Westinghouse Non-Proprietary Class 3

WCAP-16996-NP Revision 0 November 2010

Realistic LOCA Evaluation Methodology Applied to the Full Spectrum of Break Sizes (FULL SPECTRUM LOCA Methodology)

Volume III Full Spectrum LOCA Uncertainty Methodology and Demonstration Plant Analysis



WESTINGHOUSE NON-PROPRIETARY CLASS 3

WCAP-16996-NP Revision 0

Realistic LOCA Evaluation Methodology Applied to the Full Spectrum of Break Sizes (FULL SPECTRUM LOCA Methodology)

Author's Name	Author's Department
Dr. Cesare Frepoli*	LOCA Integrated Services
Dr. Katsuhiro Ohkawa*	LOCA Integrated Services
Dr. Liping Cao*	LOCA Integrated Services
Aaron M. Everhard*	LOCA Integrated Services
Jeffrey R. Kobelak*	LOCA Integrated Services
Dr. Jun Liao*	LOCA Integrated Services
Nikolay P. Petkov*	LOCA Integrated Services
Michael A. Shockling*	LOCA Integrated Services

November 2010

Reviewer:

er: Mitchell E. Nissley* Safety Analysis and Licensing

Approved:

d: Amy J. Colussy*, Manager LOCA Integrated Services

*Electronically approved records are authenticated in the electronic document management system.

Westinghouse Electric Company LLC 1000 Westinghouse Drive Cranberry Township, PA 16066, USA

© 2010 Westinghouse Electric Company LLC All Rights Reserved

WCAP-16996-NP.doc-111710

ACKNOWLEDGMENTS

The development of the FULL SPECTRUMTM LOCA methodology and this report has been a true team effort.

The principal contributors throughout the project were, in alphabetical order: John Besspiata, Dr. Liping Cao, Aaron Everhard, Randy Fittante, Dr. Cesare Frepoli, Robert Kemper, Jeff Kobelak, Dr. Vefa Kucukboyaci, Dr. Jun Liao, Mitch Nissley, Nikolay Petkov, Dr. Katsuhiro Ohkawa and Mike Shockling.

The development of this product span over a period of several years and individuals outside Westinghouse organization also contributed at various stages. Preliminary functional requirements benefited from the external reviewer of experts in the field such as Prof. Larry Hochreiter from the Penn State University and Dr. Tom Larson from the Idaho National Laboratory (INL). Marv Thurgood supported code activities as consultant while Prof. Satish Iyengar from the University of Pittsburgh was instrumental during the development of the statistical procedures utilized in the uncertainty methodology.

Carly Belovesick supported the first part of the development program as project manager and DFSS tools were implemented during the definition of the functional requirements by Dr. Luca Oriani as part of his CFL training.

Erin McGrew managed the second half of the project and led the completion of this report. Her project management skills were essential to the developers' team to navigate during the challenging phase of product integration and documentation and to ensure that a final quality product could be submitted for NRC review and approval on an expedited schedule.

The report benefited from the expertise of the Design Review Team which included Lou Grobmyer, Brian Ising, John Blaisdell, Naugab Lee, Andy Gagnon, Josh Hartz, Rich Schoff, Mike Young, Dr. Bob Perdue, Ray Tajc, Jason Eisenhauer, Yixing Sung, Bill Slagle and Dick Morrison. Ken Frederick from FENOC and Lou Cartin from SCE&G were also part of the Design Review Team. Moreover the support provided by Ken and Lou and their organizations represent the true motivation and driver behind this effort.

An extensive consistency review of the three volumes that comprises this topical report was performed by Meghan Leslie, therefore ensuring the various sections have been properly integrated from a technical standpoint.

Additional support provided by Doug Atkins, Fatih Aydogan, Kevin Barber, Hugo DaSilva, Dave DiBasilio, Ruben Espinosa, Dan Golden, Brian Ising, Molly McKain, Prudence Moon, Ajal Parikh and Bradley Slezak are also acknowledged.

Preparation of this report placed stringent demands on Technical and Online Publishing Services, particularly Jamie Hart and Carla Hamilton. The support of Dave Scherf for technical help for the preparation of this report and all the associated supporting documentation and calculation notes is deeply appreciated.

ii

Finally, the authors would like to acknowledge the overall support provided by the Westinghouse organization management in general, particularly the LOCA Integrated Services groups which during the duration of the development program was led by Mike Corletti, then Cathy Sherbine and Amy Colussy (for LIS-I) and Chuck Boyd (for LIS-II).

WCAP-16996-NP

:

November 2010 Revision 0

TABLE OF CONTENTS

LIST OF TABLES	xxii
LIST OF FIGURES	
EXECUTIVE SUMMARY	cxlviii

VOLUME 1

1	ROAI	OMAP OF	FULL SPECTRUM LOCA (FSLOCA) METHODOLOGY	1-1
	1.1	BACKO	GROUND	1-1
	1.2		NG OF FSLOCA EM DEVELOPMENT TO REGULATORY	
		GUIDA	NCE, REGULATORY GUIDE 1.203 (EMDAP)	1-2
		1.2.1	EMDAP Element 1 (Step 1): Analysis Purpose, Transient Class and	
			Power Plant Class	1-4
		1.2.2	EMDAP Element 1 (Step 2): Specification of Figures of Merit	1-5
		1.2.3	EMDAP Element 1 (Steps 3 and 4): Phenomena Identification and	
			Ranking Table	1-5
		1.2.4	EMDAP Element 2 (Step 5): Specify Objectives for Assessment Base	1-5
		1.2.5	EMDAP Element 2 (Steps 6, 7 and 8): Definition of the Assessment	
			Base and Applicability	1-5
		1,2.6	EMDAP Element 2 (Step 9): Determine Experimental Uncertainties as	
			Appropriate	1-6
		1.2.7	EMDAP Element 3 (Steps 10, 11 and 12): Develop Evaluation Model	1-6
		1.2.8	EMDAP Element 4 (Steps 13, 14 and 15): Bottom-Up Evaluation of	
			Models	1-7
		1.2.9	EMDAP Element 4 (Steps 16, 17, 18 and 19): Top-Down Evaluation of	
			Models	1-7
		1.2.10	EMDAP Element 4 (Step 20): Determine Evaluation Model Biases and	
			Uncertainties	1-8
	1.3	ORGAN	NIZATION OF THE REPORT	1-9
	1.4	REFER	ENCES	1-12
2	EVAL	UATION	MODEL FUNCTIONAL REQUIREMENTS	2-1
	2.1	INTRO	DUCTION	2-1
	2.2	FIGUR	ES OF MERIT (EMDAP STEP 2)	2-2
	2.3	PHENC	MENA IDENTIFICATION AND RANKING TABLE (EMDAP STEPS 3	
		AND 4))	2-2
		2.3.1	LOCA Scenario Specification	2-3
		2.3.2	Identification of System, Components, Processes and Ranking	2-8
		2.3.3	PIRT: Summary and Conclusions	2-42
	2.4	REQUI	REMENT ANALYSIS/ASSESSMENT FOR <u>W</u> COBRA/TRAC-TF2	
		MODE	LS	2-44
		2.4.1	Assessment Process	2-45
		2.4.2	Review of WCOBRA/TRAC and TRAC-PF1/MOD2 Capabilities and	
			Assessment Results	2-45

2.5	WCOBRA/TRAC-TF2 DEVELOPMENT STRATEGY	2-50
	2.5.1 General Structure Functional Requirements for WCOBRA/TRAC-T	
	2.5.2 Functional Requirements for 3D Vessel Module	
	2.5.3 Functional Requirements for 1D (Loops) Module	
	2.5.4 Software Development Plan for <u>WCOBRA/TRAC-TF2</u>	
2.6	DEVELOPMENT OF THE ASSESSMENT DATABASE	
	2.6.1 Objective for the Assessment Base	
•	2:6.2 Definition of the Assessment Base (SETs and IETs)	
	2.6.3 Evaluation of the Assessment Base (SETs and IETs)	
	2.6.4 Additional Assessment.	
2.7	REFERENCES	
	DBRA/TRAC-TF2 CONSERVATION EQUATIONS	
3.1	INTRODUCTION.	
3.2	VESSEL COMPONENT CONSERVATION EQUATIONS (MODEL BASIS).	
	3.2.1 Three-Field Equation Formulation	
	3.2.2 Vessel Component Three-Field Conservation Equations	
	3.2.3 Subchannel Coordinate Formulation	
3.3	VESSEL COMPONENT COMPUTATIONAL CELL STRUCTURE	
	(MODEL AS CODED)	
	3.3.1 Introduction	
	3.3.2 Vessel Component Computational Mesh	
	3.3.3 Vessel Component Finite-Difference Equations	
	3.3.4 Source, Viscous, and Turbulence Terms	
3.4	CONSERVATION EQUATIONS FOR ONE-DIMENSIONAL COMPONENT	
	(MODEL BASIS)	
	3.4.1 Introduction	
	3.4.2 Conservation of Mass	
	3.4.3 Conservation of Momentum	
	3.4.4 Conservation of Energy	
	3.4.5 Closure of the Conservation Equations	
3.5	ONE-DIMENSIONAL COMPONENT COMPUTATIONAL CELL	
	STRUCTURE (MODEL AS CODED)	
	3.5.1 Introduction	
	3.5.2 One-Dimensional Component Computational Mesh	
	3.5.3 One-Dimensional Component Finite Difference Formulation	
3.6	NUMERICAL SOLUTION METHOD	
	3.6.1 Introduction	
. •	3.6.2 Vessel Component Numerical Solution	
	3.6.3 One-Dimensional Component Numerical Solution	
	3.6.4 Network Matrix Equation	
	3.6.5 WCOBRA/TRAC-TF2 Solution Routines	
	3.6.6 Numerical Stability	
3.7	REFERENCES	3-80

4	_	DBRA/TRAC-TF2 FLOW REGIME MAPS AND INTERFACIAL AREA	
	4.1	INTRODUCTION	
	4.2	VESSEL COMPONENT NORMAL WALL FLOW REGIMES	4-1
· •		4.2.1 Introduction	
		4.2.2 Small Bubble Regime	
		4.2.3 Small to Large Bubble Regime	
		4.2.4 Churn-Turbulent Flow Regime	4-10
		4.2.5 Film/Drop Flow Regime	4-12
	4.3	VESSEL COMPONENT HOT WALL FLOW REGIMES	4-13
		4.3.1 Introduction	4-13
		4.3.2 Inverted Annular Flow Regime	4-14
		4.3.3 Inverted Liquid Slug Flow Regime	4-15
		4.3.4 Dispersed Droplet Flow Regime	4-16
		4.3.5 Falling Film Regime	4-17
		4.3.6 Top Deluge Flow Regime	4-18
		4.3.7 Interfacial Area Transport Equation	4-19
	4.4	ONE-DIMENSIONAL COMPONENT FLOW REGIMES	
		4.4.1 Introduction	
•		4.4.2 Bubbly Slug Flow Regime	
		4.4.3 Churn Flow Regime	
		4.4.4 Annular-Mist Flow Regime	
		4.4.5 Horizontal Stratified Flow	
		4.4.6 Wavy-Dispersed Flow	
	4.5	REFERENCES	
5	WCC	DBRA/TRAC-TF2 MOMENTUM TRANSFER MODELS	5 1
5	<u>w</u> cc 5.1	INTRODUCTION	
	5.1	VESSEL COMPONENT WALL SHEAR MODELS	
		VESSEL COMPONENT WALL SHEAR MODELS	
	5.3		
	5.4	VESSEL COMPONENT INTERFACIAL SHEAR MODELS	
		5.4.1 Small Bubble Flow Regime Interfacial Drag	
		5.4.2 Small-to-Large Bubble Flow Regime Interfacial Drag	
		5.4.3 Churn-Turbulent Flow Regime Interfacial Drag	
		5.4.4 Film/Drop Flow Regime	
		5.4.5 Inverted Annular Flow Regime	
		5.4.6 Inverted Liquid Slug Regime	
		5.4.7 Dispersed Droplet Flow Regime	
		5.4.8 Falling Film Flow Regime	
		5.4.9 Top Deluge Flow Regime	
	5.5	VESSEL COMPONENT INTERCELL DRAG	5-33
	5.6	VESSEL COMPONENT ENTRAINMENT AND DE-ENTRAINMENT	
		MODELS	
		5.6.1 Introduction	
		5.6.2 Entrainment in Film Flow	5-35

• .

	•	5.6.3	Entrainment During Bottom Reflood	5-40
		5.6.4	Entrainment During Top Down Reflood	5-45
		5.6.5	Spacer Grid Droplet Breakup Model	5-52
		5.6.6	De-entrainment in Film Flow	5-58
		5.6.7	Crossflow De-entrainment	5-59
		5.6.8	De-entrainment at Area Changes	5-62
		5.6.9	De-entrainment at Solid Surfaces and Liquid Pools	
	5.7	ONE-DI	IMENSIONAL COMPONENT INTERFACIAL DRAG MODELS	
		5.7.1	Introduction	5-64
		5.7.2	Bubbly Slug Flow	5-64
		5.7.3	Annular Mist	
		5.7.4	Churn Turbulent Flow	
		5.7.5	Horizontal Stratified Flow	
		5.7.6	Wavy Dispersed Flow	
	5.8		IMENSIONAL COMPONENT WALL DRAG MODELS	
	5.0	5.8.1	Homogeneous Flow	
		5.8.2	Horizontal Stratified Flow	
)	5.9		MENSIONAL COMPONENT FORM LOSS	
	5.10		LOSS AT THE JUNCTION BETWEEN A 1D COMPONENT AND	
	5.10		SEL COMPONENT	5-95
	5.11		OMPONENT MOMENTUM CONVECTION	
	5.12		AL FLOW MODEL	
	J.12	5.12.1	PF1 Critical Flow Model Option (ICFLOW=2)	
		5.12.1	Homogeneous Relaxation Model Option (ICFLOW=3)	
		5.12.2	Model as Coded	
		5.12.3	Model as Coded (ICFLOW=3 Option)	
	5.13		MODEL as Coded (ICFLOW - 5 Option)	
			ENCES	
	5.14	REFER	ENCES	
6	<u>W</u> CO	BRA/TRA	C-TF2 INTERFACIAL HEAT AND MASS TRANSFER MODELS	6-1
	6.1		DUCTION	6-1
	6.2	VESSEI	L COMPONENT INTERFACIAL HEAT AND MASS TRANSFER	
		MODEI	LS	6-1
		6.2.1	Small Bubble Regime	6-1
		6.2.2	Small to Large Bubble Regime	6-4
		6.2.3	Churn-Turbulent Regime	6-7
		6.2.4	Film/Drop Regime	6-10
		6.2.5	Inverted Annular Regime	6-12
		6.2.6	Inverted Liquid Slug Regime	6-14
		6.2.7	Dispersed Droplet Flow Regime	6-16
		6.2.8	Falling Film Regime	6-17
		6.2.9	Top Deluge Flow Regime	6-19
		6.2.10	Effect of Grid Spacers on Interfacial Heat Transfer	
		6.2.11	Effect of Non-Condensables	

	6 2 1 2		()5
	6.2.12	Condensation Ramp Model at Low Pressure	
6.3	6.2.13	Vessel Component Interfacial Mass Transfer IMENSIONAL COMPONENT INTERFACIAL HEAT AND MASS	0-20
0.3		FER MODELS	6 22
	6.3.1		
	6.3.1	Bubbly Slug Flow Regime	
	6.3.2 6.3.3	Annular-Mist Flow Regime	
	6.3.3	Horizontal Stratified Flow Regime	
	6.3.4		
	6.3.6	Wavy Dispersed Flow Regime Special Model: Cold Leg Condensation Model	
	6.3.0 6.3.7	Effect of Non-Condensables	
	6.3.8	One-Dimensional Component Interfacial Mass Transfer	
<i>с</i> н	6.3.9	Additional Remarks on Interfacial Heat Transfer Models as Coded	
6.4	REFER	ENCES	6-63
WCC	BRA/TRA	AC-TF2 WALL HEAT TRANSFER MODELS	7-1
$\frac{11}{7.1}$		DUCTION	
7.2		L COMPONENT WALL HEAT TRANSFER MODELS	
7.2	7.2.1	Convection to Single-Phase Liquid.	
	7.2.2	Saturated and Subcooled Nucleate Boiling	
	7.2.3	Critical Heat Flux and Wall Temperature at CHF	
	7.2.4	Transition Boiling	
	7.2.5	Minimum Film Boiling Wall Temperature	
	7.2.6	Inverted Annular Film Boiling	
	7.2.7	Dispersed Flow Film Boiling	
	7.2.8	Single-Phase Vapor	
	7.2.9	Grid Rewet Model	
	7.2.9	Wall to Fluid Heat Transfer	
	7.2.10	Heat Flux Splitting in <u>W</u> COBRA/TRAC-TF2	
7 2		IMENSIONAL COMPONENT WALL HEAT TRANSFER	
7.3			
	7.3.1	Single-Phase Liquid Natural Convection	
	7.3.2	Single-Phase Liquid Forced Convection	
	7.3.3	Nucleate Boiling	
	7.3.4	Critical Heat Flux	
	7.3.5	Transition Boiling	
	7.3.6	Minimum Film Boiling Temperature	
	7.3.7	Film Boiling Heat Transfer	
	7.3.8	Convection to Single-Phase Vapor	
	7.3.9	Heat Transfer to Two-Phase Mixtures	
	7.3.10	Condensation Heat Transfer	
	7.3.11	Wall to Fluid Heat Transfer	
7.4	REFER	ENCES	7-93

WCAP-16996-NP

8.1 8.2 8.3	CONDU 8.2.1	DUCTION JCTOR GEOMETRIES MODELED IN THE VESSEL	
	8.2.1	JCTOR GEOMETRIES MODELED IN THE VESSEL	0
8.3			
8.3		Conduction Equation	
8.3	8.2.2	Calculation of Thermal Conductance	8
	FUEL R	OD MODELING	
	8.3.1	Fuel Rod Quench Front Model	
	8.3.2	Pellet-Cladding Gap Conductance Model	8-
8.4	FUEL R	OD DEFORMATION MODEL	8.
	8.4.1	Deformation Mechanisms	8.
	8.4.2	Effects of Fuel Rod Deformation on Core Thermal-Hydraulics	8-
8.5	CLADD	DING REACTION MODEL	8-
8.6	[] ^{a,c} MODEL	8-
	8.6.1	Fuel Relocation Following [] ^{a,c} Burst	8-
	8.6.2	Thermal Conductivity Model of Relocated Fuel	
	8.6.3	Burst Node Heat Transfer Enhancement Model	
8.7	UNHEA	TED CONDUCTOR MODEL IN THE VESSEL	
8.8		JCTOR MODELING IN ONE-DIMENSIONAL COMPONENTS	
8.9		VG CONSIDERATIONS	
8.10		USIONS	
8.11		ENCES	
9.1	INTROI	C-TF2 REACTOR KINETICS AND DECAY HEAT MODELS	
9.2	DECAY	HEAT SOURCE	
9.3	+	N HEAT	
9.4	ACTINI	DE DECAY HEAT SOURCE	
9.5	SPACE	DEPENDENT HEAT SOURCE MODEL	
9.6	ENERG	Y DEPOSITION MODELING	9
	9.6.1	Introduction	
	9.6.2	Generalized Energy Deposition Model	9-
9.7	DECAY	HEAT UNCERTAINTY EVALUATION	9-
9.8		OR POINT KINETICS VALIDATION	
9.9	JUSTIF	ICATION OF SIMPLIFICATIONS AND ASSUMPTIONS	9.
	9.9.1	Actinide Decay Power	
	9.9.2	WCOBRA/TRAC-TF2 Fission Energy Accounting	9-
	9.9.3	Decay Heat Absorption Effects	
9.10	GENER	ALIZED ENERGY DEPOSITION MODEL (GEDM) VALIDATION	
9.11		FACE BETWEEN NEUTRONICS AND THERMAL-HYDRAULICS	
		_S	9
9.12		OR KINETICS, DECAY HEAT, AND INTERFACE MODELS AS	
)	9-
9.13		OR KINETICS, DECAY HEAT, AND INTERFACE MODELS	
		VG CONSIDERATIONS	9.

8

	9.14	CONCLUSIONS				
	9.15	REFERENCES				
10	WCOF	BRA/TRAC-TF2 ONE-DIMENSIONAL COMPONENT MODELS	10-1			
10	<u>10.1</u>	INTRODUCTION				
	10.1	PIPE COMPONENT				
	10.2	TEE COMPONENT				
	10.4	PUMP COMPONENT				
	10.5	STEAM GENERATOR				
	10.6	PRESSURIZER COMPONENT (PRIZER)				
	10.7	VALVE COMPONENT				
	10.8	ACCUMULATOR MODELING WITH THE PIPE COMPONENT				
	10.9	BREAK AND FILL COMPONENTS				
	10.10	HTSTR COMPONENTS				
	10.11	COCO COMPONENT				
	10.12	REFERENCES				
11		THERMOPHYSICAL AND TRANSPORT PROPERTIES				
	11.1	INTRODUCTION				
	11.2	THERMOPHYSICAL AND TRANSPORT PROPERTIES OF WATER				
		11.2.1 Vessel Component Water Properties				
		11.2.2 One Dimensional Component Water Properties	11-9			
	11.3	THERMOPHYSICAL AND TRANSPORT PROPERTIES OF				
5		NON-CONDENSABLE GASES AND STEAM GAS MIXTURES				
		11.3.1 Vessel Component				
		11.3.2 One-Dimensional Components				
		11.3.3 Steam and Non-Condensable Gas Mixtures				
	11.4	THERMAL PROPERTIES OF NUCLEAR FUEL ROD MATERIALS				
		11.4.1 Uranium Dioxide				
		11.4.2 Zircaloy-4				
		11.4.3 ZIRLO [®]				
		11.4.4 Fuel Rod Gas Mixtures				
	11.5	THERMAL PROPERTIES OF STRUCTURAL MATERIALS				
		11.5.1 Vessel Component Structural Material Properties				
		11.5.2 One-Dimensional Component Structural Material Properties				
	11.6	CONCLUSIONS				
	11.7	REFERENCES	11-53			

VOLUME 2

12	ASSE	SSMENT	OF BREAK FLOW MODEL	12-1	
			DUCTION		
			12.1.1	Critical Flow in LOCA (Relation to LOCA PIRT)	12-1
		12.1.2	Assessment Objective	12-2	

x

	12.2	CRITICA	AL FLOW DATA NEEDS FOR PWR LOCA MODEL VALIDATION	12-2
	12.3	ASSESS	MENT TEST MATRIX AND BASIS FOR SELECTION	12-6
	12.4	DESCRI	PTION OF DATASETS	12-12
		12.4.1	Ardron and Ackerman	12-12
		12.4.2	Boivin	12-14
		12.4.3	Fincke and Collins	12-16
		12.4.4	Jeandey	12-18
·		12.4.5	Neusen	12-20
		12.4.6	Reocreux	12-22
		12.4.7	Seynhaeve	12-24
		12.4.8	Sozzi and Sutherland	12-26
		12.4.9	Marviken Tests 1 through 27	12-28
		12.4.10	Amos and Schrock	12-31
		12.4.11	Anderson and Benedetti (TPFL)	12-33
		12.4.12	Celata (1988)	12-35
		12.4.13	Overall	12-39
	12.5	ASSESS	MENT RESULTS	12-42
		12.5.1	Assessment Method	12-42
		12.5.2	DATA COMPARISON	12-44
		12.5.3	PARAMETRIC TREND OF PREDICTION	12-53
		12.5.4	Model Performance as Implemented in WCOBRA/TRAC-TF2	12-67
	12.6	CRITICA	AL FLOW ASSESSMENT CONCLUSIONS	12-72
		12.6.1	Scaling Consideration	12-72
		12.6.2	Break Path Geometry and Application to PWR LOCA	12-73
	12.7	OFFTAK	E ENTRAINMENT MODEL	
		12.7.1	Introduction	12-73
		12.7.2	Offtake Phenomenon	12-73
		12.7.3	Relationship to PIRT	12-74
		12.7.4	Section Objectives	
		12.7.5	Two-Phase Flow Loop Offtake Entrainment Tests	
		12.7.6	Additional Offtake Model Validation	
	12.8	REFERE	NCES	12-89
APPEN	JDIX A	RESULT	S OF CRITICAL FLOW ASSESSMENT FOR INDIVIDUAL	
			Т	12-92
13	CORE	VOID DI	STRIBUTION AND MIXTURE LEVEL SWELL	13-1
	13.1	INTROE	UCTION	13-1
	13.2		AL PROCESSES	
	13.3	<u>W</u> COBR	A/TRAC-TF2 DETERMINATION OF THE MIXTURE LEVEL	13-2
	13.4		MENT OF WCOBRA/TRAC-TF2 MIXTURE LEVEL PREDICTIONS	
		13.4.1	Introduction	
		13.4.2	ORNL-THTF Small Break Tests	
		13.4.3	Simulation of G-1 Core Uncovery Tests	13-37
			•	

xi

.

		13.4.4	Simulation of G-2 Core Uncovery Tests	
		13.4.5	JAERI-TPTF Rod Bundle Tests	
	13.5		ARY AND CONCLUSIONS	
	13.6	REFER	ENCES	13-97
14	SEPAI	RATE EFI	FECT TESTS USED TO ASSESS CORE HEAT TRANSFER MOD	EL14-1
	14.1	INTRO	DUCTION	14-1
	14.2	TEST F.	ACILITIES DESCRIPTION	
		14.2.1	Test Facilities Used to Assess Single-Phase Vapor (SPV)	14-11
		14.2.2	Test Facilities Used to Assess Dispersed Flow Film Boiling (DFF)	B)
			Heat Transfer	
		14.2.3	Test Facilities Used to Assess Reflood Heat Transfer	
	14.3		ENCES	
15	ASSES	SSMENT	OF THE VESSEL POST-CHF HEAT TRANSFER	
	15.1		DUCTION	
	15.2		AP TO THE ASSESSMENT	
	15.3		SMENT OF CHF	
	15.4		E PHASE VAPOR (SPV) HEAT TRANSFER ASSESSMENT	
		15.4.1	ORNL-THTF Uncovered Bundle Heat Transfer Test Simulations.	
		15.4.2	FLECHT SEASET Single Phase Vapor Heat Transfer Test Simula	
		15.4.3	Single Phase Vapor Heat Transfer Summary and Conclusion	
	15.5		SED FLOW FILM BOILING (DFFB)	
	,	15.5.1	Assessment Using COBRAHT-TF2	
		15.5.2	Assessment Using Test Simulations	
		15.5.3	DFFB Heat Transfer Summary and Conclusions	15-95
	15.6	REFLO	OD	
		15.6.1	WCOBRA/TRAC-TF2 Simulations of FLECHT-SEASET Test Se	ries 15-95
·		15.6.2	WCOBRA/TRAC-TF2 Simulations of FLECHT Low Flooding	
			Rate (LFR) Test Series and One Supplemental Test	15-156
		15.6.3	WCOBRA/TRAC-TF2 Simulations of FLECHT Skewed Power	
			Test Bundle	15-197
		15.6.4	WCOBRA/TRAC-TF2 Simulations of G-2 Reflood Test Bundle	15-252
		15.6.5	WCOBRA/TRAC-TF2 Simulations of FEBA	15-284
		15.6.6	Reflood Heat Transfer Assessment Summary and Conclusions	15-310
	15.7	GRID H	EAT TRANSFER MODELS	
	15.8	TIME S	TEP STUDY	15-315
	15.9	HEAT T	RANSFER COMPOSITE RESULTS	15-318
		15.9.1	Prediction of Cladding Temperatures and Quench Times	15-320
		15.9.2	Droplet Assessment	
		15.9.3	SIMULATION OF PARAMETRIC TRENDS	15-351
	15.10	SUMM	ARY AND CONCLUSIONS	15-370
	15.11	REFER	ENCES	15-371

•

t

16	HOR	IZONTAL STRATIFIED FLOW AND WAVY-DISPERSED FLOW	16-1
	16.1	INTRODUCTION	16-1
	16.2	KEY PHYSICAL PROCESSES	16-1
	16.3	TEST FACILITY DESCRIPTION	16-3
		16.3.1 Test Selection and Basis	16-6
	16.4	WCOBRA/TRAC-TF2 MODEL DESCRIPTION	16-7
	16.5	ASSESSMENT RESULTS	
	16.6	CONCLUSIONS	16-9
	16.7	REFERENCES	16-9
17	COLI	D LEG CONDENSATION: COSI EXPERIMENTS, ROSA IV SB-CL-05	
	EXPE	ERIMENT, AND UPTF-8A EXPERIMENT	17-1
	17.1	INTRODUCTION	17-1
	17.2	SMALL BREAK LOCA EXPERIMENTS – COSI AND ROSA SB-CL-05	17-2
		17.2.1 Test Facilities and Tests Description	17-2
		17.2.2 DESCRIPTION OF WCOBRA/TRAC-TF2 MODELS	
		17.2.3 WCOBRA/TRAC-TF2 Results	
		17.2.4 Small Break LOCA Experiments Conclusions	17-11
	17.3	LARGE BREAK LOCA EXPERIMENTS: UPTF TEST 8A	
		17.3.1 Introduction	17-12
		17.3.2 WCOBRA/TRAC-TF2 Model Description	17-13
		17.3.3 WCOBRA/TRAC-TF2 Results: Base Model	
		17.3.4 WCOBRA/TRAC-TF2 Results: Sensitivity Studies	
		17.3.5 Large Break LOCA Experiments Conclusions	
	17.4	OVERALL CONCLUSIONS	
	17.5	REFERENCES	17-19
18	LOOF	P SEAL CLEARANCE	
	18.1	INTRODUCTION	
	18.2	IMPORTANT PHYSICAL PROCESSES AND SCALING LAWS	
		18.2.1 ROSA	18-5
		18.2.2 PWS 2.3 Loop Seal Tests	
		18.2.3 Full-Scale Steam-Water Tests	
	18.3		
		18.3.1 WCOBRA/TRAC-TF2 Simulation of the UPTF 3-Bar and	
		<u>—</u> 15-Bar Tests	18-29
	18.4	CONCLUSIONS	18-40
	18.5	REFERENCES	18-41
19	ADD	ITIONAL LOCA HYDRODYNAMIC ASSESSMENT AGAINST LARGE SCAL	E ·
-		RIMENTS	
	19.1	INTRODUCTION	
	19.2	HYDRODYNAMIC MODELS ASSESSMENT	
		19.2.1 <u>W</u> COBRA/TRAC-TF2 Models for Entrainment	

19.3	UPPER	PLENUM TEST FACILITY TESTS	19-9
	19.3.1	Introduction	19-9
	19.3.2	UPTF Facility Description	19-9
	19.3.3	UPTF 6 ECC Bypass and Downcomer Countercurrent Flow Tes	t
		Descriptions	19-14
	19.3.4	WCOBRA/TRAC-TF2 Model for UPTF Test 6	19-14
	19.3.5	Simulation of UPTF Test 6	19-15
	19.3.6	UPTF 8A Cold Leg Condensation Test Descriptions	
	19.3.7	WCOBRA/TRAC-TF2 Model for UPTF 8A	
	19.3.8	Simulation of UPTF 8A	
	19.3.9	UPTF 25A Downcomer Entrainment/De-Entrainment and Cold	Leg
		Condensation Test Descriptions	
	19.3.10	WCOBRA/TRAC-TF2 Model for UPTF Test 25A	19-35
	19.3.11	Simulation of UPTF Test 25A	19-35
	19.3.12	UPTF 29B Upper Plenum Entrainment/De-Entrainment Test	
		Descriptions	
	19.3.13	WCOBRA/TRAC-TF2 Model for UPTF Test 29B	
	19.3.14	Simulation of UPTF Test 29B	
19.4	PERFOR	RATED PLATE FLOODING ANALYSIS	
	19.4.1	Correlations and Scaling for CCFL in a Perforated Plate	19-216
	19.4.2	WCOBRA/TRAC-TF2 Model	
	19.4.3	WCOBRA/TRAC-TF2 Simulation	19-219
19.5	FULL-L	ENGTH EMERGENCY COOLING/CORE HEAT TRANSFER	
	19.5.1	FLECHT Test Facility	
	19.5.2	WCOBRA/TRAC-TF2 Simulation	
19.6	CYLINI	DRICAL CORE TEST FACILITY (CCTF)	19-241
	19.6.1	CCTF Tests	
	19.6.2	CCTF Facility Description	
	19.6.3	CCTF Test Procedure	
	19.6.4	WCOBRA/TRAC-TF2 CCTF Model	19-243
	19.6.5	CCTF Run 62 Transient Calculation	
	19.6.6	DTMAX Sensitivity Study for CCTF 62	
19.7	CONCL	USIONS	19-294
19.8	REFERI	ENCES	19-296
ADDI	TIONAL (COMPONENT MODEL ASSESSMENTS	20-1
20.1	ACCUM	IULATOR COMPONENT	20-1
	20.1.1	Introduction	
	20.1.2	IPP Accumulator Test	
	20.1.3	Callaway Accumulator Test	
	20.1.4	Effect of Accumulator Nitrogen on PWR Reflood Transients	
	20.1.5	Conclusion	
	20.1.6	References	
	,	· · ·	

	20.2	PUMP C	COMPONENT MODEL	20-55
		20.2.1	Westinghouse Pump Data	20-55
		20.2.2	Pump Model Comparison to Data	20-58
		20.2.3	References	
	20.3	MASS A	AND ENERGY CONSERVATION ACROSS 1D/3D JUNCTION	20-72
		20.3.1	Scenario Description and WCOBRA/TRAC-TF2 Model Description	20-72
		20.3.2	Results and Conclusions	
	20.4	SUMMA	ARY AND CONCLUSIONS	20-76
21	ROSA	-IV TEST	SIMULATIONS	21-1
	21.1		DUCTION	
	21.2		ACILITY DESCRIPTION	
		21.2.1	Important Physical Phenomena and Scaling Considerations	
	21.3		IPTION OF WCOBRA/TRAC-TF2 MODEL FOR ROSA/LSTF-IV	
	21.4		ATION OF SB-CL-18, 5-PERCENT COLD LEG SIDE BREAK	
		21.4.1	Description of the SB-CL-18 Test Boundary and Initial Conditions	
		21.4.2	Steady State Calibration and Transient Calculation Procedures	
		21.4.3	Results and Conclusions From the SB-CL-18 Simulation	
	21.5		CTION SENSITIVTY STUDY: SIMULATION OF SB-CL-05,	
			ENT COLD LEG SIDE BREAK	21-10
		21.5.1	Description of the Boundary and Initial Conditions	
		21.5.2	Results and Conclusions from the SB-CL-05 Simulation	
	21.6	SIMULA	ATION OF THE 10% SIDE BREAK TEST SB-CL-14	21-14
		21.6.1	Description of the Boundary and Initial Conditions	21-14
		21.6.2	Results and Conclusions for the SB-CL-14 Simulation	
	21.7	BREAK	ORIENTATION STUDY: SIMULATION OF TOP/SIDE/BOTTOM	
		0.5% (SI	B-CL-16/12/15) AND 2.5% (SB-CL-03/01/02) COLD LEG BREAKS	21-16
		21.7.1	Description of the Boundary and Initial Conditions	21-16
		21.7.2	Discussion of Results	21-16
		21.7.3	Conclusions	21-20
	21.8	BREAK	SPECTRUM STUDY	21-20
	21.9	SIMUL	ATION OF ST-NC-02, 2% POWER NATURAL CIRCULATION TEST	Г 2 1- 2 1
		21.9.1	Natural Circulation Phenomena	21-21
		21.9.2	Description of the ST-NC-02 Natural Circulation Test	21-21
		21.9.3	Description of the Test Simulation and Boundary and Initial	
			Conditions	21-22
		21.9.4	Results and Conclusions	21-23
	21.10	COUNT	ER-CURRENT FLOW (CCFL) RESULTS AND EVALUATION	21-25
		21.10.1	CCFL in the Steam Generator U-tubes	21-25
		21.10.2	CCFL in the Vicinity of the Hot Leg Elbow (Steam Generator Inlet).	21-26
		21.10.3	CCFL at the Upper Core Plate (UCP)	
		21.10.4	Effects of Calculated CCFL on ROSA-IV SB-CL-18 Transient	
			Simulation	

21.11	BYPAS	S SENSITIVITY CALCULATIONS	21-32
	21.11.1	Hot Leg Nozzle Gap Modeling Sensitivity with the SB-CL-18 Test	21-32
	21.11.2	SB-CL-18 Simulation Without Hot Leg Nozzle Bypass Flow	
	21.11:3	Spray Nozzle Bypass Ranging Sensitivity with the SB-CL-18 Test.	21-33
21.12	SUB-CC	OOLED BREAK DISCHARGE COEFFICIENT (CD1) SENSITIVIT	Y21-34
21.13	TWO-PI	HASE BREAK DISCHARGE COEFFICIENT (CD2) SENSITIVITY	21-34
21.14	BROKE	IN LOOP PUMP RESISTANCE SENSITIVITY CALCULATION	21-35
21.15	YDRAC	S SENSITIVITY CALCULATIONS	21-36
21.16	HS_SLU	JG SENSITIVITY CALCULATIONS	21-36
	21.16.1	HS_SLUG Sensitivity with 0.5% Side Break Test SB-CL-16	21-36
	21.16.2	HS_SLUG Sensitivity with 5% Top Break test SB-CL-18	21-37
	21.16.3		
	21.16.4	Conclusion Regarding the HS_SLUG Sensitivity Simulations	21-38
21.17		SENSITIVITY CALCULATIONS	•
21.18		SETPOINT SENSITIVITY CALCULATION	
21.19	CONCL	USIONS	21-41
21.20	REFERI	ENCES	21-42
LOSS-	OF-FLUI	D TEST (LOFT) INTEGRAL TEST	22-1
22.1		DUCTION	
22.2	LOFT F.	ACILITY AND SCALING	
	22.2.1	LOFT Facility Description	
	22.2.2	LOFT Scaling Consideration	
22.3		EST DESCRIPTION	
22.4	<u>W</u> COBF	RA/TRAC-TF2 LOFT MODEL	
	22.4.1	General Modeling Considerations	
·	22.4.2	WCOBRA/TRAC-TF2 Vessel Model of the LOFT Facility	
	22.4.3	WCOBRA/TRAC-TF2 Loop Model of the LOFT Facility	
22.5	LARGE	BREAK LOFT SIMULATIONS USING WCOBRA/TRAC-TF2	
	22.5.1	Large Break LOFT Tests Description	
	22.5.2	Steady-State Calculations	
	22.5.3	Transient Calculations	22-13
	22.5.4	Conclusions	
22.6	SMALL	BREAK LOFT SIMULATION USING WCOBRA/TRAC-TF2	22-16
	22.6.1	Small Break LOFT Test Description	22-16
	22.6.2	Steady-State Calculations	22-17
	22.6.3	Transient Calculations	1
	22.6.4	Conclusions	22-19
22.7		MEDIATE BREAK LOFT SIMULATIONS USING	
	<u>W</u> COBE	RA/TRAC-TF2	
	22.7.1	Intermediate Break LOFT Tests Description	
	22.7.2	Steady-State Calculations	
	22.7.3	Transient Calculations	22-20
	22.7.4	Conclusions	22-22

	22.8	REFERI	ENCES	22-22
23	ADDI	TIONAL	VALIDATION AND NUMERICAL PROBLEMS	23-1
23	23.1		ONAL VALIDATION	
	2011	23.1.1	GE Vessel Blowdown Tests	
		23.1.2	Semiscale Tests	
	23.2		VICAL PROBLEMS	
		23.2.1	1D PIPE Manometer Problem with Non-Condensable Gases	
		23.2.2	3D VESSEL Manometer Problem with Non-Condensable Gases	
		23.2.3	1D PIPE Steam Expulsion Test	
		23.2.4	3D VESSEL Steam Expulsion Test	
		23.2.5	1D PIPE Fill and Drain Test	
		23.2.6	3D VESSEL Fill and Drain Test	
		23.2.7	Condensation Test	
24			OF COMPENSATING ERROR IN EVALUATION MODEL USING	
			C-TF2	
	24.1		DUCTION	24-1
	24.2		FICATION OF HIGHLY RANKED PHENOMENA AND MODEL	
			SMENT	24-2
	24.3		FICATION OF POSSIBLE COMPENSATING ERRORS IN MODEL	
			SMENT	
	•	24.3.1	Possible Compensating Errors in Separate Effects Test Simulations	
		24.3.2	Possible Compensating Errors in Integral Effects Test Simulations	24-10
	24.4		INSATING ERROR ASSESSMENT OF SELECTED HIGHLY	
			D PHENOMENA IN SETS AND IETS	
	24.5		ERY AND BYPASSING OF ECC	
	24.6		HF HEAT TRANSFER	
		24.6.1	Summary of Assessment with Stand-alone COBRAHT-TF2	
		24.6.2	ORNL Film Boiling Test Simulation	
		24.6.3	G1-Blowdown Test Simulation	
		24.6.4	FLECHT SEASET 31504 Reflood Test Simulation	
		24.6.5	FLECHT-SEASET Test 31805	
		24.6.6	FLECHT-SEASET Test 31701	
		24.6.7	Conclusions	24-112
	24.7		DOWN AND POST BLOWDOWN THERMAL-HYDRAULICS/	
			INMENT	
		24.7.1	LOFT Test L2-3	
		24.7.2	LOFT Test L2-5	
		24.7.3	CCTF Run 62	
	24.8		LEVEL PREDICTION IN SB-CL-18 TEST	
		24.8.1	Core Collapsed Liquid Level	
		24.8.2	Core Mixture Level/Cladding Heat-up Elevation Prediction	24-245
		24.8.3	Level Swell Prediction	24-245

.

24.9	SUMMARY OF COMPENSATING ERROR ASSESSMENT	24-270
24.10	REFERENCES	24-270

VOLUME 3

25	PLAN	T SOURCES OF UNCERTAINTY	
	25.1	PLANT PHYSICAL CONFIGURATION	25-1
	25.2	PLANT INITIAL OPERATING CONDITIONS	
		25.2.1 Core Power Parameters	
		25.2.2 Plant Fluid Conditions	25-24
	25.3	REACTOR ACCIDENT BOUNDARY CONDITIONS	25-45
	25.4	MODEL PARAMETERS	25-49
	25.5	OPERATOR ACTIONS	25-49
		25.5.1 EOP Sequences for a Small Break LOCA	25-50
		25.5.2 Variability of Plant Conditions Due to Operation Actions	25-51
	25.6	CONTAINMENT RESPONSE	
	25.7	PUMP LOCKED ROTOR	
	25.8	REFERENCES	
26	<u>w</u> coi	BRA/TRAC-TF2 MODEL OF PILOT PLANTS	
	26.1	MODELING APPROACH	
		26.1.1 Introduction	
		26.1.2 Modeling Consistency	
		26.1.3 Conclusions	
	26.2	V. C. SUMMER NUCLEAR POWER PLANT	
		26.2.1 V. C. Summer WCOBRA/TRAC-TF2 Nodalization	
		26.2.2 V. C. Summer Reference Case and Allowable Plant Operating	
		Conditions	
		26.2.3 Plant Operating Range	
	26.3	BEAVER VALLEY UNIT 1 NUCLEAR POWER PLANT	
		26.3.1 Beaver Valley Unit 1 WCOBRA/TRAC-TF2 Nodalization	
		26.3.2 Beaver Valley Unit 1 Reference Case and Allowable Plant Operatin	
		Conditions	
		26.3.3 Plant Operating Range	
	26.4	STEADY STATE CALCULATION/CALIBRATION	
	26.5	REFERENCES	
27	REFE	RENCE BREAK SPECTRUM ANALYSIS	27-1
	27.1	LARGE, INTERMEDIATE, AND SMALL BREAK SPECTRA	27-1
		27.1.1 V. C. Summer (CGE)	27-1
		27.1.2 Beaver Valley Unit 1 (DLW)	27-26
	27.2	V. C. SUMMER (CGE) REFERENCE TRANSIENTS	27-49
		27.2.1 CGE Large Break Reference Transient Description	
		27.2.2 CGE Intermediate Break Reference Transient Description	
		-	

 27.2.3 CGE Small Break Reference Transient Description	.27-91 27-91 27-106 27-118 28-1 28-3 28-17 28-32 28-43 28-83 28-94 28-102 .8-102 28-111
 27.3.1 DLW Large Break Reference Transient Description	27-91 7-106 27-118 28-1 28-3 28-3 28-17 28-32 28-43 28-83 28-94 28-102 28-102 28-111
 27.3.2 DLW Intermediate Break Reference Transient Description	27-106 27-118 28-1 28-3 28-3 28-17 28-32 28-43 28-83 28-94 28-102 28-102 28-111
 27.3.3 DLW Small Break Reference Transient Description 28 SCOPING AND SENSITIVITY STUDIES 28.1 LARGE BREAK SCOPING STUDY RESULTS 28.1.1 Axial Power Distributions – LBLOCA 28.1.2 Offsite Power Availability – LBLOCA 	27-118 28-1 28-3 28-17 28-32 28-43 28-83 28-94 28-102 8-102 28-111
 28 SCOPING AND SENSITIVITY STUDIES	28-1 28-3 28-17 28-32 28-43 28-83 28-94 28-102 28-102 28-111
 28.1 LARGE BREAK SCOPING STUDY RESULTS	28-3 28-3 28-17 28-32 28-43 28-83 28-94 28-102 28-102 28-111
 28.1 LARGE BREAK SCOPING STUDY RESULTS	28-3 28-3 28-17 28-32 28-43 28-83 28-94 28-102 28-102 28-111
 28.1.1 Axial Power Distributions – LBLOCA 28.1.2 Offsite Power Availability – LBLOCA 	28-3 28-17 28-32 28-43 28-83 28-94 28-102 8-102 28-111
28.1.2 Offsite Power Availability – LBLOCA	28-17 28-32 28-43 28-83 28-94 28-102 8-102 28-111
•	28-32 28-43 28-83 28-94 28-102 28-102 28-111
	28-43 28-83 28-94 28-102 28-102 28-111
28.1.4 Break Path Resistance – LBLOCA	28-83 28-94 8-102 8-102 8-111
28.1.5 Treatment of Accumulator Elevation – LBLOCA	28-94 8-102 8-102 8-102 8-111
28.1.6 Steam Generator Hydraulics: Tube Plugging – LBLOCA	28-102 28-102 28-111
28.2 SMALL BREAK SCOPING STUDY RESULTS	28-111
28.2.1 Small Break Reference Transient Re-Baseline	
28.2.2 Axial Power Distributions – SBLOCA	0 1 2 1
28.2.3 Initial and Accident Boundary Conditions and Offsite	0 1 2 1
Power – SBLOCA	8-131
28.2.4 Time Step and Convergence Criteria Studies – SBLOCA	8-157
28.2.5 Treatment of Accumulator Elevation – SBLOCA	8-164
28.2.6 Treatment of Accumulator and SI Lines in the Broken Leg and	
Break Location – SBLOCA 2	8-168
28.2.7 Break Orientation Studies – SBLOCA	8-178
28.2.8 Interfacial Drag in the Core (Level Swell) – SBLOCA	8-194
28.2.9 Steam Generator Hydraulics: Tube Plugging – SBLOCA	8-212
28.2.10 Steam Generator Hydraulics: Interfacial Drag – SBLOCA	8-222
28.2.11 Loop Seal Clearance – SBLOCA 2	8-239
28.2.12 Horizontal Stratified Flow (HS_SLUG) – SBLOCA	8-250
29 ASSESSMENT OF UNCERTAINTY ELEMENTS	29-1
29.1 GENERATION OF MODEL UNCERTAINTY PARAMETERS AND RANGING	
DISTRIBUTIONS	29-8
29.1.1 Break Flow – [
] ^{a,c}	. 29-8
29.1.2 Broken Cold-Leg Nozzle Flow Resistance (KN) and Broken	
Loop Pump Resistance	29-17
29.1.3 Delivery and Bypassing of ECC – Bounding Approach	29-20
29.1.4 Condensation in the Downcomer	
29.1.5 Interfacial Drag in the Core Region [] ^{a,c}	29-20
29.1.6 Cold Leg Condensation (KCOSI)	
29.1.7 Horizontal Stratified Flow Regime Transition Boundary (HS_SLUG)	29-34
29.1.8 Minimum Film Boiling Temperature (T _{min})	29-34
29.1.9 Steam Binding and Entrainment – Bounding Approach	29-43

WCAP-16996-NP

		29.1.10	Non Condensable Gases/Accumulator Nitrogen – Bounding Approach	29-43
		29.1.11	Uncertainty in Loop Seal Clearance Phenomenon	29-43
		29.1.12	Steam Generator Thermal-Hydraulics	29-47
	29.2	BREAK	LOCATION, TYPE (SPLIT VS. DEGCL) AND SPLIT BREAK AREA	29-47
		29.2.1	[.] ^{a,c}	29-49
		29.2.2	Determination of the Minimum Break Size (Amin)	29-49
		29.2.3	Break Type, Split Break Area and Break Flow Model Uncertainty	
			Methodology	29-49
		29.2.4	Modeling of DECLG Breaks	29-53
		29.2.5	Modeling of Split Breaks	29-56
		29.2.6	Compliance with Regulatory Guide 1.157 on Break Type and Size	29-59
	29.3	REVIEW	V OF PLANT SCOPING STUDIES AND UNCERTAINTY IN PLANT	
		INPUT F	PARAMETERS	29-60
		29.3.1	Bounded Parameters	29-60
	,	29.3.2	Initial and Boundary Conditions (Ranged Parameters)	29-62
		29.3.3	Uncertainty Associated with Maximum Time Step Size	29-65
	29.4	CORE A	ND FUEL ROD MODEL UNCERTAINTIES	29-66
		29.4.1	Initial Reactor State Uncertainties	29-66
		29.4.2	Hot Rod Local Models Uncertainty	29-74
		29.4.3	Fuel Rod: Uncertainty on Heat Transfer to the Fluid	
	29.5	EVALUA	ATION MODEL BIASES AND UNCERTAINTY (EMDAP STEP 20)	
		29.5.1	Fuel Rod	29-119
		29.5.2	Core	29-120
		29.5.3	Upper Head	29-122
		29.5.4	Upper Plenum	29-123
		29.5.5	Steam Generator	29-123
		29.5.6	Pump Suction Piping/Loop Seal	
		29.5.7	Pump	
		29.5.8	Cold Leg/Safety Injection	29-125
		29.5.9	Accumulator	29-126
		29.5.10	Downcomer	
		29.5.11	Lower Plenum	29-128
		29.5.12	Break	29-129
	29.6	EXPERI	MENTAL UNCERTAINTIES (EMDAP STEP 9)	29-129
	29.7		ENCES	
30	TECH	NICAL BA	ASIS OF STATISTICAL PROCEDURES APPLIED IN FULL	
	SPECT	RUM LO	CA UNCERTANTY METHODOLOGY	30-1
	30.1	STATIST	FICAL METHODOLOGY ROADMAP	30-1
	30.2	STATIST	ГІСАL SAMPLING APPROACH (MONTE CARLO)	30-3
	30.3	NON-PA	RAMETRIC ORDER-STATISTICS TOLERANCE LIMITS	
		FORMU	ILATION	30-4
		30.3.1	Tolerance Intervals and Sample Size	30-10

30.4	. I			
	-	.] ^{a,c}		
30.5	OVERV	VIEW OF FULL SPECTI	RUM LOCA STATISTICAL PROCEDURI	Ξ
	(ASTRI	UM-FS)	·	
30.6	CONCL	LUSIONS ON COMPLIA	ANCE WITH 10 CFR 50.46 ACCEPTANC	E
	CRITEI	RIA		
	30.6.1	[•
] ^{a,c}		30-16
	30.6.2	[] ^{a,c}	30-16
30.7	REFER	ENCES		
			· ·	
			RATION ANALYSIS	
31.1	DEVEL		RUN MATRIX	
	31.1.1	0		
	31.1.2	Plant Operating Range		
31.2	[
	31.2.1	[] ^{a,c}	
	31.2.2	[-	31-8
	31.2.3			31-8
31.3		SIS OF RESULTS [] ^{a,c}	31-15
31.4		E] ^{a,c}	
31.5	SUMM	ARY REPORT AND CO	MPLIANCE WITH 10 CFR 50.46 CRITE	RIA31-55
MET	HODOLO	GY SUMMARY		
32.1	COMPI	LIANCE WITH 10 CFR	50.46	
32.2	COMPI	LIANCE WITH REGUL	ATORY GUIDE 1.203	32-2
	32.2.1	Regulatory Position 1,	"Evaluation Model Development and	
		Assessment Process".		32-2
	32.2.2	Regulatory Position 2,	"Quality Assurance"	
	32.2.3	Regulatory Position 3,	"Documentation"	32-15
	32.2.4	Regulatory Position 4,	"General Purpose Computer Programs"	
	32.2.5	Regulatory Position 5,	"Graded Approach to Applying the EMDA	ΑР
•				
32.3	COMPI	LIANCE WITH REGUL	ATORY POSITION WITH RESPECT TO	THE
	UNCEF		DGY	
	32.3.1	0 1	"Estimation of Overall Calculational	
		Uncertainty"		32-17
32.4	REFER	ENCES		

32

LIST OF TABLES

VOLUME 1

Table 2-1	PIRT for Full Spectrum LOCA for Westinghouse and Combustion Engineering Plants
Table 2-2	Requirement Assessment Against FSLOCA PIRT: Model Availability and Need
Table 2-3	V&V Matrix for Large Break LOCA Sub-Scenario, Phases: Blowdown and Refill
Table 2-4	V&V Matrix for Large Break LOCA Sub-Scenario, Phases: Reflood and Refill
Table 2-5	V&V Matrix for Small Break LOCA Processes, Separate Effect Tests 2-81
Table 2-6	V&V Matrix for Small Break LOCA Processes, Integral Effect Tests 2-82
Table 3-1	Timestep Size Reduction Limits
Table 3-2	Code Backup Limits
Table 4.2-1	Summary of Flow Regime Number in Vessel Components
Table 4.4-1	Summary of Flow Regime Number in 1D Components
Table 4.4.5-1	[] ^{a,c} 4-36
Table 5-1	Comparisons of Pressure Loss at Sudden Contraction (Vessel Component) 5-141
Table 5-2	Comparisons of Pressure Loss at Sudden Expansion (Vessel Component) 5-141
Table 5-3	Comparisons of Pressure Loss at Combination of Sudden Contraction and Expansion (Vessel Component)
Table 5-4	Wall Shear Dependence Upon Pipe Diameter
Table 5-5a	Irreversible Pressure Loss Coefficient
Table 5-5b	[] ^{a,c} 5-142
Table 5-6	Comparisons of Pressure Loss at Sudden Contraction (1-D Loop Component)
Table 5-7	Comparisons of Pressure Loss at Sudden Expansion (1-D Loop Component)
Table 5-8	Comparisons of Pressure Loss at Combination of Sudden Contraction and Expansion (1-D Loop Component)
Table 5-9	Critical Height Correlation Constant 5-144
Table 6-1	The Selection Logic for Condensation, Evaporation, and Flashing for 3D Vessel
Table 7.3-1	One-Dimensional Component Heat Transfer Regimes

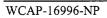


Table 8-1	Cladding Thermal Expansion Correlations	
Table 8-2	Cladding Correlations for Modulus of Elasticity (E) and Shear M	odulus (G) 8-62
Table 8-3] ^{a,c} 8-63
Table 8-4	[,] ^{a,c} 8-64
Table 8-5	[] ^{a,c} .	
Table 8-6	[] ^{a,c}	
Table 9-1	ANSI/ANS 5.1-1979	
Table 9-2	ANSI/ANS 5.1-1979	
Table 9-3	ANSI/ANS 5.1-1971	
Table 9-4	ANSI/ANS 5.1-1971	
Table 9-5	Typical Normalized Interaction Frequency Fit Data	
Table 9-6	Actinide Heat Source Data	
Table 9-7	Typical Radiation Source Timing, Strength, and Range	
Table 9-8	Typical Values for Redistribution Fraction Values	
Table 9-9	Neutron Heating Transfer Model	
Table 9-10	Gamma Photon Energy Spectrum	
Table 9-11	BUGLE-80 Gamma Kerma Data	
Table 9-12	Typical 15x15 GEDM Gamma Transfer Matrix	
Table 9-13		
Table 9-14	Decay Group Uncertainty Factors Per One Sigma (%)	
Table 9-15	Point Reactor Kinetics Validation	
Table 9-16	Actinide Isotope Nuclear Data	
Table 9-17	Prompt Fission Energy Release Data	
Table 9-18	[] ^{a,c} 9-40
Table 10-1	The Four Segments of Pump Homologous Curves	
Table 10-2	Pump Control Input Parameter	
Table 10-3	Valve Control Options	
Table 11-1	Constants for Saturated Liquid Enthalpy	11-56
Table 11-2	Constants for Saturated Vapor Enthalpy	

Table 11-3	Vessel Component Saturated Water Thermal Properties11-57
Table 11-4	Subcooled Water Density Constants
Table 11-5	Saturated Steam Internal Energy Constants
Table 11-6	Saturated Steam Enthalpy Constants
Table 11-7	Saturated Liquid Internal Energy Constants
Table 11-8	Constants for Saturated Steam Specific Heat11-63
Table 11-9	Liquid Density Constants11-64
Table 11-10	Constant Pressure Specific Heat Constants
Table 11-11	Liquid Viscosity Constants
Table 11-12	Liquid Thermal Conductivity Constants11-66
Table 11-13	Constants for Specific Heat of Air
Table 11-14	Specific Heat of Zircaloy-411-66
Table 11-15	Chemical Composition of ZIRLO [®] and Zircaloy-4 Alloys11-67
Table 11-16	Specific Heat of ZIRLO [®] Alloy11-67
	VOLUME 2
Table 12.2-1	Range of Geometrical Configurations 12-4
Table 12.2-2	Break Configuration
Table 12.2-3	Range of Physical Conditions Upstream of Discharge 12-4
Table 12.4-1	Selected Dataset and Input Variables
Table 12.4-2	Additional Dataset for Non-condensable Gas Model Validation and Input Variables
Table 12.4-3	Critical Flow Data Considered for Model Evaluation 12-8
Table 12.4-4	Marviken Test Nozzles (from pp. 51, MXC-101, EPRI/NP-2370) 12-29
Table 12.5-1	Critical Flow Data Comparison for WCOBRA/TRAC Critical Flow Model 12-46
Table 12.7.5-1	Summary of Test Parameters for Two-Phase Flow Loop Offtake Tests 12-79
Table 13.4.1-1	Comparison of Test Conditions with Typical PWR Conditions
Table 13.4.2-1	ORNL-THTF Test Simulation Matrix
Table 13.4.3-1	Comparison of PWR Rod and G-1 Test Rod Bundle 13-42
Table 13.4.3-2	G-1 Core Uncovery Test Matrix
Table 13.4.3-3	G-1 Simulation Results Summary at Model Nominal YDRAG 13-44

Table 13.4.3-4	YDRAG Values to Match G-1 Level Swell Data
Table 13.4.4-1	Comparison of 17x17-XL PWR Rod and Test Rod Bundle 13-67
Table 13.4.4-2	G2 Loop Core Uncovery Test Vessel Flow Areas
Table 13.4.4-3	G-2 Core Uncovery Test Matrix
Table 13.4.4-4	G-2 Simulation Results Summary at Model Nominal YDRAG 13-69
Table 13.4.4-5	YDRAG Values to Match G-2 Level Swell Data
Table 13.4.5-1	JAERI-TPTF Rod Bundle Uncovery Test Matrix
Table 13.4.5-2	TPTF Simulation Results Summary
Table 13.4.5-3	TPTF Simulation YDRAG Sensitivity Study Results
Table 14.1-1	SPV Heat Transfer Test Conditions
Table 14.1-2	Typical Conditions in a PWR During SPV (Blowdown, Refill, Boiloff/Recovery, Reflood)
Table 14.1-3	DFFB Heat Transfer Test Conditions 14-7
Table 14.1-4	Typical Conditions in a PWR During DFFB (Blowdown, Refill) 14-8
Table 14.1-5	Typical Conditions in a PWR During Reflood14-8
Table 14.1-6	Reflood Heat Transfer Test Conditions 14-9
Table 14.2.2.1-1	ORNL-THTF Steady-State DFFB Initial Test Condition 14-13
Table 14.2.2.1-2	ORNL-THTF Initial Test Conditions for WCOBRA/TRAC-TF2 Simulation 14-13
Table 14.2.2.2-1	Comparison of PWR Rod and G-1 Test Rod Bundle 14-22
Table 14.2.2.2-2	G-1 Initial Test Conditions
Table 14.2.2.3-1	Comparison of 17x17 PWR Fuel Rod and G-2 Test Rod 14-28
Table 14.2.2.3-2	G-2 Refill Initial Test Conditions
Table 14.2.3.1-1	Test Conditions for FLECHT-SEASET Tests 14-36
Table 14.2.3.2-1	Test Conditions for FLECHT Low Flooding Rate Tests
Table 14.2.3.3-1	Test Conditions for FLECHT Top-Skewed Power Tests 14-44
Table 14.2.3.4-1	Test Conditions for FLECHT Supplemental Test
Table 14.2.3.5-1	G-2 Reflood Tests and Conditions
Table 14.2.3.6-1	Conditions for FEBA Tests
Table 15.5.2.1-1	WCOBRA/TRAC-TF2 Calculated Fluid Conditions at Rod 1 PCT Time and Locations

Table 15.5.2.1-2	WCOBRA/TRAC-TF2 PCT Comparisons 15-26
Table 15.5.2.3-1	WCOBRA/TRAC-TF2 Cladding Temperature Comparison with the Means of the G-2 Refill Experimental Data
Table 15.5.2.3-2	WCOBRA/TRAC-TF2 PCT Comparison with the Means of the G-2 Refill Experimental Data
Table 15.6.6-1	Range of Reflood Heat Transfer Test Conditions 15-310
Table 15.9-1	Reflood Facilities Major Design Features
Table 15.9.3-1	FLECHT SEASET Sub-cooling Test Series – Test Data 15-355
Table 15.9.3-2	FLECHT SEASET Predicted Sub-cooling Sensitivity Study Results 15-355
Table 15.9.3-3	Average PCT – Based on Data for Six-foot Thermocouples 15-355
Table 15.9.3-4	FLECHT Low Flooding Rate Sub-cooling Test Series – Test Data 15-355
Table 15.9.3-5	FLECHT Low Flooding Rate Inlet Sub-cooling Sensitivity Using WCOBRA/TRAC-TF2
Table 16-1	Selected TPTF Test Data from Kawaji et al. (1987)16-11
Table 16-2	[] ^{a,c}
Table 17-1	Westinghouse COSI Test Data Average Heat Loss and Uncertainty
	Westinghouse Vertical COSI Tests Data
Table 17-2	
Table 17-3	Westinghouse Horizontal COSI Tests Data
Table 17-4	Framatome Test Data Average Heat Loss and Uncertainty 17-24
Table 17-5	Selected Framatome COSI Tests Data and Calculation for Qcond 17-25
Table 17-6	Comparison of Facilities for Cold Leg Condensation Assessment 17-26
Table 17-7	ROSA SB-CL-05 SI Condensation Test Data for SETs 17-27
Table 19.3-1	[] ^{a,c} 19-43
Table 19.3-2	[] ^{a,c}
Table 19.3-3	[] ^{a,c}
Table 19.3-4	[] ^{a,c} 19-44
Table 19.3-5	[] ^{a,c}
Table 19.3-6	[] ^{a,c}

Table 19.3-7	[] ^{a,c} 19-45
Table 19.3-8	[] ^{a,c}
Table 19.3-9	
	[] ^{a,c}
Table 19.3-10	[] ^{a,c} 19-47
Table 19.3-11	[] ^{a,c} 19-47
Table 19.3-12	Steam Mass Flows in UPTF Test 6 (all Values are in kg/sec)
Table 19.3-13	Selected Test Conditions from UPTF Test 6 (Single-Phase Steam Portion) 19-48
Table 19.3-14	Calculated Parameters for UPTF Test 6 19-49
Table 19.3-15	Calculated Cold Leg Nozzle K, $U_{DC} = 0$
Table 19.3-16	UPTF Test 8 Phase A Conditions
Table 19.3-17	[] ^{a,c}
Table 19.3-18	[/] ^{a,c} 19-51
Table 19.3-19	[] ^{a,c} 19-51
Table 19.6-1	[] ^{a,c} 19-249
Table 19.6-2	[] ^{a,c}
Table 19.6-3	[] ^{a,c}
Table 19.6-4	[] ^{a,c}
Table 19.6-5	[] ^{a,c} 19-252
Table 21.1-1	Selected ROSA-IV Test Series Description and Related Technical Reports 21-44
Table 21.2-1	Major Design Characteristics of LSTF and PWR
Table 21.2-2	Standard Operational Setpoints of the ROSA-IV Large Scale Test Facility 21-47
Table 21.4-1	Steady-State Parameter Checklist (Initial Conditions) for the SB-CL-18 Test 21-48
Table 21.4-2	Decay Heat Power Curve Used in the SB-CL-18 Test Simulation 21-49
Table 21.5-1	[] ^{a,c}
Table 21.5-2	[] ^{a,c} 21-51
Table 21.6-1	[] ^{a,c} 21-52

WCAP-16996-NP

Table 21.6-2	[·		
]'	a,c		
Table 21.6-3	[
Table 21.7-1	JAERI (Full Co	nservative) Decay He	at Curve	
Table 21.9-1				imulation 21-56
Table 22-1	Comparison of I	LOFT and PWR		
Table 22-2	Differences amo	ong LOFT Experimen	ts	
Table 22-3	LOFT/PWR Ax	ial Noding Ratio Com	parison	
Table 22-4	LOFT L2-5 Hot	Assembly Fuel Initia	l Conditions	22-25
Table 22-5	•	eak Tests <u>W</u> COBRA/	•	
	Results	•••••••••••••••••••••••••••••••••••••••		
Table 22-6	[
Table 22-7	[] ^{a,c}	
Table 22-8	[] ^{a,c}	
Table 22-9	[] ^{a,c}	
Table 22-10	LOFT L3-1 Stea	ady State Comparison		
Table 22-11	[] ^{a,c}	
Table 22-12	LOFT L5-1 Stea	ady State Comparison		
Table 22-13	[·] ^{a,c}	
Table 23.1.1-1	•	st Parameters for Sma		l Steam Blowdown 23-5
Table 23.1.1-2	Characterization	Characterization of WCOBRA/TRAC-TF2 Results Versus Test Data		
Table 23.1.2-1	Initial Condition	Initial Conditions and ECC Requirements S-07-10D Test		
Table 23.1.2-2	Sequence of Operational Procedures for Test S-07-10D 23-57			
Table 23.1.2-3	Sequence of Events for Test S-07-10D			
Table 24.2-1	•	r Large Break LOCA		vn Phase
Table 24.2-2		r Large Break LOCA		eflood Phase

xxix

LIST OF TABLES (cont.)

Fable 24.2-3V&V Matrix for Small Break LOCA Processes, Separate Effect Tests	
V&V Matrix for Small Break LOCA Processes, Integral Effect Tests	
Fable 24.6.2-1 Bundle Exit Temperatures for ORNL Tests	24-26
G-1 Blowdown Test Conditions	24-32

VOLUME 3

Table 25.2-1	Hot Assembly Rod Power Census Summary
Table 25.2-2	Peaking Factor Uncertainties
Table 25.2-3	Typical Westinghouse Plant Operation Parameters
Table 25-1	Condensed EOPs for Indian Point Unit 2, Short-Term Portion 25-54
Table 26.1-1	Core Section Axial Cell Lengths
Table 26.1-2	Hot Leg Noding Comparison
Table 26.1-3	Steam Generator Noding Comparison
Table 26.1-4	Crossover Leg Noding
Table 26.1-5	Cold Leg Noding
Table 26.2-1	Key LOCA Parameters and Scoping Study Values for V. C. Summer
Table 26.3-1	Key LOCA Parameters and Scoping Study Values for Beaver Valley Unit 1 26-43
Table 26.4-1	Criteria for an Acceptable Steady-State
Table 28.1.3-1	DTMAX Values used in LBLOCA Timestep Sensitivity
Table 28.1.3-2	PCT Results When Varying DTMAX, CGE LBLOCA Sensitivity
Table 28.1.3-3	PCT Results When Varying DTMAX, DLW LBLOCA Sensitivity 28-34
Table 28.1.4-1	Scenarios for Break Path Resistance Sensitivity Study
Table 28.2.11-1	Extent of Loop Seal Clearance Predicted for Plant Cases
Table 28.2.12-1	Flow Regime Flags
Table 29-1	Uncertainty Elements – Break Location, Type and Area Sampling Methodology
Table 29-2	Uncertainty Elements – Thermal-Hydraulic Models 29-3
Table 29-3a	Uncertainty Elements – Local Models [] ^{a,c}
Table 29-3b	Burst Strain for [] ^{a,c}
Table 29-4	Uncertainty Elements – Power-Related Parameters Defined in Section 29.4.1

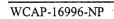
WCAP-16996-NP

Table 29-5	Initial and Boundary Conditions Considered in Uncertainty Methodology Defined in Section 29.3.2		
Table 29.1.2-1	Nozzle Loss Coefficient Assessment Data Base		
Table 29.1.11-1	Extent of Loop Seal Clearance Predicted for 3-inch SBLOCA Plant Cases in HS_SLUG Study		
Table 29.3.2-1	Comparison of Measured and Calculated Accumulator Line Resistances		
Table 29.4-1	Packing Fractions Using Various Measurements		
Table 29.4-2a	Zircaloy Rate Constants (Total Oxygen)		
Table 29.4-2b	[] ^{a,c}		
Table 29.4-3	Predictions Using Equation 29.4-2 and Cathcart-Pawel		
Table 29.4.3-1	[
] ^{a,c}		
Table 29.4.3-2	[] ^{a,c} 29-106		
Table 30-1			
·] ^{a,c}		
Table 30-2			
] ^{a,c}		
Table 30-3	Generic Rod Power Census Used for Core-Wide Oxidation Assessment		
Table 31.1-1	Calculation of Minimum Break Area		
Table 31.1-2a	Nominal and Uncertainty Range of Plant Specific Uncertainty Contributors 31-4		
Table 31.1-2b	Uncertainty Range of Plant Specific PBOT, PMID Parameters		
Table 31.2-1a	[] ^{a,c}		
Table 31.2-1b	[] ^{a,c}		
Table 31.2-1c	[] ^{a,c} 31-11		
Table 31.2-1d	[] ^{a,c}		
Table 31.2-2a	[] ^{a,c}		
Table 31.2-2b	[] ^{a,c}		
Table 31.2-2c	[] ^{a,c}		
Table 31.2-2d	[] ^{a,c}		
Table 31.3-1a	Uncertainty Attributes [
] ^{a,c}		

WCAP-16996-NP

 \geq

Table 31.3-1b	Results for [
] ^{a,c}	· · · · · · · · · · · · · · · · · · ·	
Table 31.3-2a	Uncertainty Attributes [
] ^a	^{,c}
Table 31.3-2b	Results [
] ^{a,c}	
Table 31.4-1a	Uncertainty Attributes [] ^{a,}	^{,c}
Table 31.4-1b	Results [] ^{a,c}	
Table 31.5-1	[] ^{a,c} 31-57
Table 32-1	Summary of Assessment Res	•	0
	PIRT Ranked Phenomena	·····	



LIST OF FIGURES

VOLUME 1

Figure 1-1	Evaluation Model Development and Assessment Process (EMDAP) – High Level Flow Chart (RG 1.203)
Figure 2-1	EMDAP Element 1 Process
Figure 2-3	WCOBRA/TRAC-TF2 Code Development Process
Figure 2-4	
] ^{a,c}
Figure 2-5	EMDAP Element 2
Figure 3-1	Control Volume for Cartesian Coordinates
Figure 3-2	Basic Mesh Cell
Figure 3-3	Variable Mesh Cell
Figure 3-4	Mesh Cell for Vertical Velocities
Figure 3-5	Mesh Cell for Transverse Velocities
Figure 3-6	One-Dimensional Computational Cell Structure
Figure 3-7	A Simple TRAC-PF1 Network
Figure 3-8	Transient Calculation Flow Diagram
Figure 3-9	Outer Calculation Flow Diagram
Figure 3-10	Numerical Solution Routines
Figure 3-11	WCOBRA/TRAC-TF2 Pre-pass Calculation Routines
Figure 3-12	WCOBRA/TRAC-TF2 Outer Iteration Routines
Figure 3-13	WCOBRA/TRAC-TF2 Routines for Post-Pass Calculations
Figure 3-14	Effect of Numerical Damping on Transient Value of y 3-97
Figure 4-1	Vessel Component Normal Wall Flow Regimes
Figure 4-2	Vessel Component Normal Wall Flow Regime Selection Logic
Figure 4-3	Effect of Scale on Vertical Upflow Regime Transitions Predicted by Taitel, Barnea, and Dukler (1980)
Figure 4-4	Effect of Scale on Vertical Upflow Regime Transitions (Chow, 1989) 4-47
Figure 4-5	Small to Large Bubble Regime – Formation of Large Bubbles
Figure 4-6	Vessel Component Hot Wall Flow Regimes 4-49
Figure 4-7	Hot Wall Flow Regime Selection Logic 4-50
Figure 4-8	One-Dimensional Component Flow Regime Map 4-51

WCAP-16996-NP

LIST OF FIGURES (cont.)

Figure 4-9	One-dimensional Horizontal Stratified Flow
Figure 4-10	Taitel-Dukler Transition Criteria as a Function of Pressure
Figure 4-11	Taitel-Dukler Transition Criteria as a Function of Pipe Diameter
Figure 4-12	[] ^{a,c}
Figure 4-13	[] ^{a,c}
Figure 4-14	The Hybrid Horizontal Stratification Criterion
Figure 4-15	Cross Section of Horizontal Stratified Flow
Figure 4-16	Transition Boundary for Various Tests (Continuous Line is Transition Deduced from Data, While Dashed Line is Prediction of Modified Taitel-Dukler Criterion). Note, the Ridge of Taitel-Dukler Boundary of the 0.18 m and 7.3 MPa at Low Jg* Represents a Singularity Point at Zero Relative Velocity
Figure 4-17	Horizontal Stratified Flow Regime Transition and Relevant Data
Figure 4-18	Comparison between Hybrid Horizontal Stratification Criterion and Viscous Kelvin Helmholtz Models at Various Pressures and Pipe Diameters 4-59
Figure 4-19	Horizontal Flow Regime Map Including Wavy-Dispersed Regime
Figure 4-20	Illustration of Calculation of Entrainment Fraction in Wavy-Dispersed Regime. Example for Pressure 12 MPa and Diameter 0.18 m. Note, Flow Regime Map Is Simplified to Emphasize the Entrainment in Wavy-Dispersed Flow
Figure 4-21	Schematic View of Wavy-Dispersed Flow in Cross Section
Figure 5-1	One-Dimensional Vessel Channel with Area Change
Figure 5-2	Bubble Drag Coefficients (Ishii and Chawla, 1979)5-146
Figure 5-3	Effect of Ramps on Interfacial Friction Factor. (a) Small Bubble Regime, (b) Large Bubble Regime
Figure 5-4	Interfacial Friction Factor for Smooth Films (Wallis, 1969) 5-148
Figure 5-5	Hanstock and Hanratty (1976) Film Flow Interfacial Shear
Figure 5-6a	Comparison of Droplet Data Range and Droplet Size Limits in <u>W</u> COBRA/TRAC-TF2 at 40 psia
Figure 5-6b	Comparison of Droplet Data Range and Droplet Size Limits in <u>W</u> COBRA/TRAC-TF2 at 20 psia
Figure 5-7	Impingement of a Droplet on a Grid Spacer

WCAP-16996-NP

LIST OF FIGURES (cont.)

Figure 5-7c	Leading Edge of a Wetted Grid; Effect of Vapor Velocity	5-153
Figure 5-8	The Relationship of Droplet Diameter Ratio versus Droplet Weber Number	5-154
Figure 5-9	Comparison of Equation 5-185 with Data from Whalley (1973)	5-155
Figure 5-10	Core to Film Momentum Balance in Annular Film Flow	5-156
Figure 5-11	Comparison of the Wall Friction Factors from the Churchill Model and the Blasius Model (Wall Roughness 5.0E-5 m, Pipe Diameter 0.7 m)	5-157
Figure 5-12	WCOBRA/TRAC-TF2 1D Noding	5-158
Figure 5-13	Abrupt Expansion in 1D Component	5-159
Figure 5-14	Abrupt Contraction in 1D Component	5-160
Figure 5-15	Sharp-Edged Thin-Plate Orifice	5-161
Figure 5-16	Horizontal 1D Component Connected to a PWR Downcomer Channel	5-162
Figure 5-17	Broken Cold Leg Nozzle Junction to Vessel	5-163
Figure 5-18	Horizontal 1D Component Connected to a PWR Upper Plenum Hot Leg Nozzle	5-164
Figure 5-19	TRAC-PF1/MOD1 Sub-models of the Choked Flow Models	5-165
Figure 5-20	WCOBRA/TRAC-TF2 Two-phase Choked Flow Model Matrix A	5-166
Figure 5-21	WCOBRA/TRAC-TF2 Two-phase Choked Flow Model Matrix B	5-167
Figure 5-22	WCOBRA/TRAC-TF2 Sub-models with Homogeneous Relaxation Non-equilibrium Model Option	5-168
Figure 5-23	Area Ratio in Homogeneous Non-equilibrium Relaxation Model	5-169
Figure 5-24	WCOBRA/TRAC-TF2 Choked Critical Flow Model	5-170
Figure 5-25	Possible Offtake Geometries	5-171
Figure 5-26	Determination of Actual Characteristic Height, h	5-172
Figure 6-1	Large Void Fraction Gradient Ramp for Subcooled Liquid Interfacial Area	6-68
Figure 6-2	Suppression Factor at Various Liquid Side Heat Transfer Coefficients at 0.1 MPa and 1.0 MPa using the Revised Young-Bajorek Model	6-69
Figure 6-3	Illustration of Condensation Ramp Model, Variable PCONT1 Represents ΔP_{cont}	6-70
Figure 6-4	Illustration of the Selection Logic for Condensation, Evaporation, and Flashing for 1D Components	6-71
Figure 6-5	Interfacial Mass Transfer Map for 1D Components	6-72

LIST OF FIGURES (cont.)

¢

.

Figure 6-6	WCOBRA/TRAC-TF2 Basic Flow Regime Map for 1D Components	6-73
Figure 6-7	Liquid Side Heat Transfer Coefficient Model During Condensation in Bubbly Slug Flow for 1D Components	6-74
Figure 6-8	Schematic of Flow Pattern in Annular-mist Flow	6-75
Figure 6-9	Transition from Annular-mist to Mist Fflow as a Function of Pressure for Saturated Water	6-76
Figure 6-10	Calculated Stanton Numbers for Liquid-film Flow using Saturated Water Properties	6-77
Figure 6-11	Small Break LOCA Pressure Response (DLW SBLOCA Reference Transient)	6-78
Figure 6-12	Schematic of Flow Regime and Condensation in COSI Experiments	6-79
Figure 6-13	Cross Section of Cold Leg Near the Safety Injection	6-80
Figure 6-14	Temperature Profile of the Bulk Water in the Cold Leg Measured in Westinghouse COSI Test (Test No. 010, Point 5)	6-81
Figure 6-15	Comparison between the Measured Nusselt number and Calculated Nusselt Number from the Cold Leg Condensation Correlation	6-82
Figure 6-16	Comparison of Measured Condensation Heat Transfer Rates under Different Cold Leg Water Level Cases	6-83
Figure 7.2-1	Boiling Curve	7-49
Figure 7.2-2	Heat Transfer Regime Selection Logic for Vessel Component	7-50
Figure 7.2-3	Heat Transfer Regime Map for Vessel Component	7 51
Figure 7.2-4		7-51
rigule 7.2-4	Chen Correlation Convective Multiplier F _{CHEN}	
Figure 7.2-4 Figure 7.2-5		7-52
-	Chen Correlation Convective Multiplier F _{CHEN}	7-52 7-53
Figure 7.2-5	Chen Correlation Convective Multiplier F_{CHEN} Chen Boiling Suppression Factor S_{CHEN}	7-52 7-53 7-54
Figure 7.2-5 Figure 7.2-6	Chen Correlation Convective Multiplier F _{CHEN} Chen Boiling Suppression Factor S _{CHEN} Droplet Contact Effectiveness (as coded) at Atmospheric Pressure	7-52 7-53 7-54 7-55
Figure 7.2-5 Figure 7.2-6 Figure 7.2-7	$\label{eq:chen} \begin{array}{l} \mbox{Chen Correlation Convective Multiplier } F_{CHEN} \hfill \\ \mbox{Chen Boiling Suppression Factor } S_{CHEN} \hfill \\ \mbox{Droplet Contact Effectiveness (as coded) at Atmospheric Pressure} \hfill \\ \mbox{Droplet Contact Effectiveness (as coded) at High Pressure} \hfill \\ \hfill \\ \mbox{Droplet Contact Effectiveness (as coded) at High Pressure} \hfill \\ \hfill$	7-52 7-53 7-54 7-55 7-56
Figure 7.2-5 Figure 7.2-6 Figure 7.2-7 Figure 7.2-8	$\label{eq:chen} \begin{array}{l} \mbox{Chen Correlation Convective Multiplier } F_{CHEN} & \dots & \dots \\ \mbox{Chen Boiling Suppression Factor } S_{CHEN} & \dots & \dots \\ \mbox{Droplet Contact Effectiveness (as coded) at Atmospheric Pressure } & \dots \\ \mbox{Droplet Contact Effectiveness (as coded) at High Pressure } & \dots \\ \mbox{Droplet Contact Effectiveness (as coded) at High Pressure } & \dots \\ \mbox{Transition Boiling (Model 2) Ramp } F_{FILM} & \dots \\ \end{array}$	7-52 7-53 7-54 7-55 7-56 7-57
Figure 7.2-5 Figure 7.2-6 Figure 7.2-7 Figure 7.2-8 Figure 7.2-9	$ \begin{array}{llllllllllllllllllllllllllllllllllll$	7-52 7-53 7-54 7-55 7-56 7-57 7-58
Figure 7.2-5 Figure 7.2-6 Figure 7.2-7 Figure 7.2-8 Figure 7.2-9 Figure 7.2-10	$ \begin{array}{llllllllllllllllllllllllllllllllllll$	7-52 7-53 7-54 7-55 7-56 7-57 7-58 7-59

Figure 7.2-14	Heat Flux Paths for Film Boiling	7-62
Figure 7.3-1	One-Dimensional Component Heat Transfer Regime Selection	7-90
Figure 7.3-2	Biasi CHF Correlation Switch Over Quality (from Liles, D. R., et al., 1988)	. 7-91
Figure 7.3-3	One-Dimensional Component Heat Transfer Regime Selection Process at High Void and Quality	7-92
Figure 8-1	Nuclear Fuel Rod Geometry	8-68
Figure 8-2	Heater Rod Geometry	8-68
Figure 8-3	Tube and Wall Conductor Geometries	8-69
Figure 8-4	Control Volume for Heat Balance	8-69
Figure 8-5	Noding for Fuel Rod Conduction Model	8-70
Figure 8-6	Conductance Between Nodes	8-70
Figure 8-7	Steady-State Temperature Distribution in a Flat Plate with No Internal Heat Generation	8-71
Figure 8-8	Steady-State Temperature Distribution in a Hollow Cylinder with No Internal Heat Generation	8-71
Figure 8-9	Typical Heat Transfer Noding Scheme	8-72
Figure 8-10	Examples of Heat Transfer Node Insertion	8-73
Figure 8-11	Cladding Temperature Profile with Fine Mesh Renoding	8-74
Figure 8-12	Surface Heat Flux Profile with Fine Mesh Renoding	8-74
Figure 8-13	Temperature Jump Distances for an Ideal Gap	8-75
Figure 8-14	Instantaneous Creep Rates for Westinghouse Zircaloy-4 Cladding	8-76
Figure 8-15	Instantaneous Creep Rates for Westinghouse ZIRLO [®] Cladding	8-77
Figure 8-16	Instantaneous Creep Rates for Sandvik (NRU) Cladding	8-78
Figure 8-17	Heatup Rate Scenarios	8-79
Figure 8-18	Circumferential Strain Following Rupture – Zircaloy-4 Cladding	8-80
Figure 8-19	Burst Temperature Correlation – Westinghouse ZIRLO [®] Cladding	8-81
Figure 8-20	Circumferential Strain Following Rupture – Westinghouse ZIRLO [®] Cladding	8-82
Figure 8-21	Rod Strain at Burst Elevation	8-83
Figure 8-22	Flow Area Reduction Due to Blockage – Zircaloy-4 Cladding	8-84
Figure 8-23	Flow Area Reduction Due to Blockage – ZIRLO [®] Cladding	8-85

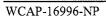


Figure 8-24	[] ^{a,c}
Figure 8-25	J
Figure 8-25	[] ^{a,c} 8-87
Figure 8-26	[
] ^{a,c}
Figure 8-27	[] ^{a,c}
Figure 8-28	[] ^{a,c} 8-88
Figure 8-29	Volumetric Increase in Fuel for Corresponding Clad Volume Increase Derived from PBF Tests (Broughton, 1981)
Figure 8-30	[
] ^{a,c}
Figure 8-31	Ι
] ^{a,c} 8-91
Figure 8-32	
5] ^{a,c}
Figure 8-33	[
] ^{a,c}
Figure 8-34	Geometry for One-Dimensional Component Conductor
Figure 8-35	Geometry for HTSTR Component Conductor
Figure 8-36	Node Located at the Interface between Two Dissimilar Materials
Figure 9-1	U-235 Fission Fraction
Figure 9-2	Pu-239 Fission Fraction
Figure 9-3	U-238 Fission Fraction
Figure 9-4	Calculated Normalized Macroscopic Cross Sections versus Core Average Water Density
Figure 9-5	$\overline{\beta}$ vs. Burnup at Various Enrichments
Figure 9-6	Prompt Neutron Lifetime
Figure 9-7	Descent Encross Deleges
	Prompt Energy Release

Figure 9-9	Delayed Group I Lambda)
Figure 9-10	Delayed Group II Lambda)
Figure 9-11	Delayed Group III Lambda	l
Figure 9-12	Delayed Group IV Lambda9-52	2
Figure 9-13	Delayed Group V Lambda	3
Figure 9-14	Delayed Group VI Lambda	ł
Figure 9-15	U-238 Capture/Fission Ratio as a Function of Initial Enrichment and Burnup 9-55	5
Figure 9-16	15x15 Material Composition Assignment Layout	5
Figure 9-17	15x15 Core Balance Fixed Source Distribution	7
Figure 9-18	15x15 Hot Assembly Fixed Source Distribution	3
Figure 9-19	15x15 Hot Rod Fixed Source Distribution)
Figure 9-20	Gamma Kerma Cross Section Energy Dependence)
Figure 9-21	Typical Heat Flux Deposition Fractions versus Coolant Density	
Figure 9-22	Typical Heat Flux Deposition Fractions versus Coolant Density)
Figure 9-23	Percent Fit Deviations for U-235 ANSI/ANS 5.1 – 1979 Plus Two Sigma 9-63	;
Figure 9-24	Percent Fit Deviations for Pu-239 ANSI/ANS 5.1 – 1979 Plus Two Sigma 9-64	ŀ
Figure 9-25	Percent Fit Deviations for U-238 ANSI/ANS 5.1 – 1979 Plus Two Sigma	;
Figure 9-26	U-235 ANSI/ANS 5.1 – 1979 Decay Heat Standard vs. Fitted Results	;
Figure 9-27	Pu-239 ANSI/ANS 5.1 – 1979 Decay Heat Standard vs. Fitted Results	7
Figure 9-28	U-238 ANSI/ANS 5.1 – 1979 Decay Heat Standard vs. Fitted Results	,
Figure 9-29	Time Dependent Reactor Period for + 0.003 ∆K Reactivity Insertion versus Time After Insertion)
Figure 9-30	Time Dependent Reactor Period for $+ 0.0015 \Delta K$ Reactivity Insertion versus Time After Insertion)
Figure 9-31	Time Dependent Reactor Period for $-0.030 \Delta K$ Reactivity Insertion versus Time After Insertion	
Figure 9-32	Total Actinide Decay Power versus Burnup and Initial Enrichment	•
Figure 9-33	Actinide Decay Power versus Burnup and Initial Enrichment	;
Figure 9-34	Capture Correction versus Burnup and Initial Enrichment	ł
Figure 9-35	WCOBRA/TRAC-TF2 Calculation Block Diagram	;

Figure 10-1	PIPE Component Noding
Figure 10-2	TEE Component Noding
Figure 10-3	PUMP Noding Diagram 10-29
Figure 10-4	93A Pump Single-Phase Homologous Head Curves
Figure 10-5	93A Pump Two-Phase Homologous Head Curves
Figure 10-6	93A Pump Single-Phase Homologous Torque Curves
Figure 10-7	93A Pump Two-Phase Homologous Torque Curves
Figure 10-8	Steam Generator Noding Diagram
Figure 10-9	Pressurizer (PRIZER) Component Noding 10-35
Figure 10-10	VALVE Component Noding
Figure 10-11	Geometry Configurations for VALVE Flow Area Calculation 10-37
Figure 10-12	Accumulator Noding Diagram
Figure 10-13	Pressure Boundary Condition Using BREAK Component 10-39
Figure 10-14	Velocity Boundary Condition Using FILL Component
Figure 10-15	ROD or SLAB Geometry HTSTR-Component with Hydraulic Cell Coupling on both the Inner and Outer Surface
Figure 11-1	WCOBRA/TRAC-TF2 Vessel Component Saturated Liquid Enthalpy Function
Figure 11-2	WCOBRA/TRAC-TF2 Vessel Component Saturated Vapor Enthalpy Function
Figure 11-3	WCOBRA/TRAC-TF2 Vessel Component Saturation Temperature
Figure 11-4	WCOBRA/TRAC-TF2 Vessel Component Saturated Liquid Density11-71
Figure 11-5	WCOBRA/TRAC-TF2 Vessel Component Saturated Vapor Density11-72
Figure 11-6	WCOBRA/TRAC-TF2 Vessel Component Saturated Liquid Viscosity11-73
Figure 11-7	WCOBRA/TRAC-TF2 Vessel Component Saturated Vapor Viscosity11-74
Figure 11-8	WCOBRA/TRAC-TF2 Vessel Component Saturated Liquid and Vapor Thermal Conductivity
Figure 11-9	WCOBRA/TRAC-TF2 Vessel Component Saturated Liquid Specific Heat11-76
Figure 11-10	WCOBRA/TRAC-TF2 Vessel Component Saturated Vapor Enthalpy11-77
Figure 11-11	WCOBRA/TRAC-TF2 Vessel Component Saturated Liquid Surface Tension

Figure 11-12	WCOBRA/TRAC-TF2 Vessel Component Superheated Vapor Enthalpy11-79
Figure 11-13	WCOBRA/TRAC-TF2 Vessel Component Superheated Vapor Temperature11-80
Figure 11-14	WCOBRA/TRAC-TF2 Vessel Component Superheated Vapor Density11-81
Figure 11-15	WCOBRA/TRAC-TF2 Vessel Component Superheated Vapor Thermal Conductivity
Figure 11-16	WCOBRA/TRAC-TF2 Vessel Component Superheated Vapor Viscosity11-83
Figure 11-17	WCOBRA/TRAC-TF2 1D Component Saturation Pressure
Figure 11-18	WCOBRA/TRAC-TF2 1D Component Saturated Vapor Density11-85
Figure 11-19	WCOBRA/TRAC-TF2 1D Component Saturated Liquid Density11-86
Figure 11-20	WCOBRA/TRAC-TF2 1D Component Saturated Vapor Enthalpy11-87
Figure 11-21	WCOBRA/TRAC-TF2 1D Component Saturated Liquid Enthalpy11-88
Figure 11-22	WCOBRA/TRAC-TF2 1D Component Saturated Vapor Specific Heat11-89
Figure 11-23	WCOBRA/TRAC-TF2 1D Component Saturated Liquid Specific Heat11-90
Figure 11-24	WCOBRA/TRAC-TF2 1D Component Saturated Vapor Viscosity11-91
Figure 11-25	WCOBRA/TRAC-TF2 1D Component Saturated Liquid Viscosity11-92
Figure 11-26	WCOBRA/TRAC-TF2 1D Component Saturated Vapor Thermal Conductivity
Figure 11-27	WCOBRA/TRAC-TF2 1D Component Saturated Liquid Thermal Conductivity
Figure 11-28	WCOBRA/TRAC-TF2 1D Component Surface Tension
Figure 11-29	MATPRO-9 and Modified NFI Thermal Conductivity for fuel density of 95% TD, for fresh fuel
Figure 11-30	Modified NFI Thermal Conductivity for fuel density of 95% TD as a function of Burnup
Figure 11-31	WCOBRA/TRAC-TF2 UO ₂ Specific Heat Model
Figure 11-32	WCOBRA/TRAC-TF2 Zircaloy-4 Thermal Conductivity Model11-99
Figure 11-33	WCOBRA/TRAC-TF2 Zircaloy-4 Specific Heat Model11-100
Figure 11-34	[] ^{a,c} 11-101
Figure 11-35	[] ^{a,c} 11-102
Figure 11-36	[] ^{a,c} 11-103

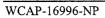
Figure 11-37

[

]^{a,c}.....11-104

VOLUME 2

Figure 12.2-1	Upstream P-T in Small and Large Break LOCAs	
Figure 12.2-2	Upstream Quality in Small and Large Break LOCAs	
Figure 12.4-1a	Upstream P-T in Ardron-Ackerman	
Figure 12.4-1b	Upstream Quality in Ardron-Ackerman	
Figure 12.4-2a	Upstream P-T in Boivin	
Figure 12.4-2b	Upstream Quality in Boivin	
Figure 12.4-3a	Upstream P-T in Fincke-Collins	
Figure 12.4-3b	Upstream Quality in Fincke-Collins	
Figure 12.4-4a	Upstream P-T in Jeandey	
Figure 12.4-4b	Upstream Quality in Jeandey	
Figure 12.4-5a	Upstream P-T in Neusen	12-21
Figure 12.4-5b	Upstream Quality in Neusen	12-21
Figure 12.4-6a	Upstream P-T in Reocreux	
Figure 12.4-6b	Upstream Quality in Reocruex	
Figure 12.4-7a	Upstream P-T in Seynhaeve	
Figure 12.4-7b	Upstream Quality in Seynhaeve	
Figure 12.4-8a	Upstream P-T in Sozzi-Sutherland	
Figure 12.4-8b	Upstream Quality in Sozzi-Sutherland	12-27
Figure 12.4-9a	Upstream P-T in Marviken Tests 1 through 27	
Figure 12.4-9b	Upstream Quality in Marviken Tests 1 through 27	
Figure 12.4-10a	Upstream P-T in Amos-Schrock	
Figure 12.4-10b	Upstream Quality in Amos-Schrock	
Figure 12.4-11a	Upstream P-T in TPFL	
Figure 12.4-11b	Upstream Quality in TPFL	
Figure 12.4-12a	Stagnation (P,DTsub)in Celata (1988) data	
Figure 12.4-12b	Critical Mass Fluxin Celata's data	
Figure 12.4-12c	Upstream P-T in Celata	
Figure 12.4-12d	Upstream Quality in Celata	



 $\overline{\}$

Figure 12.4-13a	Upstream Condition in Test Matrix	10
Figure 12.4-13b	Upstream Condition in Test Matrix	¥1
Figure 12-5-1	Pressure Profile along the Break Path	13
Figure 12.5-2	Comparison of Predicted and Measured Critical Flows 12-4	19
Figure 12.5-3a	Comparison of Predicted and Measured Critical Mass Flux with Non-condensable Gas	51
Figure 12.5-3b	Comparison of Predicted and Measured effect of Non-condensable Gas on Critical Mass Flux	52
Figure 12.5-4	Prediction Trend in Pressure Variation	54
Figure 12.5-5a	Prediction Trend in Quality Variation 12-5	56
Figure 12.5-5b	Prediction Trend Quality Variation	57
Figure 12.5-6a	Prediction Trend in Channel Length Variation in Linear Scale 12-2	59
Figure 12.5-6b	Prediction Trend in Channel Length Variation in Log Scale 12-6	50
Figure 12.5-7a	Prediction Trend in Channel Diameter in Linear Scale 12-0	52
Figure 12.5-7b	Prediction Trend in Channel Diameter in Log Scale 12-0	53
Figure 12.5-8a	Prediction Trend in Channel L/D Variation – Linear Scale 12-0	55
Figure 12.5-8b	Prediction Trend in Channel L/D Variation – Log Scale 12-0	56
Figure 12.5-9	Test 6 Noding Scheme	58
Figure 12.5-10	Test 6 Prediction of WCOBRA/TRAC-TF2 vs. Stand-Alone Model 12-0	58
Figure 12.5-11a	P(t) BC Comparison	59
Figure 12.5-11b	T(t) BC Comparison	59
Figure 12.5-12a	Impact of CD on Predicted Flow	71
Figure 12.5-12b	Observed Effective Multiplier	71
Figure 12.5-12c	Nozzle Upstream Pressure	72
Figure 12.7.2-1	Vapor Pull Through Mechanisms	30
Figure 12.7.2-2	Liquid Entrainment Mechanism	31
Figure 12.7.5-1	Diagram of the Two-Phase Flow Loop Facility	32
Figure 12.7.5-2	Schematic View of the Two-Phase Flow Loop Test Section 12-8	33
Figure 12.7.5-3	WCOBRA/TRAC-TF2 Noding Diagram of the Two-Phase Flow Loop 12-8	34



a i

Figure 12.7.5-4		nline Liquid Level for Horizontal	12-85
Figure 12.7.5-5	· • ·	nline Liquid Level for Downward-Vertical	12-86
Figure 12.7.6-1		nline Liquid Level for Upward-Vertical	12-87
Figure 12.7.6-2	ſ	_] ^{a,c}	12-88
Figure 13.4.2-1	Cross Section of the ORNL-TH	TF Test Bundle	13-10
Figure 13.4.2-2	Axial View of the ORNL-THT	F Test Bundle	13-11·
Figure 13.4.2-3	WCOBRA/TRAC-TF2 Model	of the ORNL-THTF	13-12
Figure 13.4.2-4	[
] ^{a,c}	13-13
Figure 13.4.2-5	[] ^{a,c}	13-14
Figure 13.4.2-6	[
Figure 13.4.2-7	I] ^{a,c}	13-15
11gure 13.7.2 /	L] ^{a,c}	13-16
Figure 13.4.2-8	[] ^{a,c}	12 17
Figure 13.4.2-9	[]	13-17
] ^{a,c}	13-18
Figure 13.4.2-10	[] ^{a,c}	13-19
Figure 13.4.2-11	[٦â,c	12.20
Figure 13.4.2-12	í I] ^{a,c}	13-20
	L] ^{a,c}	13-21
Figure 13.4.2-13	[] ^{a,c}	13-22
Figure 13.4.2-14	Ĺ		
· .] ^{a,c}	13-23
Figure 13.4.2-15	[] ^{a,c}	13-24

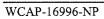


Figure 13.4.2-16	Comparison of Predicted and Measured Void Profiles for YDRAG Sensitivity Study, ORNL – THTF Test 3.09.10I	5
Figure 13.4.2-17	Comparison of Predicted and Measured Void Profiles for YDRAG Sensitivity Study, ORNL – THTF Test 3.09.10J	6
Figure 13.4.2-18	Comparison of Predicted and Measured Void Profiles for YDRAG Sensitivity Study, ORNL – THTF Test 3.09.10K	7
Figure 13.4.2-19	Comparison of Predicted and Measured Void Profiles for YDRAG Sensitivity Study, ORNL – THTF Test 3.09.10L	8
Figure 13.4.2-20	Comparison of Predicted and Measured Void Profiles for YDRAG Sensitivity Study, ORNL – THTF Test 3.09.10M	9
Figure 13.4.2-21	Comparison of Predicted and Measured Void Profiles for YDRAG Sensitivity Study, ORNL – THTF Test 3.09.10N	0
Figure 13.4.2-22	Comparison of Predicted and Measured Void Profiles for YDRAG Sensitivity Study, ORNL – THTF Test 3.09.10AA	1
Figure 13.4.2-23	Comparison of Predicted and Measured Void Profiles for YDRAG Sensitivity Study, ORNL – THTF Test 3.09.10BB	2
Figure 13.4.2-24	Comparison of Predicted and Measured Void Profiles for YDRAG Sensitivity Study, ORNL – THTF Test 3.09.10CC	3
Figure 13.4.2-25	Comparison of Predicted and Measured Void Profiles for YDRAG Sensitivity Study, ORNL – THTF Test 3.09.10DD	4
Figure 13.4.2-26	Comparison of Predicted and Measured Void Profiles for YDRAG Sensitivity Study, ORNL – THTF Test 3.09.10EE	5
Figure 13.4.2-27	Comparison of Predicted and Measured Void Profiles for YDRAG Sensitivity Study, ORNL – THTF Test 3.09.10FF	5
Figure 13.4.3-1	Westinghouse ECCS High Pressure Test Facility (G-1 Loop)	8
Figure 13.4.3-2	G-1 Test Vessel and Test Section)
Figure 13.4.3-3A	G-1 Uncovery Test Heater Rod Bundle Cross-Section)
Figure 13.4.3-3B	G-1 Uncovery Test Heater Rod Bundle Cross-Section	1
Figure 13.4.3-4	G-1 Facility Heater Rod13-52	2
Figure 13.4.3-5	G-1 Axial Power Profile	3
Figure 13.4.3-6	WCOBRA/TRAC-TF2 Model of the G-1 Test Bundle	4
Figure 13.4.3-7	Collapsed Liquid Level and Predicted Cladding Temperatures at the 8- and 10- Foot Elevations, G-1 Test 62	5

Figure 13.4.3-8	Void Fraction and Predicted Cladding Temperature at the 10- Foot Elevation, G-1 Test 62
Figure 13.4.3-9	Comparison of Predicted and Measured Mixture Level Swell for G-1 Bundle Uncovery Tests at Model Nominal YDRAG
Figure 13.4.3-10	Required YDRAG to Recover Data Versus Bundle Power
Figure 13.4.3-11	Required YDRAG to Recover Data Versus Pressure
Figure 13.4.3-12	Required YDRAG to Recover Data Versus Bundle Elevation
Figure 13.4.4-1	G-2 Test Facility Flow Schematic
Figure 13.4.4-2	G-2 Test Vessel and Test Section
Figure 13.4.4-3	G-2 Rod Bundle, Baffle Cross Section, and Bundle Instrumentation
Figure 13.4.4-4	G-2 Facility Heater Rod
Figure 13.4.4-5	G-2 Facility Axial Power Profile
Figure 13.4.4-6	WCOBRA/TRAC-TF2 Model of the G-2 Test Bundle
Figure 13.4.4-7	Collapsed Liquid Level and Predicted Cladding Temperatures at the 8- and 10- Foot Elevations, G-2 Test 716
Figure 13.4.4-8	Comparison of Predicted and Measured Mixture Level Swell for G-2 Bundle Uncovery Tests at Model Nominal YDRAG
Figure 13.4.4-9	Required YDRAG to Recover Data Versus Peak Linear Heat Rate
Figure 13.4.4-10	Required YDRAG to Recover Data Versus Pressure
Figure 13.4.4-11	Required YDRAG to Recover Data Versus Bundle Elevation
Figure 13:4.5-1	Cross Section of the JAERI-TPTF Test Bundle
Figure 13.4.5-2	Flow Diagram of the JAERI-TPTF
Figure 13.4.5-3	WCOBRA/TRAC-TF2 Model of the JAERI-TPTF
Figure 13.4.5-4	WCOBRA/TRAC-TF2 Predicted Void Fraction Profile, TPTF Test 330
Figure 13.4.5-5	WCOBRA/TRAC-TF2 Predicted Clad Temperature Profile, TPTF Test 330
Figure 13.4.5-6	Predicted Versus Measured Critical Heat Flux Elevation
Figure 13.4.5-7	Predicted Over Measured Critical Heat Flux Elevation Versus Pressure
Figure 13.4.5-8	Predicted Over Measured Critical Heat Flux Elevation Versus Linear Heat Rate
Figure 13.4.5-9	Predicted Over Measured Critical Heat Flux Elevation Versus Mass Flux 13-96

Figure 14.1-1	WCOBRA/TRAC-TF2 Heat Transfer Regime Map (from Figure 7.2-3) 14-10
Figure 14.2.2.1-1	Inlet Mass Flow Rate Forcing Function Normalized to Initial Condition, Test 3.03.6AR
Figure 14.2.2.1-2	Outlet Pressure Forcing Function Normalized to Initial Condition, Test 3.03.6AR
Figure 14.2.2.1-3	Test Section Bundle Power Forcing Function Normalized to Initial Condition, Test 3.03.6AR
Figure 14.2.2.1-4	Inlet Mass Flow Rate Forcing Function Normalized to Initial Condition, Test 3.08.6C
Figure 14.2.2.1-5	Outlet Pressure Forcing Function Normalized to Initial Condition, Test 3.08.6C
Figure 14.2.2.1-6	Test Section Bundle Power Forcing Function Normalized to Initial Condition, Test 3.08.6C
Figure 14.2.2.2-1	Diagram of G-1 Facility (from Cunningham, et al., 1974)
Figure 14.2.2.2-2	G-1 Test Vessel (from Cunningham, et al., 1974)
Figure 14.2.2.2-3	G-1 Heater Rod (from Cunningham, et al., 1974)
Figure 14.2.2.2-4	G-1 Heater Rod Axial Power Profile (from Cunningham, et al., 1974) 14-25
Figure 14.2.2.2-5	G-1 Bundle Cross Section and Instrumentation (from Cunningham, et al., 1974)
Figure 14.2.2.3-1	G-2 Test Facility Flow Schematic (from Cunningham, et al., 1975) 14-29
Figure 14.2.2.3-2	G-2 Loop Heater Rod (from Cunningham, et al., 1975)
Figure 14.2.2.3-3	G-2 Loop Heater Rod Axial Power Profile (from Cunningham, et al., 1975)
Figure 14.2.2.3-4	Test Rod Bundle, Cross Section and Instrumentation (from Cunningham, et al., 1975)
Figure 14.2.2.3-5	G-2 Loop Ground Plate (from Cunningham, et al., 1975)
Figure 14.2.2.3-6	Low Pressure UHI Refill Test Sequence of Events (from Hochreiter, et al., 1976)
Figure 14.2.3.1-1	FLECHT-SEASET Rod Bundle Cross Section (from Loftus, et al., 1981) 14-37
Figure 14.2.3.1-2	FLECHT-SEASET Axial Power Shape Profile and Grid Locations
Figure 14.2.3.2-1	FLECHT Rod Bundle Cross Section (from Rosal, et al., 1975) 14-41
Figure 14.2.3.2-2	FLECHT Cosine Axial Power Shape Profile and Grid Locations
Figure 14.2.3.3-1	FLECHT Top-Skewed Power Shape Test Bundle (from Rosal, et al., 1977) 14-45

Figure 14.2.3.3-2	FLECHT Top-Skewed Axial Power Shape 14-46
Figure 14.2.3.4-1	FLECHT Rod Bundle Cross Section (from Cadek et al., 1972) 14-49
Figure 14.2.3.4-2	FLECHT Heater Rod Schematic Diagram
Figure 14.2.3.4-3	FLECHT Axial Power Shape Profile and Grid Locations 14-51
Figure 14.2.3.6-1	FEBA Test Bundle Cross Section (from Ihle and Rust, 1984) 14-56
Figure 14.2.3.6-2	FEBA Power Shape and Grid Elevation (from Ihle and Rust, 1984) 14-57
Figure 15.1-1	WCOBRA/TRAC-TF2 Vessel Component Heat Transfer Regime Map (from Figure 7.2-3)
Figure 15.2-1	COBRAHT-TF2 Calculation Procedure
Figure 15.3-1	Predicted Versus Measured Critical Heat Flux Elevation from JAERI-TPTF Tests (from Figure 13.4.5-6)
Figure 15.4.1-1a	Heat Transfer Coefficient Comparison for ORNL-THTF Uncovered Bundle Tests (from COBRAHT-TF2)
Figure 15.4.1-1b	Ratio of Measured to Predicted Heat Transfer Coefficient vs. Vapor Film Reynolds Number for ORNL-THTF Uncovered Bundle Tests (from COBRAHT-TF2)
Figure 15.4.1-2	Cladding Temperature Profile Comparison for ORNL-THTF Uncovered Bundle Test I
Figure 15.4.1-3	Cladding Temperature Profile Comparison for ORNL-THTF Uncovered Bundle Test J
Figure 15.4.1-4	Cladding Temperature Profile Comparison for ORNL-THTF Uncovered Bundle Test K15-11
Figure 15.4.1-5	Cladding Temperature Profile Comparison for ORNL-THTF Uncovered Bundle Test L
Figure 15.4.1-6	Cladding Temperature Profile Comparison for ORNL-THTF Uncovered Bundle Test M
Figure 15.4.1-7	Cladding Temperature Profile Comparison for ORNL-THTF Uncovered Bundle Test N
Figure 15.4.1-8	Comparison of Predicted vs. Measured Cladding Temperatures for / ORNL-THTF Uncovered Bundle Tests
Figure 15.4.1-9	Vapor Temperature Profile Comparison for ORNL-THTF Uncovered Bundle Test I
Figure 15.4.1-10	Vapor Temperature Profile Comparison for ORNL-THTF Uncovered Bundle Test J

Figure 15.4.1-11	Vapor Temperature Profile Comparison for ORNL-THTF Uncovered Bundle Test K
Figure 15.4.1-12	Vapor Temperature Profile Comparison for ORNL-THTF Uncovered Bundle Test L
Figure 15.4.1-13	Vapor Temperature Profile Comparison for ORNL-THTF Uncovered Bundle Test M
Figure 15.4.1-14	Vapor Temperature Profile Comparison for ORNL-THTF Uncovered Bundle Test N
Figure 15.4.1-15	Conduction Node and Cell Vapor Temperature Profile Comparison for ORNL-THTF Uncovered Bundle Test I
Figure 15.4.2-1	Heat Transfer Coefficient Comparison for FLECHT SPV Tests (from COBRAHT-TF2)
Figure 15.4.2-2	Ratio of Predicted to Measured Heat Transfer Coefficient vs. Vapor Film Reynolds Number for FLECHT SPV Tests (from COBRAHT-TF2)
Figure 15.5.1-1	Heat Transfer Coefficient Comparison for all Thermocouples at [] ^{a,c} in ORNL Steady-State Film Boiling Tests (from COBRAHT-TF2)
Figure 15.5.1-2	Ratio of Measured to Predicted Heat Transfer Coefficient vs. Vapor Film Reynolds Number for all Thermocouples at [] ^{a,c} in ORNL Steady-State Film Boiling Tests (from COBRAHT-TF2)15-21
Figure 15.5.2.1-1	WCOBRA/TRAC-TF2 Model for the ORNL-THTF Simulations
Figure 15.5.2.1-2	ORNL-THTF 3.07.9B Axial Heater Rod Temperature Profile at 20 s of Transient
Figure 15.5.2.1-3	ORNL-THTF 3.03.6AR Axial Heater Rod Temperature Profile at 10 s of Transient
Figure 15.5.2.1-4	ORNL-THTF 3.03.6AR Transient Heater Rod Temperature at 96 in
Figure 15.5.2.1-5	ORNL-THTF 3.03.6AR Transient Heater Rod Temperature at 118 in
Figure 15.5.2.1-6	ORNL-THTF 3.03.6AR Transient Heater Rod Temperature at 143 in
Figure 15.5.2.1-7	ORNL-THTF 3.08.6C Axial Heater Rod Temperature Profile at 21 s of Transient
Figure 15.5.2.1-8	ORNL-THTF 3.08.6C Transient Heater Rod Temperature at 95 in

Figure 15.5.2.1-9	ORNL-THTF 3.08.6C Transient Heater Rod Temperature at 118 in
Figure 15.5.2.1-10	ORNL-THTF 3.08.6C Transient Heater Rod Temperature at 143 in 15-32
Figure 15.5.2.1-11	ORNL-THTF Predicted versus Measured Peak Cladding Temperature 15-33
Figure 15.5.2.2-1	WCOBRA/TRAC-TF2 Model of the G-1 Blowdown Test Simulations 15-37
Figure 15.5.2.2-2	G-1 Blowdown Test 143 Cladding Temperature Time History Comparison (24-inch Elevation)
Figure 15.5.2.2-3	G-1 Blowdown Test 143 Cladding Temperature Time History Comparison (48-inch Elevation)
Figure 15.5.2.2-4	G-1 Blowdown Test 143 Cladding Temperature Time History Comparison (72-inch Elevation)
Figure 15.5.2.2-5	G-1 Blowdown Test 143 Cladding Temperature Time History Comparison (96-inch Elevation)
Figure 15.5.2.2-6	G-1 Blowdown Test 143 Cladding Temperature Time History Comparison (120-inch Elevation)
Figure 15.5.2.2-7	G-1 Blowdown Test 143 Axial Cladding Temperature Comparison (Time = 6 Seconds
Figure 15.5.2.2-8	G-1 Blowdown Test 143 Axial Cladding Temperature Comparison (Time = 10 Seconds, PCT Time)
Figure 15.5.2.2-9	G-1 Blowdown Test 143 Axial Cladding Temperature Comparison (Time = 15 Seconds)
Figure 15.5.2.2-10	G-1 Blowdown Test 143 Axial Cladding Temperature Comparison (Time = 20 Seconds)
Figure 15.5.2.2-11	G-1 Blowdown Test 143 Axial Cladding Temperature Comparison (Time = 30 Seconds)
Figure 15.5.2.2-12	G-1 Blowdown Test 148 Cladding Temperature Time History Comparison (24-inch Elevation)
Figure 15.5.2.2-13	G-1 Blowdown Test 148 Cladding Temperature Time History Comparison (48-inch Elevation)
Figure 15.5.2.2-14	G-1 Blowdown Test 148 Cladding Temperature Time History Comparison (72-inch Elevation)
Figure 15.5.2.2-15	G-1 Blowdown Test 148 Cladding Temperature Time History Comparison (96-inch Elevation)
Figure 15.5.2.2-16	G-1 Blowdown Test 148 Cladding Temperature Time History Comparison (120-inch Elevation)

1

Figure 15.5.2.2-17	G-1 Blowdown Test 148 Axial Cladding Temperature Time History Comparison (Time = 6 Seconds)
Figure 15.5.2.2-18	G-1 Blowdown Test 148 Axial Cladding Temperature Comparison (Time = 10 Seconds, PCT Time)
Figure 15.5.2.2-19	G-1 Bolwdown Test 148 Axial Cladding Temperature Comparison (Time = 15 Seconds)
Figure 15.5.2.2-20	G-1 Blowdown Test 148 Axial Cladding Temperature Comparison (Time = 20 Seconds)
Figure 15.5.2.2-21	G-1 Blowdown Test 148 Axial Cladding Temperature Comparison (Time = 30 Seconds)
Figure 15.5.2.2-22	G-1 Blowdown Test 152 Cladding Temperature Time History Comparison (24-inch Elevation)
Figure 15.5.2.2-23	G-1 Blowdown Test 152 Cladding Temperature Time History Comparison (48 inch Elevation)
Figure 15.5.2.2-24	G-1 Blowdown Test 152 Cladding Temperature Time History Comparison (72-inch Elevation)
Figure 15.5.2.2-25	G-1 Blowdown Test 152 Cladding Temperature Time History Comparison (96-inch Elevation
Figure 15.5.2.2-26	G-1 Blowdown Test 152 Cladding Temperature Time History Comparison (120-inch Elevation)
Figure 15.5.2.2-27	G-1 Blowdown Test 152 Axial Cladding Temperature Comparison (Time = 6 Seconds)
Figure 15.5.2.2-28	G-1 Blowdown Test 152 Axial Cladding Temperature Comparison (Time = 10 Seconds, PCT Time)15-51
Figure 15.5.2.2-29	G-1 Blowdown Test 152 Axial Cladding Temperture Comparison (Time = 15 Seconds)
Figure 15.5.2.2-30	G-1 Blowdown Test 152 Axial Cladding Temperature Comparison (Time = 20 Seconds)
Figure 15.5.2.2-31	G-1 Blowdown Test 152 Axial Cladding Temperature Comparison (Time = 30 Seconds)
Figure 15.5.2.2-32	G-1 Blowdown Test 146 Cladding Temperature Time History Comparison (24-inch Elevation)
Figure 15.5.2.2-33	G-1 Blowdown Test 146 Cladding Temperature Time History Comparison (48-inch Elevation)

Figure 15.5.2.2-34	G-1 Blowdown Test 146 Cladding Temperature Time History Comparison (72-inch Elevation)
Figure 15.5.2.2-35	Blowdown Test 146 Cladding Temperature Time History Comparison (96-inch Elevation)
Figure 15.5.2.2-36	G-1 Blowdown Test 146 Cladding Temperature Time History Comparison (120-inch Elevation)
Figure 15.5.2.2-37	G-1 Blowdown Test 146 Axial Cladding Temperature Comparison (Time = 6 Seconds)
Figure 15.5.2.2-38	G-1 Blowdown Test 146 Axial Cladding Temperature Comparison (Time = 10 Seconds, PCT Time)
Figure 15.5.2.2-39	G-1 Blowdown Test 146 Axial Cladding Temperature Comparison (Time = 15 Seconds)
Figure 15.5.2.2-40	G-1 Blowdown Test 146 Axial Cladding Temperature Comparison (Time = 20 Seconds)
Figure 15.5.2.2-41	G-1 Blowdown Test 146 Axial Cladding Temperature Comparison (Time = 30 Seconds)
Figure 15.5.2.2-42	G-1 Blowdown Test 153 Cladding Temperature Time History Comparison (24-inch Elevation)
Figure 15.5.2.2-43	G-1 Blowdown Test 153 Cladding Temperature Time History Comparison (48-inch Elevation)
Figure 15.5.2.2-44	G-1 Blowdown Test 153 Cladding Temperature Time History Comparison (72-inch Elevation)
Figure 15.5.2.2-45	G-1 Blowdown Test 153 Cladding Temperature Time History Comparison (96-inch Elevation)
Figure 15.5.2.2-46	G-1 Blowdown Test 153 Cladding Temperature Time History Comparison (120-inch Elevation)
Figure 15.5.2.2-47	G-1 Blowdown Test 153 Axial Cladding Temperature Comparison (Time = 6 Seconds)
Figure 15.5.2.2-48	G-1 Blowdown Test 153 Axial Cladding Temperature Comparison (Time = 10 Seconds, PCT Time)
Figure 15.5.2.2-49	G-1 Blowdown Test 153 Axial Cladding Temperature Comparison (Time = 15 Seconds)
Figure 15.5.2.2-50	G-1 Blowdown Test 153 Axial Cladding Temperature Comparison (Time = 20 Seconds)

li

Figure 15.5.2.2-51	G-1 Blowdown Test 153 Axial Cladding Temperature Comparison (Time = 30 Seconds)15-62
Figure 15.5.2.2-52	G-1 Blowdown Test 154 Cladding Temperature Time History Comparison (24-inch Elevation)
Figure 15.5.2.2-53	G-1 Blowdown Test 154 Cladding Temperature Time History Comparison (48-inch Elevation)
Figure 15.5.2.2-54	G-1 Blowdown Test 154 Cladding Temperature Time History Comparison (72-inch Elevation)
Figure 15.5.2.2-55	G-1 Blowdown Test 154 Cladding Temperature Time History Comparison (96-inch Elevation)
Figure 15.5.2.2-56	G-1 Blowdown Test 154 Cladding Temperature Time History Comparison (120-inch Elevation)
Figure 15.5.2.2-57	G-1 Blowdown Test 154 Axial Cladding Temperature Comparison (Time = 6 Seconds)
Figure 15.5.2.2-58	G-1 Blowdown Test 154 Axial Cladding Temperature Comparison (Time = 10 Seconds, PCT Time)
Figure 15.5.2.2-59	G-1 Blowdown Test 154 Axial Cladding Temperature Comparison (Time = 15 Seconds)
Figure 15.5.2.2-60	G-1 Blowdown Test 154 Axial Cladding Temperature Comparison (Time = 20 Seconds)
Figure 15.5.2.2-61	G-1 Blowdown Test 154 Axial Cladding Temperature Comparison (Time = 30 Seconds)
Figure 15.5.2.2-62	Measured Thermocouple Data from (Cunningham, J. P., 1974)
Figure 15.5.2.3-1	WCOBRA/TRAC-TF2 Model for the G-2 Refill Test Simulations 15-75
Figure 15.5.2.3-2	G-2 Refill Test 743 Cladding Temperature Time History Comparison (12.3-inch Elevation)
Figure 15.5.2.3-3	G-2 Refill Test 743 Cladding Temperature Time History Comparison (28.7-inch Elevation)
Figure 15.5.2.3-4	G-2 Refill Test 743 Cladding Temperature Time History Comparison (45.1-inch Elevation)
Figure 15.5.2.3-5	G-2 Refill Test 743 Cladding Temperature Time History Comparison (82.0-inch Elevation)
Figure 15.5.2.3-6	G-2 Refill Test 743 Cladding Temperature Time History Comparison (118.9-inch Elevation)

liii

Figure 15.5.2.3-7	G-2 Refill Test 743 Axial Cladding Temperature at 60 s	15-78
Figure 15.5.2.3-8	G-2 Refill Test 750 Cladding Temperature Time History Comparison (12.3-inch Elevation)	
Figure 15.5.2.3-9	G-2 Refill Test 750 Cladding Temperature Time History Comparison (28.7-inch Elevation)	15-79
Figure 15.5.2.3-10	G-2 Refill Test 750 Cladding Temperature Time History Comparison (45.1-inch Elevation)	15-80
Figure 15.5.2.3-11	G-2 Refill Test 750 Cladding Temperature Time History Comparison (82.0-inch Elevation)	15-80
Figure 15.5.2.3-12	G-2 Refill Test 750 Cladding Temperature Time History Comparison (118.9-inch Elevation)	15-81
Figure 15.5.2.3-13	G-2 Refill Test 750 Axial Cladding Temperature at 60 s	
Figure 15.5.2.3-14	G-2 Refill Test 760 Cladding Temperature Time History Comparison (12.3-inch Elevation)	15-82
Figure 15.5.2.3-15	G-2 Refill Test 760 Cladding Temperature Time History Comparison (28.7-inch Elevation)	15-82
Figure 15.5.2.3-16	G-2 Refill Test 760 Cladding Temperature Time History Comparison (45.1-inch Elevation)	15-83
Figure 15.5.2.3-17	G-2 Refill Test 760 Cladding Temperature Time History Comparison (82.0-inch Elevation)	15-83
Figure 15.5.2.3-18	G-2 Refill Test 760 Cladding Temperature Time History Comparison (118.9-inch Elevation)	15-84
Figure 15.5.2.3-19	G-2 Refill Test 760 Axial Cladding Temperature at 50 s	15-84
Figure 15.5.2.3-20	G-2 Refill Test 761 Cladding Temperature Time History Comparison (12.3-inch Elevation)	15-85
Figure 15.5.2.3-21	G-2 Refill Test 761 Cladding Temperature Time History Comparison (28.7-inch Elevation)	15-85
Figure 15.5.2.3-22	G-2 Refill Test 761 Cladding Temperature Time History Comparison (45.1-inch Elevation)	15-86
Figure 15.5.2.3-23	G-2 Refill Test 761 Cladding Temperature Time History Comparison (82.0-inch Elevation)	15-86
Figure 15.5.2.3-24	G-2 Refill Test 761 Cladding Temperature Time History Comparison (118.9-inch Elevation)	15-87

Figure 15.5.2.3-25	G-2 Refill Test 761 Axial Cladding Temperature at 50 s	15-87
Figure 15.5.2.3-26	G-2 Refill Test 762 Cladding Temperature Time History Comparison (12.3-inch Elevation)	15-88
Figure 15.5.2.3-27	G-2 Refill Test 762 Cladding Temperature Time History Comparison (28.7-inch Elevation)	15-88
Figure 15.5.2.3-28	G-2 Refill Test 762 Cladding Temperature Time History Comparison (45.1-inch Elevation)	15-89
Figure 15.5.2.3-29	G-2 Refill Test 762 Cladding Temperature Time History Comparison (82.0-inch Elevation)	15-89
Figure 15.5.2.3-30	G-2 Refill Test 762 Cladding Temperature Time History Comparison (118.9-inch Elevation)	15-90
Figure 15.5.2.3-31	G-2 Refill Test 762 Axial Cladding Temperature at 50 s	15-90
Figure 15.5.2.3-32	G-2 Refill Test 767 Cladding Temperature Time History Comparison (12.3-inch Elevation)	15-91
Figure 15.5.2.3-33	G-2 Refill Test 767 Cladding Temperature Time History Comparison (28.7-inch Elevation)	15-91
Figure 15.5.2.3-34	G-2 Refill Test 767 Cladding Temperature Time History Comparison (45.1-inch Elevation)	15-92
Figure 15.5.2.3-35	G-2 Refill Test 767 Cladding Temperature Time History Comparison (82.0-inch Elevation)	15-92
Figure 15.5.2.3-36	G-2 Refill Test 767 Cladding Temperature Time History Comparison (118.9-inch Elevation)	15-93
Figure 15.5.2.3-37	G-2 Refill Test 767 Axial Cladding Temperature at 60 s	15-93
Figure 15.5.2.3-38	Comparison of G-2 Refill Test Predicted vs. Measured Peak Cladding Temperature	15-94
Figure 15.6.1-1	WCOBRA/TRAC-TF2 Transverse Noding for FLECHT-SEASET	15-102
Figure 15.6.1-2	WCOBRA/TRAC-TF2 Axial Noding for FLECHT-SEASET	15-103
Figure 15.6.1-3	FLECHT-SEASET Axial Power Shape Profile	15-104
Figure 15.6.1-4	FLECHT-SEASET 31805 Rod Temperatures at 24-inch Elevation	15-105
Figure 15.6.1-5	FLECHT-SEASET 31805 Rod Temperatures at 48-inch Elevation	15-105
Figure 15.6.1-6	FLECHT-SEASET 31805 Rod Temperatures at 72-inch Elevation	15-106
Figure 15.6.1-7	FLECHT-SEASET 31805 Rod Temperatures at 78-inch Elevation	15-106
Figure 15.6.1-8	FLECHT-SEASET 31805 Rod Temperatures at 84-inch Elevation	15-107

Figure 15.6.1-9	FLECHT-SEASET 31805 Rod Temperatures at 96-inch Elevation 15-107
Figure 15.6.1-10	FLECHT-SEASET 31805 Rod Temperatures at 120-inch Elevation
Figure 15.6.1-11	Comparison of Predicted and Estimated Quench Front Elevations for FLECHT-SEASET 31805
Figure 15.6.1-12	Comparison of Predicted and Measured Axial Temperature Profile for FLECHT-SEASET 31805 at 100 Seconds
Figure 15.6.1-13	Comparison of Predicted and Measured Axial Temperature Profile for FLECHT-SEASET 31805 at 200 Seconds
Figure 15.6.1-14	Comparison of Predicted and Measured Maximum Cladding Temperatures at all Thermocouple Elevations for FLECHT-SEASET 3180515-110
Figure 15.6.1-15	Comparison of Predicted and Measured Turn-Around Times for FLECHT-SEASET 3180515-110
Figure 15.6.1-16	FLECHT-SEASET 31805 Bundle Lower Half ΔP
Figure 15.6.1-17	FLECHT-SEASET 31805 Bundle Upper Half ΔP 15-111
Figure 15.6.1-18	FLECHT-SEASET 31805 Overall ΔP
Figure 15.6.1-19	FLECHT-SEASET 31805 Vapor Temperatures at 48-inch Elevation15-112
Figure 15.6.1-20	FLECHT-SEASET 31805 Vapor Temperatures near 72-inch Elevation15-113
Figure 15.6.1-21	FLECHT-SEASET 31805 Vapor Temperatures near 90-inch Elevation15-113
Figure 15.6.1-22	FLECHT-SEASET 31805 Vapor Temperatures near 120-inch Elevation15-114
Figure 15.6.1-23	FLECHT-SEASET 31805 Vapor Temperatures near 138-inch Elevation15-114
Figure 15.6.1-24	FLECHT-SEASET 31504 Rod Temperatures at 24-inch Elevation15-115
Figure 15.6.1-25	FLECHT-SEASET 31504 Rod Temperatures at 48-inch Elevation15-115
Figure 15.6.1-26	FLECHT-SEASET 31504 Rod Temperatures at 72-inch Elevation15-116
Figure 15.6.1-27	FLECHT-SEASET 31504 Rod Temperatures at 78-inch Elevation15-116
Figure 15.6.1-28	FLECHT-SEASET 31504 Rod Temperatures at 84-inch Elevation15-117
Figure 15.6.1-29	FLECHT-SEASET 31504 Rod Temperatures at 96-inch Elevation15-117
Figure 15.6.1-30	FLECHT-SEASET 31504 Rod Temperatures at 120-inch Elevation15-118
Figure 15.6.1-31	Comparison of Predicted and Estimated Quench Front Elevations for FLECHT-SEASET 31504
Figure 15.6.1-32	Comparison of Predicted and Measured Axial Temperature Profile for FLECHT-SEASET 31504 at 50 Seconds

lv

Figure 15.6.1-33	Comparison of Predicted and Measured Axial Temperature Profile for FLECHT-SEASET 31504 at 100 Seconds15-119
Figure 15.6.1-34	Comparison of Predicted and Measured Maximum Cladding Temperatures at all Thermocouple Elevations for FLECHT-SEASET 3150415-120
Figure 15.6.1-35	Comparison of Predicted and Measured Turn-Around Times for FLECHT-SEASET 31504
Figure 15.6.1-36	FLECHT-SEASET 31504 Bundle Lower Half ΔP 15-121
Figure 15.6.1-37	FLECHT-SEASET 31504 Bundle Upper Half ΔP 15-121
Figure 15.6.1-38	FLECHT-SEASET 31504 Overall ΔP
Figure 15.6.1-39	FLECHT-SEASET 31504 Vapor Temperatures at 48-inch Elevation
Figure 15.6.1-40	FLECHT-SEASET 31504 Vapor Temperatures near 72-inch Elevation 15-123
Figure 15.6.1-41	FLECHT-SEASET 31504 Vapor Temperatures near 90-inch Elevation 15-123
Figure 15.6.1-42	FLECHT-SEASET 31504 Vapor Temperatures at 120-inch Elevation 15-124
Figure 15.6.1-43	FLECHT-SEASET 31504 Vapor Temperatures at 138-inch Elevation15-124
Figure 15.6.1-44	FLECHT-SEASET 32013 Rod Temperatures at 24-inch Elevation 15-125
Figure 15.6.1-45	FLECHT-SEASET 32013 Rod Temperatures at 48-inch Elevation 15-125
Figure 15.6.1-46	FLECHT-SEASET 32013 Rod Temperatures at 72-inch Elevation 15-126
Figure 15.6.1-47	FLECHT-SEASET 32013 Rod Temperatures at 78-inch Elevation 15-126
Figure 15.6.1-48	FLECHT-SEASET 32013 Rod Temperatures at 84-inch Elevation 15-127
Figure 15.6.1-49	FLECHT-SEASET 32013 Rod Temperatures at 96-inch Elevation 15-127
Figure 15.6.1-50	FLECHT-SEASET 32013 Rod Temperatures at 120-inch Elevation
Figure 15.6.1-51	Comparison of Predicted and Estimated Quench Front Elevations for FLECHT-SEASET 32013
Figure 15.6.1-52	Comparison of Predicted and Measured Axial Temperature Profile for FLECHT-SEASET 32013 at 50 Seconds
Figure 15.6.1-53	Comparison of Predicted and Measured Axial Temperature Profile for FLECHT-SEASET 32013 at 100 Seconds
Figure 15.6.1-54	Comparison of Predicted and Measured Maximum Cladding Temperatures at all Thermocouple Elevations for FLECHT-SEASET 3201315-130
Figure 15.6.1-55	Comparison of Predicted and Measured Turn-Around Times for FLECHT-SEASET 32013
Figure 15.6.1-56	FLECHT-SEASET 32013 Bundle Lower Half ΔP

	· ·
Figure 15.6.1-57	FLECHT-SEASET 32013 Bundle Upper Half ΔP
Figure 15.6.1-58	FLECHT-SEASET 32013 Overall ΔP
Figure 15.6.1-59	FLECHT-SEASET 32013 Vapor Temperatures at 48-inch Elevation 15-132
Figure 15.6.1-60	FLECHT-SEASET 32013 Vapor Temperatures near 72-inch Elevation 15-133
Figure 15.6.1-61	FLECHT-SEASET 32013 Vapor Temperatures near 90-inch Elevation 15-133
Figure 15.6.1-62	FLECHT-SEASET 32013 Vapor Temperatures at 120-inch Elevation 15-134
Figure 15.6.1-63	FLECHT-SEASET 32013 Vapor Temperatures at 138-inch Elevation 15-134
Figure 15.6.1-64	FLECHT-SEASET 31203 Rod Temperatures at 24-inch Elevation 15-135
Figure 15.6.1-65	FLECHT-SEASET 31203 Rod Temperatures at 48-inch Elevation 15-135
Figure 15.6.1-66	FLECHT-SEASET 31203 Rod Temperatures at 72-inch Elevation 15-136
Figure 15.6.1-67	FLECHT-SEASET 31203 Rod Temperatures at 78-inch Elevation 15-136
Figure 15.6.1-68	FLECHT-SEASET 31203 Rod Temperatures at 84-inch Elevation 15-137
Figure 15.6.1-69	FLECHT-SEASET 31203 Rod Temperatures at 96-inch Elevation 15-137
Figure 15.6.1-70	FLECHT-SEASET 31203 Rod Temperatures at 120-inch Elevation 15-138
Figure 15.6.1-71	Comparison of Predicted and Estimated Quench Front Elevations for FLECHT-SEASET 31203
Figure 15.6.1-72	Comparison of Predicted and Measured Axial Temperature Profile for FLECHT-SEASET 31203 at 50 Seconds
Figure 15.6.1-73	Comparison of Predicted and Measured Axial Temperature Profile for FLECHT-SEASET 31203 at 100 Seconds
Figure 15.6.1-74	Comparison of Predicted and Measured Maximum Cladding Temperatures at all Thermocouple Elevations for FLECHT-SEASET 31203
Figure 15.6.1-75	Comparison of Predicted and Measured Turn-Around Times for FLECHT-SEASET 31203
Figure 15.6.1-76	FLECHT-SEASET 31203 Bundle Lower Half ΔP 15-141
Figure 15.6.1-77	FLECHT-SEASET 31203 Bundle Upper Half ΔP 15-141
Figure 15.6.1-78	FLECHT-SEASET 31203 Overall ΔP 15-142
Figure 15.6.1-79	FLECHT-SEASET 31203 Vapor Temperatures at 48-inch Elevation 15-142
Figure 15.6.1-80	FLECHT-SEASET 31203 Vapor Temperatures near 72-inch Elevation 15-143
Figure 15.6.1-81	FLECHT-SEASET 31203 Vapor Temperatures near 90-inch Elevation 15-143
Figure 15.6.1-82	FLECHT-SEASET 31203 Vapor Temperatures at 120-inch Elevation 15-144

lviii

LIST OF FIGURES (cont.)

Figure 15.6.1-83	FLECHT-SEASET 31203 Vapor Temperatures at 138-inch Elevation 15-144
Figure 15.6.1-84	FLECHT-SEASET 31701 Rod Temperatures at 24-inch Elevation 15-145
Figure 15.6.1-85	FLECHT-SEASET 31701 Rod Temperatures at 48-inch Elevation 15-145
Figure 15.6.1-86	FLECHT-SEASET 31701 Rod Temperatures at 72-inch Elevation 15-146
Figure 15.6.1-87	FLECHT-SEASET 31701 Rod Temperatures at 78-inch Elevation 15-146
Figure 15.6.1-88	FLECHT-SEASET 31701 Rod Temperatures at 84-inch Elevation 15-147
Figure 15.6.1-89	FLECHT-SEASET 31701 Rod Temperatures at 96-inch Elevation 15-147
Figure 15.6.1-90	FLECHT-SEASET 31701 Rod Temperatures at 120-inch Elevation 15-148
Figure 15.6.1-91	Comparison of Predicted and Estimated Quench Front Elevations for FLECHT-SEASET 31701
Figure 15.6.1-92	Comparison of Predicted and Measured Axial Temperature Profile for FLECHT-SEASET 31701 at 10 Seconds
Figure 15.6.1-93	Comparison of Predicted and Measured Axial Temperature Profile for FLECHT-SEASET 31701 at 30 Seconds
Figure 15.6.1-94	Comparison of Predicted and Measured Maximum Cladding Temperatures at all Thermocouple Elevations for FLECHT-SEASET 31701
Figure 15.6.1-95	Comparison of Predicted and Measured Turn-Around Times for FLECHT-SEASET 31701
Figure 15.6.1-96	FLECHT-SEASET 31701 Bundle Lower Half ΔP 15-151
Figure 15.6.1-97	FLECHT-SEASET 31701 Bundle Upper Half ΔP 15-151
Figure 15.6.1-98	FLECHT-SEASET 31701 Overall ΔP
Figure 15.6.1-99	FLECHT-SEASET 31701 Vapor Temperatures at 48-inch Elevation 15-152
Figure 15.6.1-100	FLECHT-SEASET 31701 Vapor Temperatures near 72-inch Elevation 15-153
Figure 15.6.1-101	FLECHT-SEASET 31701 Vapor Temperatures near 90-inch Elevation
Figure 15.6.1-102	FLECHT-SEASET 31701 Vapor Temperatures at 120-inch Elevation
Figure 15.6.1-103	FLECHT-SEASET 31701 Vapor Temperatures at 138-inch Elevation 15-154
Figure 15.6.1-104	Comparison of Predicted and Measured Maximum Temperatures for FLECHT-SEASET Simulations
Figure 15.6.2-1	WCOBRA/TRAC-TF2 Transverse Noding for FLECHT-LFR 15-161
Figure 15.6.2-2	
	WCOBRA/TRAC-TF2 Axial Noding for FLECHT-LFR

•

Figure 15.6.2-4	FLECHT 05029 Rod Temperatures at 24-inch Elevation 15-164
Figure 15.6.2-5	FLECHT 05029 Rod Temperatures at 48-inch Elevation 15-164
Figure 15.6.2-6	FLECHT 05029 Rod Temperatures at 72-inch Elevation 15-165
Figure 15.6.2-7	FLECHT 05029 Rod Temperatures at 78-inch Elevation 15-165
Figure 15.6.2-8	FLECHT 05029 Rod Temperatures at 84-inch Elevation
Figure 15.6.2-9	FLECHT 05029 Rod Temperatures at 96-inch Elevation
Figure 15.6.2-10	FLECHT 05029 Rod Temperatures at 120-inch Elevation 15-167
Figure 15.6.2-11	Comparison of Predicted and Estimated Quench Front Elevations for FLECHT 05029
Figure 15.6.2-12	Comparison of Predicted and Measured Axial Temperature Profile for FLECHT 05029 at 50 Seconds
Figure 15.6.2-13	Comparison of Predicted and Measured Axial Temperature Profile for FLECHT 05029 at 100 Seconds
Figure 15.6.2-14	Comparison of Predicted and Measured Maximum Cladding Temperatures at all Code Uncertainty Elevations for FLECHT 05029
Figure 15.6.2-15	FLECHT 05029 Bundle Lower Half ΔP
Figure 15.6.2-16	FLECHT 05029 Bundle Upper Half ΔP
Figure 15.6.2-17	FLECHT 05029 Overall ΔP
Figure 15.6.2-18	FLECHT 05029 Vapor Temperatures at 84-inch Elevation 15-171
Figure 15.6.2-19	FLECHT 05029 Vapor Temperatures near 120-inch Elevation 15-172
Figure 15.6.2-20	FLECHT 05029 Vapor Temperatures near Bundle Exit 15-172
Figure 15.6.2-21	FLECHT 05132 Rod Temperatures at 24-inch Elevation
Figure 15.6.2-22	FLECHT 05132 Rod Temperatures at 48-inch Elevation 15-173
Figure 15.6.2-23	FLECHT 05132 Rod Temperatures at 72-inch Elevation 15-174
Figure 15.6.2-24	FLECHT 05132 Rod Temperatures at 78-inch Elevation 15-174
Figure 15.6.2-25	FLECHT 05132 Rod Temperatures at 84-inch Elevation 15-175
Figure 15.6.2-26	FLECHT 05132 Rod Temperatures at 96-inch Elevation 15-175
Figure 15.6.2-27	FLECHT 05132 Rod Temperatures at 120-inch Elevation 15-176
Figure 15.6.2-28	Comparison of Predicted and Estimated Quench Front Elevations for FLECHT 05132

•	
Figure 15.6.2-29	Comparison of Predicted and Measured Axial Temperature Profile for FLECHT 05132 at 50 Seconds
Figure 15.6.2-30	Comparison of Predicted and Measured Axial Temperature Profile for FLECHT 05132 at 100 Seconds
Figure 15.6.2-31	Comparison of Predicted and Measured Maximum Cladding Temperatures at all Code Uncertainty Elevations for FLECHT 05132
Figure 15.6.2-32	FLECHT 05132 Bundle Lower Half ΔP 15-179
Figure 15.6.2-33	FLECHT 05132 Bundle Upper Half ΔP 15-179
Figure 15.6.2-34	FLECHT 05132 Overall ΔP
Figure 15.6.2-35	FLECHT 05132 Vapor Temperatures at 84-inch Elevation 15-180
Figure 15.6.2-36	FLECHT 05132 Vapor Temperatures near 120-inch Elevation 15-181
Figure 15.6.2-37	FLECHT 05132 Vapor Temperatures near Bundle Exit 15-181
Figure 15.6.2-38	FLECHT 04641 Rod Temperatures at 24-inch Elevation 15-182
Figure 15.6.2-39	FLECHT 04641 Rod Temperatures at 48-inch Elevation 15-182
Figure 15.6.2-40	FLECHT 04641 Rod Temperatures at 72-inch Elevation 15-183
Figure 15.6.2-41	FLECHT 04641 Rod Temperatures at 78-inch Elevation 15-183
Figure 15.6.2-42	FLECHT 04641 Rod Temperatures at 84-inch Elevation
Figure 15.6.2-43	FLECHT 04641 Rod Temperatures at 96-inch Elevation
Figure 15.6.2-44	FLECHT 04641 Rod Temperatures at 120-inch Elevation 15-185
Figure 15.6.2-45	Comparison of Predicted and Estimated Quench Front Elevations for FLECHT 0464115-185
Figure 15.6.2-46	Comparison of Predicted and Measured Axial Temperature Profile for FLECHT 04641 at 50 Seconds15-186
Figure 15.6.2-47	Comparison of Predicted and Measured Axial Temperature Profile for FLECHT 04641 at 100 Seconds15-186
Figure 15.6.2-48	Comparison of Predicted and Measured Maximum Cladding Temperatures at all Code Uncertainty Elevations for FLECHT 04641
Figure 15.6.2-49	FLECHT 04641 Bundle Lower Half ΔP15-188
Figure 15.6.2-50	FLECHT 04641 Bundle Upper Half ΔP 15-188
Figure 15.6.2-51	FLECHT 04641 Overall ΔP
Figure 15.6.2-52	FLECHT 04641 Vapor Temperatures at 84-inch Elevation 15-189
Figure 15.6.2-53	FLECHT 04641 Vapor Temperatures near 120-inch Elevation 15-190

Figure 15.6.2-54	FLECHT 04641 Vapor Temperatures near Bundle Exit	. 15-190
Figure 15.6.2-55	FLECHT 0791 Cladding Temperature at 24 inches	. 15-191
Figure 15.6.2-56	FLECHT 0791 Cladding Temperature at 48 inches	. 15-191
Figure 15.6.2-57	FLECHT 0791 Cladding Temperature at 72 inches	. 15-192
Figure 15.6.2-58	FLECHT 0791 Cladding Temperature at 96 inches	. 15-192
Figure 15.6.2-59	FLECHT 0791 Cladding Temperature at 120 inches	. 15-193
Figure 15.6.2-60	FLECHT 0791 Quench Front Progression	. 15-193
Figure 15.6.2-61	Maximum Cladding Temperature Comparison	. 15-194
Figure 15.6.2-62	FLECHT 0791 Differential Pressure 0-2 ft	. 15-194
Figure 15.6.2-63	FLECHT 0791 Differential Pressure 0-4 ft	. 15-195
Figure 15.6.2-64	FLECHT 0791 Differential Pressure 0-6 ft	. 15-195
Figure 15.6.2-65	FLECHT 0791 Differential Pressure 0-8 ft	. 15-196
Figure 15.6.2-66	Comparison of Predicted and Measured Clad Temperatures for FLECHT Low Flooding Rate Simulations	. 15-196
Figure 15.6.3-1	WCOBRA/TRAC-TF2 Transverse Noding for FLECHT Top-Skewed Test Bundle	. 15-203
Figure 15.6.3-2	WCOBRA/TRAC-TF2 Axial Noding for FLECHT Top-Skewed Test Bundle	. 15-204
Figure 15.6.3-3	<u>W</u> COBRA/TRAC-TF2 Axial Power Shape for FLECHT Top-Skewed Test Bundle	. 15-205
Figure 15.6.3-4	FLECHT 15305 Rod Temperatures at 24-inch Elevation	. 15-206
Figure 15.6.3-5	FLECHT 15305 Rod Temperatures at 48-inch Elevation	. 15-206
Figure 15.6.3-6	FLECHT 15305 Rod Temperatures at 72-inch Elevation	. 15-207
Figure 15.6.3-7	FLECHT 15305 Rod Temperatures at 96-inch Elevation	. 15-207
Figure 15.6.3-8	FLECHT 15305 Rod Temperatures at 120-inch Elevation	. 15-208
Figure 15.6.3-9	FLECHT 15305 Rod Temperatures at 126-inch Elevation	. 15-208
Figure 15.6.3-10	FLECHT 15305 Rod Temperatures at 132-inch Elevation	. 15-209
Figure 15.6.3-11	Comparison of Predicted and Estimated Quench Front Elevations for FLECHT 15305	. 15-209
Figure 15.6.3-12	Comparison of Predicted and Measured Axial Temperature Profile for FLECHT 15305 at 100 Seconds	. 15-210

lxii

Figure 15.6.3-13	Comparison of Predicted and Measured Axial Temperature Profile for FLECHT 15305 at 300 Seconds	0
Figure 15.6.3-14	Comparison of Predicted and Measured Maximum Cladding Temperatures at all Code Uncertainty Elevations for FLECHT 1530515-21	1
Figure 15.6.3-15	FLECHT 15305 Bundle Lower Half ΔP	2
Figure 15.6.3-16	FLECHT 15305 Bundle Upper Half ΔP 15-21	2
Figure 15.6.3-17	FLECHT 15305 Overall ΔP	3
Figure 15.6.3-18	FLECHT 15305 Vapor Temperatures at 84-inch Elevation 15-21	3
Figure 15.6.3-19	FLECHT 15305 Vapor Temperatures at 120-inch Elevation 15-21	4
Figure 15.6.3-20	FLECHT 15305 Vapor Temperatures at 132-inch Elevation 15-21	4
Figure 15.6.3-21	FLECHT 13812 Rod Temperatures at 24-inch Elevation 15-21	5
Figure 15.6.3-22	FLECHT 13812 Rod Temperatures at 48-inch Elevation 15-21	5
Figure 15.6.3-23	FLECHT 13812 Rod Temperatures at 72-inch Elevation 15-21	6
Figure 15.6.3-24	FLECHT 13812 Rod Temperatures at 96-inch Elevation	6
Figure 15.6.3-25	FLECHT 13812 Rod Temperatures at 120-inch Elevation	7
Figure 15.6.3-26	FLECHT 13812 Rod Temperatures at 126-inch Elevation	7
Figure 15.6.3-27	FLECHT 13812 Rod Temperatures at 132-inch Elevation 15-21	8
Figure 15.6.3-28	Comparison of Predicted and Estimated Quench Front Elevations for FLECHT 13812	8
Figure 15.6.3-29	Comparison of Predicted and Measured Axial Temperature Profile for FLECHT 13812 at 100 Seconds	9
Figure 15.6.3-30	Comparison of Predicted and Measured Axial Temperature Profile for FLECHT 13812 at 300 Seconds	9
Figure 15.6.3-31	Comparison of Predicted and Measured Maximum Cladding Temperatures at all Code Uncertainty Elevations for FLECHT 13812 15-22	0
Figure 15.6.3-32	FLECHT 13812 Bundle Lower Half ΔP	1 ·
Figure 15.6.3-33	FLECHT 13812 Bundle Upper Half ΔP	1
Figure 15.6.3-34	FLECHT 13812 Overall ΔP	2
Figure 15.6.3-35	FLECHT 13812 Vapor Temperatures at 84-inch Elevation	2
Figure 15.6.3-36	FLECHT 13812 Vapor Temperatures near 120-inch Elevation 15-22	3
Figure 15.6.3-37	FLECHT 13812 Vapor Temperatures at 132-inch Elevation 15-22	3

Figure 15.6.3-38	FLECHT 15713 Rod Temperatures at 24-inch Elevation	15-224
Figure 15.6.3-39	FLECHT 15713 Rod Temperatures at 48-inch Elevation	15-224
Figure 15.6.3-40	FLECHT 15713 Rod Temperatures at 72-inch Elevation	15-225
Figure 15.6.3-41	FLECHT 15713 Rod Temperatures at 96-inch Elevation	15-225
Figure 15.6.3-42	FLECHT 15713 Rod Temperatures at 120-inch Elevation	15-226
Figure 15.6.3-43	FLECHT 15713 Rod Temperatures at 126-inch Elevation	15-226
Figure 15.6.3-44	FLECHT 15713 Rod Temperatures at 132-inch Elevation	15-227
Figure 15.6.3-45	Comparison of Predicted and Estimated Quench Front Elevations for FLECHT 15713	15-227
Figure 15.6.3-46	Comparison of Predicted and Measured Axial Temperature Profile for FLECHT 15713 at 100 Seconds	15-228
Figure 15.6.3-47	Comparison of Predicted and Measured Axial Temperature Profile for FLECHT 15713 at 300 Seconds	15-228
Figure 15.6.3-48	Comparison of Predicted and Measured Maximum Cladding Temperatur at all Code Uncertainty Elevations for FLECHT 15713	
Figure 15.6.3-49	FLECHT 15713 Bundle Lower Half ΔP	15-230
Figure 15.6.3-50	FLECHT 15713 Bundle Upper Half ΔP	15-230
Figure 15.6.3-51	FLECHT 15713 Overall ΔP	15-231
Figure 15.6.3-52	FLECHT: 15713 Vapor Temperatures at 84-inch Elevation	15-231
Figure 15.6.3-53	FLECHT 15713 Vapor Temperatures near 120-inch Elevation	15-232
Figure 15.6.3-54	FLECHT 15713 Vapor Temperatures at 132-inch Elevation	15-232
Figure 15.6.3-55	FLECHT 13914 Rod Temperatures at 24-inch Elevation	15-233
Figure 15.6.3-56	FLECHT 13914 Rod Temperatures at 48-inch Elevation	15-233
Figure 15.6.3-57	FLECHT 13914 Rod Temperatures at 72-inch Elevation	15-234
Figure 15.6.3-58	FLECHT 13914 Rod Temperatures at 96-inch Elevation	15-234
Figure 15.6.3-59	FLECHT 13914 Rod Temperatures at 120-inch Elevation	15-235
Figure 15.6.3-60	FLECHT 13914 Rod Temperatures at 126-inch Elevation	15-235
Figure 15.6.3-61	FLECHT 13914 Rod Temperatures at 132-inch Elevation	15-236
Figure 15.6.3-62	Comparison of Predicted and Estimated Quench Front Elevations for FLECHT 13914	15-236

Figure 15.6.3-63	Comparison of Predicted and Measured Axial Temperature Profile for FLECHT 13914 at 100 Seconds	15-237
Figure 15.6.3-64	Comparison of Predicted and Measured Axial Temperature Profile for FLECHT 13914 at 300 Seconds	15-237
Figure 15.6.3-65	Comparison of Predicted and Measured Maximum Cladding Temperatures at all Code Uncertainty Elevations for FLECHT 13914	
Figure 15.6.3-66	FLECHT 13914 Bundle Lower Half ΔP	15-239
Figure 15.6.3-67	FLECHT 13914 Bundle Upper Half ΔP	15-239
Figure 15.6.3-68	FLECHT 13914 Overall ΔP	15-240
Figure 15.6.3-69	FLECHT 13914 Vapor Temperatures at 84-inch Elevation	15-240
Figure 15.6.3-70	FLECHT 13914 Vapor Temperatures at 120-inch Elevation	15-241
Figure 15.6.3-71	FLECHT 13914 Vapor Temperatures at 132-inch Elevation	15-241
Figure 15.6.3-72	FLECHT 13609 Rod Temperatures at 24-inch Elevation	15-242
Figure 15.6.3-73	FLECHT 13609 Rod Temperatures at 48-inch Elevation	15-242
Figure 15.6.3-74	FLECHT 13609 Rod Temperatures at 72-inch Elevation	15-243
Figure 15.6.3-75	. FLECHT 13609 Rod Temperatures at 96-inch Elevation	15-243
Figure 15.6.3-76	FLECHT 13609 Rod Temperatures at 120-inch Elevation	15-244
Figure 15.6.3-77	FLECHT 13609 Rod Temperatures at 126-inch Elevation	15-244
Figure 15.6.3-78	FLECHT 13609 Rod Temperatures at 132-inch Elevation	15-245
Figure 15.6.3-79	Comparison of Predicted and Estimated Quench Front Elevations for FLECHT 13609	15-245
Figure 15.6.3-80	Comparison of Predicted and Measured Axial Temperature Profile for FLECHT 13609 at 100 Seconds	15-246
Figure 15.6.3-81	Comparison of Predicted and Measured Axial Temperature Profile for FLECHT 13609 at 300 Seconds	15-246
Figure 15.6.3-82	Comparison of Predicted and Measured Maximum Cladding Temperatures at all Code Uncertainty Elevations for FLECHT 13609	15-247
Figure 15.6.3-83	FLECHT 13609 Bundle Lower Half ΔP	15-248
Figure 15.6.3-84	FLECHT 13609 Bundle Upper Half ΔP	15-248
Figure 15.6.3-85	FLECHT 13609 Overall ΔP	15-249
Figure 15.6.3-86	FLECHT 13609 Vapor Temperatures at 84-inch Elevation	15-249
Figure 15.6.3-87	FLECHT 13609 Vapor Temperatures at 120-inch Elevation	15-250

Figure 15.6.3-88	FLECHT 13609 Vapor Temperatures at 132-inch Elevation
Figure 15.6.3-89	Comparison of Predicted and Measured Maximum Clad Temperatures for FLECHT Top-Skewed Power Test Simulations
Figure 15.6.4-1	WCOBRA/TRAC-TF2 Axial Noding for G-2 Reflood Simulations 15-256
Figure 15.6.4-2	WCOBRA/TRAC-TF2 Transverse Noding for G-2 Reflood Simulations 15-257
Figure 15.6.4-3	G-2 Bundle Cross Section
Figure 15.6.4-4	G-2 Reflood Test 550 Rod Temperatures at 29-inch Elevation 15-259
Figure 15.6.4-5	G-2 Reflood Test 550 Rod Temperatures at 45-inch Elevation 15-259
Figure 15.6.4-6	G-2 Reflood Test 550 Rod Temperatures at 70-inch Elevation 15-260
Figure 15.6.4-7	G-2 Reflood Test 550 Rod Temperatures at 82-inch Elevation 15-260
Figure 15.6.4-8	G-2 Reflood Test 550 Rod Temperatures at 94-inch Elevation 15-261
Figure 15.6.4-9	G-2 Reflood Test 550 Rod Temperatures at 111-inch Elevation
Figure 15.6.4-10	G-2 Reflood Test 550 Rod Temperatures at 135-inch Elevation 15-262
Figure 15.6.4-11	Axial Temperature Profile for G-2 Reflood Test 550 at 57 Seconds 15-262
Figure 15.6.4-12	Axial Temperature Profile for G-2 Reflood Test 550 at 87 Seconds 15-263
Figure 15.6.4-13	Axial Temperature Profile for G-2 Reflood Test 550 at 137 Seconds 15-263
Figure 15.6.4-14	G-2 Reflood Test 550 Bundle Lower Half ΔP 15-264
Figure 15.6.4-15	G-2 Reflood Test 550 Bundle Upper Half ΔP
Figure 15.6.4-16	G-2 Reflood Test 550 Overall ΔP 15-265
Figure 15.6.4-17	G-2 Reflood Test 550 Vapor Temperatures near 109-inch Elevation 15-265
Figure 15.6.4-18	G-2 Reflood Test 550 Vapor Temperatures at 137-inch Elevation 15-266
Figure 15.6.4-19	Maximum Cladding Temperatures for G-2 Reflood Test 550 15-266
Figure 15.6.4-20	G-2 Reflood Test 562 Rod Temperatures at 29-inch Elevation 15-267
Figure 15.6.4-21	G-2 Reflood Test 562 Rod Temperatures at 45-inch Elevation 15-267
Figure 15.6.4-22	G-2 Reflood Test 562 Rod Temperatures at 70-inch Elevation 15-268
Figure 15.6.4-23	G-2 Reflood Test 562 Rod Temperatures at 82-inch Elevation 15-268
Figure 15.6.4-24	G-2 Reflood Test 562 Rod Temperatures at 94-inch Elevation
Figure 15.6.4-25	G-2 Reflood Test 562 Rod Temperatures at 111-inch Elevation 15-269
Figure 15.6.4-26	G-2 Reflood Test 562 Rod Temperatures at 135-inch Elevation 15-270
Figure 15.6.4-27	Axial Temperature Profile for G-2 Reflood Test 562 at 34 Seconds 15-270

WCAP-16996-NP

L

.

Eigung 15 6 4 29	Avial Temperature Drafile for C. 2 Defled Test 562 at 64 Seconds 15 271
Figure 15.6.4-28	Axial Temperature Profile for G-2 Reflood Test 562 at 64 Seconds
Figure 15.6.4-29	Axial Temperature Profile for G-2 Reflood Test 562 at 114 Seconds 15-271
Figure 15.6.4-30	G-2 Reflood Test 562 Bundle Lower Half ΔP 15-272
Figure 15.6.4-31	G-2 Reflood Test 562 Bundle Upper Half ΔP 15-272
Figure 15.6.4-32	G-2 Reflood Test 562 Overall ΔP
Figure 15.6.4-33	G-2 Reflood Test 562 Vapor Temperatures near 109-inch Elevation 15-273
Figure 15.6.4-34	G-2 Reflood Test 562 Vapor Temperatures at 137-inch Elevation 15-274
Figure 15.6.4-35	Maximum Cladding Temperatures for G-2 Reflood Test 562 15-274
Figure 15.6.4-36	G-2 Reflood Test 568 Rod Temperatures at 29-inch Elevation
Figure 15.6.4-37	G-2 Reflood Test 568 Rod Temperatures at 45-inch Elevation 15-275
Figure 15.6.4-38	G-2 Reflood Test 568 Rod Temperatures at 70-inch Elevation 15-276
Figure 15.6.4-39	G-2 Reflood Test 568 Rod Temperatures at 82-inch Elevation 15-276
Figure 15.6.4-40	G-2 Reflood Test 568 Rod Temperatures at 94-inch Elevation 15-277
Figure 15.6.4-41	G-2 Reflood Test 568 Rod Temperatures at 111-inch Elevation 15-277
Figure 15.6.4-42	G-2 Reflood Test 568 Rod Temperatures at 135-inch Elevation 15-278
Figure 15.6.4-43	Axial Temperature Profile for G-2 Reflood Test 568 at 49 Seconds 15-278
Figure 15.6.4-44	Axial Temperature Profile for G-2 Reflood Test 568 at 79 Seconds 15-279
Figure 15.6.4-45	Axial Temperature Profile for G-2 Reflood Test 568 at 129 Seconds 15-279
Figure 15.6.4-46	G-2 Reflood Test 568 Bundle Lower Half ΔP 15-280
Figure 15.6.4-47	G-2 Reflood Test 568 Bundle Upper Half ΔP 15-280
Figure 15.6.4-48	G-2 Reflood Test 568 Overall ∆P15-281
Figure 15.6.4-49	G-2 Reflood Test 568 Vapor Temperatures near 109-inch Elevation 15-281
Figure 15.6.4-50	G-2 Reflood Test 568 Vapor Temperatures at 137-inch Elevation 15-282
Figure 15.6.4-51	Maximum Cladding Temperatures for G-2 Reflood Test 568 15-282
Figure 15.6.4-52	Predicted and Measured Maximum Cladding Temperatures for G-2 Reflood Test Simulations
Figure 15.6.5-1	WCOBRA/TRAC-TF2 Transverse Noding for FEBA 15-287
Figure 15.6.5-2	WCOBRA/TRAC-TF2 Axial Noding for FEBA 15-288
Figure 15.6.5-3	Rod Temperatures for FEBA Test 223 at 2770 mm Reference Elevation 15-289
Figure 15.6.5-4	Rod Temperatures for FEBA Test 223 at 2225 mm Reference Elevation 15-289

Figure 15.6.5-5	Rod Temperatures for FEBA Test 223 at 2125 mm Reference Elevation 15-290
Figure 15.6.5-6	Rod Temperatures for FEBA Test 223 at 2025 mm Reference Elevation 15-290
Figure 15.6.5-7	Rod Temperatures for FEBA Test 223 at 1925 mm Reference Elevation 15-291
Figure 15.6.5-8	Rod Temperatures for FEBA Test 223 at 1625 mm Reference Elevation 15-291
Figure 15.6.5-9	Rod Temperatures for FEBA Test 223 at 1135 mm Reference Elevation 15-292
Figure 15.6.5-10	Comparison of Predicted and Measured Axial Temperature Profiles for FEBA Test 223 at 75 Seconds
Figure 15.6.5-11	Comparison of Predicted and Measured Axial Temperature Profiles for FEBA Test 223 at 150 Seconds
Figure 15.6.5-12	Rod Temperatures for FEBA Test 234 at 2770 mm Reference Elevation 15-294
Figure 15.6.5-13	Rod Temperatures for FEBA Test 234 at 2225 mm Reference Elevation 15-294
Figure 15.6.5-14	Rod Temperatures for FEBA Test 234 at 2125 mm Reference Elevation 15-295
Figure 15.6.5-15	Rod Temperatures for FEBA Test 234 at 2025 mm Reference Elevation 15-295
Figure 15.6.5-16	Rod Temperatures for FEBA Test 234 at 1925 mm Reference Elevation 15-296
Figure 15.6.5-17	Rod Temperatures for FEBA Test 234 at 1625 mm Reference Elevation 15-296
Figure 15.6.5-18	Rod Temperatures for FEBA Test 234 at 1135 mm Reference Elevation 15-297
Figure 15.6.5-19	Comparison of Predicted and Measured Axial Temperature Profiles for FEBA Test 234 at 75 Seconds
Figure 15.6.5-20	Comparison of Predicted and Measured Axial Temperature Profiles for FEBA Test 234 at 150 Seconds
Figure 15.6.5-21	Rod Temperatures for FEBA Test 216 at 2770 mm Reference Elevation 15-299
Figure 15.6.5-22	Rod Temperatures for FEBA Test 216 at 2225 mm Reference Elevation 15-299
Figure 15.6.5-23	Rod Temperatures for FEBA Test 216 at 2125 mm Reference Elevation 15-300
Figure 15.6.5-24	Rod Temperatures for FEBA Test 216 at 2025 mm Reference Elevation 15-300
Figure 15.6.5-25	Rod Temperatures for FEBA Test 216 at 1925 mm Reference Elevation 15-301
Figure 15.6.5-26	Rod Temperatures for FEBA Test 216 at 1625 mm Reference Elevation 15-301
Figure 15.6.5-27	Rod Temperatures for FEBA Test 216 at 1135 mm Reference Elevation 15-302
Figure 15.6.5-28	Comparison of Predicted and Measured Axial Temperature Profiles for FEBA Test 216 at 75 Seconds
Figure 15.6.5-29	Comparison of Predicted and Measured Axial Temperature Profiles for FEBA Test 216 at 150 Seconds

Figure 15.6.5-30	Rod Temperatures for FEBA Test 229 at 2770 mm Reference Elevation 15-304
Figure 15.6.5-31	Rod Temperatures for FEBA Test 229 at 2225 mm Reference Elevation 15-304
Figure 15.6.5-32	Rod Temperatures for FEBA Test 229 at 2125 mm Reference Elevation 15-305
Figure 15.6.5-33	Rod Temperatures for FEBA Test 229 at 2025 mm Reference Elevation 15-305
Figure 15.6.5-34	Rod Temperatures for FEBA Test 229 at 1925 mm Reference Elevation 15-306
Figure 15.6.5-35	Rod Temperatures for FEBA Test 229 at 1625 mm Reference Elevation 15-306
Figure 15.6.5-36	Rod Temperatures for FEBA Test 229 at 1135 mm Reference Elevation 15-307
Figure 15.6.5-37	Comparison of Predicted and Measured Axial Temperature Profiles for FEBA Test 229 at 75 Seconds
Figure 15.6.5-38	Comparison of Predicted and Measured Axial Temperature Profiles for FEBA Test 229 at 150 Seconds
Figure 15.6.5-39	Comparison of Predicted and Measured Maximum Clad Temperatures for FEBA Simulations
Figure 15.7-1	Temperature Profile Near a Spacer Grid from FEBA 223 15-313
Figure 15.7-2	Temperature Profile Near a Spacer Grid from ORNL Test M 15-313
Figure 15.7-3	Temperature Profile Near a Spacer Grid from ORNL Test N 15-314
Figure 15.8-1	Peak Cladding Temperature Comparison for FLECHT Test 31701 15-316
Figure 15.8-2	Quench Front Progression Comparison for FLECHT Test 31701 15-316
Figure 15.8-3	Peak Cladding Temperature Comparison for FLECHT Test 31805 15-317
Figure 15.8-4	Quench Front Progression Comparison for FLECHT Test 31805 15-317
Figure 15.9.1-1	Blowdown Cooling Rates for the G-1 Blowdown Heat Transfer Tests 15-322
Figure 15.9.1-2	Comparison of Predicted and Measured Quench Times in the G-1 Blowdown Heat Transfer Tests
Figure 15.9.1-3	Comparison of Predicted and Measured Clad Temperatures for the G-2 Refill Tests
Figure 15.9.1-4	Comparison of Predicted and Measured Maximum Clad Temperatures for all Reflood Separate Effects Tests Simulated
Figure 15.9.1-5	Comparison of Predicted and Measured Quench Times for the FLECHT SEASET Reflood Separate Effects Tests Simulated
Figure 15.9.1-6	Comparison of Predicted and Measured Quench Times for the FLECHT Low Flooding Rate Reflood Separate Effects Tests Simulated

x

Figure 15.9.1-7	Comparison of Predicted and Measured Quench Times for the FLECHT Skewed Reflood Separate Effects Tests Simulated	5-325
Figure 15.9.1-8	Comparison of Predicted and Measured Turn-Around Times for Each Reflood Separate Effects Tests Simulated1	5-325
Figure 15.9.1-9	Comparison of Predicted and Measured Time above 1600°F for the FLECHT Reflood Separate Effects Tests Simulated1	5-326
Figure 15.9.2-1	WCOBRA/TRAC-TF2 Film Boiling Model Components 1	5-333
Figure 15.9.2-2	Calculated Mass Flows as a Function of Elevation for G-1 Test 154 at 10 Seconds into the Test	5-334
Figure 15.9.2-3	Calculated Phase Velocities as a Function of Elevation for G-1 Test 154 at 10 Seconds into the Test 1	5-334
Figure 15.9.2-4	Calculated Volume Fraction as a Function of Elevation for G-1 Test 154 at 10 Seconds into the Test 1	5-335
Figure 15.9.2-5	Calculated Droplet Size as a Function of Elevation for G-1 Test 154 at 10 Seconds into the Test1	5-335
Figure 15.9.2-6	Calculated Droplet (Entrained Phase) Interfacial Surface Area as a Function of Elevation for G-1 Test 154 at 10 Seconds into the Test 1	5-336
Figure 15.9.2-7	Calculated Heater Rod Surface Temperature, Spacer Grid Temperature, and Vapor Temperature as a Function of Elevation for G-1 Test 154 at 10 Seconds into the Test	.5-336
Figure 15.9.2-8	Calculated Heater Rod Surface Heat Flux and Heat Transfer Mode as a Function of Elevation for G-1 Test 154 at 10 Seconds into the Test 1	5-337
Figure 15.9.2-9	Calculated Mass Flowrates as a Function of Elevation for ORNL Test 3.08.6C at 59.5 Seconds into the Test	5-337
Figure 15.9.2-10	Calculated Phase Velocities as a Function of Elevation for ORNL Test 3.08.6C at 59.5 Seconds into the Test1	5-338
Figure 15.9.2-11	Calculated Phase Volume Fraction as a Function of Elevation for ORNL Test 3.08.6C at 59.5 Seconds into the Test1	5-338
Figure 15.9.2-12	Calculated Droplet Diameter as a Function of Elevation for ORNL Test 3.08.6C at 59.5 Seconds into the Test1	5-339
Figure 15.9.2-13	Calculated Droplet Interfacial Area as a Function of Elevation for ORNL Test 3.08.6C at 59.5 Seconds into the Test1	5-339
Figure 15.9.2-14	Calculated Heater Rod Surface Temperature, Spacer Grid Temperature, and Vapor Temperature as a Function of Elevation for ORNL Test 3.08.6C at 59.5 Seconds into the Test	5-340

Figure 15.9.2-15	Calculated Heater Rod Surface Heat Flux and Heat Transfer Mode as a Function of Elevation for ORNL Test 3.08.6C at 59.5 Seconds into the Test 15-340
Figure 15.9.2-16	Calculated Mass Flowrate of Each Phase as a Function of Elevation for FLECHT SEASET Test 31701 at 10 Seconds into the Test
Figure 15.9.2-17	Calculated Vapor and Entrained (Droplet) Velocities as a Function of Elevation for FLECHT SEASET Test 31701 at 10 Seconds into the Test 15-341
Figure 15.9.2-18	Calculated Phase Volume Fractions as a Function of Elevation for FLECHT SEASET Test 31701 at 10 Seconds into the Test
Figure 15.9.2-19	Calculated Heater Rod Surface Temperature, Spacer Grid Temperature, and Vapor Temperature as a Function of Elevation for FLECHT SEASET Test 31701 at 10 Seconds into the Test
Figure 15.9.2-20	Calculated Heater Rod Heat Flux as a Function of Elevation for FLECHT SEASET Test 31701 at 10 Seconds into the Test
Figure 15.9.2-21	Calculated Net Vapor Generation Rate as a Function of Elevation for FLECHT SEASET Test 31701 at 10 Seconds into the Test
Figure 15.9.2-22	Comparison of Calculated Droplet Size and Drop Velocity at the Three-Foot Elevation with FLECHT SEASET Test Data for Test 31701 (1 - 10 s)
Figure 15.9.2-23	Comparison of Calculated Droplet Size and Drop Velocity at the Nine-Foot Elevation with FLECHT SEASET Test Data for Test 31701 (1 - 10 s)
Figure 15.9.2-24	Calculated Droplet Diameter as a Function of Elevation for FLECHT SEASET Test 31701 at 10 Seconds into the Transient
Figure 15.9.2-25	Calculated Droplet Interfacial Area/Volume as a Function of Elevation for FLECHT SEASET Test 31701 at 10 Seconds into the Test
Figure 15.9.2-26	Comparison of Calculated Droplet Size Frequency for FLECHT SEASET Test 31701 (Results are from the 9-foot Elevation for 1 to 8 Seconds
Figure 15.9.2-27	Calculated Mass Flow for Each Phase as a Function of Elevation for FLECHT SEASET Test 31805 at 100 Seconds into the Test
Figure 15.9.2-28	Calculated Phase Velocities as a Function of Elevation for FLECHT SEASET Test 31805 at 100 Seconds into the Test
Figure 15.9.2-29	Calculated Phase Void Fractions for Each Phase as a Function of Elevation for FLECHT SEASET Test 31805 at 100 Seconds into the Transient
Figure 15.9.2-30	Calculated Net Vapor Generation as a Function of Elevation for FLECHT SEASET Test 31805 at 100 Seconds into the Transient

ø

Figure 15.9.2-31	Calculated Heater Rod Surface Temperature, Spacer Grid Temperature, and Vapor Temperature as a Function of Elevation for FLECHT SEASET Test 31805 at 100 Seconds into the Test
Figure 15.9.2-32	Calculated Heater Rod Surface Heat Flux as a Function of Elevation for FLECHT SEASET Test 31805 at 100 Seconds into the Test
Figure 15.9.2-33	Calculated Droplet Diameter as a Function of Elevation for FLECHT SEASET Test 31805 at 100 Seconds into the Test
Figure 15.9.2-34	Calculated Droplet Interfacial Surface Area/Volume as a Function of Elevation for FLECHT SEASET Test 31805 at 100 Seconds into the Test 15-350
Figure 15.9.2-35	Comparison of Calculated Drop Size and Velocities with FLECHT SEASET Test Data for Test 31805 at 6 ft $(30 - 40 s)$
Figure 15.9.3-1	Effect of Flooding Rate on Heat Transfer Coefficient as Determined from Experimental Data (Lee et al., 1982)
Figure 15.9.3-2	Predicted Effect of Flooding Rate on Heat Transfer Coefficient 15-357
Figure 15.9.3-3	Effect of Flooding Rate on Clad Temperature at the 72-inch Elevation as Determined from Experimental Data (Lee et al., 1982)
Figure 15.9.3-4	Predicted Effect of Flooding Rate on Clad Temperature at the 72-inch Elevation
Figure 15.9.3-5	Effect of Flooding Rate on Quench Front Advance as Determined from Experimental Data (Lee et al., 1982)
Figure 15.9.3-6	Predicted Effect of Flooding Rate on Quench Front Advance
Figure 15.9.3-7	Effect of Pressure on Heat Transfer Coefficient as Determined from Experimental Data (Lee et al., 1982)
Figure 15.9.3-8	Predicted Effect of Pressure on Heat Transfer Coefficient
Figure 15.9.3-9	Predicted Effect of Pressure on Heat Transfer Coefficient (FLECHT Low Flooding Rate)
Figure 15.9.3-10	Effect of Pressure on Clad Temperature at the 72-inch Elevation as Determined from Experimental Data (Lee et al., 1982)
Figure 15.9.3-11	Predicted Effect of Pressure on Clad Temperature at the 72-inch Elevation (FLECHT SEASET)
Figure 15.9.3-12	Predicted Effect of Pressure on Clad Temperature at the 72-inch Elevation (FLECHT Low Flooding Rate)
Figure 15.9.3-13	Effect of Pressure on Quench Front Advance as Determined from Experimental Data (Lee et al., 1982)

.

Predicted Effect of Pressure on Quench Front Advance (FLECHT SEASET)
Effect of Pressure on Quench Front Advance (FLECHT Low Flooding Rate)
Effect of Subcooling on Temperature Rise and Quench Time as Determined from Experimental Data (Lee et al., 1982)
Comparison of Clad Temperatures at 6-ft. and <u>W</u> COBRA/TRAC-TF2 Prediction of Sensitivity to Inlet Subcooling in FLECHT SEASET 15-367
Comparison of Quench Times at 6-ft. and <u>W</u> COBRA/TRAC-TF2 Prediction of Sensitivity to Inlet Subcooling in FLECHT SEASET 15-367
Comparison of Clad Temperatures at 6-ft. and <u>WCOBRA/TRAC-TF2</u> Prediction of Sensitivity to Inlet Subcooling in FLECHT LFR Facility
Comparison of Quench Times at 6-ft. and <u>W</u> COBRA/TRAC-TF2 Prediction of Sensitivity to Inlet Subcooling in FLECHT LFR Facility
Comparison of Clad Temperatures at 10-ft. and <u>W</u> COBRA/TRAC-TF2 Prediction of Sensitivity to Inlet Subcooling in FLECHT Skewed Power Facility
Comparison of Quench Times at 10-ft. and <u>W</u> COBRA/TRAC-TF2 Prediction of Sensitivity to Inlet Subcooling in FLECHT Skewed Power Facility
The Schematic Plot of the TPTF Facility (Nakamura et al., 1983) 16-15
T Shaped Mixers used in TPTF (Anoda et al., 1989) 16-16
Test Section and Measurement Instruments (Kawaji et al., 1987) 16-17
TPTF Test Data on WCOBRA/TRAC-TF2 Flow Regime Map 16-18
WCOBRA/TRAC-TF2 Input Models for TPTF. The Fill Component Corresponds to the Location of L/D=17 in the TPTF Facility
Comparison Between Measured Void Fraction in TPTF Run 722 and Predicted Void Fraction
Comparison Between Measured Void Fraction in TPTF Run 845 and Predicted Void Fraction

] ^{a,c}
Figure 17-1	COSI Facility Arrangement

WCAP-16996-NP

Figure 17-2	Westinghouse COSI Test Section Arrangement
Figure 17-3	Depiction of Flow Patterns in the Test Section as Deduced from Data 17-30
Figure 17-4	Illustration of Condensation in COSI Test Section
Figure 17-5	· []
] ^{a,c}
Figure 17-6	Comparison of Westinghouse Test Section and Framatome Test Section in Cross Section of Cold Leg
Figure 17-7	General Structure of Cold Leg from Crossover Leg to Downcomer in the ROSA Facility
Figure 17-8	Schematics of ECCS Configuration in ROSA IV SB-CL-05 17-35
Figure 17-9	<u>W</u> COBRA/TRAC-TF2 Single TEE Noding Diagram for Westinghouse Vertical COSI, Framatome COSI, and ROSA IV SB-CL-05; for Westinghouse Vertical COSI, the Inclination angle of SI Line is 45°
Figure 17-10	WCOBRA/TRAC-TF2 Two-TEE Noding Diagram for Framatome Inverse COSI Tests
Figure 17-11a	Comparison between Measured Westinghouse COSI Condensation Heat Transfer Rate and <u>W</u> COBRA/TRAC-TF2 Predicted Condensation Heat Transfer Rate
Figure 17-11b	Predicted Heat Transfer Rate for Westinghouse COSI (TEE junction cell is number 4)
Figure 17-12	Comparison between Measured Framatome COSI Condensation Heat Transfer Rate and <u>WCOBRA/TRAC-TF2</u> Predicted Condensation Heat Transfer Rate. Data in Circles Are Tests with High SI Temperature (~80C) 17-40
Figure 17-13	Comparison between Measured ROSA SB-CL-05 SI Condensation Heat Transfer Rate and <u>W</u> COBRA/TRAC-TF2 Predicted Condensation Heat Transfer Rate
Figure 17-14	Steam Temperature Profile in Cold Leg in ROSA Test No. 1
Figure 17-15	Steam Temperature Profile in Cold Leg in ROSA Test No. 2 17-43
Figure 17-16	Steam Temperature Profile in Cold Leg in ROSA Test No. 3
Figure 17-17	Steam Temperature Profile in Cold Leg in ROSA Test No. 4 17-45
Figure 17-18	Comparison between Measured Condensation Heat Transfer Rate and <u>W</u> COBRA/TRAC-TF2 Predicted Condensation Heat Transfer Rate for All Validation Cases
Figure 17-19	Cold Leg Piping Region of UPTF Test Facility 17-47

Figure 17-20	WCOBRA/TRAC-TF2 Single TEE Model for UPTF-8 A 17-48
Figure 17-21	Comparison between Measured Fluid Temperature and <u>W</u> COBRA/TRAC-TF2 Predicted Water Temperature at Pump Exit 17-49
Figure 17-22	Comparison between Measured Fluid Temperature and <u>W</u> COBRA/TRAC-TF2 Predicted Water Temperature near Injection Point 17-50
Figure 17-23	Comparison between Measured Fluid Temperature and <u>W</u> COBRA/TRAC-TF2 Predicted Water Temperature at Downstream of Injection Point
Figure 17-24	Comparison between Measured Fluid Temperature and <u>W</u> COBRA/TRAC-TF2 Predicted Water Temperature at Outlet of Cold Leg 17-52
Figure 17-25	Comparison between the Predicted Water Temperatures at Injection Cell of Cold Leg in ECC Injection Angel Sensitivity Study
Figure 17-26	Comparison between the Predicted Water Temperatures at Downstream Cell of Cold Leg in ECC Injection Angel Sensitivity Study
Figure 17-27	Comparison between the Predicted Water Temperatures at Outlet of Cold Leg in ECC Injection Angel Sensitivity Study
Figure 17-28	Comparison between the Predicted Water Temperatures at Injection Cell of Cold Leg in Cold Leg Noding Sensitivity Study
Figure 17-29	Comparison between the Predicted Water Temperatures at Downstream of Injection Cell in Cold Leg in Cold Leg Noding Sensitivity Study
Figure 17-30	Comparison between the Predicted Water Temperatures at Outlet of Cold leg in Cold Leg Noding Sensitivity Study
Figure 17-31	[] ^{a,c}
Figure 17-32	[] ^{a,c}
Figure 17-33	[] ^{a,c}
Figure 17-34	[] ^{a,c} 17-62
Figure 17-35	[] ^{a,c}
Figure 17-36	
] ^{a,c} 17-64

WCAP-16996-NP

Figure 17-37	[
] ^{a,c}	17-65
Figure 17-38	í l	/
] ^{a,c}	17-66
Figure 18.1-1	Loop Seal Clearing and Refilling	18-3
Figure 18.1-2	Loop Seal Clearing Process	18-4
Figure 18.2.1-1a	Measured Pressure Drop in Broken Loop of ROSA 5% Break (Kumamaru, et al., 1989)	18-6
Figure 18.2.1-1b	Measured Pressure Drop in Broken Loop of ROSA 10% Break (Koizumi and Tasaka, 1988)	18-6
Figure 18.2.2-1	PWS 2.3 U-Tube Test Facility	18-13
Figure 18.2.2-2	Taitel-Dukler Flow Regime Map, Comparing 1/3-Scale Pipe at 14.7 psia and Full-Scale Pipe at 1000 psia	18-14
Figure 18.2.2-3	PWS 2.3 U-Tube Residual Liquid Level Remaining After Test as a Function of Test Gas Flow rate	18-15
Figure 18.2.2-4	PWS 2.3 U-Tube Horizontal and Vertical Leg Average Void Fractions During Test	18-16
Figure 18.2.2-5	PWS 2.3 U-Tube Horizontal Average Void Fraction During Test Compared with Average Void Fraction after Test	18-17
Figure 18.2.2-6	Pressure Difference Across the PWS 2.3 U-Tube	18-18
Figure 18.2.2-7	PWS 2.3 U-Tube Normalized Level and Limit Lines	18-19
Figure 18.2.2-8	PWS 2.3 U-Tube Flow Regimes Observed Under the Limit Line	18-20
Figure 18.2.2-9	Hysteresis in Loop Seal Limit Line	18-21
Figure 18.2.2-10	Effect of Increased Geometric Scale on Limit Lines	18-22
Figure 18.2.2-11	Effect of Increased Pressure and Scale on Limit Lines	18-23
Figure 18.2.2-12	IVO Full-Scale Final Void Fraction and Limit Lines	18-24
Figure 18.2.3-1	UPTF Facility and Single Loop Seal (Liebert and Emmerling, 1998)	18-26
Figure 18.2.3-2	Lines of Constant Gas Velocity Compared to UPTF Data for 3-Bar and 15-Bar Loop Seal Tests	18-27
Figure 18.2.3-3	UPTF and PWS 2.3 Compared to the Ishii Correlation and Data Base	18-28
Figure 18.3-1	WCOBRA/TRAC-TF2 Model of the UPTF Separate Effects Loop Seal Clearing Tests	18-31

Figure 18.3-2	Comparison of <u>W</u> COBRA/TRAC-TF2 Calculations and UPTF Data for the 3-Bar Tests
Figure 18.3-3	Comparison of <u>W</u> COBRA/TRAC-TF2 Calculations Total System Mass for UPTF 3-bar and 15-bar $j_g^* \approx 0.1$ Cases
Figure 18.3-4	Comparison of <u>W</u> COBRA/TRAC-TF2 Calculations and UPTF Data for the 15-Bar Tests
Figure 18.3-5	Comparison of Calculated vs. Measured Residual Liquid Levels
Figure 18.3-6	Calculated Residual Liquid Levels and CCFL Limit (Ku = 3.2) for 1000 psia
Figure 18.3-7a	Measured Pressure Drop for UPTF 3-Bar and 15-Bar Loop Seal Tests (from Liebert and Emmerling, 1998)
Figure 18.3-7b	Calculated Loop Seal Pressure Drop for 3-Bar, 15-Bar, and 1000 psia 18-35
Figure 18.3-8a	Calculated Pressure Drop for 15-Bar and $j_g^* \approx 0.07$
Figure 18.3-8b	Calculated Pressure Drop for 15-Bar and $j_g{}^{*}\approx 0.18\ldots 18{}^{-36}$
Figure 18.3-8c	Calculated Pressure Drop for 15-Bar and $j_g^* \approx 0.32$
Figure 18.3-9a	Comparison of Pressure Drop in Bends for $j_g^* \approx 0.05$ 3-bar Case
Figure 18.3-9b	Comparison of Pressure Dropin Bends for $j_g^* \approx 0.05$ 15-bar Case
Figure 18.3-9c	Comparison of Pressure Dropin Bends for $j_g^* \approx 0.22$ 3-bar Case
Figure 18.3-9d	Comparison of Pressure Dropin Bends for $j_g^* \approx 0.22$ 15-bar Case 18-39
Figure 19.3-1	UPTF Plan View
Figure 19.3-2	UPTF Test Vessel and Primary Loop
Figure 19.3-3	UPTF Reactor Vessel
Figure 19.3-4	UPTF Upper Plenum Structures
Figure 19.3-5	Dummy Fuel Assembly and End Box with Flow Restrictor (A) or Spider (B)
Figure 19.3-6	UPTF Core Simulator Injection Assembly 19-57
Figure 19.3-7	UPTF Steam Generator Simulators and Water Separators
Figure 19.3-8	UPTF System Configuration for Test 6 (MPR-1163) 19-59
Figure 19.3-9	WCOBRA/TRAC-TF2 VESSEL Component Axial View for UPTF Bypass Tests

Figure 19.3-10	WCOBRA/TRAC-TF2 VESSEL Component Sections 1 and 2 for UPTF Bypass Tests	19-61
Figure 19.3-11	WCOBRA/TRAC-TF2 VESSEL Component Sections 3 and 4 for UPTF Bypass Tests	19-62
Figure 19.3-12	WCOBRA/TRAC-TF2 VESSEL Component Sections 5 and 6 for UPTF Bypass Tests	19-63
Figure 19.3-13	WCOBRA/TRAC-TF2 VESSEL Component Sections 7 and 8 for UPTF Bypass Tests	19-64
Figure 19.3-14	WCOBRA/TRAC-TF2 One-Dimensional Component Model for UPTF Test 6	19-65
Figure 19.3-15	Total Core Steam Injection, UPTF Test 6 – Run 131	19-66
Figure 19.3-16	Steam Generator Simulator Steam Injection, UPTF Test 6 - Run 131	19-67
Figure 19.3-17	Intact Loop ECC Injection, UPTF Test 6 – Run 131	19-68
Figure 19.3-18	Measured Absolute Pressures in the Upper Plenum and Downcomer, UPTF Test 6 – Run 131	19-69
Figure 19.3-19	Predicted Absolute Pressures in the Upper Plenum and Downcomer, UPTF Test 6 – Run 131	19-69
Figure 19.3-20	Measured Downcomer Fluid Temperature at Level 21, UPTF Test 6 – Run 131	19-70
Figure 19.3-21	Predicted Downcomer Fluid Temperature at Level 21, UPTF Test 6 – Run 131	19-70
Figure 19.3-22	Measured Downcomer Fluid Temperature at Level 01, UPTF Test 6 – Run 131	19-71
Figure 19.3-23	Predicted Downcomer Fluid Temperature at Level 01, UPTF Test 6 – Run 131	19-71
Figure 19.3-24	Predicted Liquid Flow at Bottom of the Downcomer in Intact Side, UPTFTest 6 – Run 131	19-72
Figure 19.3-25	Predicted Liquid Flow at Bottom of the Downcomer in Broken Side, UPTF Test 6 – Run 131	19-72
Figure 19.3-26	Measured Axial Differential Pressures in Downcomer, UPTF Test 6 – Run 131	19-73
Figure 19.3-27	Predicted Axial Differential Pressures in Downcomer, UPTF Test 6 – Run 131	19-73
Figure 19.3-28	Measured Azimuthal Differential Pressures in Downcomer at Level 06, UPTF Test 6 – Run 131	19-74

Figure 19.3-29	Predicted Azimuthal Differential Pressures in Downcomer at Level 06, UPTF Test 6 – Run 131	'4
Figure 19.3-30	Measured Azimuthal Differential Pressures in Downcomer at Level 22, UPTF Test 6 – Run 131	'5
Figure 19.3-31	Predicted Azimuthal Differential Pressures in Downcomer at Level 22, UPTF Test 6 – Run 131	'5
Figure 19.3-32	Comparison on Differential Pressure in Lower Plenum, UPTF Test 6 – Run 131	'6
Figure 19.3-33	Total Core Steam Injection, UPTF Test 6 – Run 132 19-7	'7
Figure 19.3-34	Steam Generator Simulator Steam Injection, UPTF Test 6 - Run 132 19-7	8
Figure 19.3-35	Intact Loop ECC Injection, UPTF Test 6 – Run 132 19-7	'9
Figure 19.3-36	Measured Absolute Pressures in the Upper Plenum and Downcomer, UPTF Test 6 – Run 132	60
Figure 19.3-37	Predicted Absolute Pressures in the Upper Plenum and Downcomer, UPTF Test 6 – Run 132	50
Figure 19.3-38	Measured Downcomer Fluid Temperature at Level 21, UPTF Test 6 – Run 132	1
Figure 19.3-39	Predicted Downcomer Fluid Temperature at Level 21, UPTF Test 6 – Run 132	1
Figure 19.3-40	Measured Downcomer Fluid Temperature at Level 01, UPTF Test 6 – Run 132 19-8	2
Figure 19.3-41	Predicted Downcomer Fluid Temperature at Level 01, UPTF Test 6 – Run 132	2
Figure 19.3-42	Predicted Liquid Flow at Bottom of the Downcomer in Intact Side, UPTF Test 6 – Run 132	3
Figure 19.3-43	Predicted Liquid Flow at Bottom of the Downcomer in Broken Side, UPTF Test 6 – Run 132	3
Figure 19.3-44	Measured Axial Differential Pressures in Downcomer, UPTF Test 6 – Run 132	4
Figure 19.3-45	Predicted Axial Differential Pressures in Downcomer, UPTF Test 6 – Run 132	4
Figure 19.3-46	Measured Azimuthal Differential Pressures in Downcomer at Level 06, UPTF Test 6 – Run 132	5
Figure 19.3-47	Predicted Azimuthal Differential Pressures in Downcomer at Level 06, UPTF Test 6 – Run 13219-8	5

WCAP-16996-NP

Figure 19.3-48	Measured Azimuthal Differential Pressures in Downcomer at Level 22, UPTF Test 6 – Run 132	9-86
Figure 19.3-49	Predicted Azimuthal Differential Pressures in Downcomer at Level 22, UPTF Test 6 – Run 132	9-86
Figure 19.3-50	Comparison on Differential Pressure in Lower Plenum, UPTF Test 6 – Run 132	9-87
Figure 19.3-51	Total Core Steam Injection, UPTF Test 6 – Run 133 1	9-88
Figure 19.3-52	Steam Generator Simulator Steam Injection, UPTF Test 6 - Run 133 1	9-89
Figure 19.3-53	Intact Loop ECC Injection, UPTF Test 6 – Run 133 1	9-90
Figure 19.3-54	Measured Absolute Pressures in the Upper Plenum and Downcomer, UPTF Test 6 – Run 133	9-91
Figure 19.3-55	Predicted Absolute Pressures in the Upper Plenum and Downcomer, UPTF Test 6 – Run 133	9-91
Figure 19.3-56	Measured Downcomer Fluid Temperature at Level 21, UPTF Test 6 – Run 133	9-92
Figure 19.3-57	Predicted Downcomer Fluid Temperature at Level 21, UPTF Test 6 – Run 133	9-92
Figure 19.3-58	Measured Downcomer Fluid Temperature at Level 01, UPTF Test 6 – Run 133	9-93
Figure 19.3-59	Predicted Downcomer Fluid Temperature at Level 01, UPTF Test 6 – Run 133	9-93
Figure 19.3-60	Predicted Liquid Flow at Bottom of the Downcomer in Intact Side, UPTF Test 6 – Run 133	9-94
Figure 19.3-61	Predicted Liquid Flow at Bottom of the Downcomer in Broken Side, UPTF Test 6 – Run 133	9-94
Figure 19.3-62	Measured Axial Differential Pressures in Downcomer, UPTF Test 6 – Run 133	9-95
Figure 19.3-63	Predicted Axial Differential Pressures in Downcomer, UPTF Test 6 – Run 133	9-95
Figure 19.3-64	Measured Azimuthal Differential Pressures in Downcomer at Level 06, UPTF Test 6 – Run 133	9-96
Figure 19.3-65	Predicted Azimuthal Differential Pressures in Downcomer at Level 06, UPTF Test 6 – Run 133	9-96
Figure 19.3-66	Measured Azimuthal Differential Pressures in Downcomer at Level 22, UPTF Test 6 – Run 133	9-97

WCAP-16996-NP

Figure 19.3-67	Predicted Azimuthal Differential Pressures in Downcomer at Level 22, UPTF Test 6 – Run 133	19-97
Figure 19.3-68	Comparison on Differential Pressure in Lower Plenum, UPTF Test 6 – Run 133	19-98
Figure 19.3-69	Total Core Steam Injection, UPTF Test 6 – Run 135	19-99
Figure 19.3-70	Steam Generator Simulator Steam Injection, UPTF Test 6 - Run 135	19-100
Figure 19.3-71	Intact Loop ECC Injection, UPTF Test 6 – Run 135	19-101
Figure 19.3-72	Measured Absolute Pressures in the Upper Plenum and Downcomer, UPTF Test 6 – Run 135	19-102
Figure 19.3-73	Predicted Absolute Pressures in the Upper Plenum and Downcomer, UPTF Test 6 – Run 135	19-102
Figure 19.3-74	Measured Downcomer Fluid Temperature at Level 21, UPTF Test 6 – Run 135	19-103
Figure 19.3-75	Predicted Downcomer Fluid Temperature at Level 21, UPTF Test 6 – Run 135	19-103
Figure 19.3-76	Measured Downcomer Fluid Temperature at Level 01, UPTF Test 6 – Run 135	19-104
Figure 19.3-77	Predicted Downcomer Fluid Temperature at Level 01, UPTF Test 6 – Run 135	19-104
Figure 19.3-78	Predicted Liquid Flow at Bottom of the Downcomer in Intact Side, UPTF Test 6 – Run 135	19-105
Figure 19.3-79	Predicted Liquid Flow at Bottom of the Downcomer in Broken Side, UPTF Test 6 – Run 135	19-105
Figure 19.3-80	Measured Axial Differential Pressures in Downcomer, UPTF Test 6 – Run 135	19-106
Figure 19.3-81	Predicted Axial Differential Pressures in Downcomer, UPTF Test 6 – Run 135	19-106
Figure 19.3-82	Measured Azimuthal Differential Pressures in Downcomer at Level 06, UPTF Test 6 – Run 135	19-107
Figure 19.3-83	Predicted Azimuthal Differential Pressures in Downcomer at Level 06, UPTF Test 6 – Run 135	19-107
Figure 19.3-84	Measured Azimuthal Differential Pressures in Downcomer at Level 22, UPTF Test 6 – Run 135	19-108
Figure 19.3-85	Predicted Azimuthal Differential Pressures in Downcomer at Level 22, UPTF Test 6 – Run 135	19-108

Figure 19.3-86	Comparison on Differential Pressure in Lower Plenum, UPTF Test 6 – Run 135	19-109
Figure 19.3-87	Total Core Steam Injection, UPTF Test 6 – Run 136	19-110
Figure 19.3-88	Intact Loop ECC Injection, UPTF Test 6 – Run 136	
Figure 19.3-89	Measured Absolute Pressures in the Upper Plenum and Downcomer, UPTF Test 6 – Run 136	
Figure 19.3-90	Predicted Absolute Pressures in the Upper Plenum and Downcomer, UPTF Test 6 – Run 136	
Figure 19.3-91	Measured Downcomer Fluid Temperature at Level 21, UPTF Test 6 – Run 136	
Figure 19.3-92	Predicted Downcomer Fluid Temperature at Level 21, UPTF Test 6 – Run 136	19-113
Figure 19.3-93	Measured Downcomer Fluid Temperature at Level 01, UPTF Test 6 – Run 136	19-114
Figure 19.3-94	Predicted Downcomer Fluid Temperature at Level 01, UPTF Test 6 – Run 136	19-114
Figure 19.3-95	Predicted Liquid Flow at Bottom of the Downcomer in Intact Side, UPTF Test 6 – Run 136	19-115
Figure 19.3-96	Predicted Liquid Flow at Bottom of the Downcomer in Broken Side, UPTF Test 6 – Run 136	
Figure 19.3-97	Measured Axial Differential Pressures in Downcomer, UPTF Test 6 – Run 136	19-116
Figure 19.3-98	Predicted Axial Differential Pressures in Downcomer, UPTF Test 6 – Run 136	19-116
Figure 19.3-99	Measured Azimuthal Differential Pressures in Downcomer at Level 06, UPTF Test 6 – Run 136	19-117
Figure 19.3-100	Predicted Azimuthal Differential Pressures in Downcomer at Level 06, UPTF Test 6 – Run 136	19-117
Figure 19.3-101	Measured Azimuthal Differential Pressures in Downcomer at Level 22, UPTF Test 6 – Run 136	19-118
Figure 19.3-102	Predicted Azimuthal Differential Pressures in Downcomer at Level 22, UPTF Test 6 – Run 136	19-118
Figure 19.3-103	Comparison on Differential Pressure in Lower Plenum, UPTF Test 6 – Run 136	19-119
Figure 19.3-104	Lower Plenum Fluid Inventory, UPTF Test 6 – Run 131	19-120

WCAP-16996-NP

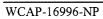
Figure 19.3-105	Lower Plenum Fluid Inventory, UPTF Test 6 – Run 132 19-121
Figure 19.3-106	Lower Plenum Fluid Inventory, UPTF Test 6 – Run 133 19-122
Figure 19.3-107	Lower Plenum Fluid Inventory, UPTF Test 6 – Run 135 19-123
Figure 19.3-108	Lower Plenum Fluid Inventory, UPTF Test 6 – Run 136 19-124
Figure 19.3-109	Comparison between Measured and Predicted Penetration Rates in UPTF Test 6
Figure 19.3-110	Comparison between Measured and Predicted Refill Periods versus Nominal Steam Flow Rate for Lower Plenum in UPTF Test 6 19-126
Figure 19.3-111	Downcomer CCFL Behavior for UPTF Test 6 19-127
Figure 19.3-112	Estimated Mass Distribution, UPTF Test 6 - Run 131 19-128
Figure 19.3-113	Predicted Mass Distribution, UPTF Test 6 – Run 131 19-128
Figure 19.3-114	Estimated Mass Distribution, UPTF Test 6 - Run 132 19-129
Figure 19.3-115	Predicted Mass Distribution, UPTF Test 6 – Run 132 19-129
Figure 19.3-116	Estimated Mass Distribution, UPTF Test 6 – Run 133 19-130
Figure 19.3-117	Predicted Mass Distribution, UPTF Test 6 – Run 133 19-130
Figure 19.3-118	Estimated Mass Distribution, UPTF Test 6 – Run 135 19-131
Figure 19.3-119	Predicted Mass Distribution, UPTF Test 6 – Run 135 19-131
Figure 19.3-120	Estimated Mass Distribution, UPTF Test 6 – Run 136 19-132
Figure 19.3-121	Predicted Mass Distribution, UPTF Test 6 – Run 136 19-132
Figure 19.3-122	Vessel Condensation Efficiency, UPTF Test 6 – Run 131 19-133
Figure 19.3-123	Vessel Condensation Efficiency, UPTF Test 6 – Run 132 19-134
Figure 19.3-124	Vessel Condensation Efficiency, UPTF Test 6 – Run 133 19-135
Figure 19.3-125	Vessel Condensation Efficiency, UPTF Test 6 – Run 135 19-136
Figure 19.3-126	Vessel Condensation Efficiency, UPTF Test 6 – Run 136 19-137
Figure 19.3-127	Comparison of Vessel Condensation Efficiency versus Nominal Steam Flow Rate, UPTF Test 6; Experimental Condensation Efficiency is Estimated by MPR (MPR-1163, 1990); Predicted Condensation Efficiency is Evaluated Using Steam Flow Rate at Break
Figure 19.3-128	Comparison of Vessel Condensation Efficiency versus Nominal Steam Flow Rate with Various DC Condensation Multipliers, UPTF Test 6; Predicted Condensation Efficiency is Evaluated Using Steam Flow Rate at Inlet of Broken Cold Leg

,

Figure 19.3-129	Comparison of Filling Period from Start of ECC Injection to End of Lower Plenum Filling with Various DC Condensation Multipliers versus Nominal Steam Flow Rate, UPTF Test 6. Note, Run 132 did not Fill the Lower Plenum at the End of the Calculation.	19-140
Figure 19.3-130	Comparison of Length of Refill Period from Start of ECC Injection to End of Lower Plenum Filling versus Nominal Steam Flow Rate with Various DTMAX, UPTF Test 6	19-141
Figure 19.3-131	Location of Fluid Thermocouples, Differential and Absolute Pressure Measurements in Broken Cold Leg of Loop 04	19-142
Figure 19.3-132	Moody Diagram	19-143
Figure 19.3-133	Cold Leg Steam Flow Rate (Top) and Downcomer Pressure (Bottom) for Test Run 131	19-144
Figure 19.3-134	Cold Leg Fluid Temperature (Top) and Cold Leg to Downcomer Pressure Drop (Bottom) for Test Run 131	19-145
Figure 19.3-135	Cold Leg Steam Flow Rate (Top) and Downcomer Pressure (Bottom) for Test Run 132.	19-146
Figure 19.3-136	Cold Leg Fluid Temperature (Top) and Cold Leg to Downcomer Pressure Drop (Bottom) for Test Run 132	19-147
Figure 19.3-137	Cold Leg Steam Flow rate (Top) and Downcomer Pressure (Bottom) for Test Run 133	19-148
Figure 19.3-138	Cold Leg Fluid Temperature (Top) and Cold Leg to Downcomer Pressure Drop (Bottom) for Test Run 133	19-149
Figure 19.3-139	Cold Leg Steam Flow rate (Top) and Downcomer Pressure (Bottom) for Test Run 135	19-150
Figure 19.3-140	Cold Leg Fluid Temperature (Top) and Cold Leg to Downcomer Pressure Drop (Bottom) for Test Run 135	19-151
Figure 19.3-141	Cold Leg Steam Flow Rate (Top) and Downcomer Pressure (Bottom) for Test Run 136	19-152
Figure 19.3-142	Cold Leg Fluid Temperature (Top) and Cold Leg to Downcomer Pressure Drop (Bottom) for Test Run 136	19-153
Figure 19.3-143	An Illustration of Downcomer and Broken Cold Leg Nozzle Noding	19-154
Figure 19.3-144	Comparison between Measured Pressure Loss and Predicted Pressure Loss across Broken Cold Leg Nozzle for UPTF 6-131	19-155
Figure 19.3-145	Comparison between Measured Pressure Loss and Predicted Pressure Loss across Broken Cold Leg Nozzle for UPTF 6-132	19-156

(

Figure 19.3-146	Comparison between Measured Pressure Loss and Predicted Pressure Loss across Broken Cold Leg Nozzle for UPTF 6-133
Figure 19.3-147	Comparison between Measured Pressure Loss and Predicted Pressure Loss across Broken Cold Leg Nozzle for UPTF 6-135
Figure 19.3-148	Comparison between Measured Pressure Loss and Predicted Pressure Loss across Broken Cold Leg Nozzle for UPTF 6-136
Figure 19.3-149	Cold Leg Piping Region of UPTF Facility and Cold Leg Noding 19-160
Figure 19.3-150	System Configuration for UPTF-8A
Figure 19.3-151	Observation on Temperature Distribution in UPTF-8 Experiments (MPR Associates, 1992) and Comparison with Predictions from <u>W</u> COBRA/TRAC-TF2
Figure 19.3-152	WCOBRA/TRAC-TF2 Vessel Model for UPTF Test 8A
Figure 19.3-153	WCOBRA/TRAC-TF2 Loop Model for UPTF-8 A
Figure 19.3-154	Comparison between the Measured Steam Flow Rates and the <u>WCOBRA/TRAC-TF2</u> Predicted Steam Flow Rates in the Cold Leg of the Loop 2
Figure 19.3-155	ECC Injection Flow Rate to Cold Leg in Loop 2
Figure 19.3-156	Comparison between Measured Fluid Temperature and <u>W</u> COBRA/TRAC-TF2 Predicted Water Temperature at Pump Exit
Figure 19.3-157	Comparison between Measured Fluid Temperature and <u>W</u> COBRA/TRAC-TF2 Predicted Water Temperature near Injection Point 19-168
Figure 19.3-158	Comparison between Measured Fluid Temperature and <u>W</u> COBRA/TRAC-TF2 Predicted Water Temperature at Downstream of Injection Point
Figure 19.3-159	Comparison between Measured Fluid Temperature and <u>W</u> COBRA/TRAC-TF2 Predicted Water Temperature at Outlet of Cold Leg 19-170
Figure 19.3-160	Predicted Flow Regime Number of Cell Face 4 of Cold Leg
Figure 19.3-161	Predicted Flow Regime Number of Cell Face 5 of Cold Leg 19-172
Figure 19.3-162	Predicted Flow Regime Number of Cell Face 6 of Cold Leg 19-173
Figure 19.3-163	Predicted Flow Regime Number of Cell Face 7 of Cold Leg 19-174
Figure 19.3-164	System Configuration for UPTF Test 25, Phase A (Run 242) and Phase B (Run 241)
Figure 19.3-165	Steam Flow Rate for UPTF Test 25, Phase A (Run 242) 19-176
Figure 19.3-166	ECC Flow Rate for UPTF Test 25, Phase A (Run 242) 19-177



.

Figure 19.3-167	Drainage Flow Rate for UPTF Test 25, Phase A (Run 242) 19-178
Figure 19.3-168	WCOBRA/TRAC-TF2 Loop Model for UPTF Test 25A 19-179
Figure 19.3-169	Absolute Pressure in the Upper Plenum and Downcomer for UPTF Test 25A
Figure 19.3-170	Measured Downcomer Fluid Temperature at Level 28 for UPTF Test 25A
Figure 19.3-171	Predicted Downcomer Fluid (Vapor) Temperature at Level 28 for UPTF Test 25A
Figure 19.3-172	Measured Downcomer Fluid Temperature at Level 24 for UPTF Test 25A
Figure 19.3-173	Predicted Downcomer Fluid (Liquid) Temperature at Level 24 for UPTF Test 25A
Figure 19.3-174	Differential Pressure between Upper Plenum and Downcomer for UPTF Test 25A
Figure 19.3-175	Axial Differential Pressure in Downcomer for UPTF Test 25A 19-185
Figure 19.3-176	Axial Differential Pressures in Downcomer for UPTF Test 25A; Curve 2 is in Broken Quadrant and Curves 1, 3 and 4 are in Intact Quadrants
Figure 19.3-177	Broken Loop Steam Flow Rate for UPTF Test 25A
Figure 19.3-178	Broken Loop Liquid Flow Rate for UPTF Test 25A 19-188
Figure 19.3-179	Void Height versus Steam Flow Rate for UPTF Test 25A 19-189
Figure 19.3-180	Cold Leg Temperature near ECC Injection for UPTF Test 25A 19-190
Figure 19.3-181	Cold Leg Temperature Downstream of ECC Injection for UPTF Test 25A 19-191
Figure 19.3-182	Cold Leg Temperature at Exit of Cold Leg for UPTF Test 25A 19-192.
Figure 19.3-183	Cold Leg Temperature near ECC Injection for UPTF Test 25A with KCOSI=0.4
Figure 19.3-184	Cold Leg Temperature Downstream of ECC Injection for UPTF Test 25A with KCOSI=0.4
Figure 19.3-185	Cold Leg Temperature at Exit of Cold Leg for UPTF Test 25A with KCOSI=0.4 19-195
Figure 19.3-186	Axial Differential Pressures in Downcomer for UPTF Test 25A with KCOSI=0.4
Figure 19.3-187	Broken Loop Steam Flow Rate for UPTF Test 25A with KCOSI=0.4 19-197.

Figure 19.3-188	Broken Loop Liquid Flow Rate for UPTF Test 25A with KCOSI=0.4 19-198
Figure 19.3-189	Differential Pressure between Upper Plenum and Downcomer for UPTF Test 25A with XC=0.4
Figure 19.3-190	Axial Differential Pressure in Downcomer for UPTF Test 25A with XC=0.4
Figure 19.3-191	Axial Differential Pressures in Downcomer for UPTF Test 25A with XC=0.4
Figure 19.3-192	Void Height versus Steam Flow Rate for UPTF Test 25A with XC=0.4 19-202
Figure 19.3-193	System Configuration for UPTF, Test 29 Phase B (Run 212) (MPR-1213, 1990)
Figure 19.3-194	Injection Rates into Core Simulator, UPTF 29B
Figure 19.3-195	WCOBRA/TRAC-TF2 Vessel Component for UPTF Test 29B 19-205
Figure 19.3-196	Illustration of Jet Channel and Global Channel in Upper Plenum
Figure 19.3-197	Section 5 of Upper Plenum Noding Model for UPTF Test 29B 19-207
Figure 19.3-198	WCOBRA/TRAC-TF2 Loop Model for UPTF Upper Plenum Test 19-208
Figure 19.3-199	Quasi-Steady State Upper Plenum Mass for Phase I of UPTF Test 29B 19-209
Figure 19.3-200	Quasi-Steady State Upper Plenum Mass for Phase II of UPTF Test 29B 19-210
Figure 19.3-201	Quasi-Steady State Upper Plenum Mass for Phase III of UPTF Test 29B19-211
Figure 19.3-202	Quasi-Steady State Upper Plenum Mass for Phase IV of UPTF Test 29B 19-212
Figure 19.3-203	Quasi-Steady State Upper Plenum Mass for Phase V of UPTF Test 29B 19-213
Figure 19.3-204	Quasi-Steady State Upper Plenum Mass for Phase VI of UPTF Test 29B 19-214
Figure 19.4-1	Flooding Model for a Perforated Plate
Figure 19.4-2	Flooding Velocities for the Nitrogen/Water System at [] ^{a,c} Compared with the Air/Water Test (Hsieh, 1980) and Northwestern Flooding Limit
Figure 19.4-3	Flooding Velocities for Saturated Liquid and Vapor at [] ^{a,c} Compared with Northwestern Flooding Limit (<u>WCOBRA/TRAC-TF2</u>) 19-223
Figure 19.4-4	Flooding Velocities for Saturated Liquid and Vapor at [] ^{a,c} Compared with Northwestern Flooding Limit (<u>WCOBRA/TRAC-TF2</u>) 19-224
Figure 19.4-5	Liquid Mass Flow Rates through Perforated Plate at [] ^{a,c} (WCOBRA/TRAC-TF2)
Figure 19.4-6	Vapor/Liquid Mass Flow Rates through Perforated Plate at [] ^{a,c} (<u>W</u> COBRA/TRAC-TF2)

Figure 19.4-7	Liquid Mass Flow rates through Perforated Plate at [] ^{a,c} (WCOBRA/TRAC-TF2)	19-227
Figure 19.4-8	Vapor/Liquid Mass Flow rates through Perforated Plate at [] ^{a,c} (<u>W</u> COBRA/TRAC-TF2)	19-228
Figure 19.5-1	Mass Inventory Measurements in the FLECHT Facilities	19-232
Figure 19.5-2	Predicted and Measured Carryover Fraction, FLECHT-SEASET Test 31805	19-233
Figure 19.5-3	Predicted and Measured Carryover Fraction, FLECHT-SEASET Test 31701	19-234
Figure 19.5-4	Predicted and Measured Carryover Fraction, FLECHT-SEASET Test 31203	19-235
Figure 19.5-5	Predicted and Measured Carryover Fraction, FLECHT Test 04641	19-236
Figure 19.5-6	Predicted and Measured Carryover Fraction, FLECHT Test 05029	19-237
Figure 19.5-7	Predicted and Measured Carryover Fraction, FLECHT Top Skewed Test 15305	19-238
Figure 19.5-8	Predicted and Measured Carryover Fraction, FLECHT Top Skewed Test 13609	19-239
Figure 19.5-9	Predicted and Measured Carryover Fraction, FLECHT Top Skewed Test 13812	19-240
Figure 19.6-1	Top View of Primary Loop Piping	19-253
Figure 19.6-2	Diagram of CCTF Pressure Vessel	19-254
Figure 19.6-3	CCTF Cross Sections (a) Pressure Vessel (b) Upper Plenum Internals	19-255
Figure 19.6-4	Axial Power Profile of Heated Rods in CCTF	19-256
Figure 19.6-5	CCTF Test Sequence for Run 62	19-257
Figure 19.6-6	CCTF Vessel Noding Diagram	19-258
Figure 19.6-7	CCTF Section 1 Noding	19-259
Figure 19.6-8	CCTF Section 2 Noding	19-260
Figure 19.6-9	CCTF Section 3 Noding	19 -2 61
Figure 19.6-10	CCTF Section 4 Noding	19-262
Figure 19.6-11	CCTF Section 5 Noding	19-263
Figure 19.6-12	CCTF Section 6 Noding	19-264
Figure 19.6-13		

ľ

Figure 19.6-14	CCTF Loop Component Diagram	6
Figure 19.6-15	Dimensions of Hot Leg in CCTF Facility 19-26	7
Figure 19.6-16	Noding Diagram of Hot Leg 19-26	7
Figure 19.6-17	Dimension of Crossover Leg, Pump Simulator, Cold Leg, and ECC Port in CCTF Facility	8
Figure 19.6-18	Noding Diagram of Crossover Leg, Pump Simulator, Cold Leg, and ECC Port in Loop 1; Other Intact Loops are Identical to Loop 1	8
Figure 19.6-19	Steam Generator Component Diagram	9
Figure 19.6-20	CCTF Run 62 Cladding Temperature at 6.0 ft for Channel 9 (Rod 6) 19-27	0
Figure 19.6-21	CCTF Run 62 Cladding Temperature at 8.0 ft for Channel 9 (Rod 6) 19-27	1
Figure 19.6-22	CCTF Run 62 Cladding Temperature at 10.0 ft for Channel 9 (Rod 6) 19-27	2
Figure 19.6-23	CCTF Run 62 Vapor Temperature at 6.0 ft for Channel 9 19-27	3
Figure 19.6-24	CCTF Run 62 Liquid Level in Core 19-274	4
Figure 19.6-25	CCTF Run 62 Liquid Level in Upper Plenum	5
Figure 19.6-26	CCTF Run 62 Pressure Difference from Lower Plenum to Upper Plenum 19-27	5
Figure 19.6-27	CCTF Run 62 Pressure Difference from Lower Plenum to Top of Downcomer	7
Figure 19.6-28	CCTF Run 62 Pressure Difference across Intact Loop 19-27	3
Figure 19.6-29	CCTF Run 62 Pressure Difference across Broken Loop 19-27	9
Figure 19.6-30	CCTF Run 62 Pressure Difference across Steam Generators; Averaged for 3 Intact Loops)
Figure 19.6-31	CCTF Run 62 Temperature Rise across Steam Generator of Loop 1 19-28	1
Figure 19.6-32	CCTF Run 62 Temperature Rise across Steam Generator of Loop 2 19-282	2
Figure 19.6-33	CCTF Run 62 Temperature Rise across Steam Generator of Loop 3 19-282	3
Figure 19.6-34	CCTF Run 62 Total (Liquid and Vapor) Mass Flow Rate in Intact Loop Hot Leg	1
Figure 19.6-35	CCTF Run 62 Total (Liquid and Vapor) Mass Flow Rate in Broken Loop Hot Leg	5
Figure 19.6-36	CCTF Run 62 Core Inlet Mass Flow Rate	5
Figure 19.6-37	CCTF Run 62 Time Step Sensitivity Study: Cladding Temperature at 6.0 ft	7

Ę

Figure 19.6-38	CCTF Run 62 Time Step Sensitivity Study: Cladding Temperature at 8.0 ft
Figure 19.6-39	CCTF Run 62 Time Step Sensitivity Study: Cladding Temperature at 10.0 ft
Figure 19.6-40	CCTF Run 62 Time Step Sensitivity Study: Collapsed Liquid Level in Core
Figure 19.6-41	CCTF Run 62 Time Step Sensitivity Study: Collapsed Liquid Level in Upper Plenum
Figure 19.6-42	CCTF Run 62 Time Step Sensitivity Study: Pressure Difference from Lower Plenum to Upper Plenum
Figure 19.6-43	CCTF Run 62 Time Step Sensitivity Study: Pressure Difference from Cold Leg Nozzle to Upper Plenum
Figure 20.1-1	IPP Loop #2 Accumulator Line Schematic
Figure 20.1-2	WCOBRA/TRAC-TF2 Model of Accumulator and SI Line in IPP and Callaway Test Models
Figure 20.1-3	Predicted Accumulator Pressure (Solid Line) Compared with Measured Test Data (Dashed Line)
Figure 20.1-4	Predicted Accumulator Flow Rate
Figure 20.1-5	Predicted Gas Temperature at Top of Accumulator
Figure 20.1-6	Comparison of CALLAWAY Accumulator Blowdown Test Data and <u>W</u> COBRA/TRAC-TF2 Prediction of Accumulator Pressure
Figure 20.1-7	Comparison of CALLAWAY Accumulator Blowdown Test Data and <u>W</u> COBRA/TRAC-TF2 Prediction of Accumulator Gas Volume
Figure 20.1-8	Comparison of CALLAWAY Accumulator Blowdown Test Data and <u>W</u> COBRA/TRAC-TF2 Prediction of Accumulator Gas Temperature
Figure 20.1-9	Best-fit Calculation of Polytropic Exponent from CALLAWAY Accumulator Blowdown <u>W</u> COBRA/TRAC-TF2 Prediction
Figure 20.1-10	Accumulator Liquid Level for LOFT Test L2-5 (Bayless et al., 1982) 20-20
Figure 20.1-11	Accumulator Pressure for LOFT Test L2-5 (Bayless et al., 1982) 20-21
Figure 20.1-12	Intact Loop Cold Leg Density for LOFT Test L2-5 (Bayless et al., 1982) 20-22
Figure 20.1-13	 (a) Core Liquid Level Plots for LOFT Test L2-5 (Bayless et al., 1982) (b) Fuel Rod Clad Temperatures (Bayless et al., 1982)
Figure 20.1-14	Fluid Density and Clad Temperature in Core at a) 27 inches, b) 44 inches Above Bottom of Core (Mackley and Birchley, 1985)

Figure 20.1-15	Suppression Tank Pressure for LOFT Test L2-5 (Bayless et al., 1982) 20-25
Figure 20.1-16	
] ^{a,c}
Figure 20.1-17	[] ^{a,c} 20-27
Figure 20.1-18	[] ^{a,c} 20-28
Figure 20.1-19	[20.20
] ^{a,c}
Figure 20.1-20	[] ^{a,c}
Figure 20.1-21	
] ^{a,c}
Figure 20.1-22	Γ
] ^{a,c}
Figure 20.1-23	[] ^{a,c}
Figure 20.1-24	ACHILLES Rig Configured for Best-Estimate Transients
-	WCOBRA/TRAC-TF2 Model of ACHILLES Test
Figure 20.1-25	
Figure 20.1-26	Cross Section of ACHILLES Cluster
Figure 20.1-27	Measured and Predicted Accumulator Pressure
Figure 20.1-28	Measured and Predicted Accumulator Discharge Line Mass Flow Rate
Figure 20.1-29	Measured and Predicted Pressure at Top of Downcomer
Figure 20.1-30	Measured and Predicted Pressure Loss from Top of Downcomer to Break 20-40
Figure 20.1-31	Measured and Predicted Gas Flow Rate from Top of Downcomer to Break 20-41
Figure 20.1-32	Measured and Predicted Downcomer Liquid Level
Figure 20.1-33	Measured and Predicted Test Section Liquid Level
Figure 20.1-34	Measured and Predicted Cladding Temperature at 1.08m (3.54 ft) 20-44
Figure 20.1-35	Measured and Predicted Cladding Temperature at 2.01m (6.59 ft) 20-45
Figure 20.1-36	Measured and Predicted Cladding Temperature at 2.65m (8.69 ft) 20-46
Figure 20.1-37	Measured and Predicted Accumulator Pressure (Broken Pipe Pressure Loss Sensitivity Study)
Figure 20.1-38	Measured and Predicted Accumulator Discharge Line Mass Flow Rate (Broken Pipe Pressure Loss Sensitivity Study)

Figure 20.1-39	Measured and Predicted Pressure at Top of Downcomer (Broken Pipe Pressure Loss Sensitivity Study)	. 20-49
Figure 20.1-40	Measured and Predicted Downcomer Liquid Level (Broken Pipe Pressure Loss Sensitivity Study)	. 20-50
Figure 20.1-41	Measured and Predicted Test Section Liquid Level (Broken Pipe Pressure Loss Sensitivity Study)	. 20-51
Figure 20.1-42	Measured and Predicted Cladding Temperature at 1.08m (3.54 ft) (Broken Pipe Pressure Loss Sensitivity Study)	. 20-52
Figure 20.1-43	Measured and Predicted Cladding Temperature at 2.01m (6.59 ft) (Broken Pipe Pressure Loss Sensitivity Study)	. 20-53
Figure 20.1-44	Measured and Predicted Cladding Temperature at 2.65m (8.69 ft) (Broken Pipe Pressure Loss Sensitivity Study)	. 20-54
Figure 20.2-1	Cross-Sectional View of the Westinghouse Scale Model Pump	. 20-60
Figure 20.2-2	Scale Model Homologous Head Single-Phase Data in the Pumping Mode, Forward and Reverse Flow	. 20-61
Figure 20.2-3	Scale Model Homologous Head Single-Phase Data in the Dissipation Mode, Forward Flow	. 20-62
Figure 20.2-4	Data Scatter for Dissipative Mode 1/3-Scale Pump Data (Cudlin, 1977)	20-63
Figure 20.2-5	Schematic of the Air/Water Test Facility	20-64
Figure 20.2-6	Homologous Head Curves and Westinghouse Air/Water Data	20-65
Figure 20.2-7	Single-Phase and Fully Degraded Pump Head Curves Compared With Two-Phase Data	20-66
Figure 20.2-8	Pump Single-Phase and Fully Degraded Torque Curves, Compared With Two-Phase Data	20-67
Figure 20.2-9	Two-Phase Multiplier and Pumping Mode Data	20-68
Figure 20.2-10	Two-Phase Multiplier and All Two-Phase Data	20-69
Figure 20.2-11	$M(\alpha)$ for Pump Torque (Referred to as $N(\alpha)$ in Equation 10-9)	20-70
Figure 20.2-12	Westinghouse Pump Head Curves Compared With LOFT Pump Head Curves	20-71
Figure 20.3-1	Scenario and Noding Diagram for 1D/3D Mass and Energy Test	20-73
Figure 20.3-2	Mass Conservation for 1D/3D Mass and Energy Test	20-74
Figure 20.3-3	Energy Conservation for 1D/3D Mass and Energy Test	20-75
Figure 21.2-1	Schematic Diagram of LSTF	21-57

Figure 21.3-1	WCOBRA/TRAC-TF2 Model of LSTF Pressure Vessel	. 21-58
Figure 21.3-2	LSTF Pressure Vessel Sections 1 and 2	. 21-59
Figure 21.3-3	LSTF Pressure Vessel Sections 3 and 4	. 21-60
Figure 21.3-4	LSTF Pressure Vessel Sections 5 and 6	. 21-61
Figure 21.3-5	LSTF Pressure Vessel Sections 7 and 8	. 21-62
Figure 21.3-6	LSTF Pressure Vessel Sections 9 and 10	. 21-63
Figure 21.3-7	ROSA-IV LSTF Core Simulator Map	21-64
Figure 21.3-8	WCOBRA/TRAC-TF2 Loop Noding Diagram of LSTF	21-65
Figure 21.3-9	Hot Leg (Including Pressurizer), Steam Generator and Cross-Over Leg Noding	21-66
Figure 21.4-1	Pressurizer Pressure	
Figure 21.4-2	Break Flows	
Figure 21.4-3	Cross-Over Leg A Differential Pressures	. 21-69
Figure 21.4-4	Cross-Over Leg B Differential Pressures	. 21-70
Figure 21.4-5	Inner Vessel Differential Pressures	. 21-71
Figure 21.4-6	Calculated and Measured Peak Cladding Temperatures	21-72
Figure 21.4-7	SG-A U-tube Upflow Side Differential Pressures	21-73
Figure 21.4-8	SG-B U-tube Upflow Side Differential Pressures	21-74
Figure 21.4-9	SG-A U-tube Downflow Side Differential Pressures	21-75
Figure 21.4-10	SG-B U-tube Downflow Side Differential Pressures	21-76
Figure 21.4-11	SG-A Inlet-to-Outlet Differential Pressures	21-77
Figure 21.4-12	SG-B Inlet-to-Outlet Differential Pressures	21-78
Figure 21.4-13	SG-A Inlet Plenum Collapsed Liquid Levels	21-79
Figure 21.4-14	SG-B Inlet Plenum Collapsed Liquid Levels	21-80
Figure 21.4-15	Upper Plenum to SG-A Inlet Differential Pressures	21-81
Figure 21.4-16	Upper Plenum to SG-B Inlet Differential Pressures	21-82
Figure 21.4-17	Upper Plenum Differential Pressures	21-83
Figure 21.4-18	Downcomer Differentail Pressures	21-84
Figure 21.4-19	Comparison of Calculated and Measured Accumulator Injection Flows Loop A	21-85

Figure 21.4-20	Comparison of Calculated and Measured Accumulator Injection Flows Loop
Figure 21.5-1	Core Power
Figure 21.5-2	Pump Speed
Figure 21.5-3	Loop Flow Rates
Figure 21.5-4	Break Flows
Figure 21.5-5	Calculated Break Spool Void Fraction
Figure 21.5-6	Pressurizer Pressures
Figure 21.5-7	Steam Generator Secondary Side Pressures
Figure 21.5-8	Steam Generator SGA U-tube Differential Pressures
Figure 21.5-9	Steam Generator SGB U-tube Differential Pressures
Figure 21.5-10	Cross-Over Leg A Differential Pressures
Figure 21.5-11	Cross-Over Leg B Differential Pressures
Figure 21.5-12	Upper Plenum Differential Pressures
Figure 21.5-13	Upper Plenum to SGA Inlet Differential Pressures
Figure 21.5-14	Upper Plenum to SGB Inlet Differential Pressures
Figure 21.5-15	Downcomer Differential Pressures
Figure 21.5-16	Core Differential Pressures
Figure 21.5-17	Core Differential Pressures for SB-CL-05 and SB-CL-18
Figure 21.5-18	Cold Leg A Pumped ECCS Injection Flows (CLA)
Figure 21.5-19	Total Pumped ECCS Injection Flows (CLA plus CLB)
Figure 21.5-20	Accumulator Hot (ACH) Liquid Level
Figure 21.5-21	Calculated and Measured Peak Cladding Temperatures
Figure 21.6-1	Loop-A Pump Speed Comparison
Figure 21.6-2	Loop-B Pump Speed Comparison
Figure 21.6-3	Comparison of Loop-A Flow Rates21-110
Figure 21.6-4	Comparison of Loop-B Flow Rates
Figure 21.6-5	Comparison of Break Flows
Figure 21.6-6	Comparison of Fluid Density in the Break Spool
Figure 21.6-7	Comparison of Loop-B Cross-Over Leg Differential Pressures

WCAP-16996-NP

Figure 21.6-8	Comparison of System Pressures	21-115
Figure 21.6-9	Comparison of SG-A U-tube Inlet-to-top Differential Pressures	21-116
Figure 21.6-10	Comparison of SG-B U-tube Inlet-to-top Differential Pressures	21-117
Figure 21.6-11	Comparison of SG-A U-tube Outlet-to-top Differential Pressures	21-118
Figure 21.6-12	Comparison of SG-B U-tube Outlet-to-top Differential Pressures	21-119
Figure 21.6-13	Comparison of SG_A Inlet Plenum Draining	21-120
Figure 21.6-14	Comparison of Core Collapsed Liquid Levels	21-121
Figure 21.6-15	Calculated Accumulator Injection Flows	21-122
Figure 21.6-16	High Power Rod (Rod 1) Cladding Temperature	21-123
Figure 21.7-1	Break Unit Configuration used in 2.5% Cold Leg Break Tests, SB-CL-01, 02, and 03 (Koizumi, et al., 1987)	21-124
Figure 21.7-2	WCOBRA/TRAC-TF2 Nodalization of LSTF Break Unit	21-125
Figure 21.7-3	Comparison of Predicted and Measured Primary System Pressure (ROSA-IV 2.5-Percent Cold Leg Break)	21-126
Figure 21.7-4	Comparison of Predicted and Measured Break Flow rates (ROSA-IV 2.5-Percent Cold Leg Break)	21-127
Figure 21.7-5	Comparison of Predicted and Measured Mixture Levels in Broken Cold Leg (ROSA-IV 2.5-Percent Cold Leg Break Runs)	21-128
Figure 21.7-6	Comparison of Predicted and Measured Core Collapsed Liquid Levels (ROSA-IV 2.5-Percent Cold Leg Break Runs)	21-129
Figure 21.7-7	Cladding Temperature of B-20 Rod at Position 7 (8.67-ft Elevation) for Side, Bottom, and Top Break Experiments	21-130
Figure 21.7-8	Predicted and Measured Differential Pressures in SGA Uphill Side	21-131
Figure 21.7-9	Predicted and Measured Differential Pressures in SGB Uphill Side	21-132
Figure 21.7-10	Calculated Accumulator Injection Flows	21-133
Figure 21.7-11	Break Unit Configuration used in the 0.5% Break Tests, SB-CL-12, -15, and -16	21-134
Figure 21.7-12	Comparison of Predicted and Measured Broken Cold Leg Liquid Levels, ROSA 0.5-Percent Cold Leg Break Runs	21-135
Figure 21.7-13	Comparison of Predicted and Measured Core Collapsed Liquid Levels, ROSA 0.5-Percent Cold Leg Break Runs	21-136

Figure 21.7-14	Comparison of Predicted and Measured Integrated Break Flows, ROSA 0.5-Percent Cold Leg Break Runs
Figure 21.8-1	Break Flow Comparison
Figure 21.8-2	System Pressure Comparison
Figure 21.8-3(a)	Cross-over Leg A Vapor Flows
Figure 21.8-3(b)	Cross-over Leg B Vapor Flows
Figure 21.8-4	Core Collapsed Levels
Figure 21.8-5(a)	Steam Generator A U-tubes Upflow Differential Pressures
Figure 21.8-5(b)	Steam Generator B U-tubes Upflow Differential Pressures
Figure 21.9-1	ST-NC-02 Primary Pressure and Loop Flow Rate (Figure taken from Reference 9) (Y. Kikuta, et.al., "Nonuniform Steam Generator U-Tube Flow Distribution During Natural Circulation Tests in ROSA-IV Large Scale Test Facility," 1988.)
Figure 21.9-2	Primary Side Circulation Flow as a Function of Primary Side Inventory 21-146
Figure 21.9-3	ST-NC-02 Primary and Secondary System Pressures
Figure 21.9-4	Steam Generator U-tube Upflow Side Differential Pressures
Figure 21.9-5	Core Differential Pressure
Figure 21.9-6	Upper Plenum Differential Pressure
Figure 21.9-7	Downcomer Differential Pressure
Figure 21.9-8	Downcomer-to-Upper Plenum Differential Pressure
Figure 21.9-9	SG Primary-to-Secondary Side Heat Transfer Coefficients
Figure 21.9-10	Steam Generator Primary-to-Secondary Side Temperature Difference
Figure 21.9-11	Steam Generator SGA U-tube Uphill Void Fraction
Figure 21.9-12	Steam Generator SGA U-tube Downhill Void Fraction
Figure 21.9-13	Steam Generator SGB U-tube Uphill Void Fraction
Figure 21.9-14	Steam Generator SGB U-tube Downhill Void Fraction
Figure 21.10.1-1	Calculated Counter-current Flow at the Inlet of Steam Generator U-tubes (Simulation of 10% Break Test SB-CL-14)
Figure 21.10.1-2	Calculated Counter-current Flow at the Inlet of Steam Generator U-tubes (Simulation of 5% Break Test SB-CL-18)
Figure 21.10.1-3	Calculated Counter-current Flow at the Inlet of Steam Generator U-tubes (Simulation of 2.5% Break Test SB-CL-01)

WCAP-16996-NP

.

Figure 21.10.1-4	Calculated Counter-current Flow at the Inlet of Steam Generator U-tubes (Simulation of 0.5% Break Test SB-CL-12)	21-162
Figure 21.10.1-5	Calculated Counter-current Flow at the Inlet of Steam Generator U-tubes (Simulation of the Natural Circulation Test SB-CL-12)	21-163
Figure 21.10.2-1	Calculated Counter-current Flow at the Hot Leg Elbows and SG Inlets (Simulation of 10% Break Test SB-CL-14)	21-164
Figure 21.10.2-2	Calculated Counter-current Flow at the Hot Leg Elbows and SG Inlets (Simulation of 5% Break Test SB-CL-18)	21-165
Figure 21.10.2-3	Calculated Counter-current Flow at the Hot Leg Elbows and SG Inlets (Simulation of 2.5% Break Test SB-CL-01)	21-166
Figure 21.10.2-4	Calculated Counter-current Flow at the Hot Leg Elbows and SG Inlets Simulation of 0.5% Break Test SB-CL-12)	21-167
Figure 21.10.3-1	Calculated Counter-current Flow Conditions at the Top of the Peripheral CCFL Channel 72	21-168
Figure 21.10.3-2	Calculated Counter-current Flow Conditions at the Top of the Inner Average CCFL Channel 14	21-169
Figure 21.10.3-3	Calculated Counter-current Flow Conditions at the Top of the Inner Hot CCFL Channel 11	21-170
Figure 21.10.3-4	Calculated UCP Counter-current Flow Conditions (10% Break Test SB-CL-14).	21-171
Figure 21.10.3-5	Calculated UCP Counter-current Flow Conditions (2.5% Break Test SB-CL-01)	21-172
Figure 21.10.3-6	Calculated UCP Counter-current Flow Conditions (0.5% Break Test SB-CL-12)	21-173
Figure 21.10.4-1	Counter-current Flow Periods in Relation to the Steam Generator A Uphill Side Differential Pressure	21-174
Figure 21.10.4-2	Counter-current Flow Periods in Relation to the Steam Generator A Inlet Plenum Collapsed Level	21-175
Figure 21.10.4-3	Counter-current Flow Periods in Relation to the Steam Generator B Uphill Side Differential Pressure	21-176
Figure 21.10.4-4	Counter-current Flow Periods in Relation to the Steam Generator B Inlet Plenum Collapsed Level	21-177
Figure 21.10.4-5	Calculated Velocities at Upper Core Plate Outer Jet Channel 73 (top of peripheral CCFL Channel 72)	21-178

Figure 21.10.4-6	Calculated Velocities at Upper Core Plate Average Jet Channel 20 (top of CCFL Channel 14)	21-179
Figure 21.10.4-7	Calculated Velocities at Upper Core Plate Hot Jet Channel 19 (top of CCFL Channel 14)	َ 21-180
Figure 21.10.4-8	Counter-current Flow Periods in Relation to the Liquid Pool Level above UCP	21-181
Figure 21.10.4-9	Counter-current Flow Periods in Relation to the Inner Vessel Level	21-182
Figure 21.10.4-10	Calculated Hot Leg Flow Rates	21-183
Figure 21.10.4-11	Calculated CCFL at UCP Outer Jet Channel 73	21-184
Figure 21.10.4-12	Calculated and Measured Cladding Temperatures of Low Power Rods at 7.33-ft Elevation	21-185
Figure 21.10.4-12	Calculated and Measured Cladding Temperatures of Low Power Rods at 7.33-ft Elevation	21-186
Figure 21.10.4-13	Calculated and Measured Cladding Temperatures of High Power Rods at 7.33-ft Elevation	21-187
Figure 21.10.4-13	Calculated and Measured Cladding Temperatures of High Power Rods at 7.33-ft Elevation	21-188
Figure 21.10.4-14	Calculated and Measured Cladding Temperatures of Average Power Rods at 7.33-ft Elevation	21-189
Figure 21.10.4-14	Calculated and Measured Cladding Temperatures of Average Power Rods at 7.33-ft Elevation	21-190
Figure 21.11.1-1	SB-CL-18 Cross-Over Leg A Differential Pressures	21-191
Figure 21.11.1-2	SB-CL-18 Cross-Over Leg B Differential Pressures	21-192
Figure 21.11.1-3	Inner Vessel Differential Pressures (LP+Core+UCP)	21-193
Figure 21.11.1-4	Downcomer Differential Pressures	21-194
Figure 21.11.1-5	Lower Plenum Differential Pressures	21-195
Figure 21.11.1-6	Upper Plenum Differential Pressures	21-196
Figure 21.11.1-7	Peak Cladding Temperatures	21-197
Figure 21.11.2-1	SB-CL-18 Cross-Over Leg A Differential Pressures	21-198
Figure 21.11.2-2	SB-CL-18 Cross-Over Leg B Differential Pressures	21-199
Figure 21.11.2-3	Inner Vessel Differential Pressures (LP+Core+UCP)	21-200
Figure 21.11.2-4	Downcomer Differential Pressures	21-201

۰.

Figure 21.11.2-5	Lower Plenum Differential Pressures	-202
Figure 21.11.2-6	Upper Plenum Differential Pressures	-203
Figure 21.11.2-7	Peak Cladding Temperatures	-204
Figure 21.11.3-1	SB-CL-18 Cross-Over Leg A Differential Pressures	-205
Figure 21.11.3-2	SB-CL-18 Cross-Over Leg B Differential Pressures	-206
Figure 21.11.3-3	Inner Vessel Differential Pressures (LP+Core+UCP)	-207
Figure 21.11.3-4	Downcomer Differential Pressures	-208
Figure 21.11.3-5	Lower Plenum Differential Pressures	-209
Figure 21.11.3-6	Upper Plenum Differential Pressures	-210
Figure 21.11.3-7	Peak Cladding Temperatures	-211
Figure 21.12-1	Break Flows	-212
Figure 21.12-2	Calculated Break Void Fraction	-213
Figure 21.12-3	Cross-Over Leg A Differential Pressures	-214
Figure 21.12-4	Cross-Over Leg B Differential Pressures	-215
Figure 21.12-5	Pressurizer Pressures	-216
Figure 21.12-6	SGA U-tubes Inlet-to-Top Differential Pressure	-217
Figure 21.12-7	SGB U-tubes Inlet-to-Top Differential Pressures	-218
Figure 21.12-8	SGA U-tubes Outlet-to-Top Differential Pressures	-219
Figure 21.12-9	SGB U-tube Outlet-to-Top Differential Pressures	-220
Figure 21.12-10	SGA Inlet Plenum Collapsed Liquid Levels	-221
Figure 21.12-11	SGB Inlet Plenum Collapsed Liquid Levels	-222
Figure 21.12-12	Upper Plenum to SGA Inlet Differential Pressures	-223
Figure 21.12-13	Upper Plenum to SGB Inlet Differential Pressures	-224
Figure 21.12-14	Downcomer Differential Pressures	-225
Figure 21.12-15	Upper Plenum Differential Pressures	-226
Figure 21.12-16	Inner Vessel (LP+Core+UP) Differential Pressures	-227
Figure 21.12-17	Lower Plenum Differential Pressures	-228
Figure 21.12-18	Peak Cladding Temperatures	-229
Figure 21.12-19	Accumulator A Injection Flows	-230

Figure 21.13-1	Break Flows
Figure 21.13-2	Calculated Break Void Fraction
Figure 21.13-3	Cross-Over Leg A Differential Pressures
Figure 21.13-4	Cross-Over Leg B Differential Pressures
Figure 21.13-5	Pressurizer Pressures
Figure 21.13-6	SGA U-tubes Inlet-to-Top Differential Pressure
Figure 21.13-7	SGB U-tubes Inlet-to-Top Differential Pressures
Figure 21.13-8	SGA U-tubes Outlet-to-Top Differential Pressures
Figure 21.13-9	SGB U-tube Outlet-to-Top Differential Pressures
Figure 21.13-10	SGA Inlet Plenum Collapsed Liquid Levels
Figure 21.13-11	SGB Inlet Plenum Collapsed Liquid Levels
Figure 21.13-12	Upper Plenum to SGA Inlet Differential Pressures
Figure 21.13-13	Upper Plenum to SGB Inlet Differential Pressures
Figure 21.13-14	Downcomer Differential Pressures
Figure 21.13-15	Upper Plenum Differential Pressures
Figure 21.13-16	Inner Vessel (LP+Core+UP) Differential Pressures
Figure 21.13-17	Lower Plenum Differential Pressures
Figure 21.13-18	Peak Cladding Temperatures
Figure 21.13-19	Accumulator A Injection Flows
Figure 21.14-1	Pump A Differential Pressures
Figure 21.14-2	SB-CL-18 Cross-Over Leg A Differential Pressures
Figure 21.14-3	SB-CL-18 Cross-Over Leg B Differential Pressures
Figure 21.14-4	Inner Vessel Differential Pressures (LP+Core+UCP)
Figure 21.14-5	Downcomer Differential Pressures
Figure 21.14-6	Lower Plenum Differential Pressures
Figure 21.14-7	Upper Plenum Differential Pressures
Figure 21.14-8	Hot Leg A Differential Pressures
Figure 21.14-9	Hot Leg B Differential Pressures
Figure 21.14-10	Peak Cladding Temperatures

Figure 21.15-1	SB-CL-18 Cross-Over Leg A Differential Pressures
Figure 21.15-2	SB-CL-18 Cross-Over Leg B Differential Pressures 21-261
Figure 21.15-3	Inner Vessel Differential Pressures (LP+Core+UCP) 21-262
Figure 21.15-4	Upper Plenum Differential Pressures
Figure 21.15-5	Downcomer Differential Pressures
Figure 21.15-6	Peak Cladding Temperatures
Figure 21.16.1-1	Calculated Break Flow Rates
Figure 21.16.1-2	Calculated Pressurizer and Steam Generator Secondary Pressures
Figure 21.16.1-3	Calculated Steam Generator U-tube Uphill Side Differential Pressures
Figure 21.16.1-4	Calculated Cross-Over Leg A Differential Pressures
Figure 21.16.1-5	Calculated Cross-Over Leg B Differential Pressures
Figure 21.16.1-6	Calculated Downcomer Differential Pressures
Figure 21.16.1-7	Calculated Upper Plenum Differential Pressures
Figure 21.16.1-8	Calculated Hot Leg Differential Pressures
Figure 21.16.1-9	Calculated Core Differential Pressures
Figure 21.16.1-10	Calculated Peak Cladding Temperatures
Figure 21.16.2-1	Calculated Break Flow Rates
Figure 21.16.2-2	Calculated Pressurizer and Steam Generator Secondary Pressures 21-275
Figure 21.16.2-3	Calculated Steam Generator U-tube Uphill Side Differential Pressures
Figure 21.16.2-4	Calculated Cross-Over Leg A Differential Pressures
Figure 21.16.2-5	Calculated Cross-Over Leg B Differential Pressures
Figure 21.16.2-6	Calculated Downcomer Differential Pressures
Figure 21.16.2-7	Calculated Upper Plenum Differential Pressures
Figure 21.16.2-8	Calculated Hot Leg Differential Pressures
Figure 21.16.2-9	Calculated Core Differential Pressures
Figure 21.16.2-10	Calculated Peak Cladding Temperatures
Figure 21.16.3-1	Calculated Break Flow Rates
Figure 21.16.3-2	Calculated Pressurizer and Steam Generator Secondary Pressures 21-283
Figure 21.16.3-3	Calculated Steam Generator U-tube Uphill Side Differential Pressures

Figure 21.16.3-4	Calculated Cross-Over Leg A Differential Pressures
Figure 21.16.3-5	Calculated Cross-Over Leg B Differential Pressures
Figure 21.16.3-6	Calculated Downcomer Differential Pressures
Figure 21.16.3-7	Calculated Upper Plenum Differential Pressures
Figure 21.16.3-8	Calculated Hot Leg Differential Pressures
Figure 21.16.3-9	Calculated Core Differential Pressures
Figure 21.16.3-10	Calculated Peak Cladding Temperatures
Figure 21.17-1	Cold Leg Void Fractions at the SI Injection Nodes
Figure 21.17-2	Mixture Flow at the Broken Cold Leg Nozzle (interface with the vessel) 21-291
Figure 21.17-3	Total SI Condensation Heat Rate at Cold Leg Injection Node in CLA 21-292
Figure 21.17-4	Cold Leg Fluid Temperatures at SI Injection Nodes
Figure 21.17-5	Cold Leg Pressures at SI Injection Nodes
Figure 21.17-6	Accumulator Injection Flows
Figure 21.17-7	Broken Cold Leg Void at Break Off-take Node
Figure 21.17-8	Break Void Fractions
Figure 21.17-9	Fluid Temperatures at the Break
Figure 21.17-10	Break Flow Rates
Figure 21.17-11	Integrated Break Flows
Figure 21.17-12	Integrated Break Flow Difference (KCOSI_low-KCOSI_high)
Figure 21.18-1	Calculated Primary and Steam Generator Secondary Pressures
Figure 21.18-2	Calculated Break Flows
Figure 21.18-3	Calculated Draining of Steam Generator U-tubes Uphill Side
Figure 21.18-4	Calculated Upper Plenum Differential Pressures
Figure 21.18-5	Calculated Upper Plenum to Steam Generator Inlet Differential Pressures 21-303
Figure 21.18-6	Calculated Cross-Over Leg Differential Pressures (Bottom-to-Pump Inlet) 21-304
Figure 21.18-7	Calculated Loop Flow Rates
Figure 21.18-8	Calculated Core Differential Pressures
Figure 21.18-9	Calculated Peak Cladding Temperatures
Figure 22-1	Schematic of LOFT Facility

Figure 22-2	LOFT Reactor Vessel Diagram with Flow Paths	22-32
Figure 22-3	LOFT Reactor Core and Arrangement of Incore Instrumentation	22-33
Figure 22-4	LOFT <u>W</u> COBRA/TRAC-TF2 Vessel Model	22-34
Figure 22-5	Section Views of LOFT WCOBRA/TRAC-TF2 Vessel Model	22-35
Figure 22-6	Section Views of LOFT WCOBRA/TRAC-TF2 Vessel Model	22-36
Figure 22-7	Section Views of LOFT WCOBRA/TRAC-TF2 Vessel Model	22-37
Figure 22-8	Arrangement of WCOBRA/TRAC Core Channels	22-38
Figure 22-9	LOFT Intact Loop WCOBRA/TRAC-TF2 Model	22-39
Figure 22-10	LOFT Active Loop Steam Generator <u>W</u> COBRA/TRAC-TF2 Model	22-40
Figure 22-11(a)	Inactive (Broken) Loop Break Orifice and Cold Leg Modeling – LOFT Large Break	22-41
Figure 22-11(b)	Inactive (Broken) Loop Break Orifice and Cold Leg Modeling – LOFT Small Break	22-42
Figure 22-11c)	Inactive (Broken) Loop Break Orifice (Gillas and Carpenter, 1980) and Cold Leg Modeling – LOFT Intermediate Break	22-43
Figure 22-12	LOFT Inactive (Broken) Loop Hot Leg WCOBRA/TRAC-TF2 Model	22-44
Figure 22-13	Typical Time History of Cladding Temperature during a LOFT Large break Test Transient	22-45
Figure 22-14	Predicted (Component 500) and Measured (PE-PC-005) Pressure, Test L2-2	22-46
Figure 22-15	Predicted (Component 500) and Measured (PE-PC-005) Pressure, Test L2-3	22-47
Figure 22-16	Predicted (Component 500) and Measured (PE-PC-005) Pressure, Test L2-5	22-48
Figure 22-17	Predicted (Component 500) and Measured (PE-PC-005) Pressure, Test LB-1	22-49
Figure 22-18	Predicted (Component 900) and Measured (FR-BL-216) Mass Flow Rate in Broken Hot Leg, Test L2-2	22-50
Figure 22-19	Predicted (Component 900) and Measured (FR-BL-116) Mass Flow Rate in Broken Hot Leg, Test L2-3	22-51
Figure 22-20	Predicted (Component 900) and Measured (FR-BL-002) Mass Flow Rate in Broken Hot Leg, Test L2-5	22-52

WCAP-16996-NP

J

Figure 22-21	Predicted (Component 900) and Measured (FR-BL-205) Mass Flow Rate in Broken Hot Leg, Test LB-1
Figure 22-22	Predicted (Component 96) and Measured (FR-BL-116) Mass Flow Rate in Broken Cold Leg, Test L2-2
Figure 22-23	Predicted (Component 96) and Measured (FR-BL-216) Mass Flow Rate in Broken Cold Leg, Test L2-3
Figure 22-24	Predicted (Component 96) and Measured (FR-BL-001) Mass Flow Rate in Broken Cold Leg, Test L2-5
Figure 22-25	Predicted (Component 96) and Measured (FR-BL-105) Mass Flow Rate in Broken Cold Leg, Test LB-1
Figure 22-26	Predicted (Component 300) and Measured (FT-P139-27) Mass Flow Rate in Intact Hot Leg, Test L2-2
Figure 22-27	Predicted (Component 300) and Measured (Figures 69, 78, Prassinos, et. al, 1979) Mass Flow Rate in Intact Hot Leg, Test L2-3 22-59
Figure 22-28	Predicted (Component 300) and Measured (FR-PC-201) Mass Flow Rate in Intact Hot Leg, Test L2-5
Figure 22-29	Predicted (Component 810) and Measured (FR-PC-105) Mass Flow Rate in Intact Cold Leg, Test LB-1
Figure 22-30a	Predicted (Component 840) and Measured (FT-P120-36) Volumetric Flow Rate and Predicted (Component 840) Void Fraction from Accumulator, Test L2-2
Figure 22-30b	Predicted (Component 850) and Measured (LIT-P120-087) Liquid Level in Accumulator, Test L2-2
Figure 22-30c	Measured Liquid Levels in Downcomer and Core Regions, Test L2-2 22-64
Figure 22-30d	Predicted Liquid Levels in Downcomer and Core Region, Test L2-2 22-65
Figure 22-30e	Predicted and Measured Liquid Levels in Core Regions, Test L2-2 22-66
Figure 22-31a	Predicted (Component 840) and Measured (FT-P120-36) Volumetric Flow Rate and Predicted (Component 840) Void Fraction from Accumulator, Test L2-3
Figure 22-31b	Predicted (Component 850) and Measured (LIT-P120-084) Liquid Level in Accumulator, Test L2-3
Figure 22-31c	Measured Liquid Levels in Downcomer and Core Regions, Test L2-3
Figure 22-31d	Predicted Liquid Levels in Downcomer and Vessel Core Regions, Test L2-3

Figure 22-31e	Predicted Liquid Levels in Downcomer and Vessel Core Regions, Test L2-3	22-71
Figure 22-32a	Predicted (Component 850) Accumulator Volumetric Flow Rate and Void Fraction, Test L2-5	22-72
Figure 22-32b	Predicted (Component 850) and Measured Accumulator Water Level, Test L2-5	22-73
Figure 22-32c	Measured Liquid Levels in Downcomer and Core Regions, Test L2-5	22-74
Figure 22-32d	Predicted Liquid Levels in Downcomer and Vessel Core Regions, Test L2-5	. 22-75
Figure 22-32e	Predicted and Measured Liquid Levels in Vessel Core Regions, Test L2-5	22-76
Figure 22-33a	Predicted (Component 840) and Measured (FT-P120-36-1) Volumetric Flow Rate and Predicted (Component 840) Void Fraction from Accumulator, Test LB-1	22-77
Figure 22-33b	Predicted (Component 850) and Measured (LIT-P120-044, LIT-P120-087) Accumulator Water Level, Test LB-1	22-78
Figure 22-33c	Predicted Liquid Levels in Downcomer and Vessel Core Regions, Test LB-1	22-79
Figure 22-33e	Predicted Liquid Level in Vessel Core Regions and Measured Vessel LowerPlenum Fluid Temperature, Test LB-1	22-80
Figure 22-34	Predicted (2.72 ft) and Measured Cladding Temperature in the Hot Channel, Test L2-2	22-81
Figure 22-35	Predicted (2.79 ft) and Measured Cladding Temperature in the Hot Channel, Test L2-3	22-82
Figure 22-36	Predicted (1.54 ft) and Measured Cladding Temperature in the Hot Channel, Test L2-5	22-83.
Figure 22-37	Predicted (2.79 ft) and Measured Cladding Temperature in Hot Channel, Test LB-1	22-84
Figure 22-38	Impact of Critical Flow Model Uncertainties on PCS Pressure, Test L2-3	22-85
Figure 22-39	Impact of Critical Flow Model Uncertainties on Cold Leg Break Flow, Test L2-3	22-86
Figure 22-40	Impact of Critical Flow Model Uncertainties on Cladding Temperature, Test L2-3	22-87
Figure 22-41	Predicted (Component 810) and Measured Fluid Temperatures in Intact Cold Leg, Test L2-5	22-88

Figure 22-42	Predicted and Measured Inlet and Outlet Fluid Temperature in Intact Loop Steam Generator, Test L2-5
Figure 22-43	Predicted (Component 600) Pressure Difference Across Intact Loop Pump, Test L2-5
Figure 22-44	Predicted (Rod 1 at 2.18 ft.) and Measured Centerline Fuel Temperature, Test LB-1
Figure 22-45	Predicted and Measured Core Power, Test L2-5
Figure 22-46	Predicted and Measured Primary System Pressure, Test L3-1 22-93
Figure 22-47	Predicted and Measured Steam Generator Secondary Side Pressure, Test L3-1
Figure 22-48	Predicted and Measured Cold Leg Break Flow and Void Fraction Before the Break, Test L3-1
Figure 22-49	Predicted and Measured Accumulator Liquid Level, Test L3-1
Figure 22-50	Predicted and Measured Accumulator Pressure, Test L3-1
Figure 22-51	Measured Primary and SG Secondary Pressure, Test L3-1
Figure 22-52	Impact of SG Secondary Side Pressure on Primary Pressure, Test L3-1 22-99
Figure 22-53	Impact of Critical Flow Model Uncertainties on Primary Pressure, Test L3-1
Figure 22-54	Impact of Critical Flow Model Uncertainties on Break Flow, Test L3-1 22-101
Figure 22-55	Predicted and Measured Primary System Pressure, Test L5-1 22-102
Figure 22-56	Predicted and Measured Cold Leg Break Flow and Break Upstream Void Fraction, Test L5-1
Figure 22-57	Predicted and Measured Primary and Steam Generator Secondary Side Pressure, Test L5-1
Figure 22-58	Predicted and Measured Hot Assembly Cladding Temperature, Test L5-1
Figure 22-59	Predicted and Measured Accumulator Liquid Level, Test L5-1
Figure 22-60	Impact of Critical Flow Model Uncertainties on Primary Pressure, Test L5-1
Figure 22-61	Impact of Critical Flow Model Uncertainties on Break Flow, Test L5-1 22-108
Figure 22-62	Impact of Critical Flow Model Uncertainties on Cladding Temperature, Test L5-1

cvi

LIST OF FIGURES (cont.)

Figure 22-63	Impact of Horizontal Stratification in the Intact Hot Leg on Cladding Temperature, Test L5-1	22-110
Figure 22-64	Impact of Horizontal Stratification in the Intact Hot Leg on Break Flow, Test L5-1	22-111
Figure 22-65	Impact of Horizontal Stratification in the Intact Hot Leg on Cladding Temperature, Test L5-1	22-112
Figure 22-66	Measured Liquid Levels in Reactor Vessel Core Region, Test L5-1	22-113
Figure 22-67	Predicted Liquid Levels in Upper Plenum and Vessel Core Regions (Base Case), Test L5-1	22-113
Figure 22-68	Predicted Liquid Levels in Upper Plenum and Vessel Core Regions (with HS_SLUG=0.1) for Test L5-1	22-114
Figure 22-69	Predicted Flow Regime and Liquid Flow Rate in the Hot Leg for both the Base case and Sensitivity case (with HS_LUG=0.1) for Test L5-1	22-115
Figure 23.1.1-1	Small Blowdown Vessel	23-6
Figure 23.1.1-2	Small Blowdown Vessel Instrumentation	23-7
Figure 23.1.1-3	WCOBRA/TRAC-TF2 Model of the GE Vessel Blowdown Facility	23-8
Figure 23.1.1-4	Comparison of Predicted and Measured Void Fraction at Level 1, Test 8-21-1	23-9
Figure 23.1.1-5	Comparison of Predicted and Measured Void Fraction at Level 2, Test 8-21-1	23-10
Figure 23.1.1-6	Comparison of Predicted and Measured Void Fraction at Level 3, Test 8-21-1	.23-11
Figure 23.1.1-7	Comparison of Predicted and Measured Void Fraction at Level 4, Test 8-21-1	23-12
Figure 23.1.1-8	Comparison of Predicted and Measured Void Fraction at Level 5, Test 8-21-1	23-13
Figure 23.1.1-9	Comparison of Predicted and Measured Void Fraction at Level 6, Test 8-21-1	23-14
Figure 23.1.1-10	Comparison of Predicted and Measured Void Fraction at Level 1, Test 8-25-1	23-15
Figure 23.1.1-11	Comparison of Predicted and Measured Void Fraction at Level 2, Test 8-25-1	23-16
Figure 23.1.1-12	Comparison of Predicted and Measured Void Fraction at Level 3, Test 8-25-1	23-17

t

Figure 23.1.1-13	Comparison of Predicted and Measured Void Fraction at Level 4, Test 8-25-1
Figure 23.1.1-14	Comparison of Predicted and Measured Void Fraction at Level 5, Test 8-25-1
Figure 23.1.1-15	Comparison of Predicted and Measured Void Fraction at Level 6, Test 8-25-1
Figure 23.1.1-16	Comparison of Predicted and Measured Void Fraction at Level 1, Test 8-28-1
Figure 23.1.1-17	Comparison of Predicted and Measured Void Fraction at Level 2, Test 8-28-1
Figure 23.1.1-18	Comparison of Predicted and Measured Void Fraction at Level 3, Test 8-28-1
Figure 23.1.1-19	Comparison of Predicted and Measured Void Fraction at Level 4, Test 8-28-1
Figure 23.1.1-20	Comparison of Predicted and Measured Void Fraction at Level 5, Test 8-28-1
Figure 23.1.1-21	Comparison of Predicted and Measured Void Fraction at Level 6, Test 8-28-1
Figure 23.1.1-22	Comparison of Predicted and Measured Void Fraction at Level 1, Test 9-1-1
Figure 23.1.1-23	Comparison of Predicted and Measured Void Fraction at Level 2, Test 9-1-1
Figure 23.1.1-24	Comparison of Predicted and Measured Void Fraction at Level 3, Test 9-1-1
Figure 23.1.1-25	Comparison of Predicted and Measured Void Fraction at Level 4, Test 9-1-1
Figure 23.1.1-26	Comparison of Predicted and Measured Void Fraction at Level 5, Test 9-1-1
Figure 23.1.1-27	Comparison of Predicted and Measured Void Fraction at Level 6, Test 9-1-1
Figure 23.1.1-28	Comparison of Predicted and Measured Void Fraction at Level 1, Test 9-15-1
Figure 23.1.1-29	Comparison of Predicted and Measured Void Fraction at Level 2, Test 9-15-1

Figure 23.1.1-30	Comparison of Predicted and Measured Void Fraction at Level 3, Test 9-15-1	23-35
Figure 23.1.1-31	Comparison of Predicted and Measured Void Fraction at Level 4, Test 9-15-1	
Figure 23.1.1-32	Comparison of Predicted and Measured Void Fraction at Level 5, Test 9-15-1	
Figure 23.1.1-33	Comparison of Predicted and Measured Void Fraction at Level 6, Test 9-15-1	
Figure 23.1.1-34	Comparison of Predicted and Measured Void Fraction at Level 1, Test 1004-3	
Figure 23.1.1-35	Comparison of Predicted and Measured Void Fraction at Level 2, Test 1004-3	
Figure 23.1.1-36	Comparison of Predicted and Measured Void Fraction at Level 3, Test 1004-3	
Figure 23.1.1-37	Comparison of Predicted and Measured Void Fraction at Level 4, Test 1004-3	
Figure 23.1.1-38	Comparison of Predicted and Measured Void Fraction at Level 5, Test 1004-3	
Figure 23.1.1-39	Comparison of Predicted and Measured Void Fraction at Level 6, Test 1004-3	
Figure 23.1.1-40	Comparison of Predicted and Measured Void Fraction at Level 1, Test 1004-2	
Figure 23.1.1-41	Comparison of Predicted and Measured Void Fraction at Level 2, Test 1004-2	23-46
Figure 23.1.1-42	Comparison of Predicted and Measured Void Fraction at Level 3, Test 1004-2	23-47
Figure 23.1.1-43	Comparison of Predicted and Measured Void Fraction at Level 4, Test 1004-2	
Figure 23.1.1-44	Comparison of Predicted and Measured Void Fraction at Level 5, Test 1004-2	
Figure 23.1.1-45	Comparison of Predicted and Measured Void Fraction at Level 6, Test 1004-2	
Figure 23.1.2-1	Semiscale Mod-3 Facility Overview	
Figure 23.1.2-2	Plan View of Semiscale Mod-3 Core for S-07-10D Test	

(

Figure 23.1.2-3	Semiscale S-07-10D Test Axial Power Profile in Relation to Vessel Instrumentation	-61
Figure 23.1.2-4	Semiscale Mod-3 Pressure Vessel and Downcomer – Cross Section Showing Instrumentation	-62
Figure 23.1.2-5	WCOBRA/TRAC-TF2 Semiscale Mod 3 Vessel Model 23-	-63
Figure 23.1.2-6	Semiscale S-07-10D Test Upper Plenum Pressure (Hot Leg Backpressure)	.64
Figure 23.1.2-7	Semiscale S-07-10D Test Lower Plenum Fluid Temperature	-65
Figure 23.1.2-8	Semiscale S-07-10D Test Core Power Decay	66
Figure 23.1.2-9	Semiscale S-07-10D Test Core Collapsed Liquid Level	·67
Figure 23.1.2-10	Density Measurement Recorded During Semiscale S-07-10D Test 23-	·68
Figure 23.1.2-11	Semiscale S-07-10D Clad Temperature at Elevation = 354 cm (from the Bottom of the Core)	·69
Figure 23.1.2-12	Semiscale S-07-10D Clad Temperature at Elevation = 322 cm (from the Bottom of the Core)	.70
Figure 23.1.2-13	Semiscale S-07-10D Clad Temperature at Elevation = 277 cm (from the Bottom of the Core)	.71
Figure 23.1.2-14	Semiscale S-07-10D Clad Temperature at Elevation = 254 cm (from the Bottom of the Core)	.72
Figure 23.1.2-15	Semiscale S-07-10D Clad Temperature at Elevation = 226 cm (from the Bottom of the Core)	73
Figure 23.1.2-16	Semiscale S-07-10D Clad Temperature at Elevation = 208 cm (from the Bottom of the Core)	.74
Figure 23.1.2-17	Semiscale S-07-10D Clad Temperature at Elevation = 190 cm (from the Bottom of the Core)	75
Figure 23.1.2-18	Semiscale S-07-10D Clad Temperature at Elevation = 181 cm (from the Bottom of the Core)	76
Figure 23.1.2-19	Semiscale S-07-10D Clad Temperature at Elevation = 167 cm (from the Bottom of the Core)	77
Figure 23.1.2-20	Semiscale S-07-10D Clad Temperature Elevation = 135 cm (from the Bottom of the Core)	78
Figure 23.1.2-21	Semiscale S-07-10D Clad Temperature at Elevation = 112 cm (from the Bottom of the Core)	79

7,

Figure 23.1.2-22	Semiscale S-07-10D Clad Temperature at Elevation = 71 cm (from the Bottom of the Core)	80
Figure 23.1.2-23	Semiscale S-07-10D Clad Temperature at Elevation = 48 cm (from the Bottom of the Core)	81
Figure 23.1.2-24	Semiscale S-07-10D Clad Temperature at Elevation = 7 cm (from the Bottom of the Core)	82
Figure 23.1.2-25	Semiscale S-07-10D Collapsed Liquid Level	33
Figure 23.1.2-26	Semiscale S-07-10D Void Fraction at Inlet of the Core (502 cm below CL Centerline)	34
Figure 23.1.2-27	Semiscale S-07-10D Void Fraction at 483 cm below CL Centerline 23-8	35
Figure 23.1.2-28	Semiscale S-07-10D Void Fraction at 323 cm below CL Centerline	36
Figure 23.1.2-29	Semiscale S-07-10D Void Fraction at 313 cm below CL Centerline	37 [.]
Figure 23.1.2-30	Semiscale S-07-10D Void Fraction at 243 cm below CL Centerline	38
Figure 23.1.2-31	Semiscale S-07-10D Void Fraction at 164 cm below CL Centerline 23-8	39
Figure 23.1.2-32	Semiscale S-07-10D Void Fraction at Core Outlet (11 cm below CL Centerline)) 0
Figure 23.1.2-33	Semiscale S-07-10D Mixture Level) 1
Figure 23.2.1-1	Schematic and Nodalization Diagram for the Oscillating Manometer (note that Nodes 1 and 20 are each Connected to a PIPE Component not Depicted in the Diagram)	94
Figure 23.2.1-2	WCOBRA/TRAC-TF2 Results for Liquid Velocity at the Bottom of the Tube	€
Figure 23.2.1-3	WCOBRA/TRAC-TF2 Results for Liquid Velocity at the Bottom of the Tube	96
Figure 23.2.2-1	WCOBRA/TRAC-TF2 Model of the Manometer Test Problem using the VESSEL Component) 9
Figure 23.2.2-2	Velocity at the Bottom Gap of the 3D Manometer)0
Figure 23.2.2-3	Collapsed Liquid Levels and Total System Mass in the 3D Manometer)1
Figure 23.2.3-1	Nodalization and Schematic for Steam Expulsion Test using 1D Pipe 23-10)5
Figure 23.2.3-2	Pressure Profile in the 1D Pipe for the Steam Expulsion Test, Superheated Steam Case)6
Figure 23.2.3-3	Pressure Profile in the 1D Pipe for the Steam Expulsion Test, Superheated Steam Case)7

Figure 23.2.3-4	Void Fraction Profile in the 1D Pipe for the Steam Expulsion Test, Superheated Steam Case	23-108
Figure 23.2.3-5	Liquid Velocity Profile in the 1D Pipe for the Steam Expulsion Test, Superheated Steam Case	23-109
Figure 23.2.3-6	Steam Velocity Profile in the 1D Pipe for the Steam Expulsion Test, Superheated Steam Case	23-110
Figure 23.2.3-7	Liquid Temperature Profile in the 1D Pipe for the Steam Expulsion Test, Superheated Steam Case	23-111
Figure 23.2.3-8	Vapor Temperature Profile in the 1D Pipe for the Steam Expulsion Test, Superheated Steam Case	23-112
Figure 23.2.3-9	Pressure Profile in the 1D Pipe for the Steam Expulsion Test, Saturated Steam Case	23-113
Figure 23.2.3-10	Void Fraction Profile in the 1D Pipe for the Steam Expulsion Test, Saturated Steam Case	23-114
Figure 23.2.3-11	Liquid Velocity Profile in the 1D Pipe for the Steam Expulsion Test, Saturated Steam Case	23-115
Figure 23.2.3-12	Steam Velocity Profile in the 1D Pipe for the Steam Expulsion Test, Saturated Steam Case	23-116
Figure 23.2.3-13	Liquid Temperature Profile in the 1D Pipe for the Steam Expulsion Test, Saturated Steam Case	23-117
Figure 23.2.3-14	Vapor Temperature Profile in the 1D Pipe for the Steam Expulsion Test, Saturated Steam Case	23-118
Figure 23.2.4-1	Steam Expulsion Test using 3D Vessel	23-121
Figure 23.2.4-2	Collapsed Liquid Level in the Vessel for the Steam Expulsion Test, Superheated Steam Case	23-122
Figure 23.2.4-3	Pressure Profile in the 3D Vessel for Steam Expulsion Test, Superheated Steam Case	23-123
Figure 23.2.4-4	Void Fraction Profile in the 3D Vessel for the Steam Expulsion Test, Superheated Steam Case	23-124
Figure 23.2.4-5	Liquid Temperature Profile in the 3D Pipe for the Steam Expulsion Test, Superheated Steam Case	23-125
Figure 23.2.4-6	Vapor Temperature Profile in the 3D Vessel for the Steam Expulsion Test, Superheated Steam Case	23-126
Figure 23.2.4-7	Liquid Velocity Profile in the 3D Vessel for the Steam Expulsion Test, Superheated Steam Case	23-127

Figure 23.2.4-8	Vapor Velocity Profile in the 3D Vessel for the Steam Expulsion Test, Superheated Steam Case, Superheated Steam Case	23-128
Figure 23.2.4-9	Collapsed Liquid Level in the Vessel for the Steam Expulsion Test, Saturated Steam Case	23-129
Figure 23.2.4-10	Pressure Profile in the 3D Vessel for the Steam Expulsion Test, Saturated Steam Case	23-130
Figure 23.2.4-11	Void Fraction Profile in the 3D Vessel for the Steam Expulsion Test, Saturated Steam Case	23-131
Figure 23.2.4-12	Liquid Temperature Profile in the 3D Pipe for the Steam Expulsion Test, Saturated Steam Case	23-132
Figure 23.2.4-13	Vapor Temperature Profile in the 3D Vessel for the Steam Expulsion Test, Saturated Steam Case	23-133
Figure 23.2.4-14	Liquid Velocity Profile in the 3D Vessel for the Steam Expulsion Test, Saturated Steam Case	23-134
Figure 23.2.4-15	Vapor Velocity Profile in the 3D Vessel for the Steam Expulsion Test, Saturated Steam Case	23-135
Figure 23.2.5-1	Fill and Drain Model using 1D Pipe	23-138
Figure 23.2.5-2	Predicted Void Fraction between 10 s and 20 s in the 1D Fill and Drain Problem without Steam Injection	23-139
Figure 23.2.5-3	Predicted Pressure between 10 s and 20 s in the 1D Fill and Drain Problem without Steam Injection	23-140
Figure 23.2.5-4	Predicted Void Fraction between 10 s and 20 s in the 1D Fill and Drain Problem with Steam Injection	23-141
Figure 23.2.5-5	Predicted Pressure between 10 s and 20 s in the 1D Fill and Drain Problem without Steam Injection	23-142
Figure 23.2.6-1	Fill and Drain Model using 3D Vessel	23-145
Figure 23.2.6-2	Predicted Collapsed Liquid Level in the 3D Fill and Drain Problem without Steam Injection	23-146
Figure 23.2.6-3	Predicted Void Fraction between 10 s and 20 s in the 3D Fill and Drain Problem without Steam Injection	23-147
Figure 23.2.6-4	Predicted Pressure between 10 s and 20 s in the 3D Fill and Drain Problem without Steam Injection	23-148
Figure 23.2.6-5	Predicted Pressure between 10 s and 20 s in the 3D Fill and Drain Problem without Steam Injection	23-149

Figure 23.2.6-6	Predicted Collapsed Liquid Level in the 3D Fill and Drain Problem with Steam Injection
Figure 23.2.6-7	Predicted Void Fraction between 10 s and 20 s in the 3D Fill and Drain Problem with Steam Injection
Figure 23.2.6-8	Predicted Pressure between 10 s and 20 s in the 3D Fill and Drain Problem with Steam Injection
Figure 23.2.7-1	3D Vessel Model used in the Condensation Test Problem
Figure 23.2.7-2	Void Fraction in the Condensation Test Problem, Vapor only Case
Figure 23.2.7-3	Flow Regime in the Condensation Test Problem, Vapor Only Case 23-157
Figure 23.2.7-4	Heat Transfer to Vapor and Vapor Velocity in the Condensation Test Problem, Vapor Only Case
Figure 23.2.7-5	Heat Transfer to Liquid and Liquid Velocity in the Condensation Test Problem, Vapor Only Case
Figure 23.2.7-6	Void Fraction and Relative Humidity in the Condensation Test Problem, Vapor and Non-Condensable Gas Case
Figure 23.2.7-7	Total, Steam, and Non-Condensable Gas Partial Pressures in the Condensation Test Problem, Vapor and Non-Condensable Gas Case
Figure 23.2.7-8	Gas, Liquid, Saturation, and Dew point Temperatures in the Condensation Test Problem, Vapor and Non-Condensable Gas Case
Figure 24.5-1	Comparison of Vessel Condensation Efficiency versus Nominal Steam Flow Rate, UPTF Test 6; The Experimental Condensation Efficiency is Estimated by MPR (MPR-1163, 1990)
Figure 24.5-2	ECC Liquid Temperature Comparison near Vessel Inlet
Figure 24.5-3	Downcomer Void Height Comparison in UPTF Test 25A
Figure 24.5-4	Broken Loop Steam Flow Rate in UPTF Test 25A
Figure 24.5-5	Cold Leg Temperature at Exit of Cold Leg for UPTF Test 25A 24-18
Figure 24.6.1-1	Heat Transfer Coefficient Comparison for ORNL-THTF
Figure 24.6.1-2	Prediction Error as a Function of Vapor Reynolds Number
Figure 24.6.1-3	Heat Transfer Coefficient Comparison for FLECHT SPV Tests
Figure 24.6.1-4	Ratio of Measured to Predicted Heat Transfer Coefficient vs. Vapor Film Reynolds Number for FLECHT SPV Tests (from COBRAHT-TF2)
Figure 24.6.1-5	Average Heat Transfer Coefficient Comparison for ORNL Steady-State Film Boiling Tests

Figure 24.6.1-6	Predicted Heat Flux Bias vs. Rev for ORNL Data	. 24-23
Figure 24.6.1-7	Predicted Heat Flux Bias vs. Void Fraction for DFFB Data	. 24-24
Figure 24.6.2-1	ORNL Test 3.03.36AR – Vapor Temperature and TLIQ (=Tsat) at Bundle Exit Calculated by <u>W</u> COBRA/TRAC-TF2	. 24-27
Figure 24.6.2-2	ORNL Test 3.08.6C – Vapor Temperature and TLIQ (=Tsat) at Bundle Exit Calculated by <u>W</u> COBRA/TRAC-TF2	. 24-28
Figure 24.6.3-1	Cladding Temperature During LBLOCA for Three-Loop Plant	. 24-33
Figure 24.6.3-2	Mass Flux at PCT Location During Blowdown (0-30 Seconds)	. 24-34
Figure 24.6.3-3	Void Fraction at PCT Location During Blowdown (0-30 Seconds)	. 24-35
Figure 24.6.3-4	Axial Cladding Temperature Distribution at Blowdown PCT Time (7.5 Seconds after Break)	. 24-36
Figure 24.6.3-5	Axial Cladding Temperature Profile at End of Blowdown Cooling Time (11.5 Seconds after Break)	. 24-37
Figure 24.6.3-6	Blowdown Cooling Rates for the G 1 Blowdown Heat Transfer Tests	. 24-38
Figure 24.6.3-7	Cladding Axial Temperature at Start of Test (6 Seconds), 15, 20, 30 Seconds for Case 1 (Test 148)	. 24-39
Figure 24.6.3-8	Cladding Axial Temperature at Start of Test (6 Seconds), 15, 20, 30 Seconds for Case 2 (Test 143)	. 24-40
Figure 24.6.3-9	Cladding Axial Temperature at Start of Test (6 Seconds), 15, 20, 30 Seconds for Case 3 (Test 152)	. 24-41
Figure 24.6.3-10	Cladding Axial Temperature at Start of Test (6 Seconds), 15, 20, 30 Seconds for Case 4 (Test 146)	. 24-42
Figure 24.6.3-11	Cladding Axial Temperature at Start of Test (6 Seconds), 15, 20, 30 Seconds for Case 5 (Test 154)	. 24-43
Figure 24.6.3-12	Cladding Axial Temperature at Start of Test (6 Seconds), 15, 20, 30 Seconds for Case 6 (Test 153)	. 24-44
Figure 24.6.3-13	WCOBRA/TRAC-TF2 Heat Transfer Regime Map	. 24-45
Figure 24.6.3-14	Vapor Fraction at 72-inch Elevation for G-1 Test 148 (Case 1)	. 24-46
Figure 24.6.3-15	Heat Flux to Vapor at 72-inch Elevation for G-1 Test 148 (Case 1)	. 24-47
Figure 24.6.3-16	Heat Flux to Liquid at 72-inch Elevation for G-1 Test 148 (Case 1)	. 24-48
Figure 24.6.3-17	Vapor Fraction at 72-inch Elevation for G-1 Test 146 (Case 4)	. 24-49
Figure 24.6.3-18	Heat Flux to Vapor at 72-inch Elevation for G-1 Test 146 (Case 4)	. 24-50
Figure 24.6.3-19	Heat Flux to Liquid at 72-inch Elevation for G-1 Test 146 (Case 4)	. 24-51

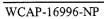


Figure 24.6.3-20	Effect of Reduced T _{min} on Cladding Axial Temperature at 26 Seconds for Case 1 (Test 148)	. 24-52
Figure 24.6.3-21	Effect of Reduced T _{min} on Axial Vapor Temperature at 26 Seconds for Case 1 (Test 148)	. 24-53
Figure 24.6.3-22	Effect of Reduced D _{DROP} on Cladding Axial Temperature at 26 Seconds for Case 1 (Test 148)	. 24-54
Figure 24.6.3-23	Effect of Reduced D _{DROP} on Axial Vapor Temperature at 26 Seconds for Case 1 (Test 148)	. 24-55
Figure 24.6.3-24	Effect of Reduced T _{min} on Cladding Axial Temperature at 22 Seconds for Case 4 (Test 146)	. 24-56
Figure 24.6.3-25	Effect of Reduced T _{min} on Axial Vapor Temperature at 22 Seconds for Case 4 (Test 146)	. 24-57
Figure 24.6.3-26	Effect of Reduced D_{DROP} on Cladding Axial Temperature at 22 Seconds for Case 4 (Test 146).	. 24-58
Figure 24.6.3-27	Effect of Reduced D _{DROP} on Axial Vapor Temperature at 22 Seconds for Case 4 (Test 146)	, 24-59
Figure 24.6.4-1	TCLAD vs. Time at 6 ft for FLECHT-31504	24-62
Figure 24.6.4-2	TCLAD vs. Time at 9.3 ft for FLECHT-31504	24-63
Figure 24.6.4-3	Lower DP vs. Time for FLECHT-31504	24-64
Figure 24.6.4-4	Upper DP vs. Time for FLECHT-31504	24-65
Figure 24.6.4-5	Quench Front Elevation vs. Time for FLECHT-31504	24-66
Figure 24.6.4-6a	Vapor Temperature Profile Prediction at 200 Seconds in FLECHT-31504	24-67
Figure 24.6.4-6b	Vapor Temperature Profile Prediction at 260 Seconds Compared against Data taken at 200 Seconds	24-68
Figure 24.6.4-7	Void Fraction Profile Comparison when the Quench Front is at 60 inches (Prediction at 260 and Data at 200 Seconds) in FLECHT-31504	24-69
Figure 24.6.4-8	Drop Velocity vs. Diameter Comparison at ~1ft above Quench Front (Prediction at 260 and Data at 200~206 Seconds) in FLECHT-31504	24-70
Figure 24.6.4-9	Bundle Vapor Flow Comparison (Prediction at 260 and Data at 200 Seconds) in FLECHT-31504	24-71
Figure 24.6.4-10	Heat Transfer to Vapor Comparison (Prediction at 260 and Data at 200 Seconds) in FLECHT-31504	24-72
Figure 24.6.4-11	Heat Transfer to Liquid Comparison (Prediction at 260 and Data at 200 Seconds) in FLECHT-31504	24-73

Figure 24.6.4-12	Predicted Fraction of Heat Transfer to Liquid in FLECHT-31504	24-74
Figure 24.6.4-13	Vapor Reynolds Number Comparison (Prediction at 260 and Data at 200 Seconds) in FLECHT-31504	24-75
Figure 24.6.4-14	Vapor Nusselt Number Comparison (Prediction at 260 and Data at 200 Seconds) in FLECHT-31504	24-76
Figure 24.6.5-1	Comparison of Measured Void Fraction Distribution Reported for FLECHT-SEASET Tests 31805 and 31701	24-79
Figure 24.6.5-2	TCLAD Profile at 100 Seconds in FLECHT-31805	24-80
Figure 24.6.5-3	Heat Transfer Coefficient vs. Time at ~6 ft in FLECHT-31805	24-81
Figure 24.6.5-4	Axial Comparison of Predicted and Measured HTC in FLECHT-SEASET 31805	24-82
Figure 24.6.5-5	Void Fraction Profile in FLECHT-SEASET 31805	24-83
Figure 24.6.5-6	Measured Void Fraction near 6 ft in FLECHT-SEASET 31805	24-84
Figure 24.6.5-7	Measured Clad Temperature, Void Fraction at 6 ft in FLECHT-SEASET 31805 (Only one Legend is shown but all Available Thermocouples are Plotted)	24-85
Figure 24.6.5-8	Measured HTC, Void Fraction at 6 ft in FLECHT-SEASET 31805 (Only one Legend is shown but all Available Thermocouples are Plotted)	24-86
Figure 24.6.5-9	Expanded View of Measured Clad Temperature, Void Fraction at 6 ft in FLECHT-SEASET 31805 (Only one Legend is shown but all Available Thermocouples are Plotted)	24-87
Figure 24.6.5-10	Expanded View of Measured HTC, Void Fraction at 6 ft in FLECHT-SEASET 31805 (Only one Legend is shown but all Available Thermocouples are Plotted)	24-88
Figure 24.6.5-11	Predicted Clad Temperature, Void Fraction at 6 ft in FLECHT-SEASET 31805	24-89
Figure 24.6.5-12	Predicted HTC, Void Fraction at 6 ft in FLECHT-SEASET 31805	24-90
Figure 24.6.5-13	Void Fraction Comparison at 6 ft in FLECHT-SEASET 31805	24-91
Figure 24.6.5-14	Measured Clad Temperature, Void Fraction at 10 ft in FLECHT-31805 (Only one Legend is shown but all Available Thermocouples are Plotted)	24-92
Figure 24.6.5-15	Measured HTC, Void Fraction at 10 ft in FLECHT-SEASET 31805 (Only one Legend is shown but all Available Thermocouples are Plotted)	24-93
Figure 24.6.5-16	Predicted Clad Temperature, Void Fraction at 10 ft in FLECHT-SEASET 31805	24-94

Figure 24.6.5-17	Predicted HTC, Void Fraction at 10 ft in FLECHT-SEASET 31805 24-95
Figure 24.6.5-18	Void Fraction Comparison at 10-11 ft in FLECHT-SEASET 31805 24-96
Figure 24.6.5-19	Void Fraction Axial Profile Comparison [] ^{a,c}] ^{a,c} 24-97
Figure 24.6.6-1	Void Fraction Measurement at 5-7 ft for FLECHT-SEASET 31701 24-100
Figure 24.6.6-2	Measured Clad Temperature, Void Fraction for FLECHT-SEASET 31701 24-101
Figure 24.6.6-3	Measured HTC, Void Fraction Relation for FLECHT-SEASET 31701
Figure 24.6.6-4	Predicted Clad Temperature, Void Fraction Relation at 6 ft for FLECHT-SEASET 31701
Figure 24.6.6-5	Predicted HTC, Void Fraction Relation at 6 ft for FLECHT-SEASET 31701
Figure 24.6.6-6	Comparison of Predicted and Measured Void Fraction Relation at 6-7 ft for FLECHT-SEASET 31701
Figure 24.6.6-7	Void Fraction Measurement at 9-11 ft for FLECHT-SEASET 31701 24-106
Figure 24.6.6-8	Measured Clad Temperature, Void Fraction Relation at 10 ft for FLECHT-SEASET 31701
Figure 24.6.6-9	Measured HTC, Void Fraction Relation at 10 ft for FLECHT-SEASET 31701
Figure 24.6.6-10	Predicted Clad Temperature, Void Fraction Relation at 10 ft for FLECHT-SEASET 31701
Figure 24.6.6-11	Predicted HTC, Void Fraction Relation at 10 ft for FLECHT-SEASET 3170124-110
Figure 24.6.6-12	Comparison of Measured and Predicted Void Fraction at 10 ft for FLECHT-SEASET 3170124-111
Figure 24.7.1-1	LOFT Measurement/Prediction Locations
Figure 24.7.1-2	.LOFT L2-3 Data vs. Predicted Hot Rod Cladding Temperature24-117
Figure 24.7.1-3	Predicted Vapor Flowrate at Top and Bottom of Hot Assembly
Figure 24.7.1-4	Predicted Entrained Drop Flowrate at Top and Bottom of Hot Assembly24-119
Figure 24.7.1-5	LOFT L2-3 Data vs. Predicted Steam Temperature at Top of Hot Assembly
Figure 24.7.1-6	LOFT L2-3 Data vs. Predicted Steam Temperature at Bottom of Hot Assembly
Figure 24.7.1-7	Predicted Hot Rod Vapor Heat Transfer Coefficient at PCT Elevation

Figure 24.7.1-8	Predicted Hot Rod Liquid Heat Transfer Coefficient at PCT Elevation	23
Figure 24.7.1-8a	Predicted Hot Rod Liquid Heat Transfer Coefficient at PCT Elevation (Expanded Scale)	24
Figure 24.7.1-9	Measured and Predicted Intact Loop Pressure	25
Figure 24.7.1-10	Predicted Downcomer Collapsed Liquid Level (1- Intact, 2-Broken Side) 24-12	26
Figure 24.7.1-11	Predicted and Measured Core Collapsed Liquid Level (Line 5-Estimated from the Liquid Detector)	27
Figure 24.7.1-12	Predicted Upper Plenum Collapsed Liquid Level	28
Figure 24.7.1-13	Measured and Predicted Intact Loop Hot Leg Flowrate	29
Figure 24.7.1-14	Measured and Predicted Intact Loop Hot Leg Mixture Density	60
Figure 24.7.1-15	Measured and Predicted Intact Loop Hot Leg Mixture Velocity	31
Figure 24.7.1-15a	Measured and Predicted Intact Loop Pressure Comparison	2
Figure 24.7.1-16	Measured and Predicted Intact Loop Cold Leg Flowrate	3
Figure 24.7.1-17	Measured and Predicted Intact Loop Cold Leg Flowrate	4
Figure 24.7.1-18	Measured and Predicted Intact Loop Cold Leg Mixture Density 24-13	5
Figure 24.7.1-19	Measured and Predicted Intact Loop Cold Leg Mixture Density 24-13	6
Figure 24.7.1-20	Measured and Predicted Intact Loop Cold Leg Mixture Velocity 24-13	7
Figure 24.7.1-21	Measured and Predicted Intact Loop Cold Leg Mixture Velocity 24-13	8
Figure 24.7.1-22	Measured and Predicted Hot Leg Break Flowrate	9
Figure 24.7.1-23	Measured and Predicted Broken Loop Hot Leg Mixture Density 24-14	0
Figure 24.7.1-24	Measured and Predicted Broken Loop Hot Leg Mixture Velocity	1
Figure 24.7.1-25	Predicted Void Fraction in Upper Plenum at Loop Level	2
Figure 24.7.1-26	Predicted Void Fraction in Upper Plenum above Upper Core Plate	.3
Figure 24.7.1-27	Measured and Predicted Cold Leg Break Flowrate	.4
Figure 24.7.1-28	Measured and Predicted Broken Cold Leg Mixture Density 24-14	.5
Figure 24.7.1-29	Measured and Predicted Broken Cold Leg Mixture Velocity 24-14	6
Figure 24.7.1-30	Mid-Elevation Cladding Temperature Comparison in Sensitivity Run with CD2=1.05	7
Figure 24.7.1-31	Predicted Vapor Flowrate at Top and Bottom of Hot Assembly in Sensitivity Run with CD2=1.05	8

Figure 24.7.1-32	Predicted Entrained Drop Flowrate at Top and Bottom of Hot Assembly in Sensitivity Run with CD2=1.05
Figure 24.7.1-33	Predicted Hot Rod Liquid Heat Transfer Coefficient at PCT Elevation in Sensitivity Run with CD2=1.05
Figure 24.7.2-1	Measured vs. Predicted Hot Rod Cladding Temperature
Figure 24.7.2-2	Predicted Vapor Flowrate at Top and Bottom of Hot Assembly
Figure 24.7.2-3	Predicted Entrained Drop Flowrate at Top and Bottom of Hot Assembly 24-157
Figure 24.7.2-4	LOFT L2-5 Data vs. Predicted Steam Temperature at Top of Hot Assembly
Figure 24.7.2-5	LOFT L2-5 Data vs. Predicted Steam Temperature at Bottom of Hot Assembly
Figure 24.7.2-6	Predicted Hot Rod Vapor Heat Transfer Coefficient at PCT Elevation
Figure 24.7.2-7	Predicted Hot Rod Liquid Heat Transfer Coefficient at PCT Elevation
Figure 24.7.2-7a	Predicted Hot Rod Liquid Heat Transfer Coefficient at PCT Elevation (with Expanded Scale)
Figure 24.7.2-8	Measured and Predicted Intact Loop Pressure
Figure 24.7.2-9	Predicted Downcomer Collapsed Liquid Level (1- Intact, 2-Broken side) 24-164
Figure 24.7.2-10	Predicted and Measured Core Collapsed Liquid Level (Line 2-Estimated from the Liquid Detector)
Figure 24.7.2-11	Predicted Upper Plenum Collapsed Liquid Level
Figure 24.7.2-12	Measured and Predicted Intact Loop Hot Leg Flowrate
Figure 24.7.2-13	Measured and Predicted Intact Loop Hot Leg Mixture Density 24-168
Figure 24.7.2-14	Measured and Predicted Intact Loop Hot Leg Mixture Velocity
Figure 24.7.2-15	Measured and Predicted Intact Loop Cold Leg Flowrate
Figure 24.7.2-16	Measured and Predicted Intact Loop Cold Leg Flowrate
Figure 24.7.2-17	Measured and Predicted Intact Loop Cold Leg Mixture Density
Figure 24.7.2-18	Measured and Predicted Intact Loop Cold Leg Mixture Density 24-173
Figure 24.7.2-19	Measured and Predicted Intact Loop Cold Leg Mixture Velocity 24-174
Figure 24.7.2-20	Measured and Predicted Intact Loop Cold Leg Mixture Velocity
Figure 24.7.2-21	Measured and Predicted Hot Leg Break Flowrate
Figure 24.7.2-22	Measured and Predicted Hot Leg Mixture Density

Figure 24.7.2-23	Measured and Predicted Broken Loop Hot Leg Mixture Velocity	24-178
Figure 24.7.2-24	Predicted Void Fraction in Upper Plenum at Loop Level	24-179
Figure 24.7.2-25	Predicted Void Fraction in Upper Plenum at Exit of CCFL Region	24-180
Figure 24.7.2-26	Measured and Predicted Cold Leg Break Flowrate	24-181
Figure 24.7.2-27	Measured and Predicted Broken Cold Leg Mixture Density	24-182
Figure 24.7.2-28	Measured and Predicted Broken Cold Leg Mixture Velocity	24-183
Figure 24.7.2-29	Predicted Broken Cold Leg Nozzle DP	24-184
Figure 24.7.2-30	Predicted Broken Cold Leg Pressure Drop to the Break Plane	24-185
Figure 24.7.3-1a	Pressure, Differential Pressure, Liquid Level and Mass Flowrate Instrumentation Location in Pressure Vessel	24-190
Figure 24.7.3-1b	Top View of Primary Loop Piping	24-191
Figure 24.7.3-2	Core Inlet Flow Comparison	24-192
Figure 24.7.3-3	CCTF Run 62 WCOBRA/TRAC-TF2 vs. Data – Cladding Temperature Comparison at 3.33 ft	24-193
Figure 24.7.3-4	CCTF Run 62 WCOBRA/TRAC-TF2 vs. Data Cladding Temperature Comparison at 6 ft	24-194
Figure 24.7.3-5	CCTF Run 62 WCOBRA/TRAC-TF2 vs. Data Cladding Temperature Comparison at 6.68 ft	24-195
Figure 24.7.3-6	CCTF Run 62 WCOBRA/TRAC-TF2 vs. Data Cladding Temperature Comparison at 8 ft	24-196
Figure 24.7.3-7	CCTF Run 62 WCOBRA/TRAC-TF2 vs. Data Cladding Temperature Comparison at 10 ft	24-197
Figure 24.7.3-8	CCTF Run 62 WCOBRA/TRAC-TF2 vs. Data Vapor Temperature Comparison at 6 ft	24-198
Figure 24.7.3-9	CCTF Run 62 WCOBRA/TRAC-TF2 vs. Data Vapor Temperature Comparison at 8 ft	24-199
Figure 24.7.3-10	CCTF Run 62 WCOBRA/TRAC-TF2 vs. Data Comparison Void Fraction from 2.1 to 2.71 m	24-200
Figure 24.7.3-11	CCTF Run 62 WCOBRA/TRAC-TF2 vs. Data Comparison Void Fraction from 2.71 to 3.32 m	24-201
Figure 24.7.3-12	CCTF Run 62 WCOBRA/TRAC-TF2 vs. Data Comparison Void Fraction from 3.32 to 3.93 m	24-202

Figure 24.7.3-13	CCTF Run 62 <u>W</u> COBRA/TRAC-TF2 vs. Data Comparison Void Fraction from 3.93 to 4.54 m	24-203
Figure 24.7.3-14	CCTF Run 62 <u>W</u> COBRA/TRAC-TF2 vs. Data Comparison Void Fraction from 4.54 to 5.15 m	24-204
Figure 24.7.3-15	CCTF Run 62 WCOBRA/TRAC-TF2 vs. Data Comparison Void Fraction from 5.15 to 5.76 m	24-205
Figure 24.7.3-16	CCTF Run 62 <u>W</u> COBRA/TRAC-TF2 vs. Data Comparison Void Fraction from Top of Upper Core Plate to Bottom of Upper Support Plate	24-206
Figure 24.7.3-17	CCTF Run 62 <u>W</u> COBRA/TRAC-TF2 vs. Data Collapsed Liquid Level in Core	24-207
Figure 24.7.3-18	CCTF Run 62 <u>W</u> COBRA/TRAC-TF2 vs. Data Collapsed Liquid Level in Upper Plenum	24-208
Figure 24.7.3-19	CCTF Run 62 WCOBRA/TRAC-TF2 vs. Data Pressure in Upper Plenum	24-209
Figure 24.7.3-20	CCTF Run 62 WCOBRA/TRAC-TF2 vs. Data Pressure Difference from Lower Plenum to Upper Plenum	24-210
Figure 24.7.3-21	CCTF Run 62 WCOBRA/TRAC-TF2 vs. Data Pressure Difference from Lower Plenum to Top of Downcomer	24-211
Figure 24.7.3-22	CCTF Run 62 <u>W</u> COBRA/TRAC-TF2 vs. Data Pressure Difference from Upper Plenum to Intact Cold Leg Nozzle (Intact Loop ΔP)	24-212
Figure 24.7.3-23	CCTF Run 62 <u>W</u> COBRA/TRAC-TF2 vs. Data Pressure Difference from Upper Plenum to Steam Generator (Intact Loop ΔP)	24-213
Figure 24.7.3-24	CCTF Run 62 <u>W</u> COBRA/TRAC-TF2 vs. Data Pressure Difference from Inlet to Outlet Plenum of Steam Generator (Intact Loop ΔP)	24-214
Figure 24.7.3-25	CCTF Run 62 <u>W</u> COBRA/TRAC-TF2 vs. Data Pressure Difference across RCP (Intact Loop ΔP)	24-215
Figure 24.7.3-26	CCTF Run 62 <u>W</u> COBRA/TRAC-TF2 vs. Data Pressure Difference from RCP to Downcomer (Intact Loop ΔP)	24-216
Figure 24.7.3-27	CCTF Run 62 Pressure Difference from UP to SG	24-217
Figure 24.7.3-28	CCTF Run 62 Pressure Difference from UP to PUMP	24-218
Figure 24.7.3-29	CCTF Run 62 <u>W</u> COBRA/TRAC-TF2 vs. Data Pressure Difference in Broken Loop Hot Leg (Broken Loop ΔP)	24-219
Figure 24.7.3-30	CCTF Run 62 <u>W</u> COBRA/TRAC-TF2 vs. Data Pressure Difference from Upper Plenum to Steam Generator in Broken Loop (Broken Loop ΔP)	24-220

Figure 24.7.3-31	CCTF Run 62 <u>W</u> COBRA/TRAC-TF2 vs. Data Pressure Difference from Inlet to Outlet Plenum of Steam Generator in Broken Loop (Broken Loop ΔP)	24-221
Figure 24.7.3-32	CCTF Run 62 <u>W</u> COBRA/TRAC-TF2 vs. Data Pressure Difference across RCP in Broken Loop (Broken Loop ΔP)	24-222
Figure 24.7.3-33	CCTF Run 62 <u>W</u> COBRA/TRAC-TF2 vs. Data Pressure Difference from RCP to CV (Broken Loop ΔP)	24-223
Figure 24.7.3-34	CCTF Run 62 <u>W</u> COBRA/TRAC-TF2 vs. Data Vapor Mass Flowrate in Intact Hot Leg	24-224
Figure 24.7.3-35	CCTF Run 62 <u>W</u> COBRA/TRAC-TF2 vs. Data Vapor Velocity in Intact Hot Leg	24-225
Figure 24.7.3-36	CCTF Run 62 <u>W</u> COBRA/TRAC-TF2 vs. Data Vapor Density in Intact Hot Leg	24-226
Figure 24.7.3-37	CCTF Run 62 <u>W</u> COBRA/TRAC-TF2 vs. Data Liquid Mass Flowrate in Intact Hot Leg	24-227
Figure 24.7.3-38	CCTF Run 62 <u>W</u> COBRA/TRAC-TF2 vs. Data Total Mass Flowrate in Intact Hot Leg	24-228
Figure 24.7.3-39	CCTF Run 62 <u>W</u> COBRA/TRAC-TF2 vs. Data Vapor Mass Flowrate in Intact Cold Leg	24-229
Figure 24.7.3-40	CCTF Run 62 <u>W</u> COBRA/TRAC-TF2 vs. Data Liquid Mass Flowrate in Intact Cold Leg	24-230
Figure 24.7.3-41	CCTF Run 62 <u>W</u> COBRA/TRAC-TF2 vs. Data Total Mass Flowrate in Intact Cold Leg	
Figure 24.7.3-42	CCTF Run 62 <u>W</u> COBRA/TRAC-TF2 vs. Data Liquid Mass Flowrate in Broken Hot Leg	24-232
Figure 24.7.3-43	CCTF Run 62 <u>W</u> COBRA/TRAC-TF2 vs. Data Vapor Mass Flowrate in Broken Hot Leg	24-233
Figure 24.7.3-44	CCTF Run 62 <u>W</u> COBRA/TRAC-TF2 vs. Data Total Mass Flowrate in Broken Hot Leg	24-234
Figure 24.7.3-45	CCTF Run 62 <u>W</u> COBRA/TRAC-TF2 vs. Data Vapor Mass Flowrate in Broken Cold Leg	24-235
Figure 24.7.3-46	CCTF Run 62 <u>W</u> COBRA/TRAC-TF2 vs. Data Pressure in Upper Plenum in Higher Containment Pressure Case	24-236
Figure 24.7.3-47	CCTF Run 62 <u>W</u> COBRA/TRAC-TF2 vs. Data Cladding Temperature Comparison at 6 ft in Higher Containment Pressure Case	24-237

1

Figure 24.7.3-48	CCTF Run 62 WCOBRA/TRAC-TF2 vs. Data Cladding Temperature Comparison at 6.68 ft in Higher Containment Pressure Case	238
Figure 24.7.3-49	Core Inlet Flow Comparison in Higher Containment Pressure Case	239
Figure 24.7.3-50	CCTF Run 62 WCOBRA/TRAC-TF2 vs. Data Collapsed Liquid Level in Core in Higher Containment Pressure Case	240
Figure 24.7.3-51	CCTF Run 62 <u>W</u> COBRA/TRAC-TF2 vs. Data Collapsed Liquid Level in Upper Plenum in Higher Containment Pressure Case	241
Figure 24.8.1-1	Core DP Comparison in SB-CL-18 Simulation	247
Figure 24.8.1-2	Pump Speed used in Test and in Simulation	248
Figure 24.8.1-3	SB-CL-18 Core DP Comparison with Core Inlet Liquid Velocity	249
Figure 24.8.1-4	SB-CL-18 Core DP Comparison with Pump DP in Loop A and B 24-2	250
Figure 24.8.1-5	Primary Side Circulation Flow as a Function of Primary Side Inventory 24-2	251
Figure 24.8.1-6	Core DP Comparison with the Void Fraction in Downhill side on Steam Generator and Cross-over Leg	252
Figure 24.8.1-7	Core DP Comparison with Axial Vapor Velocity at UCP (Curve-3=Inner High Power, Curve-4=Inner Low Power, Curve-5=Outer Low Power)	253
Figure 24.8.1-8	Core DP Comparison with the Hot Leg Nozzle Liquid Flowrates	254
Figure 24.8.1-9	DP Comparison from Upper Plenum to Steam Generator Inlet	255
Figure 24.8.1-10	DP Comparison from Steam Generator Inlet to Outlet Plenum	255
Figure 24.8.1-11	Core DP Comparison with Void Fraction in Cross-over Leg Piping 24-2	256
Figure 24.8.1-12	Inner Vessel DP Comparison	257
Figure 24.8.1-13	Downcomer to Upper Plenum Pressure Difference	257
Figure 24.8.1-14	Core DP Comparison for SB-CL-01 (2.5%)	258
Figure 24.8.1-15	Loop-A Loopseal Bottom to Pump DP Comparison for SB-CL-01 (2.5%)	259
Figure 24.8.1-16	Loop-B Loopseal Bottom to Pump DP Comparison for SB-CL-01 (2.5%)	260
Figure 24.8.1-17	Downcomer to Upper Plenum Pressure Difference in SB-CL-01 (2.5%)	261
Figure 24.8.1-18	Core Collapsed Liquid Level Comparison for SB-CL-14 (10%)	
Figure 24.8.1-19	Steam Generator Inlet to Top of Tube DP Comparison for SB-CL-14 (10%)	263



Ľ

Figure 24.8.1-20	Comparison of Loop-A Cross-Over Leg Differential Pressures	264
Figure 24.8.1-21	Comparison of Loop-B Cross-Over Leg Differential Pressures	265
Figure 24.8.2-1	Comparison of Predicted Mixture Level and Test Data	266
Figure 24.8.2-2	Comparison of Predicted Mixture Level and Test Data, and YDRAG Sensitivity	267
Figure 24.8.3-1	Comparison of Predicted Level Swell against Measured	268
Figure 24.8.3-2	Impact of YDRAG Variation on Predicted Level Swell	269
·	VOLUME 3	
Figure 25.2-1	Typical Assembly Power Map and Assembly Power Distribution, Beginning of Cycle	-29
Figure 25.2-2	Typical Assembly Power Map and Assembly Power Distribution, End of Cycle	-30
Figure 25.2-3	Typical Hot Assembly Fuel Rod Power Distribution	-31
Figure 25.2-4	Hot Assembly Rod Power Census for Typical Westinghouse Fuel Designs 25	-32
Figure 25.2-5	Relative Axial Power Distribution at BOL and EOL During Full Power Steady-State Conditions	-33
Figure 25.2-6	Typical Transient Axial Power Distributions	-34
Figure 25.2-7	Envelope of Peak Linear Heat Rates as a Function of Core Height for a Typical Westinghouse Core Design	-35
Figure 25.2-8	Typical Steady-State Peaking Factors Versus Peaking Factor Design Limit 25	-36
Figure 25.2-9	Effect of Load Follow Maneuver Period on Decay Heat Equilibrium Fraction for Various Times After Trip25	-37
Figure 25.2-10	Typical Measurement of Enthalpy Rise Hot Channel Factor $F_{\Delta H}$	-38
Figure 25.2-11	Typical Measurement of Total Peaking Factor F _Q	-39
Figure 25.2-12	Effect of Burnup on (a) Baseload PLHR, (b) Fuel Average Temperature, (c) Decay Heat Equilibrium Fraction	-40
Figure 25.2-13	Bottom and Middle Third Integrals for a Typical Low Peaking Factor Core Design	-41
Figure 25.2-14	Bottom and Middle Third Integrals for a Typical High Peaking Factor Core Design, Relaxed ΔI Bands	-42
Figure 25.2-15	Effect of Unlimited F_Q and ΔI Bands on Bottom and Middle Third Integrals 25	-43
Figure 25.2-16	Typical WCOBRA/TRAC-TF2 Axial Power Distribution	-44
Figure 25.6-1	Comparison of Analysis and Experiment for Scale Model Flywheel Tests 25	-59

Figure 25.6-2	[] ^{a,c}	50
Figure 26.2-1	Virgil C. Summer Vessel Profile	
Ū.		
Figure 26.2-2	Virgil C. Summer Vessel Component Elevations	
Figure 26.2-3	Virgil C. Summer Vessel Model Noding Diagram	
Figure 26.2-4	Virgil C. Summer Vessel Sections 1 through 3	
Figure 26.2-5	Virgil C. Summer Vessel Sections 4 through 6	26
Figure 26.2-6	Virgil C. Summer Vessel Sections 7 through 9	27
Figure 26.2-7	Virgil C. Summer Upper Plenum Structure Map	28
Figure 26.2-8	Virgil C. Summer Loop Model Noding Diagram	29
Figure 26.2-9	Virgil C. Summer Steam Generator Component Noding Diagram	30
Figure 26.2-10	Virgil C. Summer Reference Case Axial Power Distribution	31
Figure 26.3-1	Beaver Valley Unit 1 Vessel Profile	14
Figure 26.3-2	Beaver Valley Unit 1 Vessel Component Elevations	45
Figure 26.3-3	Beaver Valley Unit 1 Vessel Model Noding Diagram	16
Figure 26.3-4	Beaver Valley Unit 1 Vessel Section 1	17
Figure 26.3-5	Beaver Valley Unit 1 Vessel Section 2	18
Figure 26.3-6	Beaver Valley Unit 1 Vessel Section 3	19
Figure 26.3-7	Beaver Valley Unit 1 Vessel Section 4	50
Figure 26.3-8	Beaver Valley Unit 1 Vessel Section 5	51
Figure 26.3-9	Beaver Valley Unit 1 Vessel Section 6	52
Figure 26.3-10	Beaver Valley Unit 1 Vessel Section 7	53
Figure 26.3-11	Beaver Valley Unit 1 Vessel Section 8	54
Figure 26.3-12	Beaver Valley Unit 1 Vessel Section 9	55
Figure 26.3-13	Beaver Valley Unit 1 Upper Plenum Structure Map	56
Figure 26.3-14	Beaver Valley Unit 1 Loop Model Noding Diagram	57
Figure 26.3-15	Beaver Valley Unit 1 Steam Generator Component Noding Diagram	58
Figure 26.3-16	Beaver Valley Unit 1 Reference Case Axial Power Distribution	59
Figure 27.1.1.1-1	Rod 1 Peak Cladding Temperature, CGE LBLOCA	-3
Figure 27.1.1.1-2	Rod 1 Peak Cladding Temperature Location, CGE LBLOCA	-4

Figure 27.1.1.1-3	Break Flow, CGE LBLOCA	
Figure 27.1.1.1-4	RCS Pressure, CGE LBLOCA	
Figure 27.1.1.1-5	Accumulator Mass Flow Rate, CGE LBLOCA	
Figure 27.1.1.1-6	Vessel Fluid Mass, CGE LBLOCA	
Figure 27.1.1.1-7	Safety Injection Flow Rate, CGE LBLOCA	
Figure 27.1.1.1-8	Containment Pressure, CGE LBLOCA	
Figure 27.1.1.2-1	Rod 1 Peak Cladding Temperature, CGE IBLOCA	
Figure 27.1.1.2-2	Total Break Flow, CGE IBLOCA	
Figure 27.1.1.2-3	RCS Pressure, CGE IBLOCA	
Figure 27.1.1.2-4	Accumulator Mass Flow Rate, CGE IBLOCA	
Figure 27.1.1.2-5	Vessel Fluid Mass, CGE IBLOCA	
Figure 27.1.1.3-1	Break Void Fraction, CGE SBLOCA	
Figure 27.1.1.3-2	RCS Pressure, CGE SBLOCA	
Figure 27.1.1.3-3	Upper Head Collapsed Liquid Level, CGE SBLOCA	
Figure 27.1.1.3-4	Break Flow, CGE SBLOCA	
Figure 27.1.1.3-5	Rod 1 Peak Cladding Temperature, CGE SBLOCA	
Figure 27.1.1.3-6	Loop 1 Loop Seal Differential Pressure, CGE SBLOCA	
Figure 27.1.1.3-7	Loop 2 Loop Seal Differential Pressure, CGE SBLOCA	
Figure 27.1.1.3-8	Loop 3 Loop Seal Differential Pressure, CGE SBLOCA	
Figure 27.1.2.1-1	Rod 1 Peak Cladding Temperature, DLW LBLOCA	
Figure 27.1.2.1-2	Rod 1 Peak Cladding Temperature Location, DLW LBLOCA	
Figure 27.1.2.1-3	Total Break Flow, DLW LBLOCA	
Figure 27.1.2.1-4	RCS Pressure, DLW LBLOCA	
Figure 27.1.2.1-5	Accumulator Mass Flow, DLW LBLOCA	
Figure 27.1.2.1-6	Vessel Fluid Mass, DLW LBLOCA	
Figure 27.1.2.1-7	Intact Loop Safety Injection Flow, DLW LBLOCA	
Figure 27.1.2.1-8	Containment Backpressure, DLW LBLOCA	
Figure 27.1.2.2-1	Rod 1 Peak Cladding Temperatures, DLW IBLOCA	
Figure 27.1.2.2-2	Total Break Flow, DLW IBLOCA	

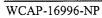


Figure 27.1.2.2-3	RCS Pressure, DLW IBLOCA	. 27-38
Figure 27.1.2.2-4	Accumulator Mass Flow Rate, DLW IBLOCA	. 27-39
Figure 27.1.2.2-5	Vessel Fluid Mass, DLW IBLOCA	. 27-40
Figure 27.1.2.3-1	RCS Pressure, DLW SBLOCA	. 27-42
Figure 27.1.2.3-2	Upper Head Collapsed Liquid Level, DLW SBLOCA	. 27-43
Figure 27.1.2.3-3	Break Flow Rate, DLW SBLOCA	. 27-44
Figure 27.1.2.3-4	Rod 1 Peak Cladding Temperature, DLW SBLOCA	. 27-45
Figure 27.1.2.3-5	Loop 1 Loop Seal Differential Pressure, DLW SBLOCA	. 27-46
Figure 27.1.2.3-6	Loop 2 Loop Seal Differential Pressure, DLW SBLOCA	. 27-47
Figure 27.1.2.3-7	Loop 3 Loop Seal Differential Pressure, DLW SBLOCA	. 27-48
Figure 27.2.1-1	Peak Cladding Temperatures, CGE LBLOCA Reference Transient	. 27-51
Figure 27.2.1-2	Rod 1 Peak Cladding Temperature Location, CGE LBLOCA Reference Transient	. 27-52
Figure 27.2.1-3	Vessel Side Break Flow, CGE LBLOCA Reference Transient	. 27-53
Figure 27.2.1-4	Pump Side Break Flow, CGE LBLOCA Reference Transient	. 27-54
Figure 27.2.1-5	Lower Plenum Collapsed Liquid Level, CGE LBLOCA Reference Transient	. 2 [;] 7-55
Figure 27.2.1-6	Vapor Mass Flow Rate Near PCT Elevation, CGE LBLOCA Reference Transient	27-56
Figure 27.2.1-7	RCS Pressure, CGE LBLOCA Reference Transient	27-57
Figure 27.2.1-8	Accumulator Flow Rate, CGE LBLOCA Reference Transient	27-58
Figure 27.2.1-9	Containment Pressure, CGE LBLOCA Reference Transient	27-59
Figure 27.2.1-10	Vessel Fluid Mass, CGE LBLOCA Reference Transient	27-60
Figure 27.2.1-11	Core Collapsed Liquid Levels, CGE LBLOCA Reference Transient	27-61
Figure 27.2.1-12	Downcomer Collapsed Liquid Level, CGE LBLOCA Reference Transient	27-62
Figure 27.2.1-13	Safety Injection Flow, CGE LBLOCA Reference Transient	27-63
Figure 27.2.2-1	Break Flow, CGE IBLOCA Reference Transient	27-65
Figure 27.2.2-2	Void Fraction at the Break, CGE IBLOCA Reference Transient	27-66
Figure 27.2.2-3	RCS Pressure, CGE IBLOCA Reference Transient	27-67
Figure 27.2.2-4	Core Collapsed Liquid Levels, CGE IBLOCA Reference Transient (2=Hot Assembly, 3=Guide Tube, 4=OH/SC/SM, 5=Low Power)	27-68

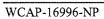


Figure 27.2.2-5	Downcomer Collapsed Liquid Levels, CGE IBLOCA Reference Transient 27-69
Figure 27.2.2-6	Peak Cladding Temperatures, CGE IBLOCA Reference Transient
Figure 27.2.2-7	Vapor Flowrate in the Hot Assembly, CGE IBLOCA Reference Transient 27-71
Figure 27.2.2-8	Accumulator Flow Rate, CGE IBLOCA Reference Transient 27-72
Figure 27.2.2-9	Vessel Fluid Mass, CGE IBLOCA Reference Transient
Figure 27.2.2-10	Safety Injection Flow, CGE IBLOCA Reference Transient
Figure 27.2.2-11	Safety Injection and Break Flow, CGE IBLOCA Reference Transient
Figure 27.2.3-1	Break Flow Void Fraction, CGE SBLOCA Reference Transient 27-78
Figure 27.2.3-2	Safety Injection Flow, CGE SBLOCA Reference Transient
Figure 27.2.3-3	RCS and Steam Generator Secondary Side Pressure, CGE SBLOCA Reference Transient
Figure 27.2.3-4	Upper Head Collapsed Liquid Level, CGE SBLOCA Reference Transient 27-81
Figure 27.2.3-5	Break Flow, CGE SBLOCA Reference Transient
Figure 27.2.3-6	Core Collapsed Liquid Levels, CGE SBLOCA Reference Transient (2=Hot Assembly, 3=Guide Tube, 4=OH/SC/SM, 5=Low Power) 27-83
Figure 27.2.3-7	Rod 1 Cladding Temperature, CGE SBLOCA Reference Transient 27-84
Figure 27.2.3-8	Loop 1 Loop Seal Pressure Differential, CGE SBLOCA Reference Transient
Figure 27.2.3-9	Loop 2 Loop Seal Pressure Differential, CGE SBLOCA Reference Transient
Figure 27.2.3-10	Loop 3 Loop Seal Pressure Differential, CGE SBLOCA Reference Transient
Figure 27.2.3-11	Accumulator Flow, CGE SBLOCA Reference Transient
Figure 27.2.3-12	Vessel Fluid Mass, CGE SBLOCA Reference Transient
Figure 27.2.3-13	Safety Injection and Break Flow, CGE SBLOCA Reference Transient
Figure 27.3.1-1	Peak Cladding Temperatures, DLW LBLOCA Reference Transient
Figure 27.3.1-2	Peak Cladding Temperature Location, DLW LBLOCA Reference Transient 27-94
Figure 27.3.1-3	Vessel Side Break Flow, DLW LBLOCA Reference Transient
Figure 27.3.1-4	Pump Side Break Flow, DLW LBLOCA Reference Transient
Figure 27.3.1-5	Lower Plenum Collapsed Liquid Level, DLW LBLOCA Reference Transient

Figure 27.3.1-6	Vapor Mass Flow in Hot Assembly Near PCT Elevation, DLW LBLOCA Reference Transient
Figure 27.3.1-7	RCS Pressure, DLW LBLOCA Reference Transient
Figure 27.3.1-8	Accumulator Mass Flow Rate, DLW LBLOCA Reference Transient
Figure 27.3.1-9	Containment Pressure, DLW LBLOCA Reference Transient
Figure 27.3.1-10	Vessel Fluid Mass, DLW LBLOCA Reference Transient
Figure 27.3.1-11	Core Collapsed Liquid Levels, DLW LBLOCA Reference Transient 27-103
Figure 27.3.1-12	Downcomer Collapsed Liquid Level, DLW LBLOCA Reference Transient 27-104
Figure 27.3.1-13	Safety Injection Flow, DLW LBLOCA Reference Transient
Figure 27.3.2-1	Break Flow, DLW IBLOCA Reference Transient
Figure 27.3.2-2	Void Fraction at the Break, DLW IBLOCA Reference Transient
Figure 27.3.2-3	RCS Pressure, DLW IBLOCA Reference Transient
Figure 27.3.2-4	Core Collapsed Liquid Levels, DLW IBLOCA Reference Transient (2=Hot Assembly, 3=Guide Tube, 4=OH/SC/SM, 5=Low Power)27-110
Figure 27.3.2-5	Downcomer Collapsed Liquid Levels, DLW IBLOCA Reference Transient27-111
Figure 27.3.2-6	Peak Cladding Temperatures, DLW IBLOCA Reference Transient
Figure 27.3.2-7	Vapor Flowrate in Hot Assembly Channel, DLW IBLOCA Reference Transient
Figure 27.3.2-8	Accumulator Flow, DLW IBLOCA Reference Transient
Figure 27.3.2-9	Vessel Fluid Mass, DLW IBLOCA Reference Transient
Figure 27.3.2-10	Safety Injection Flow, DLW IBLOCA Reference Transient
Figure 27.3.2-11	Safety Injection and Break Flow, DLW IBLOCA Reference Transient27-117
Figure 27.3.3-1	Void Fraction at the Break, DLW SBLOCA Reference Transient
Figure 27.3.3-2	Safety Injection Flow, DLW SBLOCA Reference Transient
Figure 27.3.3-3	RCS and Steam Generator Secondary Side Pressure, DLW SBLOCA Reference Transient
Figure 27.3.3-4	Upper Head Collapsed Liquid Level, DLW SBLOCA Reference Transient
Figure 27.3.3-5	Break Flow, DLW SBLOCA Reference Transient
Figure 27.3.3-6	Core Collapsed Liquid Levels, DLW SBLOCA Reference Transient (2=Hot Assembly, 3=Guide Tube, 4=OH/SC/SM,
	5=Low Power)

Figure 27.3.3-7	Hot Rod Cladding Temperature, DLW SBLOCA Reference Transient
Figure 27.3.3-8	Loop 1 Loop Seal Differential Pressure, DLW SBLOCA Reference Transient
Figure 27.3.3-9	Loop 2 Loop Seal Differential Pressure, DLW SBLOCA Reference Transient
Figure 27.3.3-10	Loop 3 Loop Seal Differential Pressure, DLW SBLOCA Reference Transient
Figure 27.3.3-11	Accumulator Flow, DLW SBLOCA Reference Transient
Figure 27.3.3-12	Vessel Fluid Mass, DLW SBLOCA Reference Transient
Figure 27.3.3-13	Safety Injection Flow and Break Flow, DLW SBLOCA Reference Transient
Figure 28.1.1-1	Axial Power Distribution, CGE Axial Power Distribution Sensitivity
Figure 28.1.1-2	Rod 1 Peak Cladding Temperatures, CGE Axial Power Distribution Sensitivity
Figure 28.1.1-3	Peak Cladding Temperature Location, CGE Axial Power Distribution Sensitivity
Figure 28.1.1-4	Lower Plenum Collapsed Liquid Level, CGE Axial Power Distribution Sensitivity
Figure 28.1.1-5	Hot Assembly Collapsed Liquid Level, CGE Axial Power Distribution Sensitivity
Figure 28.1.1-6	Vessel Fluid Mass, CGE Axial Power Distribution Sensitivity
Figure 28.1.1-7	Axial Power Distribution, DLW Axial Power Distribution Sensitivity
Figure 28.1.1-8	Peak Cladding Temperatures, DLW Axial Power Distribution Sensitivity 28-12
Figure 28.1.1-9	Peak Cladding Temperature Location, DLW Axial Power Distribution Sensitivity
Figure 28.1.1-10	Lower Plenum Collapsed Liquid Level, DLW Axial Power Distribution Sensitivity
Figure 28.1.1-11	Hot Assembly Collapsed Liquid Level, DLW Axial Power Distribution Sensitivity
Figure 28.1.1-12	Vessel Fluid Mass, DLW Axial Power Distribution Sensitivity
Figure 28.1.2-1	Safety Injection Flow, CGE Offsite Power Availability Sensitivity
Figure 28.1.2-2	Intact Loop Pump Speed, CGE Offsite Power Availability Sensitivity
Figure 28.1.2-3	Broken Loop Pump Speed, CGE Offsite Power Availability Sensitivity

Figure 28.1.2-4	Accumulator and Safety Injection Flow Rates, CGE Offsite Power Availability Sensitivity
Figure 28.1.2-5	Hot Assembly Vapor Mass Flow Rate, CGE Offsite Power Availability Sensitivity
Figure 28.1.2-6	Peak Cladding Temperatures, CGE Offsite Power Availability Sensitivity 28-24
Figure 28.1.2-7	Safety Injection Flow, DLW Offsite Power Availability Study
Figure 28.1.2-8	Intact Loop Pump Speed, DLW Offsite Power Availability Study 28-26
Figure 28.1.2-9	Broken Loop Pump Speed, DLW Offsite Power Availability Study 28-27
Figure 28.1.2-10	Peak Cladding Temperature, DLW Offsite Power Availability Study 28-28
Figure 28.1.2-11	Hot Assembly Vapor Mass Flow Rate, DLW Offsite Power Availability Study
Figure 28.1.2-12	Lower Plenum Liquid Subcooling, DLW Offsite Power Availability Study 28-30
Figure 28.1.2-13	Lower Plenum Collapsed Liquid Level, DLW Offsite Power Availability Study
Figure 28.1.3-1	Vessel Fluid Mass, run004 of CGE Timestep Sensitivity Study (DTMAX) 28-35
Figure 28.1.3-2	Peak Cladding Temperature, run004 of CGE Timestep Sensitivity Study (DTMAX)
Figure 28.1.3-3	Vessel Fluid Mass, run007 of CGE Timestep Sensitivity Study (DTMAX) 28-37
Figure 28.1.3-4	Peak Cladding Temperature, run007 of CGE Timestep Sensitivity Study (DTMAX)
Figure 28.1.3-5	Vessel Fluid Mass, run001 of DLW Timestep Sensitivity Study (DTMAX) 28-39
Figure 28.1.3-6	Peak Cladding Temperature, run001 of DLW Timestep Sensitivity Study (DTMAX)
Figure 28.1.3-7	Vessel Fluid Mass, run004 of DLW Timestep Sensitivity Study (DTMAX) 28-41
Figure 28.1.3-8	Peak Cladding Temperature, run004 of DLW Timestep Sensitivity Study (DTMAX)
Figure 28.1.4-1	[] ^{a,c} 28-47
Figure 28.1.4-2	[] ^{a,c} 28-48
Figure 28.1.4-3	[] ^{a,c}
Figure 28.1.4-4	[] ^{a,c}

Figure 28.1.4-5	[] ^{a,c}
Figure 28.1.4-6	[.] ^{a,c}
Figure 28.1.4-7	[] ^{a,c}
Figure 28.1.4-8	[] ^{a,c}
Figure 28.1.4-9] ^{a,c}
Figure 28.1.4-10	[] ^{a,c}
Figure 28.1.4-11	[] ^{a,c}
Figure 28.1.4-12	[] ^{a,c}
Figure 28.1.4-13	[] ^{a,c}
Figure 28.1.4-14	[] ^{a,c}
Figure 28.1.4-15	[] ^{a,c}
Figure 28.1.4-16	[] ^{a,c}
Figure 28.1.4-17	[] ^{a,c}
Figure 28.1.4-18	[] ^{a,c}
Figure 28.1.4-19	[] ^{a,c}
Figure 28.1.4-20	. [] ^{a,c}
Figure 28.1.4-21	[] ^{a,c}
Figure 28.1.4-22	[] ^{a,c}

)

Figure 28.1.4-23	•[
	•	^{[]a,c}
Figure 28.1.4-24	[] ^{a,c}
Figure 28.1.4-25	Ι] ^{a,c}
Figure 28.1.4-26	[] ^{a,c}
Figure 28.1.4-27	[] ^{a,c}
Figure 28.1.4-28	[] ^{a,c}
Figure 28.1.4-29	[] ^{a,c}
Figure 28.1.4-30	[] ^{a,c}
Figure 28.1.4-31	[] ^{a,c}
Figure 28.1.4-32	[] ^{a,c}
Figure 28.1.4-33	[] ^{a,c}
Figure 28.1.4-34	[-] ^{a,c}
Figure 28.1.4-35	[] ^{a,c}
Figure 28.1.4-36	[] ^{a,c}
Figure 28.1.5-1	[] ^{a,c}
Figure 28.1.5-2	[] ^{a,c}
Figure 28.1.5-3	ſ] ^{a,c}
Figure 28.1.5-4	ſ	,
-	L] ^{a,c}
Figure 28.1.5-5	L] ^{a,c} 28-89

WCAP-16996-NP

.

J

	•
] ^{a,c}	Figure 28.1.5-6
·	Figure 28.1.5-7
] ^{a,c}	Figure 28.1.5-8
] ^{a,c}	Figure 28.1.5-9
] ^{a,c}	Figure 28.1.6-1
] ^{a,c}	Figure 28.1.6-2
] ^{a.c} 28-97	Figure 28.1.6-3
] ^{a,c}	Figure 28.1.6-4
] ^{a,c} 28-99	Figure 28.1.6-5
] ^{a,c} 28-100	Figure 28.1.6-6
] ^{a,c}	Figure 28.1.6-7
at Break, CGE SBLOCA Reference Transient Re-Baseline 28-103	Figure 28.2.1-1
CGE SBLOCA Reference Transient Re-Baseline	Figure 28.2.1-2
ollapsed Liquid Level, CGE SBLOCA Reference Transient	Figure 28.2.1-3
GE SBLOCA Reference Transient Re-Baseline	Figure 28.2.1-4
Loop Seal Differential Pressure, CGE SBLOCA Reference Baseline	Figure 28.2.1-5
Loop Seal Differential Pressure, CGE SBLOCA Reference Baseline	Figure 28.2.1-6
3 Loop Seal Differential Pressure, CGE SBLOCA Reference Baseline	Figure 28.2.1-7
g Temperature, CGE SBLOCA Reference Transient	Figure 28.2.1-8
] ^{a,c} 28-113	Figure 28.2.2-1
] ^{a,c} 28-114	Figure 28.2.2-2
	Figure 28.2.2-3
] ^{a,c}	Figure 28.2.2-4

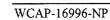


Figure 28.2.2-5	[.] ^{a,c}		
Figure 28.2.2-6	[] ^{a,c}			
Figure 28.2.2-7	[
Figure 28.2.2-8	. [·				
Figure 28.2.2-9	. [·	
Figure 28.2.2-10	[] ^{a,c} 28-122
Figure 28.2.2-11	[
1 iguit 20.2.2-11	L] ^{a,c}			
Figure 28.2.2-12	[] ^{a,c}			
Figure 28.2.2-13	[
] ^{a,c}		
Figure 28.2.2-14	[] ^{a,c}			
Figure 28.2.2-15	[] ^{a,c}			
Figure 28.2.2-16	[78.0		2 0.1 0 0
	-				
Figure 28.2.2-17	[] ^{a,c}		
Figure 28.2.2-18	[J ^{a,c}		
Figure 28.2.3-1	ſ				
0	Ľ] ^{a,c}	••••••		
Figure 28.2.3-2	[] ^{a,c}			
Figure 28.2.3-3	[-			
Figure 28.2.3-4	ſ]	·····	
I IGUIO 20.2.J-T	L	,] ^{a,c}		
				-	

WCAP-16996-NP

November 2010 Revision 0

Figure 28.2.3-5	[] ^{a,c}
Figure 28.2.3-6	.[] ^{a,c}
Figure 28.2.3-7	[] ^{a,c}
Figure 28.2.3-8	[] ^{a,c}
Figure 28.2.3-9	[
Figure 28.2.3-10	Ĩ] ^{a,c}
Figure 28.2.3-11	[] ^{a,c}
Figure 28.2.3-12] ^{a,c}
Figure 28.2.3-13	[] ^{a,c}
Figure 28.2.3-14	[] ^{a,c}
Figure 28.2.3-15	[] ^{a,c}
Figure 28.2.3-16] ^{a,c}
-	-] ^{a,c}
Figure 28.2.3-17	[] ^{a,c}
Figure 28.2.3-18	l] ^{a,c}
Figure 28.2.3-19	[] ^{a,c}
Figure 28.2.3-20	[] ^{a,c}
Figure 28.2.3-21	[] ^{a,c}

.

Figure 28.2.3-22	[] ^{a,c}
Figure 28.2.3-23	[.] ^{a,c}
Figure 28.2.3-24	[] ^{a,c}
Figure 28.2.4-1	[] ^{a,c}
Figure 28.2.4-2	[·	
] ^{a,c}
Figure 28.2.4-3	[] ^{a,c} 28-160
Figure 28.2.4-4	[] ^{a,c}
Figure 28.2.4-5	[] ^{a,c}
		-
Figure 28.2.4-6	[] ^{a,c} 28-163
Figure 28.2.5-1	[] ^{a,c} 28-165
Figure 28.2.5-2	[] ^{a,c}
Figure 28.2.5-3	[] ^{a,c}
Figure 28.2.6-1	[] ^{a,c}
Figure 28.2.6-2	[] ^{a,c}
Figure 28.2.6-3	[
] ^{a,c} 28-171
Figure 28.2.6-4	[] ^{a,c} 28-172
E'	r] 28-172
Figure 28.2.6-5	l] ^{a,c}
Figure 28.2.6-6	[
] ^{a,c}
Figure 28.2.6-7	[
] ^{a,c} 28-175
Figure 28.2.6-8	[] ^{a,c} 28-176
Figure 28.2.6-9	ſ	
	L] ^{a,c} 28-177

WCAP-16996-NP

).

		LIST OF FIGURES (cont.)
Figure 28.2.7-1	[] ^{a,c}
Figure 28.2.7-2	[
] ^{a,c}
Figure 28.2.7-3	[] ^{a,c}
Figure 28.2.7-4	[] ^{a,c}
Figure 28.2.7-5	[] ^{a,c}
Figure 28.2.7-6	[] ^{a,c}
Figure 28.2.7-7	ָ [] ^{a,c}
Figure 28.2.7-8	[
] ^{a,c}
Figure 28.2.7-9	[] ^{a,c}
Figure 28.2.7-10	· [] ^{a,c}
Figure 28.2.7-11	[] ^{a,c}
Figure 28.2.7-12	[] ^{a,c} 28-190
Figure 28.2.7-13	[1ª.¢ 20.101
	_] ^{a,c}
Figure 28.2.7-14	[] ^{a,c}
Figure 28.2.7-15	[]
1 iguite 20.2.7-13	L] ^{a,c}
Figure 28.2.8-1	[
] ^{a,c}
Figure 28.2.8-2	[] ^{a,c}
Ti	r]
Figure 28.2.8-3	[] ^{a,c}
Figure 28.2.8-4	[
•	-] ^{a,c}
Figure 28.2.8-5	[
T: 00.00.0	r] ^{a,c}
Figure 28.2.8-6	[] ^{a,c}
Figure 28.2.8-7	[] ^{a,c} 28-202
	-	,

WCAP-16996-NP

cxxxix

LIST OF FIGURES (cont.)

Figure 28.2.8-8	[] ^{a,c} 28-203
Figure 28.2.8-9	[
] ^{a,c}		
Figure 28.2.8-10		٦ ^{a,c}			
Figure 28.2.8-11	[]			
Figure 28.2.8-11	L] ^{a,c}			
Figure 28.2.8-12	[
] ^{a,c}			
Figure 28.2.8-13	[да, С		
Eigung 20 2 9 14	r]		
Figure 28.2.8-14	[] ^{a,c}	
Figure 28.2.8-15	[] ^{a,c} 28-210
Figure 28.2.8-16	[·] ^{a,c}
Figure 28.2.9-1	- .[
	-] ^{a,c}			
Figure 28.2.9-2	· [78.0		00.014
T: 00 0 0 2	r				
Figure 28.2.9-3	[] ^{a,c}		
Figure 28.2.9-4	[-		
5	-] ^{a,c}		
Figure 28.2.9-5	[
			.] ^{u,o}	······	
Figure 28.2.9-6	[] ^{a,c} 28-218
Figure 28.2.9-7	[] ^{a,c} 28-219
Figure 28.2.9-8	[] ^{a,c}			28.220
T ' 20 2 0 0	r]	•••••••••••••••••••••••••••••••••••••••		
Figure 28.2.9-9	l] ^{a,c} 28-221
Figure 28.2.10-1	[٦a,c	
Figure 28.2.10-2	[J	
	L] ^{a,c}		

WCAP-16996-NP

Figure 28.2.10-3	[] ^{a,c}
Figure 28.2.10-4	.[] ^{a,c}
Figure 28.2.10-5	[] ^{a,c}
Figure 28.2.10-6	[
Figure 28.2.10-7	[-1.0] ^{a,c}
] ^{a,c}	
Figure 28.2.10-8	[] ^{a,c}
Figure 28.2.10-9	[] ^{a,c}
Figure 28.2.10-10	[] ^{a,c}
Figure 28.2.10-11	[
] ^{a,c}
Figure 28.2.10-12	[] ^{a,c}
Figure 28.2.10-13	[、] ^{a,c}
Figure 28.2.10-14	[] ^{a,c}
Figure 28.2.10-15	[78.0	
]","	
Figure 28.2.10-16	[] ^{a,c}
Figure 28.2.11-1	[] ^{a,c}	
Figure 28.2.11-2	[] ^{a,c}	
Figure 28.2.11-3	[
Figure 29 2 11 4	г	l] ^{a,c}
Figure 28.2.11-4	L		J
Figure 28.2.11-5	[] ^{a,c}	

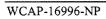


Figure 28.2.11-6	[
-	_] ^{a,c}
Figure 28.2.11-7	[···	
	-] ^{a,c}
Figure 28.2.11-8	[[^{a,c}
Figure 28.2.12-1	[] ^{a,c}
Figure 28.2.12-2	[] ^{a,c}
Figure 28.2.12-3	[]	
5	L] ^{a,c}
Figure 28.2.12-4	[
] ^{a,c}
Figure 28.2.12-5	[
·] ^{a,c}
Figure 28.2.12-6	[
] ^{a,c}
Figure 28.2.12-7	[
] ^{a,c}
Figure 28.2.12-8	[] ^{a,c}
] *
Figure 28.2.12-9	[] ^{a,c}
-	-	-
Figure 28.2.12-10	l] ^{a,c}
Figure 28.2.12-11	[] ^{a,c}
Figure 28.2.12-12	[] ^{a,c}
Figure 28.2.12-13	[] ^{a,c}
Figure 28.2.12-14	[
] ^{a,c}
Figure 28.2.12-15	[
] ^{a,c}
Figure 28.2.12-16	[
] ^{a,c}
Figure 28.2.12-17	[18. 00.000
] ^{a,c}

Figure 28.2.12-18	[
Figure 28.2.12-19	[] ^{a,c}	
Figure 28.2.12-20	[
Figure 28.2.12-21		
Figure 28.2.12-22	τ] ^{a,c} 28-274
Figure 29.1.1-1	[] ^{a,c}	
Figure 29.1.1-2	[] ^{a,c}	
Figure 29.1.1-3	ſ	
Figure 29.1.1-4		
Figure 29.1.1-5	Branchline Quality Versus Mainline Liquid Level for H Configuration	
Figure 29.1.1-6	Branchline Quality Versus Mainline Liquid Level for D Configuration	
Figure 29.1.5-1	Predicted Versus Measured Level Swell for the G1 and Simulations with [] ^{a,c}	G2 Boiloff 29-25
Figure 29.1.5-2	G1 and G2 [] ^{a,c}	
Figure 29.1.5-3	[.] ^{a,c}	
Figure 29.1.5-4	Predicted Versus Measured Level Swell for the G1 and Simulations with [G2 Boiloff] ^{ª,c} 29-28
Figure 29.1.5-5	Differential Pressure in the Test Bundle for [FLECHT-SEASET Test 31504] ^{a,c} ,
Figure 29.1.5-6	Quench Profile for [] ^{a,c} , FLE Test 31504	CHT-SEASET



Figure 29.1.6-1 [

] ^{a,c}	3
Figure 29.1.8-1	Dispersed Flow Cooling	7
Figure 29.1.8-2	Inverted Annular Cooling	7
Figure 29.1.8-3	Histogram of T_{min} Values Based on G1 and G2 Test Data [
] ^{a,c}	8
Figure 29.1.8-4	T _{min} Variation with Re (From Appendix N, Boyack et al., 1989)	9
Figure 29.1.8-5	T _{min} Variation with Pressure (From Appendix N, Boyack et al., 1989)	9
Figure 29.1.8-6	Method for Determining Quench Temperature [] ^{a,c} 29-4	0
Figure 29.1.8-7	Predicted vs. Measured Quench Temperatures from G1 Blowdown Simulations	0
Figure 29.1.8-8	Predicted vs. Measured Quench Temperatures from FLECHT SEASET Forced Reflood Test Simulations	-1
Figure 29.1.8-9	Predicted vs. Measured Quench Temperatures from FLECHT Low Flooding Rate Forced Reflood Test Simulations	1
Figure 29.1.8-10	Predicted vs. Measured Quench Temperatures from FLECHT Skewed Forced Reflood Test Simulations	2
Figure 29.1.11-1	Predicted vs. Measured Residual Liquid Level Comparison for the UPTF Loop Seal HS_SLUG Study	6
Figure 29.1.11-2	Pressure Drop across the Loop Seal for UPTF Loop Seal HS_SLUG Study 29-4	6
Figure 29.2.3-1	LOCA Frequency Evaluation Obtained using Expert Elicitation Presented by R. L. Tregoning, et al. (2007)	2
Figure 29.2.4-1	DECLG Break Noding Scheme	4
Figure 29.2.4-2	Guillotine Break Noding Used in <u>W</u> COBRA/TRAC-TF2	5
Figure 29.2.5-1	Split Break Noding Scheme	7
Figure 29.2.5-2	Split Break Noding Used in <u>W</u> COBRA/TRAC-TF2	8
Figure 29.4-1	Effect of Load Follow on F _Q	1
Figure 29.4-2	F _Q Histogram for Full Power Points of Load Follow Maneuver; Solid Line Indicates Uniform Range Assumed	2

Figure 29.4-3	
---------------	--

[

·] ^{a,c}	
Figure 29.4-4	ZIRLO [®] Cladding Burst Temperature Data and Correlation .	
Figure 29.4-5	[] ^{a,c}	
Figure 29.4-6	[] ^{a,c}	
Figure 29.4-7	[] ^{a,c} 29-82
Figure 29.4-8	[] ^{a,c}	
Figure 29.4-9	[] ^{a,c}	
Figure 29.4-10	[] ^{a,c} 29-85
Figure 29.4-11	[
] ^{a,c}	
Figure 29.4-12	[] ^{a,c} 29-87
Figure 29.4-13	[] ^{a,c}	
Figure 29.4-14	Distribution of Packing Fraction Data	
Figure 29.4-15	[] ^{a,c}	
Figure 29.4-16	[·	[^{a,c} 29-96]
⁻ Figure 29.4-18	Thermal Conductivity of UO ₂	-
Figure 29.4.3-1	[
Figure 29.4.3-2	[] ^{a,c}	
Figure 29.4.3-3	[] ^{a,c}	
Figure 29.4.3-4	Heat Transfer Coefficient vs. Time from FLECHT 31805, 6	ft 29-108
Figure 29.4.3-5	Predicted vs. Measured Heat Transfer Coefficients from For- Tests at Elevations 6-ft and 10-ft	
Figure 29.4.3-6		l ^{a,c} 29-109

Figure 29.4.3-7	FLECHT 31203 6-ft Elevation Cladding Temperature Comparison for Local and Global Heat Transfer Multiplier of [] ^{a,c}
Figure 29.4.3-8	FLECHT 31203 6-ft Elevation Cladding Temperature Comparison for Local and Global Heat Transfer Multiplier of [] ^{a,c}
Figure 29.4.3-9	FLECHT 31203 8-ft Elevation Cladding Temperature Comparison for Local and Global Heat Transfer Multiplier of [] ^{a,c}
Figure 29.4.3-10	FLECHT 31203 8-ft Elevation Cladding Temperature Comparison for Local and Global Heat Transfer Multiplier of [] ^{a,c}
Figure 29.4.3-11	FLECHT 31203 10-ft Elevation Cladding Temperature Comparison for Local and Global Heat Transfer Multiplier of [] ^{a,c}
Figure 29.4.3-12	FLECHT 31203 10-ft Elevation Cladding Temperature Comparison for Local and Global Heat Transfer Multiplier of [] ^{a,c}
Figure 29.4.3-13	FLECHT 31504 6-ft Elevation Cladding Temperature Comparison for Local and Global Heat Transfer Multiplier of [] ^{a,c}
Figure 29.4.3-14	FLECHT 31504 6-ft Elevation Cladding Temperature Comparison for Local and Global Heat Transfer Multiplier of [] ^{a,c}
Figure 29.4.3-15	FLECHT 31504 8-ft Elevation Cladding Temperature Comparison for Local and Global Heat Transfer Multiplier of [] ^{a,c}
Figure 29.4.3-16	FLECHT 31504 8-ft Elevation Cladding Temperature Comparison for Local and Global Heat Transfer Multiplier of [] ^{a,c}
Figure 29.4.3-17	FLECHT 31504 10-ft Elevation Cladding Temperature Comparison for Local and Global Heat Transfer Multiplier of [] ^{a,c}
Figure 29.4.3-18	FLECHT 31504 10-ft Elevation Cladding Temperature Comparison for Local and Global Heat Transfer Multiplier of [] ^{a,c}
Figure 29.4.3-19	FLECHT 31805 6-ft Elevation Cladding Temperature Comparison for Local and Global Heat Transfer Multiplier of [] ^{a,c}
Figure 29.4.3-20	FLECHT 31805 6-ft Elevation Cladding Temperature Comparison for Local and Global Heat Transfer Multiplier of [] ^{a,c}
Figure 29.4.3-21	FLECHT 31805 8-ft Elevation Cladding Temperature Comparison for Local and Global Heat Transfer Multiplier of [] ^{a,c}
Figure 29.4.3-22	FLECHT 31805 8-ft Elevation Cladding Temperature Comparison for Local and Global Heat Transfer Multiplier of [] ^{a,c}
Figure 29.4.3-23	FLECHT 31805 10-ft Elevation Cladding Temperature Comparison for Local and Global Heat Transfer Multiplier of [] ^{a,c}

Figure 29.4.3-24	FLECHT 31805 10-ft Elevation Cladding Temperature Comparison for Local and Global Heat Transfer Multiplier of [] ^{a,c}
Figure 31.1-1	Description of Break Area Regions
Figure 31.1-2	Noding Diagram for Minimum Break Area Determination
Figure 31.1-3	Uncertainty Range of the Demonstration Plant PBOT and PMID
Figure 31.3-1	
Figure 31.3-2] ^{a,c}
Figure 31.3-3	[] ^{a,c}
Figure 31:3-4	[] ^{a,c}
Figure 31.3-5	[] ^{a,c}
Figure 31.3-6	[] ^{a,c}
Figure 31.3-7	[] ^{a,c}
Figure 31.3-8	[] ^{a,c}
Figure 31.3-9	[] ^{a,c} 31-29
Figure 31.3-10	[] ^{a,c}
Figure 31.3-11	[] ^{a,c}
Figure 31.3-12	[] ^{a,c}
Figure 31.3-13	[] ^{a,c}
Figure 31.4-1	[] ^{a,c}
Figure 31.4-2	[] ^{a,c}
Figure 31.4-3	[] ^{a,c} 31-40
Figure 31.4-4	[] ^{a,c} 31-41
Figure 31.4-5	[] ^{a,c}

WCAP-16996-NP

1-44
1-45
I-46
1-47
l <i>-</i> 48
1-49
-50
1-51
-52
-53
-54

EXECUTIVE SUMMARY

Westinghouse's previously approved best-estimate Large Break loss-of-coolant accident (LBLOCA) methodology (or Evaluation Model (EM)) is described in WCAP-16009-P-A (Nissley et al., 2005). The methodology is referred to as the Automated Statistical Treatment of Uncertainty Method (ASTRUM) and is applicable to Westinghouse designed 3- and 4-loop plants with emergency core cooling system (ECCS) injection into the cold legs, Westinghouse designed 2-loop plants with upper plenum injection (UPI) and Combustion Engineering designs. The ASTRUM EM is based on the use of <u>W</u>COBRA/TRAC as the system code. The ASTRUM EM was also submitted as part of the AP1000^{TM1} Design Control Document (APP-GW-GL-700, Rev. 17).

The ASTRUM EM addressed Large Break LOCA scenarios with a minimum size of 1.0 ft². In this report the applicability of the Westinghouse best-estimate LOCA EM was extended to consider smaller break size, therefore including what traditionally are defined as Small and Intermediate Break LOCA scenarios. The new realistic LOCA EM is called FULL SPECTRUM^{TM1} LOCA (FSLOCA^{TM1}) methodology. The term 'Full Spectrum' specifies that the new EM is intended to resolve the full spectrum of LOCA scenarios which result from a postulated break in the cold leg of a PWR (While this EM is also applicable for analysis of breaks at other loop locations, such as the hot leg, these breaks are not limiting compared with the cold leg break). The break sizes considered in the Westinghouse FULL SPECTRUM LOCA include any break size in which break flow is beyond the capacity of the normal charging pumps, up to and including a double ended guillotine (DEG) rupture with a break flow area equal to two times the pipe area.

As in previous EMs, the FULL SPECTRUM LOCA methodology was patterned after the Code Scaling, Applicability, and Uncertainty (CSAU) methodology developed under the guidance of the U.S. Nuclear Regulatory Commission (NRC) (Boyack et al., 1989). The development roadmap is consistent with Regulatory Guide 1.203.

For the FULL SPECTRUM LOCA methodology <u>W</u>COBRA/TRAC was modified by replacing the 1D Module (based on TRAC-PD2) with the TRAC-PF1/MOD2 code and adding a few improvements to the 3D module (based on Westinghouse modified COBRA-TF). One of the major changes is the addition of an explicit non-condensable gas transport equation within the 3D module. The replacement of TRAC-PD2 with TRAC-PF1/MOD2 allows the extension of a two-fluid, six-equation formulation of the two-phase flow to the 1D loop components. This new code has been named <u>W</u>COBRA/TRAC-TF2 where "TF2" is an identifier that reflects the use of a three-field (TF) formulation of the 3D module derived by COBRA-TF and a two-fluid (TF) formulation of the 1D module based on TRAC-PF1/MOD2.

With the exception of the additional tracking of a non-condensable gas field, and few minor upgrades needed to address Small Break LOCA scenarios, the Vessel model is equivalent to the Vessel model of the approved version of <u>WCOBRA/TRAC</u>. Requests for additional information (RAIs) identified during the early review of the code that led to the approval of the original CQD (Bajorek et al., 1998) and

^{1.} FULL SPECTRUM[™], FSLOCA[™], AP1000[™], and ZIRLO[™] are trademarks or registered trademarks in the United States of Westinghouse Electric Company LLC, its subsidiaries and/or its affiliates. These marks may be used and/or registered in other countries throughout the world. All rights reserved. Unauthorized use is strictly prohibited. Other names may be trademarks of their respective owners.

subsequent ASTRUM EM (Nissley et al., 2005), and associated responses should still be applicable. In a few instances, as in the downcomer region, a more refined noding scheme has been adopted to improve accuracy or provide more consistency across the various test facilities. Such noding choices have been justified by assessing the model against large and full scale experiments.

The FULL SPECTRUM LOCA EM is intended to be applicable to all PWR fuel designs with Zirconium alloy cladding. Most of the data considered in the methodology is based on Zircaloy-4 and ZIRLO^{TM1}.

]^{a,c}

The uncertainty methodology is based on a direct Monte Carlo sampling of the uncertainty attributes. The overall uncertainty is bounded using a non-parametric statistical method similar to the ASTRUM EM. However, sample size is increased to reduce the variability of the estimator. The break size spectrum is divided in two regions. Region-I provides coverage of what typically are defined as Small Break LOCA scenarios and stretch into Intermediate Break LOCA. Region-II starts from Intermediate Break size and include what typically are defined Large Break LOCA scenarios. A 95/95 joint-probability statement is developed for the key parameters that are needed to demonstrate compliance with 10 CFR 50.46 acceptance criteria.

The code models, their assessment, and conclusions on model biases and uncertainties are aimed to be generic and applicable to the same class of plants covered by the ASTRUM EM. When modeling aspects are specific to a particular PWR design, the choice was made to focus attention on the Westinghouse 3-loop PWR with cold leg ECCS injection. Therefore, the demonstration plant analysis is limited to such a design.

FULL SPECTRUMTM, FSLOCATM, AP1000TM, and ZIRLOTM are trademarks or registered trademarks in the United States of Westinghouse Electric Company LLC, its subsidiaries and/or its affiliates. These marks may be used and/or registered in other countries throughout the world. All rights reserved. Unauthorized use is strictly prohibited. Other names may be trademarks of their respective owners.

25 PLANT SOURCES OF UNCERTAINTY

We have, to this point, assessed the ability of WCOBRA/TRAC-TF2 to simulate the key phenomena identified in the PIRT. In addition, it has been demonstrated that compensating errors or bias, due to the increase in scale from the experiments to the PWR; result in a more conservative estimate of the LOCA analysis results relative to several key phenomena. However, there may be differences in PWR response to the LOCA, which may result in some models being more important for the PWR than for the experiment. In addition, variability in plant initial and boundary conditions introduce additional uncertainty. In this section, these additional aspects are discussed. The objective of this section is to develop a plan for performing various sensitivity or scoping studies with the PWR models described in Section 26, in order to identify those parameters which have an important influence on the calculation of the PCT in the PWR, and to make decisions about which variables should be considered for uncertainty propagation.

For some parameters, the uncertainty will be explicitly treated within the uncertainty analysis. For other parameters, a bounding approach may be employed (such as for the containment back-pressure).

25.1 PLANT PHYSICAL CONFIGURATION

The plant physical configuration consists of those parameters which define the geometrical and hydraulic configuration of the reactor at the time the LOCA occurs. These parameters are listed and defined below:

- 1. Dimensions
- 2. Flow resistances
- 3. Pressurizer location, relative to broken loop
- 4. Accumulator Tank Elevation
- 5. Hot assembly location, relative to vessel upper internals
- 6. Hot assembly type
- 7. Steam generator tube plugging level

Dimensions

Reactor dimensions, volumes, and surface areas are obtained directly from component drawings. Some variability exists in these dimensions due to tolerances and approximations which may have been made in geometrical calculations. Dimensions also vary from nominal due to thermal expansion. Thermal expansion is estimated to increase volumes by about [

]^{a,c}

Fuel assembly grids, control rod guide tubes, and steam generator tubes may be affected, in some cases, by high stresses resulting from the combination of seismic and LOCA loads, an assumption required by 10 CFR 50, Appendix A, General Design Criterion 4. A dynamic analysis of the Reactor Coolant System -(RCS) under combined seismic and LOCA loads is performed to demonstrate that key RCS components will continue to perform their safety function. Structural analyses performed as part of the original plant design basis have confirmed that Emergency Core Cooling System (ECCS) safety function and core shutdown capability are maintained. These analyses have also indicated that for some plants, the pressure differentials and structural movements which are predicted may result in minor deformation of fuel assembly grids, control rod guide tubes, and/or steam generator tubes. In the case of the fuel assembly, some crushing of the grids in assemblies at the periphery of the core may be calculated. This may push fuel rods closer together, reducing the available flow area. Steam generator tubes may be slightly deformed at support plate locations, reducing the flow area through the tube bundle and increasing the flow resistance during reflood. For larger breaks, control rod guide tubes may be displaced from their nominal positions, preventing control rod insertion and causing the core to shutdown on voids early in the LOCA, and to remain shut down due to boron alone. These deformations, while not compromising safety functions, were found to affect the LOCA analysis results.

The combined effects of LOCA and seismic loads may potentially lead to some degree of grid crushing in the core, due to the baffle plates impacting the peripheral assemblies. If the impact on the peripheral assemblies is large enough, these assemblies may subsequently impact in-board assemblies, and so on. If the loads are large enough for grid damage to occur, test data and analyses show that the damage is typically limited to no more than two rows or rods per assembly, with elevations towards the mid-plane of the core.

 $]^{a,c}$

]^{a,c}

WCAP-16996-NP

ſ

ſ

November 2010 Revision 0

Modeling Approach

ſ

ſ

]^{a,c}

Flow Resistance

The flow resistance in the vessel and loops during a LOCA is as much a function of the models used to calculate the friction factor, as it is the plant configuration. However, flow resistance is included in this category because some changes in plant configuration affect this parameter. The steady-state hydraulic resistance of virtually all the major components in a PWR was determined from scaled testing. The accuracy of the loss coefficients obtained from these tests has, over the years, been confirmed by the accurate prediction of steady-state flow and temperature conditions of operating reactors during numerous plant startup cycles. The accuracy of these predictions, using loss coefficients for subcomponents which are typically subject to large uncertainties may also be a result of the fact that the pressure distribution in a reactor circuit consists of many components. [

]^{a,c} The uncertainty in the

pressure drop under LOCA transient conditions is discussed in Section 29.1.2.

WCAP-16996-NP

]^{a,c}

25-3

When the LOCA occurs, reverse flow through some components and two-phase flow may significantly increase the uncertainty of the predicted flow resistance. One area in particular where reverse flow introduces additional resistance not present during normal operation is the broken cold leg inlet nozzle. Another area where additional resistance is introduced is the broken loop pump.

During several large scale ECCS tests conducted in the past years, it was observed that there was a significant pressure drop across the inlet nozzle of the broken cold leg. In the Cylindrical Core Test Facility (CCTF) reflood tests, this pressure drop was observed to result in a significant pressurization of the downcomer during reflood, resulting in increased reflood rates (Akimoto et al., 1984). Part of this loss was attributed to the increased dynamic head resulting from the reverse flow from a large reservoir, the reactor vessel, to the cold leg nozzle. Other contributors were losses associated with two-phase flow. A review of recent Upper Plenum Test Facility (UPTF) data has confirmed this finding as described in Section 29.1.2.

During a cold leg break, the flow rate through the broken loop pump increases substantially, to the point where the pump acts as a resistance. The effect of this additional flow resistance must also be taken into account, and is a source of additional uncertainty. The flow in the intact loop typically continues in the same direction at lower flow rates, therefore the predicted pressure drop is less subject to uncertainty.

Modeling Approach

Pressurizer Location

The pressurizer may be on the broken loop or one of the unbroken loops. Its location arises as a source of uncertainty because it may introduce some asymmetry into the reactor configuration at the time of the LOCA.

]^{a,c}

Modeling Approach

ſ

ſ

Accumulator Tank Elevation

The accumulator tanks may sit below, at, or above the cold leg elevation. The elevation of the accumulator relative to the cold leg will impact the maximum flow during accumulator injection, the duration of accumulator injection, and the amount of liquid which remains in the accumulator after accumulator injection into the cold leg terminates.

]^{a,c}



Modeling Approach

Hot Assembly Location

Approximately 40 percent of the fuel assemblies in the core of a PWR lie beneath control rod guide tubes which extend into the upper head. These guide tubes, arranged in an approximate checkerboard pattern, house reactor control rods used for reactor control and shutdown, and extend into the reactor vessel upper head. The remaining fuel assemblies lie below open holes in the core plate, flow mixers attached to the core plate, or support columns of several possible designs (Section 26). As a result, for larger breaks (during the blowdown phase) the fuel assemblies will receive varying amounts of flow from the upper head and upper plenum depending on their position. [

·]^{a,c}

Modeling Approach

The configuration of the guide tubes is such that specific modeling of these flowpaths is considered necessary, particularly in view of the connection to the upper head, which contains a large volume of water. Consequently, the core and upper plenum geometry in the <u>WCOBRA/TRAC-TF2</u> model is designed to specifically include separate channels for guide tubes and core plate open hole locations. As described in Section 26, each reactor internal layout is examined, and the hot assembly is located where reduced direct flow is expected to occur.

Hot Assembly Type

The basic design of a PWR fuel assembly has remained essentially unchanged through the years; the standard Westinghouse fuel assembly, for example, consists of an array of fuel rods in a 14x14, 15x15, or 17x17 square matrix. Approximately 90 percent of the matrix is occupied by fuel rods; the remainder is occupied by thimble tubes. Five or more spacer grids hold the array together; some or all of the grids contain mixing vanes which serve to enhance flow turbulence, improving heat transfer during normal operation.

Variations in this standard design may occur to achieve improved fuel utilization. Typical changes made to a fuel assembly design are the following:

1. Changes in Fuel Rod Diameter – The fuel rod may be "optimized" by reducing its diameter, thus reducing the overall amount of fuel required. These changes are marginal in nature. For example, the standard Westinghouse 14x14 fuel rod diameter is 0.422 inches. For the optimized designs the diameter is 0.400 inches. Since smaller rods are designed to the same linear powers as standard rods, their surface heat fluxes and adiabatic heating rates are slightly higher. On the other hand, the amount of coolant in the core is also higher, because of the larger flow area.

2. Changes in Grid Design – The grid may be made of stainless steel, Inconel, or zirconium alloys. Typically, if the fuel rod diameter has been changed, the grids are modified slightly such that the overall hydraulic loss is the same as the standard design.

An additional design improvement is to incorporate additional mixing vane grids along portions of the rod, which further improve heat transfer characteristics, and offset reductions in departure from nucleate boiling (DNB) margin brought about by a smaller rod.

- 3. Changes in Fuel Enrichment Axial and radial "blankets" are sometimes provided to reduce neutron leakage from the core. These blankets consist of regions of low reactivity fuel, or annular fuel. These blankets affect the axial and radial power distribution in the core, and are explicitly considered when these distributions are calculated.
- 4. Burnable Absorbers Burnable absorbers are often used to reduce soluble boron requirements and improve power distributions. Burnable poisons may be accessory (i.e., loaded in thimbles) or integral (i.e., coatings or dopings of the fuel). Burnable absorbers affect axial and radial power distributions in the core, and are explicitly accounted for in core design calculations. Integral absorbers may also cause the internal pressure of the fuel rod, which generally increases with burnup, to increase at a different rate. Rod internal pressure causes swelling and possible burst during the LOCA.
- 5. Changes in Cladding Material New alloys more resistant to corrosion are being developed. Their plastic strain characteristics may be different, and may therefore affect the LOCA results.
- 6. Other Changes Minor modifications in upper and lower fuel assembly tie plates, mixing vane grid design, and removal of thimble plugging devices, are other changes which may occur from reload to reload, but which are not expected to change the LOCA results significantly.

Modeling Approach

[

]^{a,c}

Steam Generator Tube Plugging Level

Steam generator tubes may require plugging for various reasons. Typically, tube plugging takes place during a normal outage. Plugs are inserted into each end of the degraded tube. This removes the tube completely from the RCS volume, and reduces the total flow area through the steam generator. The increased resistance and reduced volume may affect the blowdown transient and reflood behavior for larger breaks or the loop seal clearing in small breaks, and is a variation which must be considered in the LOCA analysis.

Modeling Approach

[

]^{a,c}

25.2 PLANT INITIAL OPERATING CONDITIONS

Reactor operating conditions and their variations are described by two groups of parameters:

1. Core power parameters. These parameters define the core power distribution and fuel stored energy at the time of the LOCA.

- a. Total core power
- b. Peak linear heat rate (PLHR)
- c. Hot assembly peak linear heat rate

d. Hot rod average power

- e. Hot assembly average power
- f. Axial power distribution
- g. Low power region relative power
- h. Time-in-Cycle
- i. Reactor operating power history
- j. Moderator temperature coefficient (MTC)
- k. Hot full power (HFP) boron concentration
- 2. Reactor primary fluid conditions. These parameters describe the primary fluid thermodynamic state at the time of the LOCA.
 - a. Core average fluid temperature
 - b. Pressurizer pressure
 - c. Loop flow rate
 - d. Upper head fluid temperature
 - e. Pressurizer level
 - f. Accumulator water temperature
 - g. Accumulator pressure
 - h. Accumulator water volume
 - i. Accumulator line resistance
 - j. Accumulator boron concentration

The basis for the choice of these parameters is discussed in the following sections.

25.2.1 Core Power Parameters

A summary of the core modeling is given below. There are four core channels and []^{a,c} where the fuel rods are defined as:

Rod 1: The rod in the core with the highest linear heat rate, assumed to also have the highest average power and to reside in the assembly with the highest average power.

Rod 2: All the other (average) rods in the highest power assembly.

Rod 3: All the average rods in the assemblies residing under non-guide tube structures (e.g. support columns, free standing mixers, orifice plates, and open holes).

Rod 4: All the average rods in the assemblies residing under guide tubes.

Rod 5: All the average rods in the assemblies residing on the periphery of the core.

[

]^{a,c}

There are three distinct regions (the hot assembly, the two average channels, and the low power channel) which serve to resolve the radial power distribution in the core.

Each fuel rod group has parameters describing the peak linear heat rate, the average linear heat rate, the axial distribution of power, and the number of physical rods modeled by the rod group. [

]^{a,c}

The axial and radial core power distributions are of basic importance to the uncertainty analysis. The parameters which affect these distributions, and their variations, are described in the following section.

25.2.1.1 Core Power Distributions

The nuclear design of the reactor core meets constraints on the local power distribution in the fuel. Power distributions are typically characterized in terms of hot channel factors. These factors relate peak pellet power and hot rod power to core average quantities. These factors and other terms which will be used are defined below:

Core average heat flux (AFLUX) is the average thermal power produced per unit length of active fuel, kW/ft.

Peak linear heat rate (PLHR) is the maximum linear heat rate produced in the reactor, kW/ft.

Hot assembly peak heat rate (HAPHR) is the peak linear heat rate of an average rod in the hot assembly, kW/ft.

Hot assembly average power (HAFLUX) is the average power per unit length in the hot assembly, kW/ft.

Hot rod average power (HRFLUX) is the average power per unit length in the hot rod, kW/ft.

Total peaking factor (F_Q) is the ratio of the peak linear heat rate to the core average linear heat rate (PLHR/AFLUX).

Enthalpy rise peaking factor ($F_{\Delta H}$) is the ratio of hot rod average power to core average linear heat rate (HRFLUX/AFLUX).

PWR power distributions are often separated into their respective radial and axial components. The radial component is sensitive to the fuel and absorber loading pattern and the presence of control rods. Radial distributions change slowly with time and fuel depletion and are relatively insensitive to power level, xenon concentration/distribution, axial burnup distribution, and axial fuel design feature. By contrast, PWR axial distributions are relatively insensitive to the loading pattern but are quite sensitive to control bank position, xenon concentration/distribution, coolant density distribution, and reactor power.

The existence of this radial/axial power distribution separability is frequently utilized by the nuclear designer. As noted above, PWR radial power distributions are slowly varying in time, provided that the presence of control rods is accounted for accurately. Axial power distributions are more dependent upon the plant operating parameters such as current power level, recent changes in power level/distribution, and control bank position. These characteristics allow the analysis of transient three-dimensional power distributions to be performed by superposition of transient axial power distributions on steady-state, appropriately rodded, radial power distributions rather than the rigorous direct solution for the three-dimensional power distribution. While the methods and calculations used to design reload cores are extremely reliable, and have been confirmed by measurements taken in many operating reactors, it is a normal practice to design cores with some margin, such that measured power distributions will always fall below the core power limits, even when measurement uncertainties are added. These core power limits are determined from the body of safety analyses which support the FSAR and Technical Specifications, and ensure that regulatory limits will not be exceeded for any postulated transient.

Assembly power distributions in a typical Westinghouse designed PWR reload core are shown in Figures 25.2-1 and 25.2-2. The radial power distribution can be divided into three core regions: a low power peripheral region, fresh high power assemblies distributed throughout the core, and average power regions also distributed throughout the core. These figures show the predicted power of assemblies in a reload core. This is a typical low leakage core loading pattern, in which high burnup assemblies are situated around the periphery of the core, while fresh and low burnup assemblies are in the interior of the core.

]^{a,c}

ſ

Within the fuel assembly, individual fuel rods vary in power due to the presence of burnable absorbers and water holes near the thimble tubes. Figure 25.2-3 is a histogram showing the distribution of rod powers within the high power assembly of several different fuel designs. The powers are expressed as a fraction of the maximum power allowed by the technical specifications. The maximum calculated rod power is therefore more than four percent lower than the maximum allowed value, to accommodate measurement uncertainties during surveillance. It can be seen that most of the fuel rods are at powers near the middle of the distribution, and that the hot assembly power distribution can be modeled with a single average rod and a single hot rod. The cumulative distribution is shown in Figure 25.2-4, and the average hot assembly power calculated from these distributions summarized in Table 25.2-1, and is seen to lie approximately $\begin{bmatrix} & a \\ & b \end{bmatrix}^{a,c}$ below the maximum calculated (hot rod) value.

The steady-state axial power distribution also varies as a function of time. Figure 25.2-5 shows the core average axial power distribution at the beginning of cycle life (BOL), and end of cycle life (EOL) for the typical reload core illustrated in Figures 25.2-1 and 25.2-2. During the cycle, the steady-state axial peak moves away from the center of the core as the core is depleted.

While a PWR is designed to easily follow load demand, the most likely state of the reactor is full power and equilibrium conditions. Under these conditions, the axial peaking is relatively low. Measurements taken of the maximum peaking factor at hot full power (HFP), nominal conditions are usually well below the technical specification limits. The margin to peaking factor limits is intended to allow for the less frequent occurrence of transient reactor operation, usually consisting of power reductions and increases to follow load.

In summary, it is seen that the design of a core (its geometry, fuel enrichment, and loading pattern) establishes the maximum radial peaking in the core. The radial distribution is determined almost entirely by the core loading, and cannot be easily changed by external controls in normal operation. Hence, to assure that the measured hot rod power will always lie below the limit, core designs are set allowing for additional margin beyond the four percent required by technical specifications.

25.2.1.2 Transient Power Distributions

Short term changes in reactor power distributions are typically attributable to changes in reactor power level. Changes in power level may require control rod motion, and result in changes in coolant density profiles and xenon distribution. Changes in xenon distribution are a strong function of the magnitude and duration of the power change maneuver as well as the operating strategy used during the maneuver.

We stinghouse methodology used to generate axial power distributions has been previously reviewed by the USNRC. Two distinct methods are employed in design based on the ΔI technical specifications employed. (ΔI is a measure of the axial power distribution, and is the flux difference between the top and bottom halves of the core.)

CAOC methodology (Morita et al., 1974) requires the core designer to simulate various types of load follow maneuvers throughout the cycle to establish the limiting axial power distributions. The approach taken is conservative in that daily load follow swings to various power levels are assumed throughout the cycle. This method is used with plants whose ΔI technical specification is defined as an allowable band (typically ±5 percent) about a target ΔI .

Another approach is used for plants with a fixed ΔI technical specification. The RAOC methodology (Miller et al., 1983) considers the core parameters (power level, xenon distribution, and control rod position) that can affect power distributions and establishes the maximum variability possible in these parameters throughout a given cycle. These parameters are then treated as independent variables and all possible combinations are checked. Any axial shapes that are found to be within the ΔI operating space defined by the technical specifications are taken to be possible. Although conservative, the RAOC approach is analytically easier to implement than CAOC.

Typical transient distributions generated by the RAOC methodology are shown in Figure 25.2-6. The limiting distributions are used to develop an envelope of peak linear heat rate (or peaking factor, when normalized to the core average) as a function of elevation as shown in Figure 25.2-7. It is these transient shapes which sometimes approach the technical specification limit for F_Q , which is also shown in Figure 25.2-7. [

]^{a,c}

The basic characteristic of the axial power distribution (near zero at each end of the core, with one or two maxima) suggests several ways by which the distribution can be characterized in terms of a small number of parameters. [

]^{a,c}

Despite the sensitivity of the core axial power shape to reactor transient operation, the occurrence of high PLHR power shapes, even with constant daily load follow is relatively rare.

An additional characteristic of these transient power shapes is that fission products do not have sufficient time to build up in the high power region of the fuel rod. Consequently, were the reactor to shut down for any reason at the time the maximum transient linear shapes occurred, the decay heat generated is substantially lower at the peak power location than if the core had been operating indefinitely at these PLHR's. This phenomenon is not credited in the FULL SPECTRUM LOCA methodology.

The reactor heat source is made up of three major constituents. Fission energy is by far the largest component of the heat, comprising from roughly 93 to 100 percent of the total heat source for full power operation. The stored energy contribution to the LOCA transient is, therefore, directly related to the fission rate distribution at the time of the LOCA. The magnitudes of the decay and actinide heat sources make them a small contribution to the stored energy component. The decay and actinide components are, however, the principal contributors to core heat generation later in the LOCA transient since the fission rate during this portion of the transient is negligible. The decay and actinide heat sources are independent of the instantaneous fission rate at any given point in time but dependent upon the fission rate time history. Their concentrations determine the decay power available since the decay power for radionuclide decay is determined by the product of the energy release per decay, the decay constant, and the concentration. The concentration of a non-absorbing fission product is dependent upon the fission rate time history, the fission product yield per fission, and the decay constant. Since the yield and time constant for a given fission

product are constant for a specified isotope, the time dependent fission product concentration depends only upon the fission rate time history.

Decay heat is the result of a multitude of radionuclide decays (approximately 350 isotopes). These decay processes have been simplified in the ANSI/ANS 5.1-1979 decay heat standard to a summation of 23 exponentials for each fissile isotope. In the absence of significant absorption or isotope decay chain cross-coupling, the ANSI/ANS 5.1-1979 decay heat standard is a 23 group "pseudo-nuclide" representation of the fission product decay process. The magnitude of the decay heat source at any given point in the reactor, therefore, depends on the time history of the fission rate. The decay heat source for a given point in the reactor will be in effective equilibrium (production rate = decay rate) only if the fission rate has been maintained for the period of time corresponding to ten to twenty time constants for that nuclide. Figure 25.2-9 illustrates a point evaluation of decay equilibrium fraction versus sinusoidal fission rate period. [

]^{a,c}

25.2.1.3 Power Distribution Uncertainties

After a core has been designed and loaded, it is monitored to confirm that the core operates as designed, and to ensure that the reactor is operating within specified limits. The detailed reactor power distribution is monitored by means of in-core detectors. (There are several other core monitoring systems as well.) The readings from these detectors (which are fission chambers and convert the local neutron flux to a current signal) are transformed to fission rate distributions using analytical factors, based on the specific core design (Spier et al., 1988).

The core power distribution is measured during steady-state operation at regular intervals. The following quantities are typically obtained as the result of measurement and data processing:

- $F_{\Delta H}$ The enthalpy rise hot channel factor is the ratio of the integral of local power along the rod (pin) with the highest integrated power in the core to the average rod power.
- $F_{xy}(z)$ The elevation dependent radial peaking factor is the maximum local power density in the plane at elevation z divided by the average power density of the plane.
- $F_Q(z)$ The elevation dependent heat flux hot channel factor is the maximum local linear power density at elevation z divided by core average linear power density.

Because the above peaking factors are derived from a combination of instrument measurements and analytical model calculation, the uncertainty associated with these factors is a combination of the two factors.

The peaking factors defined above are typically measured on a monthly basis. In addition to the peaking factors defined above, the core axial flux difference is measured on a continual basis by the ex-core nuclear

WCAP-16996-NP

detectors. This measurement is equivalent to the axial flux difference discussed previously, and provisions are incorporated in the plant computer to provide alarms if limits are exceeded.

The calculational uncertainty on radial power distribution $(F_{\Delta H})$ has been shown (Spier et al., 1988) to be bounded by a factor of []^{a,c} through benchmarks to critical experiments and other data. There is also an additional uncertainty associated with measuring the radial power distribution, which is bounded by a factor of four percent. It is desirable to assure that the plant will not routinely experience flux map measurements which exceed the $(F_{\Delta H})$ limit after a four percent uncertainty is applied due to combined effects of calculational and measurement uncertainties. To accomplish this, Westinghouse standard practice is to design the core such that it is predicted to be at least []^{a,c} below the $(F_{\Delta H})$ limit on a bestestimate basis. With this approach, the most probable condition is for the core to be measured at least []^{a,c} below the technical specification limit after measurement uncertainty is applied. Typical measurements shown in Figure 25.2-10 show this is indeed the case.

The margin inherent in the design as it relates to the total peaking factor $F_{O}(z)$ is also reflected in typical

measurements. Design calculations are performed to conservatively calculate the possible effects of adverse xenon distributions on the maximum total peaking factor. These penalty factors are generated assuming xenon transients are initiated in the core and shift the axial distribution to the full range allowed by the technical specifications. The most probable condition for the core is at an equilibrium xenon condition which will produce F_Q values well below the limits. The total peaking factor measurement for a typical core during a cycle is shown in Figure 25.2-11. The measured values include an uncertainty of 8.15 percent which bounds measurement uncertainty, manufacturing variability, and rod bow effects.

Nuclear design calculations are performed assuming nominal pellet diameter, density, etc. These calculations form the basis of the analytic factors used to convert in-core measurements to rod power. A study of the effect of variables such as pellet diameter (Chelemer and Tong, 1962) and rod bow (Argall et al., 1979) showed that these variables introduce an additional uncertainty to point measurements.

Since rod bow occurs only at high burnups, this uncertainty does not have to be applied at beginning of cycle. However, both factors are currently applied to the hot rod peaking factor measurement for the entire cycle. These factors are not applied to measurements of the hot assembly and hot rod power. Local linear heat rate depends on the local mass of UO_2 per unit length, or more specifically, per pellet and also on the local channel geometry. The local mass varies as a result of manufacturing variations in pellet dimensions and fuel enrichment.

]^{a,c}

A similar statement can be made for rod bow. [

]^{a,c}

A detailed study of the in-core flux mapping system and its accuracy was performed by Westinghouse (Spier et al., 1988). Because the "measured" values of $F_{\Delta H}$ and F_Q are actually inferred values obtained

from the raw measurement using core model group constants, error contributions from both measurement and modeling sources were considered. Two uncertainties are defined: a measurement uncertainty, to be applied to the inferred peaking factor during normal core surveillance such that the true values are bounded at a high confidence level, and a calculational uncertainty, to be applied to the calculated peaking factors during the core design such that the true values are bounded at a high confidence level. The two uncertainties contain several common components, and so are similar in magnitude. In the best-estimate LOCA methodology, we are concerned with the calculational uncertainty of the predicted peaking factors.

The calculational uncertainty is composed of several independent subcomponents which are summarized in Table 25.2-2. Some of these components are related to uncertainties which should be applied only to the hot rod. In subsequent application of these uncertainties (Section 29.4), these components will be applied separately when considering the calculational uncertainties associated with groups of fuel rods such as the hot assembly. [

]^{a,c}

A final uncertainty related to the power distribution is that associated with the total core power. Core power is inferred from an energy balance using feedwater flow and temperature, and steam flow and pressure. The maximum error from this measurement is typically ± 2 percent, []^{a,c}. Some plants have employed improved uncertainty measurement systems which reduce this uncertainty below 2 percent.

25.2.1.4 The Effect of Fuel Burnup on Power Distributions

Core burnup has the following effects on the state of the core, which may affect the LOCA transient.

 Burnup tends to initially reduce the fuel average temperature not only because the linear power is being reduced, but also because such phenomena as pellet cracking and cladding creep tend to increase the gap conductance. There are also additional considerations later in life which will affect the fuel average temperature as the rod continues to accrue burnup. The effect of burnup on fuel temperature is illustrated in Figure 25.2-12. [1^{a,c}

2. Burnup generates fission gases which collect in the fuel rod, raising its internal pressure. During a LOCA, this higher pressure may result in more cladding swelling, burst, and blockage.

3. Burnup generates fission products such that heat generated from decay of these products following core shutdown initially increases rapidly; however, an equilibrium value is reached fairly early in the cycle.

The Westinghouse PAD code (Foster and Sidener, 2000) is used to calculate the initial fuel rod properties.

25.2.1.5 Power Distribution Modeling Approach

Summarizing the preceding sections, the core power distribution is seen to exhibit the following characteristics:

- 1. The radial power distribution is primarily controlled by core geometry, fuel enrichment, burnable absorber loading, and core loading patterns. It is relatively insensitive to operational procedures such as load follow.
- 2. The axial power distribution is sensitive to operational procedures (such as load follow), which produce non-equilibrium xenon distributions in the core, and core burnup. Large axial power distribution variations have a small effect on the radial power distribution. Axial power distributions which produce the limiting F_0 occur during transient operation.
- 3. The power distribution in the core is well described by the following parameters: the average linear heat rate, the hot assembly linear heat rate, the low power assembly linear heat rate, and the peak linear heat rate.
- 4. The average power of the rods in the assembly which contains the hot rod is typically $\begin{bmatrix} \\ \\ \end{bmatrix}^{a,c}$ or more lower than the hot rod.
- 5. The axial peak power may occur at any location within approximately two feet from the ends of the core, during both transient and steady-state conditions.
- 6. Burnup tends to reduce radial and axial peaking, and fuel stored energy and increases fuel rod gap pressure.

As described in Section 26, the PWR core is modeled with sufficient detail to resolve both the radial and axial power distributions present in the core. The radial power distribution is resolved using [

]^{a,c}

There are several parameters which play a role in the calculation of rod power in <u>WCOBRA/TRAC-TF2</u>. Each parameter, in turn, contributes some uncertainty. Based on the general discussion of power distributions, the parameters as used in <u>WCOBRA/TRAC-TF2</u> are described in more detail below. A final summary of uncertainty contributors is presented later in this section, after the discussion of the fuel rod model.

As described previously, there are four core channels and [

Rod 1: The rod in the core with the highest linear heat rate, assumed to also have the highest average power and to reside in the assembly with the highest average power.

]^{a,c}

Rod 2: An average rod in the highest power assembly.

WCAP-16996-NP

Rod 3: An average rod in the assemblies residing under support columns.

Rod 4: An average rod in the assemblies residing under guide tubes.

Rod 5: An average rod in the assemblies residing on the periphery of the core.

[

Each fuel rod has input parameters describing the average linear heat rate, and the axial distribution of power relative to the core average linear heat rate. The important parameters used in WCOBRA/TRAC-TF2 for these fuel rods are described below. The "0" designates initial, or steady-state values of parameters which will change during the LOCA transient.

]^{a,c}

The reactor power parameters described below are directly related to several quantities which are also measured in the plant during normal operation. These are the total peaking factor (F_Q), the hot channel factor ($F_{\Delta H}$), and the axial flux difference (AFD). Other quantities of lesser importance are the moderator temperature coefficient (MTC) and the coolant boron concentration. The technical specifications call for specific uncertainties and margins to be applied to the measured values of some of these quantities before they are compared to the Technical Specification limit. In the discussion below, these quantities will normally be described in terms of calculated or expected values, without local uncertainties, and will be designated with subscript BE (Best-Estimate).

Initial Core Average Linear Heat Rate

The parameter defining core power in <u>W</u>COBRA/TRAC-TF2 is the core average linear heat rate, calculated by:

$$AFLUX(0) = P(0)/(NFR*L)$$

(25-1)

where:

L = nominal active fuel length P(0) = initial core power NFR = total number of fuel rods

There is a tendency for the fuel pellet stack (L) to shrink during the cycle, which would increase AFLUX based on Equation 25-1. However, [

]^{a,c} The only uncertainty affecting AFLUX is the core power measurement uncertainty, which results from calorimetric errors in measuring feedwater flow and temperature. As noted in Section 25.2.1.3, the range of this error is estimated as []^{a,c}

The axial power distributions of the core average rods (Rods 3, 4, and 5) are determined from the required attributes of the hot rod and hot assembly rod (Rods 1 and 2). These distributions will be illustrated later in the section, when the power distribution modeling is described.

Peak Linear Heat Rate (PLHR)

The peak linear heat rate (PLHR) for the hot rod (Rod 1) [defined by:

For the hot rod, the PLHR can also be expressed as,

]^{a,c}

The variation due to transient operation is the result of assumed load follow operations and other operational transients, which introduce relatively short lived skewed power shapes with relatively high peaking factors compared to equilibrium conditions, when the plant returns to full power. Limiting transient power distributions are generated during the core design analysis to confirm that maximum values remain below limits established in the Technical Specifications. The calculated maximum peaking factor is obtained from the envelope that is generated by these distributions. Peaking factors encountered during normal steady-state operation will normally be far below these calculated values (Figure 25.2-8).

ſ

[

]^{a,c}

(25-2)

 $]^{a,c}$

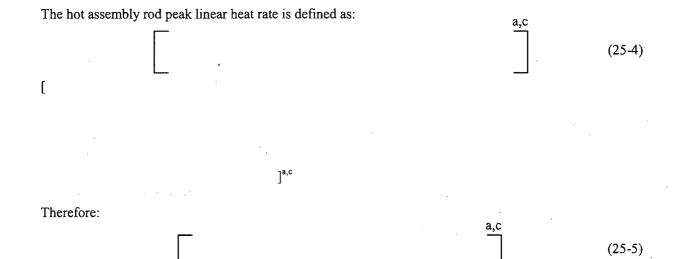
(25-3)

a,c

a,c

FGAM is a measure of how much of the nuclear energy generated in the hot rod is deposited as thermal energy outside of the rod, and is part of the fuel rod nuclear model in <u>WCOBRA/TRAC-TF2</u> described in Volume I of this report. The actual thermal power calculated to be produced by <u>WCOBRA/TRAC-TF2</u> in the hot rod is slightly lower than the nuclear power, due to redistribution of the power to the moderator and surrounding rods. The uncertainty in FGAM(1,0) from its best-estimate value is due to uncertainty in the assumed surrounding ród powers and fluid conditions. This uncertainty is described in Section 29.4.1.2, which addresses core and fuel rod model uncertainties.

Hot Assembly Rod Peak Linear Heat Rate



Typically, the relationship in power of the hottest rod in an assembly to the assembly average will depend upon details in the design of that assembly, such as the location of the hot rod in the assembly. In this analysis, it is conservatively assumed that the hottest rod in the core resides in the hottest assembly, and the peak power is offset by a constant factor equal to the difference in average power. Further discussion of the validity of this assumption is provided in the next subsection.

There are two items to consider when developing the relationship between the hot rod, which is a single rod, and the hot assembly rod, which represents the average of all the rods in the hot assembly minus the hot rod. The first item is the actual difference between the hot rod and the hot assembly rod powers. The second is the difference in the uncertainty associated with various quantities for the hot rod and the hot assembly rod.

Examination of rod census data indicates that the minimum difference between the hot rod and the hot assembly average rod is []^{a,c}. Absent all uncertainties, this is a conservative estimate of the relationship which will exist between the hot rod and the hot assembly average rod during normal operation for the entire fuel cycle. As a general approach, the hot assembly average rod power will be calculated using the []^{a,c} difference. However, if additional information is available in the form

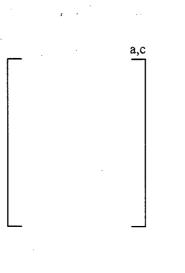
of a core design limit, an alternative and less conservative approach may be taken to bound the hot assembly average power. In Equations 25-4 and 25-5 and the discussion that follows, it is assumed that the general approach (where the difference is []^{a,c} is taken.

A second consideration is the uncertainty associated with the hot rod and with the hot assembly average rod. For a single rod at a single axial location, the following uncertainties exist:

- 1. Uncertainty in the actual linear heat rate, relative to what is predicted.
- 2. Uncertainty in the actual fuel pellet geometry. The pellet at a particular location may be slightly larger or be slightly more enriched than the value intended during manufacture.
- 3. Uncertainty in the hot rod subchannel geometry. The subchannel may be slightly distorted due to rod bow.

The overall uncertainty for the hot assembly average rod peaking factor should be less than that for the hot rod, since we are concerned with the average value over a number of rods, [$]^{a,c}$. This is indicated in Table 25.2-2.

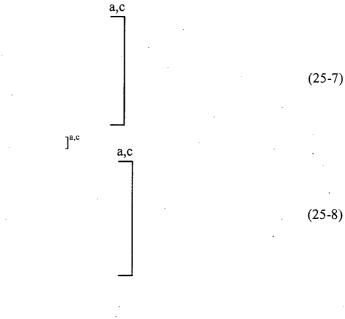
For a single axial location on a single rod, all of these uncertainties must be considered. Since the local axial linear heat rate as specified by F_Q is defined at a single location, all of these uncertainties must be considered for the hot rod, hence the full column of numbers in Table 25.2-2 for the hot rod F_Q . For integral quantities such as the rod total power as specified by $F_{\Delta H}$, local uncertainties such as pellet dimensions should not contribute significantly to the integral uncertainty. [



(25-6)

]^{a,c}

[



]^{a,c}

When the hot assembly average rod is considered, additional uncertainties due to assembly radial peaking drop out.

The result of the application of these different uncertainties is that the uncertainty associated with the power on the hot rod is typically larger than the uncertainty associated with the power in the hot assembly average rod. These uncertainties are discussed in Sections 29.4.1.2 and 29.4.2.1.

Hot Rod Average Linear Heat Rate

]^{a,c}

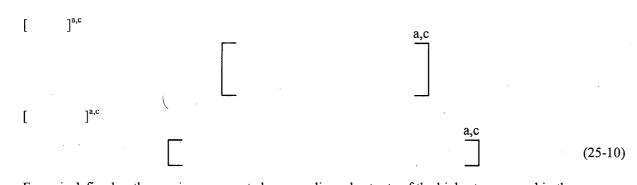
ſ

[

Since the hot rod has a very small effect on the hot assembly fluid conditions (it is only one rod among about 150), its total power is not as important as the power in the hot assembly rod. However, total power will affect hot rod gap pressure and cladding burst times.



WCAP-16996-NP



 $F_{\Delta H,BE}$ is defined as the maximum expected average linear heat rate of the highest power rod in the core, relative to the core average linear heat rate. Typically, the calculated $F_{\Delta H,BE}$ for a core design is augmented by four percent to account for calculational and measurement uncertainties and up to an additional $\begin{bmatrix} \\ \end{bmatrix}^{a,c}$ for "good measure." The reason for the application of additional margin in $F_{\Delta H}$ that, unlike total peaking factor, there are few alternatives short of reducing power if the measured value exceeds the designed value. $F_{\Delta H}$ becomes lower at high burnups, although there may be an increase in mid cycle as poisons are depleted.

Hot Assembly Average Linear Heat Rate

The hot assembly rod (Rod 2) average linear heat rate during steady-state is defined as:

]^{a,c}

ି [

(25 - 12)

a,c

]^{a,c}

25-21

(25-11)

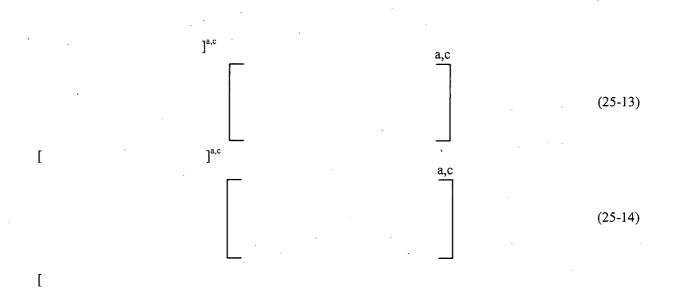
The actual thermal power produced in the hot assembly rod relative to its nuclear power may be slightly different from the hot rod, due to different levels of redistribution. [

As discussed in Section 25.2.1.1, a review of a large number of core designs in two-, three-, and four-loop plants indicates that the minimum difference between the hot rod and the hot assembly average rod is

 $\begin{bmatrix} \\ \end{bmatrix}^{a,c} \text{lower (Figure 25.2-4). This is a conservative estimate of the relationship which will exist between the hot rod and the hot assembly average rod during normal operation, during the entire fuel cycle. The relative nuclear power generated in the hot assembly average rod is therefore assumed to be <math display="block">\begin{bmatrix} \\ \end{bmatrix}^{a,c} \text{lower than the best-estimate value of the hot rod relative nuclear power, } F_{\Delta H,BE}. As previously discussed, however, if additional information is available in the form of a core design limit, an alternative and less conservative approach may be taken to bound the hot assembly average power.$

Axial Power Distribution

Axial power distributions vary widely due to burnup and transient operation. The distributions have been considered in prior evaluation models using [



]^{a,c}

Low Power Region (PLOW)

The power in the average rod (Rod 5) of the low power region of assemblies is determined from the core design and usually varies from [

 $]^{a,c}$ If this region has a low power, the interior channels (Rods 3 and 4) have a higher power. A relative power [$]^{a,c}$ of the core average is typical of current and future low leakage loading patterns. An average value expected for future cycles is assumed as discussed in Section 29.3.1.

Time-in-Cycle

As discussed in Section 25.2.1.4, the time-in-cycle impacts a number of different parameters significant to the LOCA transient behavior. The fuel peaking factors, initial stored energy, rod internal pressure, and decay heat are several examples of burnup dependent parameters. The impact of the time-in-cycle is considered in the uncertainty analysis as discussed in Section 29.4.1.1, Volume 3 of this topical.

Prior Operating History

As discussed previously, the power distributions which generate high peaking factors are relatively short lived. A detailed accounting of the buildup of fission products would show that after shutdown, the axial power distribution would revert back to the original, steady-state distribution. This effect will be

]^{a,c}

Moderator Temperature Coefficient (MTC)

The moderator temperature coefficient (MTC) affects reactor shutdown during the first few seconds of blowdown. The larger (more positive) this value, the less responsive the reactor is to the increased fluid temperature which occurs in the first second or two of the LOCA.

]^{a,c}

Hot Full Power (HFP) Boron Concentration

The initial primary fluid boron concentration coupled with the moderator temperature coefficient discussed previously dictate the core power response during the blowdown phase of a LOCA transient. The initial HFP boron concentration is modeled [

J^{a,c}

The modeling of the various power distribution parameters described above is summarized as follows. The core designer defines the core loading pattern and other constraints which will give the expected maximum $(F_{Q,max})$ and baseload $(F_{Q,ss})$ hot rod peaking factors which meet the Technical Specification limits. The values analyzed in the LOCA analysis for the hot rod and hot assembly rod are derived from these expected values. []^{a,c}

WCAP-16996-NP

November 2010 Revision 0

]^{a,c}

(More details on this uncertainty treatment are provided in Section 29.4.) In Figure 25.2-16, a typical axial power distribution as input into the <u>W</u>COBRA/TRAC-TF2 PWR model is shown. The hot rod peak power is offset by []^{a,c} from the hot assembly average rod power (assuming the general approach), and is offset from the average rod power by the total axial peaking ($F_{\Delta H}$). The low power rod is offset from the average rod power, in turn, by the factor PLOW.

25.2.2 Plant Fluid Conditions

The plant fluid conditions listed at the beginning of this section are those which are sufficient to define an overall thermodynamic state of the fluid. Since <u>W</u>COBRA/TRAC-TF2 calculates a steady-state condition prior to the LOCA, the thermodynamic state cannot be over-specified. Thus, four basic quantities are defined for the primary fluid; its average temperature, pressure, volume, and flow rate. Then, the states of significant fluid regions which are isolated from the RCS during steady-state, but which subsequently become part of the RCS during the LOCA, such as the upper head and the accumulator, are defined. The section below is a brief description of how fluid conditions typically are controlled in a PWR.

25.2.2.1 Overview of Plant Fluid Conditions

A nuclear power plant is equipped with a variety of control systems. For example, the reactor control system in conjunction with the electric load demand program controls the neutron generation rate within the core such that core heat generation rates are proportional to the demanded electric power output. Other control systems are available for control of plant response to rapid disturbances arising from abnormal conditions and for the control of processes which maintain the plant in an economically desirable operating condition.

The static and dynamic behavior of the power production process can only be determined by reliable and accurate measurements of process variables. The application of these measurements by the control and protection systems is then accomplished in a manner which assures proper corrective action and provides protection for the plant and public against extreme accidents. This is normally accomplished by the feedback process where process variables are controlled to a predetermined value, commonly referred to as a setpoint. When measurements deviate from the setpoint, the deviation is noted as an error by the controller(s) and action is taken to restore the process to its correct state point or condition.

Setpoints generally represent either a desired, or "target," value for a process control variable, or a limit or bounding value, that a process control variable may have. In the case of a "target" or control setpoint, variation from the desired value will result in some corrective action to return the plant to the control setpoint. For example, the pressurizer water level control setpoint is approximately 35 percent of the full-scale reading of the measurement span, with either heaters or spray being actuated with a ± 5 percent variation of full span from the 35 percent span. Violation of limiting or bounding setpoints results in a more radical plant response.

From the preceding example of the pressurizer, it is readily seen that relatively small variations from control setpoints will result in plant control systems initiating corrective action. These small spans are called control bands. Thus, for a plant maintained at equilibrium conditions, the process control parameters may be taken to vary from their respective setpoints by no more than the bounds of their respective control

bands. In particular, for process parameters which are subject to automatic control, such as the pressurizer level, the likelihood of the process parameter being significantly different from the target value is extremely small. For those process parameters subject to less frequent surveillance, the potential variation may be larger.

Trip setpoints define the limits within which the plant may operate. Again referring to the example of the pressurizer, the plant will continue to operate temporarily with a pressurizer water level between 17 and 92 percent of full-scale of the measured span, with the plant control systems acting to achieve a level of between 30 to 40 percent of full-scale reading. Owing to operator and/or automatic actions however, prolonged operation outside the control bands is extremely unlikely. The trip setpoints are established to allow the plant flexibility in responding to changes in operating conditions while providing for the health and safety of the public.

Plant operation parameter variations that are significant for LOCA analyses are listed in Table 25.2-3 for a typical PWR. All but primary side loop flow may be considered process control parameters for a nuclear power plant; direct controlling of primary coolant flow rate is not provided for. For a typical plant, the variability of these parameters about their nominal or setpoint values is seen to be small, with a control band of about [$]^{a,c}$ on primary loop pressure and fluid temperature, [$]^{a,c}$ on core power, and about [$]^{a,c}$ on water volumes.

25.2.2.2 Fluid Conditions Modeling Approach

In addition to the process parameters identified in Table 25.2-3, additional RCS fluid conditions have been found to be important in past LOCA analyses. The reactor vessel upper head is supplied by a small bypass flow from the upper downcomer. While the incoming fluid is at the temperature of the cold leg (T_{cold}), the upper head fluid may be at a different average temperature because of the low bypass flow rate which results in some flow from the upper plenum, which is at a higher temperature (T_{hot}). The initial temperature of the fluid in the upper head (T_{UH}) has been found to strongly affect the blowdown PCT in other evaluation models (for Large Break LOCA). Typically, plants can be separated into two categories: those with sufficient bypass flow to maintain (T_{UH}) near (T_{cold}), and those with low bypass flow, in which (T_{UH}) remains close to T_{hot} .

The bypass flow mentioned above is one component of several bypass flows, which reduce the core flow rate relative to the loop flow rate by about four to eight percent. This bypass flow has an indirect effect on the LOCA transient by affecting the fluid temperature rise through the core, but is not expected to affect the LOCA transient directly.

Not all the process parameters described in Section 25.2.2.1 are independent. Typically, if core power, primary flow, and secondary temperature and pressure are specified, the primary fluid temperature and pressure will seek appropriate levels consistent with these boundary conditions. In the modeling of these parameters, the secondary side conditions are adjusted as required to obtain primary side conditions consistent with the Technical Specifications and planned operation. Since the secondary-side model is rather detailed, the secondary-side conditions required to achieve the appropriate primary-side conditions are generally consistent with expected operational values.

Although the accumulator is isolated from the RCS by a check valve during normal operation, it is considered part of the RCS in this methodology. The performance of the accumulator during the LOCA depends on several factors including the water and cover gas initial pressure, temperature, and volume. These are all subject to some variation. Typically, pressure and volume are controlled to within plus or minus 10 percent or less. Since the accumulators reside within containment, the long term temperature of the containment atmosphere will affect the accumulator water temperature. The variation in containment temperature is likely to be seasonal to some degree, and is limited in most plants to a maximum value to avoid problems with equipment degradation. In general, therefore, the accumulator temperature range is plant specific. The accumulator line is subject to the same uncertainties as identified earlier for flow resistance; however, plant startup tests reduce this uncertainty to some extent as discussed in Section 29.3.2, Volume 3.

While accumulator boron concentration is not likely to have a significant effect on the LOCA PCT, it is modeled to ensure that recriticality does not occur in the short-term following a LOCA.

The parameters chosen to represent the reactor initial fluid conditions are:

- 1. Average fluid temperature (T_{avg}) , degrees F
- 2. Pressurizer pressure (P_{RCS}), psia
- 3. Loop flow rate (W_{loop}) , gpm per loop
- 4. Upper head fluid temperature (T_{UH}) , degrees F
- 5. Pressurizer level (L_p) , percent of full span
- 6. Accumulator temperature (T_{ACC}) , degrees F
- 7. Accumulator pressure, (P_{ACC}) psia

8. Accumulator water volume, (V_{ACC}) cubic feet

- 9. Accumulator line fl/D (K_{ACC})
- 10. Accumulator boron concentration, (C_{ACC}) ppm

The effects that the above parameters have on the LOCA transient are considered as part of the uncertainty analysis. The treatment of the fluid condition uncertainties is discussed in Section 29.3.2, Volume 3.

WCAP-16996-NP

Table 25.2-1 Hot Assembly Rod Power Census Summary									
	-								
<u> </u>									
		- Mitagan an area							

			/)
· · ·		· · · · · · · · · · · · · · · · · · ·			
			· · · ·		
· ·					
· · · ·					
				,	
	• •				

Notes:

1. Spier et al. (1988)

2. Chelemer and Tong (1962)

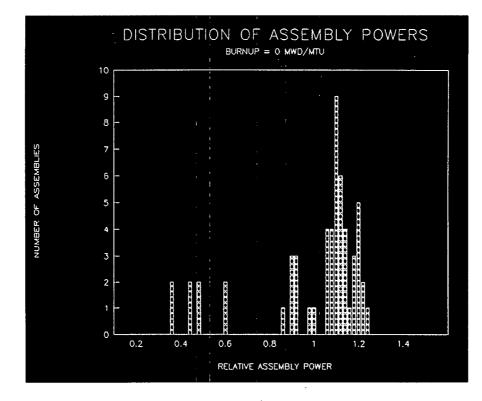
3. Argall et al. (1979)

4. Uncertainties are given in terms of one standard deviation divided by average value (coefficient of variation), percent. The total uncertainty is the square root sum of squares of the components.

Table 25.2-3 Typical Westinghouse Plant Operation Parameters							

25-28

				0 10	ID/HTU				
				1379 PF					
				1.35 PI	AK F.				
	4 0.85	74 1.11	6A 1.08	7A 1 19	8A 1.07	68 1.10	88 1.06 (58 0.46]
	0.88	1.24	1.11	1,32	1.13	1.18	1.24	0.75	
	33400	•	20900	10	21100	20200	12800	30800	
				54	78	64	74	64	
	74 1.11	56 0.92	74 1,14	0,98	- 1,18	1.09	1.12	0.60	
	1.24	0.97	1.24	1.07	1.29	1,15	1,31	0.92	
	BA 1,06	7A 1, 15	08 1.23	8A 1 09	BA 1.11	XA 1.21	08 1, 13	7B 0.90	
	1.11	1.25	1.35	1,10	1,10	1.35	1.19	1.24	
	20900	٥	12800	20500	18900	•	15400	· •	
	7A 1.19	5A	64	74	68	54	78	4	
	1.19	1.07	6A 1.09	74 1 20	58 1.18 1.27	³⁴ 1.08 1.14	/8 1.10 1.28	0.44	
	0	31900	20500	1.31	18500	25400	0	28900	1
	BA 1.07	76 1.19	^{5A} 1.12	58 11 18	60 1.10	74 1.14	74 0.92		
	1,13	1.29	1.20	1,27	1.32	1.32	1,27		
				1					
	⁶⁸ 1, 10	6A 1.09	7A 1.21	5A 1.08	74 1.14	7A 0.90	5A 0.36		
	1.16	1.15	1.35	1.14	1.32	1.19,	0.60		
-	20200	20700	•	25400	•	0	36100		
		74	ab	<u> </u>	74	34	i		
	68 1.08 1.24	1,10	1, 12	78 1.10	0.92	0.35			
	12800	0	15400	0	0	38100	· ·		VERAGE POWER
				1 j		1		AB	VERAGE BURNUP
	58 0.48	6A 0.80	78 0.90	0.44		_,	×		
	0.75	0.93	1.23	0.80					
	30600	20000	•	27000	1, 2, 3, .	. IN UPPER	LEFT CORNE		5
	L	ļ	L		1 X IN C	ORNER INDI			
	QUADRANT OF PEAK								
	REGIO	NO. 1 ASSBA P		JCUM, BURI JRNUP SHAI			NO. POH		
	•	9		27700	0	68		15 1830	
	5A 50	24		11100 11600 '	0	7A 78 .		10 08	o o o o
	8A	40		20300	0				





WCAP-16996-NP

November 2010 Revision 0

			16600 H	PM				
			1.38 P	EAK F ₃				
4 0.92 0.94	7A 1.22 1.27	5A 1.05 1.11	7A 1.20	6A 1.05	68 1.03 1.09	08 0,99 1,12	58 0.53 0.75	
48800	20700	38900	21200	38600	37200	29100	38500	
7A 1.22 1.27	58 0.96 1.01	7A 1.23 1.29	5A 0.98 1.07	78 1.32	6A 1.04	7A 1.14 1.25	8A 0.62 0.66	
20700	48800	20700	48300	21400	38100	18600	29900	
6A 1.05	7A 1.24 1.29	68 1.11 1.19	8A 1.01 1.07	6A 1.04 1,13	7A 1,25 1,31	68 1.04	78 0.83 1.10	
38900	20700	31900	37500	38500	20900	32700	13500	
7A 1.28 1 30	5A 0.98 1.07	6A 1.01	7A 1.22 1.28	68 1,05 (5A 1.02 1.07	78 1,15 1,31	4 0.47 0.75	
21200	48300	37600	20500	38400	42700	18700	34300	
.6A 1.05 1.13	78 1.32	6A 1.04 1.13	58 1.05 1.14	68 1.09	7A 1.21 1,28	74 0.90 1.18		
38600	21400	36500	35400	35300 '	20200	15 100		
68 1.03 1.09	6A 1.04 1.13	7A 1,25 1,31	5A 1.02 1.07	7A 1.21 1 1.20	7A 1.03	5A 0.43 0 80		
37200	38000	20900	42700	20200	16800	42800		
58 0.99 1.12	7A 1,14 1,25	08 1.04 1.14	78 1j. 15 1j. 31	7A 0.90 '	5A 0.43 0.80			
29100	18500	32700	, 18700	15100 ;	42800		MP AS	VERAGE POWER SSEMBLY P. VERAGE BURNUP
58 0.53 0.75	6A 0.83 0.88	78 0.83 1.10	0,47			×.		
38600	29700	13500	34400			GION 1. 2.	9,	
				X IN C	ORNER INDIC	ATES ASSEN		
REGION			CUN. BURM			ND. POWE SSBY SHAR		
4 5.A	9 24	0.81 4	8900 820 4800 1350	00	68 7A	J 2 1.0 50 1.1		
38 84	40		9700 1210 9100 1580		70 .	24 1.1		

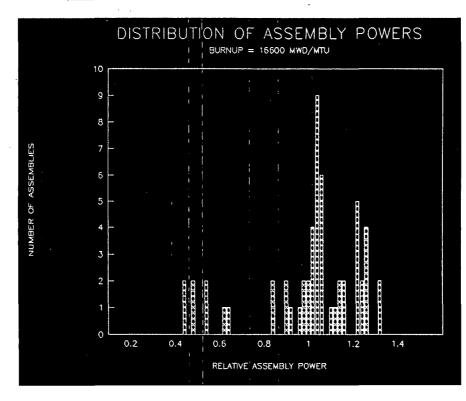


Figure 25.2-2 Typical Assembly Power Map and Assembly Power Distribution, End of Cycle

WCAP-16996-NP

25-31

a,c

· · ·

Figure 25.2-3 Typical Hot Assembly Fuel Rod Power Distribution

WCAP-16996-NP

November 2010 Revision 0

25-32

a,c

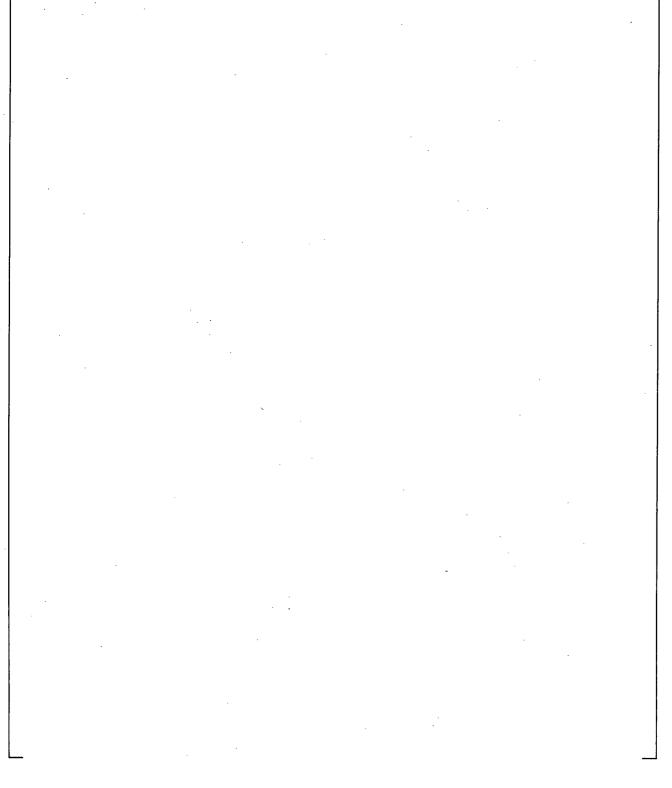


Figure 25.2-4 Hot Assembly Rod Power Census for Typical Westinghouse Fuel Designs

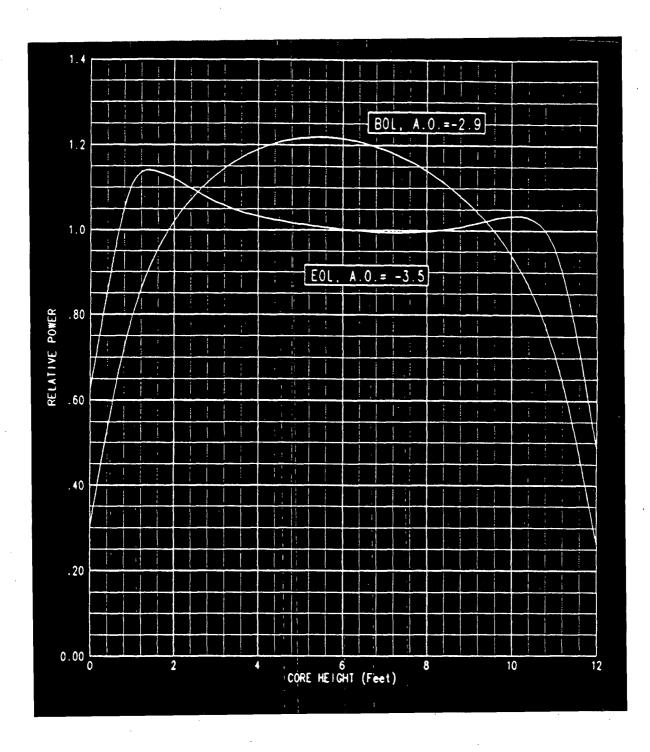


Figure 25.2-5 Relative Axial Power Distribution at BOL and EOL During Full Power Steady-State Conditions

WCAP-16996-NP

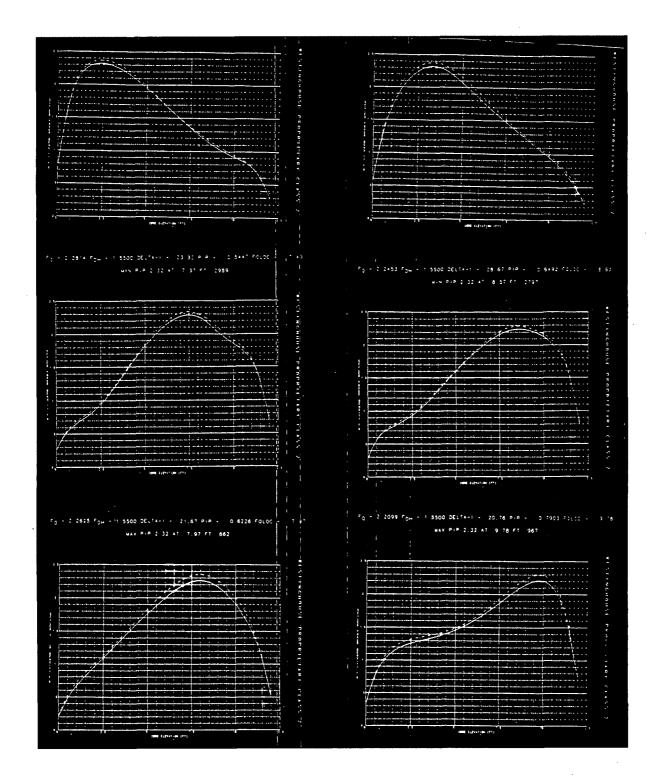


Figure 25.2-6 Typical Transient Axial Power Distributions

WCAP-16996-NP

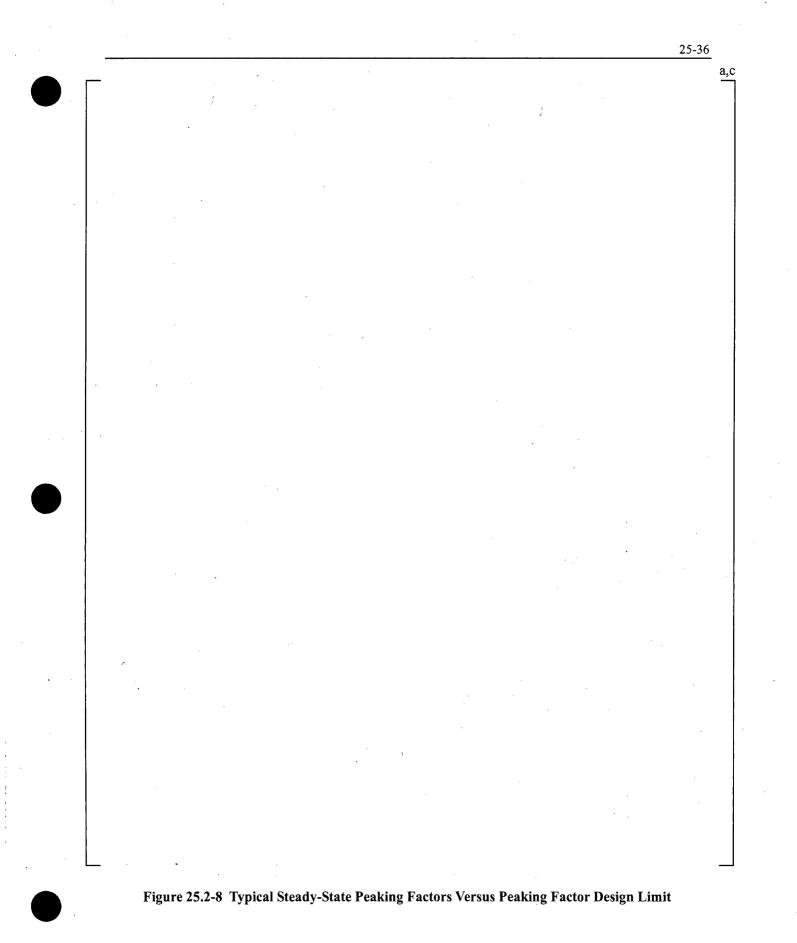
November 2010 Revision 0

2.4 11 2.3 2.2 2.1 • 6 2.0 11 +1.9 MAX1MUM (FQ + P(REL) 1.2 1.6 1.2 1.5 1.2 1.5 1.2 1.2 1.3 - 0 1. 1 1.1 1 1.2 1.1 1.0 o .90 .80 L 4 5 6 CORE HEIGHT 10 11 12 9 3 8 (FEET)

Figure 25.2-7 Envelope of Peak Linear Heat Rates as a Function of Core Height for a Typical Westinghouse Core Design

WCAP-16996-NP

5



WCAP-16996-NP

25-37

a,c

Figure 25.2-9

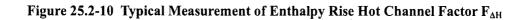
Effect of Load Follow Maneuver Period on Decay Heat Equilibrium Fraction for Various Times After Trip

WCAP-16996-NP

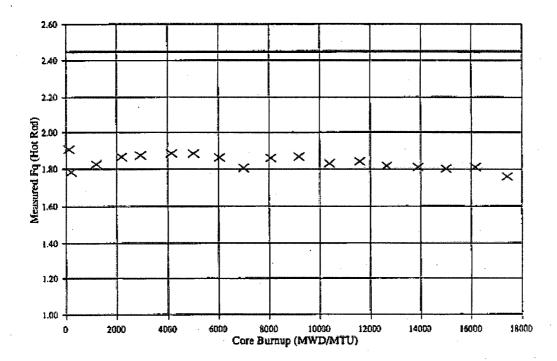
November 2010 Revision 0

1.80 1:70 Measured F-Delta-H (Hot Rod) 1.40 × $_{\star}$ \times × × × к× \times × 2 × 1.30 1.20) 8000 10000 1 Core Burnup (MWD/MTU) 0 2000 4000 6000 12000 14000 16000 18000

 \times Measured — Tech Spec



WCAP-16996-NP



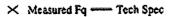


Figure 25.2-11 Typical Measurement of Total Peaking Factor F_Q

November 2010 Revision 0

25-40

a,c

Figure 25.2-12Effect of Burnup on (a) Baseload PLHR, (b) Fuel Average Temperature, (c) Decay
Heat Equilibrium Fraction

.

WCAP-16996-NP

Figure 25.2-13 Bottom and Middle Third Integrals for a Typical Low Peaking Factor Core Design

WCAP-16996-NP

25-41

a,c

Figure 25.2-14 Bottom and Middle Third Integrals for a Typical High Peaking Factor Core Design, Relaxed AI Bands

WCAP-16996-NP_

25-42

a,c

25-43 a,c

Figure 25.2-15 Effect of Unlimited F_Q and ΔI Bands on Bottom and Middle Third Integrals

WCAP-16996-NP

November 2010 Revision 0

	· · ·				· · ·	<u>25-44</u> a,
-						
				-		
	·					
				•		
	•					
				. Ť		
						•
,						
				· · · · ·	•	
					<i></i>	
			•			
•						
				,		
				•		
_		•				

WCAP-16996-NP

November 2010 Revision 0

25.3 REACTOR ACCIDENT BOUNDARY CONDITIONS

The reactor accident boundary conditions are defined as those conditions outside the RCS pressure boundary which affect the LOCA transient. The break itself is considered a boundary condition. The following parameters are included in this category:

- 1. Break Location
- 2. Break Type
- 3. Break Size
- 4. Offsite Power
- .5. Safety Injection Flow
- 6. Safety Injection Temperature
- 7. Safety Injection Delay
- 8. Containment Pressure
- 9. Single Failure
- 10. Control Rod Drop/Drop Time
- 11. Steam Generator Secondary Side

One of the key accident boundary conditions is the postulated break. In a realistic sense, the pipe is not expected to fail. However, for the plant safety analysis and the assessment of the ECCS performance, it is postulated that the main reactor coolant piping will fail. The break parameters are discussed below.

Break Location

Break Type

Break Size

Once it is postulated that the reactor coolant pipe can fail, then all points on the piping have equal probability of failure. If a complete circumferential crack is postulated, piping analysis calculations show that the ends of the severed pipe would separate approximately one inch with a limited lateral displacement of one-half of the pipe wall thickness (Mendler, 1975). This limited displacement is the result of pipe and structural constraints. The time history of axial and lateral displacement of the piping are computed by loop dynamic analysis models.

The mechanical analysis indicates that if the reactor coolant pipe fails, the most probable break geometry is a limited displacement circumferential split break in which the flow comes out of the break in a circumferential direction. The only way that a limited displacement circumferential break can open up into a full double-ended guillotine break is by substantial lateral movement of the piping. The larger lateral displacement can only occur if the pump supports fail for the cold leg break, or the steam generator supports fail for the hot leg break. Additional mechanical analysis indicates that there is insufficient pipe whip energy to crimp the ends of the pipes to create guillotine breaks of smaller area. This is due to the rigidity of the pipes and limited axial displacement of the pipe. Therefore, based on the above mechanical considerations, the range of most probable breaks that should be investigated are the limited displacement breaks or split breaks. The only guillotine break that is possible is the full double-ended guillotine which is caused by larger lateral displacement of the reactor coolant pipes. For smaller split breaks, the orientation of the break becomes increasing significant to the LOCA transient behavior. As such, the orientation of the break relative to the pipe must be considered for smaller break sizes.

Modeling Approach

]^{a,c}

Offsite Power

ſ

Offsite power determines whether RCS pumps initially remain on, and whether pumped safety injection (and containment safeguards) come on with only valve opening and alignment delays. The effect of the RCS pumps on the LOCA transient may be significantly different, depending on whether they are assumed to coast down or continue running (until operator action is taken, if applicable).

Modeling Approach

Variations in this parameter will be considered in the scoping analysis [

]^{a,c}

Safety Injection Flow

Safety injection (SI) flow varies depending on the single failure assumed, and on the specific plant pump and injection line configuration. Current methods, which are also used in currently accepted evaluation models, provide conservative estimates of minimum and maximum flow, which take into account several uncertainties.

Additionally, for smaller break sizes there is the potential for switchover to recirculation mode to occur prior to meeting the transient termination criteria. The safety injection flow rate in recirculation mode may differ from the injection mode flow rate, and there may be a period of safety injection interruption during switchover.

Modeling Approach

ſ

]^{a,c}

Safety Injection Temperature

SI temperature may vary, depending on the location of the refueling water storage tank (RWST), and on controls imposed by Technical Specifications. The safety injection temperature may also change as a result of switching to recirculation mode.

Modeling Approach

[

]^{a,c}

Safety Injection Delay

SI delays vary depending on whether loss of offsite power is assumed to occur.

Modeling Approach

Scoping study results will be used to examine the effect of delayed injection, resulting from delayed diesel start or other delays. [

]^{a,c}

Containment Pressure

The containment pressure is dependent on the mass and energy release from the RCS during the LOCA. Studies have shown that the containment pressure response is most highly sensitive to the value of the heat transfer coefficient used for heat transfer to passive heat sinks. In the computer codes used to calculate the pressure transient, this heat transfer coefficient is set at an upper bound to minimize calculated containment pressure.

Modeling Approach

A minimum containment pressure is calculated considering run-specific mass and energy releases as discussed in Section 25.6.

Single Failure Assumption

There are two types of single failures which may have an effect on the LOCA transient. If loss of an entire train is assumed, then the flow to the RCS is minimized, since this assumption results in the loss of both high and low head pumped flows. However, this assumption also leads to reduced cooling of the containment, since the train includes containment sprays and fan coolers. If the assumed single failure is the loss of a low head pump only, this results in a higher flow to the RCS, but also increases containment cooling, which reduces containment pressure. The negative effect of lower containment pressure may offset the positive effect of higher pumped flow to the RCS.

Modeling Approach

In order to simplify the analysis, the loss of a train may be assumed for the determination of pumped ECCS flow during the LOCA, while the train will be assumed to operate in the calculation of containment backpressure. This will result in a conservatively low containment backpressure. Alternatively, a more complete analysis using consistent assumptions may be performed on a plant-by-plant basis.

Control Rod Drop/Drop Time

If it is demonstrated that combined seismic and LOCA loads do not distort the control rod guide tubes, then the control rods may be assumed to drop during the LOCA. While this assumption has a negligible effect on the LOCA PCT/MLO transient for larger breaks, advantage may be taken of the negative reactivity introduced by the control rods when determining boron requirements to prevent short term recriticality. This, in turn, may affect the boron concentration assumed in the LOCA analysis. For smaller breaks, control rod insertion is necessary to preclude re-criticality in the core. In addition, slightly higher core flow rates would occur, since the thimble tubes would no longer be empty. [

Modeling Approach

ſ

Steam Generator Secondary Side

]^{a,c}

Downstream of the main steam isolation valve (MSIV), a steam turbine stop valve can halt the flow from the secondary side. For LBLOCA applications, it is conservative to assume the SG secondary side is isolated early, maximizing the secondary side pressure and temperature and eliminating the steam generator as a heat removal path during the early part of the transient. [

For SBLOCA applications, the main steam safety valve (MSSV) actuates to relieve the building secondary side pressure resulting from heat transfer from the primary side during the natural circulation phase.

]^{a,c}

Modeling Approach

ſ

25-48

]^{a,c}

]^{a,c}

1^{a,c}

25.4 MODEL PARAMETERS

The assessment studies of Volume 2 were performed such that all models and correlations were used within ranges expected to occur during analysis of a PWR. Many of the experiments were of sufficient complexity that the appropriate model interactions would also occur. The resulting comparisons between data and prediction yielded the basis for the uncertainty methodology detailed in Section 29, Volume 3.

The Westinghouse methodology for combining biases and uncertainties considers the effect of all medium and high-ranked phenomena from the Phenomena Identification Ranking Table (PIRT), as detailed earlier in Table 2-1. A discussion of how each of the phenomena is considered is provided in Section 29.5, Volume 3.

25.5 OPERATOR ACTIONS

Upon the initiation of a transient in a plant, the operators use the plant's Emergency Operating Procedures (EOPs) to sequentially verify that automatic safeguards features are functioning correctly and follow prescribed operations to restore any malfunctioning systems. Eventually, the EOPs are used to begin plant recovery or to secure operations. Operator actions must be examined to determine the different transient scenarios that could develop and affect the severity of a small break LOCA transient and/or challenge the assumptions made in the LOCA analysis calculations.

The EOPs have been developed to direct the operators to analyze and respond to symptoms ascertained from measured plant parameters or trends of those parameters. During the initial stages of an accident or transient, the plant response can be similar for different events. The large number of changing parameters and their rates of change may prevent immediate diagnosis of the exact type of event; for example, LOCA, steam generator tube rupture, and steam line breaks. Therefore, the EOPs are based upon a hierarchy directing that important, common actions are performed early, based upon the symptoms observed; eventually, the EOPs branch to increasingly specific categories of accidents or transients.

The EOPs are formulated to handle many different events, including beyond design basis accident scenarios. [

]^{a,c} Upon first review, there appear to be numerous actions that could be followed leading to a variety of outcomes. However, when the event is a design basis small break LOCA involving no more than the limiting single failure, implementation of the EOPs can be significantly streamlined because certain actions, verifications, or branch points and their outcomes are already known. The EOPs can even be further streamlined for specific small break LOCA scenarios. For example, when analyzing a given case for an assumed failure of a diesel generator or a train of safety injection (consistent with the FSLOCA single failure assumption), the symptoms that the operator will observe and the system responses to the operator's actions are known. The EOPs can then be reduced to only a few pages when operations that are unnecessary for the specific small break LOCA scenario are eliminated because key plant symptoms are known a priori.

25.5.1 EOP Sequences for a Small Break LOCA

Table 25-1 is a condensation of the EOPs relevant to the short-term portion of a small break LOCA at the Indian Point Unit 2 plant. While Table 25-1 is specific to Indian Point Unit 2, plants typically follow a generic template for the generation of EOPs, and plant-to-plant differences in the EOP structure are not expected to be important for the purpose of performing a LOCA safety analysis. [

25.5.1.1 Adverse Containment Conditions

In adverse containment conditions, a few parameters are evaluated against specifications that are dependent upon containment conditions. The values to use when adverse containment conditions exist are given in parentheses throughout the rest of this section. Adverse containment conditions are defined as:

]^{a,c}

 $P_{CONT} > 4 psig$

or

ſ

Containment radiation level $> 10^5$ R/hr

Either or both of these conditions would probably be met at some time during the small break LOCA transients of interest. Actions are based upon measurement comparisons against the adverse conditions criteria.

25.5.1.2 Continuously Monitored Conditions

In addition to the sequential steps prescribed in the EOPs, there are a few key items continuously monitored as the procedures are followed. These are listed in "Foldouts" to a given procedure where they apply. Two of these items, both of which are in procedure [$]^{a,c}$ of Table 25-1, are important to the boundary conditions assumed for small break LOCA analysis calculations. They are as follows (values in parentheses are typical values for adverse containment conditions):

WCAP-16996-NP

 $]^{a,c}$

25.5.1.3 Inadequate Core Cooling

ſ

ſ

Another condition the operator will monitor following a small break LOCA event is to verify that the core is being adequately cooled. To establish that adequate core cooling exists, the EOPs require that the temperature readings of the core exit thermocouples do not exceed 1200°F. If this criterion is not met, the operator will enter the Inadequate Core Cooling Procedure FR-C.1, which directs the operator to depressurize the steam generator secondary side. If this depressurization is performed, it may significantly affect the small break LOCA transient, [

]^{a,c}

25.5.2 Variability of Plant Conditions Due to Operation Actions

The condensed procedures in Table 25-1 show the importance of operator actions in defining the conditions during the short-term phases of a small break LOCA. The process is summarized chronologically as follows:

A review of the operations in Table 25-1 shows that the majority of the efforts undertaken by the operators are categorized as "verify operation or status." Although the operators continuously analyze equipment status and respond to failures throughout the entire operation, selected equipment failures are prescribed as boundary conditions to any given LOCA analysis calculation and the responses may, therefore, be defined a priori for an analysis. It may be assumed that an operator will spend more or less time on a given EOP step attempting to remedy an equipment failure. However, given an assumption concerning the failure of certain equipment for a defined analysis scenario, that equipment will still be unavailable as far as the

WCAP-16996-NP

November 2010 Revision 0

]^{a,c}

]^{a,c}

LOCA analysis boundary conditions are concerned. Furthermore, the operators have little latitude in the operations that may be attempted while working through the EOPs during the response to an accident. The possibility of various equipment failures is addressed within the procedures. When a failure is noted during a given step in the EOPs, the operators are directed immediately to an alternate action under a "Response Not Obtained" column. There, specific actions such as verifying or cycling a switch position or sending an operator into the field to perform a manual action are listed to attempt to remedy the failure. If the failure remains after the alternate action is taken, the operators note the failure and return to the subsequent actions directed by the EOPs.

Although some variability in the overall response times may occur from the operators spending time attempting to rectify individual failures – for example, time spent attempting to restart a failed safety injection pump – the net result is manifested only in terms of a few boundary conditions to a LOCA analysis. The only ones with potentially significant variability that could affect the ECCS performance prior to the time of PCT during a given small break LOCA calculation, are as follows:

· [

]^{a,c}

Table 25-1	Condensed EC	Ps for Indian Point Un	it 2, Short-Term F	ortion		
				ļ		
	·····					
,						. <u></u>
					<u> </u>	
		· .				
<u></u>				<u></u>		
		<u></u>				·····
· · · · · · · · · · · · · · · · · · ·						
			· · · · · · · · · · · · · · · · · · ·			
		· .				

Table 25-1 Condensed EOPs for Indian Point Unit 2, Short-Term Portion (cont.) .								
		-						
		· · · · · · · · · · · · · · · · · · ·		_				
<u></u>								
						•		
· ·								
				_			<u> </u>	<u></u>
		<u>, </u>						
		· · ·						
							•	
······································								

25-55

25-56

	· · · · · · · · · · · · · · · · · · ·	- -
		· · · · · · · · · · · · · · · · · · ·
$\left \right $	· · · · · · · · · · · · · · · · · · ·	
	· · · · · · · · · · · · · · · · · · ·	
	``````````````````````````````````````	
	•	
-		
		· · · · · · · · · · · · · · · · · · ·
-		
	X .	

# **25.6 CONTAINMENT RESPONSE**

The containment pressure analyzed in the FSLOCA methodology is calculated using the COCO code (Bordelon, 1974). The COCO containment code was integrated into the WCOBRA/TRAC-TF2 thermal-hydraulic code. The mass and energy releases from WCOBRA/TRAC-TF2 are passed into COCO every timestep. COCO then calculates the containment pressure based on the containment model and the mass and energy releases, and passes the pressure back to WCOBRA/TRAC-TF2 as a boundary condition at the break. The COCO code is used to calculate the containment pressure [

# ]^{a,c}

The containment model for COCO is designed to calculate a conservatively low containment pressure, including the effects of all the installed pressure reducing systems and processes. The previous approach for calculating the containment pressure using the COCO code was described in Appendix A of (Bordelon et al., 1974). The same approach is generally followed within the FULL SPECTRUM LOCA method, with some exceptions as described herein.

Consistent values were used for inputs shared between the <u>W</u>COBRA/TRAC-TF2 model and COCO model (such as the safety injection temperature), with the exception of the single failure assumption. The failure of a single-train of ECCS was assumed for the LOCA transient calculation, but all trains of containment spray, fan coolers, etc. are assumed to be in operation for the calculation of the containment pressure in order to further reduce the calculated containment pressure. The values for inputs pertinent only to the containment model were typically selected to provide a minimum containment pressure (e.g. maximum heat transfer areas and volumes are modeled for containment heat sinks).

#### ]^{a,c}

ſ

#### **25.7 PUMP LOCKED ROTOR**

The pump model includes transfer of momentum from the pump to the fluid, as described by Equation 10-1. Variable pump speed is taken into account through Equation 10-10. The pressure difference through the pump, and the torque applied by the fluid on the pump rotor are calculated using empirically determined single and two-phase homologous curves. The data used to obtain these curves is described in Section 10.4, Volume 1.

If the pumps lose power during the LOCA, the broken loop pump rotation will accelerate, while the intact loop pumps will coast down. Such an acceleration will impose centripetal stresses on the pump's flywheel. If the flywheel fails, there is a small chance that the rotor will become locked. [

[

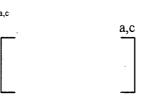
]^{a,c}

. 1 .

WCAP-16996-NP

November 2010 Revision 0

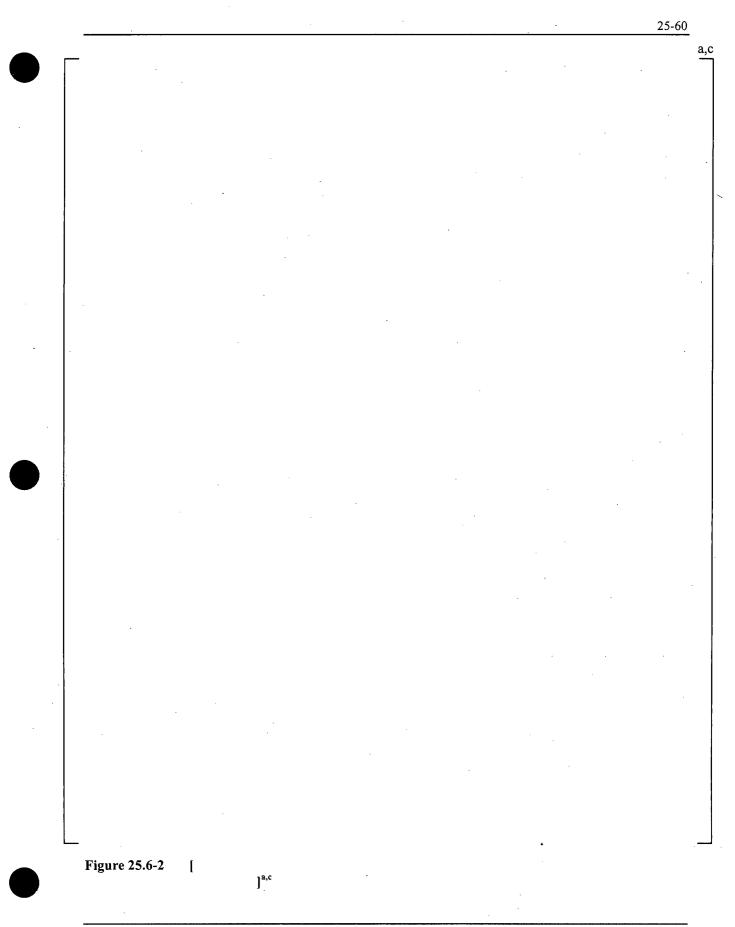
]^{a,c}



November 2010 Revision 0

25-59

a,c



WCAP-16996-NP

# **25.8 REFERENCES**

- 1. American Nuclear Society, 1979, "American National Standard for Decay Heat Power in Light Water Reactors," ANSI/ANS-5.1-1979.
- 2. Akimoto, H., et al., 1984, "Pressure Drop through Broken Cold Leg During Reflood Phase of Loss-of-Coolant Accident of PWR," Journal of Nuclear Science and Technology, 21 [16].
- 3. Argall, B. M., et al., 1979, "Fuel Rod Bow Evaluation," WCAP-8691, Revision 1.
- 4. Bajorek, S. M., et al., March 1998, "Code Qualification Document for Best Estimate LOCA Analysis," Volume 1 Revision 2, and Volumes 2 through 5, Revision 1, WCAP-12945-P-A (Proprietary).
- 5. Bordelon, F. M. and Murphy, E. T., 1974, "Containment Pressure Analysis Code (COCO)," WCAP-8327 (Proprietary), WCAP-8306 (Non-Proprietary).
- 6. Bordelon, F. M., et al., 1974, "Westinghouse Emergency Core Cooling System Evaluation Model – Summary," WCAP-8339.
- 7. Bordelon, F. M., et al., 1975, "The Westinghouse ECCS Evaluation Model: Supplementary Information," WCAP-8471-P-A (Proprietary).
- 8. Chelemer, H. and Tong, L. S., 1962, "Engineering Hot Channel Factors for Open Lattice Cores," <u>Nucleonics</u>, 20, Number 9.
- 9. Foster and Sidener, July 2000, "Westinghouse Improved Performance Analysis and Design Model (PAD 4.0)," WCAP-15063-P-A, Revision 1, with Errata (Proprietary).
- 10. Letter from Johnson, W. J. to Richardson, J. E., December 1990, "Steam Generator Tube Deformation," NS-NRC-90-3557.
- 11. Mendler, O. J., 1975, "Method of Analysis and Evaluation of Jet Impingement Loads from Postulated Pipe Breaks," WCAP-8957.
- 12. Miller, R. W., et al., 1983, "Relaxation of Constant Axial Offset Control/F_q Surveillance Technical Specification," WCAP-10216-P-A.
- 13. Morita, T., et al., 1974, "Power Distribution Control and Load Following Procedures," WCAP-8385-P-A.
- 14. Salvatori, R., 1973, "Topical Report, Reactor Coolant Pump Integrity in LOCA," WCAP-8163.
- 15. Spier, E. M., et al., 1988, "Evaluation of Nuclear Hot Channel Factor Uncertainty," WCAP-7308-L-P-A.

WCAP-16996-NP

- 16. Stucker, D. L., et al., 1991, "Westinghouse ECCS Evaluation Model: Revised Large Break LOCA Power Distribution Methodology," WCAP-12909-P.
- 17. U.S. Nuclear Regulatory Commission, 1989, "Best-Estimate Calculations of Emergency Core Cooling System Performance," Regulatory Guide 1.157.

• (

# 26 WCOBRA/TRAC-TF2 MODEL OF PILOT PLANTS

# 26.1 MODELING APPROACH

## **26.1.1 Introduction**

All U.S. designed light water Pressurized Water Reactors (PWRs) have the same fundamental design. The functions of the major system components such as the reactor vessel, pressurizer, steam generators, and pumps are the same, and most have similar design features. Differences between PWR systems are primarily due to loop design and the Emergency Core Cooling System (ECCS) configuration. Operating Westinghouse units, for example, have loop designs that are 2x2 (two-loop), 3x3 (three-loop), and 4x4 (four-loop), while Combustion Engineering units, Westinghouse advanced plants (AP600, AP1000), and Babcock and Wilcox (B&W) units have a 2x4 loop arrangement. With the exception of size, and the B&W once-through steam generator, individual loop flow paths in each type of system are similar.

At a higher level, the reactor vessel internals for various PWRs are also similar. However, there are differences in the design details of the internal structures in various vessel regions. In some older Westinghouse plants for example, the lower support plate is curved while in other plants it is flat. Within the core, there are differences in fuel design. Some plants have a thermal shield in the downcomer, while others have a neutron pad attached to the core barrel. B&W plants include vent valves in their core barrels. The upper plenums and upper heads contain control rod guide tubes and support structures that may have slightly different designs and arrangements.

The differences in the various PWR designs lead to differences in flow areas, volumes, and surface areas within various regions of the PWR primary system. The <u>WCOBRA/TRAC-TF2</u> nodalization for a PWR Reactor Coolant System (RCS) must model specific flow paths and regions within the system. Thus, the PWR design itself dictates, to an extent, the specific nodalization and inputs for a plant model. [

 $]^{a,c}$  The following sections describe how a RCS is modeled using <u>W</u>COBRA/TRAC-TF2. Two three-loop plant models are described in detail to show a consistent modeling approach that can accommodate different plants. The relationship between the plant nodalizations and the nodalizations for the experimental tests is discussed.

#### Noding Strategy and Modeling Philosophy

Given that a degree of noding sensitivity to the results is unavoidable, there must be a specific relationship between the noding scheme used for the PWR compared to the noding scheme for the experiment simulations (since these simulations form the validation basis for the physical models in the code). Reinforcing noding consistency to the extent practical between the SETs, IETs and the PWR will ensure that same conclusions with respect to biases and uncertainties derived from the code and model assessments will be applicable to the PWR LOCA simulations for which the EM was designed. Exceptions to this noding philosophy are discussed on a case by case basis. The definition of an optimal noding strategy to apply to a specific region or component is ideally an iterative process between a realistic modeling of the test features while maintaining consistency across tests facilities and the PWR which span over a full range of scales. [

]^{a,c} The result of this process is the generation of modeling guidelines which were applied in the modeling the SETs, IETS and PWR presented in Volume 2 of this Topical Report.

The resulting consistency in the application of the modeling guidelines for the PWR relative to the test facilities is presented in Section 26.1.2.

#### **26.1.2 Modeling Consistency**

Volume 2 documented simulations of experimental tests in a broad range of facilities using <u>WCOBRA/TRAC-TF2</u>. These tests were modeled so that a consistent noding methodology could be established for use in PWRs and other experimental facilities. This section compares the experimental test and RCS noding in various regions. The RCS noding is described in detail for both V. C. Summer and Beaver Valley Unit 1 in subsequent sub-sections.

WCAP-16996-NP

[

]^{a,c}

## **Core Axial Noding**

The axial noding in a PWR core and in tests with simulated cores is established by the overall heated length and the location of spacer grids. Table 26.1-1 lists input parameters used in modeling experimental tests with heated bundles, and the PWR models. The table lists the number of grids, the number of axial hydraulic cells used to model the core, and the range of cell heights. As can be seen in this table, the average cell heights for all of the test models and the plant models fall within a narrow range.

#### **Core Lateral Noding**

The grouping of assemblies in <u>WCOBRA/TRAC-TF2</u> models for the large scale experimental tests and PWRs depends on the relative radial power distribution in addition to the potential flow delivery from the upper plenum. Three large scale experimental test facilities having heated cores were modeled: CCTF (Section 19), ROSA (Section 21), and LOFT (Section 22). Consistency between the lateral core nodalization in these tests and the PWR models can be characterized as follows:

<u>Hot Assembly</u> – A hot assembly is modeled in the PWR, with plant-specific input determining the possible lateral power distributions. The hot assembly in the PWR is surrounded by one of the average assembly channels. A hot assembly was modeled in each of these experimental facilities based on the radial power profile imposed on the test bundles. For LOFT, the central assembly was the hot assembly. This assembly was cross-connected to an average core channel. In CCTF, test bundles 29 to 32 were approximately one-fourth the size of a typical PWR bundle and all had the same relative high power. These four bundles were grouped and modeled as a single hot assembly, which was connected laterally to the low and medium powered assemblies below open holes and guide tubes. The ROSA hot assembly modeled a total of 8 high-power bundles, which represent one-third of the entire heated core. The ROSA hot assembly had cross-flow links to both the average and low power channels (bundles).

<u>Upper Plenum Structures</u> – The PWR hot assembly is assumed to reside in a location in which the flow is restricted from above. Other channels represent the core regions below support columns and guide tubes, or the low power peripheral assemblies. In LOFT, the hot channel was the central bundle, which had the highest power. The LOFT core had two other channels; one representing the four bundles beneath guide tubes, and another representing the four corner assemblies. The corner bundles were located below structures similar to support columns. In CCTF, the core was modeled by four channels; a hot channel, a channel for the bundles below guide tubes, a channel for bundles beneath open core plate holes, and a channel representing the eight low power bundles on the core perimeter beneath support columns. In the ROSA model, the hot assembly is modeled as being located below open holes and guide tubes. The ROSA model had two other channels; one representing the average power assemblies and another for the outer lower power assemblies.

<u>Radial Power Distribution</u> – The radial power distribution is accounted for in both the PWR models and in the LOFT, CCTF, and ROSA models by representing various regions with several <u>W</u>COBRA/TRAC-TF2 nuclear or heated rods.



#### Hot Leg Noding

Only the LOFT, CCTF, and ROSA experimental tests included hot legs that connected scaled upper plenums to functional steam generators. Table 26.1-2 lists the cell sizes in these test models and the PWR models. [

]^{a,c}

#### **Steam Generator Noding**

Table 26.1-3 compares the primary side hydraulic cell lengths in the experimental test models and the PWR models. Because the LOFT and CCTF steam generators were less than full-scale in height, fewer cells are used. While in the CCTF steam generator the cell length remained very similar to that of the PWR, the LOFT value became small. Increasing the cell size in LOFT would result in excessively coarse noding for that test. The ROSA steam generator noding and the noding for the two pilot plants are similar. The ROSA facility and both pilot plants used the same number of nodes, resulting in roughly the same cell lengths for the steam generator tubes.

#### Crossover Leg Noding

Only the LOFT and ROSA facilities had crossover legs connecting the steam generator to actual pumps. The crossover leg noding from LOFT and ROSA is compared to the plant model noding in Table 26.1-4. As can be seen in this table, the hydraulic cell lengths are similar in the PWR models. In LOFT, the number of cells was reduced to increase cell size so the cell length is closer to the PWR models. In the ROSA model, the number of cells was increased to model the deeper loop seal and decrease the cell length.

While the UPTF facility used simulators for the steam generator and pump components, [

]^{a,c}

#### **Pump Noding**

The pump is modeled as a two-cell component, with pump curves supplied as input. The LOFT pump and the plant model pumps are modeled the same way, with the exception of the pump curves. LOFT-specific pump curves are used for that facility, while pump curves appropriate for the plant-specific pump design are used in the plant models. Similar to LOFT, the ROSA pump model had two cells with ROSA-specific homologous curves.

#### **Cold Leg Noding**

Table 26.1-5 lists the separate effects and integral effects test facilities in which cold leg models were used. [

# 26.1.3 Conclusions

ſ

A set of guidelines has been established so that nodalization of test facilities and full-scale plants is done in a consistent fashion. Axial noding in the core is based on the bundle heated length and the location of spacer grids, which defines the cell height to be approximately 10 inches. Lateral noding in the core is determined by the radial power distribution and the likelihood of flow delivery due to the upper plenum internals arrangement, with a hot assembly explicitly modeled.

In the upper and lower plena, the plant models and large scale integral tests are modeled consistently. A CCFL region, which extends from the top of the active fuel to the upper core support plate, is modeled explicitly in the PWRs as well as in the UPTF, CCTF, ROSA, and LOFT models. In this region, channels are used to model the flow area through the fuel assembly nozzles extended up to the upper core plate. These channels are referred to as jet channels. The remainder of the volume in this region is modeled in a global or several global channels. The regions below the lower core support plate and above the upper core support plate are also modeled in a similar manner, with differences in noding used to account for physical differences in the various designs.

In the loop components, the number of cells and/or cell sizes used in the test models and in the PWR models are approximately the same. Differences in cell size or the number of cells, such as those in the LOFT and ROSA models, are due to unique features of the facility. In cases where the facility design required a deviation from the general guidelines, additional detail was put into the model.

While a close connection is maintained between noding for the test facilities and PWRs, an important feature of <u>WCOBRA/TRAC-TF2</u> modeling is its flexibility. The noding with <u>WCOBRA/TRAC-TF2</u> is not prescribed as was the noding in Appendix K type Evaluation Models. With <u>WCOBRA/TRAC-TF2</u>, additional noding detail is added as the actual hardware being modeled requires. Thus, additional sections can be added in the upper plenum, for example, if behavior is expected to be non-uniform as in the case of a plant with core deluge jets.

WCAP-16996-NP

]^{a,c}

In some plants, the hot assembly location may differ. The assembly location in a PWR which leads to the highest peak cladding temperature depends not only on the core design, but also on the upper plenum internals arrangement, which determines the amount of downflow cooling, and the crossflow from surrounding assemblies. The PWR hot assembly location must then be determined from review of the internals layout and the technical assessment described in subsequent sections for the specific plants to be analyzed.

Table 26.1-1	Core Section Axial Cell Lengths					
				,,		
		•				
· · · · · · · · · · · · · · · · · · ·						
						-
				· · ·		

26-7

-

Table 26.1-2	Hot Leg Noding Comparison					
			<u></u>			
	·	e				
			-			

Table 26.1-3         Steam Generator Noding Comparison					
<u> </u>				· .	

,	Table 26.1-4	Crossove	r Leg Noding		
Γ					
	<u> </u>				
					1

26-8

2	6-	9

<u>a,c</u>

Table 26.1-5     Cold Leg Noding						
		,				
		a				
				·		
			· · · · · · · · · · · · · · · · · · ·			
		\ \				

# 26.2 V. C. SUMMER NUCLEAR POWER PLANT

The vessel and loop portions of a PWR are modeled with significant detail for <u>W</u>COBRA/TRAC-TF2 within the Westinghouse FULL SPECTRUM LOCA Evaluation Model.

V. C. Summer (CGE) is a three-loop plant containing Westinghouse 17x17 VANTAGE PLUS (V+) fuel with IFMs and ZIRLO[®] cladding. The nominal core power for this plant is 2,900 MWt. V. C. Summer also has Westinghouse DELTA-75 replacement steam generators.

# 26.2.1 V. C. Summer WCOBRA/TRAC-TF2 Nodalization

The CGE vessel geometry as modeled in <u>WCOBRA/TRAC-TF2</u> is described in Section 26.2.1.1; a description of the core modeling is provided in Section 26.2.1.2, the loop geometry is described in Section 26.2.1.3, and the ECCS modeling is detailed in Section 26.2.1.4.

## 26.2.1.1 Vessel Model

Figure 26.2-1 shows the vessel drawing for the V. C. Summer three-loop PWR. Figure 26.2-2 shows the vessel major internal component elevation layout. The elevations shown on the right are relative to the inside bottom of the vessel. This elevation layout contains most of the information needed to divide the vessel into nine vertical sections. These sections are described in turn starting at the bottom of the vessel.

The bottom of vessel Section 1 is the inside vessel bottom. The bottom of vessel Section 2 is the bottom of the upper tie plate. The bottom of vessel Section 3 is defined as the beginning of the active fuel. The bottom of vessel Section 4 is the top of the active fuel. The bottom of vessel Section 5 is the elevation at the bottom of the upper core plate. The bottom of vessel Section 6 is equal to the elevation of the bottom of the hot leg inner wall. The bottom of vessel Section 7 is the elevation of the hot leg. The bottom of vessel Section 8 is the elevation at the top of the upper support plate. The bottom of vessel Section 9 is the elevation at the top of the upper guide tube in the upper head. The top of vessel Section 9 is the inside top of the vessel upper head.

After defining the elevations for each section, a noding scheme is defined following the same basic philosophy applied to the Separate Effects Test (SET) and Integral Effects Test (IET) facilities as described in Section 26.1.1 of this document. [

]^{a,c}

Figures 26.2-3 through 26.2-6 illustrate the V. C. Summer vessel noding. Figure 26.2-3 is a vertical section noding diagram. Figures 26.2-4 through 26.2-6 are the horizontal "plan" views of each section. In these figures, the numbers within the squares are the channel numbers and the numbers within the circles with arrows attached to them are the gap numbers. A gap is used to define a horizontal flow path between channels. Positive flow is in the direction indicated by the arrow. It is assumed within <u>WCOBRA/TRAC-TF2</u> that a vertical flow path for vertically stacked channels exists unless specified otherwise in the input. Upward axial flow is considered as positive flow.

As can be seen in Figures 26.2-3 through 26.2-6, 89 channels and 89 gaps are used for V. C. Summer to define the vessel. It can be seen in Figure 26.2-3 that several of the nine vertical sections are sub-divided into two or more levels. For example, the active fuel region, vessel Section 3, is divided into 14 vertical levels. By accounting for the vertical sub-division within vessel Sections 2, 3, 5 and 7, the vessel model for V. C. Summer has a total of 309 fluid cells.

Vessel Section 1 models the vertical section of the vessel from the inside bottom of the vessel to the bottom of the upper tie plate. The modeling of this section is relatively simple since there is one channel with one vertical cell and no horizontal flow gaps (Figures 26.2-3 and 26.2-4). Channel 1 completely represents Section 1 of the vessel. The top flow area of this channel/section was computed based on the net flow area at the bottom of the tie plate.

Vessel Section 2 models the vertical section of the vessel from the bottom of the upper tie plate to the bottom of the active fuel region. This section contains two vertical cells for ten channels (designated 2 through 5 and 52 through 57) and horizontal flow gaps (numbered 1 through 6 and 46 through 57). Figures 26.2-3 and 26.2-4 provide an illustration for the vertical and radial representation of this section of the vessel model.

Channels 2, 3, 4, 52, 53, 54, 55, 56, and 57 each represent one-ninth of the annulus volume between the vessel inner wall and the core barrel outer wall, and are connected by Gaps 4 through 6 and 52 through 57. Channel 5 is the lower plenum volume between the upper tie plate and the fuel nozzle elevation. [ ]^{a,c} The area at the top of

Channel 5 is equal to the sum of the areas modeled at the bottom of Channels 9 through 13 in vessel Section 3. Area variation inputs are used to vary the flow area between the lower and upper cells of Channel 5 to account for the change in flow area within this channel due to the lower support plate. The radial flow gaps modeled in vessel Section 2 are illustrated in Figure 26.2-3 with positive flow in the direction indicated in the figure. Gaps 1, 2, 3, 46, 47, 48, 49, 50, and 51 model a radial flow gap in the lower cell of vessel Section 2, with the core barrel extension blocking radial flow from the upper cell of the downcomer channels into the upper cell of lower plenum Channel 5.

Vessel Section 3 models the vertical section of the vessel from the bottom to the top of the active fuel region. The modeling is accomplished using fourteen vertical cells in fourteen channels (designated 6 through 13 and 58 through 63) and thirteen horizontal flow gaps (designated 7 through 13 and 58 through 63). Figures 26.2-3 and 26.2-4 provide an illustration for the vertical and radial representation of this section of the vessel model.

Channels 6 through 8 and 58 through 63 each represent one-ninth of the downcomer annulus volume between the vessel inner wall and the core barrel outer wall. The neutron pads are modeled in this section. Channel 9 is the volume between the core barrel inner wall and the baffle plates, which is designated as the barrel/baffle channel. For V. C. Summer, flow travels upward through this region during normal operation which is referred to as an upflow barrel/baffle design.

Channels 10 through 13, combined, represent the total volume within the baffle plates, i.e., the entire core active fuel region for all 157 assemblies. Channel 10 includes assemblies on the periphery of the core which have relatively low power. [

]^{a,c}

]^{a,c} A map of the different structures

in the upper plenum is presented in Figure 26.2-7. There are six types of upper internals in the V. C. Summer upper plenum: guide tubes, open holes, orifice plates, support columns, free-standing flow mixers, and support columns with flow mixers. [

]^{a,c}

The gaps modeled in vessel section 3 are illustrated in Figure 26.2-4. The 144-inch active fuel length is divided into fourteen axial cells. The grids and their associated form losses are modeled within this length range at their specified elevations. [

# ]^{a,c}

[

Vessel Section 4 includes the vertical section of the vessel from the top of the active fuel to the bottom of the upper core plate. This section has one vertical cell and uses fourteen channels (designated 14 through 21 and 64 through 69) and thirteen horizontal flow gaps (17 through 23 and 64 through 69) to model this portion of the vessel. Figures 26.2-3 and 26.2-5 illustrate the vertical and radial representation of this section of the vessel model.

Section 4 of the model is referred to as the CCFL region, where CCFL is the acronym for counter-current flow limitation. [

Channels 14, 15, 16, 64, 65, 66, 67, 68, and 69 each represent one-ninth of the downcomer annulus volume between the vessel inner wall and the core barrel outer wall. [

WCAP-16996-NP

November 2010 Revision 0

]^{a,c}

]^{a,c} Channel 17 is modeled with no vertical flow path into or out of the top of the channel. The gaps within vessel Section 4 are illustrated in Figure 26.2-5.

Vessel Section 5 extends vertically from the bottom of the upper core plate to the inner bottom of the hot leg. This section contains two vertical cells for fifteen channels (designated 22 through 29, 51, and 70 through 75) and fourteen horizontal flow gaps (24 through 30, 45, and 70 through 75). Figures 26.2-3 and 26.2-5 provide an illustration of the vertical and radial representation of this section of the vessel model.

Channels 22, 23, 24, 70, 71, 72, 73, 74, and 75 each represent one-ninth of the downcomer annulus volume between the vessel inner wall and the core barrel outer wall. [

]^{a,c} There is no flow into the bottom of Channel 25 from vessel Section 4. Since these Channels (27, 28, and 29) are all surrounded by the inner global upper plenum Channel 25, this region constitutes another area where CCFL may be calculated. [

]^{a,c} Similar to Channel 25, there is no flow into the bottom of Channel 51 from vessel Section 4. Figure 26.2-5 defines the gaps for vessel Section 5.

Vessel Section 6 models the vertical section of the vessel from the bottom to the top of the hot leg (inner diameter). One vertical cell in sixteen channels (designated 30 through 39 and 76 through 81) and fourteen horizontal flow gaps (designated 31 through 38 and 76 through 81) are used to model this section. Figures 26.2-3 and 26.2-5 provide an illustration for the vertical and radial representation of this section of the vessel model.

Channels 30, 31, 32, 76, 77, 78, 79, 80, and 81 each represent one-ninth of the downcomer annulus volume between the vessel inner wall and the core barrel outer wall, excluding the volume of the hot leg which passes through this region. Note that the cold legs of the loop model connect to vessel downcomer Channels 30, 76, and 79. [

]^{a,c}

ſ

November 2010 Revision 0

٦^{a,c}

Gaps 36, 37, and 38 are added to model the radial flow into the hot leg channels from the outer global Channel 34. Channels 37, 38, and 39 complete vessel Section 6, modeling the hot leg nozzles and serving as an interface to the hot legs in the loop model.

Vessel Section 7 extends vertically from the top of the hot leg to the top of the upper support plate. The section is divided into two levels with the lower cell extending from the top of the hot legs to the bottom of the deep beam. This section contains two vertical cells for thirteen channels (designated 40 through 46 and 82 through 87) and eleven horizontal flow gaps (39 through 43 and 82 through 87). Figures 26.2-3 and 26.2-6 illustrate the vertical and radial representation of this section of the vessel model.

Channels 40, 41, 42, 82, 83, 84, 85, 86, and 87 each represent one-ninth of the downcomer annulus volume between the vessel inner wall and the core barrel outer wall. Channel 45 is a vertical extension of Channel 35 in vessel Section 6.

J^{a,c} and is a vertical extension of Channel 36 from vessel Section 6. Channel 43 is the inner global region and is a vertical extension of Channel 33 from vessel Section 6. Channel 44 is the outer global region and is a vertical extension of Channel 34 from vessel Section 6. There is no vertical flow connection between Channels 43, 44, and 45 to vessel Section 8 above. Channels 40 through 42 and 82 through 87, however, connect vertically to vessel Section 8 via the upper head spray nozzles. Guide tube Channel 46 also connects vertically to vessel Section 8 through the guide tube extension. The eleven gaps in vessel Section 7 are illustrated in Figure 26.2-6.

Vessel Section 8 extends vertically from the top of the upper support plate to the top of the upper guide tube. This section has one vertical cell for five channels (designated 47 through 49, 88, and 89) and six horizontal flow gaps (14 through 16, 44, 88, and 89). Figures 26.2-3 and 26.2-6 illustrate the vertical and radial representation of this section of the vessel model.

The boundary between outer Channels 47, 88, and 89 and inner Channel 48 is formed by the cylinder which intersects the inside of the upper head sphere at the top of the upper guide tube (Figure 26.2-3). Channels 47, 88, and 89 each include one-third of the volume in the upper head outside this boundary while Channel 48 models the volume inside this boundary, excluding the volume of the upper guide tubes. There is no flow into Channel 48 from below since the upper support plate prevents direct flow communication between the upper head and the upper plenum. Channel 49 models the volume inside of the upper guide tubes. There is no flow communication between the fluid inside the upper guide tube enclosure and Channel 48 in Section 8 of the vessel.

Vessel Section 9 models the vertical section of the vessel extending from the top of the upper guide tubes to the inside top of the vessel head. Similar to Section 1 of the vessel, vessel Section 9 is modeled as one channel (50) containing one vertical cell with no horizontal flow gaps (Figures 26.2-3 and 26.2-6). The flow area at the bottom of Channel 50 (vessel Section 9) is equal to the sum of the flow area at the top of Channels 48 and 49 from vessel Section 8.

Γ

#### 26.2.1.2 Core Model

Rod 1 represents the single hot rod, which has the highest power. It is located in the hot assembly (Channel 13) which is an assembly under a support column with a flow mixer. Rod 2 represents the remaining 263 fuel rods in the hot assembly and has a power equivalent to the hot assembly average fuel rods.

Rod 5 represents the 28 assemblies in the outer low powered region (Channel 10) and contains (28 assemblies) * (264 fuel rods/assembly) fuel rods. The fuel rods in the remaining 128 assemblies are divided up in proportion to the number of assemblies used in Channels 11 and 12 in the core. The guide tube channel contains (53 assemblies) * (264 fuel rods/assembly) fuel rods that are represented by fuel rod 3. The OH/SC/FSM channel contains (75 assemblies) * (264 fuel rods/assembly) fuel rods that are represented by fuel rods.

The nuclear fuel rods are initialized with internal gas properties, and fuel average temperatures from the Westinghouse Nuclear Fuel Business Unit's PAD code (Foster and Sidener, 2000).

]^{a,c}

ſ

#### 26.2.1.3 Loop Model

The V. C. Summer loop model is presented in Figure 26.2-8, with a more detailed noding for the steam generators shown in Figure 26.2-9. As with the vessel inputs, each component in the one-dimensional loop has various cells to allow for specific changes in geometry along the component. Each component is identified by a module title, a unique component number, and connections to numbered junctions. The three loops are defined using 37 components and 41 junctions. Components and junctions are indicated by rectangles and circles, respectively, in Figures 26.2-8 and 26.2-9.

ſ

]^{a,c}

Loop 1 is the loop which contains the pressurizer. Component 11 is the hot leg and was modeled with a TEE module. Component 19, the pressurizer (PRIZER module) is connected to the secondary branch of the hot leg TEE. The primary side of the steam generator is modeled as Component 12; with the secondary side consisting of several components. TEE Component 112 is the shell of the steam generator secondary side. The feedwater connection is modeled as TEE Component 113, and the downcomer of the steam generator is PIPE Component 114. The feedwater is injected through FILL Component 17, and the steam flows through TEE Component 118 and then exits via either the Main Steam Isolation Valve (VALVE Component 218 and BREAK Component 18) or the Main Steam Safety Valve (VALVE Component 318 and BREAK Component 418). Continuing around the loop are the crossover leg (PIPE Component 13) and reactor coolant pump (PUMP Component 14). The cold leg is next, divided into two TEE components in order to model safety injection (FILL Component 63) and accumulator injection (accumulator PIPE Component 15 is the pump-side cold leg safety injection TEE and Component 16 is the

vessel-side cold leg accumulator TEE. The accumulator line is modeled as a VALVE module (Component 61) which simulates the check valve. The accumulator tank itself (Component 62) is modeled with a PIPE component and an associated input which causes an accumulator module to be invoked.

The accumulators and pressurizer components have two junctions, although they only have a single communication path with the RCS. As such, zero FILL Components 119 and 162 are provided as boundary conditions for the junction not in communication with the RCS.

Loop 2 is set up much the same way, except that the hot leg (Component 21) is modeled as a PIPE module in the absence of the pressurizer and the SI and accumulator injection points are reversed based on the actual plant ECCS configuration. Loop 3 is modeled the same as Loop 2.

[

]^{a,c}

Finally, thimble bypass is modeled using three separate PIPE modules (loop Components 50-52) connected to the bottom cells of the low power, guide tube, and OH/SC/FSM core channels in vessel Section 3 and the corresponding CCFL channels in vessel Section 4.

#### 26.2.1.4 Emergency Core Cooling Safety Injection Model

The Safety Injection System (SIS) for V. C. Summer consists of three accumulator tanks, two charging/safety injection (SI) pumps and two low head Residual Heat Removal (RHR) pumps. Each pump is connected to injection lines which inject directly into each cold leg. The accumulators are modeled to inject at a nominal pressure, a nominal temperature, and a nominal water volume. The pumped safety injection flow is modeled assuming a nominal temperature and the loss of one train of safety injection pumps (one SI and one RHR). The loss of one train of safety injection is considered as the limiting single failure assumption.

]^{a,c}

26-16

ſ

# 26.2.2 V. C. Summer Reference Case and Allowable Plant Operating Conditions

The best-estimate methodology establishes a sampling of the distribution of potential uncertainty contributors which occur due to changes in plant or model variables (Section 29). The following paragraphs describe the assumptions in the key LOCA parameters for V. C. Summer.

The reference case input values for V. C. Summer are listed in Table 26.2-1. The input values fall under three categories: 1) plant physical description, 2) plant initial operating conditions, and 3) accident boundary conditions. The values used for the reference case for each of these parameters are discussed in the following subsections.

For most of the parameters, the nominal value is assumed for the reference case. For others, a bounding or conservative value is assumed. The uncertainty associated with these parameters is accounted for in the uncertainty analysis, as shown in Section 31.

]^{a,c}

26.2.2.1 Plant Physical Description

ſ

## 26.2.2.2 Plant Initial Operating Conditions - Reactor Power

- 1. **Initial Core Average Linear Heat Rate** The core power assumed for the reference case is 100 percent of the power level (2900 MWt).
- 2. Hot Rod Peak Linear Heat Rate The total peaking factor (FQ) for the reference case is set to  $[ ]^{a,c}$ .
- 3. Hot Rod Average Linear Heat Rate  $(\mathbf{F}_{\Delta H})$  In the reference case,  $\mathbf{F}_{\Delta H}$  is set to [
- 4. **Hot Assembly Average Linear Heat Rate** The minimum difference between the power generated in the hot rod and that in the hot assembly average rod is conservatively assumed. The hot assembly average rod is assumed to be [ ]^{a,c} lower in power than the hot rod.
- 5. Hot Assembly Peak Linear Heat Rate Consistent with the average linear heat rates, the peaking factor used to calculate the peak linear heat rate generated in the hot assembly average rod is [ ]^{a,c} lower than the value assumed in the hot rod.
- Axial Power Distribution The power distribution represented by the power shape assumed for the reference case is presented in Figure 26.2-10. This power shape corresponds to
  - ]^{a,c}.
- 7. Low-Power Region (PLOW) Current and expected core designs for V. C. Summer result in a range of PLOW from [

]^{a,c} is

selected as the value for the reference case.

- 8. **Burnup** The burnup is selected from the time-in-cycle, which is a sampled attribute within the uncertainty analysis. For the reference case, a nominal cycle burnup equal to [  $]^{a,c}$  is assumed.
- 9. **Prior Operating History** The power distribution assumed to exist at the time of the LOCA is conservatively assumed to have existed since plant startup when determining fission product inventories.
- 10. **Moderator Temperature Coefficient (MTC)** The maximum value specified in the Technical Specifications for hot full power is assumed, to conservatively estimate core reactivity and fission power.
- 11. Hot Full-Power (HFP) Boron Concentration A value typical of those used in current cores is assumed.

## 26.2.2.3 Plant Initial Operating Conditions - Fluid Conditions

- Average Fluid Temperature (T_{avg}) The nominal value during normal full-power operation of 572.0°F is used for V. C. Summer.
- 2. **RCS Pressure** The nominal value (2250 psia) is assumed for the V. C. Summer reference case.

3. **Loop Flowrate** – [ ]^{a,c} loop flow is assumed for the reference case.

- 4. Upper Head Temperature  $(T_{UH})$  The appropriate best estimate value of  $T_{UH}$  is assumed.
- 5. **Pressurizer Level** The nominal value of pressurizer level is assumed.
- 6. Accumulator Water Temperature A nominal (midpoint) value within the range established for V. C. Summer is assumed.

7. Accumulator Pressure – A nominal (midpoint) value of accumulator pressure is assumed.

- 8. Accumulator Water Volume A nominal (midpoint) value of accumulator water volume is assumed.
- 9. Accumulator Line Resistance A best-estimate value of accumulator line resistance is assumed.
- 10. Accumulator Boron Concentration The Technical Specification minimum value is assumed.

## 26.2.2.4 Accident Boundary Conditions

1. Break Location – [

 $]^{a,c}$ 

]^{a,c}

- 6. Safety Injection Temperature Nominal (midpoint) values are assumed.
- 7. **Safety Injection Delay** Maximum values consistent with the offsite-power assumption (offsite power available) are used.
- 8. **Containment Pressure** A conservatively low value as calculated by <u>WCOBRA/TRAC-TF2</u> is assumed.

9. Single-Failure Assumption – [

## 26.2.3 Plant Operating Range

The [ ]^{a,c} developed by the best-estimate methodology are valid for a range of plant operating conditions. Several parameters in the reference calculation are at nominal values. The range of variation of the operating parameters is accounted for in the uncertainty analysis. This is accomplished by assuring that, in the sampling of the attributes for each run (Section 31), [

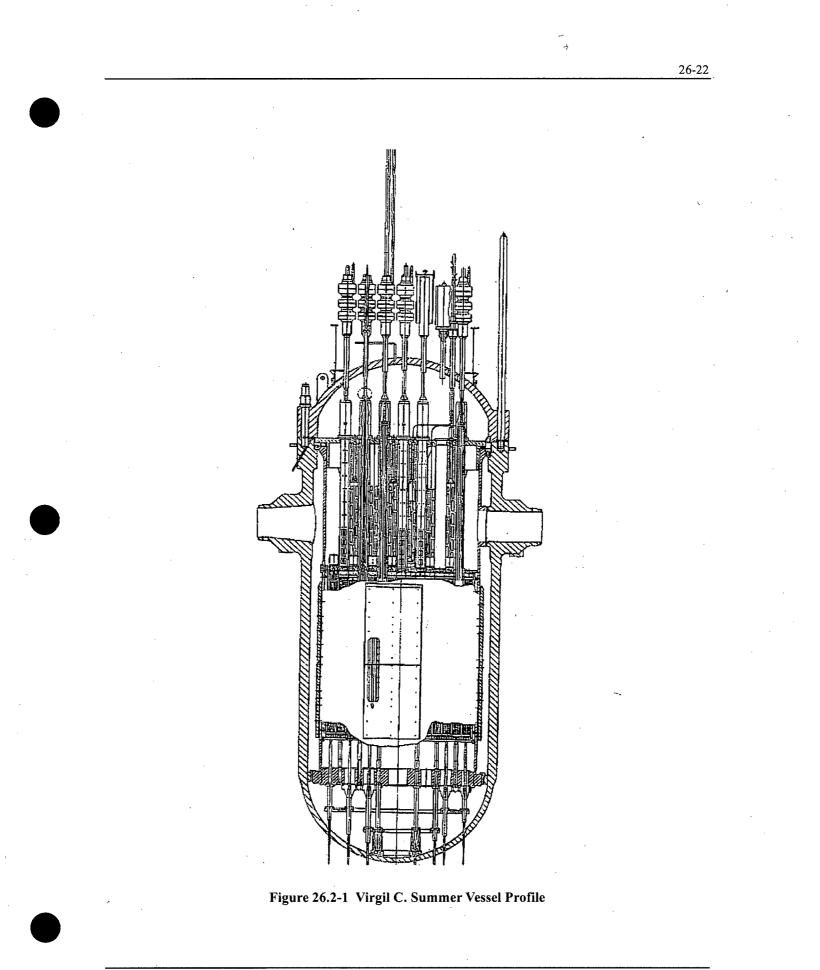
]^{a,c}. Westinghouse has processes in place with the utilities to ensure that the analyzed ranges bound the plant operation.

<b>Fable 26.2-1</b>	Key LOCA Paran	neters and Scoping	s Study Values	for V. C. Summer	, 	
					· · ·	
	. <u></u>			, ,		
	· · ·			•		
		· · · ·		<u>.</u>		
				<u> </u>		
·				,		
				· · ·		
	-	· · · · · · · · · · · · · · · · · · ·				
		<u> </u>		<u> </u>		
	······					
,						
			•			
	-					-

WCAP-16996-NP

November 2010 Revision 0

26-21



WCAP-16996-NP

November 2010 Revision 0

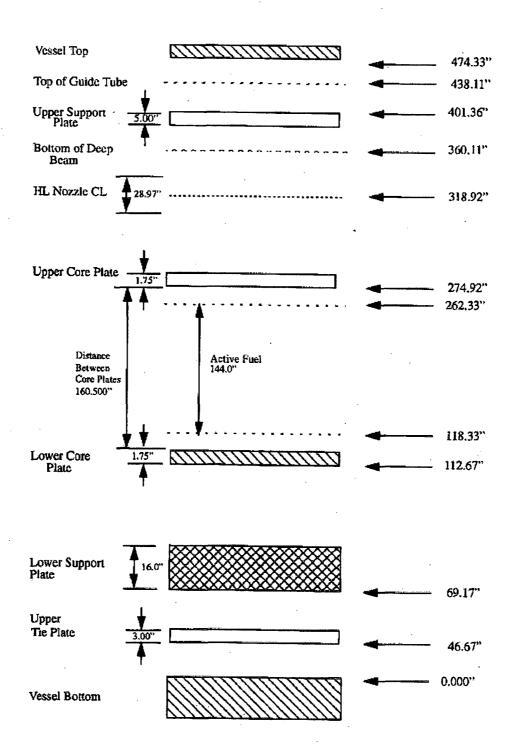
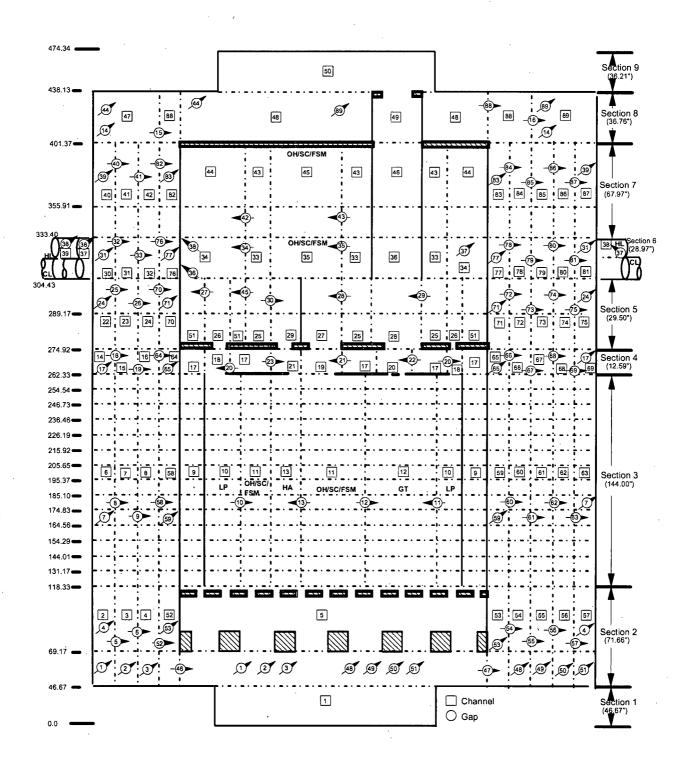
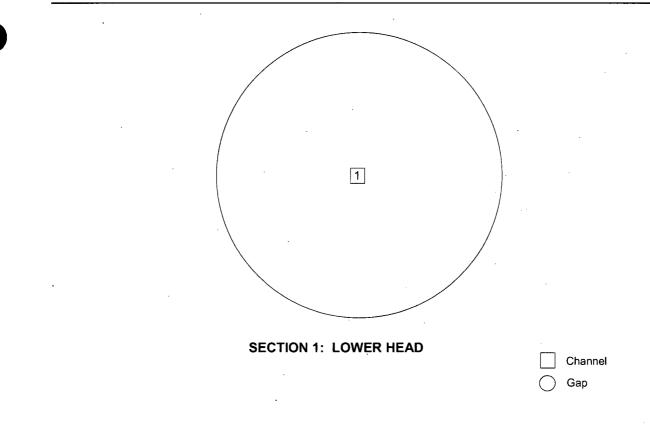


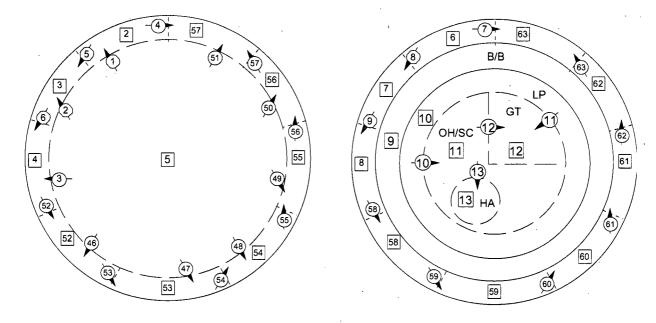
Figure 26.2-2 Virgil C. Summer Vessel Component Elevations

26-23



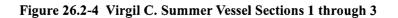
# Figure 26.2-3 Virgil C. Summer Vessel Model Noding Diagram





SECTION 2: LOWER PLENUM

SECTION 3: CORE REGION



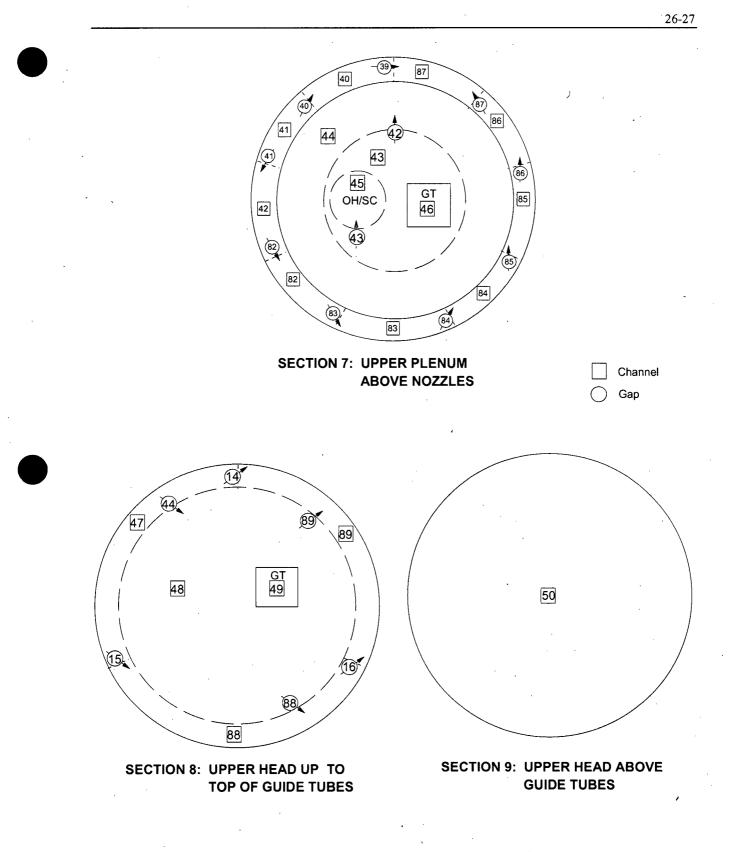
26-26

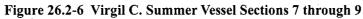
a,c

Figure 26.2-5 Virgil C. Summer Vessel Sections 4 through 6

WCAP-16996-NP

November 2010 Revision 0





WCAP-16996-NP

November 2010 Revision 0

OH OH FSM ОН SCM GT SCM GT ОН GT 2 SCM ÓН FSM GT SCM GT FSM PGT SCM 3 SCM GT SC GT OH GT OH GT OH GT FSM 4 OН PGT SCM OP SCM FSM ОН FSM ОН GT SCM OH GT 5 GT FSM GT SCM GT OH FSM GT SC GT OH GT GΤ 6 FSM SCM GT ОН OН OH GT SC GT OH OP OH GT SC OH 7 SC SCM SCM GT GT OH GT SCM GT SCM GT GT GT SCM FSM 8 ОН SC FSM OP ОН GT SCM GT FSM ОН ОН GT SC ОН GT 9 GT FSM GT SC GT FSM GT ОН GT SCM GT OH GT 10 ОН ОН FSM GT SCM ОН SCM OP SCM GT ОН PGT OH 11 sc FSM FSM ОН GT FSM GT SCM GT GT GT 12 SC PGT GT FSM ОН sc OH GT SCM 13 FSM SC GT FSM GT GT SC 14 ОН FSM FSM 15 GT - Guide Tube (53) PGT - Plugged Guide Tube (4) OH - Open Hole (37) OP - Orifice Plate (4) FSM - Free-Standing Mixer (23) SC – Support Column (13)

Figure 26.2-7 Virgil C. Summer Upper, Plenum Structure Map

Total = 157

SCM - Support Column w/ Mixer (23)

- Low Power Assemblies (LP)

WCAP-16996-NP

R

1

Μ

L

Ν

κ

J

н

G

F

Е

D

С

в

А

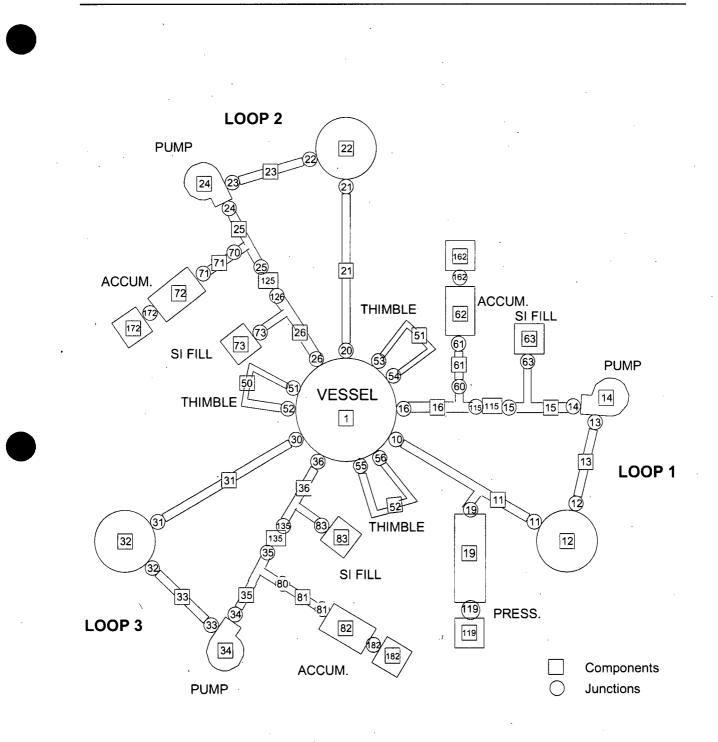


Figure 26.2-8 Virgil C. Summer Loop Model Noding Diagram

WCAP-16996-NP

November 2010 Revision 0

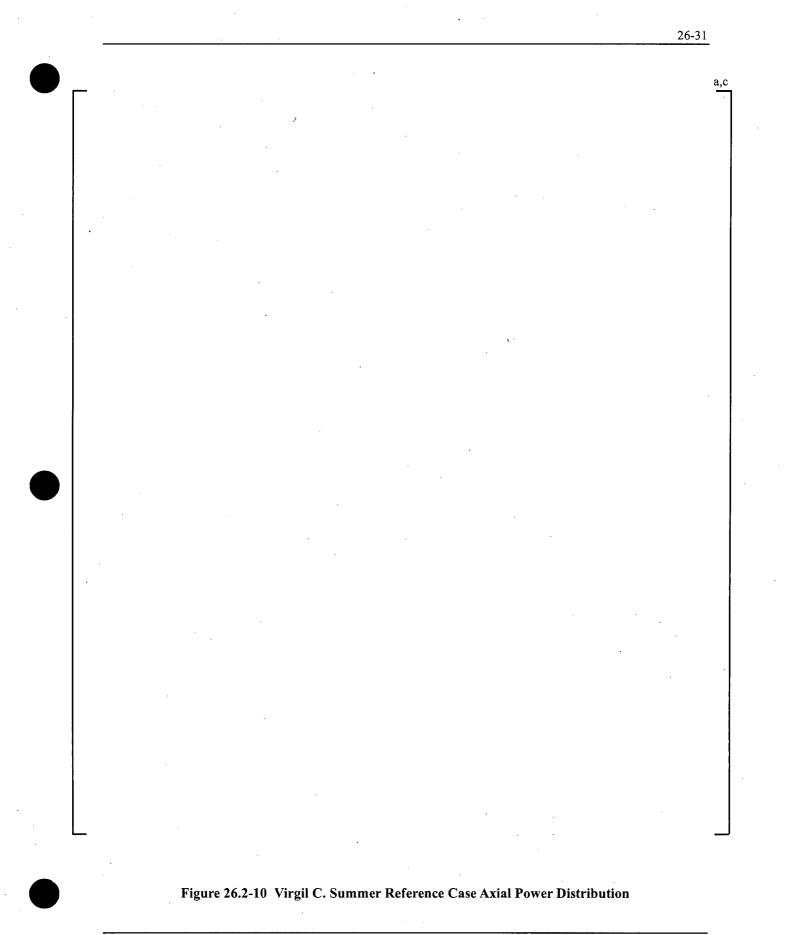
£

MSIV BREAK MSIV BREAK MSIV BREAK 18 28 38 418 428 438 X Æ 218 228 238 X MSSV BREAK MSSV BREAK MSSV BREAK 318 (228 328 218 338 (238 118 518 418 128 328 X 528 428 138 M 438 318 <u>]</u> (338) 538 (28 38 112 122 132 (113) (123) (133) FILL FIL 113 17 17 123 27 27 133 37 37 (124) (114) (134) 114 124 134 12 22 32 112 122 132 22) 32) 12 (2 LOOP 1 SG LOOP 2 SG LOOP 3 SG

Figure 26.2-9 Virgil C. Summer Steam Generator Component Noding Diagram

WCAP-16996-NP

November 2010 Revision 0



# 26.3 BEAVER VALLEY UNIT 1 NUCLEAR POWER PLANT

Beaver Valley Unit 1 is a three-loop plant containing Westinghouse 17x17 Robust Fuel Assembly (RFA-2) fuel with IFMs and ZIRLO[®] cladding. The nominal core power for this plant is 2,900 MWt. Beaver Valley Unit 1 also has Westinghouse 54F replacement steam generators.

# 26.3.1 Beaver Valley Unit 1 WCOBRA/TRAC-TF2 Nodalization

The vessel geometry as modeled in <u>WCOBRA/TRAC-TF2</u> is described in Section 26.3.1.1; while a description of the core modeling is provided in Section 26.3.1.2, the loop geometry is described in Section 26.3.1.3 and the ECCS modeling is detailed in Section 26.3.1.4.

## 26.3.1.1 Vessel Model

Figure 26.3-1 shows the vessel drawing for the Beaver Valley Unit 1 three-loop PWR. Figure 26.3-2 shows the vessel major internal component elevation layout. The elevations shown on the right are relative to the inside bottom of the vessel. This elevation layout contains most of the information needed to divide the vessel into nine vertical sections. These sections are described in turn starting at the bottom of the vessel.

The bottom of vessel Section 1 is the inside vessel bottom. The bottom of vessel Section 2 is the bottom of the upper tie plate. The bottom of vessel Section 3 is defined as the beginning of the active fuel. The bottom of vessel Section 4 is the top of the active fuel. The bottom of vessel Section 5 is the elevation at the bottom of the upper core plate. The bottom of vessel Section 6 is equal to the elevation of the bottom of the hot leg inner wall. The bottom of vessel Section 7 is the elevation of the hot leg. The bottom of vessel Section 8 is the elevation at the top of the upper support plate. The bottom of vessel Section 9 is the elevation at the top of the upper guide tube in the upper head. The top of vessel Section 9 is the inside top of the vessel upper head.

After defining the elevations for each section, a noding scheme is defined following the same basic philosophy applied to the Separate Effects Test (SET) and Integral Effects Test (IET) facilities are described in Section 26.1.1.

]^{a,c}

Figures 26.3-3 through 26.3-12 illustrate the Beaver Valley Unit 1 vessel noding. Figure 26.3-3 is a vertical section noding diagram. Figures 26.3-4 through 26.3-12 are the horizontal "plan" views of each section. In these figures, the numbers within the squares are the channel numbers and the numbers within the circles with arrows attached to them are the gap numbers. A gap is used to define a horizontal flow path between channels. Positive flow is in the direction indicated by the arrow. It is assumed within <u>WCOBRA/TRAC-TF2</u> that a vertical flow path for vertically stacked channels exists unless specified otherwise in the input. Upward axial flow is considered as positive flow.

As can be seen in Figures 26.3-3 through 26.3-12, 89 channels and 89 gaps are used for Beaver Valley Unit 1 to define the vessel. It can be seen in Figure 26.3-3 that several of the nine vertical sections are sub-divided into two or more levels. For example, the active fuel region, vessel Section 3, is divided into

14 vertical levels. By accounting for the vertical sub-division within vessel Sections 2, 3, 5 and 7, the vessel model for Beaver Valley Unit 1 has a total of 309 fluid cells.

Vessel Section 1 models the vertical section of the vessel from the inside bottom of the vessel to the bottom of the upper tie plate. The modeling of this section is relatively simple since there is one channel with one vertical cell and no horizontal flow gaps (Figures 26.3-3 and 26.3-4). Channel 1 completely represents Section 1 of the vessel. The top flow area of this channel/section was computed based on the net flow area at the top of the tie plate.

Vessel Section 2 models the vertical section of the vessel from the bottom of the upper tie plate to the bottom of the active fuel region. This section contains two vertical cells for ten channels (designated 2 through 5 and 52 through 57) and horizontal flow gaps (numbered 1 through 6 and 46 through 57). Figures 26.3-3 and 26.3-5 provide an illustration for the vertical and radial representation of this section of the vessel model.

Channels 2, 3, 4, 52, 53, 54, 55, 56, and 57 each represent one-ninth of the annulus volume between the vessel inner wall and the core barrel outer wall, and are connected by Gaps 4 through 6 and 52 through 57. Channel 5 is the lower plenum volume between the upper tie plate and the fuel nozzle elevation. [ ]^{a,c} The area at the top of Channel 5 is equal to the sum of the areas modeled at the bottom of Channels 9 through 13 in vessel Section 3. Area variation inputs are used to vary the flow area between the lower and upper cells of Channel 5 to account for the change in flow area within this channel due to the lower support plate. The radial flow gaps modeled in vessel Section 2 are illustrated in Figure 26.3-5 with positive flow in the direction indicated in the figure. Gaps 1, 2, 3, 46, 47, 48, 49, 50, and 51 model a radial flow gap in the lower cell of vessel Section 2, with the core barrel extension blocking radial flow from the upper cell of the downcomer channels into the upper cell of lower plenum Channel 5.

Vessel Section 3 models the vertical section of the vessel from the bottom to the top of the active fuel region. The modeling is accomplished using fourteen vertical cells in fourteen channels (designated 6 through 13 and 58 through 63) and thirteen horizontal flow gaps (designated 7 through 13 and 58 through 63). Figures 26.3-3 and 26.3-6 provide an illustration for the vertical and radial representation of this section of the vessel model.

Channels 6 through 8 and 58 through 63 each represent one-ninth of the downcomer annulus volume between the vessel inner wall and the core barrel outer wall. Thermal shield is modeled in this section. Channel 9 is the volume between the core barrel inner wall and the baffle plates, which is designated as the barrel/baffle channel. For Beaver Valley Unit 1, flow travels upward through this region during normal operation which is referred to as an upflow barrel/baffle design.

Channels 10 through 13, combined, represent the total volume within the baffle plates, i.e., the entire core active fuel region for all 157 assemblies. Channel 10 includes assemblies on the periphery of the core which have relatively low power. [

]^{a,c} There are five types of upper internals in the Beaver Valley Unit 1 upper plenum: guide tubes, orifice holes, support columns, free-standing flow mixers, and support columns with flow mixers. The locations of these structures in the upper plenum are

26-34

presented in Figure 26.3-13.

]^{a,c}

The gaps modeled in vessel Section 3 are illustrated in Figure 26.3-6. The 144-inch active fuel length is divided into fourteen axial cells. The grids and their associated form losses are modeled within this length range at their specified elevations. [

]^{a,c}

Vessel Section 4 includes the vertical section of the vessel from the top of the active fuel to the bottom of the upper core plate. This section has one vertical cell and uses fourteen channels (designated 14 through 21 and 64 through 69) and thirteen horizontal flow gaps (17 through 23 and 64 through 69) to model this portion of the vessel. Figures 26.3-3 and 26.3-7 illustrate the vertical and radial representation of this section of the vessel model.

Section 4 of the model is referred to as the CCFL region, where CCFL is the acronym for counter-current flow limitation.

]^{a,c}

Channels 14, 15, 16, 64, 65, 66, 67, 68, and 69 each represent one-ninth of the downcomer annulus volume between the vessel inner wall and the core barrel outer wall. [

]^{a,c}

]^{a,c} Channel 17 is modeled with no vertical flow path into or out of the top of the channel. The gaps within section 4 are illustrated in Figure 26.3-5.

Vessel Section 5 extends vertically from the bottom of the upper core plate to the inside bottom of the hot leg. This section contains two vertical cells for fifteen channels (designated 22 through 29, 51, and 70 through 75) and fourteen horizontal flow gaps (24 through 30, 45, and 70 through 75). Figures 26.3-3 and 26.3-8 provide an illustration of the vertical and radial representation of this section of the vessel model.

Channels 22, 23, 24, 70, 71, 72, 73, 74, and 75 each represent one-ninth of the downcomer annulus volume between the vessel inner wall and the core barrel outer wall. [

]^{a,c} There is no flow into the bottom of

]^{a,c} Similar to Channel 25,

Channel 25 from vessel Section 4. Since these Channels (27, 28, and 29) are all surrounded by the inner global upper plenum Channel 25, this region constitutes another area where CCFL may be calculated.

there is no flow into the bottom of Channel 51 from vessel Section 4. Figure 26.3-8 defines the gaps for vessel Section 5.

Vessel Section 6 models the vertical section of the vessel from the bottom to the top of the hot leg (inner diameter). One vertical cell in sixteen channels (designated 30 through 39 and 76 through 81) and fourteen horizontal flow gaps (designated 31 through 38 and 76 through 81) are used to model this section. Figures 26.3-3 and 26.3-9 provide an illustration for the vertical and radial representation of this section of the vessel model.

Channels 30, 31, 32, 76, 77, 78, 79, 80, and 81 each represent one-ninth of the downcomer annulus volume between the vessel inner wall and the core barrel outer wall, excluding the volume of the hot leg which passes through this region. Note that the cold legs of the loop model connect to vessel downcomer Channels 30, 76, and 79.

]^{a,c} Gaps 36, 37,

and 38 are added to model the radial flow into the hot leg channels from the outer global Channel 34. Channels 37, 38, and 39 complete vessel Section 6, modeling the hot leg nozzles and serving as an interface to the hot legs in the loop model.

WCAP-16996-NP

ſ

November 2010 Revision 0 Vessel Section 7 extends vertically from the inside top of the hot leg to the top of the upper support plate. The section is divided into two levels with the lower cell extending from the inside top of the hot legs to the bottom of the deep beam. This section contains two vertical cells for thirteen channels (designated 40 through 46 and 82 through 87) and eleven horizontal flow gaps (39 through 43 and 82 through 87). Figures 26.3-3 and 26.3-10 illustrate the vertical and radial representation of this section of the vessel model.

Channels 40, 41, 42, 82, 83, 84, 85, 86, and 87 each represent one-ninth of the downcomer annulus volume between the vessel inner wall and the core barrel outer wall. Channel 45 is a vertical extension of Channel 35 in vessel Section 6. [

]^{a,c} and is a vertical extension of Channel 36 from vessel Section 6. Channel 43 is the inner global region and is a vertical extension of Channel 33 from vessel Section 6. Channel 44 is the outer global region and is a vertical extension of Channel 34 from vessel Section 6. There is no vertical flow connection between Channels 43, 44, and 45 to vessel Section 8 above. Channels 40 through 42 and 82 through 87, however, connect vertically to vessel Section 8 via the upper head spray nozzles. Guide tube Channel 46 also connects vertically to vessel Section 8 through the guide tube extension. The eleven gaps in vessel Section 7 are illustrated in Figure 26.3-10.

Vessel Section 8 extends vertically from the top of the upper support plate to the top of the upper guide tube. This section has one vertical cell for five channels (designated 47 through 49, 88, and 89) and six horizontal flow gaps (14 through 16, 44, 88, and 89). Figures 26.3-3 and 26.3-11 illustrate the vertical and radial representation of this section of the vessel model.

The boundary between outer Channels 47, 88, and 89 and inner Channel 48 is formed by the cylinder which intersects the inside of the upper head sphere at the top of the upper guide tube (Figure 26.3-1). Channels 47, 88, and 89 each include one-third of the volume in the upper head outside this boundary while Channel 48 models the volume inside this boundary, excluding the volume of the upper guide tubes. There is no flow into Channel 48 from below since the upper support plate prevents direct flow communication between the upper head and the upper plenum. Channel 49 models the volume inside of the upper guide tubes. There is no flow communication between the fluid inside the upper guide tube enclosure and Channel 48 in Section 8 of the vessel.

Vessel Section 9 models the vertical section of the vessel extending from the top of the upper guide tubes to the inside top of the vessel head. Similar to Section 1 of the vessel, vessel Section 9 is modeled as one channel (50) containing one vertical cell with no horizontal flow gaps (Figures 26.3-3 and 26.3-12). The flow area at the bottom of Channel 50 (vessel Section 9) is equal to the sum of the flow area at the top of Channels 48 and 49 from vessel Section 8.

#### 26.3.1.2 Core Model

Rod 1 represents the single hot rod, which has the highest power. It is located in the hot assembly (Channel 13) which is an assembly under a support column with a flow mixer. Rod 2 represents the remaining 263 fuel rods in the hot assembly and has a power equivalent to the hot assembly average fuel rods.

Rod 5 represents the 28 assemblies in the outer low powered region (Channel 10) and contains (28 assemblies) * (264 fuel rods/assembly) fuel rods. The fuel rods in the remaining 128 assemblies are divided up in proportion to the number of assemblies used in Channels 11 and 12 in the core. The guide tubes contain (53 assemblies) * (264 fuel rods/assembly) fuel rods that are represented by fuel rod 3. The SC/OH/FM channel contains (75 assemblies) * (264 fuel rods/assembly) fuel rods that are represented by fuel rod 4.

The nuclear fuel rods are initialized with internal gas properties, and fuel average temperatures from the Westinghouse Nuclear Fuel Business Unit's PAD code (Foster and Sidener, 2000).

26.3.1.3 Loop Model

]^{a,c}

The Beaver Valley Unit 1 loop model is represented by Figures 26.3-14 and 26.3-15. As with the vessel inputs, each component in the one-dimensional loop has various cells to allow for specific changes in geometry along the component. Each component is identified by a module title, a unique component number, and connections to numbered junctions. The three loops are defined using 37 components and 41 junctions. Components and junctions are indicated by rectangles and circles, respectively, in Figures 26.3-14 and 26.3-15.

# [

ſ

Loop 2 is the loop which contains the pressurizer. Component 21 is the hot leg and was modeled with a TEE module. Component 29, the pressurizer (PRIZER module) is connected to the secondary branch of the hot leg TEE. The primary side of the steam generator is modeled as Component 22; with the secondary side consisting of several components. TEE Component 122 is the shell of the steam generator secondary side. The feedwater connection is modeled as TEE Component 123, and the downcomer of the steam generator is PIPE Component 124. The feedwater is injected through FILL Component 27, and the steam flows through TEE Component 128 and then exits via either the Main Steam Isolation Valve (VALVE Component 228 and BREAK Component 28) or the Main Steam Safety Valve (VALVE Component 328 and BREAK Component 428). Continuing around the loop are the crossover leg (PIPE Component 23) and reactor coolant pump (PUMP Component 24). The Loop 2 cold leg is next, divided into two TEE components in order to model safety injection (FILL Component 73) and accumulator injection (accumulator PIPE component 72). Component 25 is the pump-side cold leg safety injection TEE and Component 26 is the vessel-side cold leg accumulator TEE. The accumulator line is modeled as a VALVE module (Component 71) which simulates the check valve. The accumulator tank itself (Component 72) is modeled with a PIPE component and an associated input which causes an accumulator module to be invoked.

]^{a,c}

The accumulators and pressurizer components have two junctions, although they only have a single communication path with the RCS. As such, zero FILL Components 129 and 172 are provided as boundary conditions for the junction not in communication with the RCS.

Loop 1 is set up much the same way except that the hot leg (Component 11) is modeled as a PIPE module in the absence of the pressurizer. Loop 3 is modeled the same as Loop 1.

6 are used to model containment conditions for the transient (depending on the break type, either one or both of the components are required). [

Finally, thimble bypass is modeled using three separate PIPE modules (loop Components 50-52) connected to the bottom cells of the low power, guide tube, and SC/OH/FM core channels in vessel Section 3 and the corresponding CCFL channels in vessel Section 4.

#### 26.3.1.4 Emergency Core Cooling Safety Injection Model

]^{a,c}

The Safety Injection System (SIS) for Beaver Valley Unit 1 consists of three accumulator tanks, two charging/safety injection (SI) pumps and two low head RHR pumps. Each pump is connected to injection lines which inject directly into each cold leg. The accumulators are modeled to inject at a nominal pressure, a nominal temperature, and a nominal water volume. The pumped safety injection flow is modeled assuming a nominal temperature and the loss of one train of safety injection pumps (one SI and one RHR). The loss of one train of safety injection is considered as the limiting single failure assumption.

# ]^{a,c}

#### 26.3.2 Beaver Valley Unit 1 Reference Case and Allowable Plant Operating Conditions

The best-estimate methodology establishes a sampling of the distribution of potential uncertainty contributors which occur due to changes in plant or model variables (Section 29). The following paragraphs describe the assumptions in the key LOCA parameters for Beaver Valley Unit 1.

WCAP-16996-NP

ſ

[

]^{a,c} BREAK Component(s) 4 and/or

The reference case input values for Beaver Valley Unit 1 are listed in Table 26.3-1. The input values fall under three categories: 1) plant physical description, 2) plant initial operating conditions, and 3) accident boundary conditions. The values used for the reference case for each of these parameters are discussed in the following subsections.

For most of the parameters, the nominal value is assumed for the reference case. For others, a bounding or conservative value is assumed. The uncertainty associated with these parameters is accounted for in the uncertainty analysis, as shown in Section 31.

26.3.2.1 Plant Physical Description

I

#### 26-39

# 26.3.2.2 Plant Initial Operating Conditions – Reactor Power

1. **Initial Core Average Linear Heat Rate** – The core power assumed for the reference case is 100 percent of an uprated power level (2900 MWt).

]^{a,c}

2. Hot Rod Peak Linear Heat Rate – The total peaking factor (FQ) for the reference case is set to [ ]^{a,c}.

l^{a,c} is

- 3. Hot Rod Average Linear Heat Rate  $(\mathbf{F}_{\Delta H})$  In the reference case,  $\mathbf{F}_{\Delta H}$  is set to [
- 4. **Hot Assembly Average Linear Heat Rate** The minimum difference between the power generated in the hot rod and that in the hot assembly average rod is conservatively assumed. The hot assembly average rod is assumed to be [ ]^{a,c} lower in power than the hot rod.
- 5. Hot Assembly Peak Linear Heat Rate Consistent with the average linear heat rates, the peaking factor used to calculate the peak linear heat rate generated in the hot assembly average rod is [ ]^{a,c} lower than the value assumed in the hot rod.
- Axial Power Distribution The power distribution represented by power shape assumed for the reference case is presented in Figure 26.3-16, and corresponds to [
- 7. Low-Power Region (PLOW) Current and expected core designs for Beaver Valley Unit 1 result in a range of PLOW from [

selected as the value for the reference case.

- 8. **Burnup** The burnup is selected from the time-in-cycle, which is a sampled attribute within the uncertainty analysis. For the reference case, a nominal cycle burnup equal to [ ]^{a,c} is assumed.
- 9. **Prior Operating History** The power distribution assumed to exist at the time of the LOCA is conservatively assumed to have existed since plant startup when determining fission product inventories.
- 10. **Moderator Temperature Coefficient (MTC)** The maximum value specified in the Technical Specifications for hot full power is assumed, to conservatively estimate core reactivity and fission power.
- 11. Hot Full-Power (HFP) Boron Concentration A value typical of those used in current cores is assumed.

#### 26.3.2.3 Plant Initial Operating Conditions – Fluid Conditions

- 1. Average Fluid Temperature  $(T_{avg}) [$  $]^{a,c}$  is used for Beaver Valley Unit 1.
- 2. **RCS Pressure** The nominal value (2250 psia) is assumed for the Beaver Valley Unit 1 reference case.
- 3. **Loop Flowrate** [ ]^{a,c} loop flow is assumed for the reference case.
- 4. Upper Head Temperature  $(T_{UH})$  The appropriate best estimate value of  $T_{UH}$  is assumed.

5. **Pressurizer Level** – The nominal value of pressurizer level is assumed.

6. Accumulator Water Temperature – A nominal (midpoint) value within the range established for Beaver Valley Unit 1 is assumed.

7. Accumulator Pressure – A nominal (midpoint) value of accumulator pressure is assumed.

8. Accumulator Water Volume – A nominal (midpoint) value of accumulator water volume is assumed.

9. Accumulator Line Resistance – A best-estimate value of accumulator line resistance is assumed.

10. Accumulator Boron Concentration – The Technical Specification minimum value is assumed.

26.3.2.4 Accident Boundary Conditions

1. Break Location – [

]^{a,c}

6. Safety Injection Temperature – Nominal (midpoint) values are assumed.

- 7. **Safety Injection Delay** Maximum values consistent with the offsite-power assumption (offsite power available) are used.
- 8. **Containment Pressure** A conservatively low value was calculated by <u>WCOBRA/TRAC-TF2</u> for the reference case.

### Single-Failure Assumption – [

9.

#### **26.3.3 Plant Operating Range**

The [ ]^{a,c} developed by the best-estimate methodology are valid for a range of plant operating conditions. Several parameters in the reference calculation are at nominal values. The range of variation of the operating parameters is accounted for in the uncertainty analysis. This is accomplished by assuring that, in the sampling of the attributes for each run [

]^{a,c}

]^{a,c}. (as demonstrated in Section 31 for V. C. Summer). Westinghouse has processes in place with the utilities to ensure that the analyzed ranges bound the plant operation.

Table 26.3-1	Key LOCA Parameters and Scoping Stu	dy Values for Beaver Valley Unit 1
		· · · ·
	·	
	· · · ·	· .
		<u> </u>
	· · · · · · · · · · · · · · · · · · ·	
		· · ·
	·	
	······································	· · ·
·		
		·
	· · · · · · · · · · · · · · · · · · ·	
		······································
	· · · · · · · · · · · · · · · · · · ·	· · · · · · · · · · · · · · · · · · ·
		· · · · ·
	· · · · · · · · · · · · · · · · · · ·	· · ·
		· · · · · · · · · · · · · · · · · · ·
		·

WCAP-16996-NP

26-43

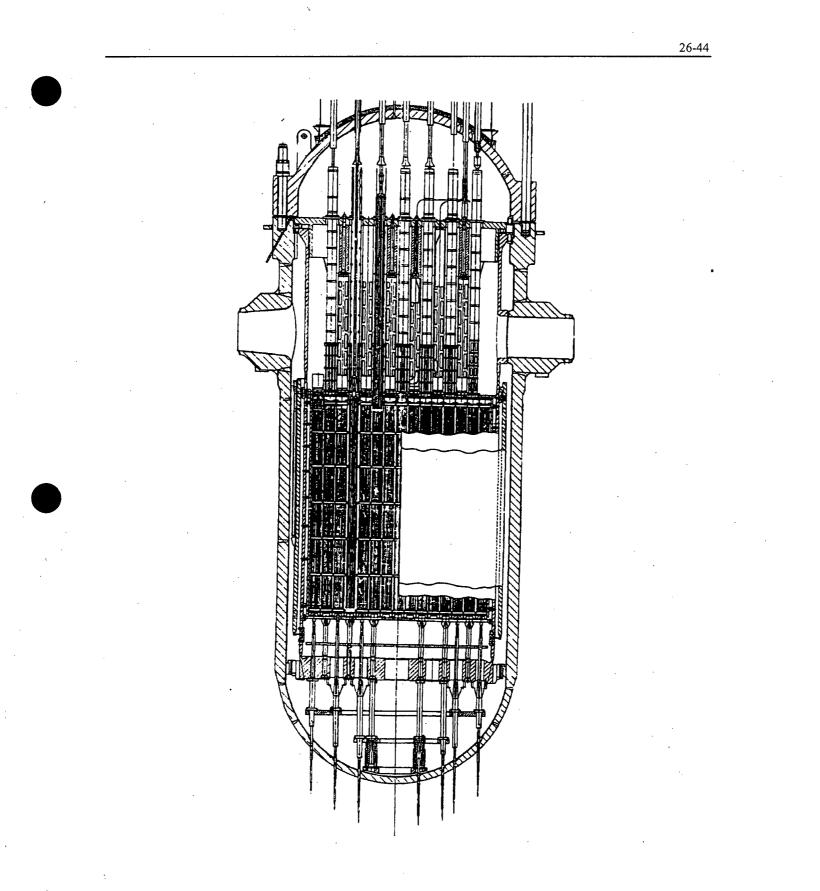
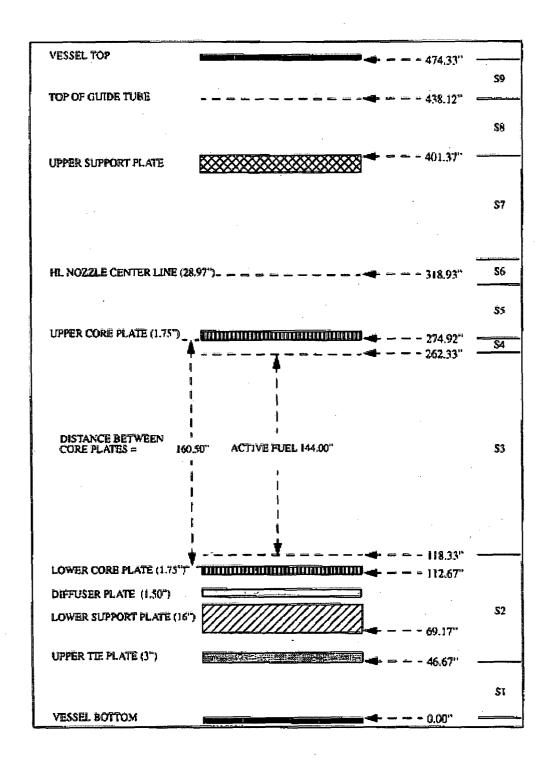


Figure 26.3-1 Beaver Valley Unit 1 Vessel Profile

WCAP-16996-NP



# Figure 26.3-2 Beaver Valley Unit 1 Vessel Component Elevations

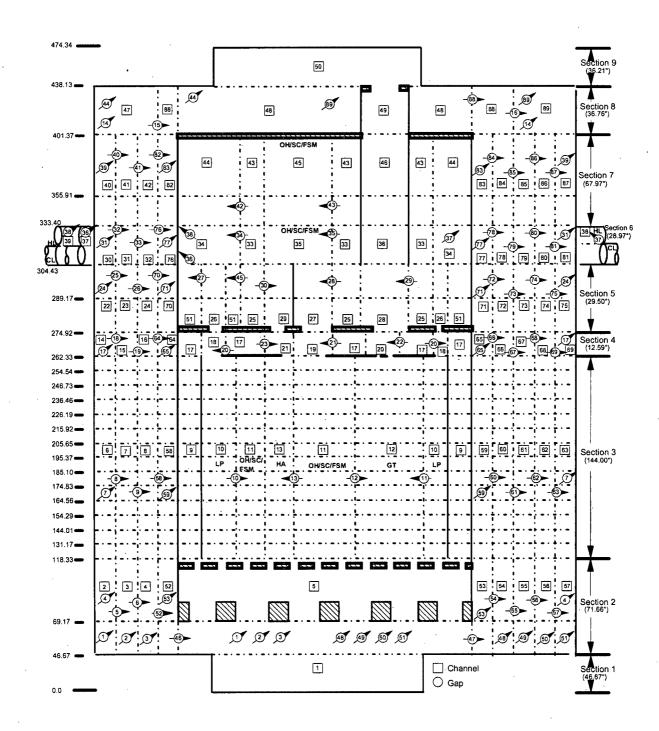
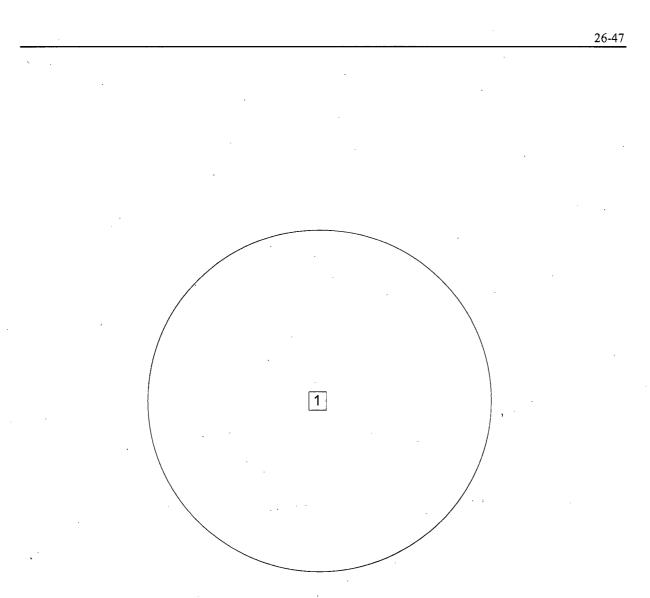


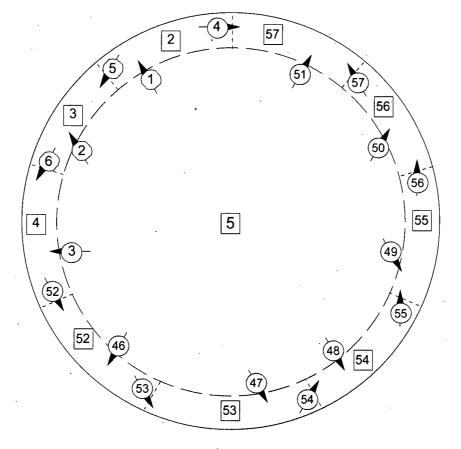
Figure 26.3-3 Beaver Valley Unit 1 Vessel Model Noding Diagram

WCAP-16996-NP

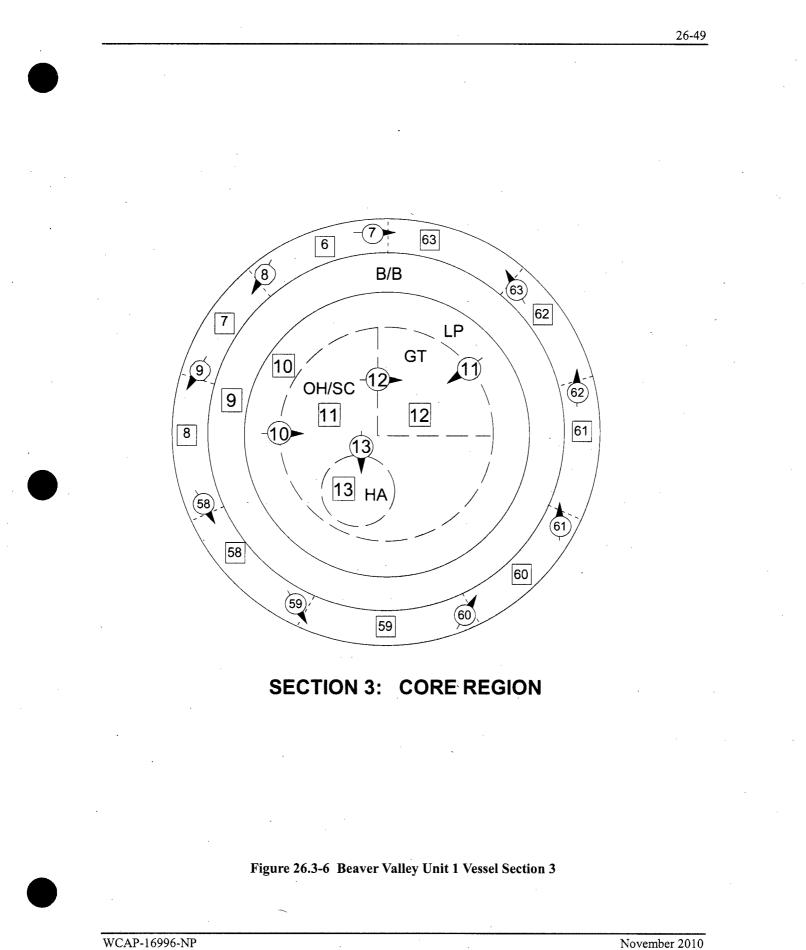


**SECTION 1: LOWER HEAD** 

Figure 26.3-4 Beaver Valley Unit 1 Vessel Section 1



# SECTION 2: LOWER PLENUM



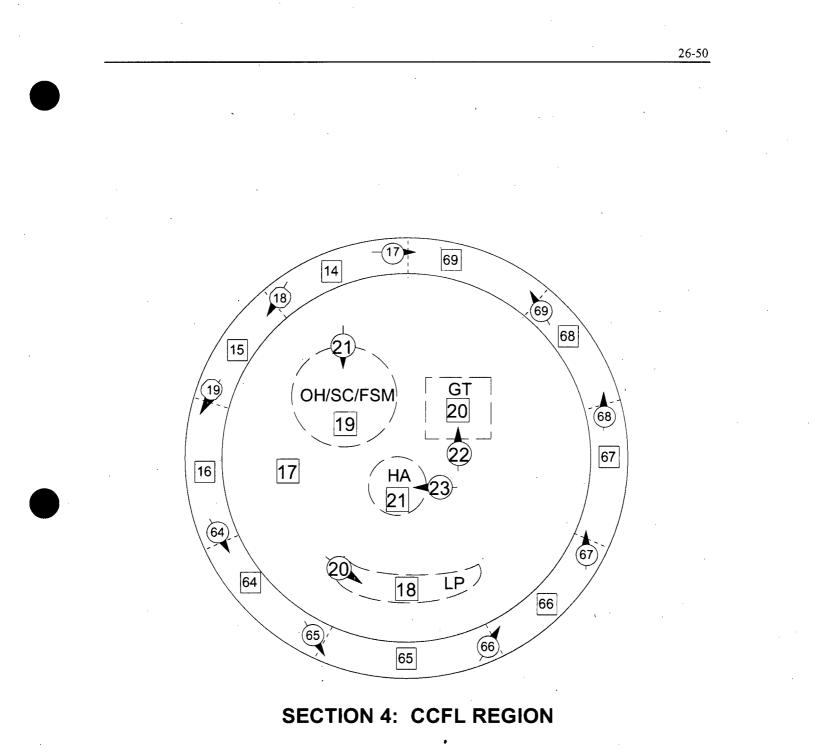
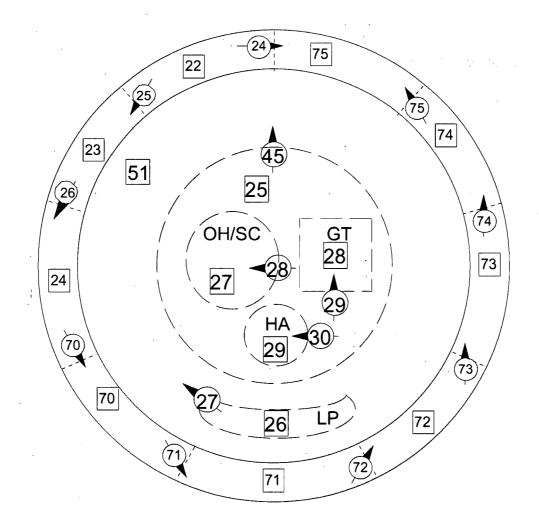


Figure 26.3-7 Beaver Valley Unit 1 Vessel Section 4

WCAP-16996-NP



# SECTION 5: UPPER PLENUM BELOW NOZZLES

Figure 26.3-8 Beaver Valley Unit 1 Vessel Section 5

WCAP-16996-NP

a.c

### Figure 26.3-9 Beaver Valley Unit 1 Vessel Section 6

WCAP-16996-NP

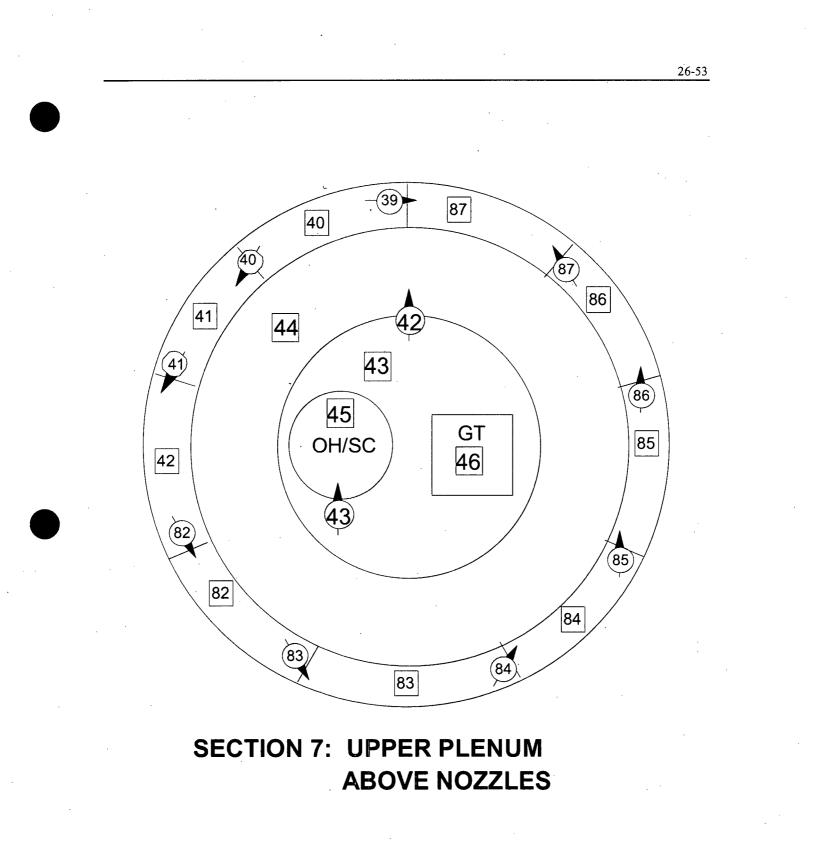
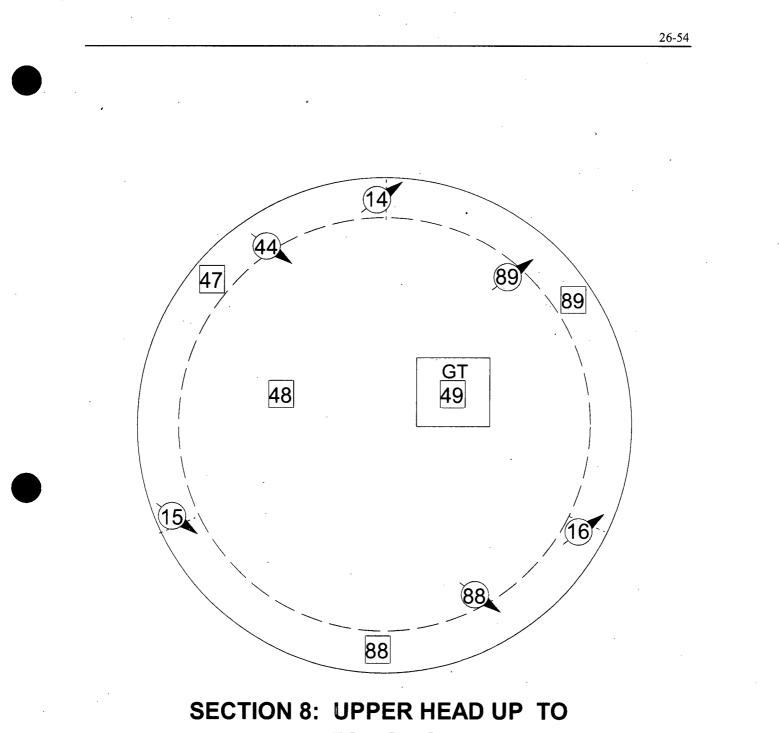


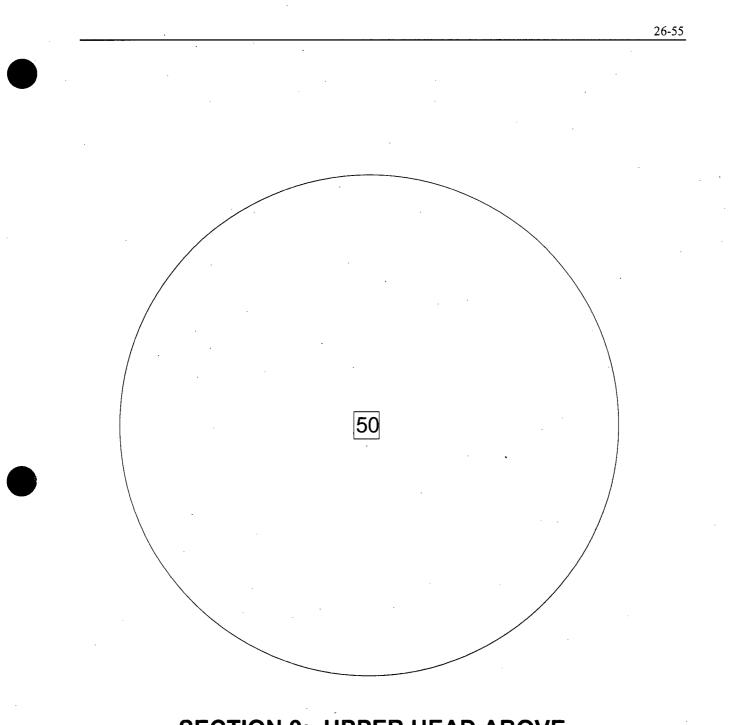
Figure 26.3-10 Beaver Valley Unit 1 Vessel Section 7

WCAP-16996-NP



TOP OF GUIDE TUBES

Figure 26.3-11 Beaver Valley Unit 1 Vessel Section 8



# SECTION 9: UPPER HEAD ABOVE GUIDE TUBES

Figure 26.3-12 Beaver Valley Unit 1 Vessel Section 9

		Ň	1		111	L	IX.	5		_	•	<b>L</b>		0	υ.	~
1								ОН	ОН	FSM						
2						ОН	GT	SCM	GŢ	SCM	GT	он		$\backslash$		
3			$\square$		SCM	он	FSM	GT	SCM	GT	FSM	PGT	SCM		$\overline{\ }$	
4				SCM	GT	он	GΤ	он	GT	он	GT	FSM	GT	SC		
5		$\left \right $	ОН	PGT	он	GT	SCM	PGT	SCM	он	SCM	GT	FSM	ОН	FSM	
6		X	GT	FSM	GT	SCM	GT	он	GT	FSM	GT	sc	GT	он	GT	
7	$\Box$	FSM	SCM	GT	он	он	он	GT	sc	GT	он	PGT	он	GT	sc	ОН
8		он	GT	SCM	GT	SCM	GT	sc	GT	SCM	GT	SCM	GT	SCM	GT	FSM
9		ОН	SC	GT	FSM	PGT	он	GT	SCM	GT	FSM	он	он	GT	SC	он
10			GT	FSM	GT	sc	GT	FSM	GT	он	GT	SCM	GT	он	GT	
11		$\left  \right\rangle$	ОН	он	FSM	GT	SCM	он	SCM	PGT	SCM	GT	он	PGT	ОН	
12		$\square$		SC	GT	FSM	GT	FSM	GT	он	GT	FSM	GT	SCM		/
13			$\overline{\ }$		SC	PGT	он	GT	SCM	GT	FSM	он	SC		$\square$	
.14						FSM	GT	SC	GT	sc	GT	FSM		$\nearrow$		
15						/		·OH	FSM	FSM						
						P C F S	GT – F H – Of SM – F C – Su CM – S	Pluggeo ben Ho Free-Sta pport 0	anding Column t Colun	Tube Mixer (13)	(23)	3)				

#### R P N M L K J H G F E D C B A

Figure 26.3-13 Beaver Valley Unit 1 Upper Plenum Structure Map

1

Low Power Assemblies (LP)

WCAP-16996-NP

November 2010 Revision 0

ĺ

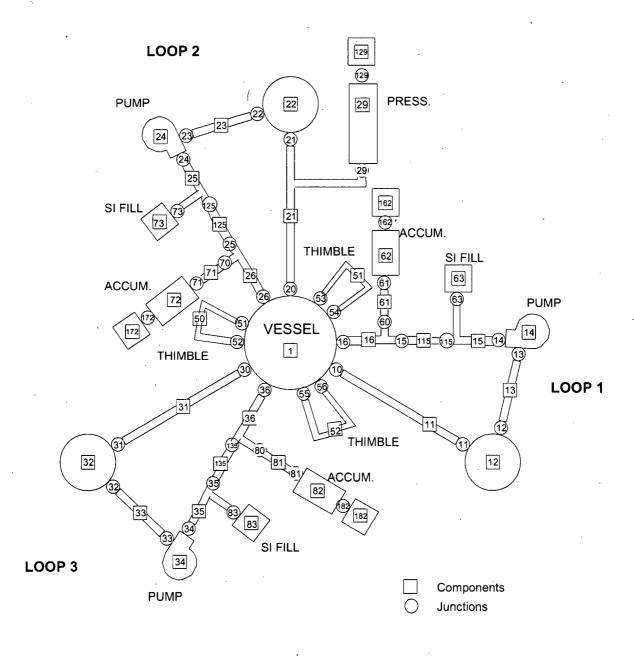


### Figure 26.3-14 Beaver Valley Unit 1 Loop Model Noding Diagram



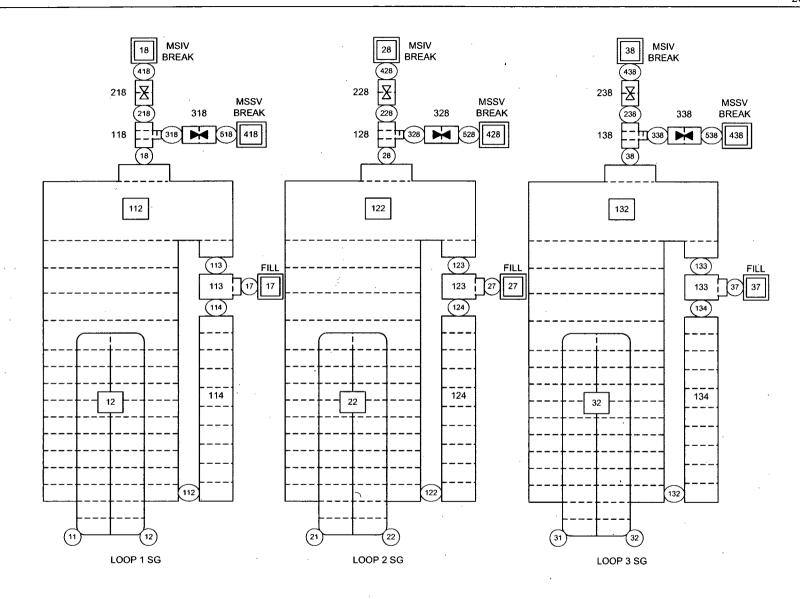


Figure 26.3-15 Beaver Valley Unit 1 Steam Generator Component Noding Diagram

a,c

Figure 26.3-16 Beaver Valley Unit 1 Reference Case Axial Power Distribution

WCAP-16996-NP

#### 26.4 STEADY STATE CALCULATION/CALIBRATION

1

Steady-state acceptance criteria are necessary because the above-mentioned fluid and core conditions are likely to differ somewhat from plant-to-plant and the degree to which these parameters are matched in the <u>WCOBRA/TRAC-TF2</u> simulation must be consistent. Table 26.4-1 shows the acceptance criteria used in <u>WCOBRA/TRAC-TF2</u> for acceptable simulation of plant conditions. A checklist for a number of significant parameters is given below, which utilizes this table to verify whether these variables have reached their acceptable steady-state values.

[

]^{a,c}

[

. .

]^{a,c}

.

<u>a,c</u>

Table 26.4-1	Criteria for an Acceptable Stea	dy-State	
· · ·			
	<u>nn an an ann ann ann ann ann an an an an</u>		
		•	
	· · · · · · · · · · · · ·		
	· · · · · ·		
<u> </u>	······································		
· · · · · · · · · · · · · · · · · · ·			·····

#### 26.5 **REFERENCES**

- Bajorek, S. M., et al., March 1998, "Code Qualification Document for Best Estimate LOCA Analysis," Volume 1 Revision 2, and Volumes 2 through 5, Revision 1, WCAP-12945-P-A (Proprietary).
- 2. Bordelon, F. M. and Murphy, E. T., 1974, "Containment Pressure Analysis Code (COCO)," WCAP-8327 (Proprietary), WCAP-8306 (Non-Proprietary).
- 3. Bordelon, F. M., et al., 1974, "Westinghouse Emergency Core Cooling System Evaluation Model – Summary," WCAP-8339.
- 4. Bordelon, F. M., et al., 1975, "The Westinghouse ECCS Evaluation Model: Supplementary Information," WCAP-8471-P-A (Proprietary).
- 5. Foster and Sidener, July 2000, "Westinghouse Improved Performance Analysis and Design Model (PAD 4.0)," WCAP-15063-P-A, Revision 1, with Errata (Proprietary).
- 6. Shimeck, D. J., March 1988, "COSI SI/Steam Condensation Experiment Analysis," WCAP-11767 (Proprietary).

### 27 REFERENCE BREAK SPECTRUM ANALYSIS

#### 27.1 LARGE, INTERMEDIATE, AND SMALL BREAK SPECTRA

The V. C. Summer (CGE) and Beaver Valley Unit 1 (DLW) plant models described in Section 26 are exercised over the full spectrum of break sizes to determine the code's ability to properly capture the phenomena identified in the PIRT process (Section 2). For each plant, a representative break size is chosen for a small, intermediate, and large break, with a more detailed description of each transient provided in Sections 27.2 (CGE) and 27.3 (DLW). The small and large break reference transients are carried forward into the scoping studies in Section 28. As was historically found and as confirmed in this section, intermediate breaks are not limiting relative to large and small breaks. An intermediate break reference transient is therefore not considered in the scoping studies.

#### 27.1.1 V. C. Summer (CGE)

#### 27.1.1.1 CGE Large Break Spectrum

The phenomena observed following a large break LOCA are generally observed regardless of break size, however the timing of events and the consequent cladding temperatures will vary. A series of transients typical of large breaks is explored, with all uncertainty parameters at a representative (model as coded) value aside from those related to the effective break area, to demonstrate the general sensitivity to break area. The range of effective break areas explored is from  $[ ]^{a,c}$  times a nominal double-ended guillotine (DEG, through the use of a discharge coefficient of  $[ ]^{a,c}$ ), or an effective break area of  $[ ]^{a,c}$  times the cold leg area.

Figure 27.1.1.1-1 shows the peak cladding temperature for the large break transients. Based on this limited set of cases, [

]^{a,c}. The location of the PCT is more a function of the power shape, and is relatively insensitive to the break size, shown in Figure 27.1.1.1-2.

The effect of increasing break area is primarily to increase the peak magnitude and decrease the duration of the total break flow, shown in Figure 27.1.1.1-3. This directly corresponds with the rate of depressurization (Figure 27.1.1.1-4) where the largest breaks depressurize the most quickly. The faster depressurization for larger breaks allows for an earlier accumulator injection, shown in Figure 27.1.1.1-5, but due to higher ECCS bypass early in the transient, the total vessel fluid mass is not replaced to the same degree it is for the smaller breaks (Figure 27.1.1.1-6) by the end of refill.

Safety injection flow is shown in Figure 27.1.1-7. [

Based on the results for the large break spectrum, a nominal DEG with break size twice the cold leg area is chosen as the reference large break and is utilized in the scoping studies in Section 28. The CGE large break reference transient is described in more detail in Section 27.2.1.

(

Figure 27.1.1.1-1 Rod 1 Peak Cladding Temperature, CGE LBLOCA

WCAP-16996-NP

November 2010 Revision 0

27-3

Figure 27.1.1.1-2 Rod 1 Peak Cladding Temperature Location, CGE LBLOCA

WCAP-16996-NP

27-4



a,c

## Figure 27.1.1.1-3 Break Flow, CGE LBLOCA



### Figure 27.1.1.1-4 RCS Pressure, CGE LBLOCA

WCAP-16996-NP

November 2010 Revision 0

27-6

a,c

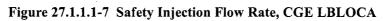
a,c

Figure 27.1.1.1-5 Accumulator Mass Flow Rate, CGE LBLOCA

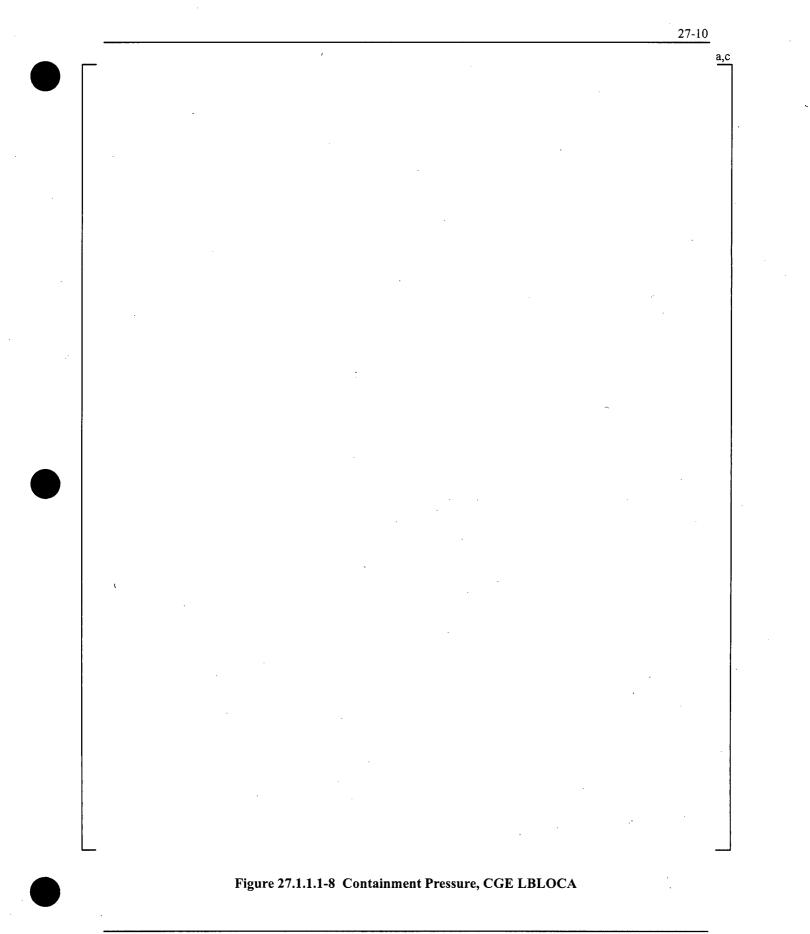


a,c

Figure 27.1.1.1-6 Vessel Fluid Mass, CGE LBLOCA



a,c



#### 27.1.1.2 CGE Intermediate Break Spectrum

]^{a,c}

Intermediate breaks have historically been shown to be non-limiting relative to both large breaks, where significant ECCS bypass prevents efficient core recovery through accumulator injection, and small breaks, where an extended natural circulation phase and vessel depressurization delays accumulator injection such that core uncovery may occur. A series of transients is explored here, with effective break areas from approximately 0.35 times the cold leg area for a 16-inch diameter break down to an 8-inch diameter break, equivalent to slightly less than 0.1 times the cold leg area.

Figure 27.1.1.2-1 shows the peak cladding temperature for the intermediate break transients. [

Figure 27.1.1.2-2 shows a continuation of the trend observed for large breaks, where decreases in effective break area lead to a prolonged period of lower break flow. This is also clear from the depressurization rate, shown in Figure 27.1.1.2-3, and the timing of accumulator injection in Figure 27.1.1.2-4.

]^{a,c} The 12-

inch break is described in more detail as the intermediate break reference transient in Section 27.2.2.

a,c

Figure 27.1.1.2-1 Rod 1 Peak Cladding Temperature, CGE IBLOCA

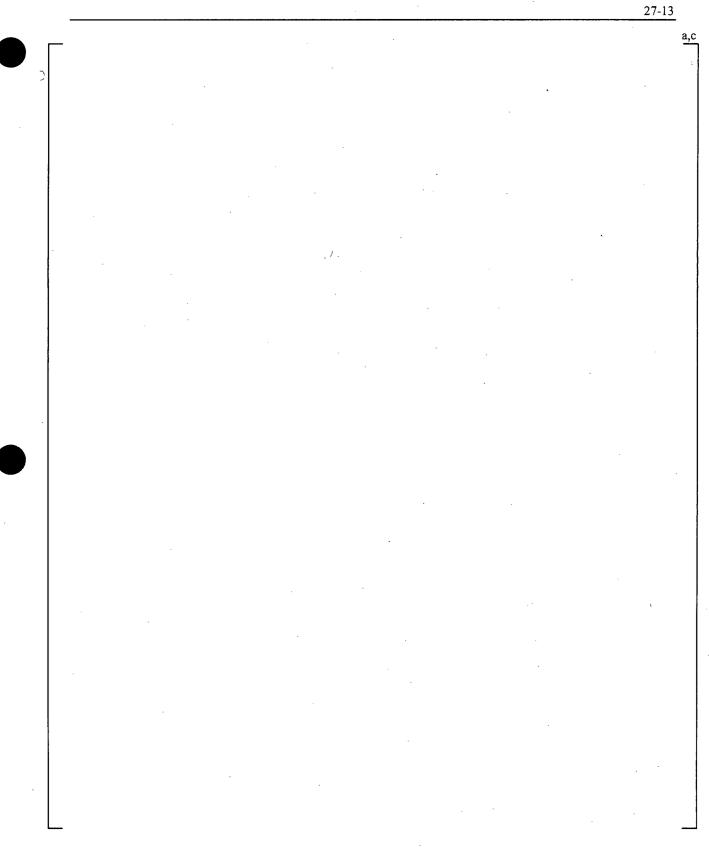


Figure 27.1.1.2-2 Total Break Flow, CGE IBLOCA

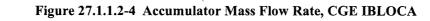
WCAP-16996-NP

a,c

# Figure 27.1.1.2-3 RCS Pressure, CGE IBLOCA

WCAP-16996-NP

١



WCAP-16996-NP

a,c

### Figure 27.1.1.2-5 Vessel Fluid Mass, CGE IBLOCA

WCAP-16996-NP

#### 27.1.1.3 CGE Small Break Spectrum

Following a small break LOCA, a relatively long transient ensues in which the timing of the major phenomena and consequently the severity of the cladding heat up are a strong function of break size. The largest of the small breaks will blow down quickly, allowing for an efficient clearing of the loop seals, rapid vessel depressurization, and early accumulator injection, resulting in a transient that is not expected to be limiting as in the case of an intermediate break. In direct contrast, an extremely small break will result in break flow so small that the high head safety injection flows are sufficient to prevent core uncovery.

Figure 27.1.1.3-1 shows the break flow void fraction for a range of break sizes from a 2-inch equivalent diameter to an 8-inch break. During blowdown, and until the natural circulation phase ends (Figure 27.1.1.3-2), the break flow is a two-phase mixture. [

]^{a,c}

]^{a,c}

All cases demonstrate the top-down draining that is characteristic of small breaks (Figure 27.1.1.3-3). [

Figure 27.1.1.3-5 shows that [

]^{a,c} Section 28.2.11 will

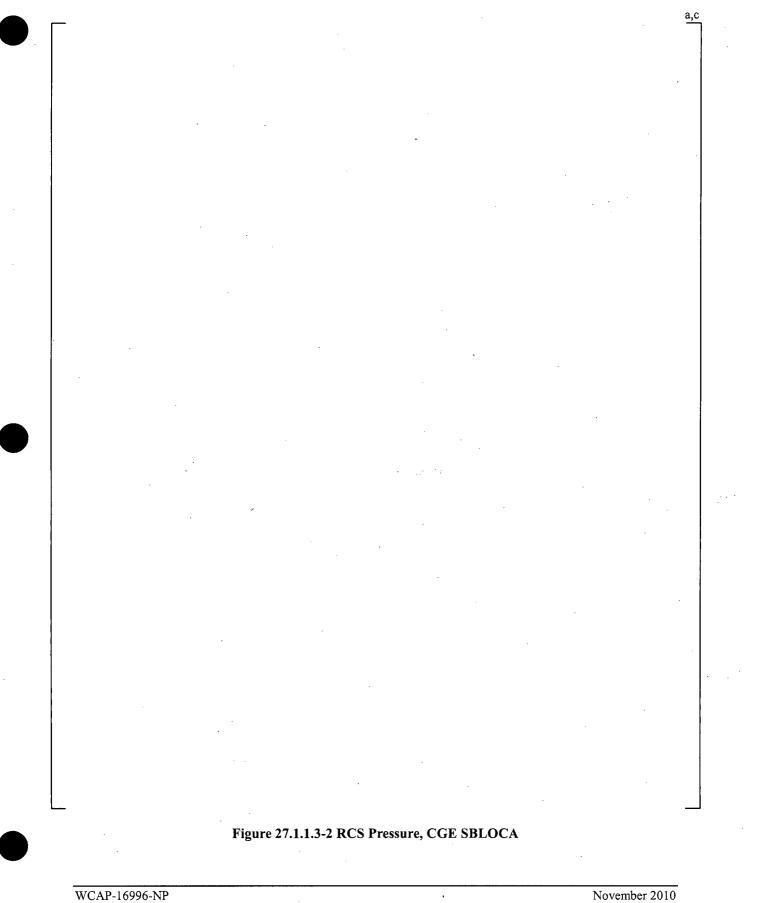
demonstrate the strong relationship between the number of loop seals that clear, and to what extent, and break size for these small breaks.

The 3-inch break is chosen as the small break reference transient and is described in more detail in Section 27.2.3.

a,c

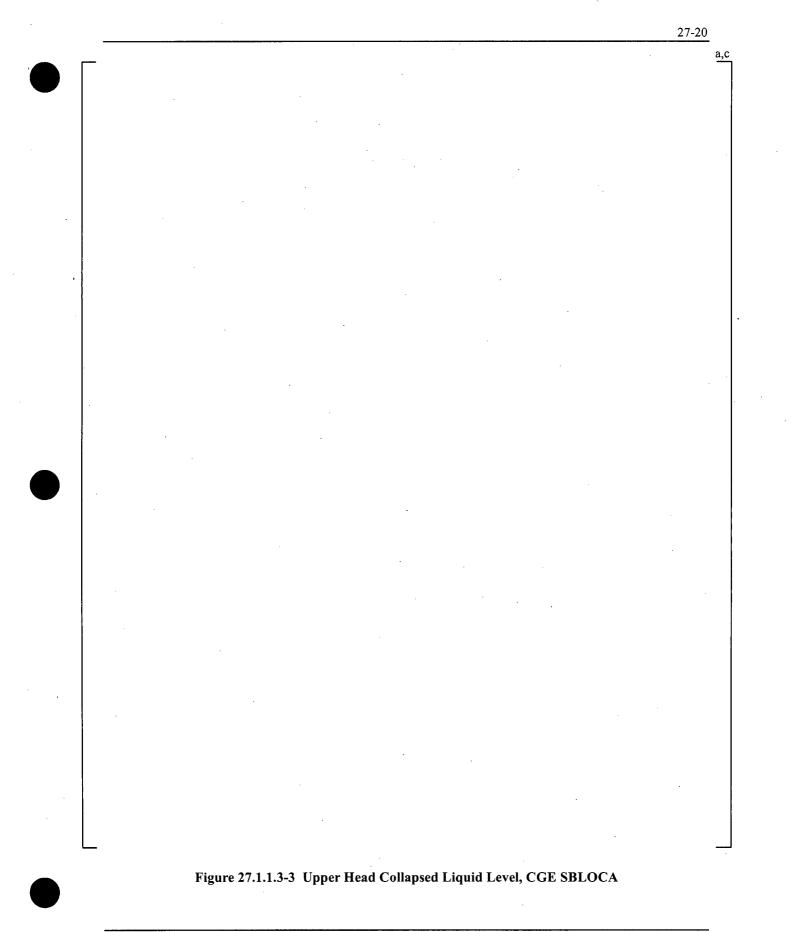
## Figure 27.1.1.3-1 Break Void Fraction, CGE SBLOCA

WCAP-16996-NP



November 2010 Revision 0

27-19



WCAP-16996-NP



6

a,c

## Figure 27.1.1.3-4 Break Flow, CGE SBLOCA

a,c

Figure 27.1.1.3-5 Rod 1 Peak Cladding Temperature, CGE SBLOCA

.

a,c

Figure 27.1.1.3-6 Loop 1 Loop Seal Differential Pressure, CGE SBLOCA

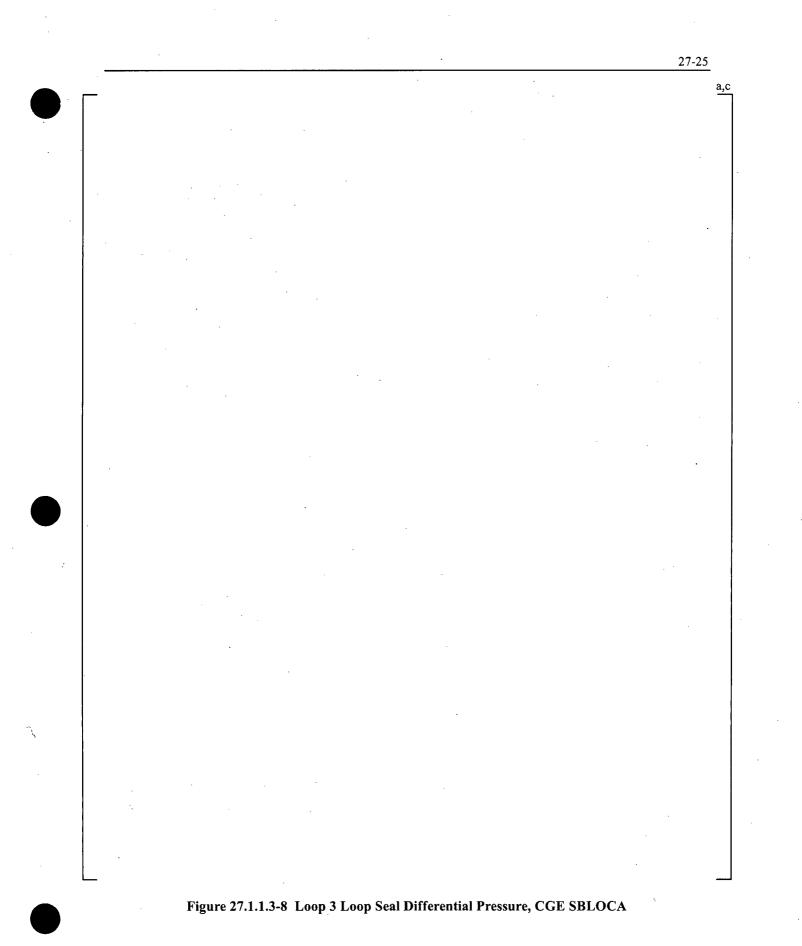
WCAP-16996-NP .

٠

a,c

Figure 27.1.1.3-7 Loop 2 Loop Seal Differential Pressure, CGE SBLOCA

WCAP-16996-NP



WCAP-16996-NP

#### 27.1.2 Beaver Valley Unit 1 (DLW)

#### 27.1.2.1 DLW Large Break Spectrum

The phenomena observed following a large break LOCA are generally observed regardless of break size, however the timing of events and the consequent cladding temperatures will vary. A series of transients typical of large breaks is explored, with all uncertainty parameters at a representative (model as coded) value aside from those related to the effective break area, to demonstrate the general sensitivity to break area. The range of break areas explored is from  $[ ]^{a,c}$  times a nominal DEG (through the use of a discharge coefficient of  $[ ]^{a,c}$ ), or an effective break area of  $[ ]^{a,c}$  times the cold leg area, down to a split break with effective break area of 0.5 times the cold leg area.

Figure 27.1.2.1-1 shows the peak cladding temperature for the large break transients. For DLW, it appears that [

 $]^{a,c}$ . The location of the PCT is more a function of the power shape, and is relatively insensitive to the break size, shown in Figure 27.1.2.1-2.

The effect of break area is primarily to increase the magnitude and decrease the duration of the total break flow, shown in Figure 27.1.2.1-3. This directly corresponds with the rate of depressurization (Figure 27.1.2.1-4) where the largest breaks depressurize the most quickly, as expected. The faster depressurization for larger breaks allows for earlier accumulator injection, shown in Figure 27.1.2.1-5, but due to higher ECCS bypass the total vessel fluid mass is not replaced to the same degree it is for the smaller breaks (Figure 28.1.2.1-6).

Safety injection flow is shown in Figure 27.1.2.1-7.

### ]^{a,c}

Based on the results for the large break spectrum, a break size of twice the cold leg area is chosen as the reference large break and is utilized in the scoping studies in Section 28. The DLW large break reference transient is described in more detail in Section 27.3.1.

WCAP-16996-NP

a,c

Figure 27.1.2.1-1 Rod 1 Peak Cladding Temperature, DLW LBLOCA

WCAP-16996-NP

a,c

## Figure 27.1.2.1-2 Rod 1 Peak Cladding Temperature Location, DLW LBLOCA

١

WCAP-16996-NP

a,c

Figure 27.1.2.1-3 Total Break Flow, DLW LBLOCA

WCAP-16996-NP

ſ

(

a,c

## Figure 27.1.2.1-4 RCS Pressure, DLW LBLOCA

WCAP-16996-NP

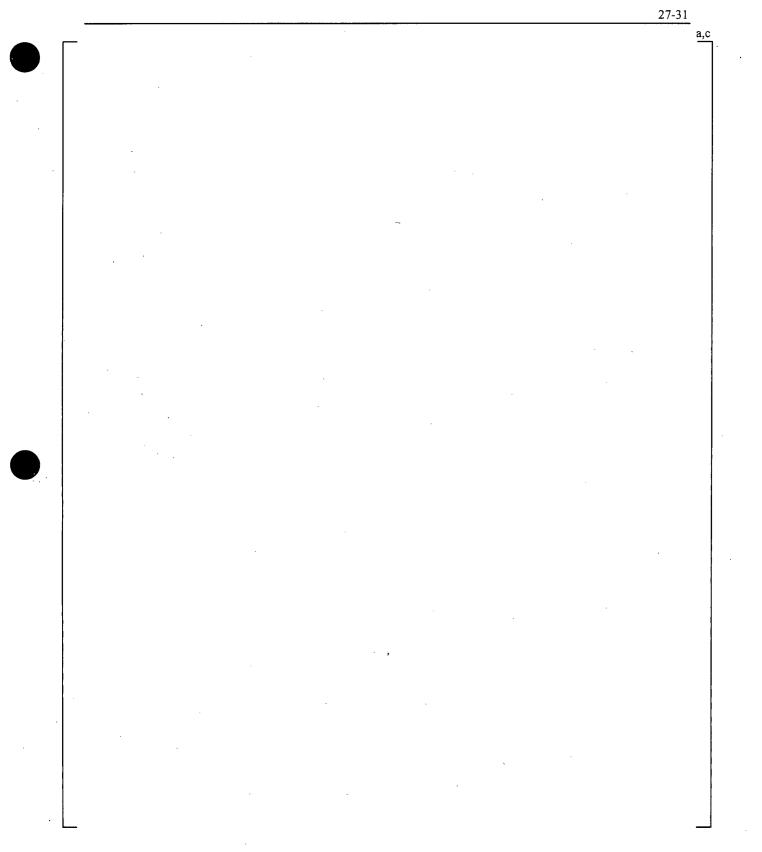


Figure 27.1.2.1-5 Accumulator Mass Flow, DLW LBLOCA

WCAP-16996-NP

November 2010 Revision 0 •

a,c

Figure 27.1.2.1-6 Vessel Fluid Mass, DLW LBLOCA

WCAP-16996-NP

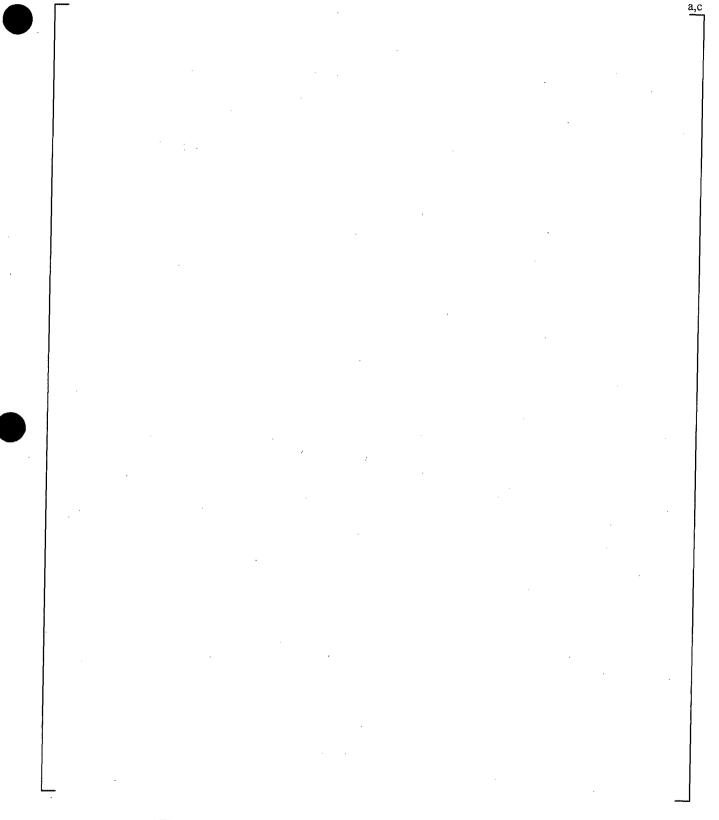
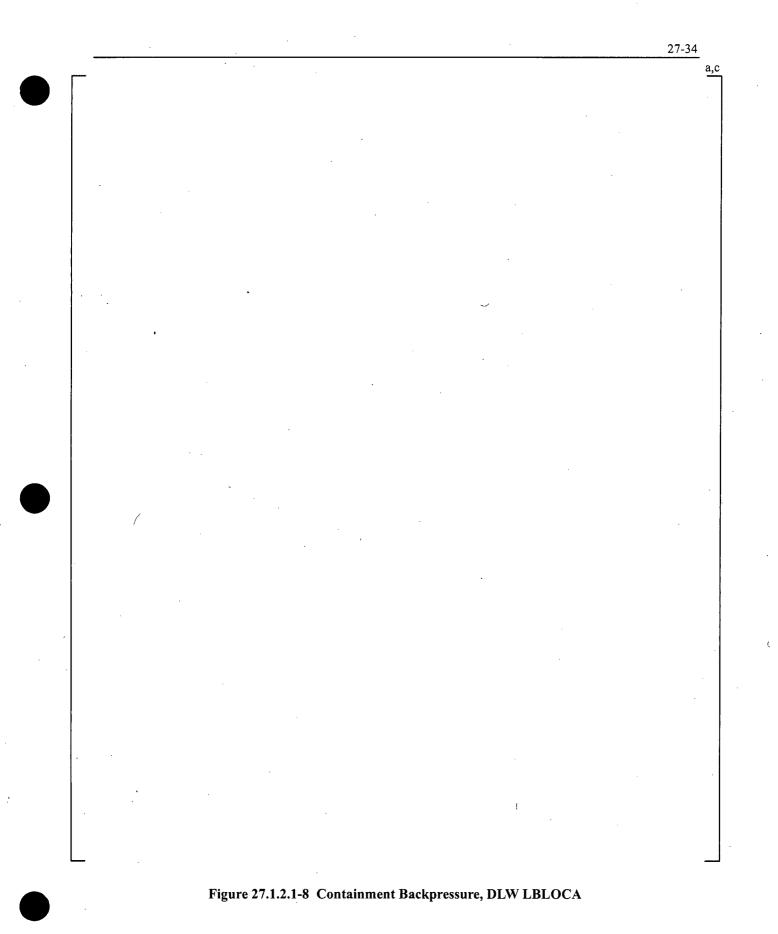


Figure 27.1.2.1-7 Intact Loop Safety Injection Flow, DLW LBLOCA

WCAP-16996-NP

27-33



WCAP-16996-NP

#### 27.1.2.2 DLW Intermediate Break Spectrum

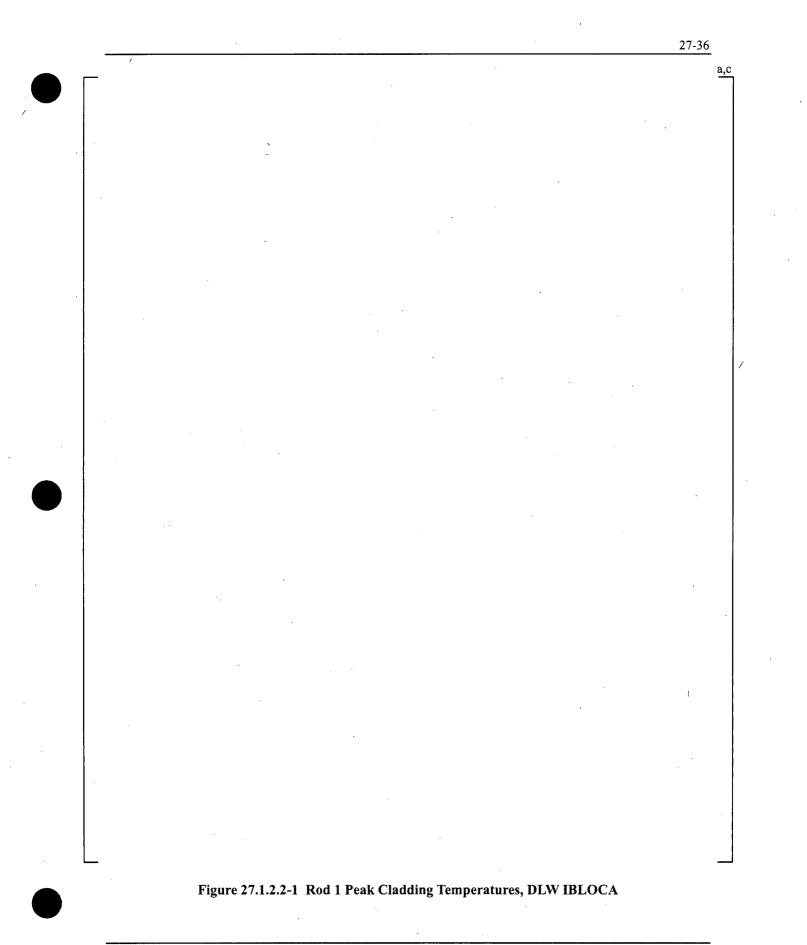
Intermediate breaks have historically been shown to be non-limiting relative to both large breaks, where significant ECCS bypass prevents efficient core recovery through accumulator injection, and small breaks, where an extended natural circulation phase and vessel depressurization delays accumulator injection such that core uncovery may occur. A series of transients is explored here, from a 16-inch diameter break with effective break area of approximately 0.34 times the cold leg area down to an 8-inch diameter break, equivalent to slightly less than 0.1 times the cold leg area.

Figure 27.1.2.2-1 shows the peak cladding temperature for the intermediate break transients. [

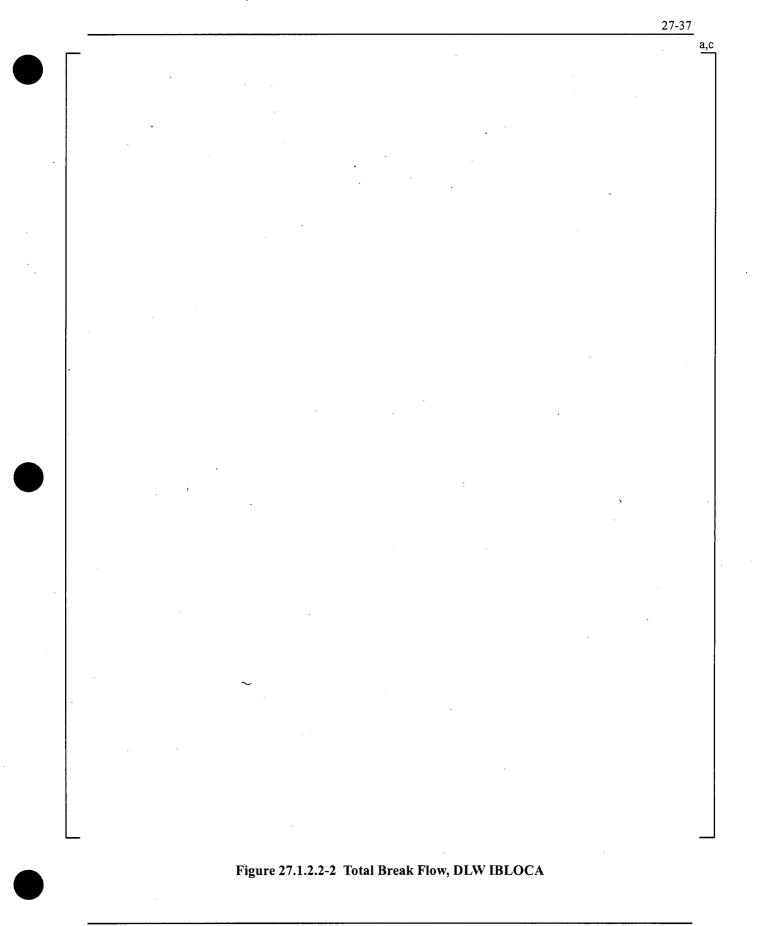
]^{a,c}

Figure 27.1.2.2-2 shows a continuation of the trend observed for large breaks, where decreases in effective break area lead to a prolonged period of lower break flow. This is also clear from the depressurization rate, shown in Figure 27.1.2.2-3, and the timing of accumulator injection in Figure 27.1.2.2-4. Figure 27.1.2.2-5 shows the relative importance of ECCS bypass, where [

^{a,c} The 12-inch break is described in more detail as the intermediate break reference transient in Section 27.3.2.



WCAP-16996-NP



WCAP-16996-NP

a,c

### Figure 27.1.2.2-3 RCS Pressure, DLW IBLOCA

WCAP-16996-NP

\



a,c

1

Figure 27.1.2.2-4 Accumulator Mass Flow Rate, DLW IBLOCA

WCAP-16996-NP

a,c

## Figure 27.1.2.2-5 Vessel Fluid Mass, DLW IBLOCA

WCAP-16996-NP

#### 27.1.2.3 DLW Small Break Spectrum

Following a small break LOCA, a relatively long transient ensues in which the timing of the major phenomena and consequently the severity of the cladding heat up are a strong function of break size. The largest of the small breaks will blow down quickly, allowing for an efficient clearing of the loop seals, rapid vessel depressurization, and early accumulator injection, resulting in a transient that is not expected to be limiting as in the case of an intermediate break. In direct contrast, an extremely small break will result in break flow so small that the high head safety injection flows are sufficient to prevent core uncovery.

Figure 27.1.2.3-1 shows RCS depressurization following a range of break sizes from a 2-inch equivalent diameter to an 8-inch break. [

]^{a,c}

All cases demonstrate the top-down draining that is characteristic of small breaks (Figure 27.1.2.3-2). [

Figure 27.1.2.3-4 shows that [

]^{a,c} Section 28.2.11 will demonstrate the strong relationship between the number of loop seals that clear, and to what extent, and break size for these small breaks.

The 3-inch break is chosen as the small break reference transient and is described in more detail in Section 27.3.3.

WCAP-16996-NP

]^{a,c}

a,c

## Figure 27.1.2.3-1 RCS Pressure, DLW SBLOCA

WCAP-16996-NP

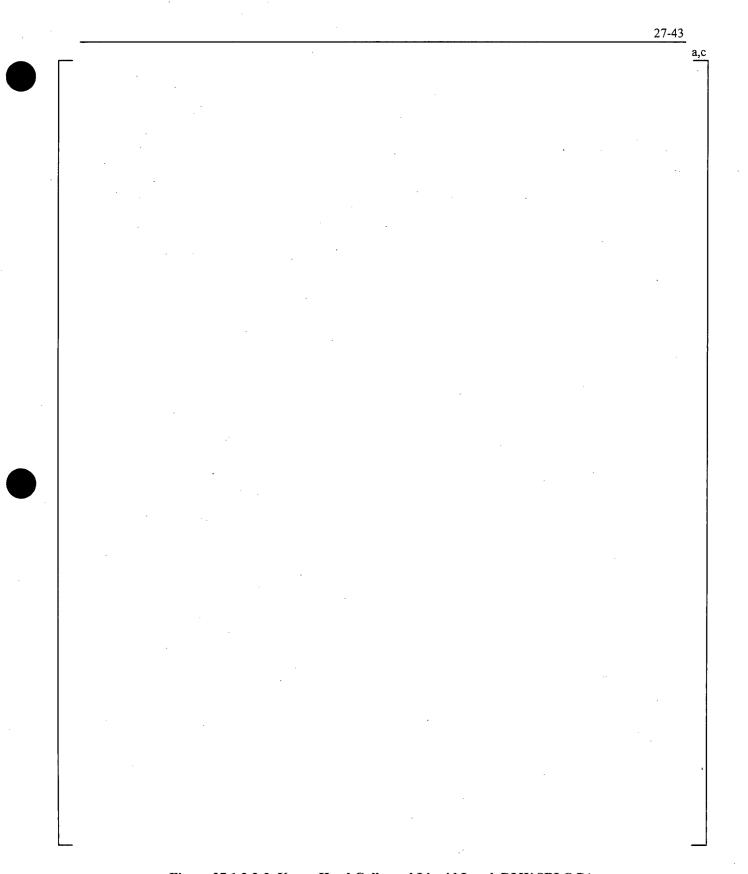
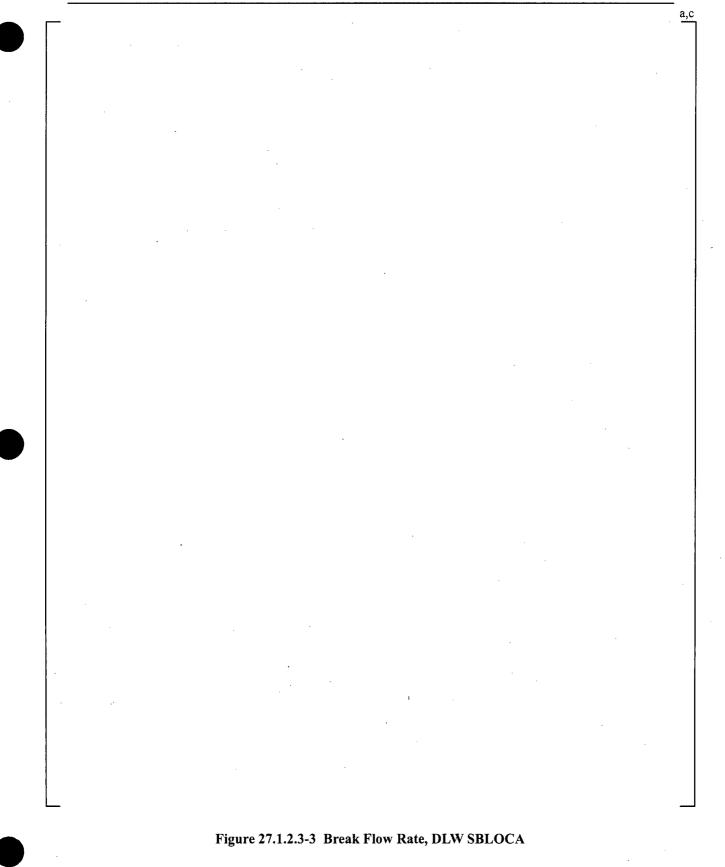


Figure 27.1.2.3-2 Upper Head Collapsed Liquid Level, DLW SBLOCA

WCAP-16996-NP



WCAP-16996-NP

|--|

a,c

## Figure 27.1.2.3-4 Rod 1 Peak Cladding Temperature, DLW SBLOCA

WCAP-16996-NP

1

27-46 a,c Figure 27.1.2.3-5 Loop 1 Loop Seal Differential Pressure, DLW SBLOCA

WCAP-16996-NP

a,c

Figure 27.1.2.3-6 Loop 2 Loop Seal Differential Pressure, DLW SBLOCA

WCAP-16996-NP

a,c

Figure 27.1.2.3-7 Loop 3 Loop Seal Differential Pressure, DLW SBLOCA

WCAP-16996-NP

### 27.2 V. C. SUMMER (CGE) REFERENCE TRANSIENTS

### 27.2.1 CGE Large Break Reference Transient Description

The CGE large break reference transient used the conditions listed in Table 26.2-1. The reference large break is a nominal double-ended guillotine break of the cold leg pipe with uncertainty attributes at representative (model as coded) values. A conservatively low containment pressure is calculated according to the mass and energy release [

]^{a,c}.

The large break LOCA transient can be divided into time periods in which specific phenomena are occurring. A convenient way to divide the transient is in terms of the various heatup and cooldown phases that the hot assembly undergoes. For each of these phases, specific phenomena and heat transfer regimes are important, as discussed below.

1. Critical Heat Flux (CHF) Phase

In this phase, the break flow is subcooled, the discharge rate is high, the core flow reverses, the fuel rods go through departure from nucleate boiling (DNB), and the cladding rapidly heats up while core power shuts down. Figure 27.2.1-1 shows the maximum cladding temperature in the core for all the fuel rods, as a function of time, and Figure 27.2.1-2 shows the PCT location as a function of time for the hot rod.

The regions of the RCS with the highest initial temperatures (upper core, upper plenum, and hot legs) begin to flash during this period. This phase is terminated when the water in the lower plenum and downcomer begin to flash. The mixture level swells and the intact loop pumps, still rotating in single-phase liquid, push this two phase mixture into the core. As the fluid in the cold leg reaches saturation conditions, the discharge flow rate at the break decreases sharply (Figures 27.2.1-3 and 27.2.1-4).

#### 2. Upward Core Flow Phase

Heat transfer is improved as the two-phase mixture is pushed into the core. The break discharge rate is reduced because the fluid is saturated at the break. Figures 27.2.1-3 and 27.2.1-4 show the break flowrate from the vessel and pump sides of the break, respectively. This phase ends as the lower plenum mass is depleted (Figure 27.2.1-5), the loops become two-phase, and the pump head degrades.

3. Downward Core Flow Phase

The break flow begins to dominate and pulls flow down through the core as the pump head degrades due to increased voiding. Figure 27.2.1-6 shows the vapor mass flow rate near the PCT elevation. While liquid and entrained liquid flows also provide cooling, the vapor flow entering the top of the core best illustrates this phase of core cooling. This period may be enhanced by flow from the upper head. Once the system has depressurized to the accumulator pressure (Figure 27.2.1-7 provides the system pressure transient), the accumulators begin to inject cold

water into the intact cold legs (Figure 27.2.1-8). During this period, due to steam upflow in the downcomer, a portion of the injected ECCS (Emergency Core Cooling System) water is calculated to be bypassed around the downcomer and out the break. As the system pressure continues to fall (Figure 27.2.1-7), the break flow and consequently the downward core flow are reduced. The system pressure approaches the containment pressure at the end of this last period of the blowdown phase, around [ $]^{a,c}$ ]

During this phase, the core begins to heat up as the system approaches containment pressure (Figure 27.2.1-9) and the vessel begins to fill with ECCS water (Figures 27.2.1-10, 27.2.1-11, and 27.2.1-12).

### 4. Refill Phase

The core continues to heat up as the lower plenum fills with ECCS water. Figure 27.2.1-5 shows the lower plenum liquid level. This phase is characterized by a rapid increase in cladding temperatures at all elevations due to the lack of liquid and steam flow in the core region. This phase ends when the ECCS water enters the core and entrainment begins, with a resulting improvement in heat transfer.

Figures 27.2.1-8 and 27.2.1-13 show the liquid flows from the intact loop accumulators and the safety injection on one of the intact loops, respectively. As water fills the lower plenum, the refill phase ends. A repressurization, which occurs as the accumulators discharge nitrogen, can be seen in the reduction in pumped flow.

#### Reflood Phase

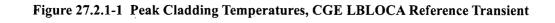
5.

During the early reflood phase, the accumulators begin to empty and nitrogen enters the system (Figure 27.2.1-8). The nitrogen surge forces water into the core, which then boils, causing system repressurization, and the lower core region begins to quench. The repressurization is illustrated by the RCS pressure (Figure 27.2.1-7). During this time, core cooling may increase due to vapor generation and liquid entrainment, but conversely the early reflood pressure spike results in loss of mass out the broken cold leg.

The pumped ECCS water aids in the filling of the downcomer throughout the reflood period. Figure 27.2.1-11 and Figure 27.2.1-12 show the core and downcomer collapsed liquid levels, respectively. Figure 27.2.1-10 shows the vessel fluid mass. As the quench front progresses further into the core, the PCT location moves to a higher elevation (Figure 27.2.1-2).

As the transient progresses, continued injection of pumped ECCS water refills the core, removes the vessel metal mass stored energy and core decay heat, and leads to an increase in the vessel fluid mass. All rods are quenched before approximately [ ]^{a,c} after the break (Figure 27.2.1-1).

a,c



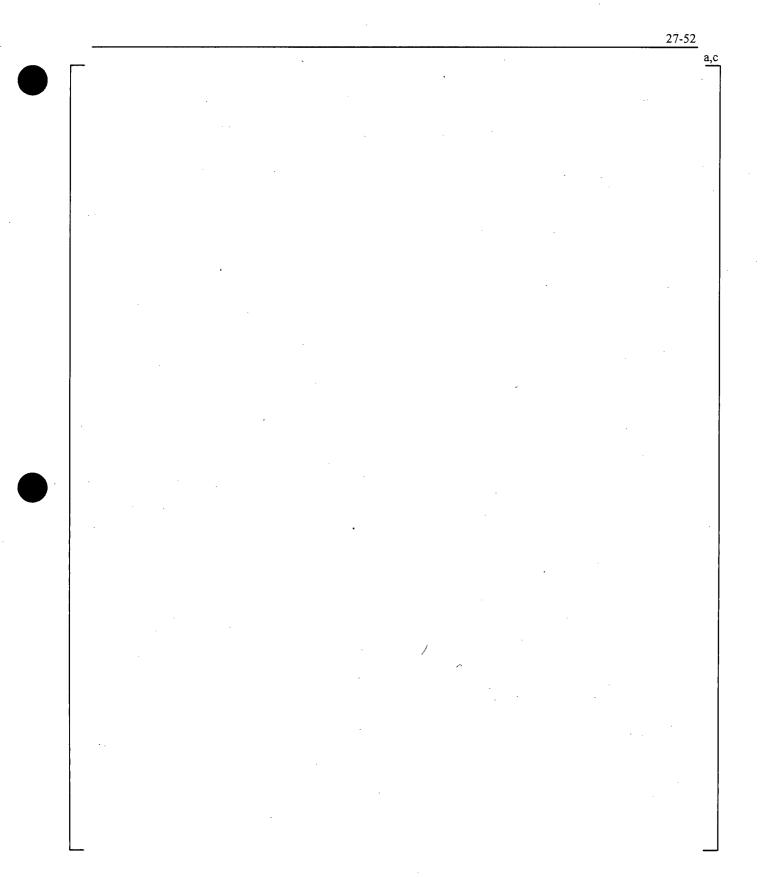


Figure 27.2.1-2 Rod 1 Peak Cladding Temperature Location, CGE LBLOCA Reference Transient

.

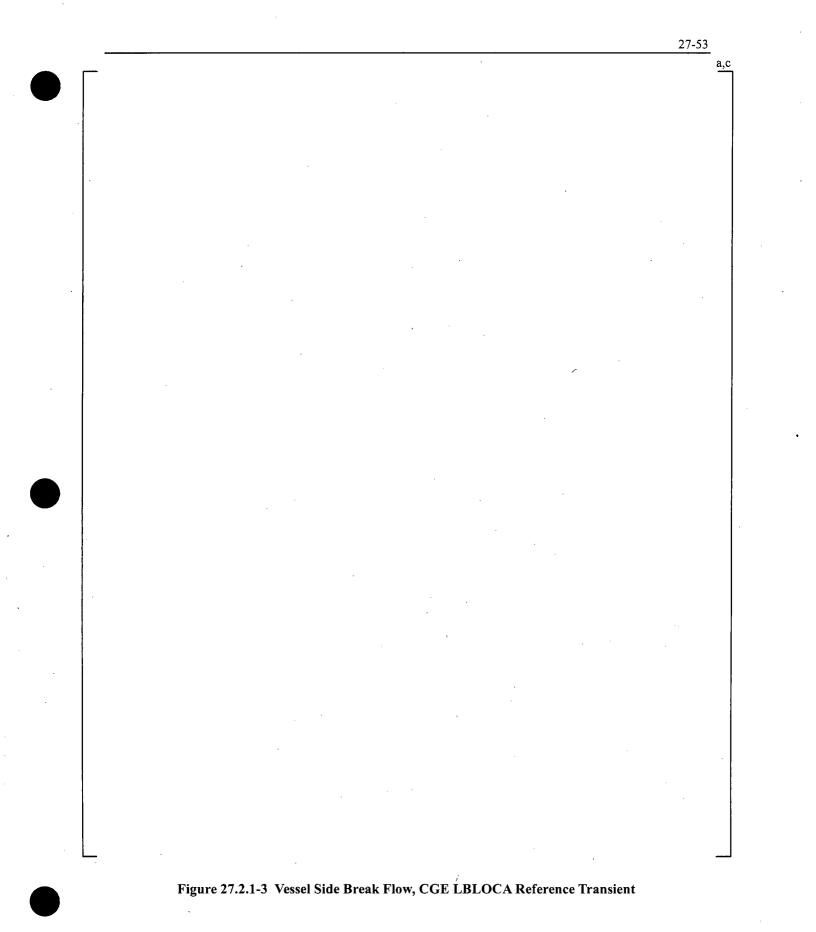
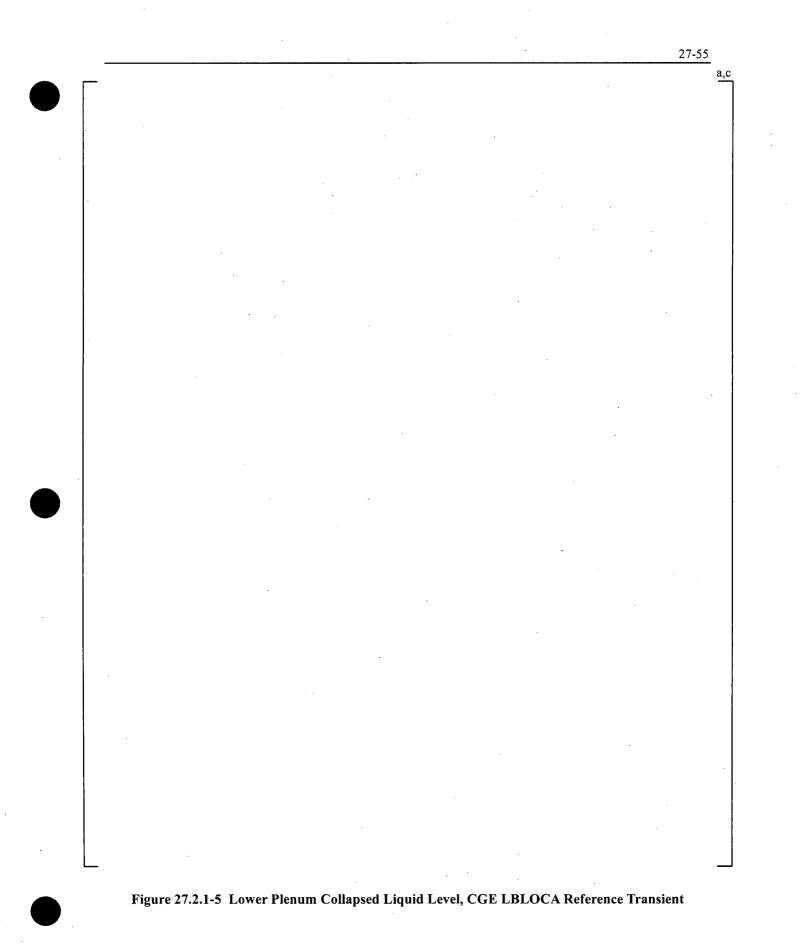


Figure 27.2.1-4 Pump Side Break Flow, CGE LBLOCA Reference Transien	[
---------------------------------------------------------------------	---

27-54

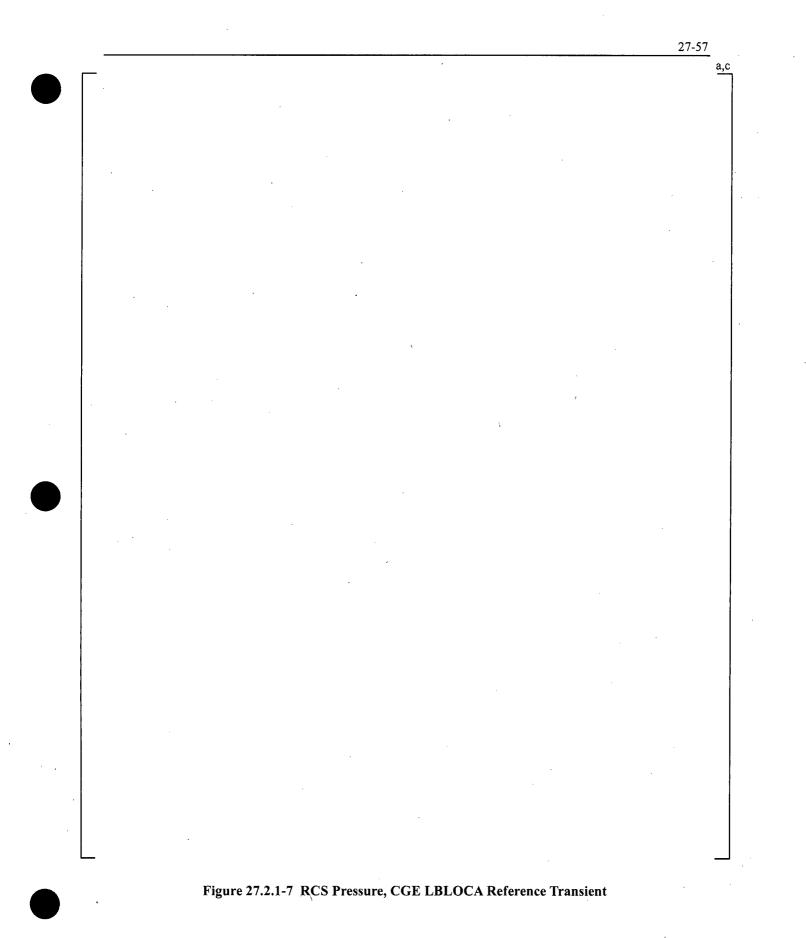
a,c



a,c

Figure 27.2.1-6 Vapor Mass Flow Rate Near PCT Elevation, CGE LBLOCA Reference Transient

WCAP-16996-NP



a,c

Figure 27.2.1-8 Accumulator Flow Rate, CGE LBLOCA Reference Transient



a,c

# Figure 27.2.1-9 Containment Pressure, CGE LBLOCA Reference Transient

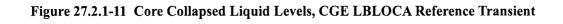
WCAP-16996-NP

a,c

Figure 27.2.1-10 Vessel Fluid Mass, CGE LBLOCA Reference Transient

WCAP-16996-NP

a,c



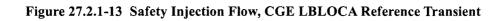
WCAP-16996-NP

0



a,c

Figure 27.2.1-12 Downcomer Collapsed Liquid Level, CGE LBLOCA Reference Transient



a,c

### 27.2.2 CGE Intermediate Break Reference Transient Description

The CGE intermediate break reference transient used the conditions listed in Table 26.2-1. The reference intermediate break is a split break of the cold leg pipe with uncertainty attributes at representative (model as coded) values and a break area consistent with a 12-inch diameter hole. A conservatively low containment pressure is calculated according to the mass and energy release [

]^{a,c}

As stated in Section 2.3.1.3, an intermediate break is classified by a monotonic depressurization, or a lack of pressure stabilization associated with small breaks, and a lack of significant ECCS bypass brought about by steam upflow in the downcomer in large breaks. As a result, effective core recovery is expected early in the transient due to largely uninhibited accumulator flow. Historically, intermediate breaks have been shown to be non-limiting as a consequence. The intermediate break LOCA transient can be divided into time periods in which specific phenomena are occurring, as discussed below.

### 1. Blowdown/Depressurization

Initially, the break flow is high and single phase at the beginning of the blowdown phase (Figures 27.2.2-1 and 27.2.2-2). Break flow reduces as the flow to the break becomes two-phase, and consequently the depressurization rate also decreases (Figure 27.2.2-3). Flashing in the vessel results from the RCS depressurization, and collapsed liquid levels in the core and downcomer drop (Figures 27.2.2-4 and 27.2.2-5). [

# ]^{a,c}

#### 2. Accumulator Injection

Once the RCS pressure reaches the accumulator check valve pressure setpoint, accumulator flow rapidly refills the majority of the lost vessel inventory (Figures 27.2.2-8 and 27.2.2-9). ECCS bypass is low, as the core and downcomer fill with nearly the entire volume of the accumulator liquid. After the accumulators have emptied, ECCS injection is reduced to a minimal amount corresponding with the high-head safety injection (HHSI) system (Figure 27.2.2-10). This results in a period of vessel fluid mass depletion through boiling within the vessel, as the HHSI is not sufficient to make up for the break flow, which continues as the vessel depressurizes.

### 3. SI Injection

This phase begins as the low-head safety injection (LHSI) system is initiated (Figure 27.2.2-10). The RCS continues to depressurize, resulting in a continually increasing amount of SI flow injection from the LHSI system. Vessel fluid inventory depletion is halted nearly immediately as the total injected flow becomes greater than that lost through the break (Figure 27.2.2-11).

a,c

Figure 27.2.2-1 Break Flow, CGE IBLOCA Reference Transient

WCAP-16996-NP

a,c

# Figure 27.2.2-2 Void Fraction at the Break, CGE IBLOCA Reference Transient

a,c



WCAP-16996-NP

a,c

Figure 27.2.2-4

## Core Collapsed Liquid Levels, CGE IBLOCA Reference Transient (2=Hot Assembly, 3=Guide Tube, 4=OH/SC/SM, 5=Low Power)

WCAP-16996-NP

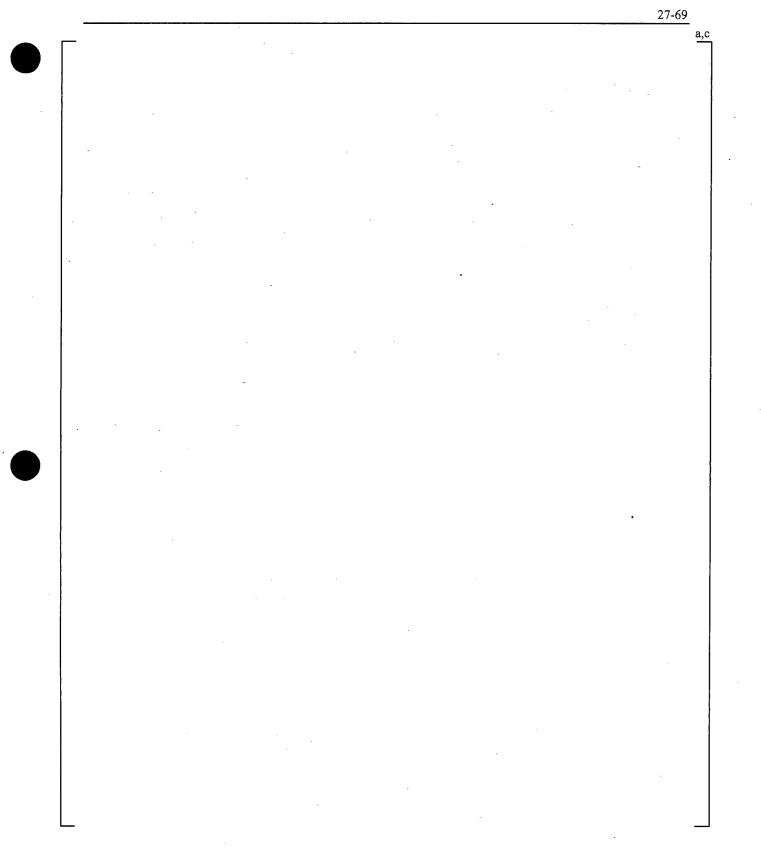


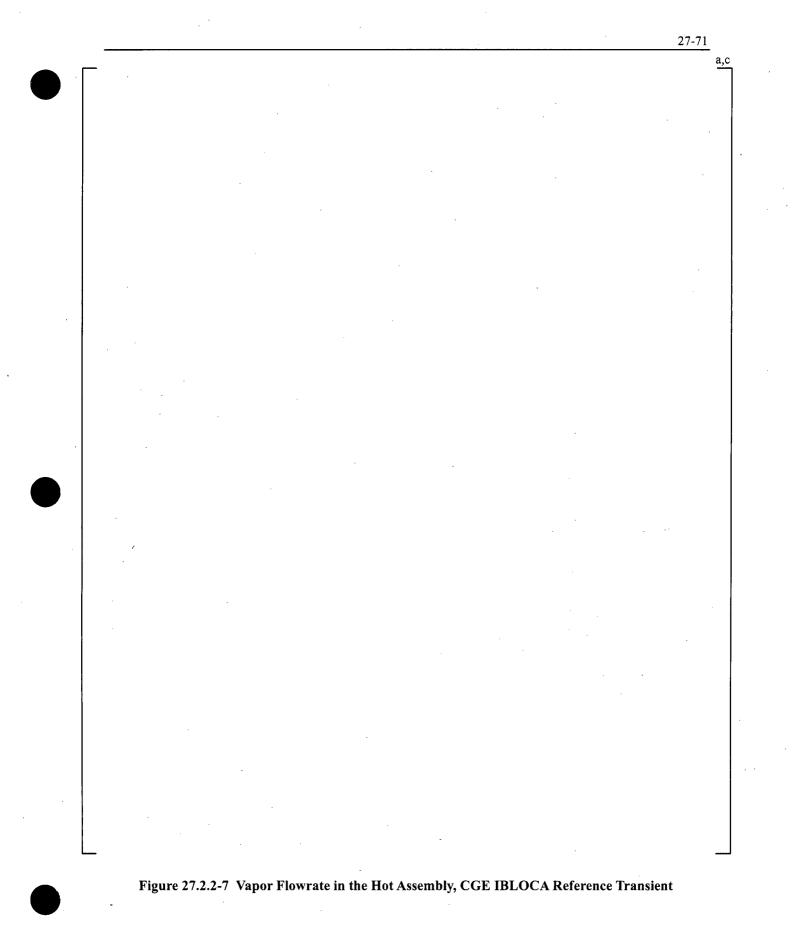
Figure 27.2.2-5 Downcomer Collapsed Liquid Levels, CGE IBLOCA Reference Transient

WCAP-16996-NP

a,c

# Figure 27.2.2-6 Peak Cladding Temperatures, CGE IBLOCA Reference Transient

WCAP-16996-NP



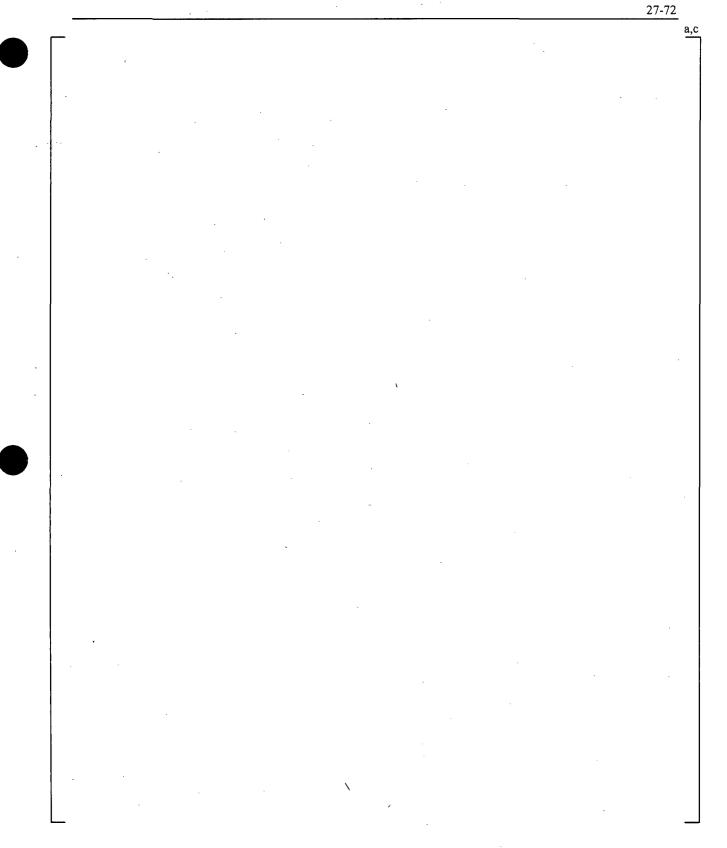
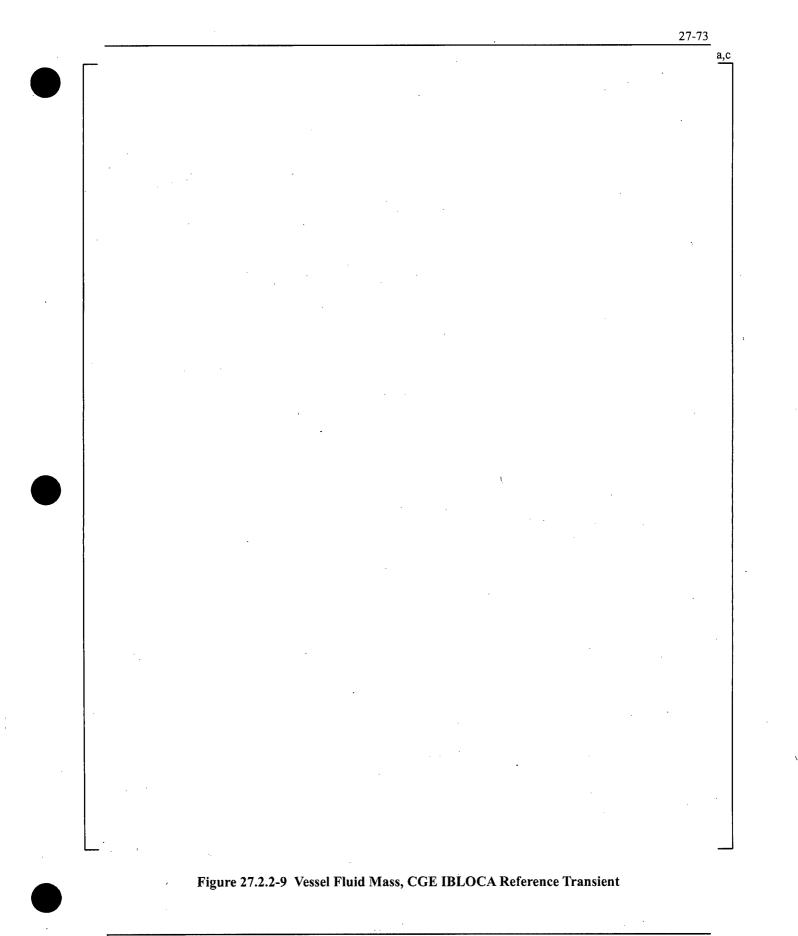


Figure 27.2.2-8 Accumulator Flow Rate, CGE IBLOCA Reference Transient



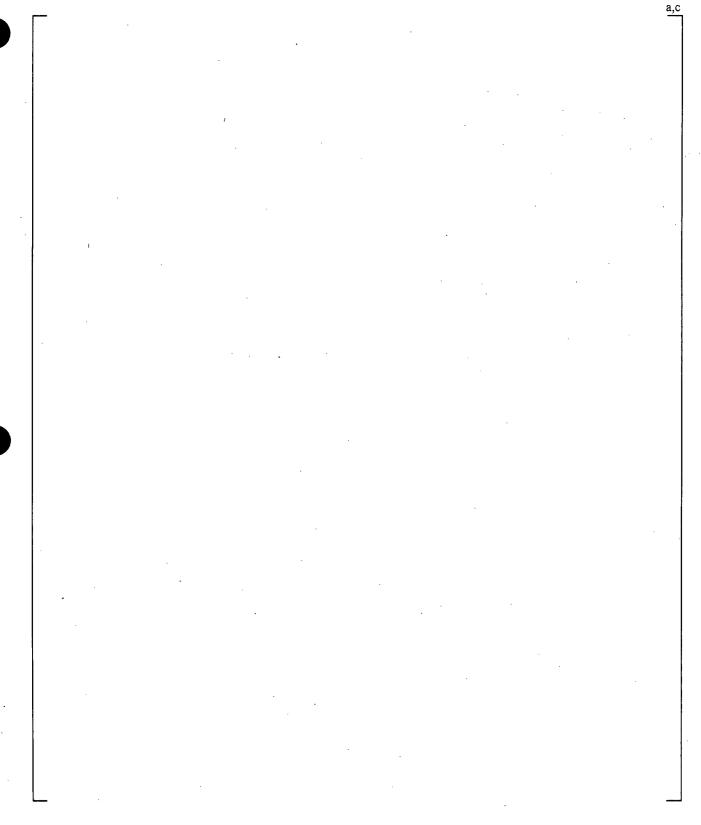
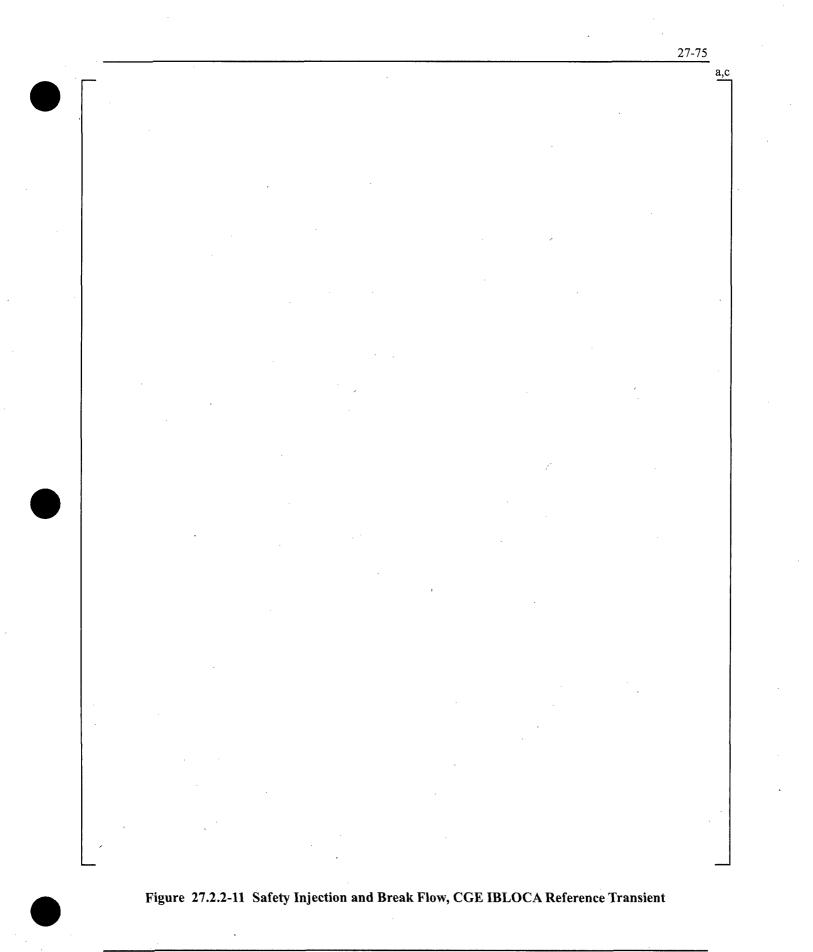


Figure 27.2.2-10 Safety Injection Flow, CGE IBLOCA Reference Transient

WCAP-16996-NP

November 2010 Revision 0

27-74



### 27.2.3 CGE Small Break Reference Transient Description

The CGE small break reference transient used the conditions listed in Table 26.2-1. The reference small break is a split break of the cold leg pipe with uncertainty attributes at representative (model as coded) values and a break area consistent with a 3-inch diameter hole. [

]^{a,c}

The small break LOCA transient can be divided into time periods in which specific phenomena are occurring, as discussed below.

### 1. Blowdown

The rapid depressurization of the RCS coincides with single-phase liquid flow through the break as shown in Figure 27.2.3-1. Following the reactor trip, initiated on a low-low pressurizer pressure setpoint, high pressure safety injection flow begins after the setpoint is reached with some delay (Figure 27.2.3-2). Phase separation begins in the upper head, upper plenum, and hot legs near the end of this period until the entire RCS eventually reaches saturation, ending the rapid depressurization [

]^{a,c}.

### 2. Natural Circulation

This quasi-equilibrium phase persists until [  $]^{4,c}$  as the RCS pressure remains slightly above the secondary side pressure (Figure 27.2.3-3). The system drains from the top down (Figure 27.2.3-4), and while significant mass is continually lost through the break (Figure 27.2.3-5), the vapor generated in the core is trapped in the upper regions by the liquid remaining in the crossover leg loop seals. [

]^{a,c}

### 3. Loop Seal Clearance

As the system drains, the liquid level in the downhill side of the pump suction piping becomes depressed to the bottom of the loop seal, allowing the steam trapped during the natural circulation phase to vent to the break (Figures 27.2.3-8, 27.2.3-9, and 27.2.3-10). The break flow and the flow through the RCS loops become primarily vapor (Figure 27.2.3-1). [

]^{a,c}

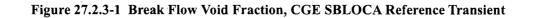
### 4. Boil-Off

With a vapor vent path established, the RCS depressurizes at a rate determined by the critical flow, which continues to be primarily single phase (Figures 27.2.3-3 and 27.2.3-1). [

]^{a,c}

## 5. Core Recovery

The RCS pressure continues to fall, and once it reaches that of the accumulator check valve setpoint, the introduction of additional ECCS water (Figure 27.2.3-11) replenishes the vessel inventory (Figure 27.2.3-12) and recovers the core mixture level. Depressurization continues as a result of break flow and condensation, and the transient is declared over as the break flow becomes less than the total injected flow (Figure 27.2.3-13).

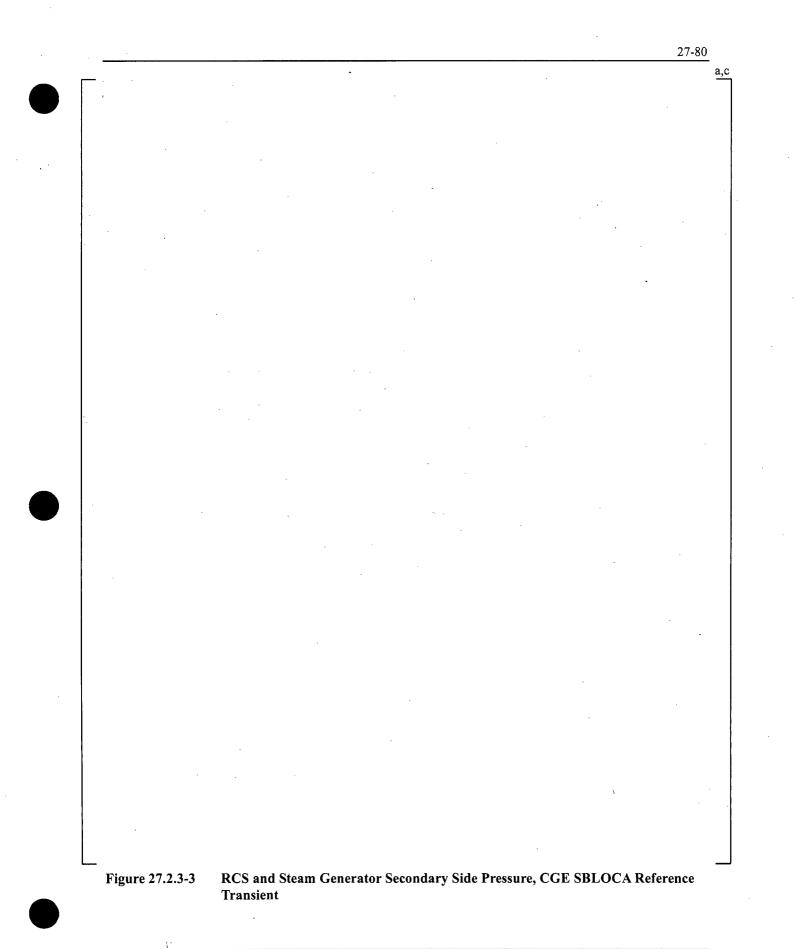


a,c

a,c

Figure 27.2.3-2 Safety Injection Flow, CGE SBLOCA Reference Transient

WCAP-16996-NP



a,c

Figure 27.2.3-4 Upper Head Collapsed Liquid Level, CGE SBLOCA Reference Transient

WCAP-16996-NP

a,c

Figure 27.2.3-5 Break Flow, CGE SBLOCA Reference Transient

WCAP-16996-NP



a,c

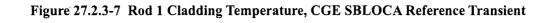
Figure 27.2.3-6

## Core Collapsed Liquid Levels, CGE SBLOCA Reference Transient (2=Hot Assembly, 3=Guide Tube, 4=OH/SC/SM, 5=Low Power)

WCAP-16996-NP



a,c



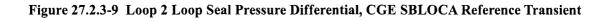
a,c

1  $\rangle$ 

Figure 27.2.3-8 Loop 1 Loop Seal Pressure Differential, CGE SBLOCA Reference Transient

WCAP-16996-NP

a,c



WCAP-16996-NP

a,c

Figure 27.2.3-10 Loop 3 Loop Seal Pressure Differential, CGE SBLOCA Reference Transient

WCAP-16996-NP

a,c

Figure 27.2.3-11 Accumulator Flow, CGE SBLOCA Reference Transient

a,c

Figure 27.2.3-12 Vessel Fluid Mass, CGE SBLOCA Reference Transient



a,c

# Figure 27.2.3-13 Safety Injection and Break Flow, CGE SBLOCA Reference Transient

WCAP-16996-NP

## 27.3 BEAVER VALLEY UNIT 1 (DLW) REFERENCE TRANSIENTS

## 27.3.1 DLW Large Break Reference Transient Description

The DLW large break reference transient used the conditions listed in Table 26.3-1. The reference large break is a nominal double-ended guillotine break of the cold leg pipe with uncertainty attributes at representative (model as coded) values. [

]^{a,c}

The large break LOCA transient can be divided into time periods in which specific phenomena are occurring. A convenient way to divide the transient is in terms of the various heatup and cooldown phases that the hot assembly undergoes. For each of these phases, specific phenomena and heat transfer regimes are important, as discussed below.

1. Critical Heat Flux (CHF) Phase

In this phase, the break flow is subcooled, the discharge rate is high, the core flow reverses, the fuel rods go through departure from nucleate boiling (DNB), and the cladding rapidly heats up while core power shuts down. Figure 27.3.1-1 shows the maximum cladding temperature in the core for all the fuel rods, as a function of time, and Figure 27.3.1-2 shows the PCT location as a function of time for the hot rod.

The regions of the RCS with the highest initial temperatures (upper core, upper plenum, and hot legs) begin to flash during this period. This phase is terminated when the water in the lower plenum and downcomer begin to flash. The mixture level swells and the intact loop pumps, still rotating in single-phase liquid, push this two phase mixture into the core. As the fluid in the cold leg reaches saturation conditions, the discharge flow rate at the break decreases sharply (Figures 27.3.1-3 and 27.3.1-4).

## 2. Upward Core Flow Phase

Heat transfer is improved as the two-phase mixture is pushed into the core. The break discharge rate is reduced because the fluid is saturated at the break. Figures 27.3.1-3 and 27.3.1-4 show the break flowrate from the vessel and pump sides of the break, respectively. This phase ends as the lower plenum mass is depleted (Figure 27.3.1-5), the loops become two-phase, and the pump head degrades.

3. Downward Core Flow Phase

The break flow begins to dominate and pulls flow down through the core as the pump head degrades due to increased voiding. Figure 27.3.1-6 shows the vapor mass flow rate near the PCT elevation. While liquid and entrained liquid flows also provide cooling, the vapor flow entering the top of the core best illustrates this phase of core cooling. This period may be enhanced by flow from the upper head. Once the system has depressurized to the accumulator pressure (Figure 27.3.1-7 provides the system pressure transient), the accumulators begin to inject cold

(Figure 27.3.1-7), the break flow and consequently the downward core flow are reduced. The system pressure approaches the containment pressure at the end of this last period of the blowdown phase, around 20-25 seconds.

During this phase, the core begins to heat up as the system reaches containment pressure (Figure 27.3.1-9) and the vessel begins to fill with ECCS water (Figures 27.3.1-10, 27.3.1-11, and 27.3.1-12).

#### Refill Phase

4.

5.

The core continues to heat up as the lower plenum fills with ECCS water. Figure 27.3.1-5 shows the lower plenum liquid level. This phase is characterized by a rapid increase in cladding temperatures at all elevations due to the lack of liquid and steam flow in the core region. This phase ends when the ECCS water enters the core and entrainment begins, with a resulting improvement in heat transfer.

Figures 27.3.1-8 and 27.3.1-13 show the liquid flows from the intact loop accumulators and the safety injection on one of the intact loops, respectively. The repressurization, which occurs as the accumulator discharges nitrogen, can be seen in the reduction in pumped flow.

#### Reflood Phase

During the early reflood phase, the accumulators begin to empty and nitrogen enters the system (Figure 27.3.1-8). The nitrogen surge forces water into the core, which then boils, causing system repressurization, and the lower core region begins to quench. The repressurization is illustrated by the RCS pressure (Figure 27.3.1-7). During this time, core cooling may increase due to vapor generation and liquid entrainment, but conversely the early reflood pressure spike results in loss of mass out the broken cold leg.

The pumped ECCS water aids in the filling of the downcomer throughout the reflood period. Figure 27.3.1-11 and Figure 27.3.1-12 show the core and downcomer collapsed liquid levels, respectively. Figure 27.3.1-10 shows the vessel fluid mass. As the quench front progresses further into the core, the PCT location moves to a higher elevation (Figure 27.3.1-2). [

# ]^{a,c}

As the transient progresses, continued injection of pumped ECCS water refills the downcomer and core, removes the vessel metal mass stored energy and core decay heat, and leads to an increase in the vessel fluid mass. [

٦^{a,c}

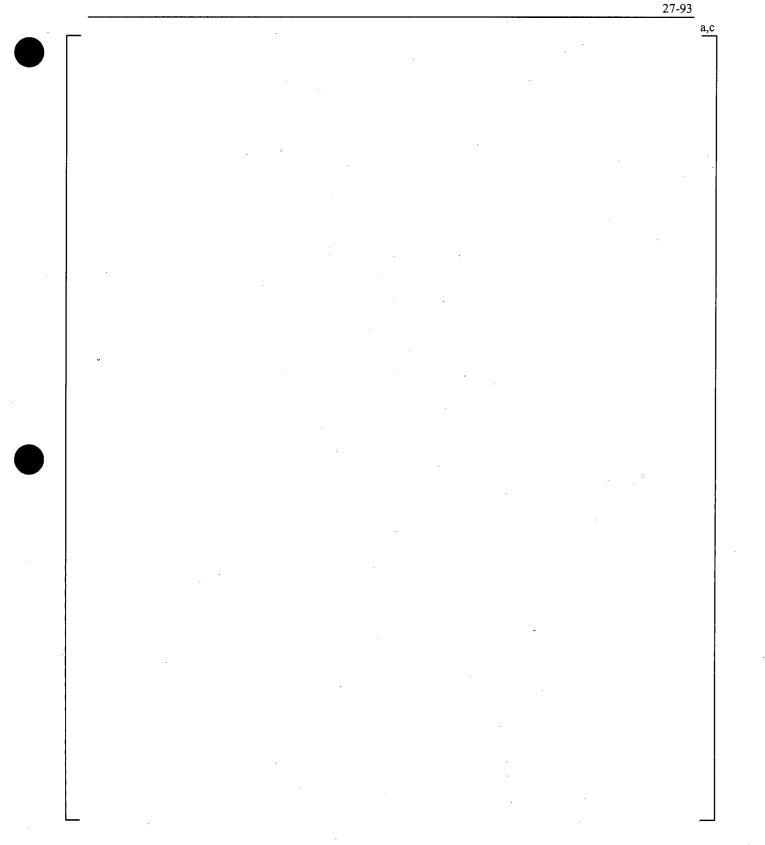


Figure 27.3.1-1 Peak Cladding Temperatures, DLW LBLOCA Reference Transient

WCAP-16996-NP

a,c

Figure 27.3.1-2 Peak Cladding Temperature Location, DLW LBLOCA Reference Transient

a,c

Figure 27.3.1-3 Vessel Side Break Flow, DLW LBLOCA Reference Transient

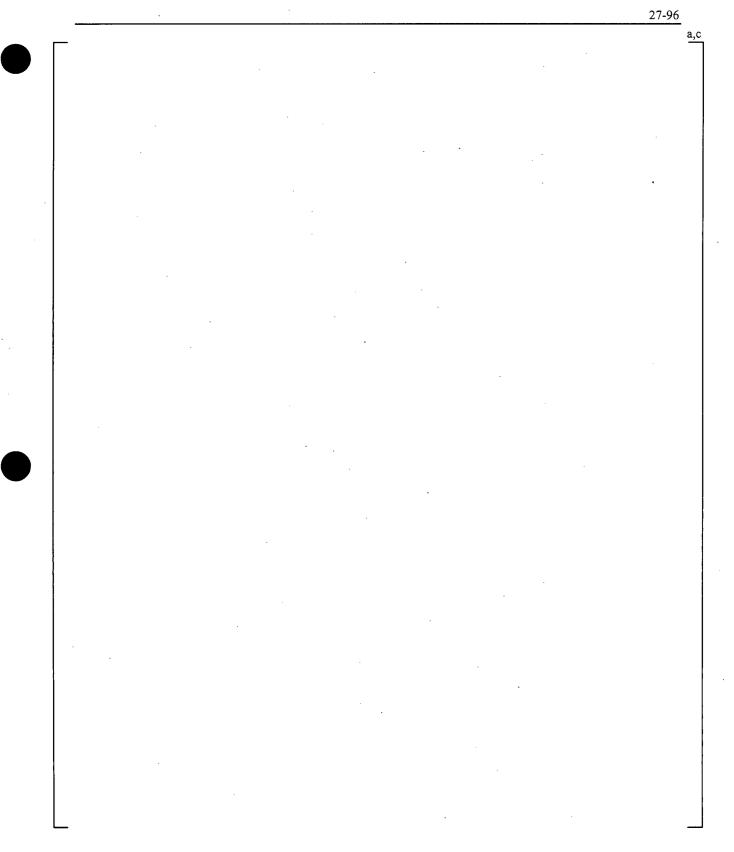


Figure 27.3.1-4 Pump Side Break Flow, DLW LBLOCA Reference Transient



Figure 27.3.1-5 Lower Plenum Collapsed Liquid Level, DLW LBLOCA Reference Transient

WCAP-16996-NP

27-97

a,c

27-98 a,c

Figure 27.3.1-6

Vapor Mass Flow in Hot Assembly Near PCT Elevation, DLW LBLOCA Reference Transient

WCAP-16996-NP

a,c

# Figure 27.3.1-7 RCS Pressure, DLW LBLOCA Reference Transient

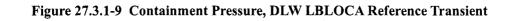
WCAP-16996-NP

a,c

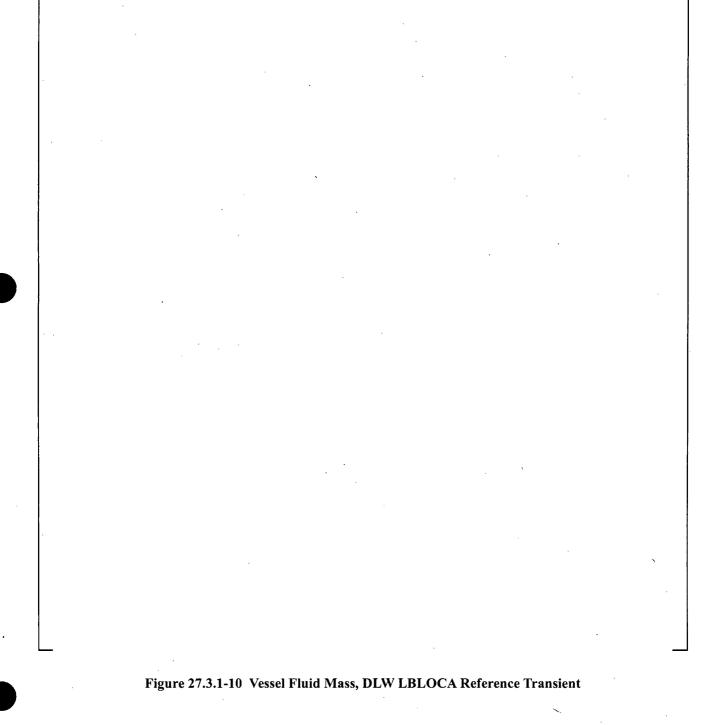


WCAP-16996-NP

a,c



a,c



2	7-	ŀ	03

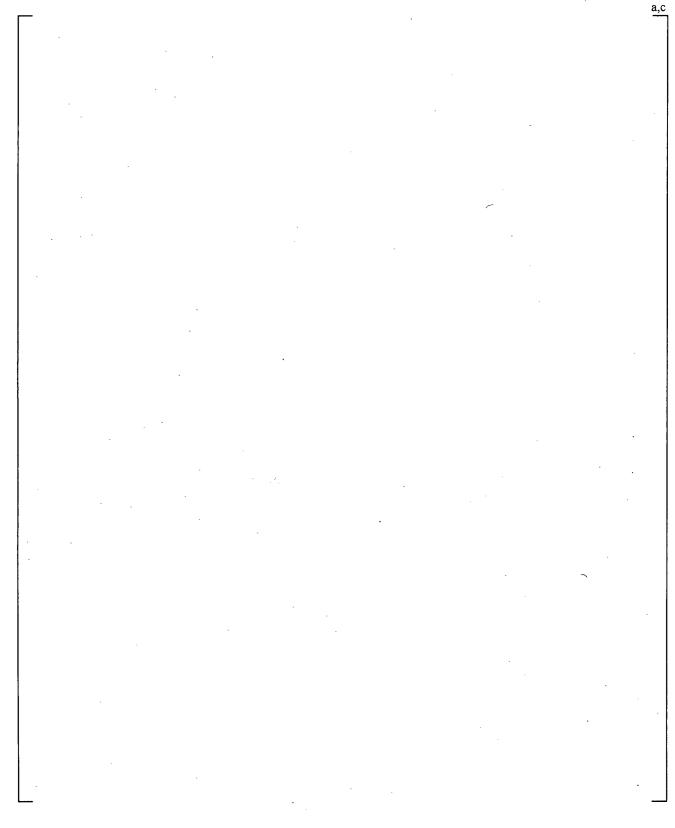
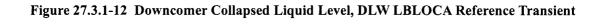
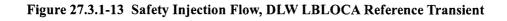


Figure 27.3.1-11 Core Collapsed Liquid Levels, DLW LBLOCA Reference Transient

a,c



a,c



# 27.3.2 DLW Intermediate Break Reference Transient Description

The DLW intermediate break reference transient used the conditions listed in Table 26.3-1. The reference intermediate break is a split break of the cold leg pipe with uncertainty attributes at representative (model as coded) values and a break area consistent with a 12-inch diameter hole. [

As stated in Section 2.3.1.3, an intermediate break is classified by a monotonic depressurization, or a lack of pressure stabilization associated with small breaks, and a lack of significant ECCS bypass brought about by steam upflow in the downcomer in large breaks. As a result, effective core recovery is expected early in the transient due to largely uninhibited accumulator flow. Historically, intermediate breaks have been shown to be non-limiting as a consequence. The intermediate break LOCA transient can be divided into time periods in which specific phenomena are occurring, as discussed below.

### 1. Blowdown/Depressurization

]^{a,c}

Initially, the break flow is high and single phase at the beginning of the blowdown phase (Figures 27.3.2-1 and 27.3.2-2). Break flow reduces as the flow to the break becomes two-phase, and consequently the depressurization rate also decreases (Figure 27.3.2-3). Flashing in the vessel results from the RCS depressurization, and collapsed liquid levels in the core and downcomer drop (Figures 27.3.2-4 and 27.3.2-5). [

]^{a,c}

#### 2. Accumulator Injection

Once the RCS pressure reaches the accumulator check valve pressure setpoint, accumulator flow rapidly refills the majority of the lost vessel inventory (Figures 27.3.2-8 and 27.3.2-9). ECCS bypass is low, as the core and downcomer fill with nearly the entire volume of the accumulator liquid. After the accumulators have emptied, ECCS injection is reduced to a minimal amount corresponding with the high-head safety injection (HHSI) system (Figure 27.3.2-10). This results in a period of vessel fluid mass depletion through boiling within the vessel, as the HHSI is not sufficient to make up for the break flow, which continues as the vessel depressurizes.

#### 3. SI Injection

This phase begins as the low-head safety injection (LHSI) system is initiated (Figure 27.3.2-10). The RCS continues to depressurize, resulting in a continually increasing amount of SI flow injection from the LHSI system. Vessel fluid inventory depletion is halted nearly immediately as the total injected flow becomes greater than that lost through the break (Figure 27.3.2-11).

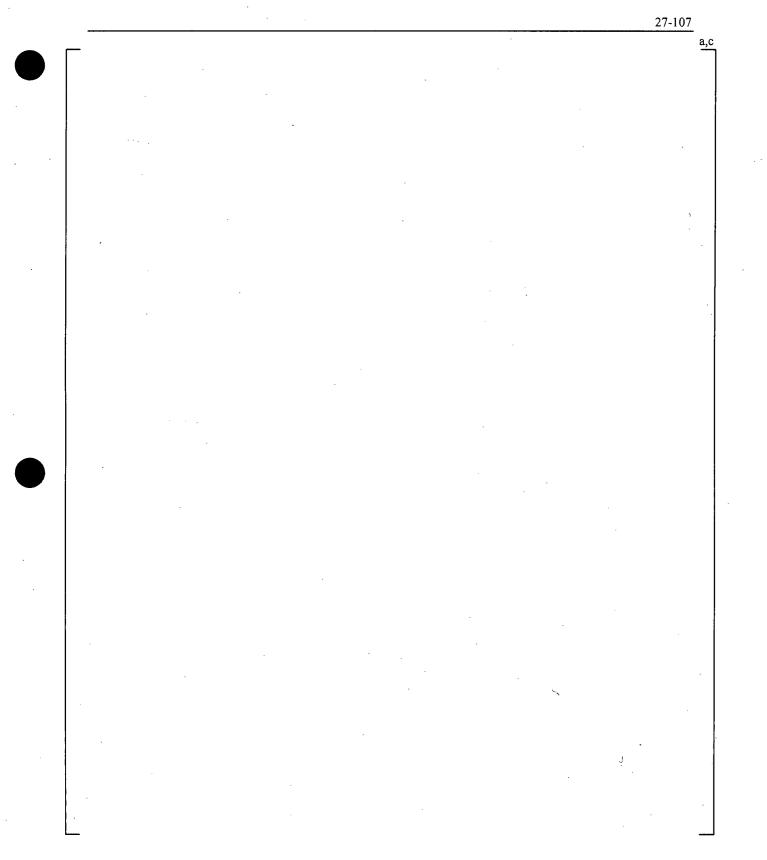


Figure 27.3.2-1 Break Flow, DLW IBLOCA Reference Transient

WCAP-16996-NP

27-108 a,c

Figure 27.3.2-2 Void Fraction at the Break, DLW IBLOCA Reference Transient

WCAP-16996-NP

a,c

Figure 27.3.2-3 RCS Pressure, DLW IBLOCA Reference Transient

WCAP-16996-NP

a,c

Figure 27.3.2-4

Core Collapsed Liquid Levels, DLW IBLOCA Reference Transient (2=Hot Assembly, 3=Guide Tube, 4=OH/SC/SM, 5=Low Power)

WCAP-16996-NP

a,c

Figure 27.3.2-5 Downcomer Collapsed Liquid Levels, DLW IBLOCA Reference Transient

WCAP-16996-NP

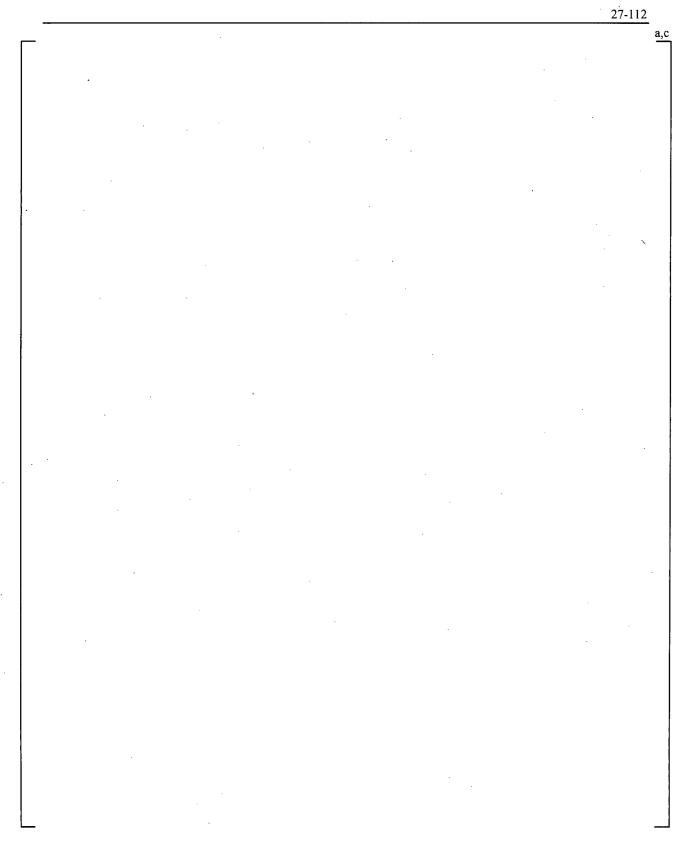


Figure 27.3.2-6 Peak Cladding Temperatures, DLW IBLOCA Reference Transient

WCAP-16996-NP

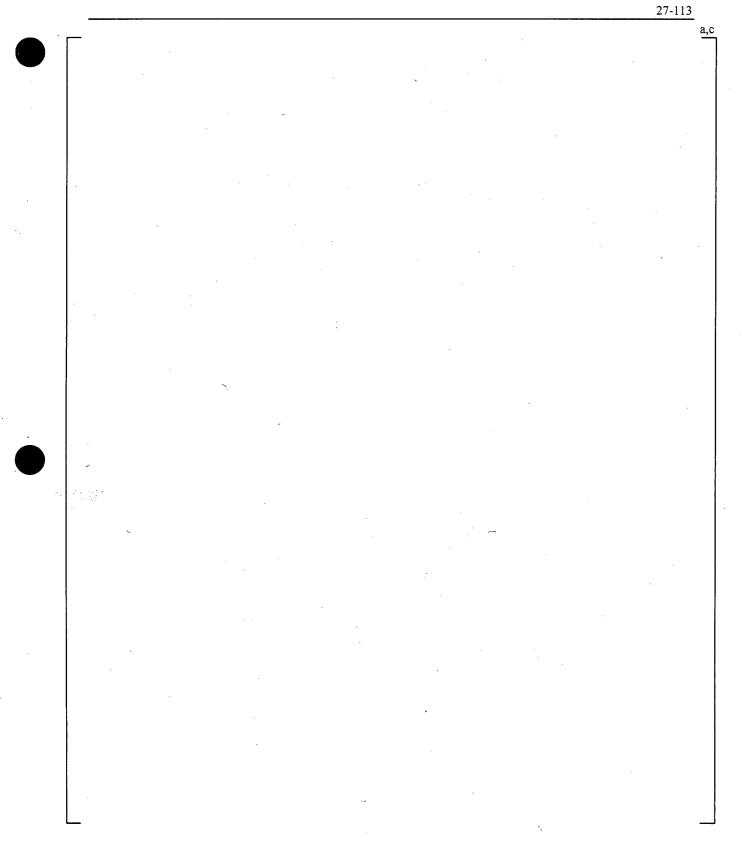


Figure 27.3.2-7 Vapor Flowrate in Hot Assembly Channel, DLW IBLOCA Reference Transient

a,c

# Figure 27.3.2-8 Accumulator Flow, DLW IBLOCA Reference Transient

WCAP-16996-NP



a,c

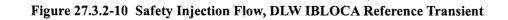
Figure 27.3.2-9 Vessel Fluid Mass, DLW IBLOCA Reference Transient

WCAP-16996-NP

`

2	7-	1	1	6

a,c



a,c

Figure 27.3.2-11 Safety Injection and Break Flow, DLW IBLOCA Reference Transient

WCAP-16996-NP .

## 27.3.3 DLW Small Break Reference Transient Description

The DLW small break reference transient used the conditions listed in Table 26.3-1. The reference small break is a split break of the cold leg pipe with uncertainty attributes at representative (model as coded) values and a break area consistent with a 3-inch diameter hole. [

The small break LOCA transient can be divided into time periods in which specific phenomena are occurring, as discussed below.

#### 1. Blowdown

The rapid depressurization of the RCS coincides with single-phase liquid flow through the break as shown in Figure 27.3.3-1. Following the reactor trip, initiated on a low-low pressurizer pressure setpoint, high pressure safety injection flow begins after the setpoint is reached with some delay (Figure 27.3.3-2). Phase separation begins in the upper head, upper plenum, and hot legs near the end of this period until the entire RCS eventually reaches saturation, ending the rapid depressurization slightly above the steam generator secondary side pressure near the main steam safety valve (MSSV) setpoint [ ]^{a,c}.

]^{a,c}

### 2. Natural Circulation

This quasi-equilibrium phase persists [ ]^{a,c} as the RCS pressure remains slightly above the secondary side pressure (Figure 27.3.3-3). The system drains from the top down (Figure 27.3.3-4), and while significant mass is continually lost through the break (Figure 27.3.3-5), the vapor generated in the core is trapped in the upper regions by the liquid remaining in the crossover leg loop seals. [

]^{a,c}

### 3. Loop Seal Clearance

As the system drains, the liquid level in the downhill side of the pump suction piping becomes depressed to the bottom of the loop seal, allowing the steam trapped during the natural circulation phase to vent to the break (Figures 27.3.3-8, 27.3.3-9, and 27.3.3-10). The break flow and the flow through the RCS loops become primarily vapor (Figure 27.3.3-1), [

]^{a,c}. Relief of a static head imbalance allows for a quick but temporary recovery of liquid levels in the core (Figure 27.3.3-6).

## 4. Boil-Off

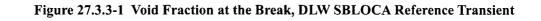
With a vapor vent path established, the RCS depressurizes at a rate determined by the critical flow, which continues to be primarily single phase (Figures 27.3.3-3 and 27.3.3-1).

]^{a,c}

# 5. Core Recovery

The RCS pressure continues to fall, and once it reaches that of the accumulator check valve setpoint, the introduction of additional ECCS water (Figure 27.3.3-11) replenishes the vessel inventory (Figure 27.3.3-12) and recovers the core mixture level. The transient is declared over as the break flow is compensated for with injected flow (Figure 27.3.3-13).

a,c



a,c

Figure 27.3.3-2 Safety Injection Flow, DLW SBLOCA Reference Transient

WCAP-16996-NP

a,c

Figure 27.3.3-3

-3 RCS and Steam Generator Secondary Side Pressure, DLW SBLOCA Reference Transient

WCAP-16996-NP

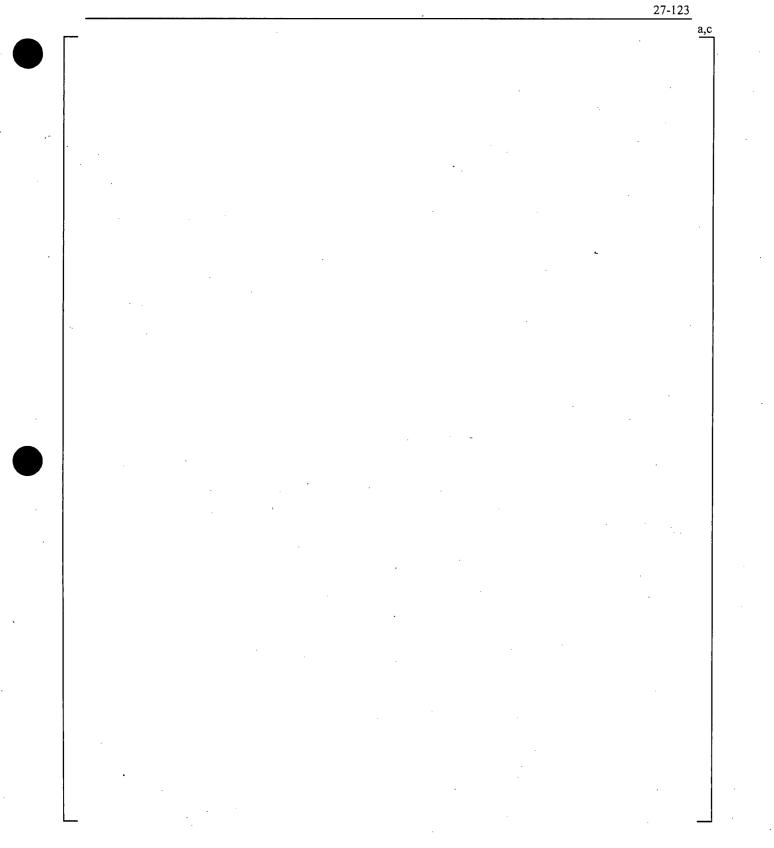


## Figure 27.3.3-4 Upper Head Collapsed Liquid Level, DLW SBLOCA Reference Transient

WCAP-16996-NP



a,c

# Figure 27.3.3-5 Break Flow, DLW SBLOCA Reference Transient

WCAP-16996-NP

November 2010 Revision 0

ì

a,c

Figure 27.3.3-6

-6 Core Collapsed Liquid Levels, DLW SBLOCA Reference Transient (2=Hot Assembly, 3=Guide Tube, 4=OH/SC/SM, 5=Low Power)

WCAP-16996-NP

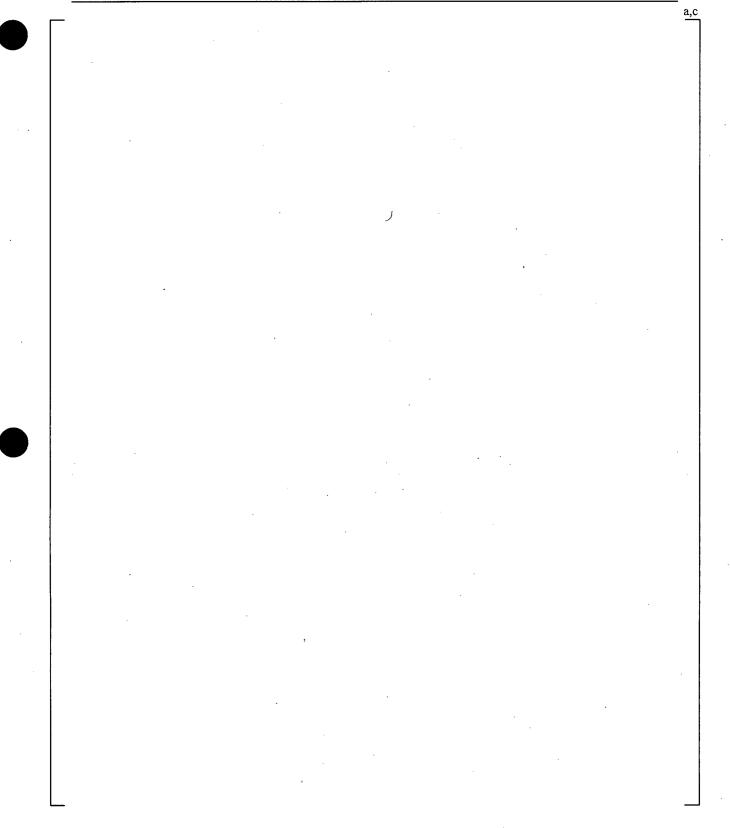


Figure 27.3.3-7 Hot Rod Cladding Temperature, DLW SBLOCA Reference Transient

WCAP-16996-NP

2<u>7-127</u>

a,c

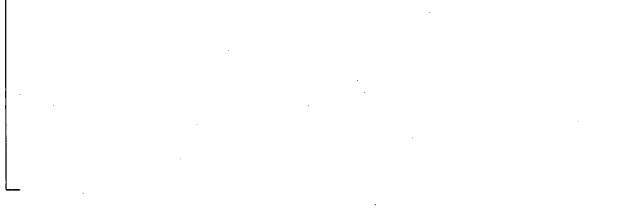


Figure 27.3.3-8 Loop 1 Loop Seal Differential Pressure, DLW SBLOCA Reference Transient

WCAP-16996-NP

Figure 27.3.3-9 Loop 2 Loop Seal Differential Pressure, DLW SBLOCA Reference Transient

WCAP-16996-NP

November 2010 Revision 0

27-128

Figure 27.3.3-10 Loop 3 Loop Seal Differential Pressure, DLW SBLOCA Reference Transient

WCAP-16996-NP

27-129

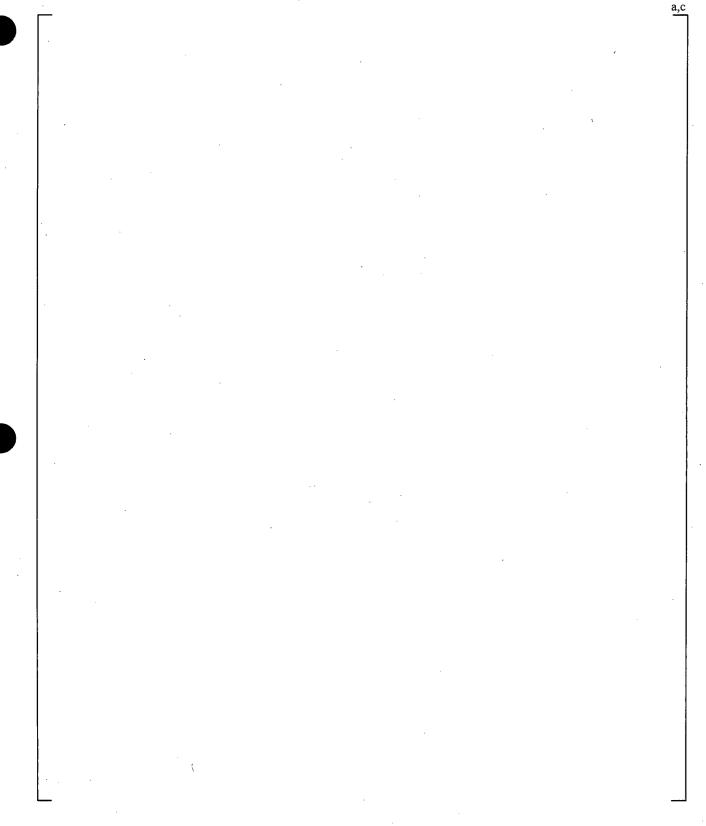


Figure 27.3.3-11 Accumulator Flow, DLW SBLOCA Reference Transient

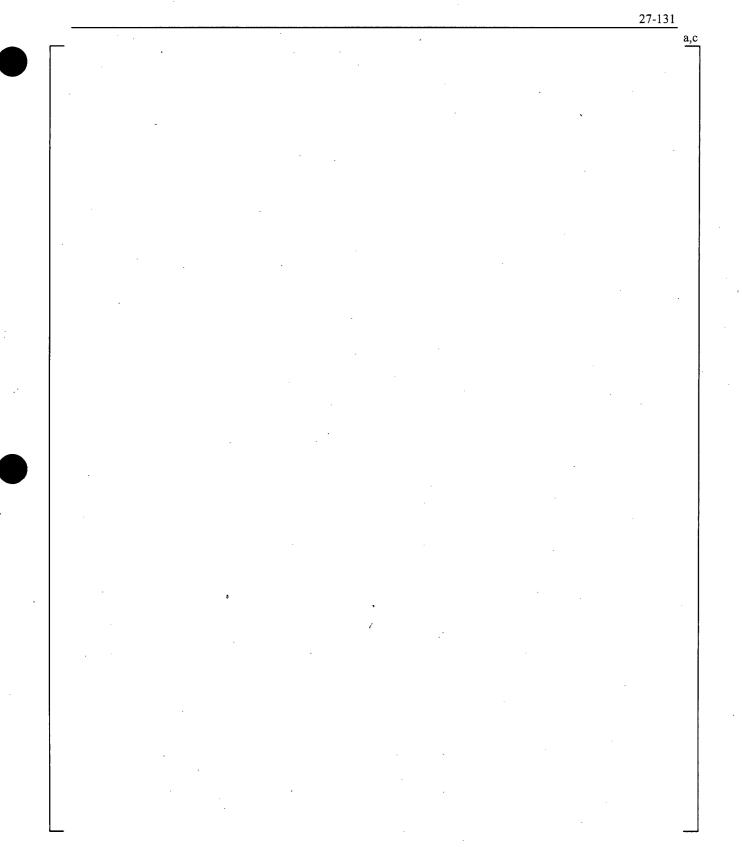


Figure 27.3.3-12 Vessel Fluid Mass, DLW SBLOCA Reference Transient

WCAP-16996-NP

ىر



.

WCAP-16996-NP

27-132

## 28 SCOPING AND SENSITIVITY STUDIES

In this section, the pilot plant models for V. C. Summer (CGE) and Beaver Valley Unit 1 (DLW) are exercised using the <u>W</u>COBRA/TRAC-TF2 code to determine the effect of variations in key LOCA parameters on the small and large break reference transients from Section 27. As was shown in Section 27, breaks typically classified as intermediate in size are less limiting than small and large breaks, and therefore are not considered in these scoping studies. The intent of the studies is to exercise the <u>W</u>COBRA/TRAC-TF2 plant models, evaluate the effects of parameters of interest to demonstrate reasonable behavior, and to determine the appropriate treatment of several parameters for the plant analysis. For those parameters for which the treatment is determined within this section, a summary of those methodology decisions supported by scoping studies is provided below.

]^{a,c}

]^{a,c}

]^{a,c}

#### **Offsite Power Availability**

Section 28.1.2 shows that [

#### Limiting Offsite Power Scenario

[

#### **Operator Action**

The availability of offsite power affects [

#### Limiting Operator Action

L

#### **Accumulator Elevation**

Section 28.1.5 shows that [

]^{a,c}

WCAP-16996-NP

November 2010 Revision 0

]^{a,c}

## Limiting Accumulator Elevation

[

#### **Break Location**

Section 28.2.6 shows that [

]^{a,c}

]^{a,c}

]^{a,c}

]^{a,c}

## Limiting Break Location

## **Break Orientation**

The ROSA break orientation study in Section 21.7 showed [

Limiting Split Break Orientation

[ ]^{a,c}

## **Steam Generator Tube Plugging**

Section 28.1.6 demonstrates [  $]^{a,c}$  and Section 28.2.9 [

## Limiting Steam Generator Tube Plugging

]^{a,c}

]^{a,c}

WCAP-16996-NP

[

## 28.1 LARGE BREAK SCOPING STUDY RESULTS

## **28.1.1** Axial Power Distributions – LBLOCA

As part of the uncertainty analysis, the axial power distribution [

transient of Section 27.2.1 and the DLW LBLOCA reference transient of Section 27.3.1 both assumed a top-skewed power distribution, which is expected to be more limiting for a nominal double-ended guillotine break due to the timing of the PCT during reflood with an upward-progressing quench front. A sensitivity case is examined for each plant where the axial power distribution is skewed more toward the bottom of the core.

## 28.1.1.1 V. C. Summer (CGE)

Figure 28.1.1-1 shows the axial power distribution used for this sensitivity compared with the reference transient. Figure 28.1.1-2 shows [

# ]^{a,c}

In addition to affecting PCT and PCT locations during blowdown, [

## -

]^{a,c}

## 28.1.1.2 Beaver Valley Unit 1 (DLW)

Overall, the behavior observed here is similar to that shown in the CGE sensitivity. Figure 28.1.1-7 shows the axial power distribution used for this sensitivity compared with the reference transient. Figure 28.1.1-8 shows [

]^{a,c}

]^{a,c}

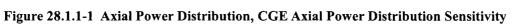
The nature of early reflood again affected by the power distributed in the lower elevations, [

WCAP-16996-NP

]^{a,c} The CGE LBLOCA reference

## 28.1.1.3 Conclusions

The axial power distribution affects cladding temperatures throughout the transient, [ $]^{a,c}$  as described in Section 29.4.1.2.



a,c

Figure 28.1.1-2 Rod 1 Peak Cladding Temperatures, CGE Axial Power Distribution Sensitivity



Figure 28.1.1-3 Peak Cladding Temperature Location, CGE Axial Power Distribution Sensitivity

WCAP-16996-NP

November 2010 Revision 0

28-7

a,c

Figure 28.1.1-4 Lower Plenum Collapsed Liquid Level, CGE Axial Power Distribution Sensitivity

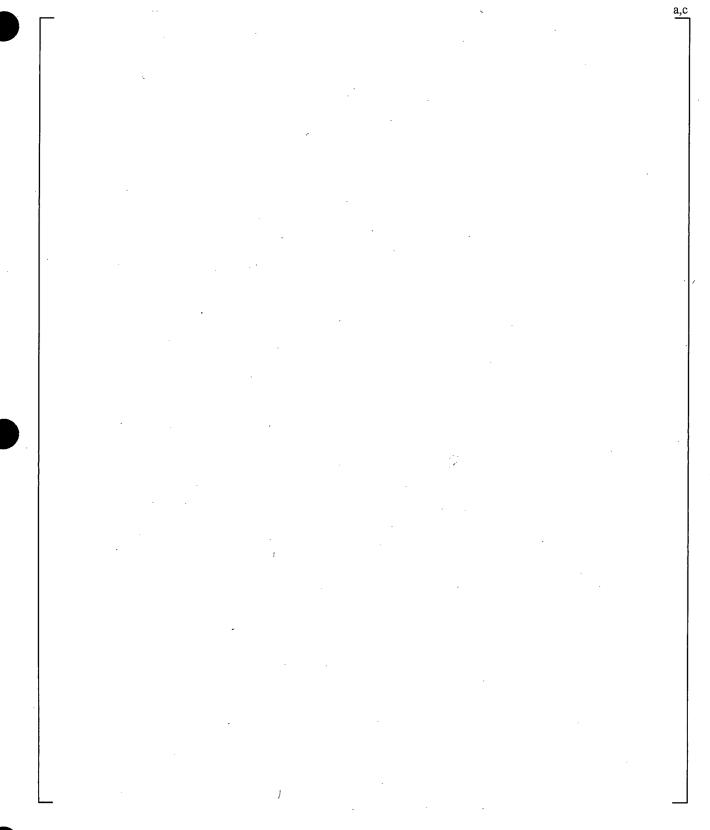
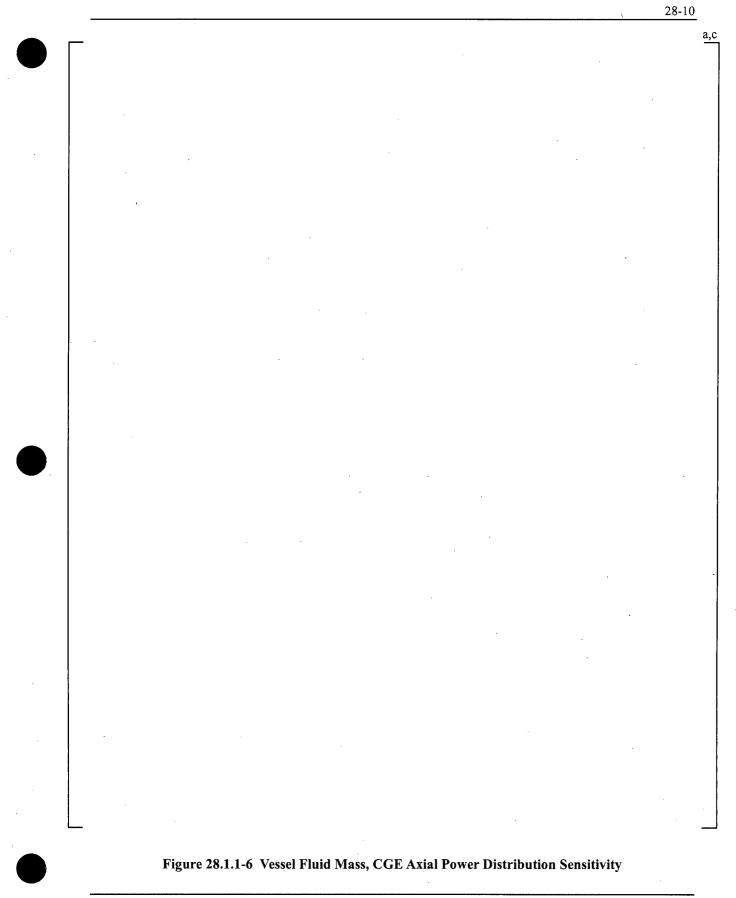


Figure 28.1.1-5 Hot Assembly Collapsed Liquid Level, CGE Axial Power Distribution Sensitivity

WCAP-16996-NP

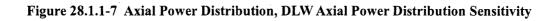
November 2010 Revision 0

28-9



WCAP-16996-NP

a,c



.

WCAP-16996-NP

1

a,c



Figure 28.1.1-8 Peak Cladding Temperatures, DLW Axial Power Distribution Sensitivity

WCAP-16996-NP

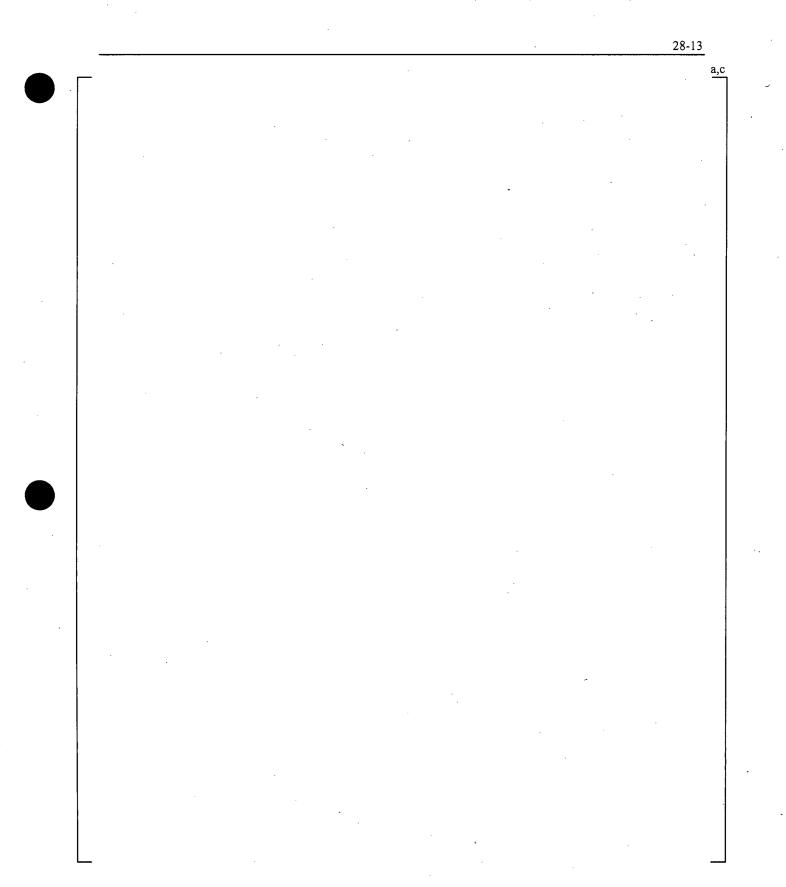


Figure 28.1.1-9 Peak Cladding Temperature Location, DLW Axial Power Distribution Sensitivity

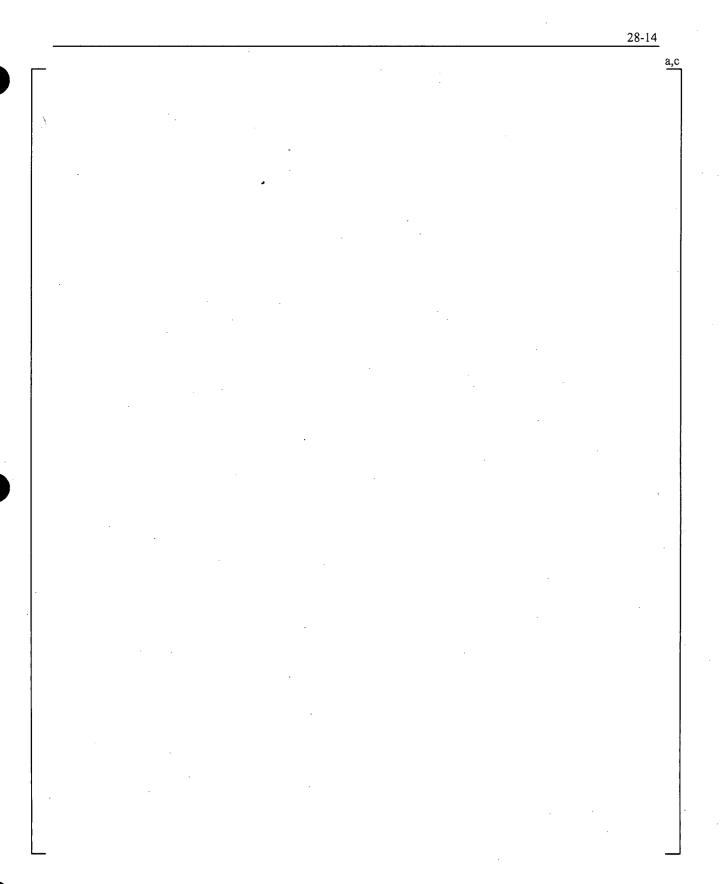


Figure 28.1.1-10 Lower Plenum Collapsed Liquid Level, DLW Axial Power Distribution Sensitivity

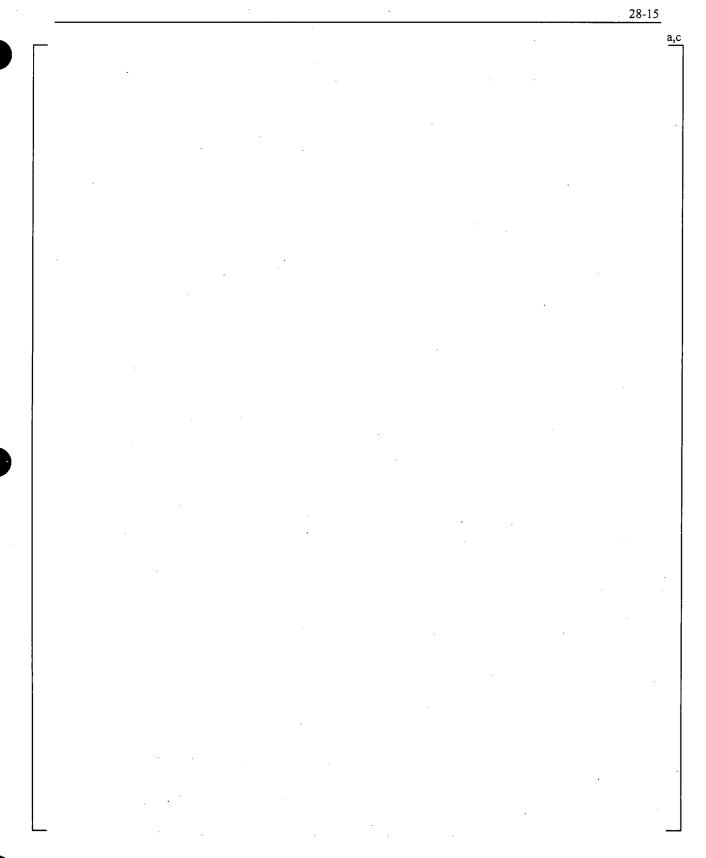
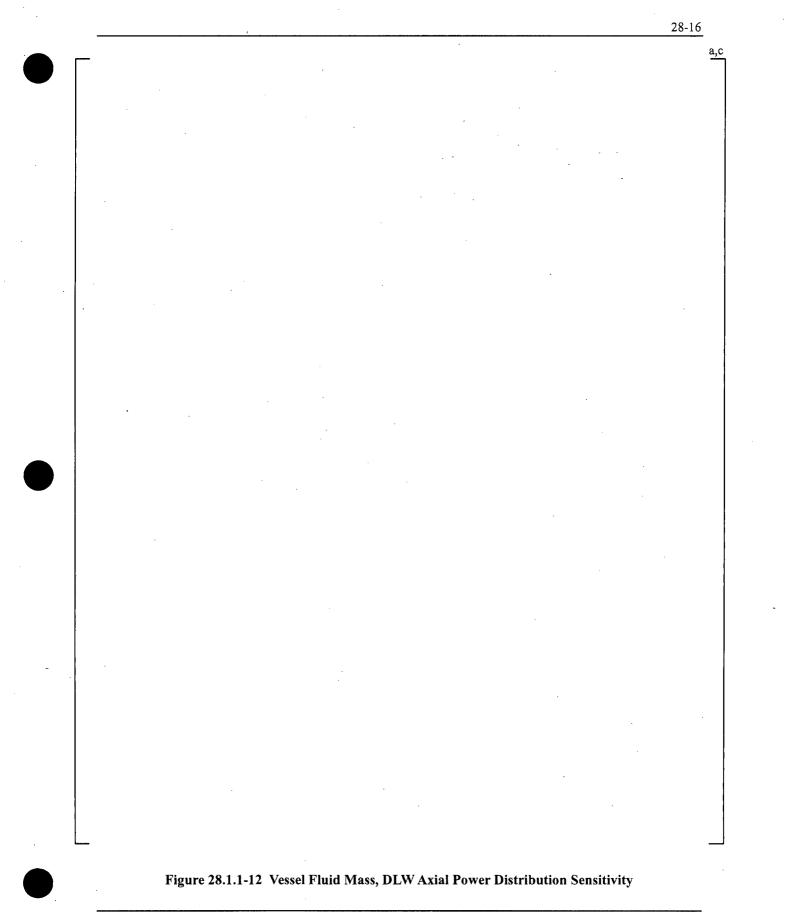


Figure 28.1.1-11 Hot Assembly Collapsed Liquid Level, DLW Axial Power Distribution Sensitivity



## 28.1.2 Offsite Power Availability – LBLOCA

The availability of offsite power affects the timing of the reactor coolant pump trip and the initiation of safety injection flow following a large break LOCA. With a loss of offsite power (LOOP), there is an extended delay in safety injection. Also with LOOP, the RCP trip is modeled [

]^{a,c} With offsite power available (OPA), the pumps continue to rotate at a fixed speed until operator trip.

#### 28.1.2.1 V. C. Summer (CGE)

With a loss of offsite power (LOOP), there is extended delay in safety injection, which for V. C. Summer results in a delay time of [ ]^{a,c} (Figure 28.1.2-1). For the LOOP case, Figure 28.1.2-2 shows the pump coastdown in the intact loops, while Figure 28.1.2-3 shows the predicted acceleration of the pump in the broken loop.

For this case, [

## 28.1.2.2 Beaver Valley Unit 1 (DLW)

For Beaver Valley Unit 1, the delay in safety injection resulting from a LOOP is [

]^{a,c} (Figure 28.1.2-7) with OPA. For the LOOP case, Figure 28.1.2-8 shows the pump coastdown in the intact loops, while Figure 28.1.2-9 shows the acceleration of the pump in the broken loop.

]^{a,c}

For the DLW reference transient, [

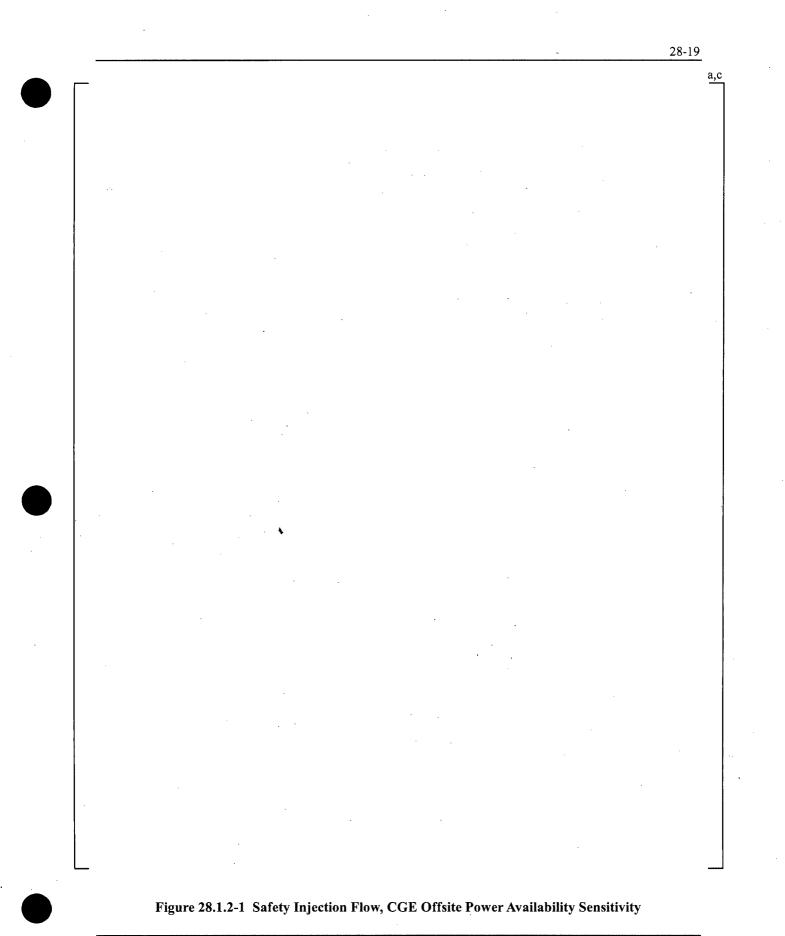
]^{a,c}

#### 28.1.2.3 Conclusions

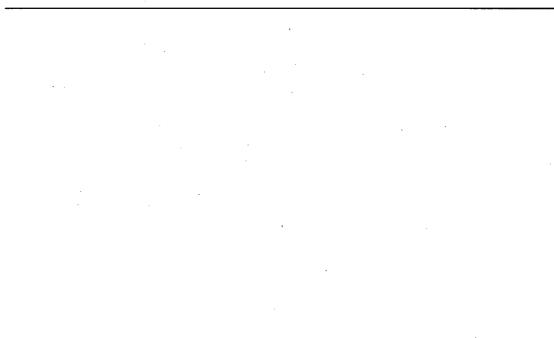
Since the availability of offsite power leads to some competing effects that affect the magnitude of blowdown cooling, the behavior of the liquid insurge following refill, and the conditions leading to

]^{a,c}

# potential downcomer and lower plenum boiling, [



WCAP-16996-NP



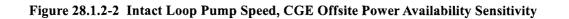


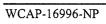






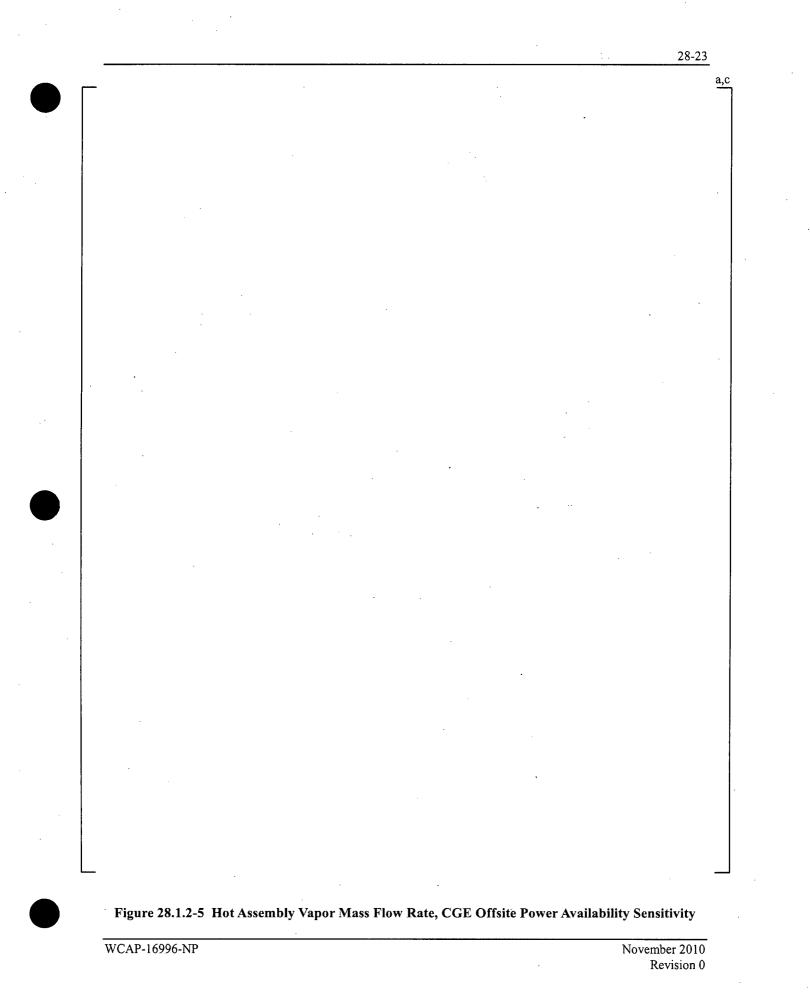


Figure 28.1.2-3 Broken Loop Pump Speed, CGE Offsite Power Availability Sensitivity

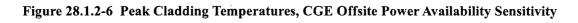


a,c

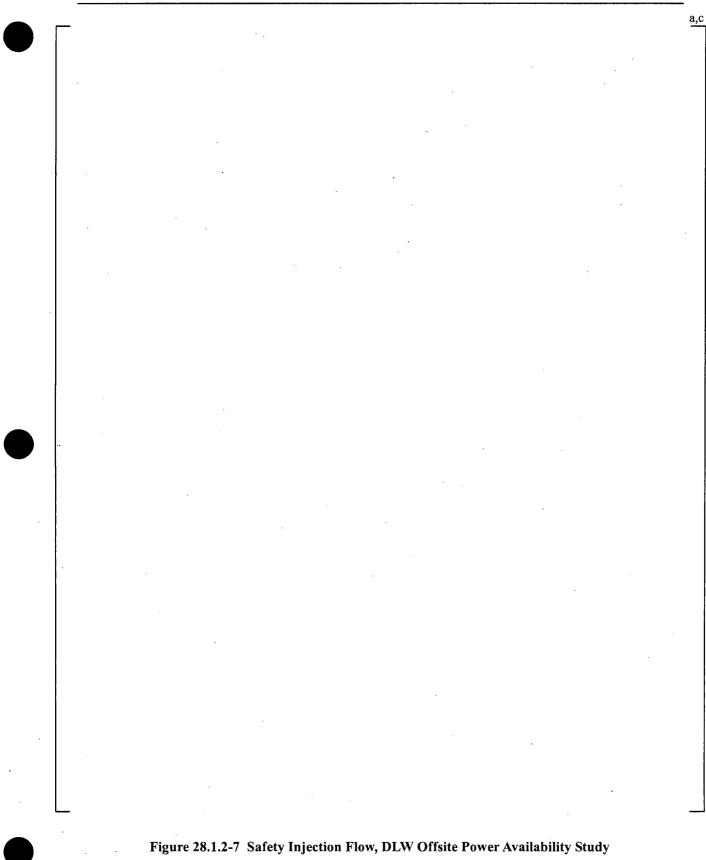
Accumulator and Safety Injection Flow Rates, CGE Offsite Power Availability Sensitivity Figure 28.1.2-4



a,c



ι,



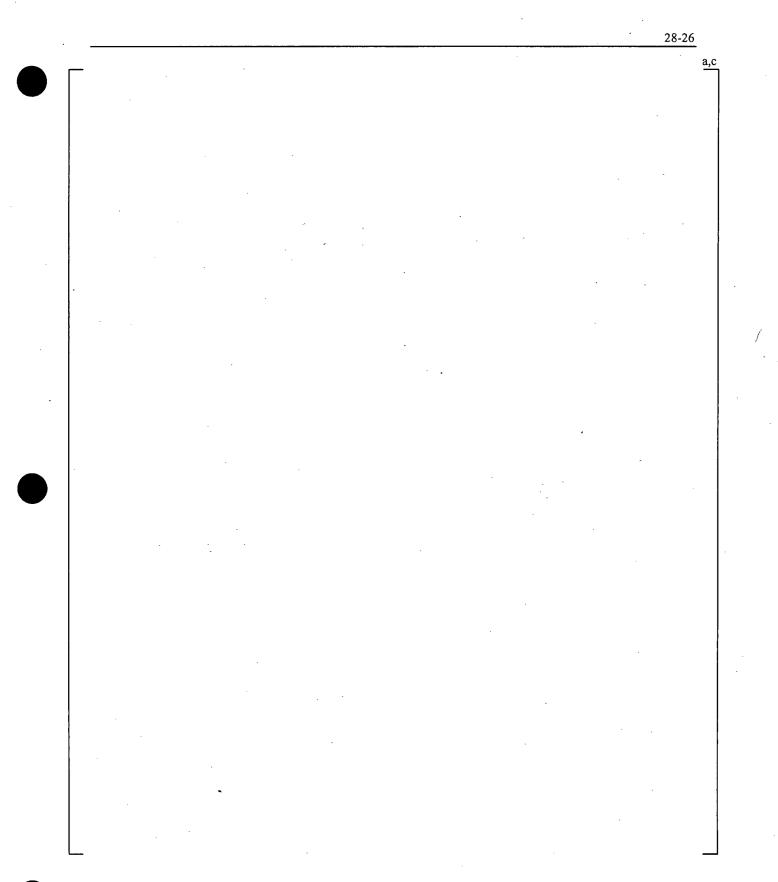
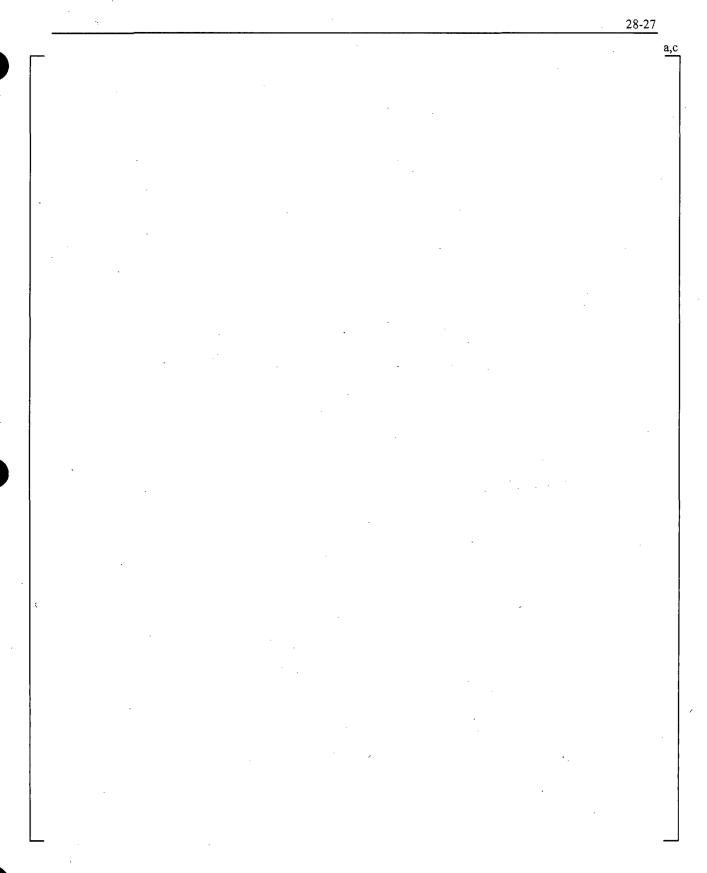
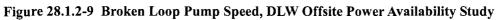
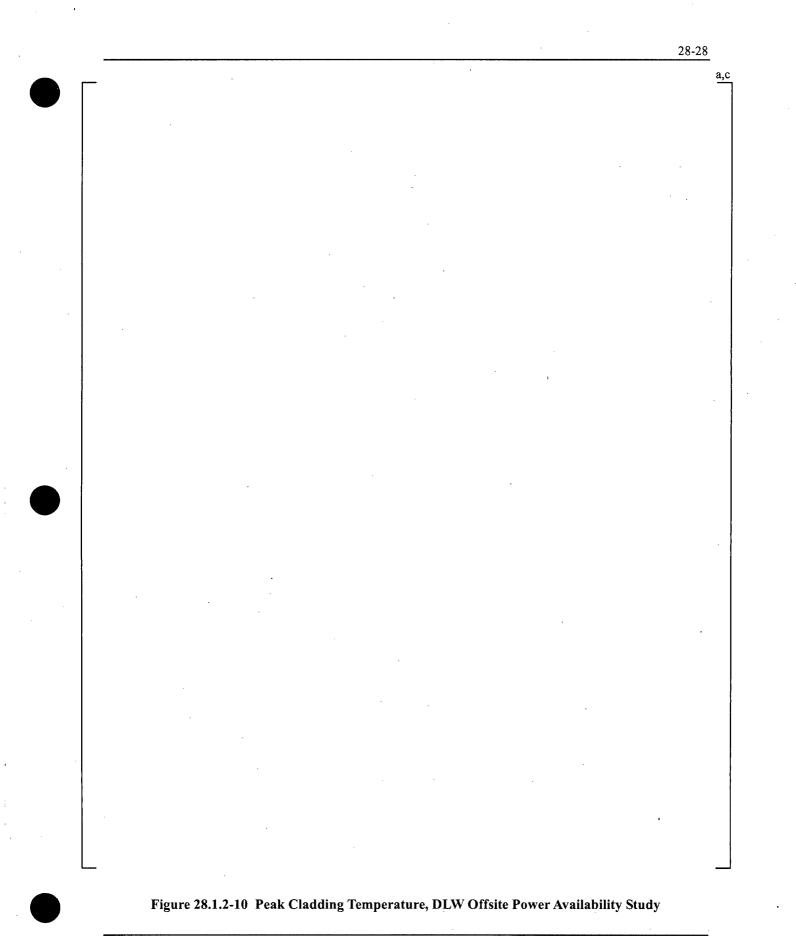


Figure 28.1.2-8 Intact Loop Pump Speed, DLW Offsite Power Availability Study

)







a,c

Figure 28.1.2-11 Hot Assembly Vapor Mass Flow Rate, DLW Offsite Power Availability Study

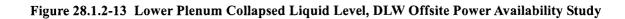
a,c

Figure 28.1.2-12 Lower Plenum Liquid Subcooling, DLW Offsite Power Availability Study

WCAP-16996-NP

November 2010 Revision 0

C



28-31

a,c

]^{a,c}

## 28.1.3 Time Step and Convergence Criteria Studies – LBLOCA

The large break spectra are executed here using a modified upper limit on the time step (DTMAX) during the blowdown/refill (prior to 100 seconds after break initiation) and reflood portions of the transient. The reference DTMAX strategy consists of [ $]^{a,c}$ .

The decrease and increase explored in this study is shown in Table 28.1.3-1.

#### 28.1.3.1 V. C. Summer (CGE)

Table 28.1.3-2 presents the peak cladding temperatures as calculated with the original and modified DTMAX. The thirteen large break transients from the LBLOCA break spectrum analysis (see Section 27.1.1.1; note that not all thirteen cases are presented there) were examined. The largest PCT difference seen when reducing the DTMAX limit [

The vessel fluid mass, PCT, and time step for the two cases showing the largest PCT difference, run004 and run007, are shown in Figure 28.1.3-1 through Figure 28.1.3-4. For both cases, [

#### ]^{a,c}

#### 28.1.3.2 Beaver Valley Unit 1 (DLW)

Table 28.1.3-3 presents the results of the DTMAX sensitivity study applied to the DLW LBLOCA break spectrum of Section 27.1.2.1. The largest difference from a DTMAX [

Figure 28.1.3-5 through Figure 28.1.3-8 show the vessel mass and PCT for the two cases with the largest PCT difference. [  $1^{a,c}$ 

28.1.3.3 Conclusions

The use of DTMAX upper limits on time step size [

 $]^{a,c}$ . The choice of DTMAX for the plant is discussed further in Section 29.3.3.

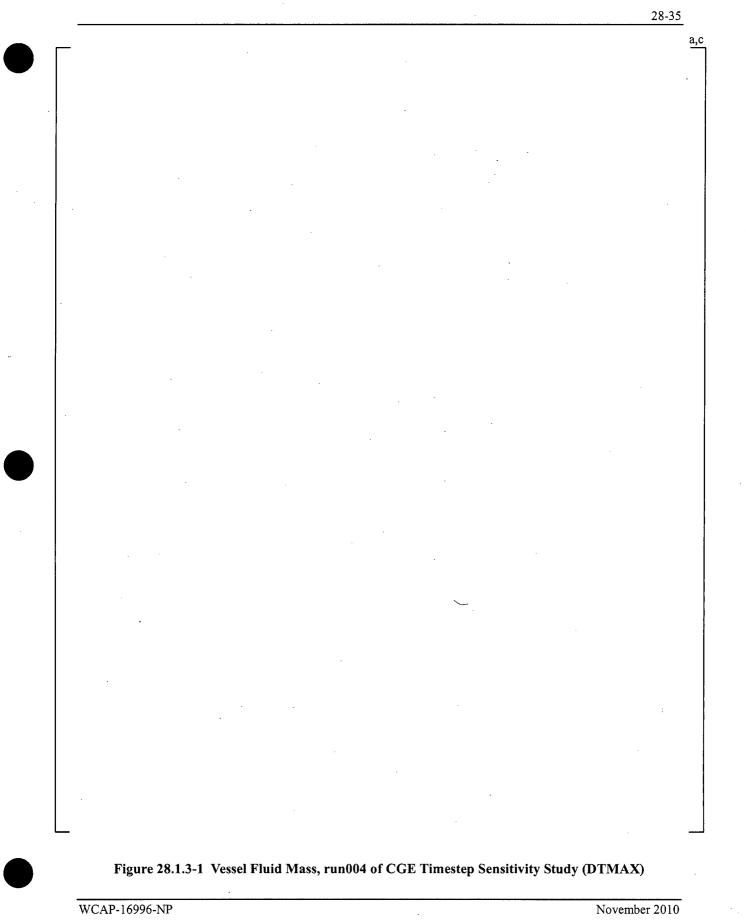


Table 28.1.3-1         DTMAX Values used in LBLOCA Timestep Sensitivity							
	·····						

		hen Varying DT	 T	, 	1
			-		
			 		1.
				, , ,, ,, ,, ,, ,, ,, ,, ,, ,, ,, ,, ,,	
	· · · ·				·
			4		
····.					

Table 28.1.3-3	PCT Results When Varying DTMAX, DLW LBLOCA Sensitivity								
	-					e			
		· ·							
					·				
						•			
r	×								

•

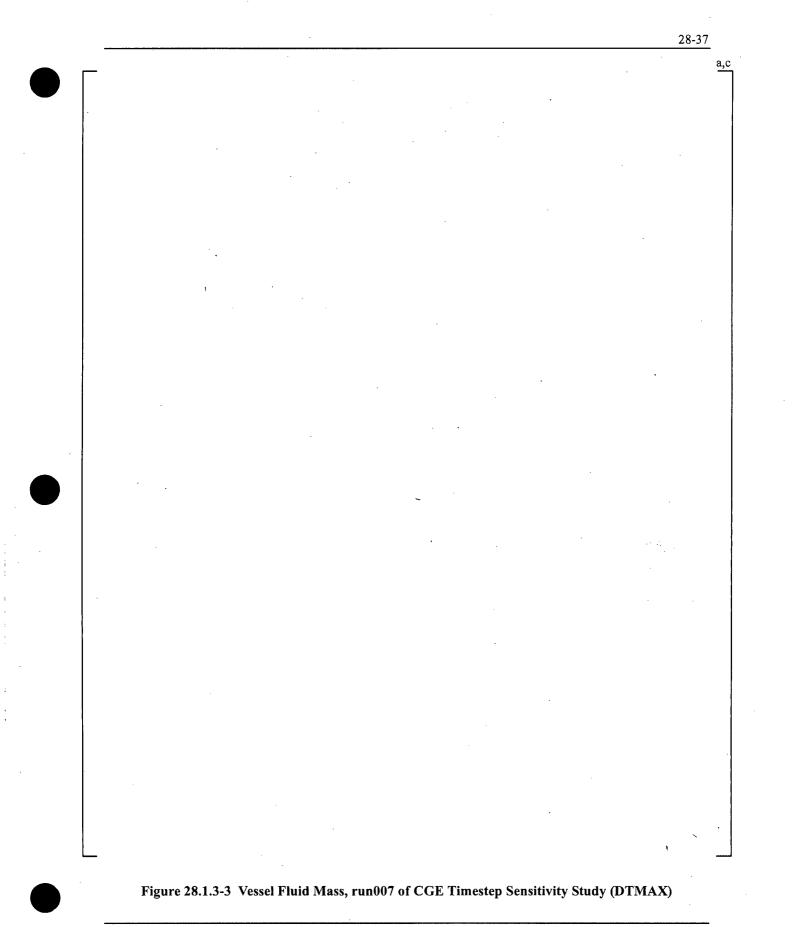


Revision 0



a,c

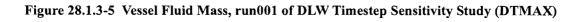
Figure 28.1.3-2 Peak Cladding Temperature, run004 of CGE Timestep Sensitivity Study (DTMAX)



a,c

Figure 28.1.3-4 Peak Cladding Temperature, run007 of CGE Timestep Sensitivity Study (DTMAX)

a,c



WCAP-16996-NP

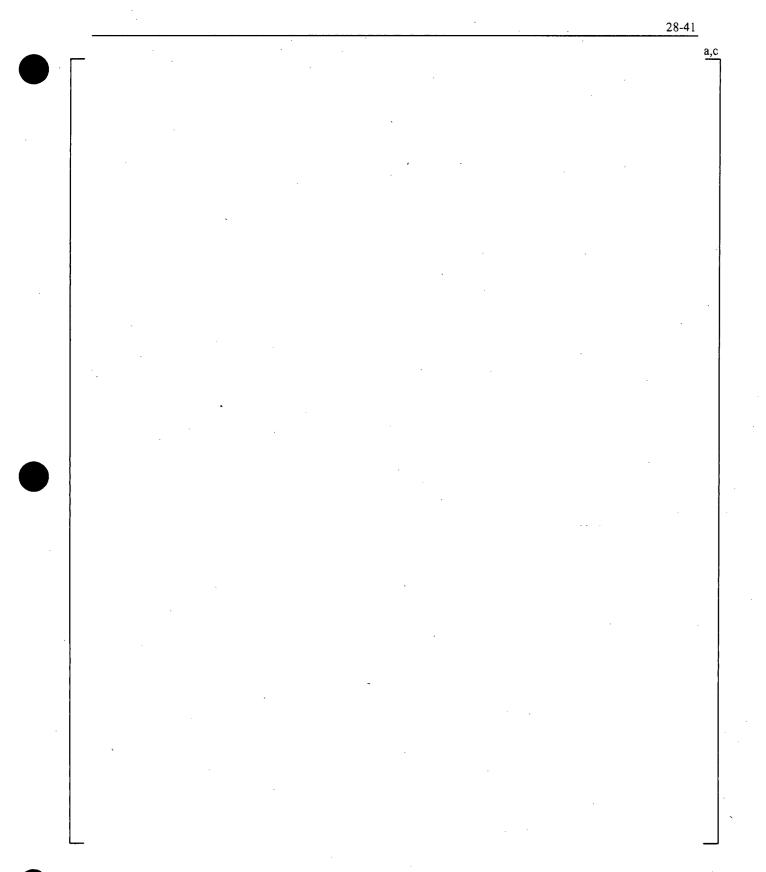
2



a,c

Figure 28.1.3-6 Peak Cladding Temperature, run001 of DLW Timestep Sensitivity Study (DTMAX)

WCAP-16996-NP



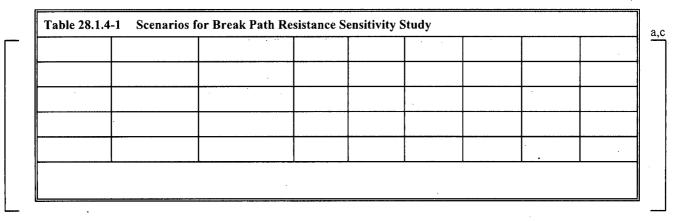


a,c

Figure 28.1.3-8 Peak Cladding Temperature, run004 of DLW Timestep Sensitivity Study (DTMAX)

## 28.1.4 Break Path Resistance – LBLOCA

To demonstrate that [



# 28.1.4.1 V. C. Summer (CGE)

[

WCAP-16996-NP

November 2010 Revision 0

]^{a,c}

~

## 28.1.4.2 Beaver Valley Unit 1 (DLW)

]^{a,c}

## 28.1.4.3 Conclusions

For a double-ended guillotine break, it has been shown that [

]^{a,c}. For a nominal split break with half the break area as the DEG break, [ $]^{a,c}$ 

WCAP-16996-NP

[_____]^{a,c}_____

· · · ·

7

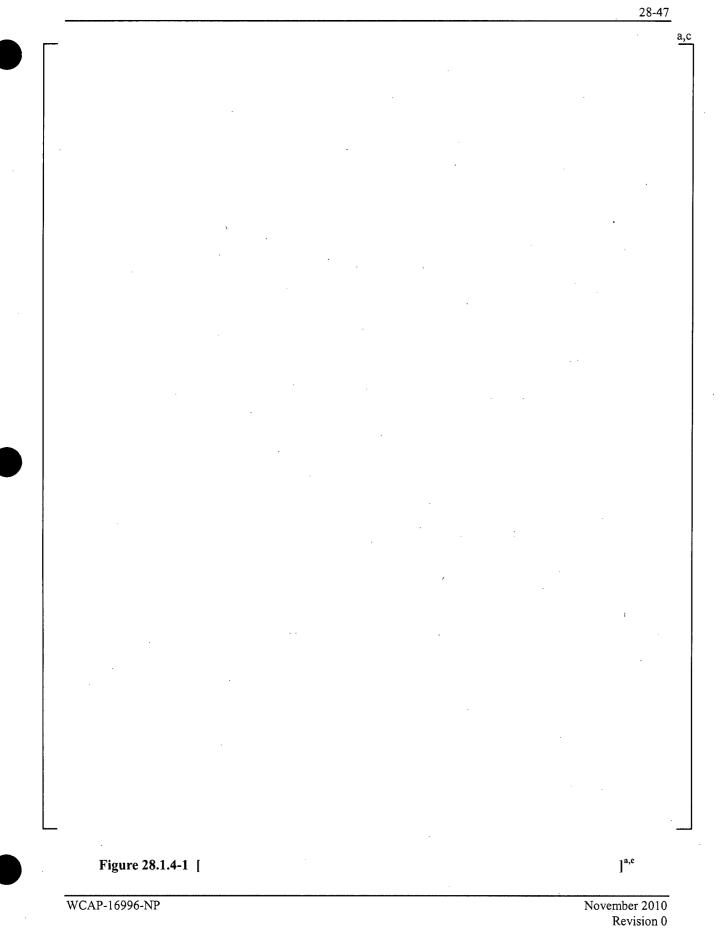
WCAP-16996-NP

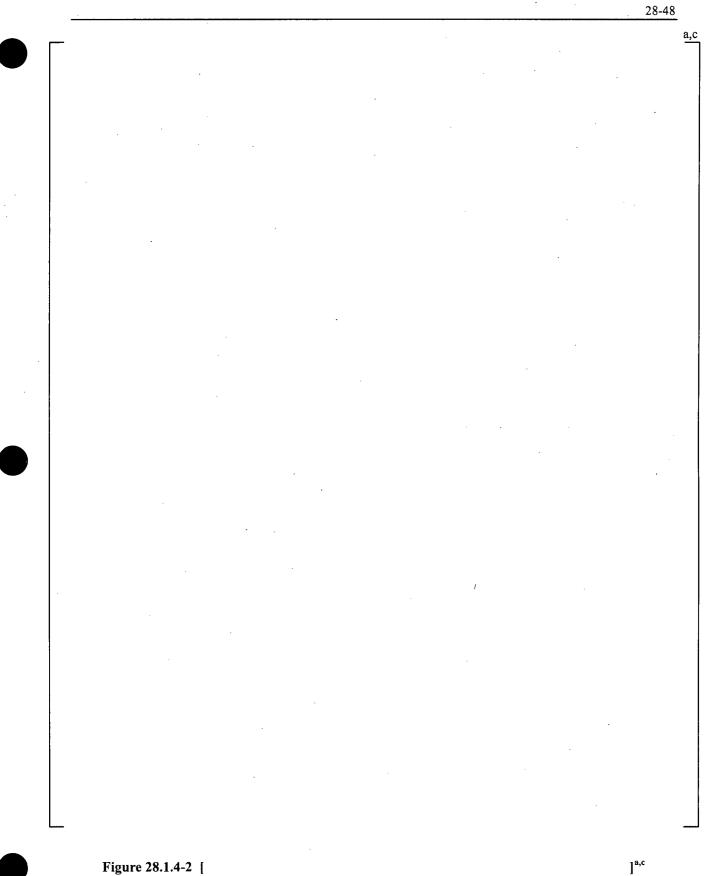
. .

.

. .

. ·





a,c

]^{a,c}

Figure 28.1.4-3 [

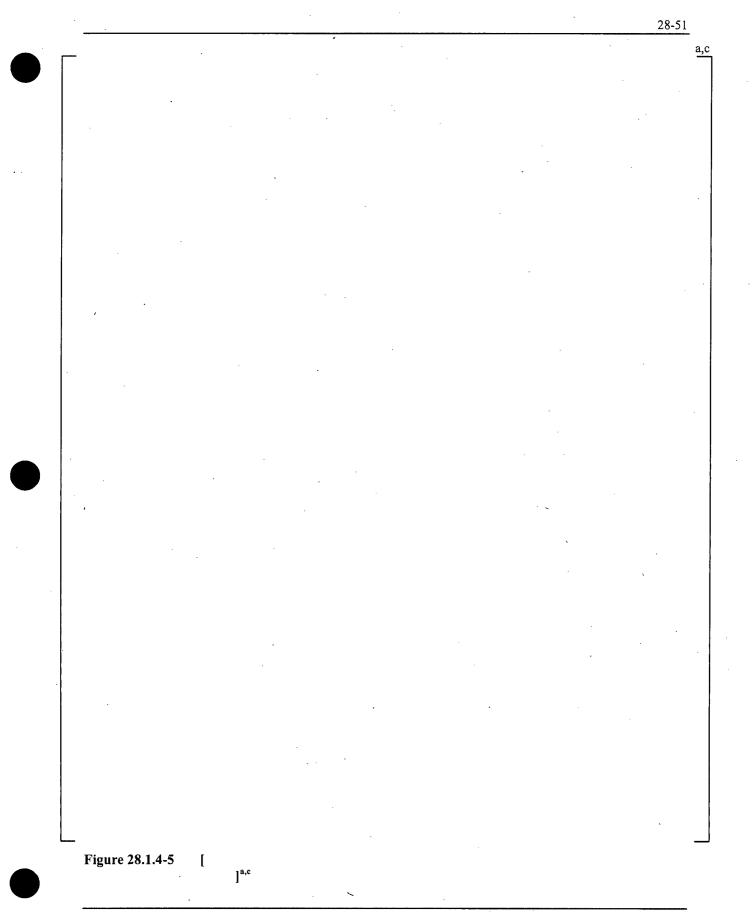
			. •						
		×							
	,				·				
			·						
				·					
			·						•
								·	
	e.								
									-
								•	
-				`					

Figure 28.1.4-4 [

]^{a,c}

WCAP-16996-NP

November 2010 Revision 0 a,c



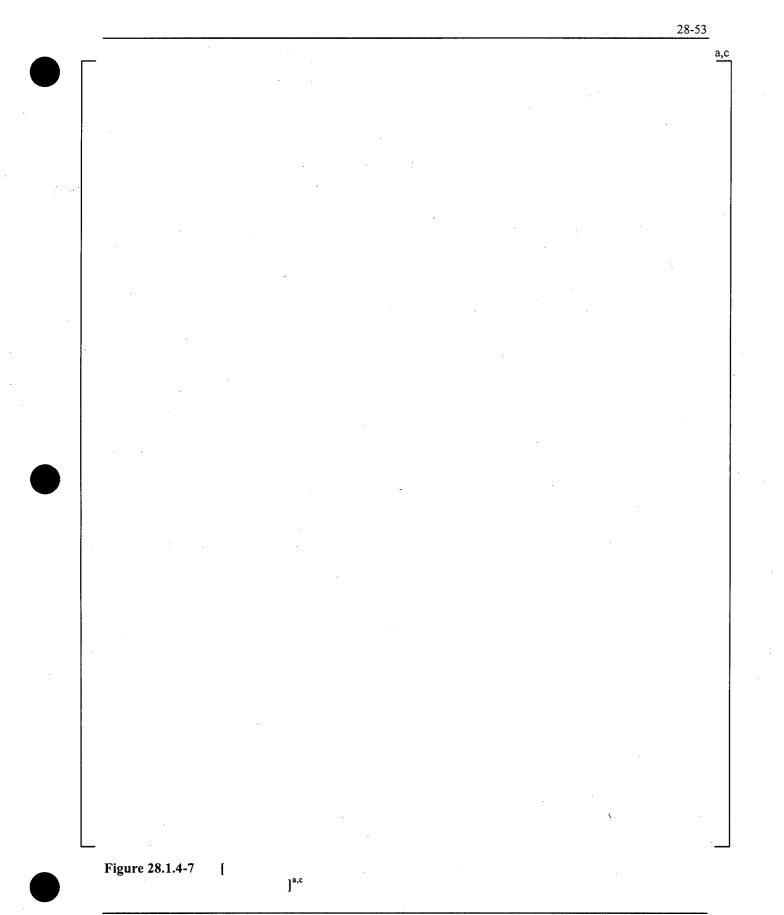
a,c

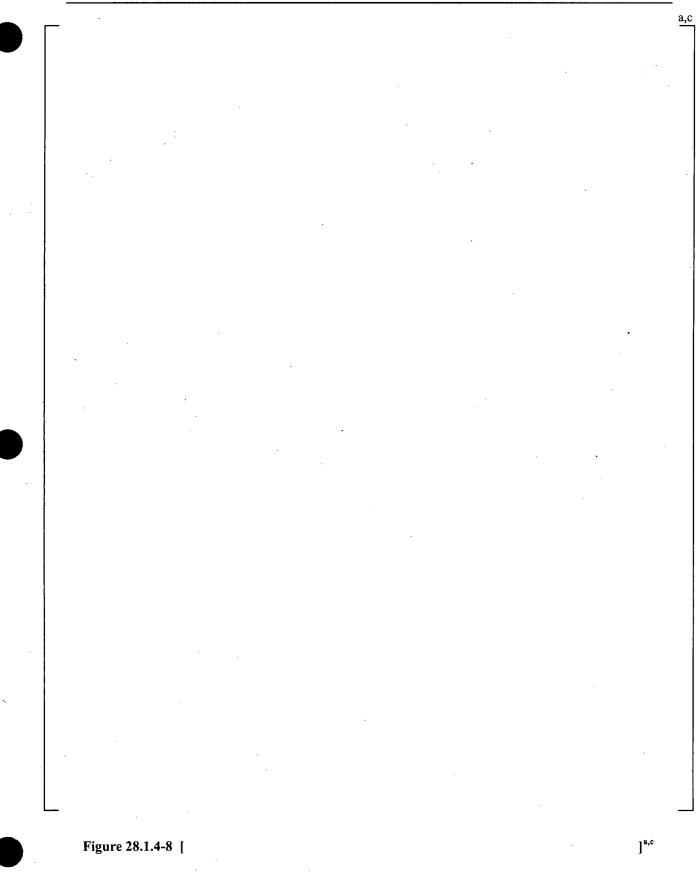
Figure 28.1.4-6

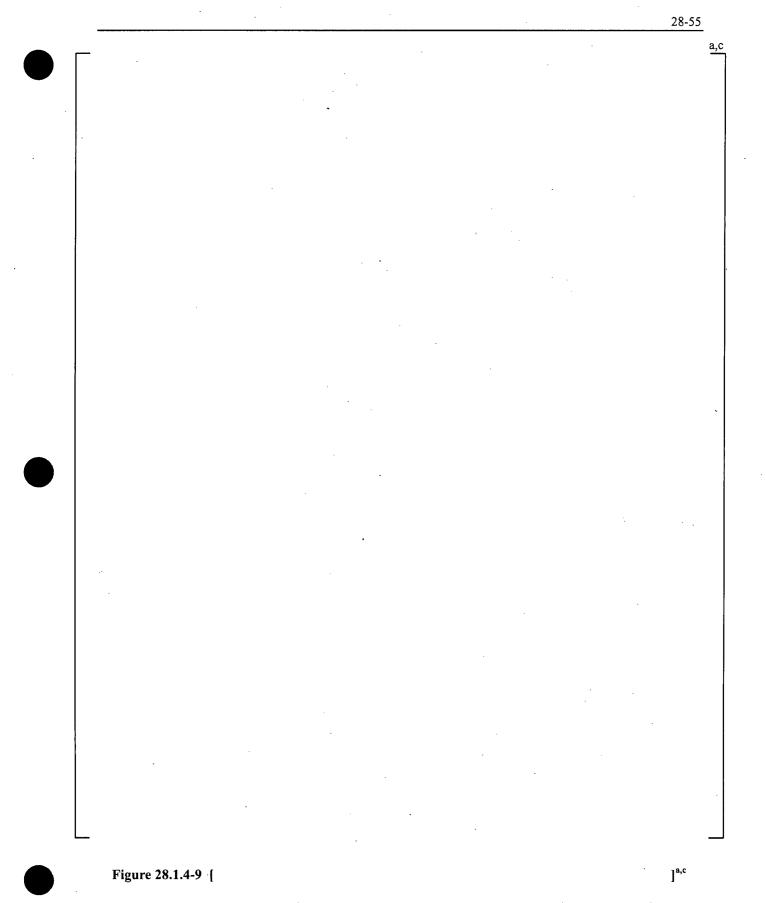
ĺ

]^{a,c}

WCAP-16996-NP









a,c

]^{a,c}

Figure 28.1.4-10 [

WCAP-16996-NP

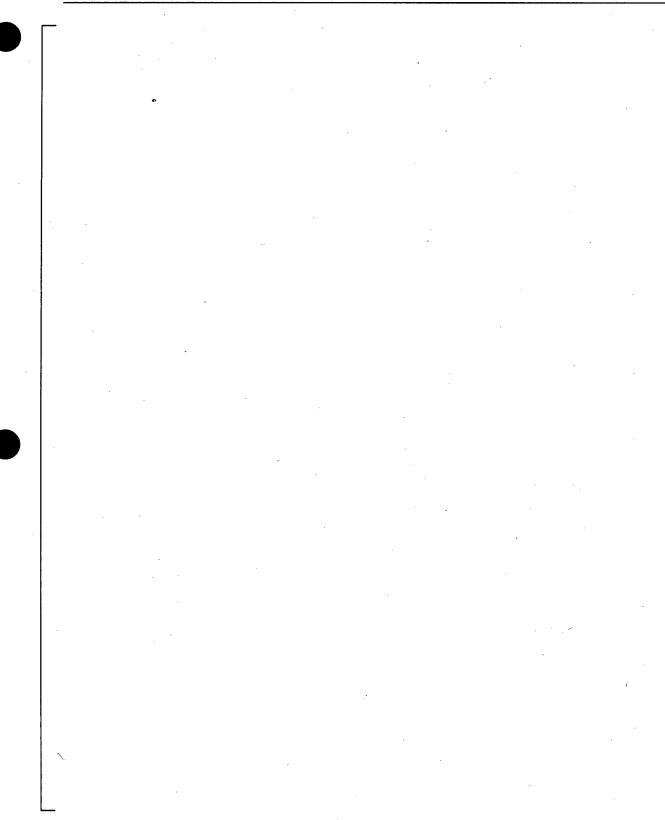
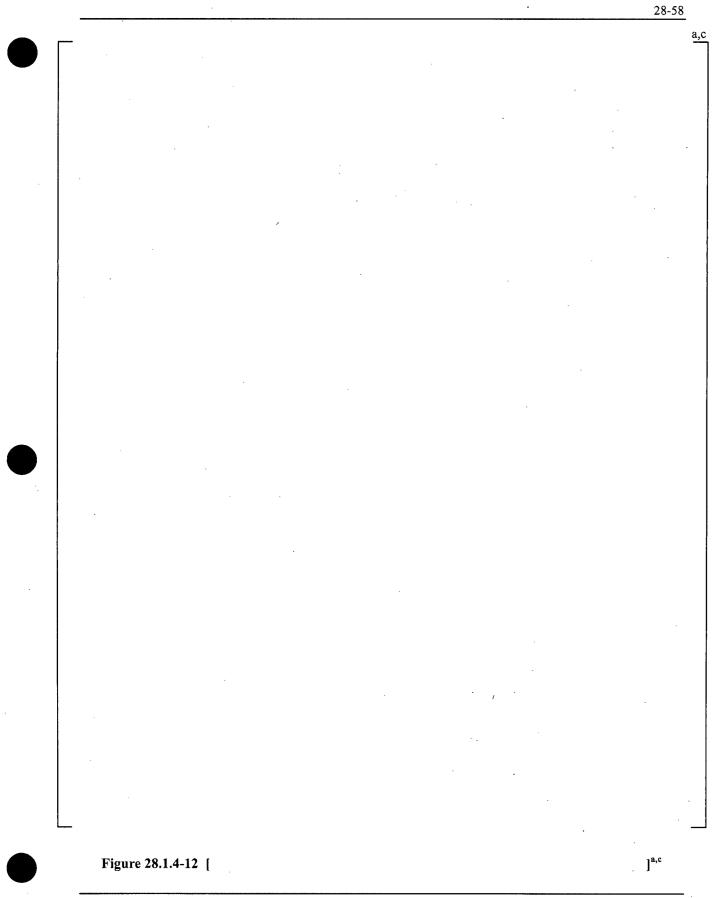


Figure 28.1.4-11 [

]^{a,c}

WCAP-16996-NP

November 2010 Revision 0 a,c



a,c

]^{a,c} Figure 28.1.4-13 [ WCAP-16996-NP

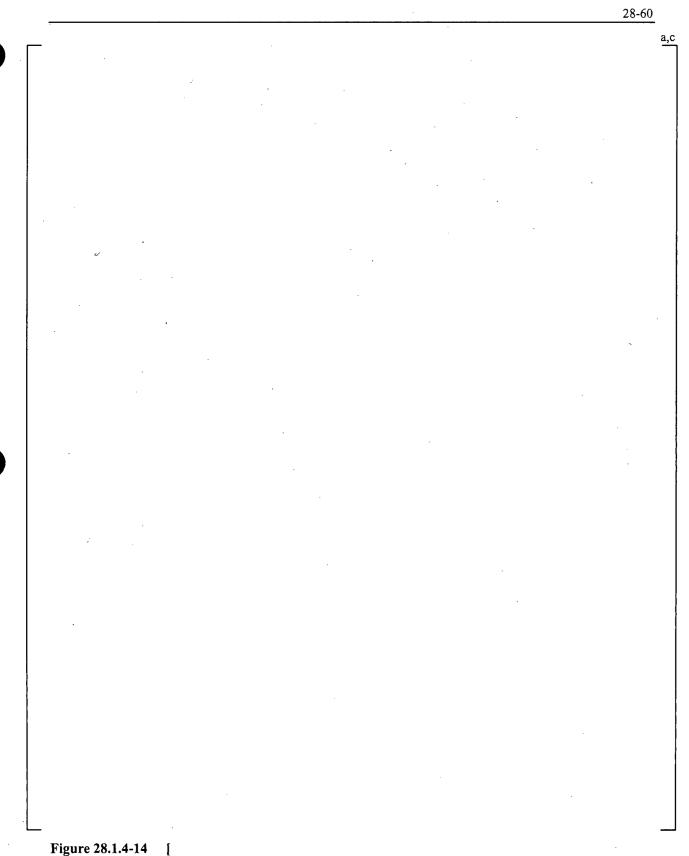


Figure 20.1.4-14 [

]^{a,c}

WCAP-16996-NP

a,c

Figure 28.1.4-15 [

]^{a,c}

WCAP-16996-NP

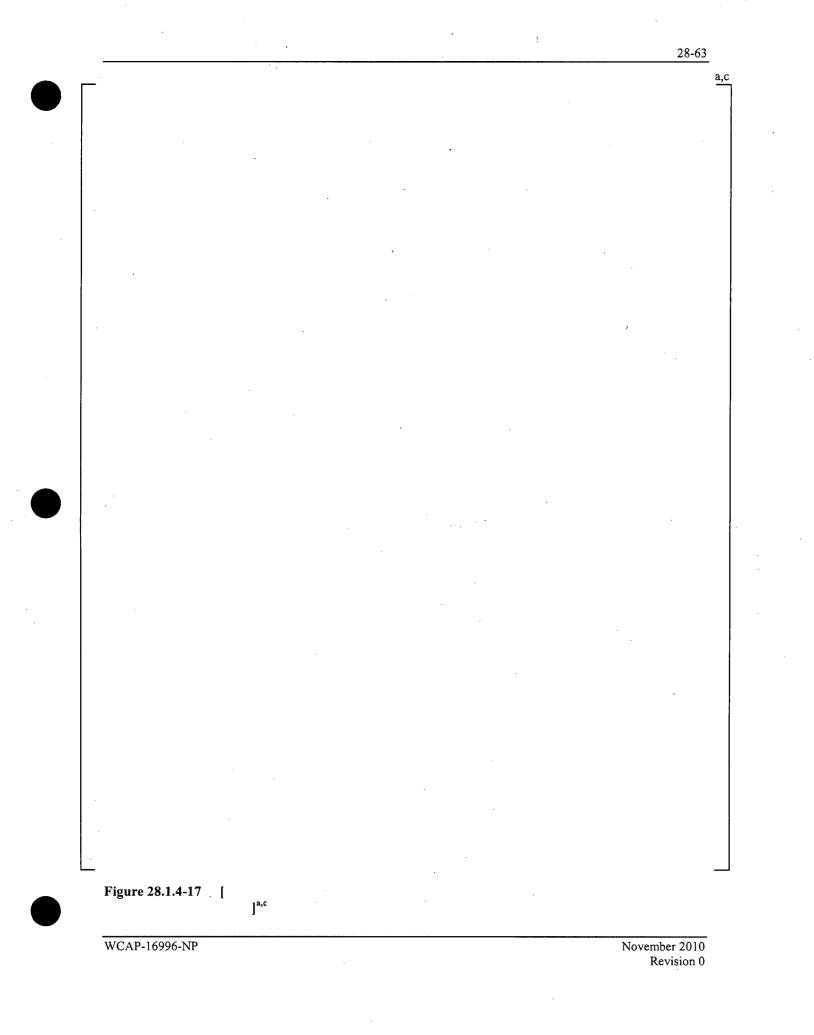
1

a,c

## Figure 28.1.4-16 [

]^{a,c}

WCAP-16996-NP



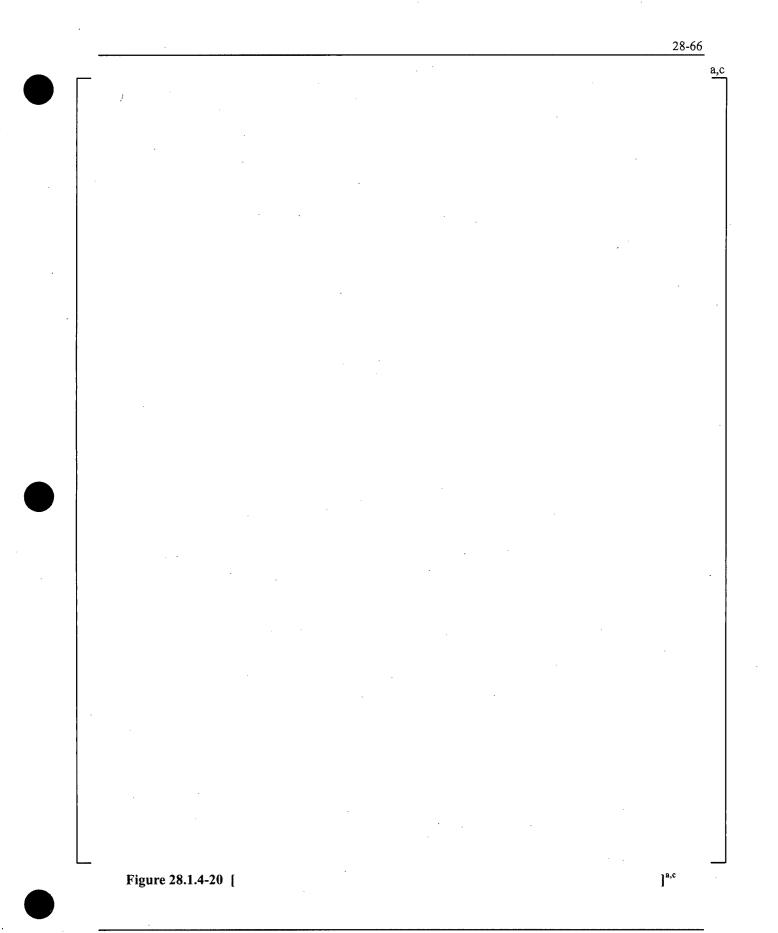
28-64 a,c Figure 28.1.4-18 [ ]^{a,c} WCAP-16996-NP November 2010 Revision 0

a,c

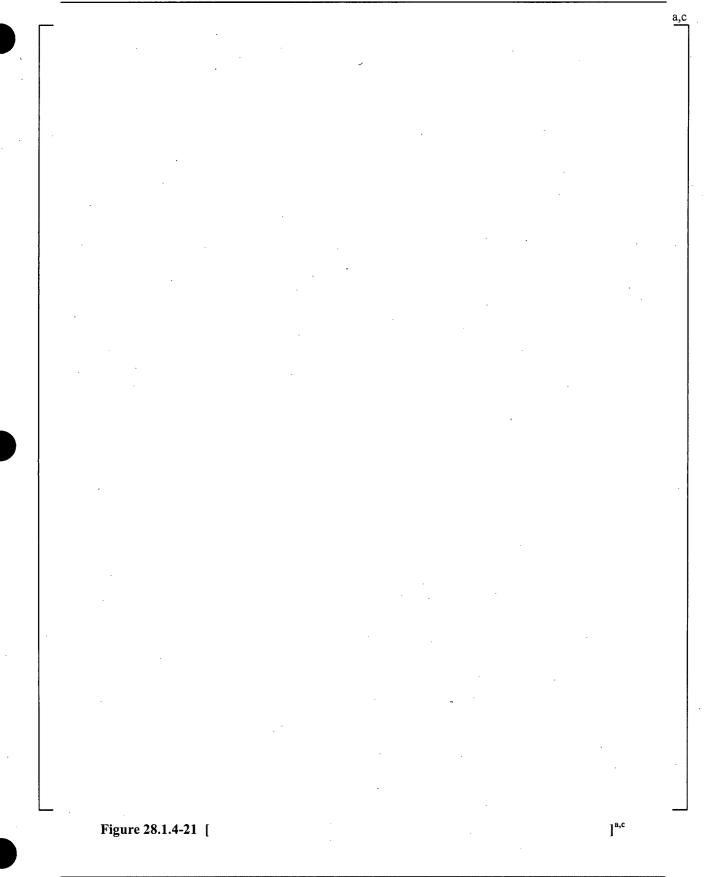
]^{a,c}

Figure 28.1.4-19 [

WCAP-16996-NP







2	8-	68

a,c

Figure 28.1.4-22 [

WCAP-16996-NP

November 2010 Revision 0

						â
_						
	、					
			/ .			
•						
				,		
					·	
_						
	Figure 28.1.4-23	[				
	-	] ^{a,c}				

WCAP-16996-NP

a,c

## Figure 28.1.4-24 [

]^{a,c}

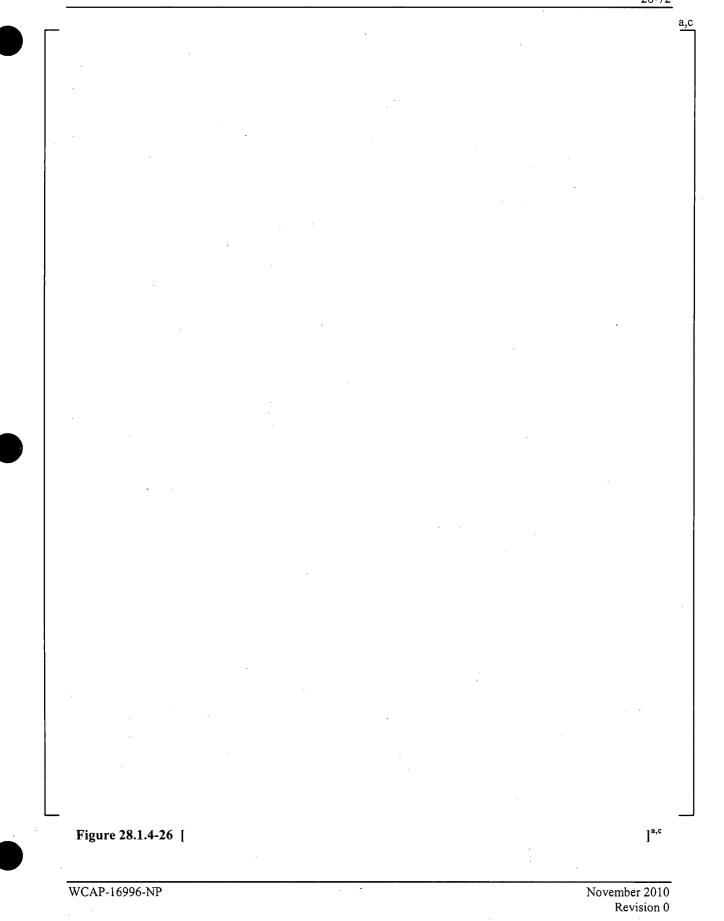
WCAP-16996-NP

a,c

Figure 28.1.4-25 [

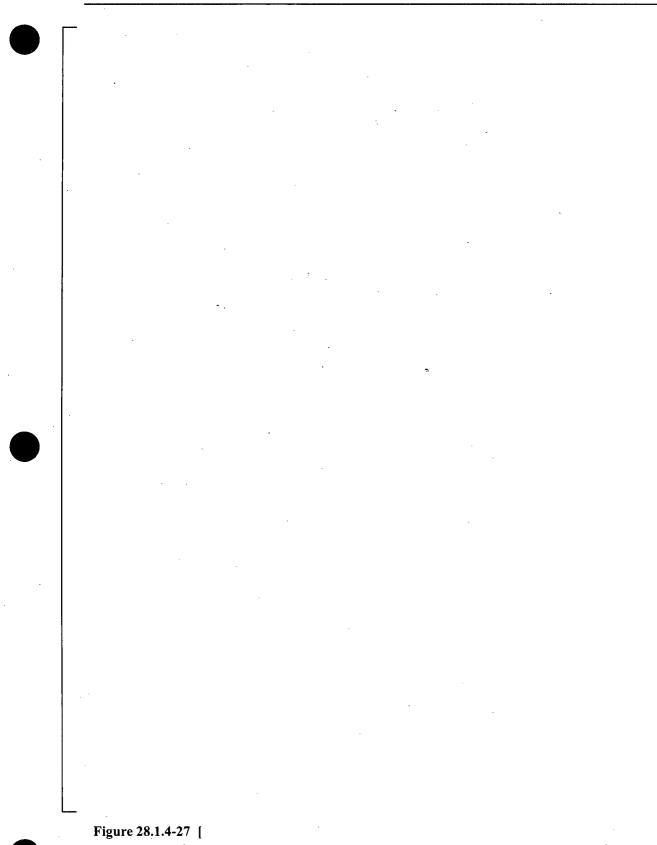
]^{a,c}

WCAP-16996-NP





a,c



]^{a,c}

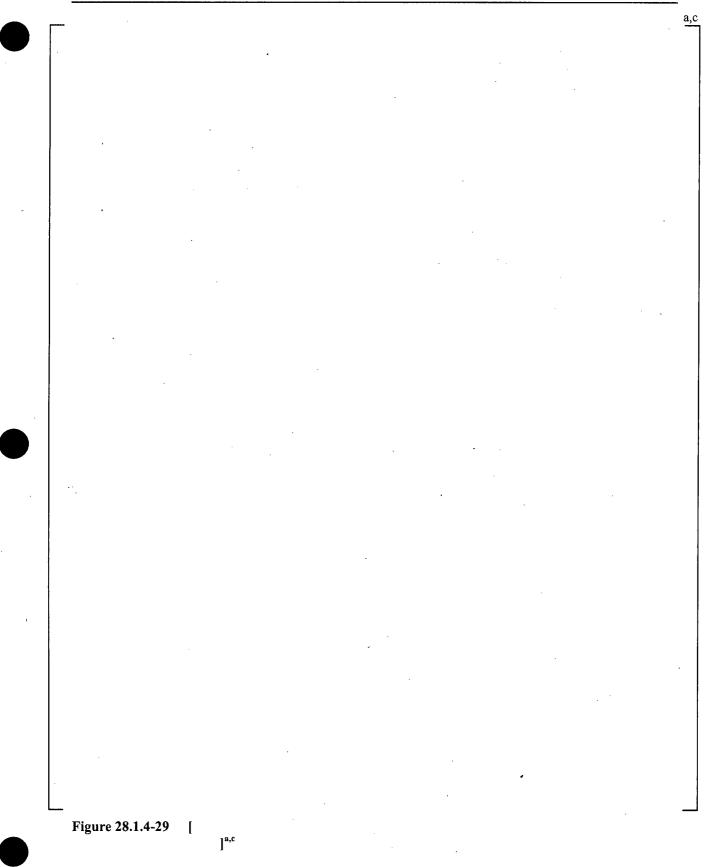
WCAP-16996-NP

	-							a,c
	-		. •		· .			
					,			
					•			·
						:	·	
·								
			,					
		、 · ·			,			
						,		
		×						

Figure 28.1.4-28 [

]^{a,c}

WCAP-16996-NP



a,c

Figure 28.1.4-30 [

WCAP-16996-NP

November 2010 Revision 0

a,c ]^{a,c}

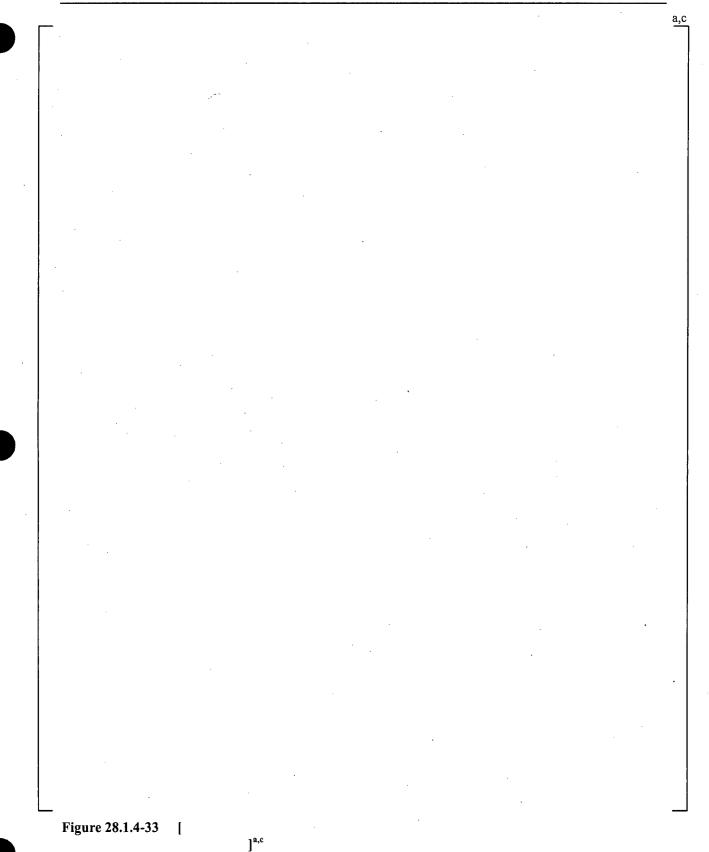
Figure 28.1.4-31 [

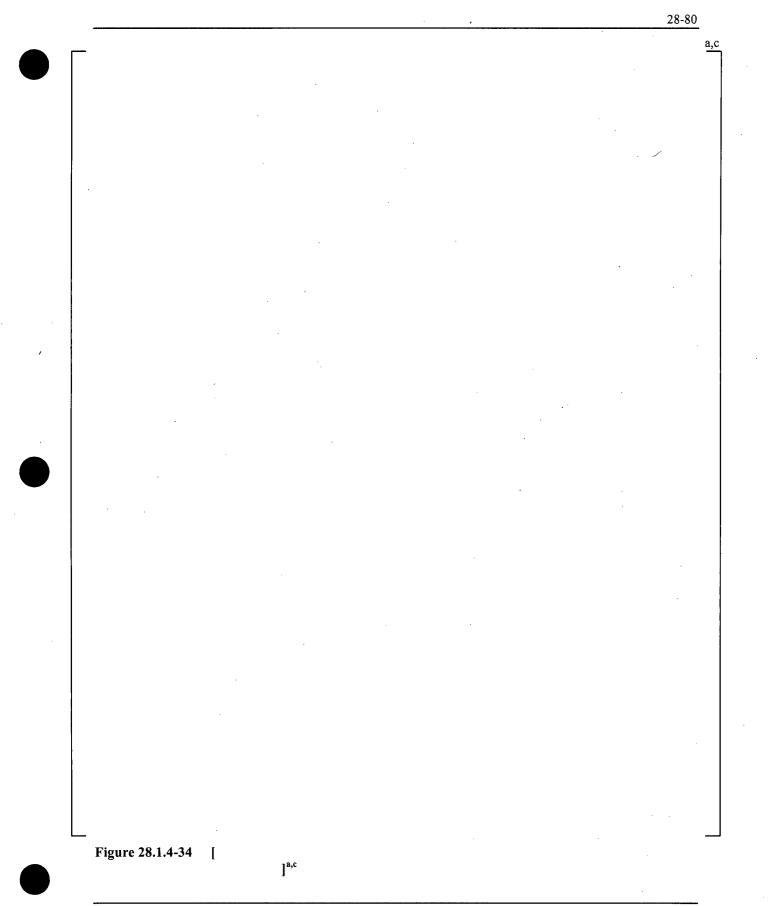
WCAP-16996-NP

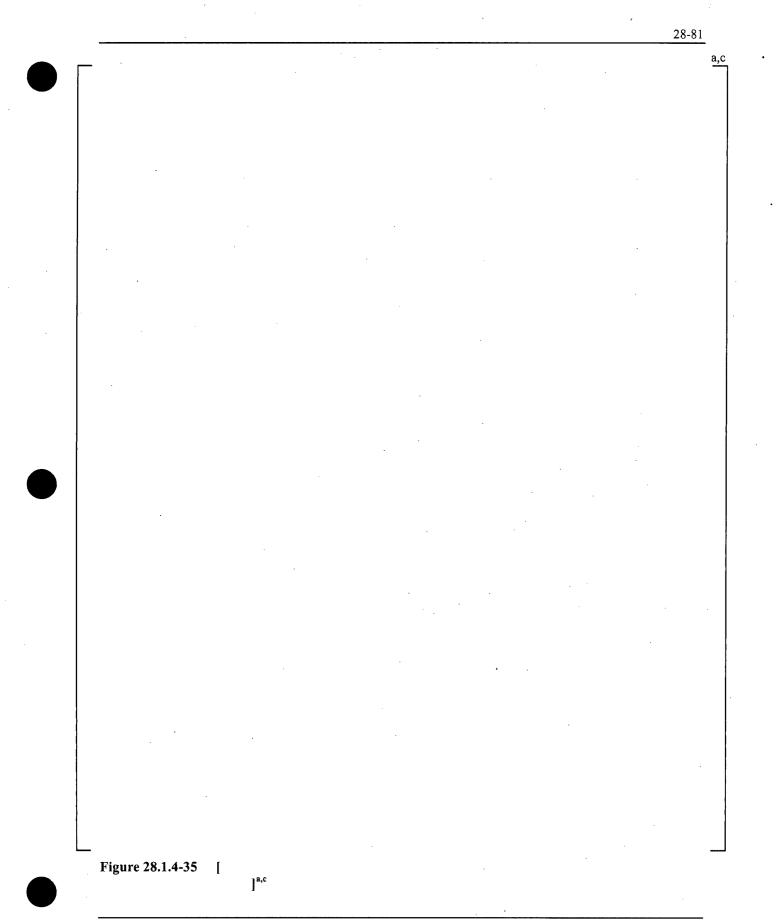
		a,c
	•	
 · · ·		
,		

WCAP-16996-NP

28-79







.

		•			28-82
					ä
·		-			
			· · · ·		
	Ň		•		
			•		
				·	
	· .·				
			,		
		· .			
Figure 28.					-

#### 28.1.5 Treatment of Accumulator Elevation – LBLOCA

In many plants, the elevation of the accumulators relative to the cold leg is loop-specific. For a large break LOCA, the initiation of accumulator injection is accompanied by a high degree of ECCS bypass, but a significant amount of accumulator liquid penetrates into the lower plenum during the refill phase. [

28.1.5.1 V. C. Summer (CGE)

]^{a,c}

The CGE large break LOCA reference transient from Section 27.2.1 is executed [

 $]^{a,c}$ . The length of the accumulator line (fL/D) was preserved in all cases. For CGE, two accumulators are [  $]^{a,c}$ . The elevations for this study were chosen to represent large but representative values that could be expected in a plant application.

It is expected that the dominance of ECCS bypass during blowdown and early refill will cause differing behavior, as a function of effective break size, in consideration to the accumulator elevation. A nominal double-ended guillotine break is explored along with breaks using a discharge coefficient (CD) of [ ]^{a,c} to evaluate this effect.

Figure 28.1.5-1 shows the PCT for the Low, Nominal, and High accumulator elevation cases [

]^{a,c}

Figure 28.1.5-4 shows the PCT for the various arrangements [

]^{a,c}

The effect of accumulator elevation for a break with a discharge coefficient of [

]^{a,c}

WCAP-16996-NP

### 28.1.5.2 Conclusions

There exists, for a given effective break area and its associated blowdown and ECCS bypass characteristics, an optimum accumulator design. Varying the elevation and consequently the timing of accumulator injection can affect the degree to which accumulator liquid fills the lower plenum. For large breaks, it has been shown [

]^{a,c}

To properly account for the variations in ECCS performance as a function of as-built accumulator elevations in a realistic manner, the plant analysis will [ ]^{a,c}.

WCAP-16996-NP



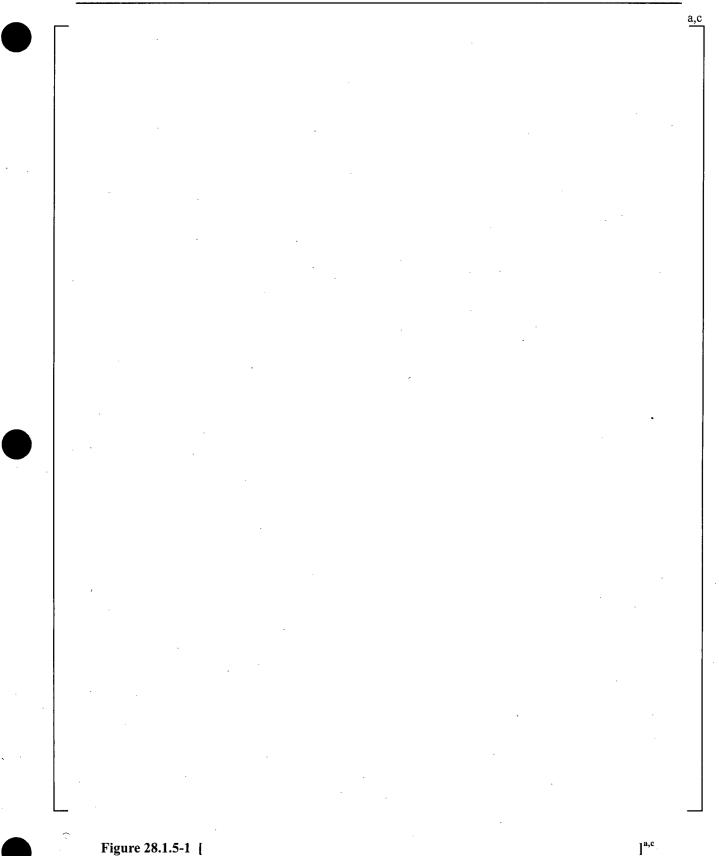
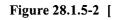


Figure 28.1.5-1 [

WCAP-16996-NP

a,c



WCAP-16996-NP

November 2010 Revision 0

a,c

Figure 28.1.5-3 [

]^{a,c}



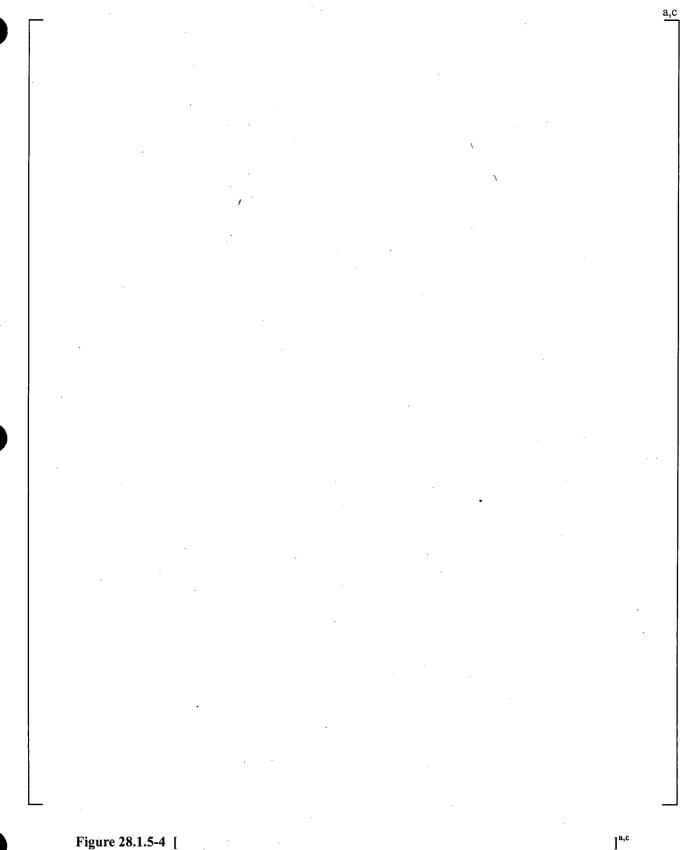


Figure 28.1.5-4 [

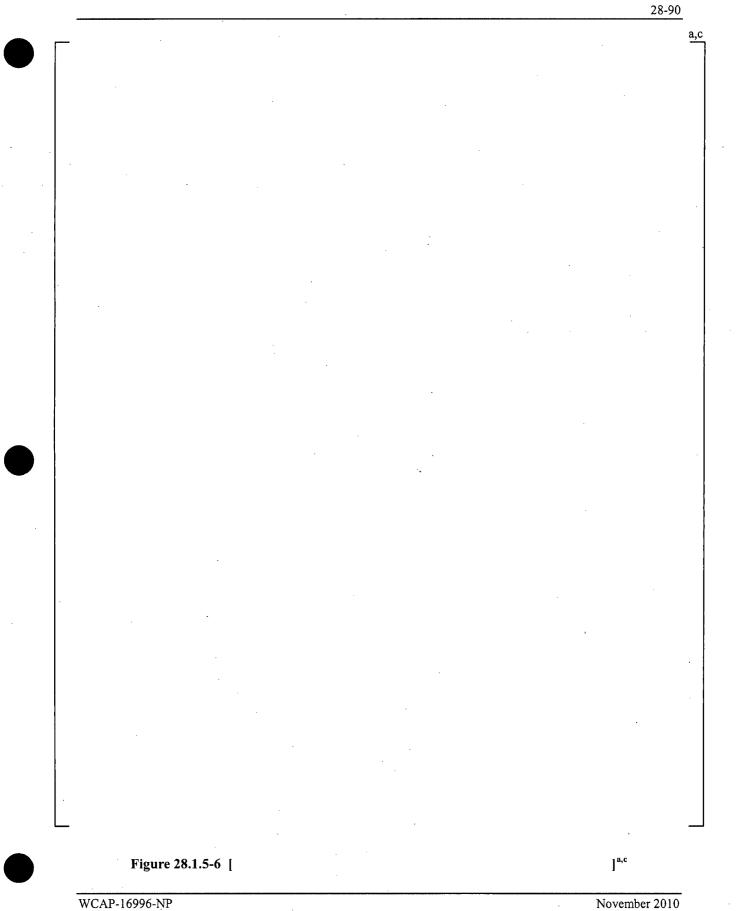
WCAP-16996-NP

a,c

Figure 28.1.5-5 [

WCAP-16996-NP

November 2010 Revision 0



Revision 0

				 Managara			 28-91	_
Γ		n Alexandria Alexandria					. 1	a
		• ·	:					
			· .					
							·	
ж. 1						ł		
	· . ·							
					·			_
	Figure 28.1.5-7 [						] ^{a,c}	_

2	8	-92
	ð	-92

a,c

]^{a,c}

Figure 28.1.5-8 [

WCAP-16996-NP

28-93

a,c

Figure 28.1.5-9 [

]^{a,c}

WCAP-16996-NP

### 28.1.6 Steam Generator Hydraulics: Tube Plugging – LBLOCA

For a large break, the additional resistance through the steam generator tubes as a result of tube plugging has two primary effects. First, it affects the relative break path resistance during blowdown, altering the conditions in the core regarding stagnation and flow reversal. Second, it inhibits steam venting during reflood, aggravating the steam binding phenomenon and reducing the rate at which the vessel fills with liquid.

Tube plugging levels of 0%, 10%, and 20% are examined here for a nominal DEG break.

#### 28.1.6.1 V. C. Summer (CGE)

Cooling during blowdown occurs slightly later, which results in a slightly higher blowdown PCT, when the tube plugging level [

#### 28.1.6.2 Conclusions

The effects of tube plugging for a large break LOCA are to [

WCAP-16996-NP

7^{a,c}

a,c



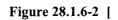
Figure 28.1.6-1 [

]^{a,c}

WCAP-16996-NP



a,c



WCAP-16996-NP

November 2010 Revision 0

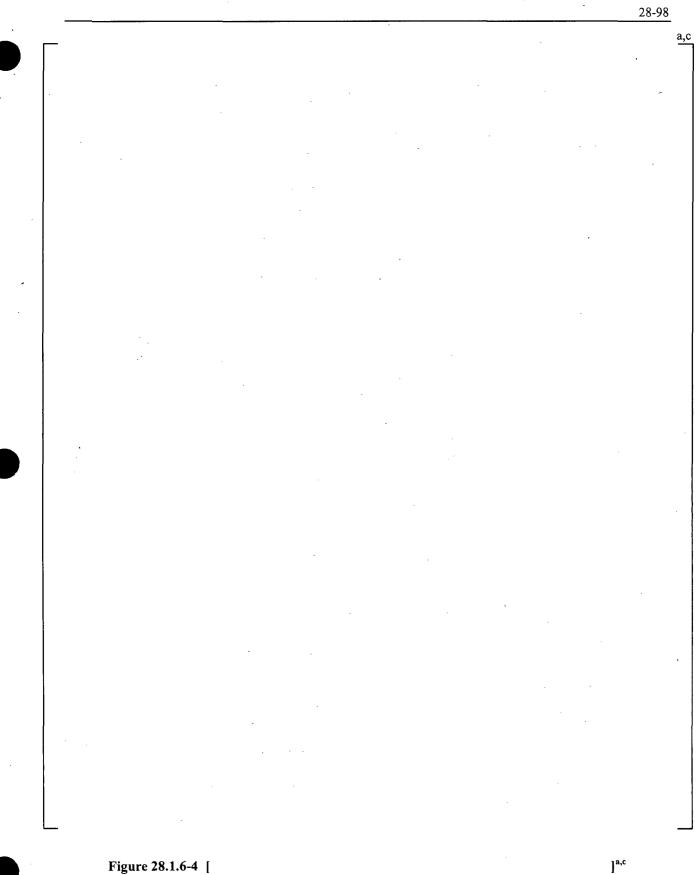
.28-97

a,c

# Figure 28.1.6-3 [

WCAP-16996-NP

November 2010 Revision 0



	<u> </u>	· • • • • • • • • • • • • • • • • • • •		 	28-99
		•			a
					• .
			·		
					· .
— — —					-

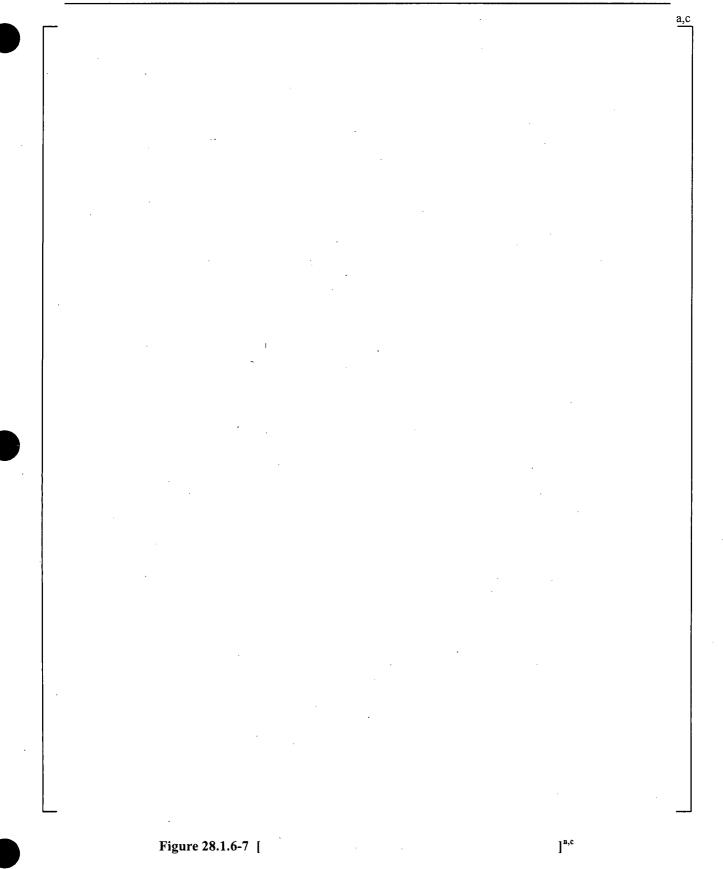
a,c

# Figure 28.1.6-6 [

WCAP-16996-NP

November 2010 Revision 0

]^{a,c}



WCAP-16996-NP

### 28.2 SMALL BREAK SCOPING STUDY RESULTS

#### 28.2.1 Small Break Reference Transient Re-Baseline

Since the V. C. Summer nominal 3-inch diameter SBLOCA transient [

]^{a,c}

#### 28.2.1.1 V. C. Summer (CGE)

Until the RCS depressurizes to the accumulator pressure, safety injection flow works to replenish lost inventory. [

]^{a,c}

For illustrative purposes, the reference transient [ SBLOCA sensitivity studies in the following subsections.  $]^{a,c}$  is used in the CGE

28-103

a,c

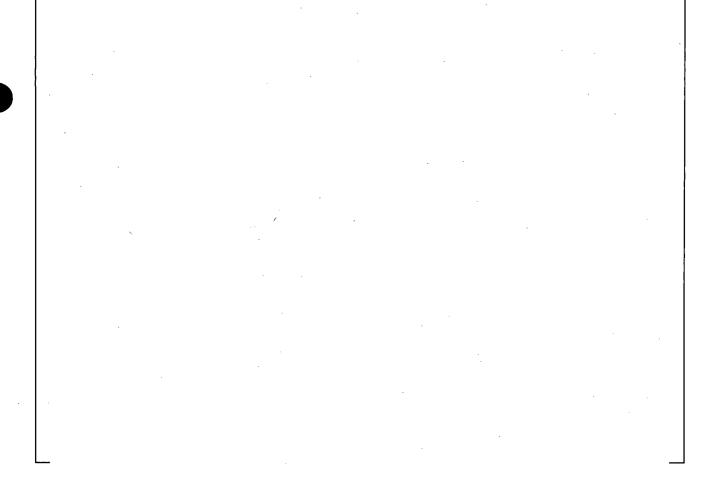


Figure 28.2.1-1 Void Fraction at Break, CGE SBLOCA Reference Transient Re-Baseline

28-10	)4
-------	----

1	· ·						a,
		-					
				•			
	[						
						·	
					. 1		
			·				
	x						
					,		
l	L						-

Figure 28.2.1-2 RCS Pressure, CGE SBLOCA Reference Transient Re-Baseline

a,c

# Figure 28.2.1-3 Upper Head Collapsed Liquid Level, CGE SBLOCA Reference Transient C Re-Baseline

WCAP-16996-NP

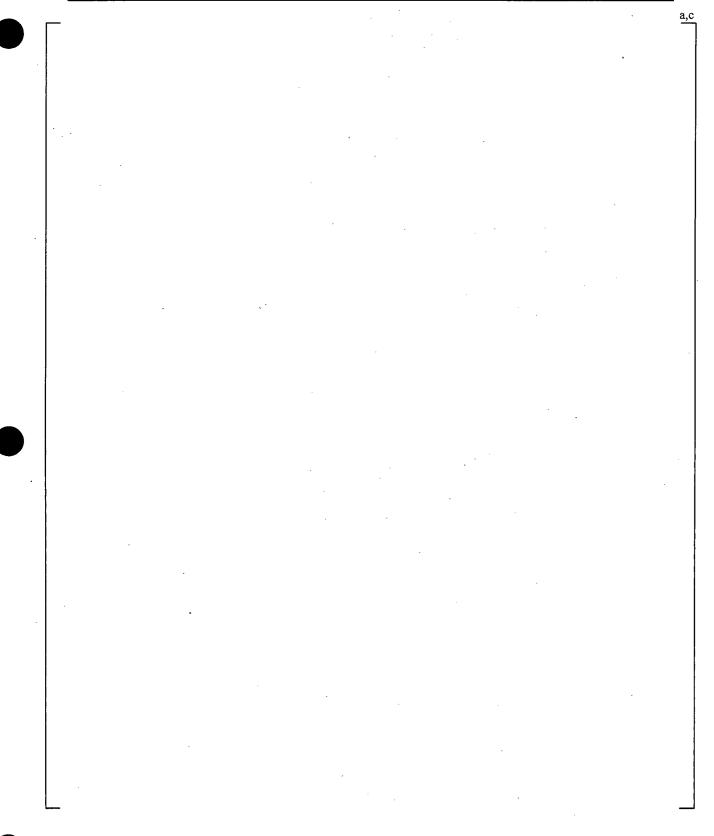


Figure 28.2.1-4 Break Flow, CGE SBLOCA Reference Transient Re-Baseline

WCAP-16996-NP

,

a,c

Figure 28.2.1-5 Intact Loop 1 Loop Seal Differential Pressure, CGE SBLOCA Reference Transient Re-Baseline

a,c

# Figure 28.2.1-6 Intact Loop 2 Loop Seal Differential Pressure, CGE SBLOCA Reference Transient Re-Baseline

WCAP-16996-NP

28-109

a,c

# Figure 28.2.1-7Broken Loop 3 Loop Seal Differential Pressure, CGE SBLOCA Reference<br/>Transient Re-Baseline

WCAP-16996-NP

a,c

Figure 28.2.1-8 Peak Cladding Temperature, CGE SBLOCA Reference Transient Re-Baseline

# 28.2.2 Axial Power Distributions – SBLOCA

As part of the uncertainty analysis, [

# ]^{a,c}. The CGE and DLW SBLOCA 3-

]^{a,c}

inch reference transients assumed top-skewed power distributions, which are expected to be more limiting for a small break as a result of higher power in the region of potential core uncovery. A sensitivity case is examined for each plant where the axial power distribution is skewed more toward the bottom.

28.2.2.1 V. C. Summer (CGE)

The 3-inch break with power skewed more toward the bottom (Figure 28.2.2-1) results in [

#### 28.2.2.2 Beaver Valley Unit 1 (DLW)

For DLW, the bottom-skewed case (Figure 28.2.2-10) results in [

J^{a,c}

# 28.2.2.3 Conclusions

In this sensitivity study, it is clear that [

]^{a,c}. All else equal, a top-skewed shape will likely be more limiting for a small break LOCA with upper core uncovery. [

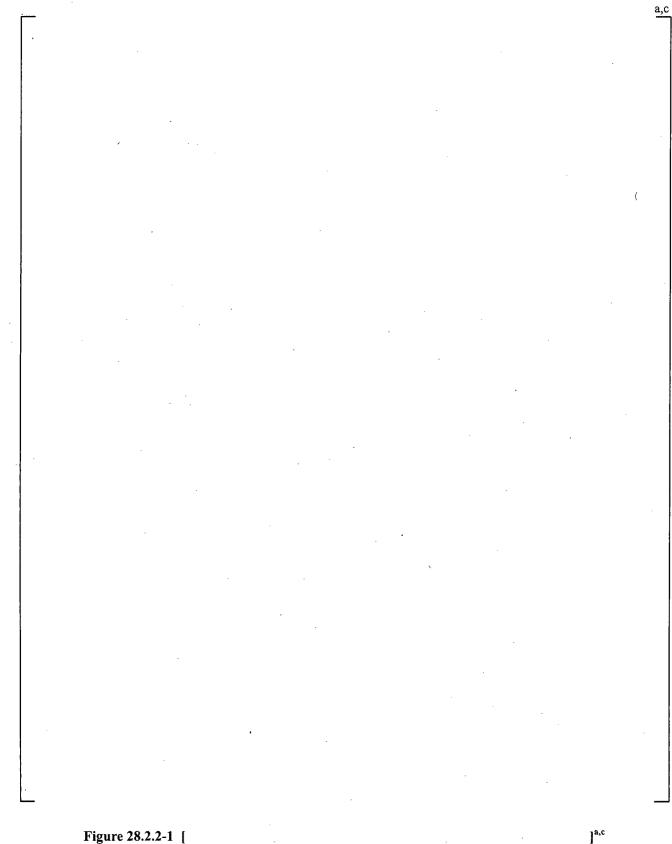


Figure 28.2.2-1 [

WCAP-16996-NP

a,c

# Figure 28.2.2-2 [

WCAP-16996-NP

November 2010 Revision 0

]^{a,c}

a,c

Figure 28.2.2-3 [

WCAP-16996-NP

November 2010 Revision 0

]^{a,c}

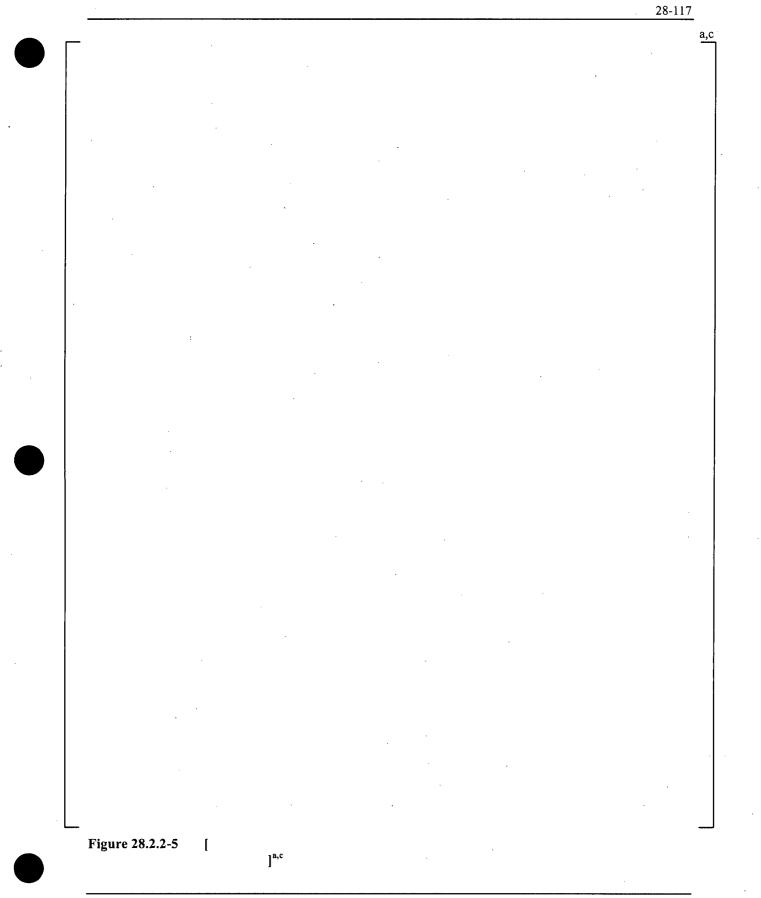
a,c

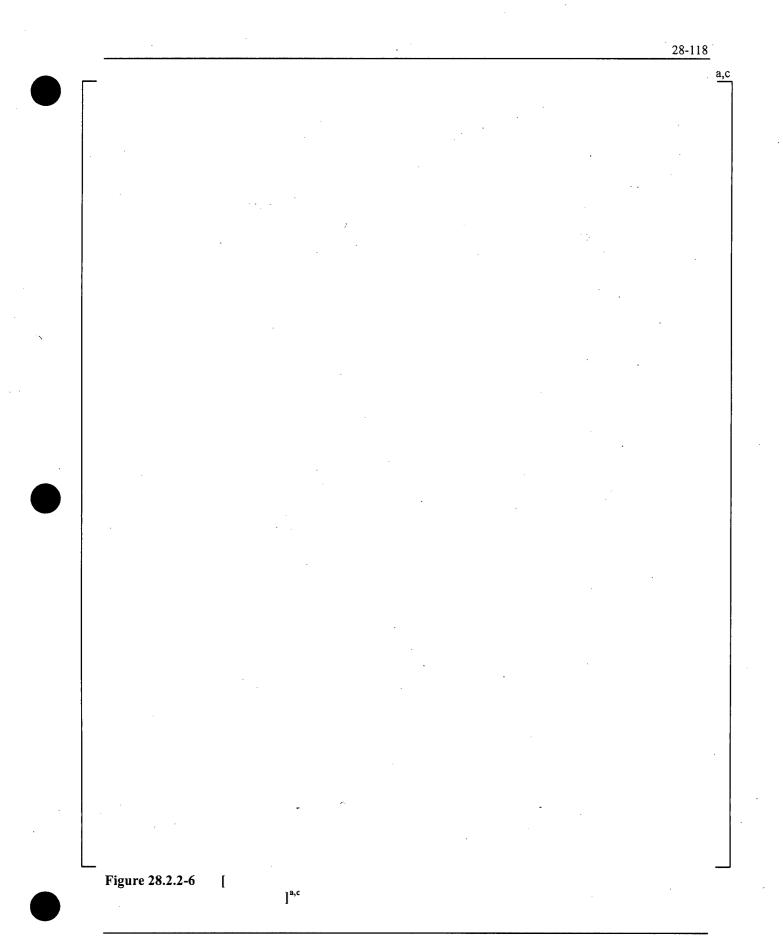
Figure 28.2.2-4

ſ

]^{a,c}

WCAP-16996-NP





a,c

0

ſ

]^{a,c}

Figure 28.2.2-7 [

WCAP-16996-NP



Figure 28.2.2-8 [

_____

]^{a,c}

a,c

a,c

– Figure 28.2.2-9 [ ]^{a,c}

) [			a,c
	•		
)			
)		Figure 28.2.2-10 [ ] ^{a,c}	

a,c

Figure 28.2.2-11 [

]^{a,c}

a,c

Figure 28.2.2-12 [

]^{a,c}

WCAP-16996-NP

 		 	 	<u></u>			28-125	5
								a,c
						·		
						÷		
	•							
			· ·					
	•				•			•
			• ·					
	·							
				٩			÷	
								28-12

a,c

Figure 28.2.2-14

[

]^{a,c}

WCAP-16996-NP

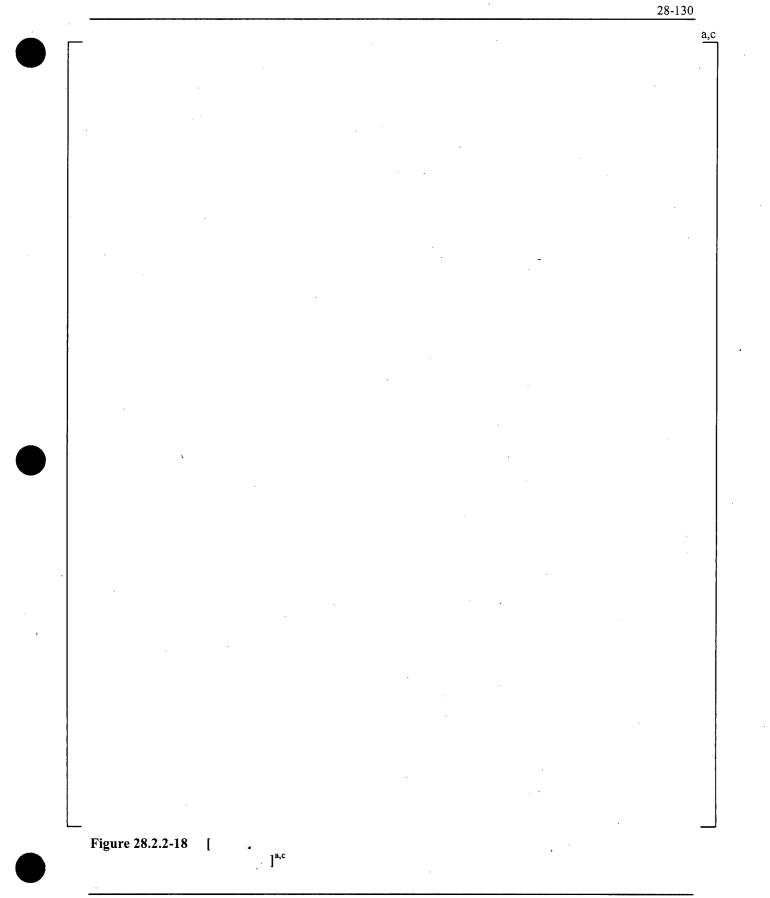
28-127	7	2	1	28-	
--------	---	---	---	-----	--

	•
	¥.
۰.	

_					 		 28-128
-							
		•			`		
						•	
					-		
				, i			
	· .						
			•				
					·		
							·
	<b>,</b>						

 					28-129
	-				
			-		
		· ·	•		
	,				
					· .
			·		
					. ,
				<i>.</i>	
 28.2.2-17					

WCAP-16996-NP



#### 28.2.3 Initial and Accident Boundary Conditions and Offsite Power - SBLOCA

In a small break LOCA, the loss of offsite power has two main effects. The delay in safety injection is increased due to the diesel generator startup, and the pumps are [

]^{a,c}. With a loss of offsite power, the delayed SI results in a longer period of time when the vessel inventory is lost without being replaced by HHSI flow, although the HHSI flow is relatively small in magnitude early in the transient compared to the break flow due to the high RCS pressure. When offsite power is available, continued pump operation can work to pump more flow toward the break, depleting vessel inventory at a greater rate than otherwise would occur for a given break size. For small breaks, however, the continued pump operation can also maintain the positive flow in the broken cold leg, impeding flow reversal and reducing the total flow out the break.

#### 28.2.3.1 Offsite Power Availability: V. C. Summer (CGE)

In addition to the 3-inch diameter SBLOCA reference transient, a 2.6-inch diameter case is also explored here.

## ]^{a,c}

#### 28.2.3.2 Offsite Power Availability: Beaver Valley Unit 1 (DLW)

In addition to the 3-inch diameter SBLOCA reference transient, a 3.2-inch diameter case is also explored here.

WCAP-16996-NP

ſ

ſ

November 2010 Revision 0

]^{a,c}

]^{a,c}

]^{a,c}

# ]^{a,c}

[

# 28.2.3.3 Offsite Power Availability: Conclusions

The availability of offsite power is observed to [

# 28.2.3.4 Operator Action

The reactor coolant pumps trip very early in the transient for the LOOP case, while the [

28-133

a,c 1 ]^{a,c} Figure 28.2.3-1 [

WCAP-16996-NP

)	
	· ·
	• ,
	•

Figure 28.2.3-2 [

]^{a,c}

WCAP-16996-NP

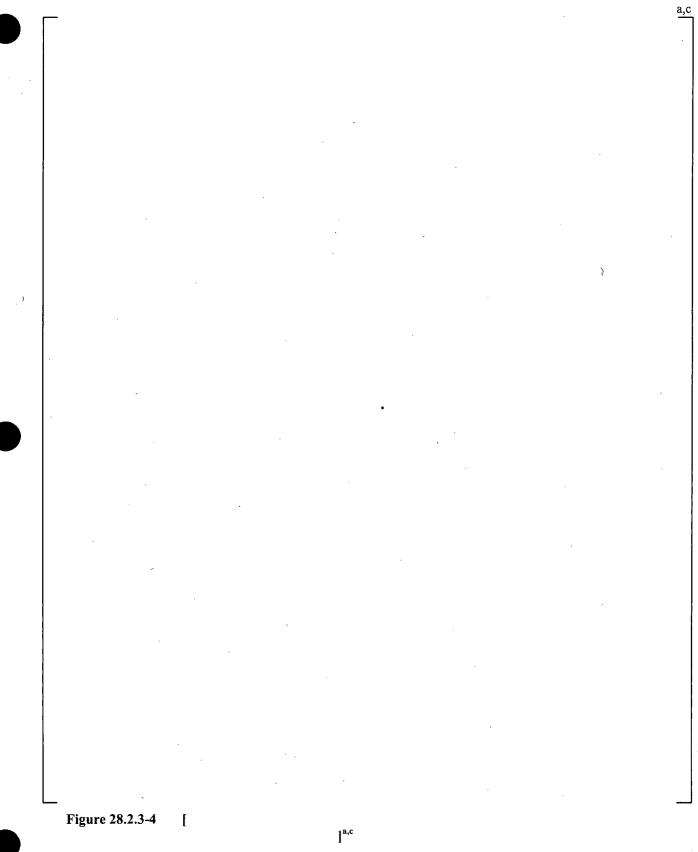
November 2010 Revision 0 a,c

a,c

Figure 28.2.3-3

[

WCAP-16996-NP



WCAP-16996-NP

a,c

?

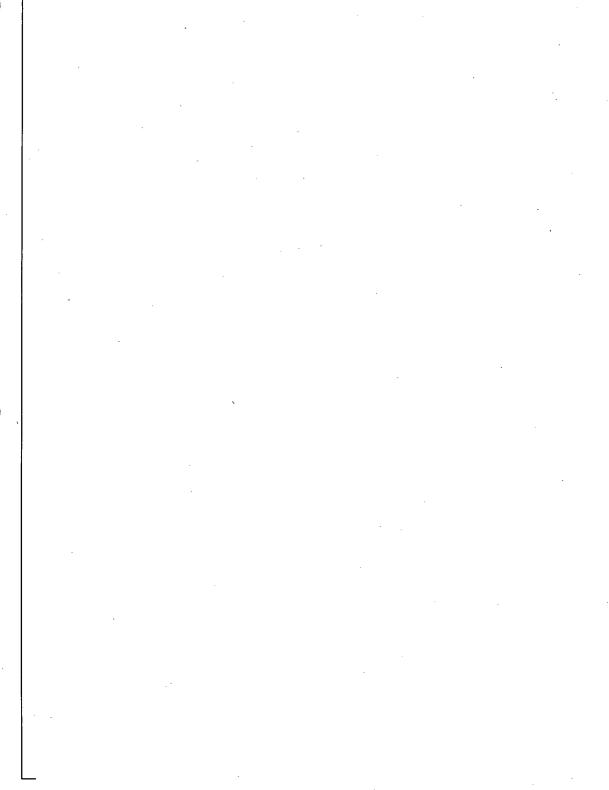


Figure 28.2.3-5 [

WCAP-16996-NP

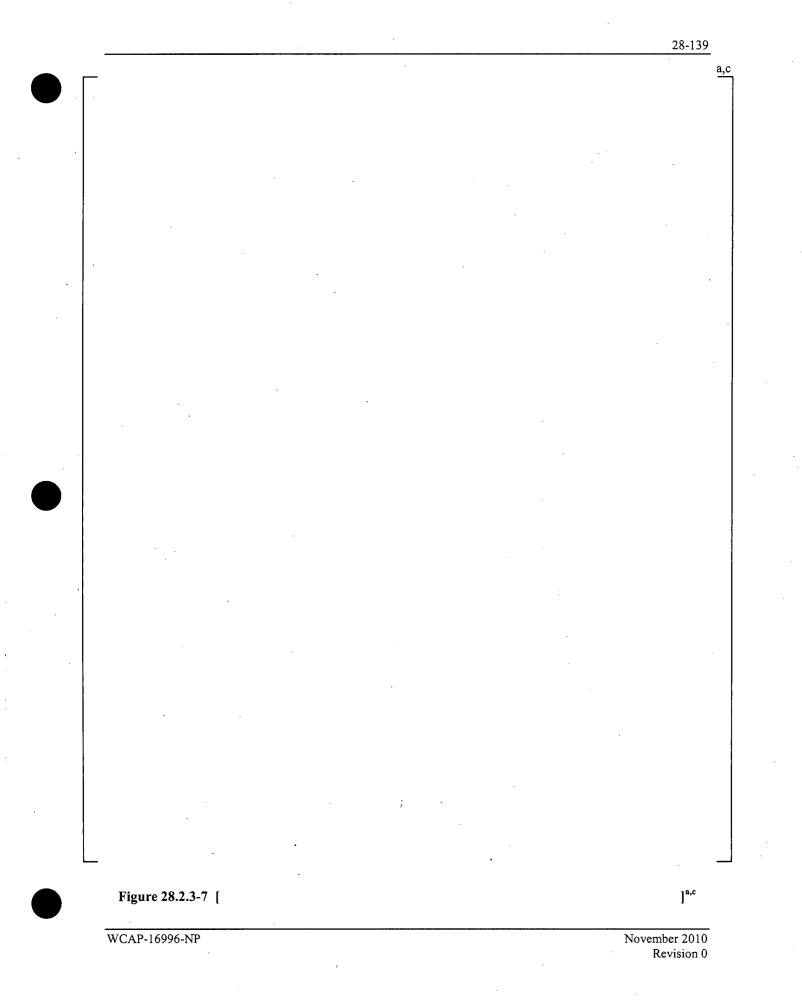
]^{a,c}

a,c

) Figure 28.2.3-6 [

]^{a,c}

WCAP-16996-NP



/					a,0
		<b>`</b>	ν.	Ŷ	
		·			
			· .		
		<b>i</b> .			
			· ·		
			м. Х		
	,				
					•
					•
			}		
					,
				· .	
		×			
-			· · · ·		
Figure 2	28.2.3-8 [				
		] ^{a,c}			

WCAP-16996-NP

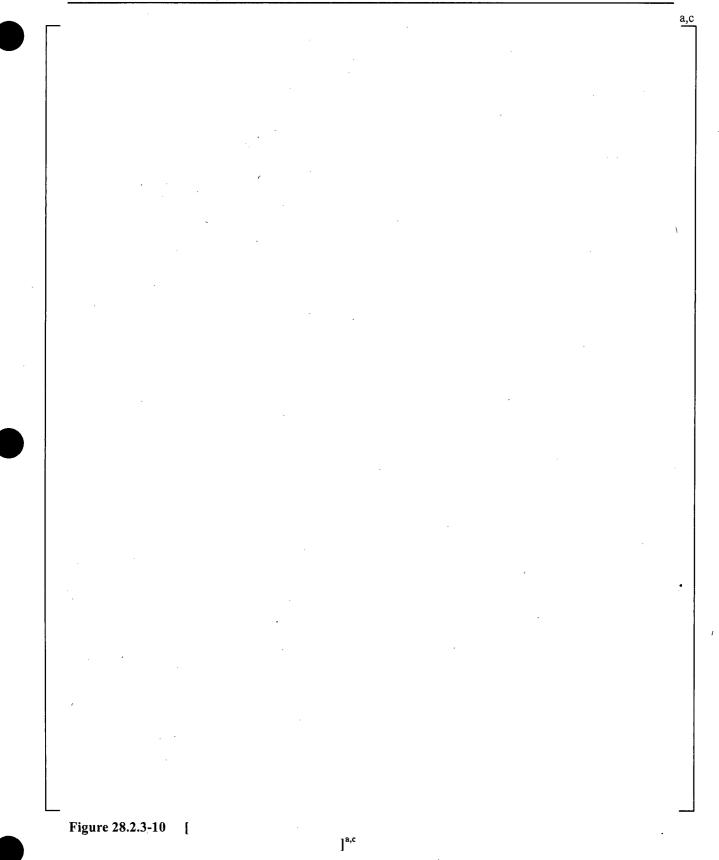
-28-	1	4	1
------	---	---	---

a,c

Figure 28.2.3-9 [

]^{a,c}

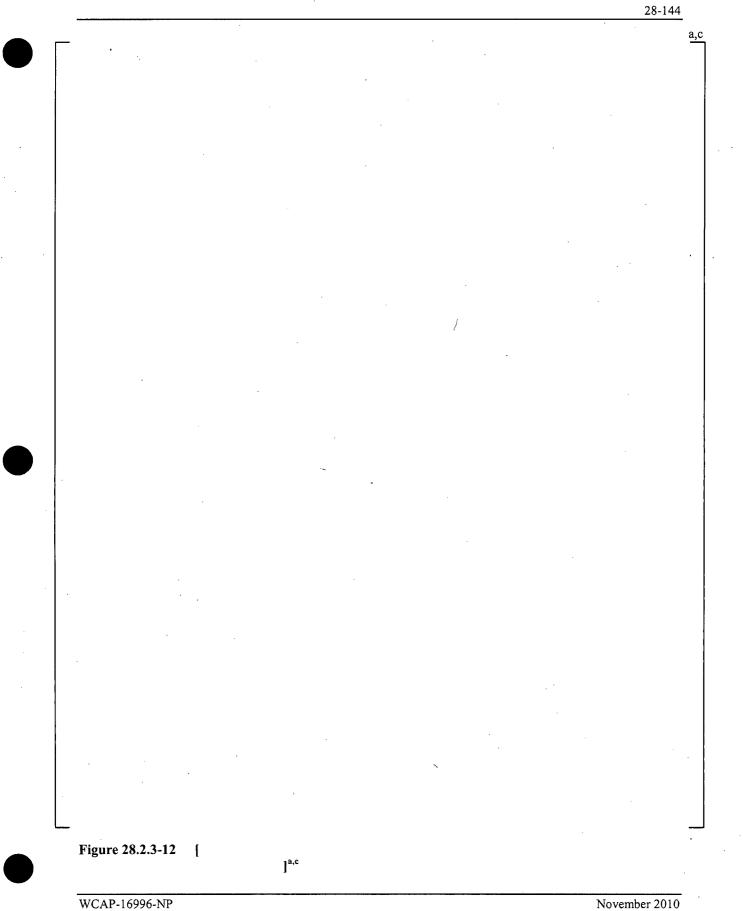
WCAP-16996-NP



WCAP-16996-NP

					28-143	_
	-				·	<u>a,c</u>
				· · · ·		
				· .		
		X				
			i			
				· .	·	
{						
					,	
			° L			
	· .					
		•				
	_					
		,				
	Figure 28.2	.3-11 [			] ^{a,c}	
					vember 2010 Revision 0	

ł



		a,c
,		
<b>Figure 28.2.3-13</b> [		<u> </u>
I IGULU MUMMU IU	l ^{a,c}	

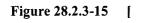
WCAP-16996-NP

	 			28-14
<b></b>				
				•
		•	· .	
		• • • • • • • • • • • • • • • • • • •		
-				
	· .			
	x			
			<b>.</b> .	
			,	
· · ·				
				•

WCAP-16996-NP

28-14	7
-------	---

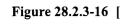
a,c



]^{a,c}

WCAP-16996-NP

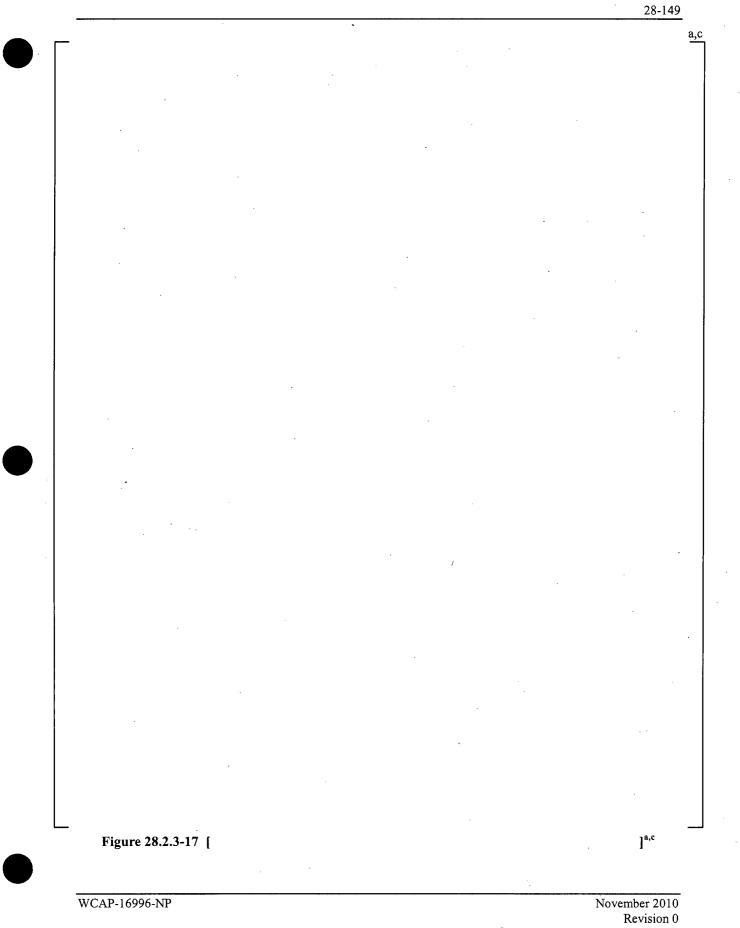
a,c



WCAP-16996-NP

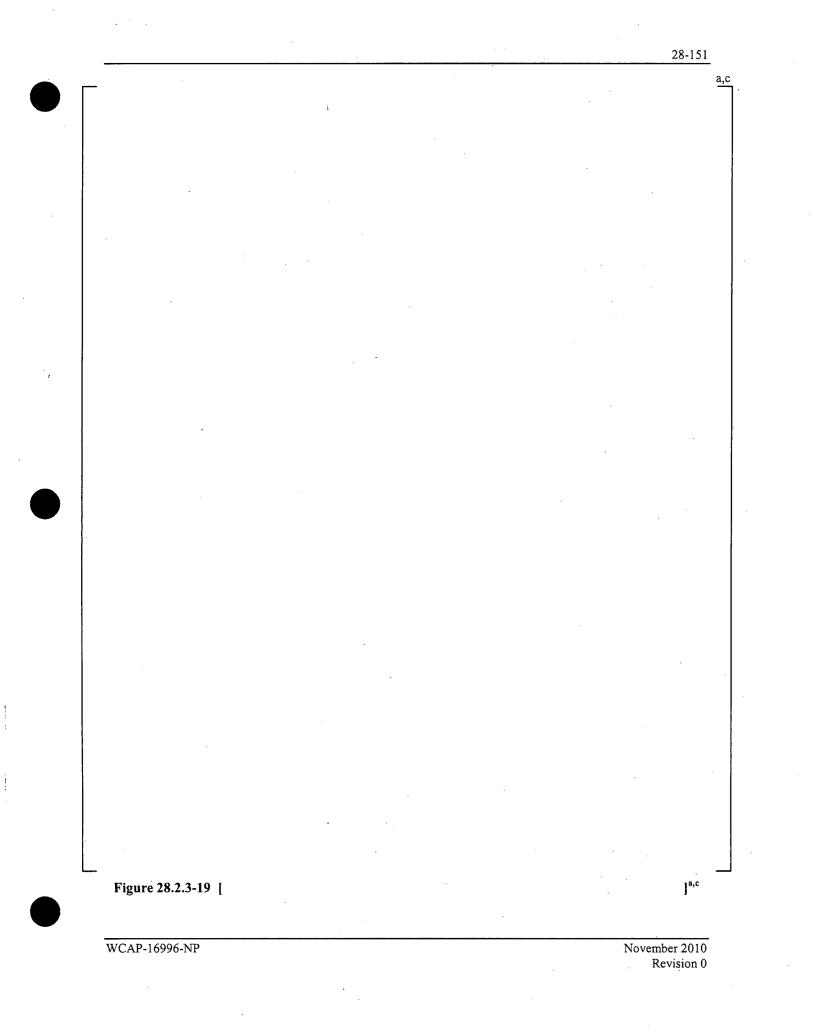
November 2010 Revision 0

]^{a,c}



a,c Figure 28.2.3-18 [ ]^{a,c}

WCAP-16996-NP



-		· · · · · · · · · · · · · · · · · · ·		28-152 a,c
	_		· · · ·	· · ·
	· .		· .	
1				
		<b>x</b>		
	· · · ·			

,

WCAP-16996-NP

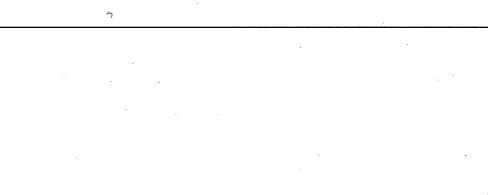


Figure 28.2.3-21 [

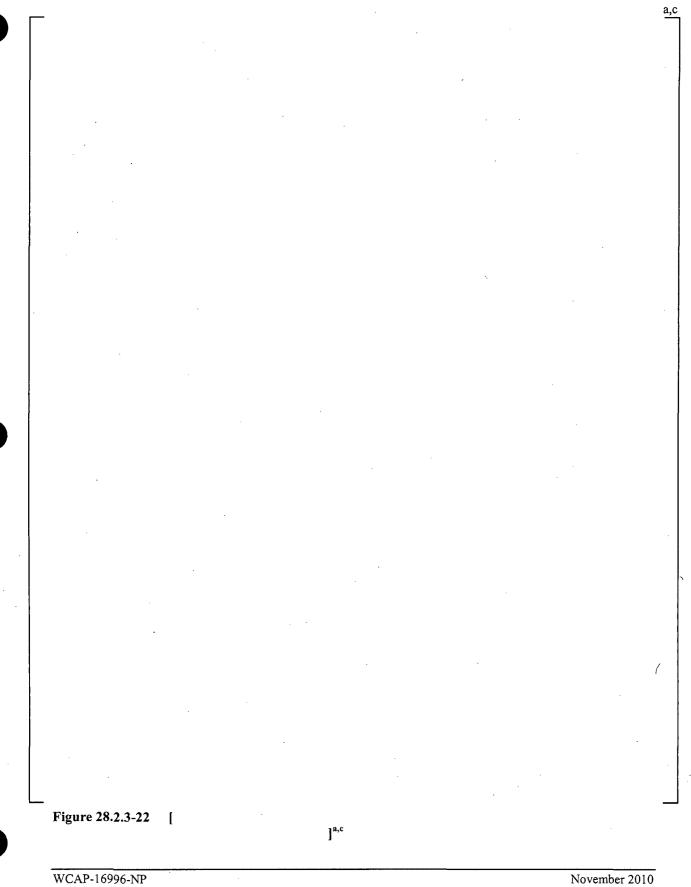
WCAP-16996-NP

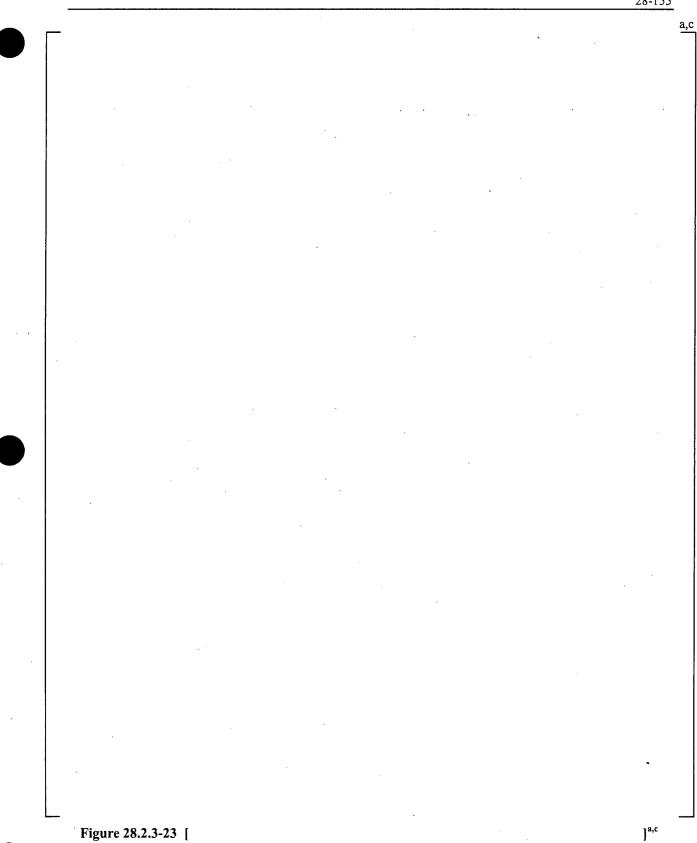
November 2010 Revision 0

]^{a,c}

28-153

a,c





ζ

WCAP-16996-NP

a,c

Figure 28.2.3-24 [

]^{a,c}

WCAP-16996-NP

]^{a,c}

### 28.2.4 Time Step and Convergence Criteria Studies – SBLOCA

The 3-inch reference transients for CGE and DLW are executed here using a modified upper limit on the time step (DTMAX). The reference DTMAX strategy uses [

]^{a,c}.

#### 28.2.4.1 V. C. Summer (CGE)

Figure 28.2.4-1 shows [

#### 28.2.4.2 Beaver Valley Unit 1 (DLW)

Similar to CGE, [

]^{a,c}

28.2.4.3 Conclusions

Changes in DTMAX upper limits [

DTMAX for the plant is discussed further in Section 29.3.3.

]^{a,c}. The choice of

WCAP-16996-NP

28-	158

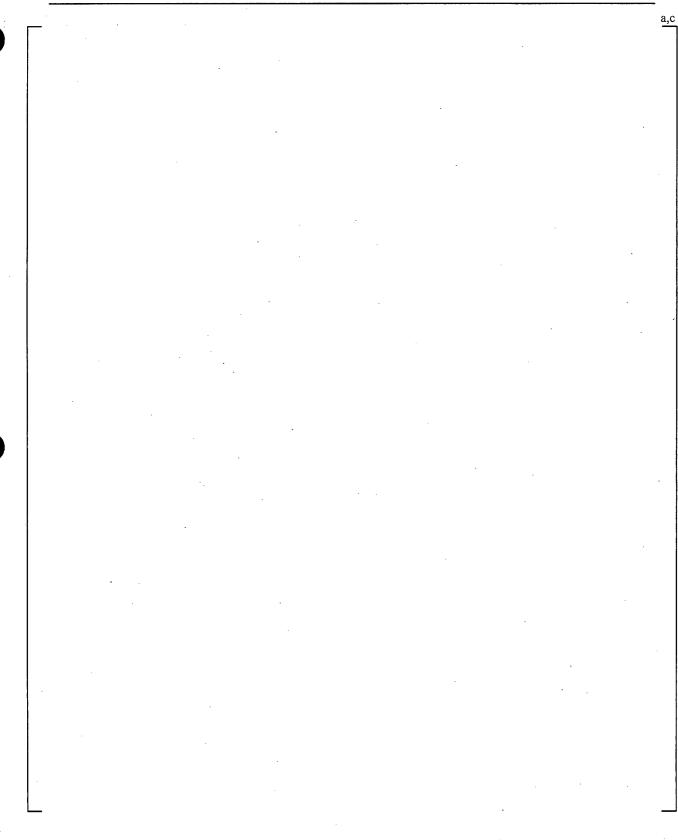


Figure 28.2.4-1 [

]^{a,c}

WCAP-16996-NP

a,c

### · · · ·

Figure 28.2.4-2 [

WCAP-16996-NP

28-160	
--------	--

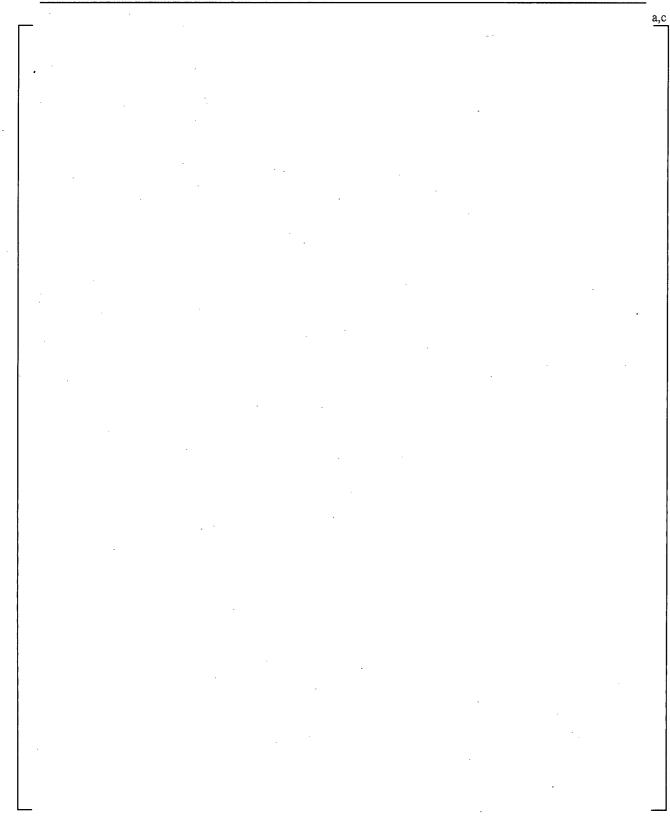


Figure 28.2.4-3 [

WCAP-16996-NP

]^{a,c}

28-161 ⁽

a,c

# Figure 28.2.4-4 [

WCAP-16996-NP

November 2010 Revision 0

]^{a,c}

					a
Γ					-
	· ·				
		,		· · ·	
		•			•
		:			
		,			
	٠				
			,		
	igure 28.2.4-5 [			•	_

WCAP-16996-NP



		a,c
	•	
 Figure 28.2.4-6 [	] ^{a,c}	

#### 28.2.5 Treatment of Accumulator Elevation – SBLOCA

In many plants, the elevation of the accumulators relative to the cold leg is loop-specific. For a small break LOCA, the initiation of accumulator injection is an important event that refills the vessel, bringing about core recovery and effectively ending the transient.

]^{a,c}

#### 28.2.5.1 V. C. Summer (CGE)

The re-baselined CGE small break LOCA reference transient from Section 28.2.1 is executed [

# 28.2.5.2 Conclusions

]^{a,c}

]^{a,c}

All else constant, it is expected that accumulators positioned at a high elevation are less limiting for a small break LOCA. [



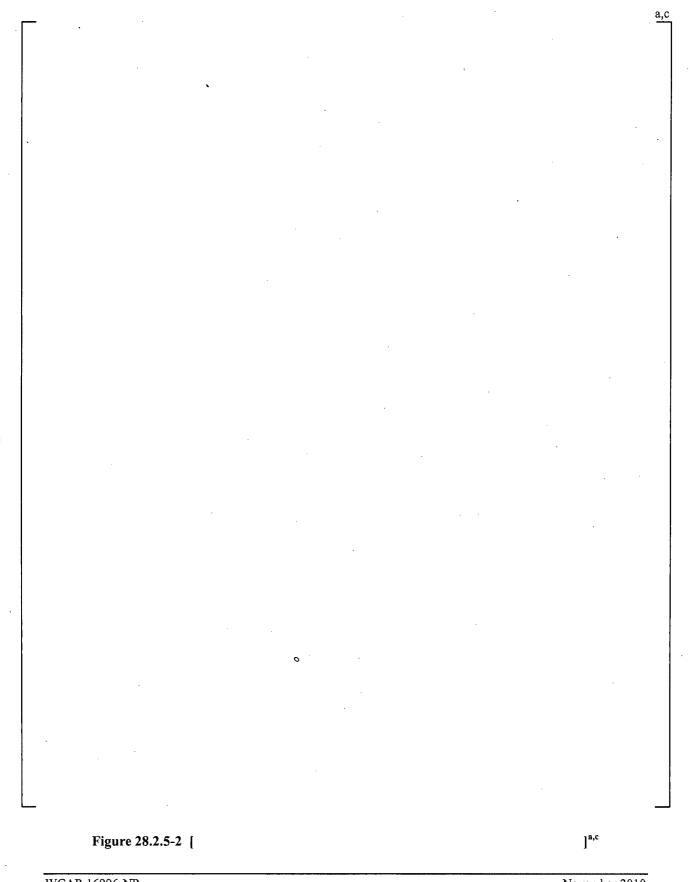
a,c

Figure 28.2.5-1 [

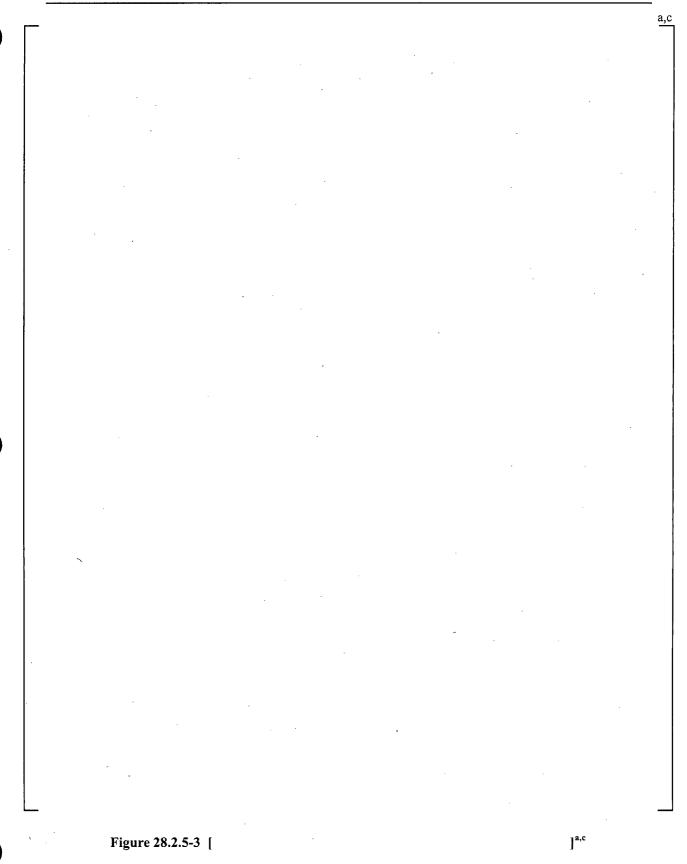
]^{a,c}

# WCAP-16996-NP

28-166



WCAP-16996-NP



WCAP-16996-NP

### 28.2.6 Treatment of Accumulator and SI Lines in the Broken Leg and Break Location – SBLOCA

For all breaks in the cold leg, [

# ]^{a,c}

## 28.2.6.1 Beaver Valley Unit 1 (DLW)

[

[

28.2.6.2 Conclusions

]^{a,c}

WCAP-16996-NP

a,c

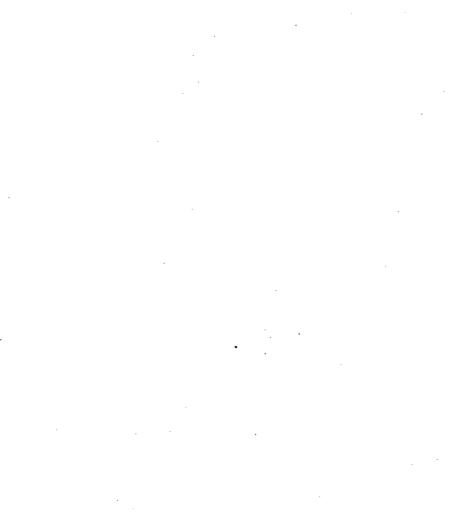


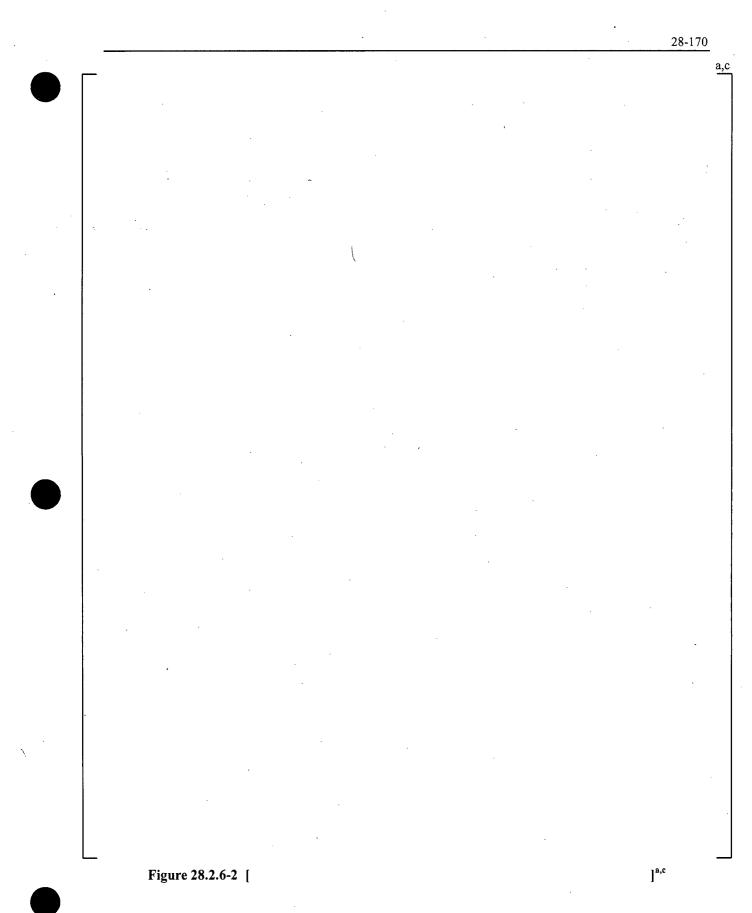
Figure 28.2.6-1 [

]^{a,c}

WCAP-16996-NP

November 2010 Revision 0

.



WCAP-16996-NP

a,c

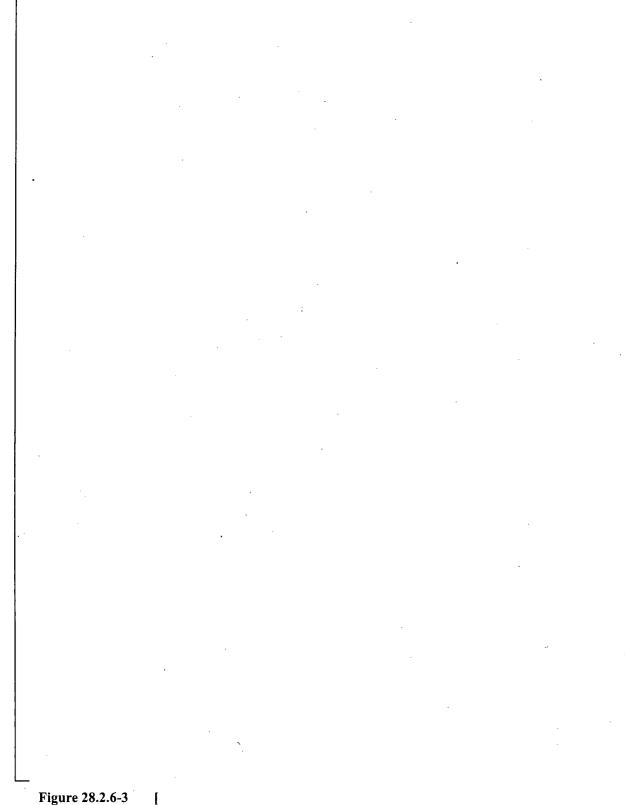


Figure 28.2.6-3

]^{a,c}

WCAP-16996-NP

Figure 28.2.6-4

[

]^{a,c}

WCAP-16996-NP

	_	,			a,c
•					
			• .		
	· ·				
				•	
	· .				
			·		
		· .			
		Υ.			
					•
			•		
		· .		на страна 1	
ļ					

Figure 28.2.6-5 [

]^{a,c}

WCAP-16996-NP

November 2010 Revision 0

.

-						
					. ·	
·						
				· .		
	· .		~			
			•			
			· .			

WCAP-16996-NP

]^{a,c}

Ì

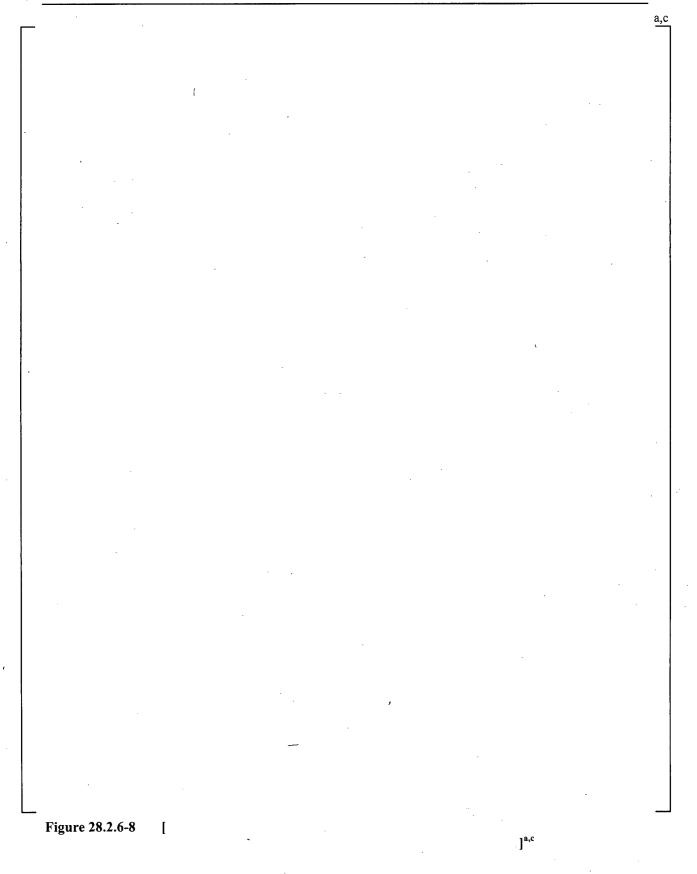
· Figure 28.2.6-7

28-175

a,c

]^{a,c}

WCAP-16996-NP



WCAP-16996-NP

28-1//
--------

							i
•							
	•						
	•						
		• .					
. ,							
						•	
	κ.						
					,		
				•			
				,			
	1						
	те 28.2.6-9 [					e 282.6-9	e 28.2.6.9

WCAP-16996-NP

## 28.2.7 Break Orientation Studies – SBLOCA

Similar to tests in the ROSA facility (see Section 21.7), a series of simulations is performed here to evaluate the plant response to a break oriented at the bottom, side, and top of the broken cold leg. The offtake model that accounts for such geometry upstream of the break is described in Section 5.13.

## 28.2.7.1 V. C. Summer (CGE)

The influence of break orientation on RCS pressure (Figure 28.2.7-1) and core collapsed liquid levels (Figure 28.2.7-2) [

### 28.2.7.2 Beaver Valley Unit 1 (DLW)

Figure 28.2.7-7 and Figure 28.2.7-8 show again that the influence of break orientation on RCS pressure and core collapsed liquid levels [

]^{a,c}

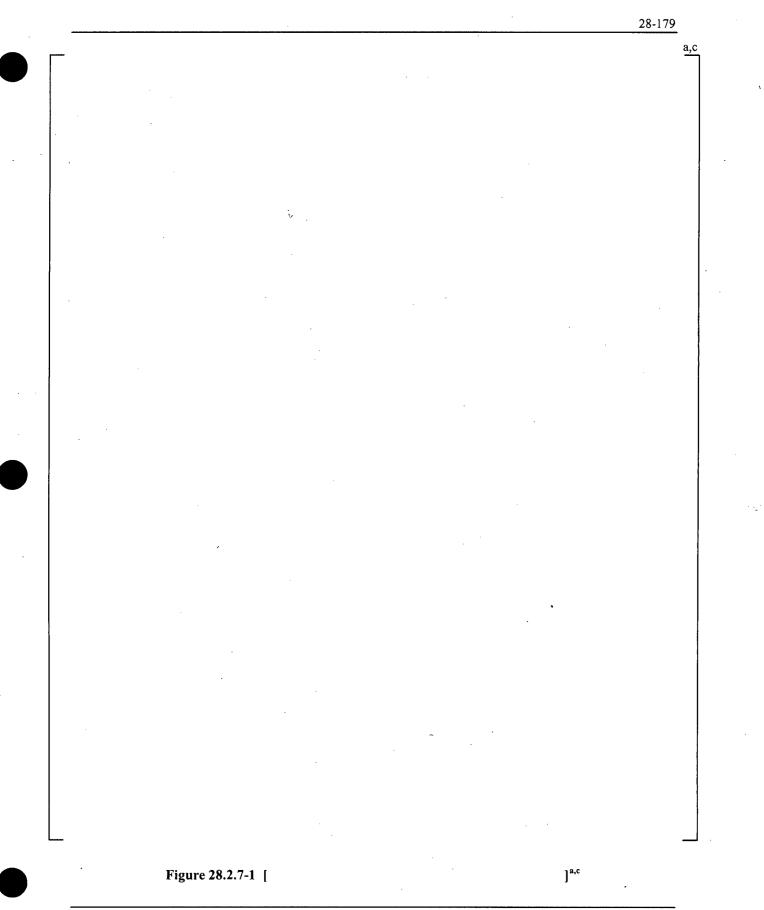
## 28.2.7.3 Conclusions

[

WCAP-16996-NP

]^{a,c}

]^{a,c}



WCAP-16996-NP

28-180
--------

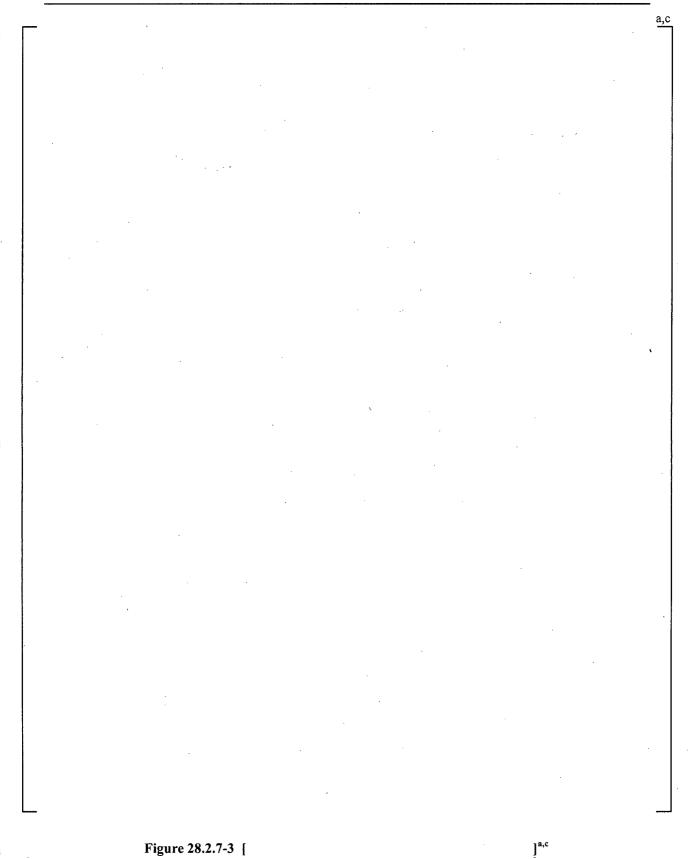
			*			
						. '
		•				
		·				
	. ,					

Figure 28.2.7-2

I

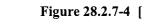
]^{a,c}

WCAP-16996-NP



WCAP-16996-NP

a,c

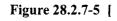


WCAP-16996-NP

November 2010 Revision 0

]^{a,c}

20-103	83	1	-	8	2	
--------	----	---	---	---	---	--



WCAP-16996-NP

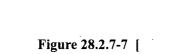
November 2010 Revision 0

]^{a,c}

a,c Figure 28.2.7-6 [ ]^{a,c}

WCAP-16996-NP

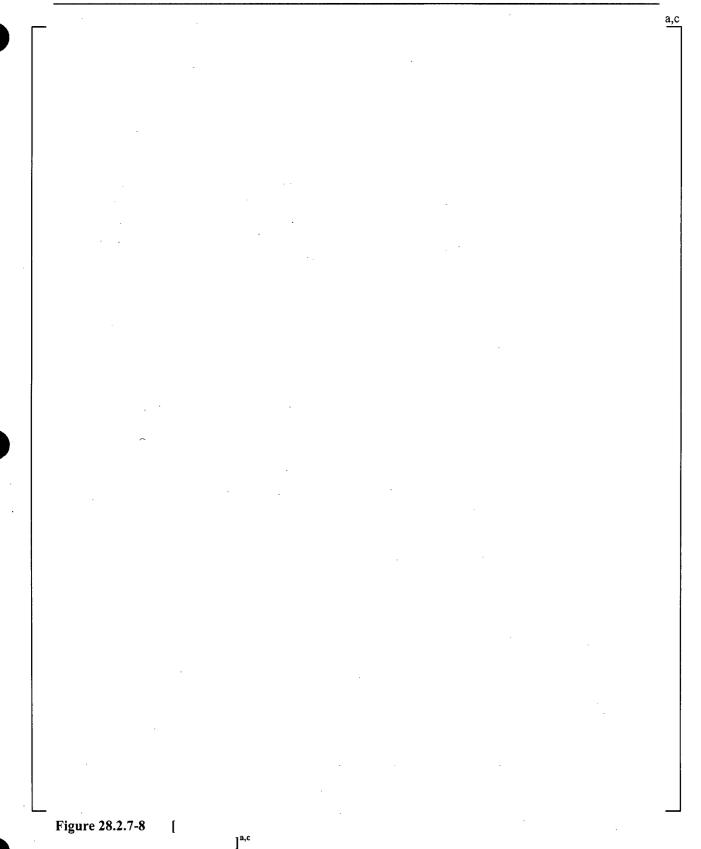






WCAP-16996-NP

28-186



WCAP-16996-NP

a,c

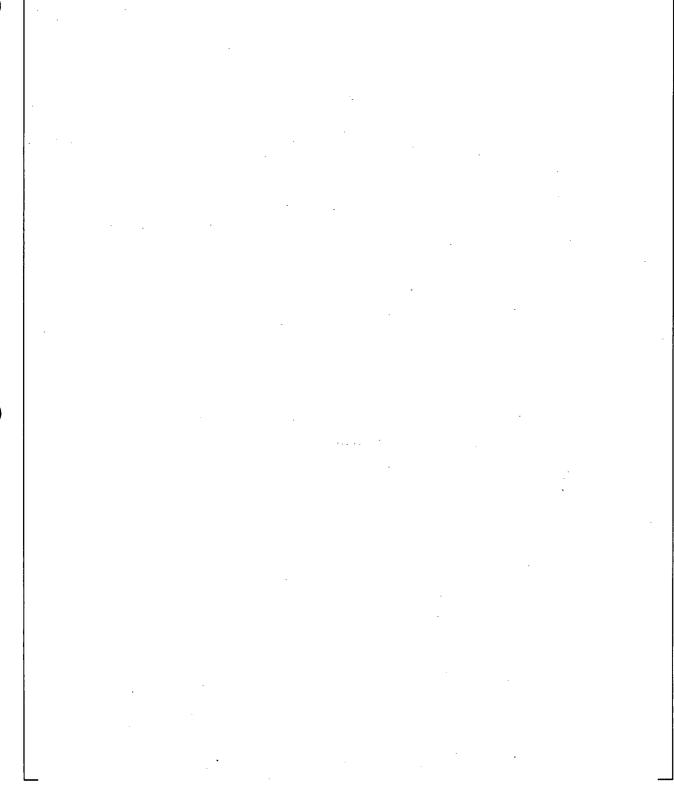
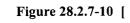


Figure 28.2.7-9 [

]^{a,c}

WCAP-16996-NP

a,c



]^{a,c}

WCAP-16996-NP

a,c

.

Figure 28.2.7-11 [

WCAP-16996-NP

November 2010 Revision 0

`]^{a,c}

a,c Figure 28.2.7-12 [ ]^{a,c}

WCAP-16996-NP

a,c

Figure 28.2.7-13 [

]^{a,c}

WCAP-16996-NP

28-192

__

]^{a,c}

Figure 28.2.7-14 [

WCAP-16996-NP

a,c

Figure 28.2.7-15 [

]^{a,c}

WCAP-16996-NP

# 28.2.8 Interfacial Drag in the Core (Level Swell) – SBLOCA

١

The effect of [

]^{a,c}

## 28.2.8.1 V. C. Summer (CGE)

[

## 28.2.8.2 Beaver Valley Unit 1 (DLW)

[

WCAP-16996-NP

November 2010 Revision 0

]^{a,c}

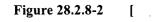
#### 28.2.8.3 Conclusions

Interfacial drag in the core affects core liquid levels, steam venting, and PCT. [  $]^{a,c}$ 

WCAP-16996-NP

28-196 a,c Figure 28.2.8-1 [ ]^{a,c} November 2010 Revision 0 WCAP-16996-NP

a,c



]^{a,c}

WCAP-16996-NP

a,c

ņ

/

]^{a,c}

Figure 28.2.8-3 [

WCAP-16996-NP

28-199
--------

Figure 28.2.8-4 [

]^{a,c}

WCAP-16996-NP

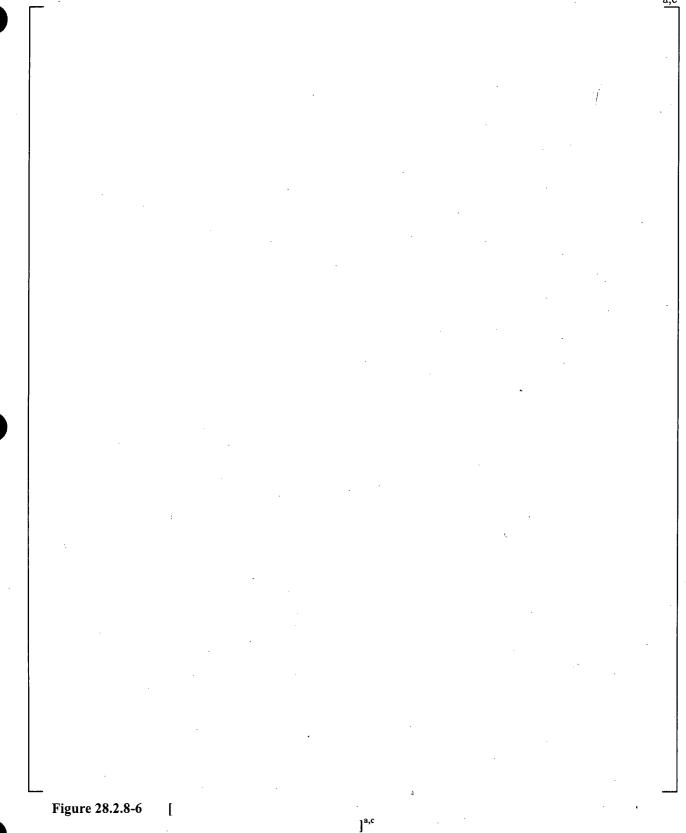
a,c

Figure 28.2.8-5 [

]^{a,c}

WCAP-16996-NP

28-201 a,c



WCAP-16996-NP

a,c

Figure 28.2.8-7 [

WCAP-16996-NP

November 2010 Revision 0

]^{a,c}

28-203

Figure 28.2.8-8 [

WCAP-16996-NP

November 2010 Revision 0

]^{a,c}

28	-204	
20	~407	

_							a
	·						
						-	
			i.				
					·		
_							-
Figure 2	8.2.8-9	[		] ^{a,c}			

WCAP-16996-NP

28-205

]^{a,c}

Figure 28.2.8-10

[

WCAP-16996-NP

a,c

# Figure 28.2.8-11 [

.

]^{a,c}

WCAP-16996-NP

<del></del>	· · · · · · · · · · · · · · · · · · ·	28-207
•		·
	· · ·	
		141-14
		ς
	<i>;</i>	

Figure 28.2.8-12 [

]^{a,c}

WCAP-16996-NP

20-200
--------

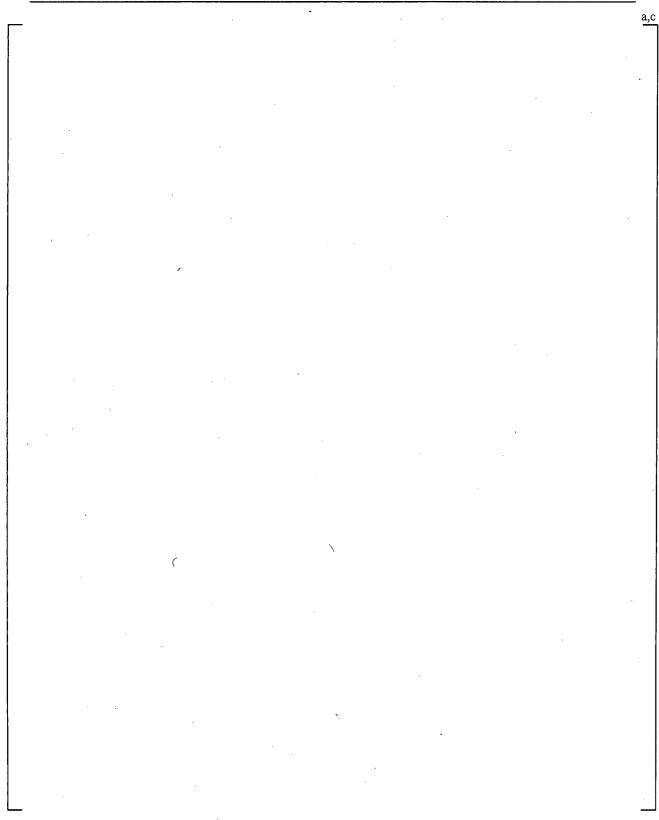


Figure 28.2.8-13 [

]^{a,c}

WCAP-16996-NP

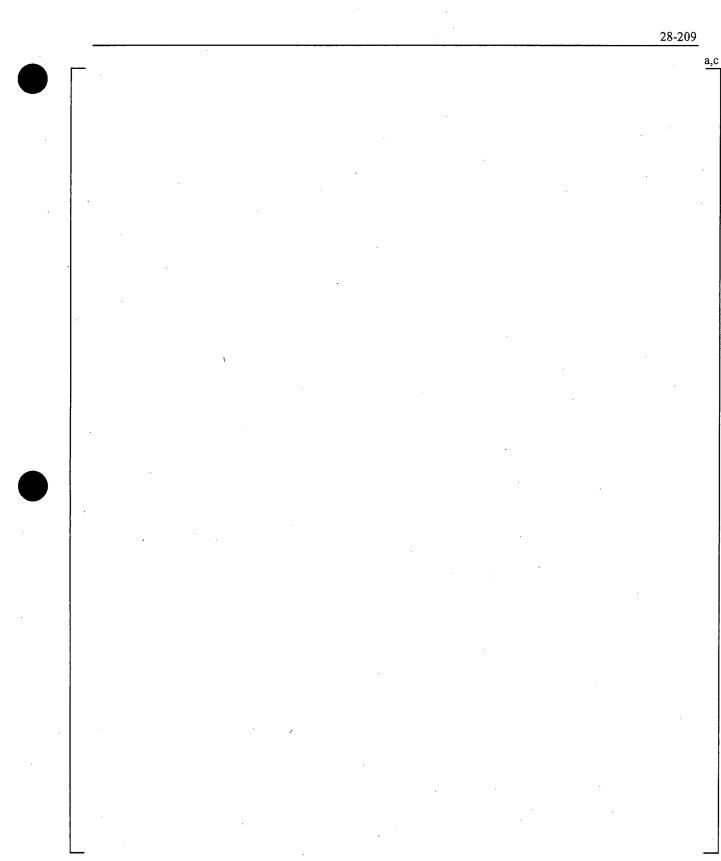


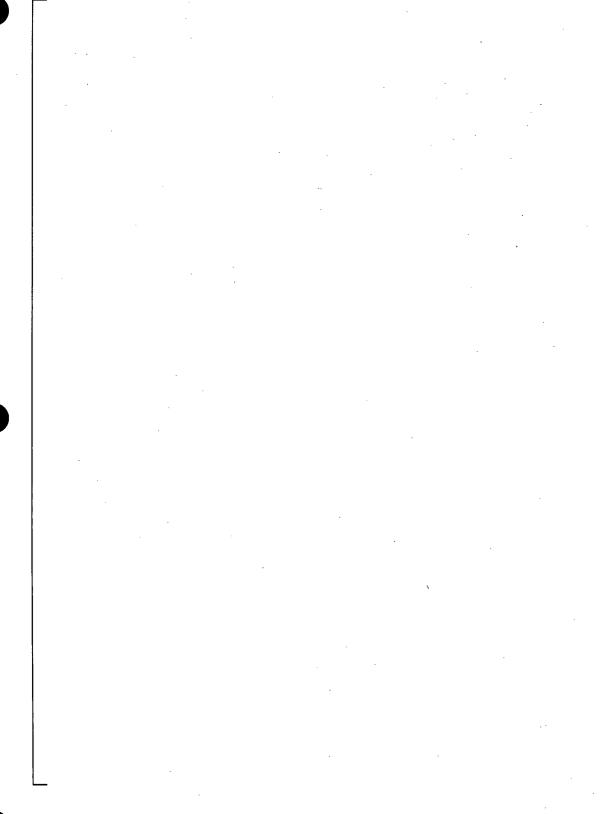
Figure 28.2.8-14 [

]^{a,c}

WCAP-16996-NP

28	1	C

a,c



.

Figure 28.2.8-15 [

WCAP-16996-NP

November 2010 Revision 0

1^{a,c}

	 28-211	-
		a,c
. '		

_____

November 2010 Revision 0

]^{a,c}

WCAP-16996-NP

Figure 28.2.8-16 [

]^{a,c}

]^{a,c}

### 28.2.9 Steam Generator Hydraulics: Tube Plugging – SBLOCA

For a small break, tube plugging affects the steam venting and condensation as a result of reduced flow and heat transfer area. A sensitivity study is performed here to assess the main effects assuming tube plugging levels of 0%, 10%, and 20%.

### 28.2.9.1 V. C. Summer (CGE)

The result of increasing the tube plugging level is a lower heat transfer area in the steam generators and a lower condensation rate. [

The vapor generation from the core is the same for all cases, but [

### 28.2.9.2 Conclusions

Although not a dominant contributor to PCT, [

 $]^{a,c}$ 

a,c Figure 28.2.9-1 ſ ]^{a,c}

WCAP-16996-NP

							a,
ſ	<b>—</b>						
							· .
		,					
		,		~		· -	
		,					
						·	
					1		
					,		
-	Figure 28.2.9-2	[	] ^{a,c}				_

WCAP-16996-NP

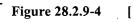
a,c

]^{8,0}

Figure 28.2.9-3 [

WCAP-16996-NP

a,c



]^{a,c}

WCAP-16996-NP

November 2010 Revision 0

 $\sim$ 

a,c

# Figure 28.2.9-5

ſ

]^{a,c}

WCAP-16996-NP



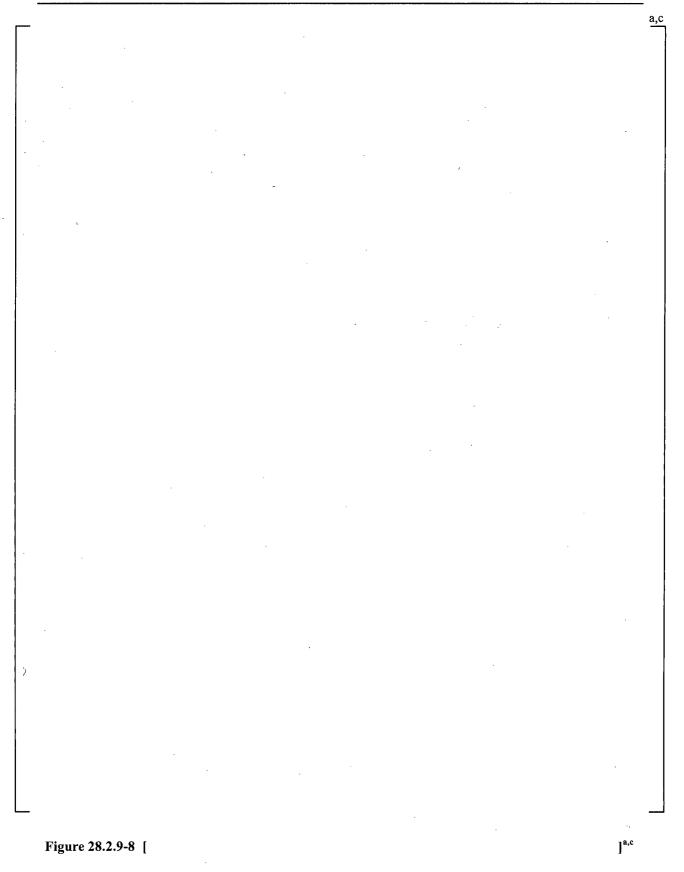
a,c

]^{a,c}

WCAP-16996-NP

Figure 28.2.9-6 [

Figure 28.2.9-7 [								a,c
						·		
					·			
			·					
			,					
			,					
		· .						
		-						
			· · ·					
Figure 28.2.9-7 [								
Figure 28.2.9-7 [								
Figure 28.2.9-7 [				· · ·				
Figure 28.2.9-7 [								
Figure 28.2.9-7 [								
Figure 28.2.9-7 [								
Figure 28.2.9-7 [								
			•					
└────────────────────────────────────								
Figure 28.2.9-7 [ ] ^{a,c}	L						-	
	<b>Figure 28.2.9-7</b>	'[		,		] ^{a,c}		



WCAP-16996-NP

a,c

Figure 28.2.9-9 [

]^{a,c}

WCAP-16996-NP

]^{a,c}

### 28.2.10 Steam Generator Hydraulics: Interfacial Drag – SBLOCA

]^{a,c}

A sensitivity study is performed to determine the effect of interfacial drag in the steam generator tubes following a small break LOCA. [

28.2.10.1 V. C. Summer (CGE)

[

### 28.2.10.2 Beaver Valley Unit 1 (DLW)

]^{a,c}

28.2.10.3 Conclusions

]^{a,c}

WCAP-16996-NP

				a
		· .		
·			,	
		(		
		(		
			· .	
	•			
_				-
Figure 28.2.1	10-1 [		] ^{a,c}	
			J	

WCAP-16996-NP



a,c

Figure 28.2.10-2 [

]^{a,c}

WCAP-16996-NP

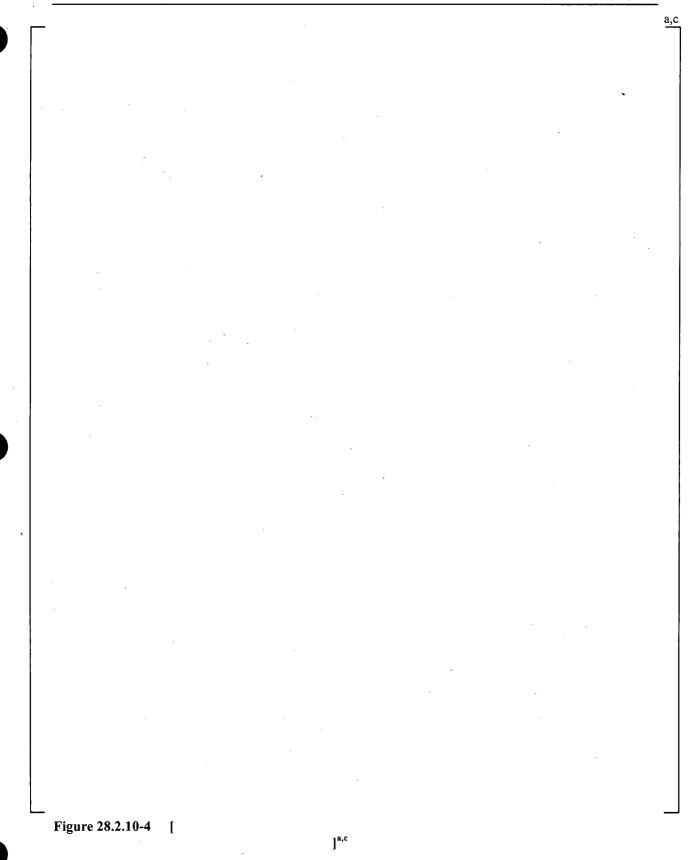
Figure 28.2.10-3 [

]^{a,c}

WCAP-16996-NP

November 2010 Revision 0 a,c

28-226



WCAP-16996-NP

a,c

Figure 28.2.10-5 [

]^{a,c}

WCAP-16996-NP

a,c

Figure 28.2.10-6 [ ]^{a,c}

WCAP-16996-NP

Γ								
		•						
						- 1		
				· .				
	•							
							u.	-
					١			
					·			
	_		2.10-7					

WCAP-16996-NP

i

a,c



Figure 28.2.10-8 [

]^{a,c}

WCAP-16996-NP

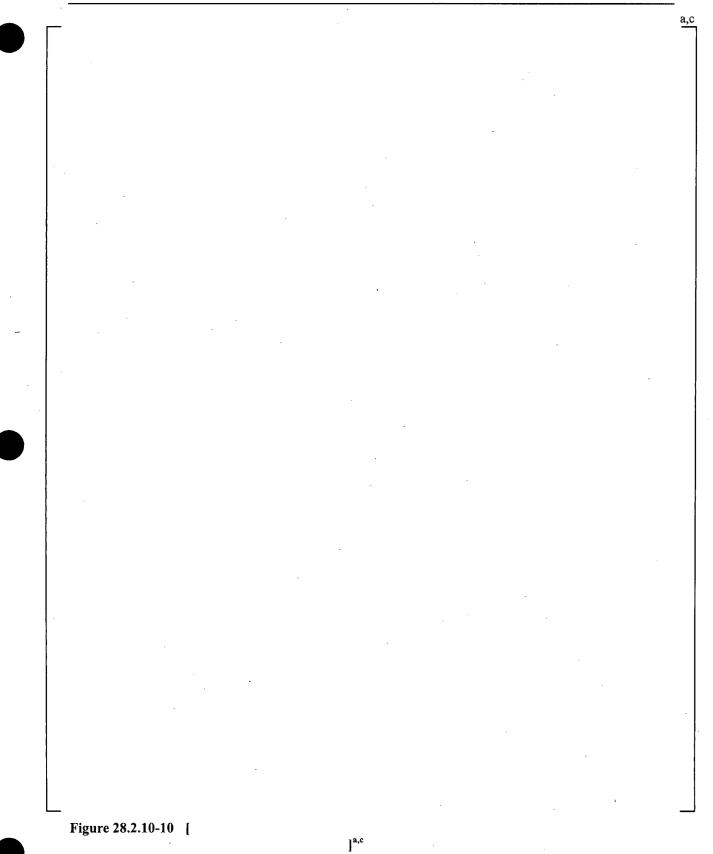
a,c

# Figure 28.2.10-9 [

WCAP-16996-NP

]^{a,c}

28-232



-								28-233
_							,	â
						•		
				,				
							a.	
		••• •						
,	,							
					. *			
· ·								
		·						
			·					
	•							
— Figure 28.2.10-1								

WCAP-16996-NP

a,c

# - Figure 28.2.10-12 [

]^{a,c}

WCAP-16996-NP

a,c

Figure 28.2.10-13 [ ]^{a,c}

WCAP-16996-NP

a,c

### Figure 28.2.10-14 [

]^{a,c}

WCAP-16996-NP

a,c

Figure 28.2.10-15 [

]^{a,c}

WCAP-16996-NP

a,c

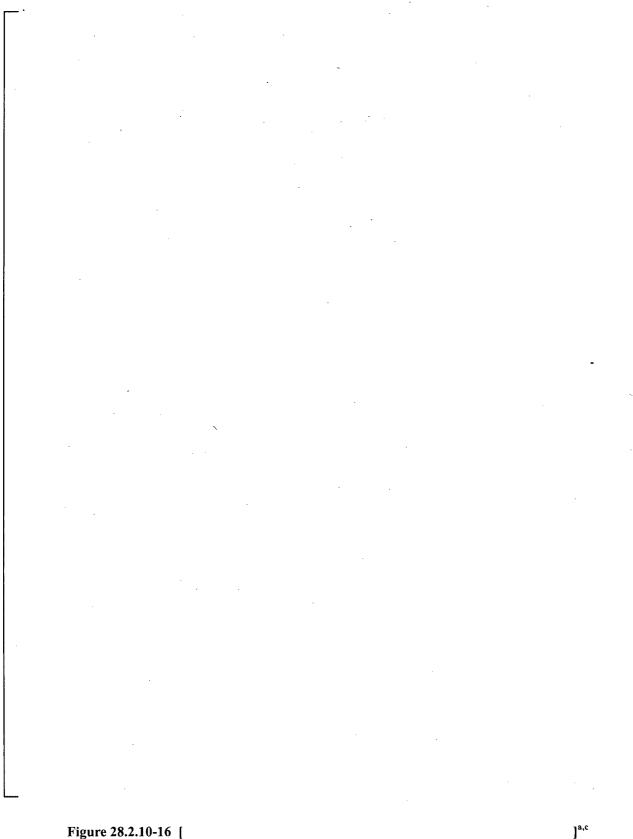


Figure 28.2.10-16 [

WCAP-16996-NP

November 2010 Revision 0

ł

### 28.2.11 Loop Seal Clearance – SBLOCA

Section 18 provides a general description of the loop seal clearance, identified as an important phenomenon in modeling small break LOCAs.

A range of small breaks is explored [

]^{a,c} At the extremes, a small break resulting in break flow less than the maximum charging flow will never clear the loop seals, while a large break LOCA will effectively clear all the loop seals during blowdown.

### 28.2.11.1 V. C. Summer (CGE)

ľ

I

#### 28.2.11.2 Beaver Valley Unit 1 (DLW)

# ]^{a,c}

]^{a,c}

#### 28.2.11.3 Conclusions

Table 28.2.11-1 shows the extent to which the loop seals cleared for the cases shown in this section, the CGE loop 2 LOOP/OPA sensitivity result from Section 28.2.3, the 3- and 4-inch transients from Section 27, and the 3-inch CGE re-baseline from Section 28.2.1. [

Further discussion of the treatment of uncertainty in loop seal clearing is provided in Section 29.1.11. The database generated for the CGE demonstration analysis in Section 31 is also [ ]^{a,c} in Section 31.3.

]^{a,c}

WCAP-16996-NP

### 28.2.11.4 References

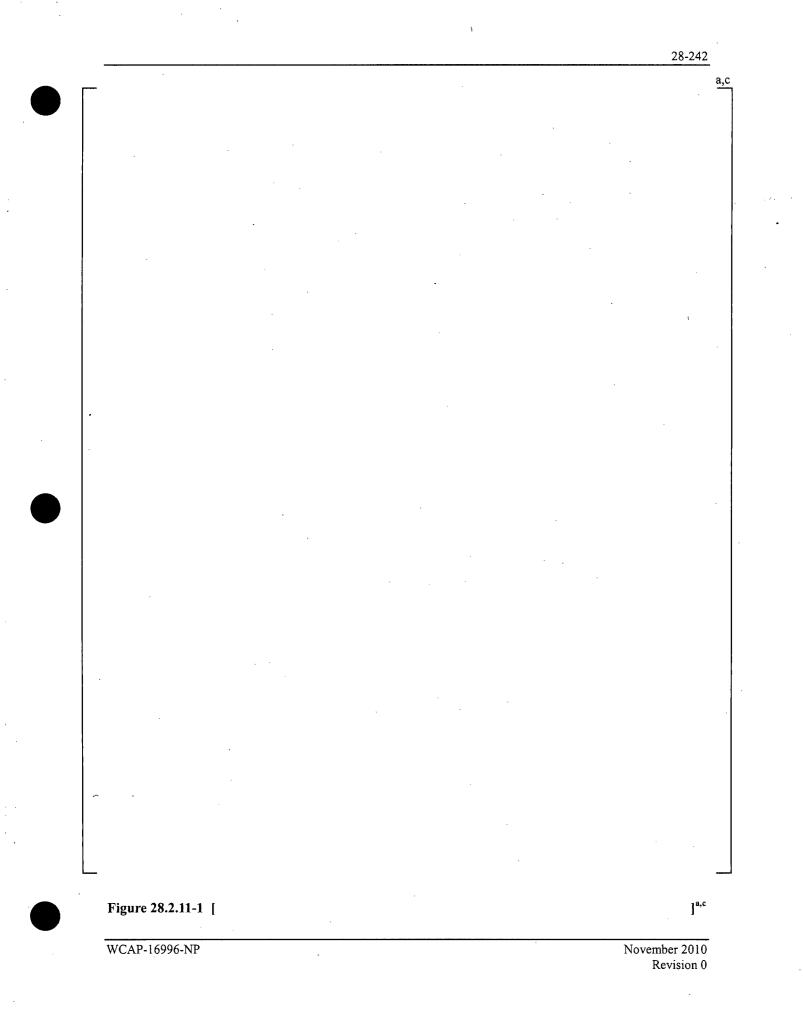
1

1.

Lee, et al., "Phenomenological Uncertainty During Loop Seal Steam Venting in a Small Break Cold Leg LOCA of a PWR," ASME 83-HT-104, 1983.

WCAP-16996-NP

· · · · · · · · · · · · · · · · · · ·			
			•
		• .	
	·		
		·	

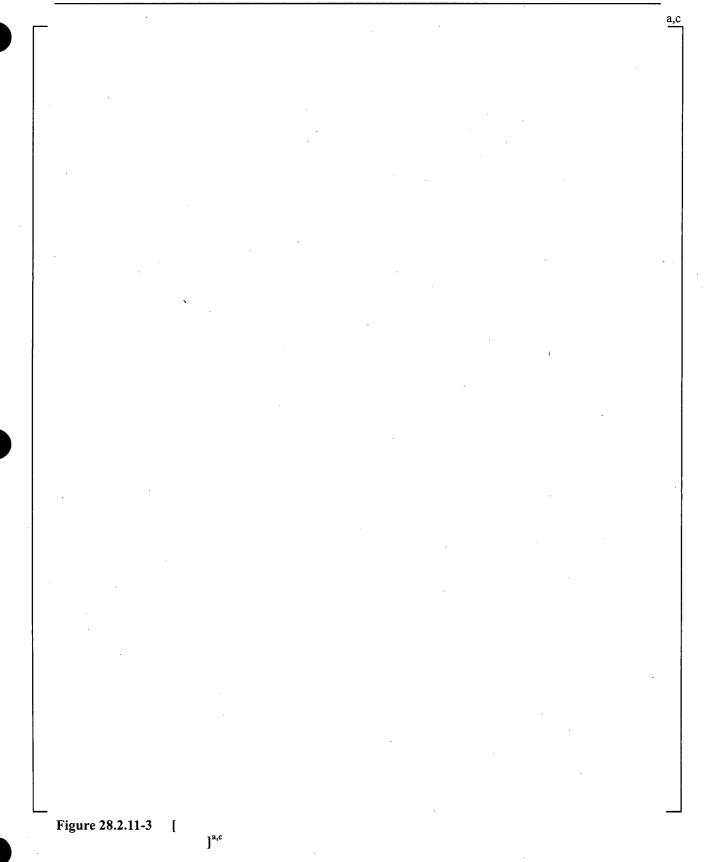


a,c

#### Figure 28.2.11-2 [

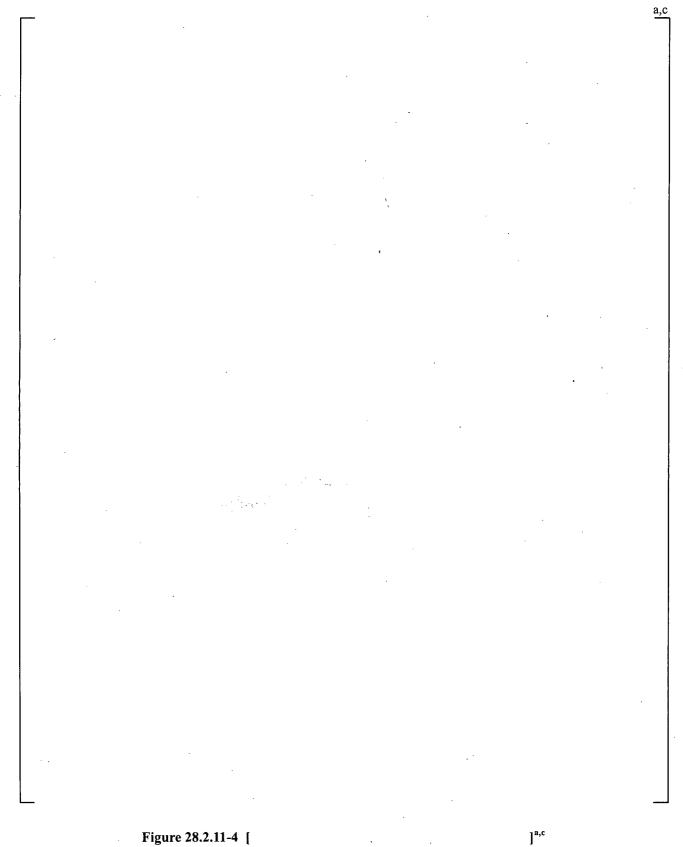
WCAP-16996-NP

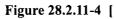
November 2010 Revision 0



WCAP-16996-NP







28-246 a,c Figure 28.2.11-5 [ ]^{a,c}

a,c

Figure 28.2.11-6 [

]^{a,c}

WCAP-16996-NP

a,c

Figure 28.2.11-7 [

ς.

WCAP-16996-NP

a,c ]^{a,c} Figure 28.2.11-8 [

WCAP-16996-NP

#### 28.2.12 Horizontal Stratified Flow (HS_SLUG) – SBLOCA

As discussed in Section 29.1.7, uncertainty in determining the transition between non-stratified and stratified flow regimes is captured [

]^{a,c}. The flow stratification in the RCS piping and in the loop seal is expected to affect the venting and loop seal clearance following a small break LOCA. Here, the 3-inch reference transients for CGE (re-baseline from Section 28.2.1) and DLW are executed using [

]^{a,c}.

]^{a,c}

28.2.12.1 V. C. Summer (CGE)

[

#### 28.2.12.2 Beaver Valley Unit 1 (DLW)

 $]^{a,c}$ 

WCAP-16996-NP

[

#### 28.2.12.3 Conclusions

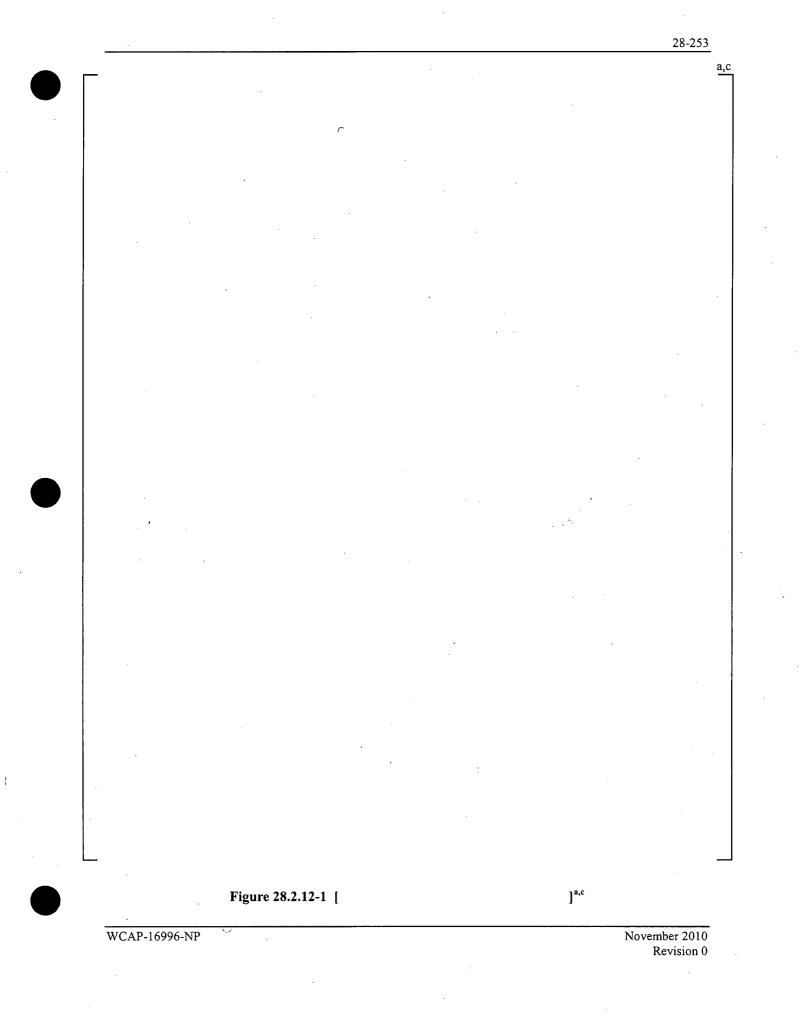
]^{a,c}

[

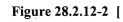
The uncertainty associated with transition to stratified flow will be accounted for [ $]^{a,c}$  as described in Section 29.1.7.

-	

Fable 28.2.12-1       Flow Regime Flags			
Flag	Flow Regime		
1	Bubbly or Slug		
2	Stratified ( $\alpha < 0.5$ )		
2.5	Wavy Dispersed ( $\alpha < 0.5$ )		
3.	Churn (Transition)		
4	Stratified $(0.5 < \alpha < 0.75)$		
4.5	Wavy-Dispersed $(0.5 < \alpha < 0.75)$		
5	Annular/Mist		
6	Stratified $(0.75 < \alpha)$		
. 6.5	Wavy-Dispersed $(0.75 < \alpha)$		



a,c



х.,

WCAP-16996-NP

November 2010 Revision 0

28-255

a,c

# Figure 28.2.12-3 [

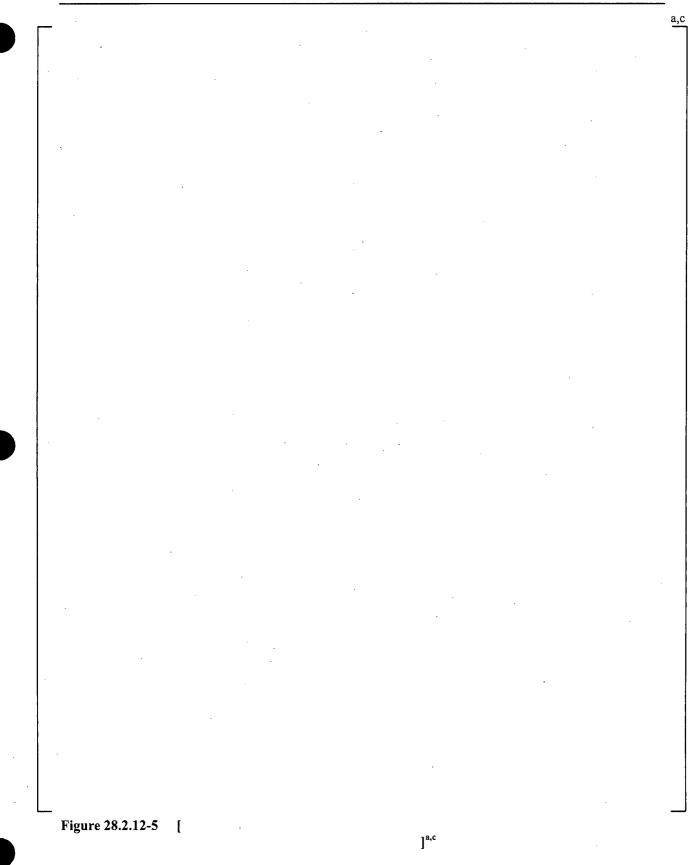
]^{a,c}

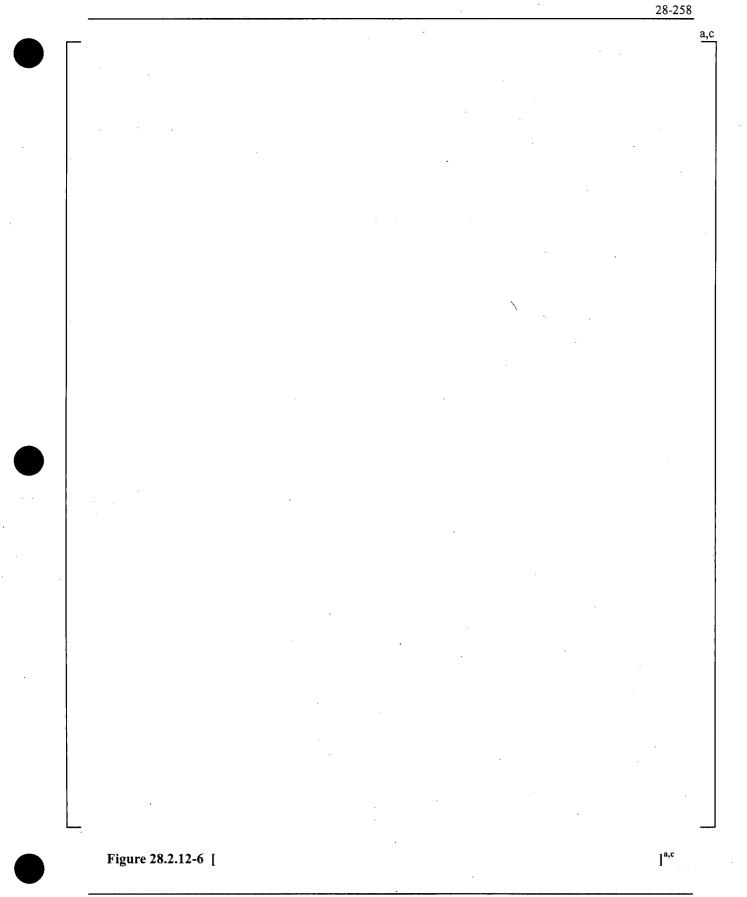
WCAP-16996-NP

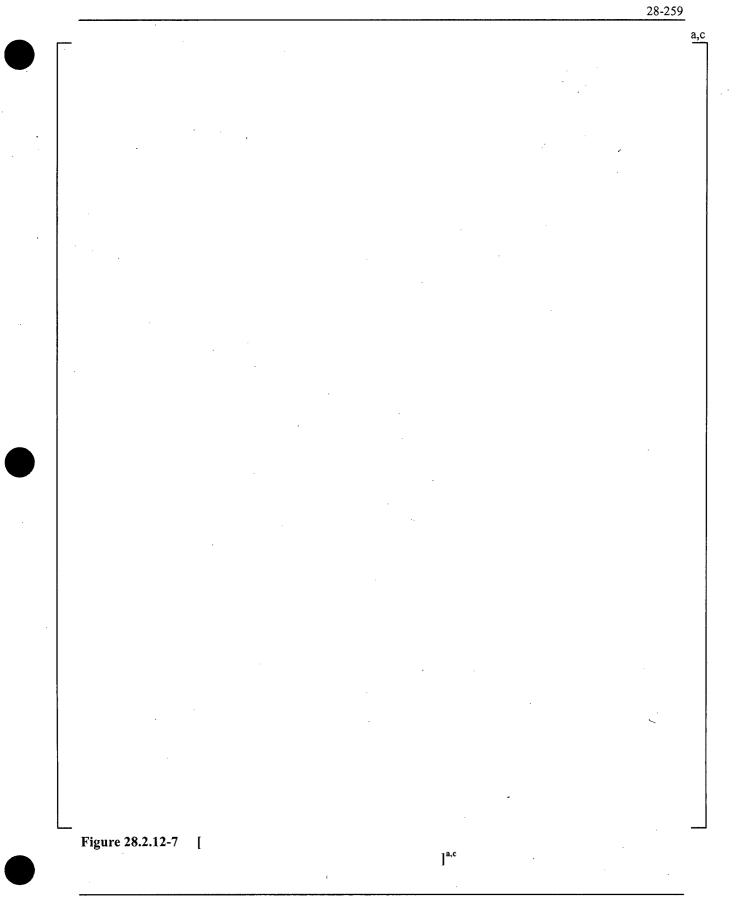
2.8	-2:	56

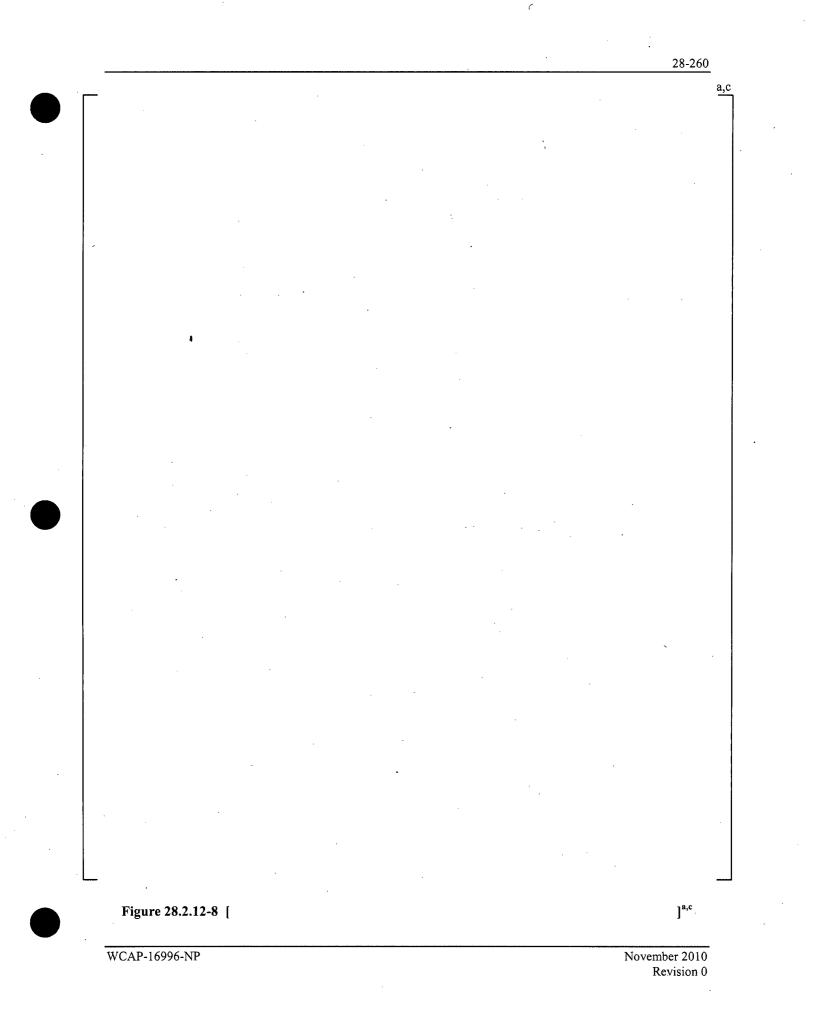
	8
•	
	•
$\sim$ $\sim$	
·	
· .	
	-
Figure 28.2.12-4 [ ] ^{a,c}	

28-257









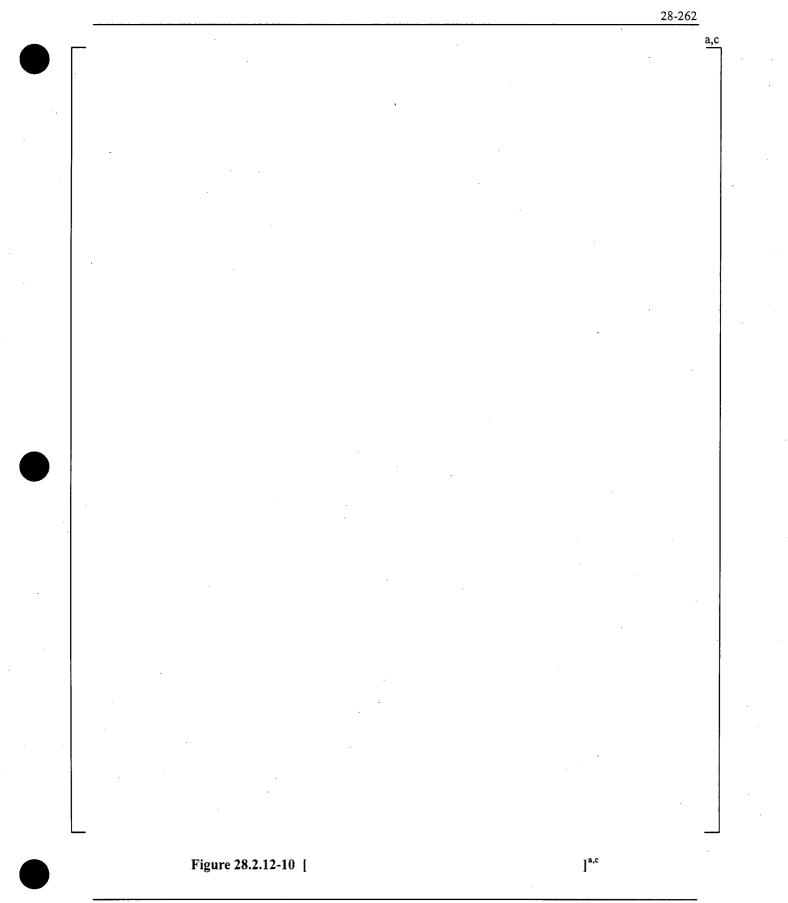
a,c

## Figure 28.2.12-9 [

]^{a,c}

WCAP-16996-NP

ſ



	·	 		28-263
				a,c
	· · · ·			
· · ·			. · ·	
		· .		
			·	
, ,				
			· ·	
			,	
			- 9.6	
	Figure 28.2.12-11 [		] ^{a,c}	

.

a,c

Figure 28.2.12-12 [

]^{a,c}

WCAP-16996-NP

a,c

# Figure 28.2.12-13 [

WCAP-16996-NP

November 2010 Revision 0

......

28-266

ī

a,c

## Figure 28.2.12-14 [

]^{a,c}

WCAP-16996-NP

28<u>-267</u>

a,c

### Figure 28.2.12-15 [

WCAP-16996-NP

November 2010 Revision 0

a,c

## Figure 28.2.12-16 [

l^{a,c}

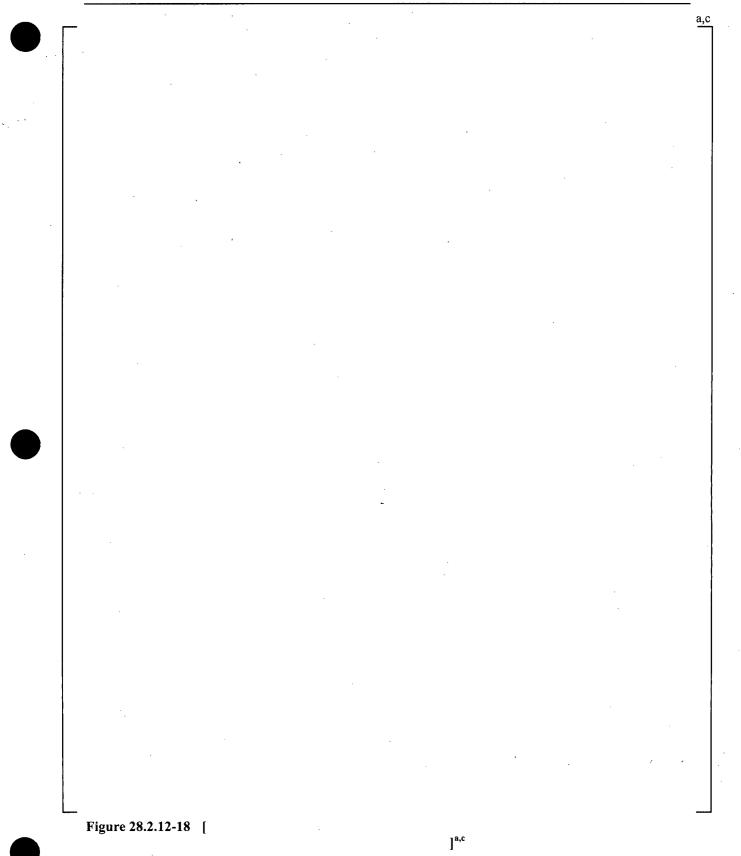
WCAP-16996-NP

a,c

Figure 28.2.12-17 [

WCAP-16996-NP

November 2010 Revision 0



WCAP-16996-NP

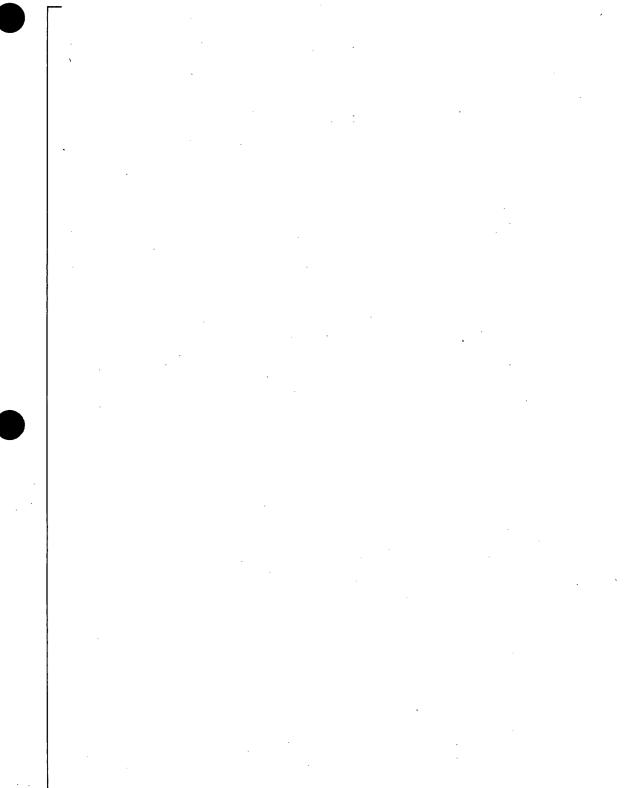


Figure 28.2.12-19 [

WCAP-16996-NP

November 2010 Revision 0

]^{a,c}

a,c

- Figure 28.2.12-20 [		] ^{a,c}		
· · ·				
	· ·			
			•	
			ł	

WCAP-16996-NP

(

a,c

Figure 28.2.12-21 [

WCAP-16996-NP

November 2010 Revision 0

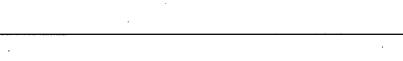


Figure 28.2.12-22 [

]^{a,c}

WCAP-16996-NP

November 2010 Revision 0

28-274

a,c

#### **29** ASSESSMENT OF UNCERTAINTY ELEMENTS

The list of dominant phenomena was identified by the PIRT discussed in Section 2. The PIRT included all processes covering the scenarios that span over the full spectrum of break sizes. A summary of the important phenomena was provided in Section 2.3.3. The code models associated with such phenomena were then assessed against an independent dataset comprised of separate effect tests (SETs) and integral effect tests (IETs). This was the subject of Sections 12 through 23. Section 24 provides a synthesis of the assessment as well as an analysis of potential compensating errors.

The code assessment exercise leads to the determination and quantification of model biases and uncertainties (EMDAP Step 20). Consistent with the CSAU roadmap, the uncertainty has to be ultimately propagated or convoluted statistically during the plant analysis. The statistical procedure used to propagate the uncertainties is the subject of Section 30. The approach is based on a Monte Carlo convolution of the uncertainty contributors. The procedure is designed to generate a sample of the LOCA 'population' and then develop probabilistic statements that show compliance with the 10 CFR 50.46 criteria.

In general, the uncertainty parameters fall into three categories:

- 1. Nominal without Uncertainty The nominal (expected or midpoint) value of the parameter is used without consideration of uncertainty when the variation in the parameter is tightly controlled, such as pressurizer level, or when the sensitivity of the transient to the value of the parameter is negligible, such as the initial RCS boron concentration. An example of a model treated as nominal without uncertainty is the offtake model (Section 29.1.1.1).
- 2. Bounded A conservative value of the parameter is used when the parameter varies gradually as a function of operating history, when the sensitivity of the transient to variations in the parameter is small, or when the effort to develop and justify a detailed uncertainty treatment is judged to exceed the benefits of doing so. Bounded plant parameters are discussed in Section 29.3.1. An example of a phenomenon treated in a bounding manner is steam binding.
- 3. Nominal with Uncertainty The Westinghouse methodology includes three categories of uncertainty contributors to the overall uncertainty assessment. These are the thermal-hydraulic model uncertainties, the power-related parameter uncertainties, and the initial and boundary condition uncertainties.

Tables 29-1 through Table 29-5 provide the list of the uncertainty contributors or parameters that are explicitly considered in the FSLOCA methodology. The uncertainty contributors [

]^{a,c} For most models, ranging capabilities on key parameters has been included in the code such that the solution can be randomly biased during the Monte

Carlo convolution of the uncertainties. The objective of Section 29.1 is to develop and justify the probability density function (PDFs) associated with such key parameters.

While a PDF was developed and justified for most of the models, in some instances a bounding approach was judged to be adequate for the purpose of the uncertainty analysis. This was the case when a complete characterization of the individual model biases and uncertainty could not be pursued, because of the complexity of the process, and/or because limitations in experimental data caused the effort of developing a detailed uncertainty treatment for each individual component to exceed the benefit of doing so. In those circumstances the objective of the exercise was to demonstrate that the biases associated with that specific complex phenomenon, albeit not quantified, are conservative with respect to engineering figures of merit in the context of a realistic but still conservative LOCA simulation. In those cases the validity of the approach was also supported by compensating error analyses (Section 24). [

The analysis of the uncertainty on the break flow is [

]^{a,c} The discussion of the break model methodology deserves a section itself and Section 29.2 is dedicated to this topic.

Core power related parameters are listed in Table 29-4. The time in cycle is the first parameter selected since many fuel related parameters are a function of burnup. The methodology is presented in Section 29.4.1.

Uncertainties associated with the fuel rod models are listed in Tables 29-3 and 29-4. Some of these parameters are characterized as local uncertainties since the effect is postulated to mainly affect the local PCT or MLO and the effect on the global T/H response is expected to be minimal. [

]^{a,c}

All the other uncertainty parameters are associated with the plant parameters listed in Table 29-5. Section 29.3 is dedicated to the topic.

Section 29.5 provides a review of the PIRT and summarizes the conclusions from the perspective of model biases and uncertainty of all phenomena ranked high (H). This corresponds to EMDAP Step 20. Finally, Section 29.6 addresses experimental accuracy in the context of Step 9 of the EMDAP roadmap.

Table 29-1         Uncertainty Elements – Break Location, Type and Area Sampling Methodology			
	· · ·		
	· · ·		
	······································		
	· · · · · · · · · · · · · · · · · · ·		

Table 29-2	Uncertainty Elements	- Thermal-Hydraulic Models	
	and the state of the		· · · · · · · · · · · · · · · · · · ·
			- •
· ·	·		·
			· · · · · · · · · · · · · · · · · · ·
		· · ·	

Table 29-3a   Uncertainty Element	nts – Local Models [	] ^{a,c}	
		· · ·	
		· · · ·	
۰. ۵.۰		•	

29-4

29-5

Table 29-3bBurst Strain for	] ^{a,c}	
		· · · ·

	· · ·

Table 29-5	Initial and Boundary Conditions Considered in Uncertainty Methodology Defined in Section 29.3.2		
	······································		
		· · · · · · · · · · · · · · · · · · ·	
		· · · · · · · · · · · · · · · · · · ·	
		· · · · · · · · · · · · · · · · · · ·	

# 29.1 GENERATION OF MODEL UNCERTAINTY PARAMETERS AND RANGING DISTRIBUTIONS

The purpose of this section is to document the development of the bias and uncertainty distributions (PDFs) for the ranging parameters associated with the global models. Key controlling parameters (or multipliers) on selected closure relationships have been coded in <u>WCOBRA/TRAC-TF2</u> to permit the explicit ranging of such uncertainties. For a small set of phenomena, a conservative approach was instead chosen to bound the bias and uncertainty of the associated models. For less influential but complex phenomena a nominal value without uncertainty was sometimes judged to be adequate. The justification of these decisions is the subject of the following subsections.

## 29.1.1 Break Flow – [

The assessment of the break flow model is presented in Section 12. A total of [

]^{a,c}

]^{a,c} were used for the determination of bias and uncertainty associated with the critical flow model prediction used in <u>WCOBRA/TRAC-TF2</u>. The main results are summarized in Section 12.5.2.

The model has the tendency to [

The break flow calculated by the code is ranged by applying a discharge coefficient (CD). The application of discharge coefficient is accomplished by modifying the break flow area and more details on implementation is provided in Sections 29.2.4 and 29.2.5 for DEG and split breaks, respectively. Here, for the purpose of defining the uncertainty analysis methodology, [

]^{a,c}

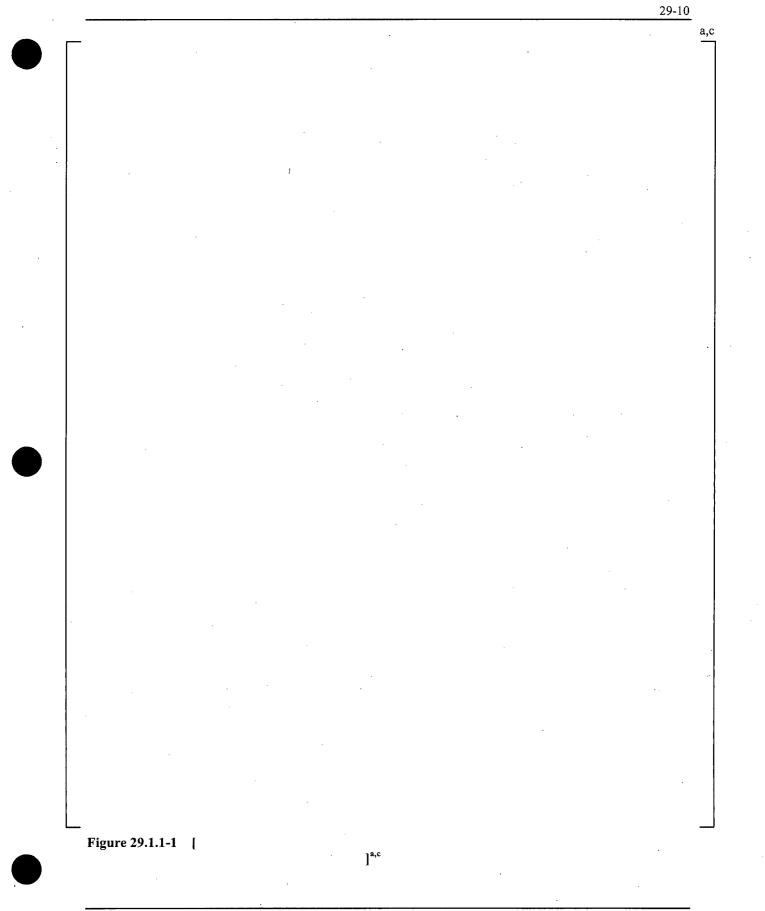
Once the break type and break area are selected, as discussed in Section 29.2, the uncertainty on the break flow model is treated by independently sampling a value [

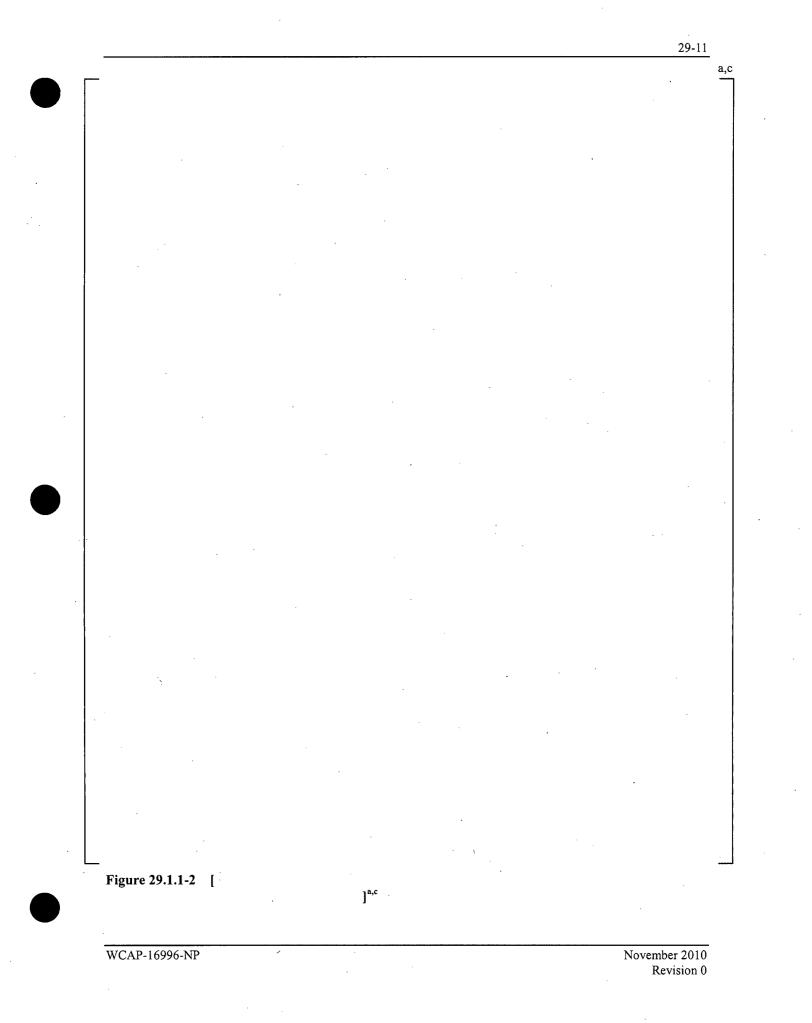
]^{a,c}

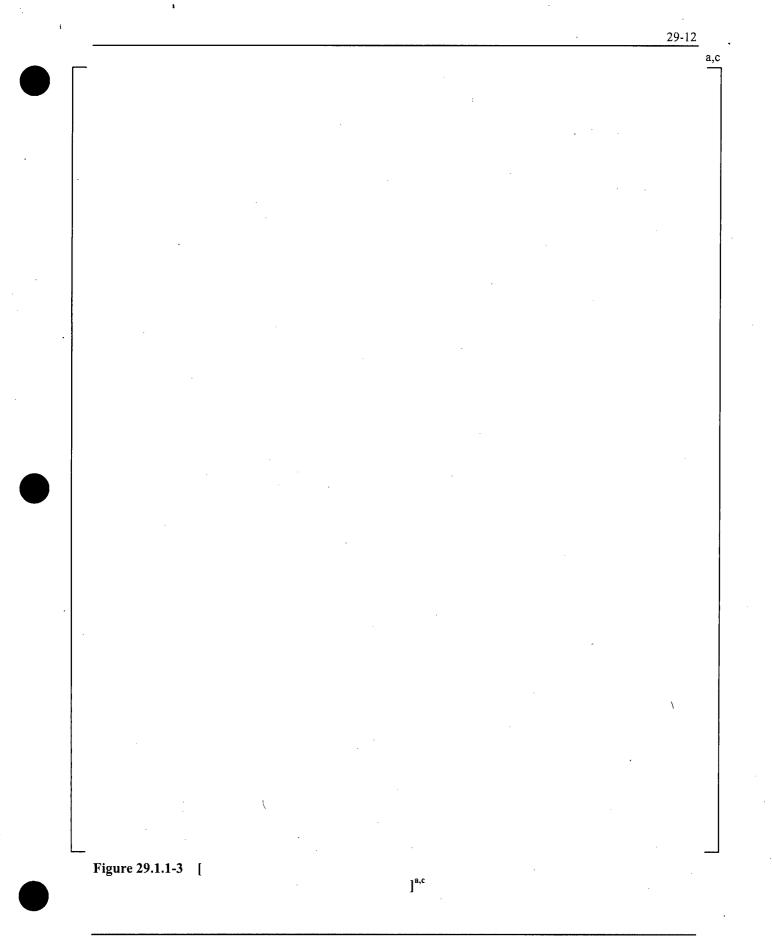
Sensitivity studies on the effect of [ ]^{a,c} on the small break LOCA transient were performed with the ROSA-IV 5% side break test SB-CL-18, Section 21.

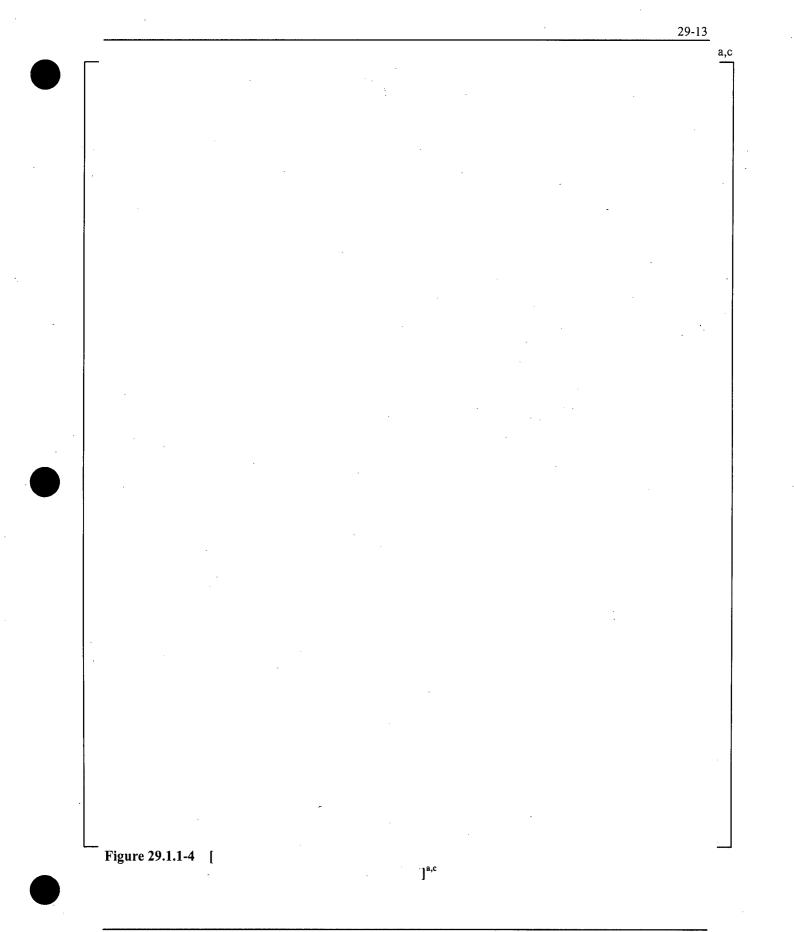
Detailed discussion of the [  $]^{a,c}$  sensitivity results is presented in Section 21.12. The sensitivity calculations showed that the [  $]^{a,c}$  multiplier has a pronounced effect on the calculated loss of inventory through the break discharge from the very beginning of the transient. This effect propagates throughout the entire transient and has a fairly significant effect on the calculated peak cladding temperature during the loop seal clearance and the boiloff period as well; see Figure 21.12-20 in Section 21.12.

The results of the [ ]^{a,c} sensitivity calculations, documented in Section 21.13, show some effect on the loop seal clearance period; higher [ ]^{a,c} tends to somewhat delay the core level recovery following the loop seal clearance depression. However, the effect of the [ ]^{a,c} multiplier on the transient is much more pronounced after the loop seal clearance. With higher [ ]^{a,c} multiplier the system depressurizes faster and boiloff heatup occurs earlier. However, with higher [ ]^{a,c} the peak cladding temperature is calculated to turn around earlier due to the sooner initiation of accumulator injection; see Figures 21.13-20 and 21.13-21 in Section 21.









#### 29.1.1.1 Break Flow - Offtake and Pull-Through Behavior

When the flow in the cold leg is stratified, the vapor pull-through (break below stratified interface)/liquid entrainment (break above stratified interface) phenomenon is especially important in determining the flow quality upstream of the break. This phenomenon is called offtake entrainment and is discussed in Section 12.7. The uncertainty associated with the offtake model could be an additional contributor to the break flow uncertainty. Note that this effect is only relevant for smaller break sizes.

]^{a,c}

WCAP-16996-NP

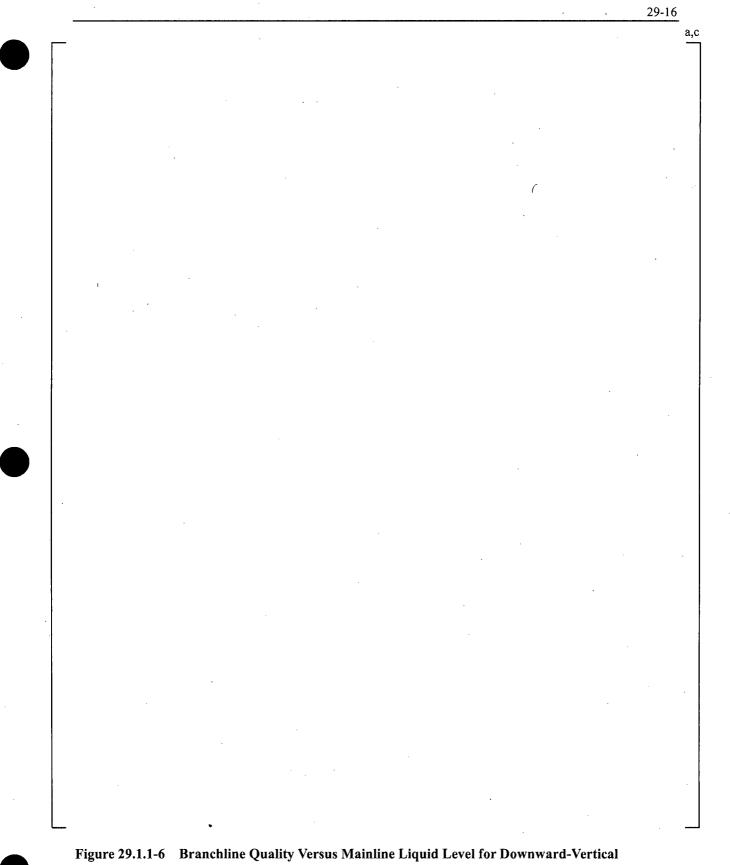
[



(

29-15

a,c



Configuration

#### 29.1.2 Broken Cold-Leg Nozzle Flow Resistance (KN) and Broken Loop Pump Resistance

The flow resistance through the broken loop cold leg nozzle was found to be of high importance during the blowdown phase of a large break LOCA in the PIRT (Section 2.3.2.14). The broken loop flow resistance, of which the pump resistance is a large contributor, was ranked high in the PIRT for large breaks (Section 2.3.2.9). This section assesses the uncertainty associated with the cold leg nozzle and broken loop pump resistance. These two large contributors to relative break path resistance, in combination with the influence from break discharge coefficient uncertainty, [

#### 29.1.2.1 Broken Cold-Leg Nozzle Flow Resistance (KN)

The uncertainty in the flow resistance through the broken loop nozzle is characterized here. Table 29.1.2-1 shows the experimental database used to establish the value and range for this parameter. The effect of geometry was established by evaluating data from full-scale UPTF tests (Section 19).

The UPTF pressure drop data (Section 19.3.5.10) was used to extract a loss coefficient (KN) by subtracting out velocity and friction effects. The way in which the loss coefficient is used at the ID/3D junction in WCOBRA/TRAC-TF2 is as a total pressure loss coefficient. For application to the ID/3D junction, the data is evaluated as a total loss coefficient by subtracting the friction pressure drop.

The UPTF range of conditions relative to PWR is shown in Table 29.1.2-1, with the pressure loss data provided in Table 19.3-16.

]^{a,c}

An additional data point is available from estimates made of the pressure loss during reflood in the CCTF test facility (Akimoto et al., 1984). These estimates indicate a pressure loss coefficient of approximately 0.5, which is well within the range of the UPTF test data. The CCTF range of conditions relative to the UPTF and PWR ranges is shown in Table 29.1.2-1.

#### 29.1.2.2 Broken Loop Pump Resistance

For large breaks, the pump flow resistance contributes to the overall loop resistance, which together with the broken cold leg nozzle resistance affects the flow reversal and stagnation in the core. For smaller breaks, the influence of flow resistance through the pump and its effect on flow to the break is at most of medium importance during the natural circulation and loop seal clearing periods. Therefore, the ranging of the broken loop pump resistance is considered for the uncertainty analysis with the expectation that such ranging will be relevant or have an effect only for larger breaks.

The pump model was developed from 1/3-scale Westinghouse pump data (Section 20.2), and assessed against four LOFT tests (Section 22). In two of the tests, the pumps continued to rotate, while in the other

]^{a,c}

(29.1.2.1-1)

two tests, the pumps were allowed to coast down. The two-phase test data extend well beyond the range expected to occur in a PWR. This can be seen in Figure 20.2-6, which shows the <u>WCOBRA/TRAC-TF2</u> pump head curves and the test data in non-dimensional (homologous) form.

Recall from Section 10.4 that the homologous curves plot the normalized head/normalized speed squared ratio ( $H/\alpha^2$ ) against the normalized flow/normalized speed ratio ( $\upsilon/\alpha$ ), where the normalization is to pump rated head, flow, and speed. In Figure 20.2-6, two-phase data are available over a normalized flow range [  $]^{a,c}$ . It was found (Section 20.2) that the uncertainty in two-phase pump head was significant when the pump was in dissipative (i.e., forward flow producing a pressure drop through the pump) operation. Pumping mode data was therefore used to determine the degradation multiplier, and it was found that predictions were largely insensitive to the nature of the degradation multiplier curve. The uncertainty in the pump will therefore be accounted for using the uncertainty in the dissipative (single phase) data.

From Figures 20.2-3 and 20.2-4 of Section 20.2, the uncertainty range of  $(H/H_R)/(Q/Q_R)^2$  is [

## ]^{a,c}

The approach on the ranging of  $(H/H_R)/(Q/Q_R)^2$  is considered to be applicable to both small and large break LOCA scenarios. To evaluate the impact of these decisions for a small break, a sensitivity calculation was performed with the ROSA-IV test SB-CL-18, Section 21.14. The ROSA-IV sensitivity performed therein was not a sensitivity on the  $(H/H_R)/(Q/Q_R)^2$  adder, but simply looks at the sensitivity on the results when the pump resistance at zero rotation point in the homologous curve (resistance when pump velocity is equal to zero) is reduced by 50%. The ROSA-IV sensitivity results presented in Section 21.14 show that the impact is small. Since during the critical time for a small break (boiloff) the pumps will most likely operate close to locked rotor conditions, this shows that ranging of the  $(H/H_R)/(Q/Q_R)^2$  is expected to have a negligible effect on the results.

Table 29.1.2-1         Nozzle Loss Coefficient Assessment Data Base			
	Test Range		
Parameter	UPTF	CCTF	PWR Range
Geometry: Vessel/Nozzle	Full Scale	1/20 Scale	Full Scale
Pressure (psia)	120 – 40	30	2250 - 40
Vapor Fraction	1.0	0-1	0-1

#### 29.1.3 Delivery and Bypassing of ECC – Bounding Approach

The delivery and bypassing of ECC water is a phenomena which is only important during a LB scenario. The ECC bypass (CCFL) models in <u>W</u>COBRA/TRAC-TF2 were assessed in Section 19.3 using UPTF full-scale data. In particular, the UPTF Test 6 series looks at ECC bypass during the blowdown period and UPTF Test 25 investigates steam-water interaction (entrainment) during reflood.

The assessment showed that the models as coded adequately predict the ECC delivery and bypassing with a moderate conservative bias that does not warrant an explicit consideration of the uncertainties.

#### 29.1.4 Condensation in the Downcomer

The model for condensation in the downcomer annulus was assessed against full-scale UPTF data in Section 19.3.5 (UPTF Test 6 series). Condensation efficiencies were estimated by MPR and calculated with two methods which provided an upper and lower bound for the uncertainty range.

Table 19.3-8 compares the predicted average condensation efficiency from <u>W</u>COBRA/TRAC-TF2, and the condensation efficiency calculated in the MPR report by two methods described in Section 19.3.5.8. The ratio of experimental to predicted efficiency was calculated as shown, [

The effect of condensation in the downcomer annulus was ranked High only during the refill phase of a LBLOCA scenario, therefore [

 $]^{a,c}$ .

]^{a,c}.

A sensitivity analysis was performed where the UPTF 6 test series was simulated by varying the downcomer condensation multiplier, XC, in Section 19.3.5.8, considering values of 0.0, 0.4, 1.0, and 1.1 to examine the effect of the condensation multiplier. Results are shown in Tables 19.3-9 and 19.3-10 and Figures 19.3-128 and 19.3-129, where, in general, [

]^{a,c}.

]^{a,c}

A sensitivity study was performed with XC=0.4 for the UPTF Test 25 in Section 19.3.11. It was observed that [

The overall assessment on the downcomer condensation during refill phase indicates that

 $]^{a,c}$ .

#### **29.1.5** Interfacial Drag in the Core Region [

From the PIRT, prediction of the mixture level swell and tracking of the mixture level are important in the later stages of a small break or intermediate break LOCA.

In a small break LOCA, as more liquid is boiled away the mixture level can eventually drop into the core. While good cooling can be maintained below the mixture level, dryout occurs above the mixture level. Heat transfer above the mixture level is limited to convection and thermal radiation to steam. Everything else being the same, the PCT in the period when the core is uncovered will increase as the mixture level decreases because steam enthalpy rise start from the location of the mixture level upward. The location of the mixture level is defined as the 'dryout' point, or the point where there is a sharp reduction in total heat transfer and most of the heat is transferred to the steam.

The location of the mixture level also determines the steam flow rate in the uncovered portion of the core, since boiling can only occur below in the two-phase region. The steam generation decreases with the magnitude of the core uncovery. As the steam flow decrease in the uncover portion of the core, this will further increase the steam temperature and enthalpy raise.

For a given mass inventory (or core collapsed liquid level) the location of the mixture level depends on the phenomenon characterized as level swell. The level swell is defined in Section 13. The mixture level swell is a function of the interfacial drag between the vapor and liquid in the two-phase region. The exact location of the dryout point also depends on other factors which are not strictly related to the swell in the two-phase region. A sharp mixture level exists when the annular film flow regime cannot develop (low bundle power and corresponding low vapor superficial velocity which are typical of the boiloff phase in a small break LOCA scenario). At higher power, CHF can occur at a lower void fraction and below the two-phase mixture level. Also the CHF model and the hydraulic mesh resolution play a role in exactly defining the location of the dryout point. Higher linear heat rate are more typical of the reflood phase an intermediate and large break LOCA scenario. Under those conditions an annular film flow regime is expected to dominate the upper region of the core.

There are several closure relationships used to calculate the interfacial drag in the various flow regime below the two-phase mixture level. [

The interfacial drag in the small bubble regime is calculated from Equation 5-67a:

]^{a,c}

The interfacial drag in the large bubble regime is calculated from Equation 5-72:

]^{a,c}

]^{a,c} As such,

]^{a,c} The

a,c

a,c

a,c

a,c

]^{a,c}

Since the interfacial drag multiplier is applied to both interfacial drag components prior to this calculation, the overall calculation is consistent and will include the effects of the multiplier.

As described by Equations 5-74a and 5-74b, the transition from small-to-large bubble flow regime [

the interfacial drag multiplier is inherent in the transition from small-to-large bubble flow regime and will include the effects of the multiplier.

interfacial drag in the film regime is calculated from Equation 5-81:

]^{a,c}

]^{a,c}

As described by Equation 5-78, the churn-turbulent regime is a linear combination of large bubble and film/drop flow regimes. [

]^{a,c}

]^{a,c}

Considering all the level swell simulations discussed in Section 13, Volume 1, only the ORNL-THTF data had detailed void fraction data for comparison against the code predictions. [

]^{a,c}

WCAP-16996-NP

[

ſ

ſ

[

.

]^{a,c}

#### ]^{a,c} The FLECHT-SEASET

test 31504 (described in Section 14.2.3.1, Volume 2) is taken as a representative test of rod heat transfer under prototypical LBLOCA reflood conditions. The <u>W</u>COBRA/TRAC-TF2 simulation of this test is addressed in Section 15.6.1, Volume 2. Figures 29.1.5-5 and 29.1.5-6 show results from a YDRAG sensitivity analysis performed for FLECHT-SEASET test 31504. [

]^{a,c}

Similarly as for the other uncertainty parameters, a sensitivity study for YDRAG was performed with ROSA-IV test SB-CL-18 to examine its role in an integral small break LOCA test. In two simulations of the SB-CL-18 test, the YDRAG parameter in the core channels was ranged between [ ]^{a,c} The results of this sensitivity are discussed in Section 21.15. [

Figure 29.1.5-1	Predicted Versus Measured	Level Swell for the G1 a	nd G2 Boiloff Simulations
	with [	] ^{a,c}	

November 2010 Revision 0

#### 29-25

a,c

•

2 · · · ·

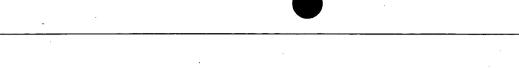
29-26

a,c

Figure 29.1.5-2 G1 and G2 [

]^{a,c}

WCAP-16996-NP



· · ·

29-27

a,c

Figure 29.1.5-3 [

]^{a,c}



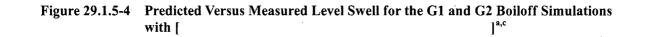


Figure 29.1.5-5 Differential Pressure in the Test Bundle for [ FLECHT-SEASET Test 31504 ]^{a,c},



## Figure 29.1.5-6 Quench Profile for [

### ]^{a,c}, FLECHT-SEASET Test 31504

WCAP-16996-NP

#### 29.1.6 Cold Leg Condensation (KCOSI)

]^{a,c}

The cold leg condensation by the cold liquid injected from the ECCS is an important phenomenon during both small and large break LOCAs (see PIRT in Section 2). [

]^{a,c} A special cold leg condensation model was developed in Section 6.3.6 to predict the cold leg condensation heat transfer rate when the cold leg is expected to be [ ]^{a,c}.

The cold leg condensation model was assessed against SBLOCA SETs, Westinghouse COSI, Framatome COSI, and ROSA IV SB-CL-05 in Section 17, and LBLOCA SETs, UPTF 8A and 25A in Sections 17 and 19. The comparison with experimental results shows that the code is able to predict condensation rates within a reasonable range of uncertainty for a SBLOCA. [

A cold leg condensation multiplier (KCOSI) was added in the code to allow a ranging capability for the cold leg condensation model for the purpose of the uncertainty analysis. In the code, the nominal cold leg condensation heat transfer rate is calculated from Equation 6-236a:

a.c

where the Nusselt number is predicted using Equation 6-236. The cold leg condensation multiplier is applied to the above equation directly, such that the cold leg condensation heat transfer rate is calculated as:

Here, the uncertainty on the cold leg condensation model is determined using the Westinghouse horizontal COSI test data and the Framatome COSI test data. [

]^{a,c}

The results with KCOSI multipliers of [ ]^{a,c} are presented in Figure 29.1.6-1. The figure reports the ratio of the predicted condensation rate to the upper/lower bound measured value for each of the COSI tests considered in the assessment (32 data points). [ ]^{a,c}

]^{a,c}

]^{a,c}

]^{a,c}

Based on the results of this sensitivity, [ is considered for Region I in the uncertainty analysis.

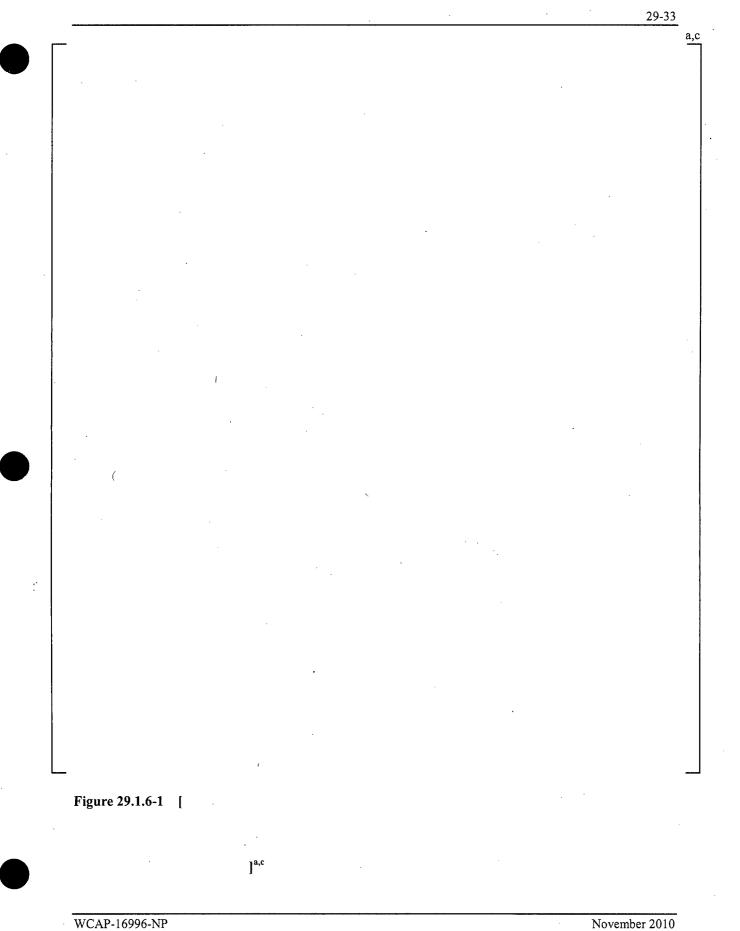
ſ

[

A KCOSI sensitivity was performed with the ROSA-IV 5% side break test SB-CL-05. Detailed discussion of the sensitivity results is presented in Section 21.17. [

WCAP-16996-NP

]^{a,c}



(

#### 29.1.7 Horizontal Stratified Flow Regime Transition Boundary (HS_SLUG)

In <u>WCOBRA/TRAC-TF2</u>, a transition criterion from the stratified flow regime to the non-stratified flow regime was developed by combining [ $]^{a,c}$ 

(Section 4.4.5). Figure 4-17 compared the transition criterion with various test data at different pressures, and different pipe diameters. [

The horizontal stratified flow regime transition boundary multiplier, HS_SLUG, is then introduced to adjust the critical relative velocity for horizontal stratified flow. The multiplier is represented by the symbol  $C_{hs_slug}$  in Equation 4-117. For the purpose of the uncertainty analysis a random value of HS_SLUG is sample with [ ]^{a,c}. It is also assumed that [

]^{a,c}

Sensitivity on the effect of the HS_SLUG multiplier on the small break LOCA transient were performed with selected ROSA-IV Test SB-CL-18. Detailed discussions of these sensitivities are documented in Section 21.16. Based on the results from the HS_SLUG sensitivity calculations presented in Section 21.16, it is concluded that the effect of the HS_SLUG ranging would have [

]^{a,c}. The effect of the HS_SLUG multiplier appears to [

]^{a,c}. The HS_SLUG sensitivity calculation performed with the 10% break test SB-CL-14, Section 21.16.3, showed [ ]^{a,c}.

]^{a,c}

#### **29.1.8** Minimum Film Boiling Temperature (T_{min})

The minimum film boiling temperature ( $T_{min}$ ), represents the minimum temperature at which liquid can maintain contact with a heated surface. It is used to define the boundary between the transition boiling heat transfer regime and the film boiling regimes. In codes such as <u>WCOBRA/TRAC-TF2</u>, TRACE, or RELAP,  $T_{min}$  is estimated in order to determine the applicable heat transfer regime, and then to select a set of correlations appropriate for that regime. In general, a simple correlation or in some instances a constant value is assumed for  $T_{min}$  in these codes.

]^{a,c}

[

It must be recognized that  $T_{min}$  is not a property or a unique value for a given geometry. The minimum film boiling temperature is the result of two competing processes: liquid evaporation and the conduction of heat to the wall surface. Evaporation of the liquid determines the repulsive force that acts on the liquid, which can be in the form of droplets or an inverted annular column. When the evaporation rate is high, it can prevent the liquid from making contact with the heated surface. If contact between the liquid and the wall does occur, the rate at which heat is conducted to the surface determines if the liquid is quickly thrown off the wall, or if the contact can be sustained. Conduction within and along the wall is affected by its material properties as well as its internal geometry and initial temperature distribution.

Figures 29.1.8-1 and 29.1.8-2 illustrate two situations encountered in the quenching of nuclear fuel rods. Figure 29.1.8.-1 shows a situation typical of the blowdown cooling phase, in which liquid is distributed in a dispersed droplet field and the subcooling is equal to or nearly zero. In this case, droplets approach the wall with a normal velocity caused by turbulent motion in the bulk fluid. Unequal evaporation on the wall-facing and fluid-facing sides of the droplet causes a repulsive force to act on the droplet. Drop-wall contact depends on the magnitudes of the repulsive force and the initial droplet momentum towards the wall. This process is described by Ganic and Rohsenow (1977) who calculated a continuous post-CHF boiling curve by considering a force balance on a droplet entering a boundary layer. Tmin in their analysis was the surface temperature when the heat flux reached a minimum.

The more complex situation typical of bottom reflood is shown in Figure 29.1.8-2, in which the liquid is in the form of an inverted annular column. In this case, wave phenomena on the surface of the liquid column must be considered. Unlike the droplet situation in Figure 29.1.8-1, the inverted annular column is much more difficult to characterize. It can consist not only of relatively large waves as shown in the figure, but also include "ripples" superimposed on the primary waves. The complexity of the inverted annular column was investigated by Vijaykumar and Dhir (1992), who used a holographic interferometer to examine the wave structures that can occur. Liquid-wall contact still depends on the relative magnitudes of the wave momentum towards the wall and the repulsive force due to evaporation. Baum (1977) developed a model for transition and film boiling that considered the forces acting on a wave near a heated wall, but  $T_{min}$  was not a major consideration.

In both Figures 29.1.8-1 and 29.1.8-2, the "wall" is the fuel rod clad, which is made of zircaloy, and is separated from the fuel pellet by a thin gap. The gap acts as a resistance to conduction from the heat source to the clad. Thus, as liquid nears contact with the clad, the effect of the gap on the transient conduction from the pellet to the clad needs to be accounted for in determining the limit at which energy can be made available to evaporate the liquid. The material property effect was examined by Dhir, Duffey, and Catton (1981), who found that zircaloy quenched faster than stainless steel.

From a consideration of the physical processes involved in rewetting, it is apparent that details of the heat transfer process must be known locally if  $T_{min}$  is to be accurately determined. While numerous correlations have been proposed for  $T_{min}$ , none have gained wide acceptance due to the large uncertainty in their estimates compared to data. The major cause of the large uncertainty is twofold. First, few of the available methods have attempted to determine  $T_{min}$  based on all of the fundamental processes, which limits their applicability. Second, while there is considerable data for  $T_{min}$ , none of the available databases included nor systematically examined parameters that must be known on a local basis. Most databases include parameters such as pressure, mass flux, and inlet subcooling, but few contain information on local parameters such as void fraction, droplet size, heat flux, clad oxidation, and axial temperature gradient. In

addition, most data for  $T_{min}$  were obtained for solid heater rods with stainless steel clad as opposed to zircaloy clad rods with a gap between the pellet and the clad as is the case in a nuclear rod. Therefore, the available data must be examined in order to identify an appropriate  $T_{min}$  value for an individual rod.

[

The  $T_{min}$  model used in <u>WCOBRA/TRAC-TF2</u> is described in Section 7, which is derived from Henry (1974). DFFB simulations were performed in Section 15.5, and reflood simulations were performed in Section 15.6. Since  $T_{min}$  defines when the rods may rewet during blowdown or quench during reflood, quench temperature comparisons are performed for select tests simulated in Sections 15.5 and 15.6. The method for determining the quench temperatures is [

]^{a,c}

Figure 29.1.8-7 provides a comparison of predicted versus measured quench temperatures at several elevations from the G-1 Blowdown experiments simulated in Section 15.5. The data values are the average of all the thermocouples located within the inner channel modeled by <u>WCOBRA/TRAC-TF2</u>. As can be seen from the figure, [

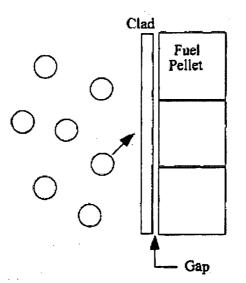
]^{a,c}

Figures 29.1.8-8 through 29.1.8-10 provide a comparison of predicted versus measured quench temperatures for the FLECHT experiments (SEASET, low flooding rate, Skewed) simulated in Section 15.6. The data values are the individual thermocouples located within the inner channel modeled by WCOBRA/TRAC-TF2. As can be seen from the figures, WCOBRA/TRAC-TF2 tends to [

WCAP-16996-NP

]^{a,c}

٦^{,a,c}





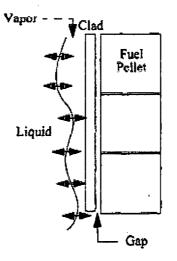


Figure 29.1.8-2 Inverted Annular Cooling

Figure 29.1.8-3 Histogram of T_{min} Values Based on G1 and G2 Test Data [

]^{a,c}

WCAP-16996-NP

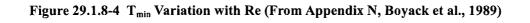
November 2010 Revision 0

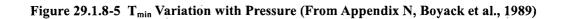
29-38

a,c



a,c





29-40

]^{a,c}

a,c

a,c

# Figure 29.1.8-6 Method for Determining Quench Temperature

. ,

Figure 29.1.8-7 Predicted vs. Measured Quench Temperatures from G1 Blowdown Simulations



a,c

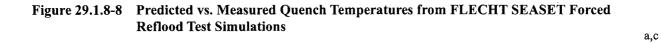


Figure 29.1.8-9 Predicted vs. Measured Quench Temperatures from FLECHT Low Flooding Rate Forced Reflood Test Simulations

Figure 29.1.8-10 Predicted vs. Measured Quench Temperatures from FLECHT Skewed Forced **Reflood Test Simulations** 

WCAP-16996-NP

29-42

a,c

# 29.1.9 Steam Binding and Entrainment – Bounding Approach

Comparisons with FLECHT (Section 19.5) indicate that WCOBRA/TRAC-TF2 is in good agreement with data regarding carryover, while CCTF comparisons (Section 19.6) indicate that WCOBRA/TRAC-TF2 overpredicts the amount of entrainment from the core. For forced reflood tests, this leads to a slightly higher predicted heat transfer. For gravity reflood tests such as CCTF, however, the excess entrainment results in an over-prediction of steam binding, which reduces the flooding rate and causes an under-prediction of core heat transfer. In addition, the comparisons with Upper Plenum Test Facility (UPTF) tests showed that when the conditions at the entrance to the upper plenum are known, WCOBRA/TRAC-TF2 underpredicts the mass retained in the upper plenum, therefore overpredicting the amount of water entrained into the loops. Based on the CCTF gravity reflood and UPTF test predictions, it is concluded that a conservative bias already exists in the calculations for core entrainment/de-entrainment and the resulting steam-binding effects, and an additional bias or uncertainty is not required.

# 29.1.10 Non Condensable Gases/Accumulator Nitrogen – Bounding Approach

This refers to the impact of the accumulators' nitrogen discharge into the RCS at the end of the accumulators' blowdown. The main effects are the compression at the top of the downcomer as a result of nitrogen discharge to the cold leg and downcomer and condensation suppression in the loops and downcomer as a result of non-condensable gas replacing steam.

Comparisons with ACHILLES test data (Section 20.1.4) indicated that <u>WCOBRA/TRAC-TF2</u> reasonably predicts the pressurization of the downcomer and the resulting insurge of water into the core. Figures 20.1-42 to 20.1-44 show that the cooling during the initial insurge of liquid in the core is reasonably predicted, with a slight over-prediction of cladding temperatures. Comparisons with LOFT L2-5 showed that the prediction of liquid discharge, the initial RCS pressurization, and the reflood/quench behavior was in good agreement with the measurement. The break flow increase due to the out-surge of liquid following the pressurization was over-predicted.

The tendency to conservatively predict downcomer pressurization and the resulting effect on the heat transfer during the initial insurge of water in the core leads to the conclusion that the effects of accumulator nitrogen will be reasonably calculated in a PWR LOCA transient without the need to explicitly account for this uncertainty in the analysis.

## 29.1.11 Uncertainty in Loop Seal Clearance Phenomenon

The loop seal starts to clear when the level formed in the downhill side of the pump suction piping reaches the top of the horizontal pipe. The timing of the onset is determined by the break flow, the vapor generation rate in the core, the condensation rate in the steam generator tubes, and the bypass flow rate. Once the clearing commences, because of the significant volume of vapor accumulated in the inner vessel, a relatively high vapor flow is maintained for a significant time such that a significant fraction or all of liquid in the loop seal is swept to the cold leg. At larger break sizes, the vapor volumetric flow is large enough to clear the loop seal in multiple loops.

For a stable loop seal clearing which may include a partially cleared loop, the remaining liquid in the horizontal leg of the pump suction piping contributes to the pressure loss through an intact loop.

The UPTF loop seal test is a quasi-steady state experiment. The test provides important full-scale single loop seal clearing separate effect data in a prototypic PWR geometry with well defined boundary conditions. The assessment of the <u>WCOBRA/TRAC-TF2</u> model against the UPTF loop seal test is discussed in Section 18. The conclusions from the assessment in Section 18 are [

]^{a,c}. Since horizontal stratification can affect the residual liquid mass after the loop seal clears and the pressure drop across the loop seal, HS_SLUG sensitivity studies are performed with the UPTF loop seal tests that are documented in Section 18. The values chosen to study are [ ]^{a,c}. Figure 29.1.11-1 shows a comparison of the predicted vs. measured residual liquid levels for the 3-bar and 15-bar HS_SLUG studies, and Figure 29.1.11-2 shows a comparison of the pressure drops for the 3-bar and 15-bar HS_SLUG studies. As seen from the figures, [

# ]^{a,c}.

For the purpose of a reasonable representation of the uncertainty associated with the loop seal clearing event during a small break LOCA, [

]^{a,c}

Section 28.2.11 showed [

١

WCAP-16996-NP

29-46

a,c

a,c

Figure 29.1.11-1 Predicted vs. Measured Residual Liquid Level Comparison for the UPTF Loop Seal HS_SLUG Study

Figure 29.1.11-2 Pressure Drop across the Loop Seal for UPTF Loop Seal HS_SLUG Study

## 29.1.12 Steam Generator Thermal-Hydraulics

There are two important phenomena associated with the steam generator thermal-hydraulic which are significant for the purpose of modeling a small break LOCA scenario:

- 1. The primary-to-secondary heat transfer and condensation in U-tubes.
- 2. The flow regime, in particular the CCFL in the primary side.

#### 29.1.12.1 Primary to Secondary Heat Transfer and Condensation Reflux

The primary to secondary side heat transfer was assessed based on the results of the simulation of the natural circulation test ST-NC-02, Section 21.9. Based on the results, it was concluded that, [

#### **29.1.12.2** Counter-current Flow Limitation (CCFL)

Assessment of the code's capability to predict counter-current flow in a small break LOCA was performed with calculated counter-current flow results extracted from simulations of a number of ROSA-IV LSTF tests, documented in more detail in Section 21.10. The overall effect of CCFL calculated at the steam generator U-tubes, hot leg elbow region and the upper core plate was evaluated in Section 21.10.4. The major conclusion made therein is that [

#### 29.2 BREAK LOCATION, TYPE (SPLIT VS. DEGCL) AND SPLIT BREAK AREA

The objective of the Westinghouse FULL SPECTRUM LOCA (FSLOCA) methodology is to cover the spectrum of LOCA scenarios that are initiated by an instantaneous rupture of a reactor coolant system (RCS) pipe. The break type considered is either a double-ended guillotine, defined as a complete severance of the pipe resulting in unimpeded flow from either end, or a split break, defined as a partial tear. The break size considered for a split includes any break size such that break flow is beyond the capacity of the normal charging pumps up to and including a double ended guillotine rupture with a break flow area two times the pipe area.

]^{a,c}.

Note that guidelines for acceptable method for the break modeling are provided in the Regulatory Position 3.1 – Second Paragraph, of Regulatory Guide 1.157. The main criteria are repeated here and divided in the following three paragraphs:

- 1. "The calculations performed should be representative of the spectrum of possible break sizes from the full double-ended break of the largest pipe to a size small enough that it can be shown that smaller breaks are of less consequence than those already considered."
- 2. "The analyses should also include the effects of longitudinal splits in the largest pipes, with the split area equal to twice the cross-sectional area of the pipe."
- 3. "The range of break sizes considered should be sufficiently broad that the system response as a function of break size is well enough defined so that interpolations between calculations, without considering unexpected behavior between the break sizes, may be made confidently."

While it is acknowledged that RG 1.157 was written with focus on a Large Break LOCA scenario, there is no reason that prevents the extension of these principles to cover the entire spectrum of break sizes and scenarios.

Section 2.3.1 provides further clarification on the LOCA scenario considered by the Westinghouse FSLOCA methodology. In particular with regard to the break location, any break is located always (conservatively) in a cold leg, while all other locations have been identified as being less limiting.

Break orientation relative to the cold leg (top, side or bottom) is another attribute that is expected to have some influence on the break flow via vapor pull-through (bottom) or entrainment offtake (top). This is known to have some effect, especially for relatively small break sizes.

The ROSA-IV program considered the effect of break orientation by simulating bottom, side, and top breaks. [

 $]^{a,c}$ 

In summary the break uncertainty attributes in the methodology are postulated to be the following:

29-48

The uncertainty on the break flow model is discussed in Section 29.1.1. The overall break modeling methodology is discussed here.

]^{a,c}

29.2.2 Determination of the Minimum Break Size (A_{min})

Consistent with the FSLOCA scenario definition, the minimum break size should correspond to a break flow rate which can be compensated by the charging pump flow. This break size  $(A_{min})$  can be determined and will be plant specific. This defines the minimum break size considered in the break area sampling. This approach leads to a probability that a very small break could be sampled and analyzed in the uncertainty analysis. The corresponding transient would be extremely long to compute but likely non-limiting in terms of core heat up. A transient termination criterion will be developed to prevent this circumstance. PCT will be reported as the initial temperature, essentially the temperature at saturation pressure, for that case.

]^{a,c}

29.2.3 Break Type, Split Break Area and Break Flow Model Uncertainty Methodology

Herein a methodology position for the treatment of the break type and for a split the break size is developed.

One key difference between the previous LBLOCA methodology (ASTRUM, Nissley, M. E., et al., 2005) and FSLOCA is that the FSLOCA methodology extends the break area spectrum considered in the analysis to cover the full range from what is historically defined as Small Breaks (SB) to Large Breaks (LB) including break sizes previously not analyzed and classified as Intermediate Breaks (IB).

The approved approach in the ASTRUM EM (Nissley, M. E., et al., 2005) considers both the break type (Split vs. DEGCL) and for the Split the break area as random variables during the Monte Carlo sampling

29.2.1

ſ

procedure. The break type is first selected (with a 50/50 chance of Split vs. DEGCL) and for the split breaks, the area is uniformly sampled between [ $]^{a,c}$ .

For the treatment of break size in FSLOCA the following two approaches were first considered:

Option 1 – [

· ]^{a,c}

Option 2 – [

]^{a,c}

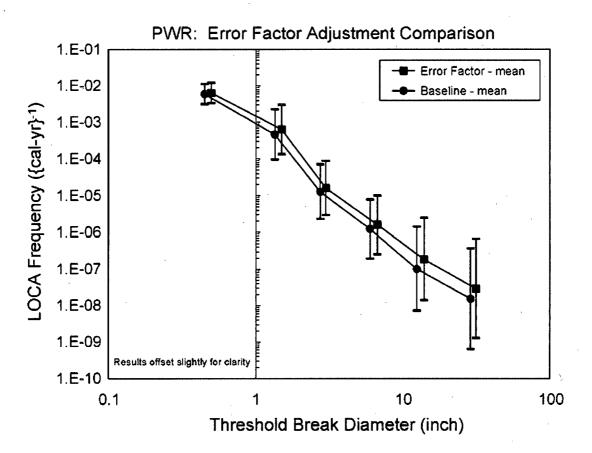
This approach provides an adequate coverage of all possible LOCA scenarios. Moreover, rather than aiming for [

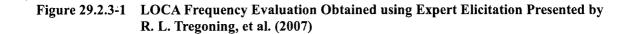
]^{a,c}

[

The uncertainty on the break flow model is treated as discussed in Section 29.1.1. The modeling methodology and treatment of model uncertainty for double-ended cold-leg guillotine (DECLG) and split breaks is described in Sections 29.2.4 and 29.2.5 respectively.

(





ţ

# 29.2.4 Modeling of DECLG Breaks

The cold-leg double-ended guillotine break is modeled as shown in Figure 29.2.4-1. [

# $]^{a,c}$

#### **Discharge Coefficient Uncertainty Strategy**

The guillotine break analysis requires explicit accounting for the uncertainties in break discharge flow.

#### The values of [

# ]^{a,c} (

#### Justification of CD Strategy

To confirm that this modeling approach achieved the desired change in flowrate, the same changes were made to the pipe model used to simulate the Marviken Test 6 experiment. The results are shown in Section 12.5.4.4, where Figure 12.5-12b confirms that discharge coefficients of 0.8 and 1.2 result in an observed 20% reduction and increase in break flow, respectively.

29-54 a,c

# Figure 29.2.4-1 DECLG Break Noding Scheme

29-55

a,c

Figure 29.2.4-2 Guillotine Break Noding Used in <u>W</u>COBRA/TRAC-TF2

)

WCAP-16996-NP

November 2010 Revision 0

]^{a,c}

#### 29.2.5 Modeling of Split Breaks

The size of a double ended guillotine break is fixed and equal to twice the cold leg cross sectional area. Therefore, any break which is smaller than twice the cold leg area is considered a split break. A large split break is possible only if the split is longitudinal. However, since there is no physical evidence that would indicate how such break types would appear (if they could in fact occur), the break geometry must be postulated.

#### **Discharge Coefficient and Break Size Uncertainty Strategy**

The noding scheme of a broken cold leg pipe for a split break is shown in Figure 29.2.5-1. [

As in the guillotine break, the code calculates the appropriate pressure drop using the TRAC momentum equations until the cell next to the break is reached. The pressure drop to the break plane is then calculated using the critical flow model.

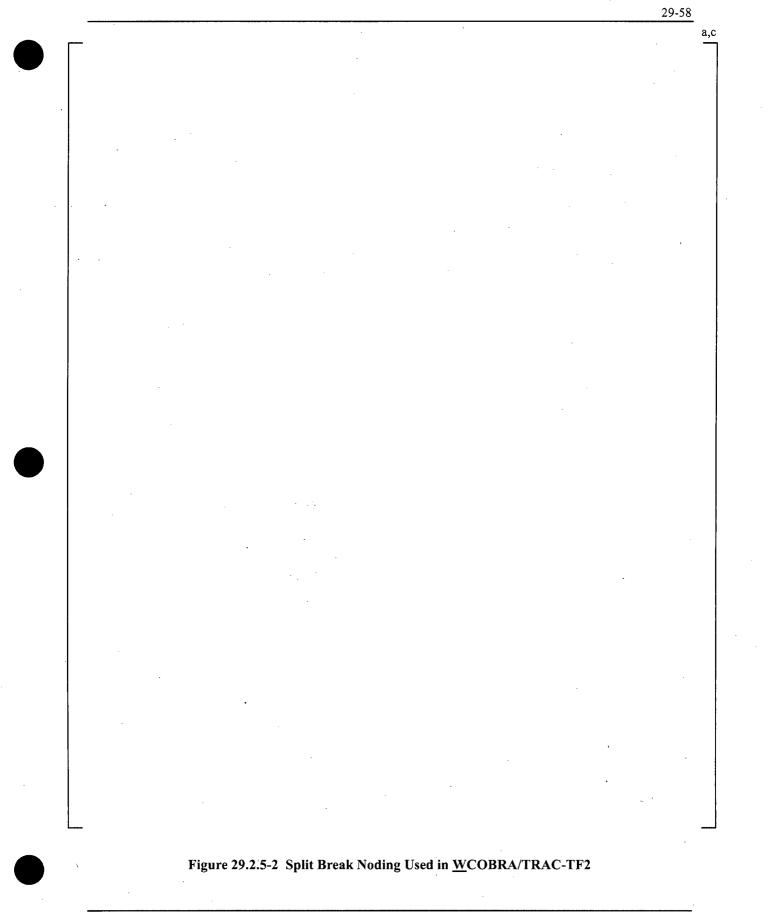
]^{a,c}

ſ

29-57

a,c

# Figure 29.2.5-1 Split Break Noding Scheme



WCAP-16996-NP

November 2010 Revision 0

## 29.2.6 Compliance with Regulatory Guide 1.157 on Break Type and Size

Regulatory Guide (RG) 1.157 states the Nuclear Regulatory Commission's (NRC's) regulatory position on the break type and size for the requirement for best-estimate LOCA (BELOCA) analysis. In this section, the compliance of the revised BELOCA sampling methodology for break type and size to RG 1.157 is examined. The following statements are found in RG 1.157:

#### **Regulatory Position 3.1 – Second Paragraph**

"The calculations performed should be representative of the spectrum of possible break sizes from the full double-ended break of the largest pipe to a size small enough that it can be shown that smaller breaks are of less consequence than those already considered. The analyses should also include the effects of longitudinal splits in the largest pipes, with the split area equal to twice the cross-sectional area of the pipe. The range of break sizes considered should be sufficiently broad that the system response as a function of break size is well enough defined so that interpolations between calculations, without considering unexpected behavior between the break sizes, may be made confidently."

#### **Regulatory Position 3.4.1**

"In analyses of hypothetical LOCAs, a spectrum of possible break sizes should be considered, as indicated in Regulatory Position 3.1. The discharge flowrate should be calculated with a critical flowrate model that considers the fluid conditions at the break location, upstream and downstream pressures, and break geometry. The critical flow model should be justified by comparison to applicable experimental data over a range of conditions for which the model is applied. The model should be a best-estimate calculation, with uncertainty in the critical flowrate included as part of the uncertainty evaluation. Best-estimate models will be considered acceptable provided their technical basis is demonstrated with appropriate data and analyses."

#### **Regulatory Position 3.15**

"Break flow may be greatly influenced by the location and specific geometry of the break. For a break in a horizontal pipe containing stratified flow, the quality of the break flow will be a strong function of the assumed location of the break on the pipe (e.g., top or bottom). Small break loss-of-coolant accident calculations should, therefore, include various assumed break locations in the spectrum of breaks analyzed."

Considering Regulatory Position 3.1, strict compliance with this position has been demonstrated in Section 29.2.3 by [

]^{a,c}

Considering Regulatory Position 3.4.1, the worst location of the break that results in the highest PCT was found [

 $]^{a,c}$ 

Considering the remarks specific to small break LOCAs in Regulatory Position 3.15, the geometry of the break was explored in the context of the ROSA experiments and WCOBRA-TRAC/TF2 simulations (Section 21), and PWR plant scoping studies (Section 28). Break orientations on the top, side, and bottom of the pipe were considered.

]^{a,c}

ſ

# 29.3 REVIEW OF PLANT SCOPING STUDIES AND UNCERTAINTY IN PLANT INPUT PARAMETERS

A review of the uncertainty associated with plant specific inputs and the treatment of those uncertainties in the FSLOCA methodology is discussed in this section. The plant input parameters and modeling approach were introduced in Section 26. Section 28 presented PWR sensitivity studies performed to identify or confirm the ranging required of potential contributors to uncertainty. A summary of the results is provided at the beginning of Section 28.

The plant input parameters treated in a bounding nature (Section 29.3.1) or as an uncertainty parameter (Section 29.3.2) are discussed in this section.

#### **29.3.1 Bounded Parameters**

The previous Westinghouse realistic large break LOCA Evaluation Model (EM) (ASTRUM) included the use of "confirmatory studies" to determine the limiting value of the following parameters for the reference transient:

- Offsite power availability
- Steam generator tube plugging level (maximum vs. minimum)
- Relative power of peripheral assemblies (maximum vs. minimum)

and, in some cases,

• Average fluid temperature in the reactor coolant system (maximum vs. minimum, if the plant being analyzed has an allowable range for the nominal value)

In addition, the confirmatory studies served to derive an appropriate (conservatively low) containment backpressure for use in the uncertainty analysis.

The limiting hot assembly location was also determined from a detailed examination of the upper plenum geometry. The location of the hot assembly is mainly important during a LBLOCA. A similar procedure to identify the limiting location is followed in the FSLOCA EM.

The "confirmatory" approach was originally developed for the 1996 EM (Bajorek, S. M., et al., 1998), which used response surfaces based on limited parametric studies of the global system response to

dominant parameters. In that EM, the reference transient played a major role in that the effect of variations in the dominant parameters was expressed as a difference in the peak cladding temperature (PCT) relative to the reference transient PCT.

In the 2005 ASTRUM EM (Nissley, M. E., et al., 2005), the reference transient had much less significance. The confirmatory studies were still used to determine the limiting value of the above parameters and to derive an appropriate containment backpressure, but the use of non-parametric order statistics eliminated the use of the reference transient in the statistical combination of uncertainties; the reference transient PCT had no direct influence on the analysis.

With the introduction of the FULL SPECTRUM LOCA EM, the method used to treat the above parameters has been re-examined. The treatment of each of these parameters in the FULL SPECTRUM LOCA EM is as described below.

#### Offsite Power Availability

ſ

The treatment of offsite power availability is an integral part of the FULL SPECTRUM LOCA uncertainty methodology and is treated [ ]^{a,c} described in Section 30.4.

#### Steam Generator Tube Plugging Level

## ]^{a,c}

#### **Relative Power of Peripheral Assemblies**

Standard core design practice is to minimize neutron leakage from the reactor core by placing assemblies on the periphery that have already been irradiated for at least one cycle. The average power of the peripheral assemblies typically varies by only a small amount from cycle to cycle. Furthermore, historical studies have shown that PLOW has a limited impact on analysis results. Core physics predictions for the plant being analyzed will be reviewed, [ ]^{a,c}

٦^{a,c}

#### Average Fluid Temperature in the Reactor Coolant System

If the plant being analyzed has an allowable range for the nominal value, the entire range will be sampled in the uncertainty analysis. Uncertainty in the measurement will also be included to augment the range beyond that of the allowable range for the nominal.

#### **Containment Backpressure**

[

#### 29.3.2 Initial and Boundary Conditions (Ranged Parameters)

The following are the parameters selected to describe the primary fluid conditions (RCS and ECCS), as discussed in Section 25.2.2.2.

- a. Average fluid temperature
- b. Pressurizer pressure
- c. Loop flowrate
- d. Upper head fluid temperature
- e. Pressurizer level
- f. Accumulator water temperature
- g. Accumulator pressure
- h. Accumulator water volume
- i. Accumulator line resistance
- j. Accumulator boron concentration

The range of variation of the operating parameters is accounted for in the uncertainty analysis. This is accomplished by assuring that, in the sampling of the attributes for each run (Section 31), the operating range is bounded. Table 29-5 presents the list of parameters that are statistically sampled in a typical analysis.

Items (a) and (b) are ranged according to measurement uncertainty. Item (c) tends to be well-controlled and measured, so the nominal thermal design flow is used. Item (d) is implicitly ranged through its relationship with the average fluid temperature, discussed in Section 25.2.2.2. Because pressurizer level, item (e) is tightly controlled relative to the average fluid temperature, it is also ranged consistently with variations in RCS average temperature.

Parameters related to the accumulator, items (f) through (i), are ranged according to plant-specific data. Specific to the line resistance, accumulator blowdown tests have been performed at dozens of plants as part of the standard plant startup testing. Standard procedures are to perform these tests for each RCS loop. The uncertainty of the line resistances measured in these tests is estimated to be about  $[ ]^{a,c}$ . For those plants for which measured accumulator line resistances are not readily available, it is considered acceptable to use

the calculated resistance as the nominal value. Westinghouse calculates accumulator line resistances using (Crane, 1988). Comparisons of pre-test calculations and test results were made for a number of plants. Table 29.3.2-1 shows that the calculations typically over-predict the measurements, conservative for large breaks in that the prediction of lower plenum and downcomer refill is delayed. For the ACHILLES test facility, the uncertainty estimated for the accumulator line resistance was 10% (Table 2.2 of Holmes, 1991). [

As described in Section 25.2.2.2, while accumulator boron concentration, item (j), is not likely to have a significant effect on the LOCA PCT, it is modeled at its nominal value without uncertainty to ensure that recriticality does not occur in the short-term following a LOCA.

#### 29.3.3 Uncertainty Associated with Maximum Time Step Size

In <u>W</u>COBRA/TRAC-TF2, a maximum allowable time step size is set by the user through the DTMAX input. In addition to the numerical convergence criteria covered in Section 3.6.5.3, the DTMAX input, in combination with the analogous minimum time step size input DTMIN, defines for the code the range of allowable time step size. The size of the time step employed by the code is then determined for each time step by the promotional and inhibitive algorithms described in Section 3.6.5.3, with a general tendency to promote (increase) the time step for increased computational efficiency. In the DTMAX range typically used to achieve reliable numerical convergence in the plant analyses, the maximum time step limit is often more restrictive than the limits imposed by the convergence criteria. As a result, <u>W</u>COBRA/TRAC-TF2 uses DTMAX as the time step throughout significant portions of the transient.

The effect of the choice of DTMAX was demonstrated for UPTF Test 6 in Section 19.3.5.9. Varying DTMAX [  $j^{a,c}$  did not result in a clear effect on the ECC penetration delay, and conservatism relative to the test data was observed for all DTMAX values.

A sensitivity of the CCTF 62 prediction in Section 19.6.6 showed that an increase in DTMAX to [ ]^{a,c} had negligible impact on the predictions, and the overall conservatism regarding cladding temperatures at the upper elevations was preserved.

The impact of DTMAX on reflood heat transfer predictions was also investigated using the FLECHT SEASET test series as described in Section 15.8. It was observed that varying DTMAX [

]^{a,c} had minimal impact on the PCT and quench front progression for the lowest and highest flooding rate tests.

Section 28.1.3 presents a DTMAX sensitivity study of the V. C. Summer and Beaver Valley Unit 1 reference large break spectra. It is observed there that DTMAX values [

Section 28.2.4 presents a DTMAX study of the reference small break spectra. DTMAX values [

]^{a,c} are not observed to introduce significant bias or additional uncertainty, and differences among the DTMAX cases originate from differences in the loop seal clearance event.

]^{a,c}

[ ]^{a,c} a Monte Carlo uncertainty analysis is implemented to combine the uncertainties and predict an upper bound to the 95th quantile PCT, MLO, and CWO (see Section 30). For any given transient, there exists inherent uncertainty in phenomena (initial insurge for LBLOCA and loop seal clearance for SBLOCA), the prediction for which is observed to differ somewhat depending on the choice of DTMAX. In the analysis, a choice of DTMAX is made and is applied in all transients. [

]^{a,c}

#### **29.4 CORE AND FUEL ROD MODEL UNCERTAINTIES**

#### **29.4.1** Initial Reactor State Uncertainties

#### 29.4.1.1 Time in Cycle

]^{a,c}

ſ

[

The NRC has initiated the formal process to revise the ECCS acceptance criteria in § 50.46, via issuance of an Advance Notice of Proposed Rulemaking (FR 40765). This initiative has several main objectives, but in the context of the FULL SPECTRUM LOCA methodology the most significant is a proposed reduction in allowable cladding oxidation to reflect the results of hydrogen pickup during normal operation. The final form of the rule and its requirements are projected to be issued in August 2011 (Clifford and Flanagan, 2009). The software and methodology requirements necessary to fully address the future rule cannot be fully defined until the rule is established in detail.

For the demonstration analysis presented in Section 31, [

]^{a,c}

To address the expected revision to § 50.46 in the context of the FULL SPECTRUM LOCA methodology, [

^{a,c} As previously stated,

]^{a,c}

however, the specific way in which the FSLOCA methodology will be modified to address the expected § 50.46 revision cannot be fully defined until the issuance of the final rule.

#### 29.4.1.2 Reactor Core Power Distributions and Global Uncertainties

Reactor core power distributions are characterized by radial and axial power distributions, as discussed in Section 25.2.1. The steady-state radial distribution is established by core loading pattern, fuel enrichment, fixed burnable poisons, etc., and is not subject to wide variation during normal operation (Section 25.2.1.1). The maximum of the radial distribution is defined by F $\Delta$ H (hot rod average power divided by the core average rod average power). Predictions of F $\Delta$ H are accurate to within []^{a,c} percent at > 95 percent probability (Section 25.2.1.3). [

]^{a,c}

Steady-state axial distributions are established by core loading pattern and burnup. The axial distribution tends to vary widely as a result of changes in external controls such as boron or control rods. The maximum of the radial distribution times maximum of the axial distribution is FQ (maximum linear heat rate divided by the core average linear heat rate). Transients are simulated in the core design process, yielding a wide range of possible power distributions and FQ values. As described in Section 25, the axial distribution is characterized by defining PBOT and PMID, the average relative power in the bottom and middle third of the core, respectively. In core design, the calculated FQ for each power distribution is augmented by [ ]^{a,c} percent prior to comparing to the Technical Specification to bound calculational, measurement, and local uncertainties.

Plants operate in "baseload" (i.e., full power, all control rods out) nearly all the time. In baseload operation, FQ varies slowly with time. However, the Technical Specifications allow for transient operation. Figure 29.4-1 shows the effect of a typical load follow maneuver on peaking factor (FQ x power), for a plant with a Technical Specification (Tech Spec) FQ limit of  $[ ]^{a,c}$ . Figure 29.4-2 shows the FQ probability distribution for the load-follow maneuver in Figure 29.4-1, for the portions of the figure where the reactor was at full power. In the Westinghouse best-estimate LOCA methodology, [

]^{a,c}

]^{a,c}

It will be assumed that for a given reactor state,  $F_Q$  (not including uncertainties) is [

]^{a,c} As seen in Figure 29.4-2, this is a conservative representation of the

actual PWR operation.

ſ

29-68

]^{a,c}

Other sources of uncertainty involve: 1) the accuracy with which the power distribution in the hot assembly and remainder of the core can be defined; 2) the accuracy with which the power at the hot spot (most limiting elevation of the hot rod) can be defined, including local uncertainties. The latter is addressed in Section 29.4.2.

The following contributors are considered, [

]^{a,c}.

- Radial power distribution
- Total peaking factor and axial power distribution
- Initial core power level
- Decay heat

ſ

• Gamma redistribution

#### **Radial Power Distribution**

The hot assembly and core radial power distribution is modeled by defining the following variables:

- Hot rod average relative power,  $F_{\Delta H}$ . The hot rod average relative power,  $F_{\Delta H}$  will be ranged according to its calculational uncertainty. This global uncertainty, as shown in Table 25.2-2, has a standard deviation equal to [  $]^{a,c}$  of the nominal value.
- Hot assembly average power is [

]^{a,c} lower than  $F_{\Delta H}$ , minimum (Section 25), [

]^{a,c}

Power in the assemblies in the core periphery (PLOW), as a percent of average assembly power ([ ]^{a,c} are typical lower and upper bounds). Variations in this parameter will have a small effect on the power of the core average rods surrounding the hot assembly. [

#### **Total Peaking Factor and Axial Power Distribution**

The axial power distribution is modeled by defining the following variables:

F _Q		=	hot rod peak relative power (total peaking factor)
[	] ^{a,c} ·	=	hot assembly peak relative power
$F_{\Delta H}$		-	hot rod average relative power
[	] ^{a,c}	-	hot assembly rod average relative power
PBOT		· =	average relative power in bottom third of core
PMID		-	average relative power in middle third of core

The initial power generation rate, as a function of elevation, is specified for the hot rod by the initial axial and radial power distributions (peaking factors  $F_Q$  and  $F_{\Delta H}$ ) on the hot rod. The uncertainty associated with the total peaking factor  $F_Q$  (a total of [ ]^{a,c}, Table 25.2-2) consists of two components; one closely coupled to the uncertainty in the hot assembly power, and one associated only with local uncertainties and therefore independent of the hot assembly. Since there is a fixed radial power distribution in the assembly, a fluctuation in the hot assembly power results in a similar fluctuation in the hot rod. This situation is illustrated in Figure 29.4-3. Fluctuations in the hot assembly rod are assumed to also affect the thermal-hydraulics (i.e., they affect the heat transfer coefficient boundary condition), and so the uncertainties are considered in the global thermal-hydraulic solution accordingly. [

#### ]^{a,c}

#### Initial Core Power, Decay Heat, Gamma Redistribution

The remaining variables, core average power, gamma redistribution, and decay heat, contribute additional uncertainty to the peak linear heat rate. The uncertainty in core power (AFLUX₀, [

]^{a,c}) was quantified in Section 25.2.1.3. Increases (decreases) in AFLUX result in proportional increases (decreases) in rod powers for all rods as described in Section 25.2.1.5.

Uncertainty in decay heat is considered through the application of ANSI/ANS 5.1-1979 Standard (DH, normal distribution). See also Section 9.7.

ſ

WCAP-16996-NP

[

2	9-	7	1

a,c

# Figure 29.4-1 Effect of Load Follow on $\mathbf{F}_{\mathbf{Q}}$

29-72

a,c

Figure 29.4-2

l

29-73

a,c

Figure 29.4-3 [

]^{a,c}

## 29.4.2 Hot Rod Local Models Uncertainty

Beside the uncertainty in hot rod local power discussed in the previous section, several other uncertainty contributors in the fuel rod models and heat transfer from the rod to the fluid contribute to the local hot spot uncertainty.

The fuel rod modeling was presented in Sections 8.3 through 8.6 (Volume 1). These included the fuel conduction model, the pellet-cladding gap conductance model, the fuel rod deformation model, the cladding reaction with water or steam models, and [  $]^{a,c}$ . The heat transfer from the fuel rod to the fluid was discussed in Section 7 and its assessment is provided in Sections 14 and 15. The discussion in Sections 7 and 8 focuses on the models as coded, while here the discussion is expanded to describe the treatment of the uncertainty associated with those models.

In particular, the following contributors are considered:

- Hot rod peaking factor
- Hot rod radial peaking, pellet geometry, enrichment, density, and rod bow uncertainties
- [

- ]^{a,c}
- Cladding burst temperature
- Cladding burst strain
- Zirconium-water reaction
- Fuel relocation
- Convective heat transfer coefficient from the rod to the fluid

Models are considered 'local' when the effect of the uncertainty in those models has an effect limited to local processes, such as the local cladding temperature or local cladding oxidation, while the impact of such uncertainties on the 'global' thermal-hydraulic process is negligible. The hot rod peaking factor uncertainty reflects the power difference between the hot rod and the hot assembly rod. The additional uncertainty related to hot rod radial peaking, pellet geometry, enrichment, density, and rod bow is captured by the local linear heat rate uncertainty. [

]^{a,c} The uncertainties in the cladding burst temperature, the cladding burst strain, Zirconium-water reaction, fuel relocation, and convective heat transfer coefficient are incorporated into [ ]^{a,c}.

In the previous ASTRUM methodology (Nissley, M. E., et al., 2005) the <u>WCOBRA/TRAC</u> solution was followed by the execution of a one-dimensional conduction code (HOTSPOT) [

HOTSPOT is essentially a one-dimensional conduction code used to resolve the heat conduction [ ]^{a,c}. Driven by boundary conditions

]^{a,c}

on the fluid side calculated with  $\underline{W}COBRA/TRAC$ , HOTSPOT was used to simulate the transient conduction [

 $]^{a,c}$ . The models in HOTSPOT were consistent with the corresponding models in <u>W</u>COBRA/TRAC.

The uncertainty methodology for the heat transfer coefficients will be discussed in more detail in Section 29.4.3. The FSLOCA methodology for modeling the hot assembly rods was discussed in Section 8 and is briefly summarized here:

# 29.4.2.1 [

[

ſ

]^{a,c}

]^{a,c}

[

# Fuel Internal Heat Generation - Local Uncertainty

As discussed in Section 29.4.1.2, the uncertainty in total peaking factor  $F_Q$  is comprised of components that are global in nature, and hence are closely coupled with hot assembly power, and components that are local in nature. The local uncertainties, which do not affect the global thermal-hydraulic solution, are accounted for [ ]^{a,c}. From Table 25.2-2, the local uncertainties in the local heat generation arise from the combination of [

expressed as:

[

]^{a,c}. The total standard deviation ( $\sigma$ ) can be

a,c

]^{a,c}

(29.4-2)

]^{a,c}

(29.4-3)

]^{a,c} The local uncertainty amounts to:

This uncertainty is considered only as a local uncertainty with [

]^{a,c}.

### **Cladding Burst Temperature**

The rupture criteria for Zircaloy-4 cladding and ZIRLO[®] cladding introduced in Section 8.4.1 are applicable for both the hot assembly rod and [ $1^{a,c}$ ]

Cladding burst is calculated by monitoring the stress on the cladding and using the cladding rupture correlations to predict the rod burst as described in Section 8.4. The cladding burst temperature can be correlated fairly well as a function of hoop stress for ZIRLO[®] cladding as shown in Figure 8-19 in Section 8.4. Figure 29.4-4 is replication of Figure 8-19 with a band of [ ]^{a,c} of the calculated burst temperature shown. The [

The [ ]^{a,c} uncertainty range on cladding burst temperature is used for both Zircaloy-4 and ZIRLO[®] cladding. The ZIRLO[®] data shown in Figure 29.4-5 actually indicates a smaller uncertainty than the assumed [ ]^{a,c}. These data were obtained by Westinghouse using a consistent testing method. The zircaloy data from Powers and Meyer (1980), which were used to develop the zircaloy burst temperature and burst strain models in Section 8.4.1 (Volume 1), show scatter more consistent with the [ ]^{a,c} range (Figure 1 of Powers and Meyer, 1980). This is believed to be at least partly attributable to the variety of testing methods used to obtain the Zircaloy-4 data. Although it is believed that the ZIRLO[®] cladding testing methods are as valid as those in Powers and Meyer, there may be some uncertainty due to the testing method, and the larger uncertainty for both cladding materials is used.

ſ

]^{a,c}

a,c

]^{a,c}.

29-78 a,c

Figure 29.4-4 ZIRLO[®] Cladding Burst Temperature Data and Correlation

.

#### **Cladding Burst Strain**

The burst strain discussed in Section 8.4, as shown in Figures 8-18 and 8-20 for the respective Zircaloy-4 and ZIRLO[®] cladding, is applied to hot assembly rod. However, the data in Figures 8-18 and 8-20 show wide scatter. Burman (1980) discussed how burst occurs randomly at "hot spots" which are the results of a wide range of azimuthal temperature gradients around the cladding. Burman also argued that in fuel rods these gradients can be larger due to random contact of the pellet against the cladding, which then causes smaller burst strains to occur.

For the cladding burst strain of [ ]^{a,c}, Figures 29.4-5 and 29.4-6 revisit the data of maximum burst strain as a function of burst temperature for the Zircaloy-4 and ZIRLO[®] cladding at different heatup rates to identify the influence of heat up rate. In both cases the scatter is very large for both alpha phase and beta phase, and low uncertainty for the alpha/beta transition region is observed. Thus, three burst temperature ranges are identified: [

Figures 29.4-7 to 29.4-9 show the Zircaloy-4 burst data in the form of histograms for burst temperature ranges [ ]^{a,c}, indicating the frequency of occurrence of a particular burst strain within a range of burst temperatures. [

 $]^{a,c}$ 

The ZIRLO[®] data are shown in Figures 29.4-10 to 29.4-12, and exhibit a similar behavior for [ ]^{a,c} except for the difference in the transition temperature. The effect of heatup rate on cladding strain is also evident in the

]^{a,c}, but the burst strains are smaller. [

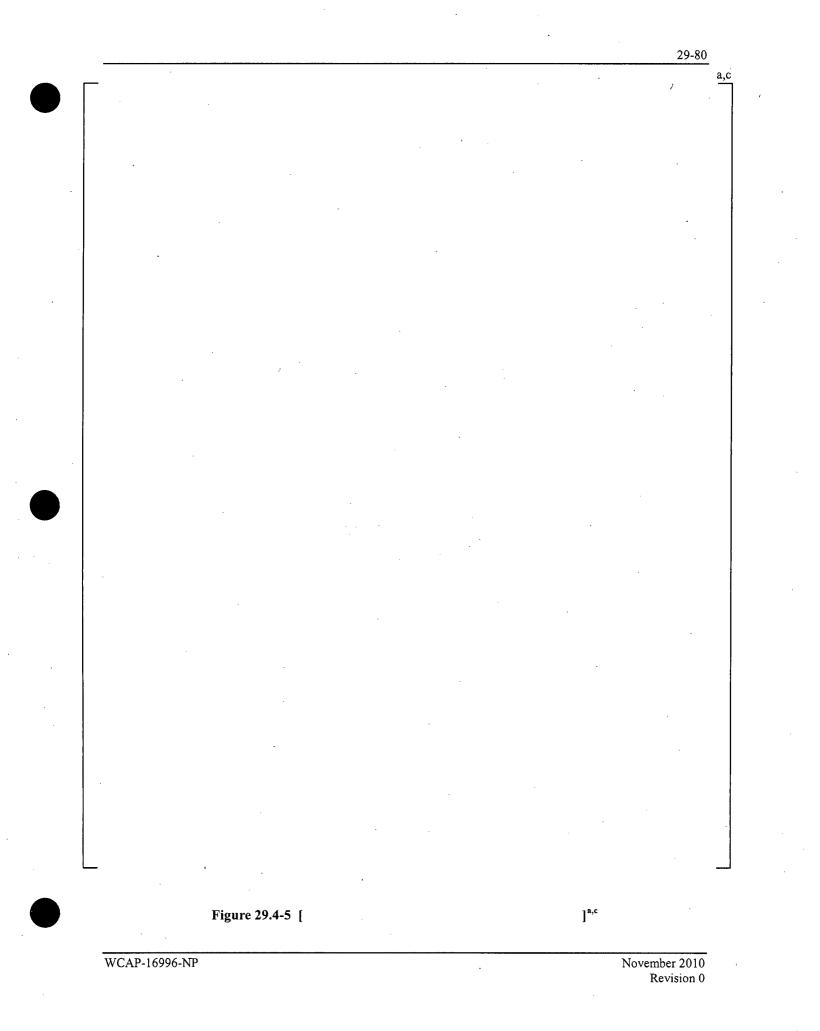
]^{a,c}

]^{a,c}

]^{a,c}

range [

ſ

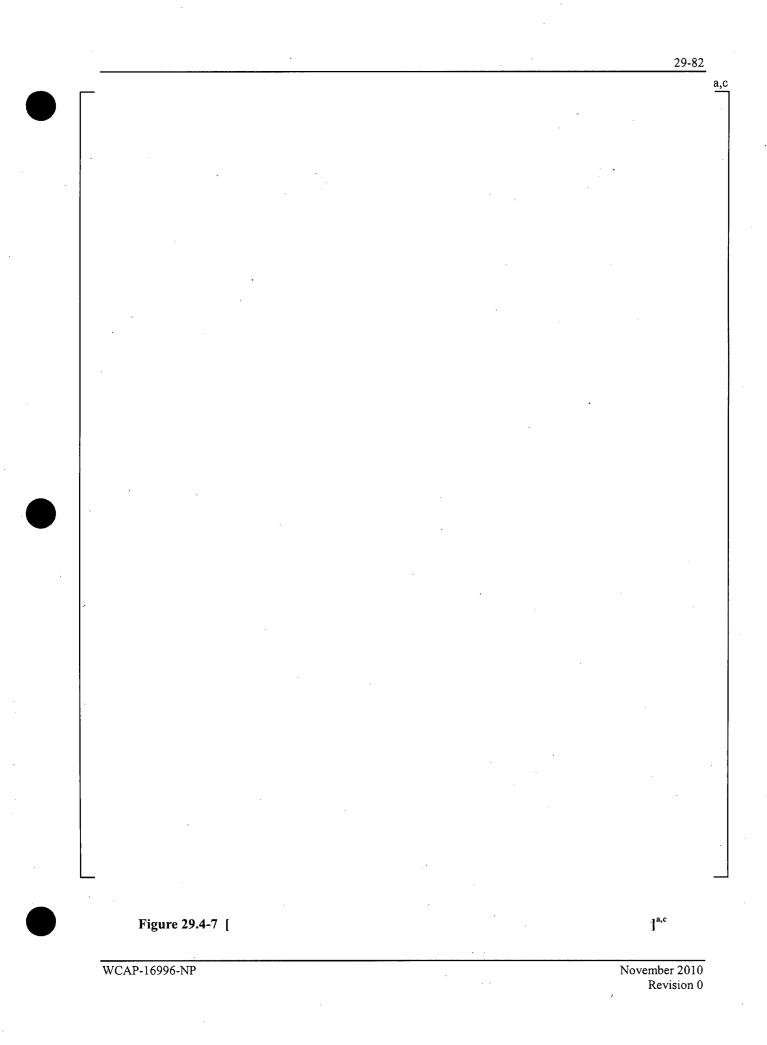


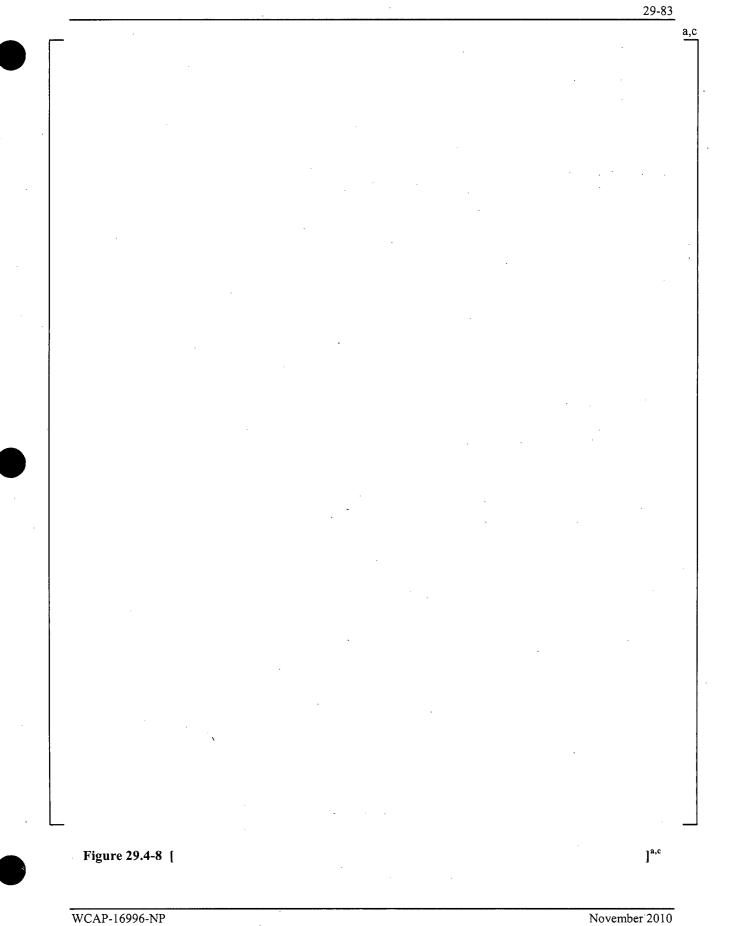
					·····			29-81
	-							a,0
	·							
		·						
					. ·			
						54 ^{- 1}		
		`						
				•				
						ζ.	ч	
L	-							
		Figure 29.4-	6 [		۰.		] ^{a,c}	
,								

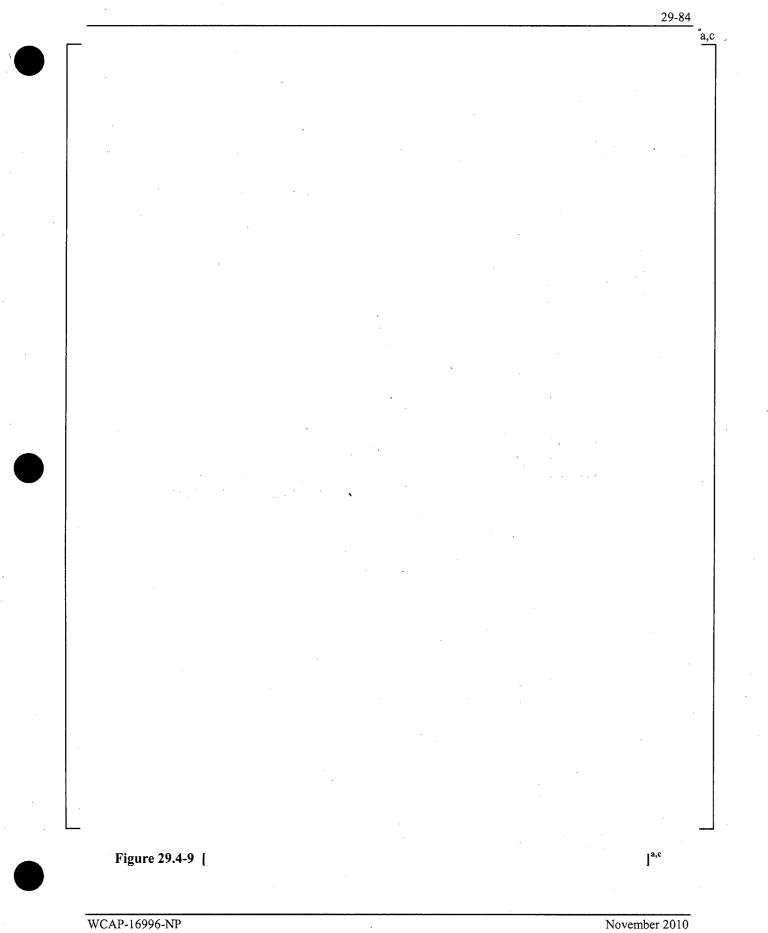
.

i

. ľ







a,c

]^{a,c}

WCAP-16996-NP

Figure 29.4-10 [

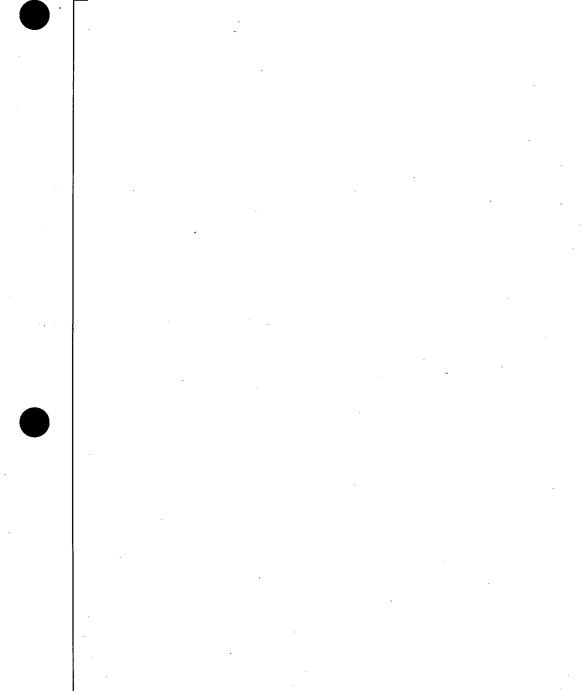


Figure 29.4-11 [

WCAP-16996-NP

November 2010 Revision 0

]^{a,c}

a,c

		29-87	
Г	<u> </u>		â
•			
L			
	Figure 29.4-12 [ ]	,c	

WCAP-16996-NP

### Fuel Relocation Following Burst

The phenomenon of fuel relocation following cladding burst was discussed in Section 8.6.1. The fuel density at the burst region of [ ]^{a,c} is measured by packing fraction. The packing fraction is the ratio of the volume of fuel within the burst region to the total volume within the burst region. The INEL (Broughton, 1981) studied data from several sources and used several measurement methods. In addition, NNC performed additional analyses using photographs of the fuel cross sections. These data are summarized in Table 29.4-1. A plot of this data versus burst strain (Figure 29.4-13) appears to confirm [ ]^{a,c}. From these different measurement

methods, the uncertainty on packing fraction was estimated.

The numbers of occurrences as a function of packing fractions are plotted in Figure 29.4-14. The range was calculated by taking the difference between the maximum and minimum value, and dividing by the average value. A histogram of the data is shown in Figure 29.4-14. [

]^{a,c}

Table 29.4-1         Packing Fractions Using Various Measurements						
Burst Strain Percent	Packing Fractions Percent (Various Measurement Methods)					
29	79	70	66	65		
35	63	70	42	63.		
42	71	67	59	58		
47	71		62	-		
48	62	70	61	74		
74	66	-	52	-		

a,c

a,c

Figure 29.4-13 [

Figure 29.4-14 Distribution of Packing Fraction Data

WCAP-16996-NP

November 2010 Revision 0

]^{a,c}

### Zirconium-Water Reaction and its Uncertainty

The zirconium-water reaction rate calculations are performed using methods described in Volume 1, Section 8.5. When [

The data upon which the ZIRLO[®] and zircaloy reaction rate equations are based are from Cathcart and Pawel (1977). The prediction interval at 95 percent probability for these equations was calculated from the data using the following equation (Draper and Smith, 1981):

$$Y + t (95\%, n-2) \left[ 1 + \frac{1}{n} + \frac{(X - \overline{X})^2}{\sum (X_i - \overline{X})^2} \right]^{1/2} s$$
(29.4-1)

Where t (95%, n-2) is the 95 percentage point of a t-distribution with n-2 degrees of freedom, to account for sample size,  $\overline{X}$  is the average of the X values, and s² is the residual mean square of the data around the reaction equation line. The equation above is the prediction interval for the next "point estimate" of the reaction rate; the uncertainty interval for the prediction of the mean of the data is smaller (the equation is similar to that above except that the 1 is missing).

The "uncertainty" cited in [

]^{a,c} A model is

(29.4-2)

assumed of the form:

ſ

ſ

$$\ln (\delta^2 / 2) = A + B(1 / T(K))$$

The regression output is shown in Table 29.4-2b. The output shows that the constants A and B are:

]^{a,c}

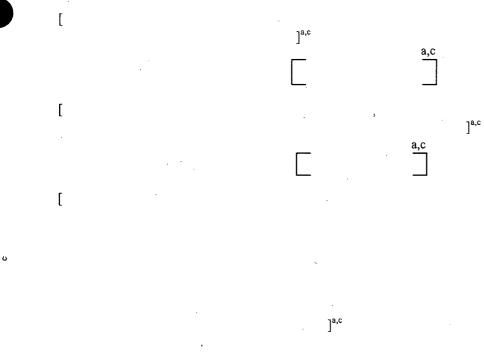
These numbers compare to those in Table A2 of Cathcart and Pawel:

A = -1.70986 B = -20100

WCAP-16996-NP

]^{a,c}

]^{a,c}_



. . .

WCAP-16996-NP

November 2010 Revision 0

. .

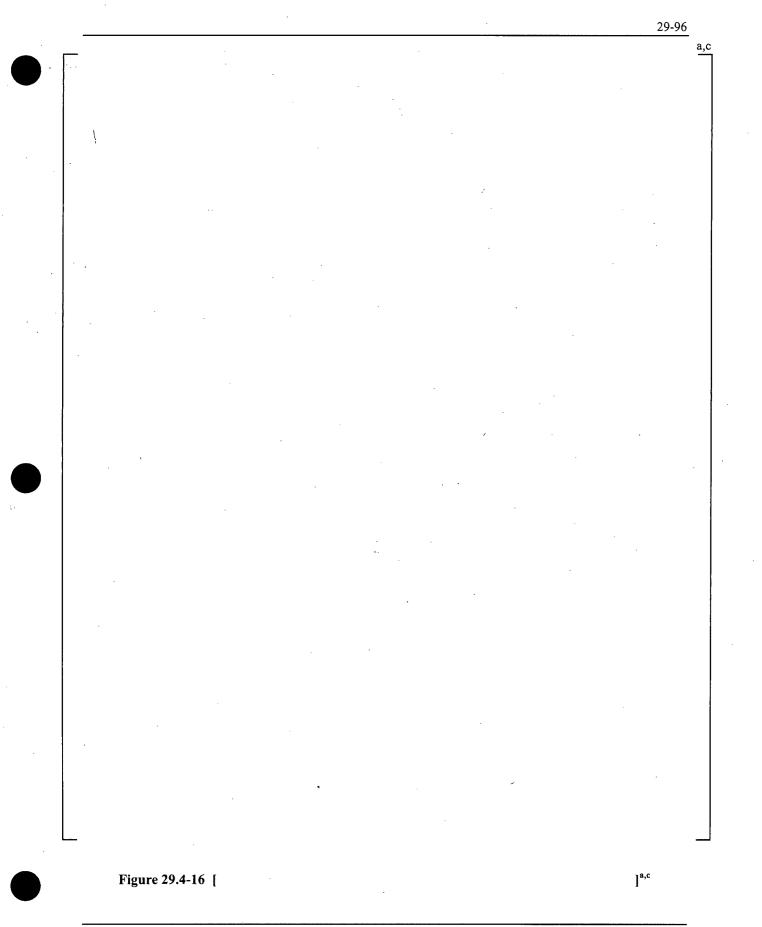
Table 29.4-2a	Zircaloy Rate Constants	s (Total Oxygen)		
T(°C)	δ²/2=ΟΧ	1/T(K)=X	(X-XBAR) ²	LN(OX)=Y
1050	4.720E-08	0.000755	1.109E-08	-16.8689
. 1101	8.070E-08	0.000727	5.968E-09	-16.3325
1153	1.390E-07	0.000701	2.573E-09	-15.7888
1203	2.180E-07	0.000677	7.274E-10	-15.3388
1253	3.300E-07	0.000655	2.280E-11	-14.9242
1304	5.080E-07	0.000634	2.694E-10	-14.4928
1352	7.690E-07	0.000615	1.235E-09	-14.0782
1404	1.130E-06	0.000596	2.940E-09	-13.6933
1454	1.640E-06	0.000578	5.109E-09	-13.3208
1504	2.280E-06	0.000562	7.704E-09	-12.9913
NTESTS:		XBAR:	$\Sigma(X-XBAR)^2$ :	· ·
10		0.000650	3.764E-08	

Table 29.4-2b [	] ^{a,c}	·
· · ·		
		-
(		

-		-			
			<u>`````````````````````````````````````</u>		
· ·					

				29-95
Г		ţ		a,c
				· .
			•	
				-
	\$			
		· · ·		
	•			
		· · ·		
			× .	
			·	•
		. '		
	•			
				•
Figure 29.4-15 [	·			] ^{a,c}

WCAP-16996-NP



WCAP-16996-NP

November 2010 Revision 0

.

#### 29.4.2.2 Initial Calibration of the Steady-State Condition for the Nuclear Rods

The initial fuel temperature and rod internal pressure for Westinghouse PWRs are calibrated against the PAD 4.0 fuel performance code (Foster and Sidener 1999). For CE PWRs, the calibration will be against the FATES3B code (CE, 1992). The calibration of initial fuel temperature is performed for [ ]^{a.c.} in FSLOCA.

The initial stored energy in the fuel is a direct function of the pellet average (radial) fuel temperature which we call TFUEL. The initial fuel temperature is a function of the peak linear heat rate and burnup.

 $]^{a,c}$ 

]^{a,c}

a,c

a,c

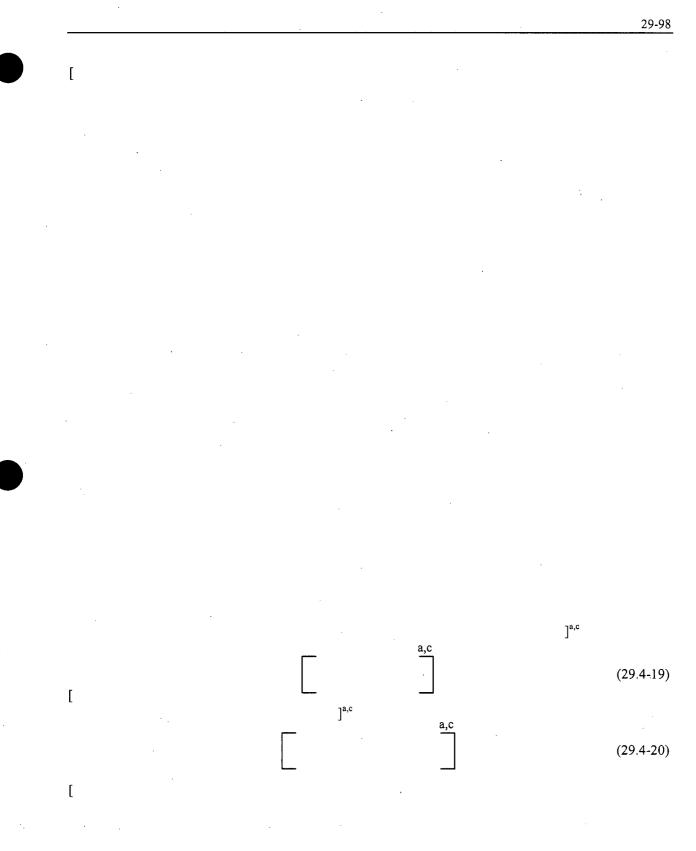
ſ

ſ

[

(29.4-17)

(29.4-18)



 $]^{a,c}$ 

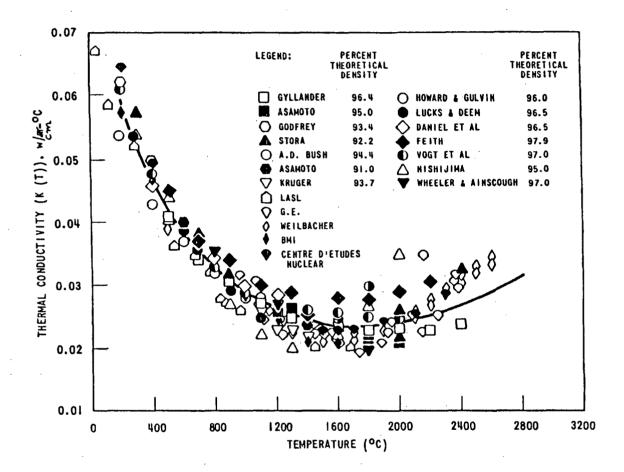


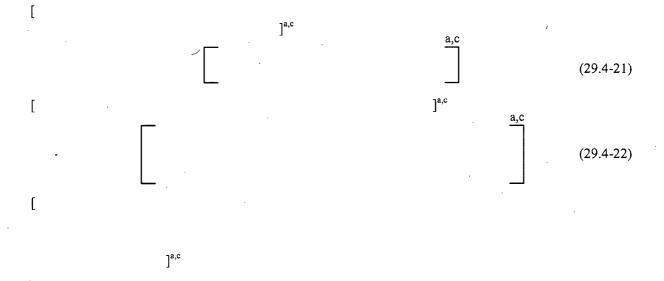
# Figure 29.4-18 Thermal Conductivity of UO₂

WCAP-16996-NP

# 29.4.3 Fuel Rod: Uncertainty on Heat Transfer to the Fluid

The methodology for uncertainty propagation considers, in addition to fuel rod model and minimum film boiling temperature uncertainties, the local variation in heat transfer from the nuclear rod to the fluid. There are several heat transfer regimes that affect the cladding temperature during a postulated LOCA accident, which depend on the fluid conditions as well as the cladding temperature itself. Models are included in the code to characterize each heat transfer regime, as described in Section 7. During a simulation, models are properly selected depending on the local flow regime, void fraction and surface temperature. Such models have been derived from a large data base which describes the fundamental heat transfer processes. The heat transfer package is then validated and assessed against prototypical data which was intended to recreate conditions expected in the reactor core during an accident, as discussed in Sections 14 and 15.





ſ

1^{a,c}

]^{a,c}

(29.4-23)

]^{a,c}

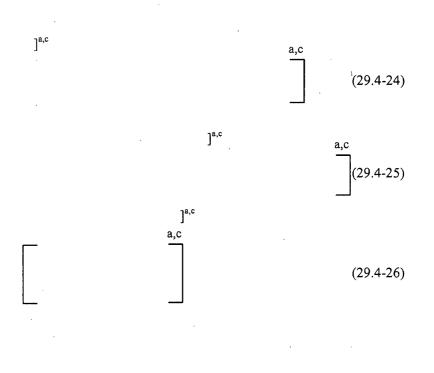
]^{a,c}

The second dataset is from FLECHT SEASET (Wong. S and Hochreiter, L.E., 1981), which are low pressure single-phase vapor tests. The COBRAHT-TF2 calculation results are presented in Section 15.4.2. Using Equation 29.4-22, the PDF is created as shown in Figure 29.4.3-2. A heat transfer multiplier sampled from this distribution in the uncertainty analysis is applied to a conduction node that is determined to be in single-phase vapor and has a [

When the code predicts a heat conduction node to be in single-phase vapor during each simulation (run) of the uncertainty analysis (Monte Carlo propagation of uncertainties), one of the single-phase vapor multipliers is applied to the single-phase heat flux as follows:



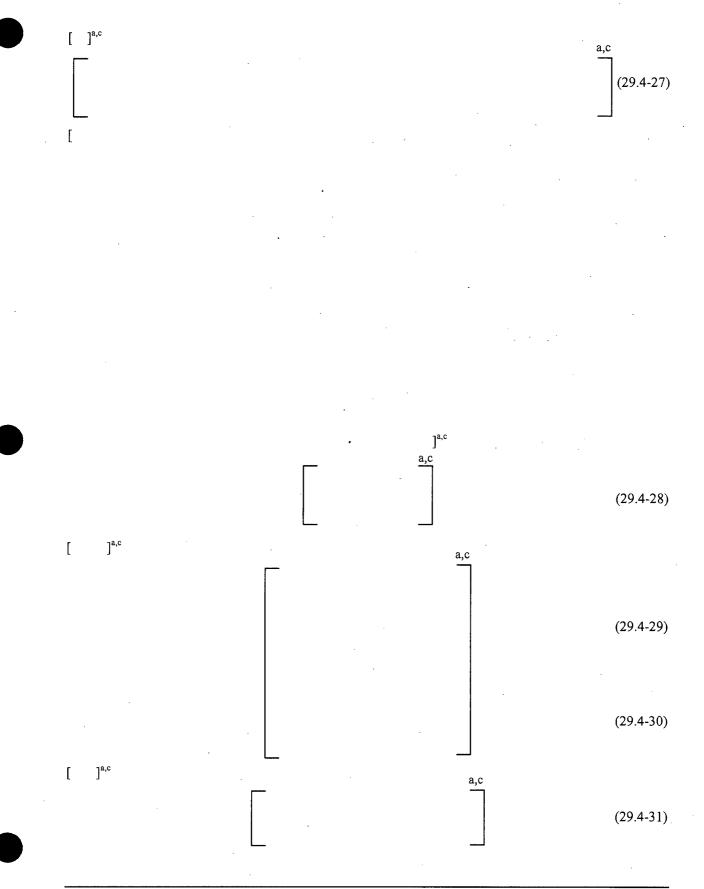
]^{a,c}



WCAP-16996-NP

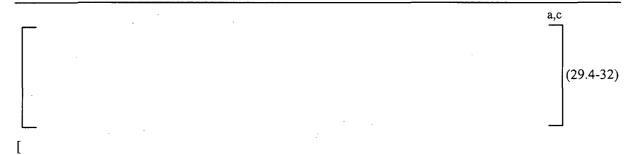
ſ

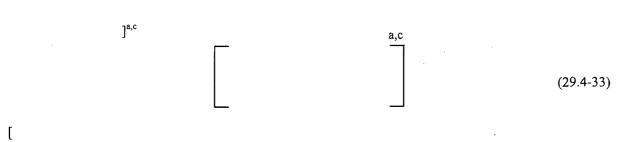
ſ



WCAP-16996-NP







WCAP-16996-NP

]^{a,c}



]^{a,c}

[

[

# 29.4.3.3 Global versus Local Heat Transfer Coefficient

(29.4-34)

a,c

]^{a,c}

]^{a,c}

# 29.4.3.4 Effect of Rod-to-Rod Radiation Heat Transfer

]^{a,c}

[

[

Section 15 documents the assessment of the <u>WCOBRA/TRAC-TF2</u> heat transfer logic for several rod bundle heat transfer experiments. Given the limited size of the experimental test sections, the presence of the housing and any thimbles and unheated rods may affect the overall heat transfer by enhancing the radiation heat flux from the rod to the cooler housing, thimble and/or rod (termed rod-to-rod radiation herein). Such phenomenon can not be neglected in the overall heat transfer assessment.

WCAP-16996-NP

Table 29.4.3-1 [	] ^{a,c}				
-	. •				
					· · · · · · · · · · · · ·
<u></u>	,				
·	· · · · ·				
	······································	<u></u>			
	-	· · ·			
		4			
			· · · · · · · · · · · · · · · · · · ·	· · ·	
			<b>4</b>	<b>.</b>	~

Table 29.4.3-2 [	] ^{a,c}		
		1	

WCAP-16996-NP

a,c Figure 29.4.3-1 [ ]^{a,c} a,c

Figure 29.4.3-2 [

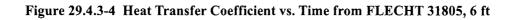
]^{a,c}

a,c

a,c

# Figure 29.4.3-3 [

j^{a,c}



WCAP-16996-NP

a,c

a,c

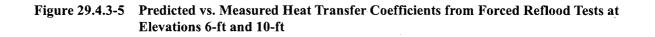


Figure 29.4.3-6 [

WCAP-16996-NP

November 2010 Revision 0

]^{a,c}

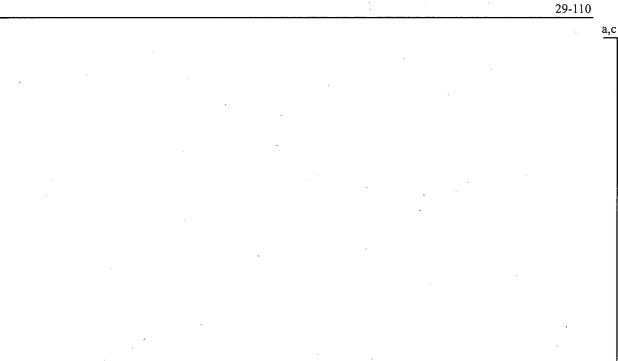
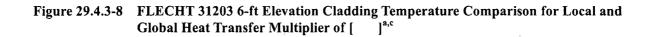


Figure 29.4.3-7 FLECHT 31203 6-ft Elevation Cladding Temperature Comparison for Local and Global Heat Transfer Multiplier of [ ]^{a,c}



WCAP-16996-NP

a,c

a,c

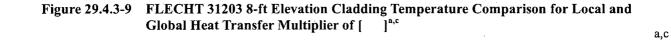


Figure 29.4.3-10 FLECHT 31203 8-ft Elevation Cladding Temperature Comparison for Local and Global Heat Transfer Multiplier of [ ]^{a,c}

WCAP-16996-NP

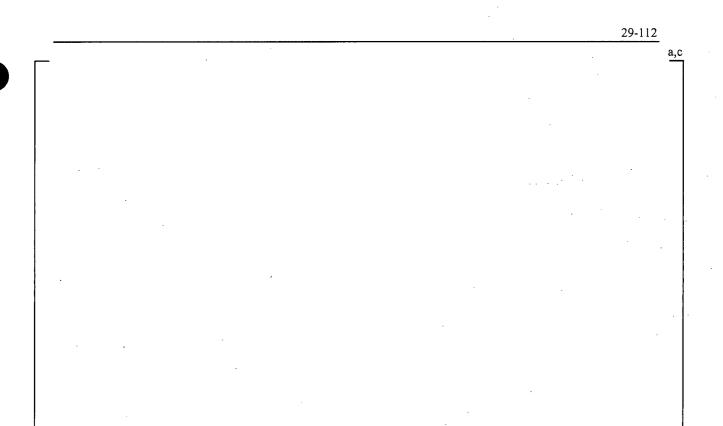


Figure 29.4.3-11 FLECHT 31203 10-ft Elevation Cladding Temperature Comparison for Local and Global Heat Transfer Multiplier of [ ]^{a,c}

Figure 29.4.3-12 FLECHT 31203 10-ft Elevation Cladding Temperature Comparison for Local and Global Heat Transfer Multiplier of [ ]^{a,c}

WCAP-16996-NP

November 2010 Revision 0 a,c

a,c

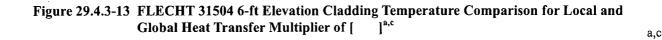


Figure 29.4.3-14 FLECHT 31504 6-ft Elevation Cladding Temperature Comparison for Local and Global Heat Transfer Multiplier of [ ]^{a,c}

a,c

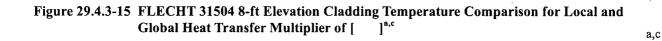


Figure 29.4.3-16 FLECHT 31504 8-ft Elevation Cladding Temperature Comparison for Local and Global Heat Transfer Multiplier of [ ]^{a,c}

)

a,c

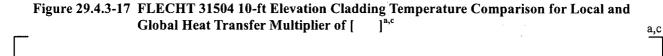


Figure 29.4.3-18 FLECHT 31504 10-ft Elevation Cladding Temperature Comparison for Local and Global Heat Transfer Multiplier of [ ]^{a,c}

WCAP-16996-NP

November 2010 Revision 0

ſ



a,c

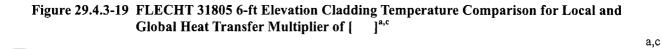


Figure 29.4.3-20 FLECHT 31805 6-ft Elevation Cladding Temperature Comparison for Local and Global Heat Transfer Multiplier of [ ]^{a,c}

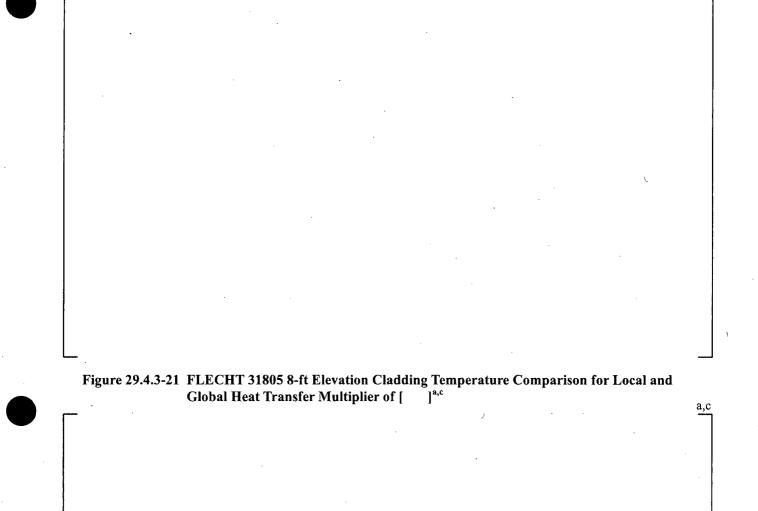


Figure 29.4.3-22 FLECHT 31805 8-ft Elevation Cladding Temperature Comparison for Local and Global Heat Transfer Multiplier of [ ]^{a,c}

WCAP-16996-NP

November 2010 Revision 0

29-117

a,c



a,c

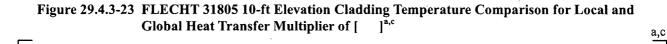


Figure 29.4.3-24 FLECHT 31805 10-ft Elevation Cladding Temperature Comparison for Local and Global Heat Transfer Multiplier of [ ]^{a,c}

# 29.5 EVALUATION MODEL BIASES AND UNCERTAINTY (EMDAP STEP 20)

According to the Regulatory Guide 1.203, a singular uncertainty statement on the overall uncertainty results can only be achieved when the individual uncertainty contributions are determined. The procedure used to obtain the convolution of such uncertainties is the subject of Section 30. The development of the individual uncertainty contributors, ranges, and probability density functions has been the objective of this section.

The uncertainty contributors are divided in two main categories:

- 1. The first main category is the uncertainty associated with the code capability of representing phenomena and processes identified as highly important by the PIRT. The capability is established by assessing the code against SET/IET experiments that were designed to simulate such processes. The combined uncertainty will reflect the degree to which the individual models, correlations and methods used within the code represent the physical phenomena, the uncertainty associated with the use of such models, and the uncertainty associated with the experimental data itself and applicability of the data to PWRs.
- 2. The second main category is the uncertainty associated with the input boundary and initial conditions and all those parameters that define the plant state at the time of the postulated LOCA event, as well as the uncertainty associated with the break location, break type and size, etc. This uncertainty is not the result of the code capability of simulating the LOCA event, but rather the uncertainty associated with the LOCA scenario event itself.

The purpose of this section is to summarize the methodology for the treatment of the uncertainty contributors contained mainly in the first category. This is in line with the intent of Step 20 of the EMDAP, which asks for the determination of the EM biases and uncertainty. Since the process started by identifying the important phenomena with the PIRT, it is useful here to structure the review following the PIRT (Section 2), by describing how each of the phenomena was considered in the uncertainty methodology.

# 29.5.1 Fuel Rod

#### **Stored Energy**

Uncertainties in the initial stored energy of the hot rod and hot assembly are large. There is a wide range of possible peaking factors and power distributions that are allowed by the Technical Specifications. For a given power distribution, [

l^{a,c} have

been considered in the uncertainty methodology by explicitly ranging them as part of the uncertainty methodology.

## **Clad Oxidation**

The metal-water reaction rate is ranged based on uncertainty estimates obtained from experimental data. This uncertainty is treated as a local uncertainty – see Table 29-3a for the numerical values.

#### **Decay Heat**

The decay heat uncertainties from the American National Standards Institute/American Nuclear Society (ANSI/ANS) 5.1-1979 standard are applied as described in Section 9.7. [

]^{a,c}

#### **Clad Deformation (Burst Strain, Relocation)**

These processes were ranked medium (M) during the periods where clad temperatures can approach those at which burst may occur. The uncertainty on cladding burst strain and temperature are obtained from the data scatter. The fuel pellet fragments packing fraction after relocation is also identified as an uncertainty contributor. Numerical values are provided in Table 29-3a and Table 29-3b.

# 29.5.2 Core

## **Critical Heat Flux (CHF)**

Assessments of the CHF predictions are discussed in Sections 13 and 15. As discussed in Sections 15 and 22, [

#### ٦^{a,c}

#### Post-Critical Heat Flux (CHF) Heat Transfer

Uncertainties in the post-CHF heat transfer are accounted for by ranging [

 $]^{a,c}$  are based on the assessments of Sections 15 and 29.4.3.

#### Rewet/T_{min}

The effects of the uncertainty on rewet/ $T_{min}$  on the post-CHF heat transfer in a large or intermediate break LOCA are discussed in Section 29.1.8. For small breaks, the uncovered portion of the rod is in single-phase vapor which is the only source of cooling until the mixture level passes through. The advancement of the mixture level determines the rod re-wetting.

#### Three-Dimensional (3D) Flow/Core Natural Circulation

The importance of correctly predicting the distribution of the downflow from the upper plenum to the core is high (H) for large breaks during the blowdown period. Uncertainties in these parameters are accounted

for by choosing the limiting hot assembly location based on consideration of the hardware in the upper plenum, and the resulting flow distribution during the downward core flow period of blowdown. Multidimensional effects are also captured by the core nodalization scheme, which uses 4 separate assembly groupings (hot assembly, assemblies on core periphery, interior assemblies located under guide tube assemblies, and interior assemblies located under other structures).

#### Void Generation/Void Distribution

During a small break, the void generation and distribution determine the location of the mixture level and the portion of core that uncovers for a given liquid inventory. The interfacial drag is the parameter controlling the void fraction in the two-phase region. The process is assigned a high (H) importance during the loop seal clearing, boiloff, and core recovery periods. For intermediate breaks, for similar considerations, this process is assigned a high (H) ranking during the accumulator injection and SI injection phases. The code has been assessed in these regards in an extreme core uncovery condition in the simulation of the Semiscale test (Section 23.1.2) with satisfactory results. [

]^{a,c} The uncertainty is treated as discussed in

#### Section 29.1.5.

In a large break LOCA, during blowdown, different considerations apply but void distribution/generation is also ranked high (H) following the multiple channel flow discussion above (see the ranking rationale for 3D Flow/Natural Circulation above). The amount and timing of liquid and vapor downflow the core receives from the upper plenum depends on the hardware and geometry directly above a particular core region. The geometry of the upper internals in the upper plenum is explicitly modeled, and the core regions under particular hardware are explicitly modeled to account for different downflow behavior. The ability of the code to calculate voiding and flow under blowdown conditions was assessed indirectly by simulating the LOFT tests (Section 22.5), [

]^{a,c} (see *Flow Reversal/Stagnation* discussion below).

#### **Entrainment/De-entrainment**

This is highly (H) important during the accumulator injection period of intermediate breaks and the reflood period in large breaks. Comparisons with FLECHT and CCTF data indicate that <u>WCOBRA/TRAC-TF2</u> overpredicts the amount of entrainment from the core. For forced reflood tests, the entrainment was accurately predicted. For gravity reflood tests such as CCTF, however, excess entrainment results in an over-prediction of steam binding, which reduces the flooding rate and causes an under-prediction of core heat transfer. In addition, the comparisons with Upper Plenum Test Facility (UPTF) tests showed that when the conditions at the entrance to the upper plenum are known, <u>WCOBRA/TRAC-TF2</u> underpredicts the mass retained in the upper plenum, therefore overpredicting the amount of water entrained into the loops. Based on the gravity reflood and UPTF test predictions, it is concluded that a conservative bias already exists in the calculations for core entrainment/de-entrainment, and an additional bias or uncertainty is not required.

#### Flow Reversal/Stagnation

This phenomenon was assigned high (H) only during the blowdown phase of a large break LOCA. Uncertainties in the blowdown flow reversal and stagnation affect the time and magnitude of the blowdown PCT, and the core-wide cooling during blowdown. Uncertainties are accounted for by varying break flowrate, via sampling of break type, split-break size, and the application of break flow multipliers based on the assessment of the critical flow model. Ranging of the broken cold-leg nozzle resistance and pump resistance also affects the flow reversal and stagnation as demonstrated in Section 28.1.4. The interactions between the stagnation point and the location of peak nuclear power are accounted for by ranging the core axial power distribution as well.

# 29.5.3 Upper Head

# Draining/Flashing/Mixture Level

The liquid inventory in the upper head initially drains through the guide tubes, until the depressurization causes flashing in this region. For large breaks, the initial depressurization is rapid and the upper head inventory can be a significant contributor to the removal of initial core stored energy. This process is therefore highly ranked in blowdown. It is considered not applicable for later periods due to depletion of inventory. The initial upper head liquid temperature is calibrated during the steady-state calculation. Upper head liquid temperature uncertainty is considered by varying the temperature based on the ranging of vessel average temperature.

#### Venting

Later in a LOCA transient, steam generated in the core will either be vented through the hot legs, the hot leg nozzle gaps, or the upper head. The ability to vent steam through the upper head is strongly dependent on the flow area of the spray nozzles, which is the flow path connecting the upper head and the downcomer. Venting has a high importance during the loop seal clearing period when it relieves some of the core two-phase level depression. Sensitivity studies of the effect of spray nozzle bypass on the small break LOCA transient, performed with the ROSA-IV test simulations, are provided in Section 21.11. The overall conclusion from the results presented in Section 21 is that [

#### ]^{a,c}

#### **Initial Fluid Temperature**

The initial fluid temperature in the upper head region will be either equal to the cold leg temperature, or close to the hot leg temperature, depending on the spray nozzle flow area. This will affect the timing at which flashing occurs in the upper head, causing the flow through the guide tubes to switch from single phase liquid to a two-phase mixture. For large breaks, the initial depressurization is rapid and the upper head inventory can be a significant contributor to the removal of initial core stored energy. The timing of flashing in the upper head has a significant effect on the downflow cooling of the core. This process is therefore highly ranked in blowdown. For the uncertainty, see a similar discussion under "Draining/Flashing/Mixture Level."

# **29.5.4** Upper Plenum

# **Hot Assembly Location**

Refer to the discussion of core 3D flow in Section 29.5.2.

#### **Entrainment/De-entrainment/Phase Separation**

The entrainment/de-entrainment in the upper plenum was ranked high (H) only for two-loop plant with UPI. The applicability of the FSLOCA EM to that type of plants is outside the scope of this report, other than the PIRT (Section 2), which sets the basis for applicability to UPI plants. For 3- and 4-loop plants with cold-leg injection, refer to discussion of core entrainment/de-entrainment in Section 29.5.2.

#### Hot Leg-Downcomer Gap Flow

Small gaps exist at the interface of the core barrel and the hot leg nozzles. These are the leakage paths that exist between the hot leg nozzles and upper downcomer region during all operating modes. For small breaks, these leakage paths are expected to have high importance during the loop seal clearing period when they provide alternative paths from the upper plenum to the cold leg break location to vent steam and relieve some two-phase level depression. The ROSA sensitivity study in Section 21.11 shows that  $\int_{a,c}^{a,c}$ .

# 29.5.5 Steam Generator

#### Primary Side Heat Transfer/Condensation in U-tubes

This refers to the heat transfer processes on the primary side of the SG tubes. If condensation occurs, it affects the amount of vapor present and the resistance to flow through the generator. For small breaks, during the blowdown period, the U-tube heat transfer from the primary to the secondary system is important and was ranked high (H); and during the loop seal clearance period the process was ranked high (H) because of the effect of condensation. The primary-to-secondary heat transfer and condensation is calculated with a conservative bias by the code as discussed in Section 29.1.12. There is no need to explicitly treat uncertainties for this phenomenon.

The effect of reduced heat transfer area due to steam generator tube plugging is [ $]^{a,c}$ .

#### Flow Regime/CCFL

This refers to the flow regime in the primary side of the steam generator, and in particular the hydraulic processes on the primary side in the SG tubes that lead to liquid holdup on the uphill side and voiding at the top of the U-tube. The potential for CCFL in the tubes and the impact of CCFL predictions on the transient was judged to be of high (H) importance during the loop seal clearing period. Based on the assessment of CCFL extracted from the ROSA-IV simulations at key locations (UCP, hot leg elbow/SG inlet, and steam generator U-tubes), the code calculations have been concluded to be biased in a conservative direction (see Section 29.1.12.2).

# **Steam Binding**

This process is only relatively important when high liquid entrainment from the upper plenum is carried into the steam generator U-tubes, while the SG is acting as a heat source. The vaporization of the liquid leads to pressure increase and a reduction of the core inlet flow rate. The steam binding is highly important (H) only during the reflood period of a large break as it affects the venting path resistance and thus the reflood in the core. Refer to the discussion of core entrainment/de-entrainment in Section 29.5.2. The effects of steam binding from steam generator tube plugging are [

]^{a,c} (see the introductory summary in Section 28).

# **Primary Flow Resistance (Two-Phase DP)**

The two-phase pressure drop through the SG primary side was rated high (H) for the loop seal clearing part of a small break LOCA transient and during the blowdown period of a large break LOCA when the SG flow resistance affects the overall loop resistance, which in turn affect the flow reversal and stagnation in the core. By sampling the break size, discharge coefficient, pump loss, broken cold leg nozzle loss, horizontal stratification transition, and axial power distribution, the effects on the break path resistance regarding the large break blowdown (see Section Flow Reversal/Stagnation discussion in 29.5.2) and small break loop seal clearance (see Section 29.1.11) are adequately ranged.

# 29.5.6 Pump Suction Piping/Loop Seal

#### **Horizontal Stratification**

The prediction of the horizontal stratified flow regime in the loop seal piping was assigned a high (H) ranking in the loop seal clearance period of a small break LOCA. The uncertainty on the flow regime transition in and out from horizontal stratified flow (or wavy-dispersed) is treated as discussed in Section 29.1.7 (HS_SLUG). [

#### Entrainment/Flow Regime/Interfacial Drag

This refers to the entrainment of liquid from the stratified layer at the bottom of the horizontal section of loop seal piping, and the carryout of this liquid from the region.

For small breaks a high (H) ranking was assigned for the loop seal clearance period when entrainment and interfacial drag determine the efficacy of clearing. The modeling of the uncertainty in the loop seal clearing phenomenon is discussed in Section 29.1.11.

# 29.5.7 Pump

#### **Coastdown Performance**

This item refers to the effect the pump has on the flow between the time when the pump is tripped and when the impeller completes its coastdown. Note that the effects of pump friction/windage losses are included in this process. For large breaks, the coastdown performance is important since it indicates when

the pumps lose their pumping capability. This helps determine the flow reversal in the core, and therefore is ranked consistently with flow reversal in the core. The process is ranked high (H) during blowdown. The intact loop pumps are in the pumping mode during the 2-phase period, and the data in this mode show little scatter (Section 20.2). However, the broken loop pump is in the dissipative mode, where the data scatter is considerable. The uncertainty treatment, therefore, focuses on the broken loop pump resistance uncertainty in the dissipative mode, described in Sections 29.1.2.2 and 20.2.

#### **Flow Resistance**

The hydraulic resistance to flow passing through the pump was ranked high for large breaks. During the reflood portion of the transient, the flow resistance is expected to have an effect on the venting path flow resistance, with an effect similar to that discussed above for the steam binding. The ranging of the pump resistance discussed before for the blowdown phase is also applicable to reflect the uncertainty in the pump flow resistance during reflood.

# 29.5.8 Cold Leg/Safety Injection

Phenomena relative to the flow delivered by accumulator safety injection on the cold leg are discussed here, as well as phenomena relative to the pumped safety injection. The accumulator is discussed separately in Section 29.5.9.

#### **Interfacial Heat Transfer (Condensation)**

This is condensation that occurs on and about the stream of subcooled water injected into the cold leg from the pumped SI system and/or the accumulator. For small breaks during the boiloff period and the recovery period, the SI flow to the cold legs is high because the system pressure is lower, so a high (H) ranking was assigned. For the intermediate breaks, condensation was assigned high (H) ranking during the accumulator injection and SI injection phases. For the large breaks, condensation is of the highest relative importance during the refill period. When the ECC water is no longer bypassed in the refill period, the condensation process at the top of the downcomer can increase the downcomer level and therefore helps to induce reflood through the core, promoting cooling. A ranking of high (H) is assigned during this period. A specific condensation model (COSI) was included in the code (Section 6, Volume 1) and is active in the cold leg in the node connected with the ECC piping when the flow regime is either stratified or wavy-dispersed or annular-mist. The model was shown to be applicable to the full spectrum of breaks and scenarios (Section 17). The uncertainty on the model was developed in Section 29.1.6 and ranging is considered in the plant analysis.

[

#### **Non-Condensable Effects**

This refers to the effect that nitrogen has on condensation in the cold leg. The rankings for this effect generally follow those assigned for condensation. For intermediate breaks, a high (H) ranking was assigned for the safety injection period to reflect the effect of nitrogen on condensation in the cold leg, which was ranked high during this period for intermediate breaks as discussed above. For the larger breaks, the effects

]^{a,c}

of non-condensable gases are important during the reflood period when the accumulators empty and the nitrogen from the accumulators is released into the primary system. In the PIRT the effect on condensation is considered to have medium (M) importance during the reflood period of a large break LOCA. The transport of the non-condensable field was added to WCOBRA/TRAC-TF2 and the effect of the non-condensable on the condensation is captured. Given the medium ranking for large break and considering that intermediate breaks are typically not limiting, the model as coded is considered adequate without consideration of uncertainties. Comparisons with ACHILLES test data (see Section 29.1.10) indicated that WCOBRA/TRAC-TF2 tends to underpredict the pressurization of the downcomer and the resulting insurge of water into the core. The tendency to underpredict downcomer pressurization, and the impact on the heat transfer during the initial insurge of water in the core, leads to the conclusion that the effects of accumulator nitrogen will be conservatively calculated and therefore the uncertainty associated with this model is bounded.

#### **Flow Regime**

Horizontal stratification was assigned a high (H) ranking in the loop seal clearance, boiloff, and recovery periods, when the two-phase level drops in the cold legs and the break uncovers. The controlling parameter is the transition boundary between horizontally stratified or wavy-dispersed flow and non-stratified flow regimes. The uncertainty on the flow regime transition in and out from horizontal stratified flow (or wavy-dispersed) is treated as discussed in Section 29.1.7 through the ranging of HS_SLUG.

#### **Spilling Flow Treatment (Pumped SI)**

The treatment of the pumped SI flow in terms of flow spilled at the break versus flow delivered is considered. Spilled flow depends on the break dimension and location on the cold leg. For small breaks, a ranking of high (H) was assigned for the boiloff and recovery periods. A ranking of high was also assigned during the safety injection phase of intermediate break and during the reflood period of a large break LOCA. The uncertainty on the amount of pumped SI flow spilling to containment and its impact to the SI delivered in the RCS is bounded in the analysis as discussed in Section 25.

# 29.5.9 Accumulator

# **Injection Flowrate/Line Resistance**

This refers to the rate at which liquid is discharged from the accumulator, which depends upon the cover gas expansion coefficient and the hydraulic resistance to accumulator flow in the check valve and in the line connecting the accumulator to the cold leg. The effect of the line resistance was ranked high (H) during the accumulator injection period of intermediate breaks, and during the refill period of large breaks. The uncertainty in the line resistance is ranged in the uncertainty analysis. Numerical values are provided in Table 29-5.

#### Nitrogen Discharge

The accumulator nitrogen provides the main source of non-condensable gas in the system during the LOCA transient. While the potential effects of non-condensables are discussed elsewhere as applicable, it is recognized that the accumulator cover gas provides the main source of non-condensable gas in the

system, and thus ranking should follow consistently. The modeling of this process was assigned a high (H) ranking for intermediate breaks during the safety injection phase. See Non-Condensable Effects discussion in Section 29.5.8.

#### **Broken Loop Accumulator Treatment**

The accumulator on the broken loop [ (Pumped SI) in Section 29.5.8. ]^{a,c}. See Spilling Flow Treatment

## 29.5.10 Downcomer

#### Condensation

In a large break LOCA condensation in the downcomer affects ECC bypass and the refill and reflood transient. Comparisons with small- and large-scale tests showed that while <u>W</u>COBRA/TRAC-TF2 predicted reasonable values of condensation efficiency, the range of uncertainty in the data interpretation is large. The condensation in the downcomer is calculated using the nominal model, which demonstrates conservatism regarding the timing of ECC bypass and the beginning of refill. Treatment of uncertainty is discussed in Section 29.1.4.

#### **Reactor Pressure Vessel Internals/Vessel Wall Stored Energy**

This is the effect of the heat release to the fluid from the downcomer metal structures. Heating of the water in the downcomer during reflood eventually causes boiling, which results in level swell, spilling of water out of the broken loop, and a reduction in reflood rate. Comparisons with CCTF Run 62 and UPTF Test 25A hot wall tests indicated that the combined effects of downcomer boiling and entrainment on downcomer level during reflood are well predicted (Figure 19.6-28 and Figures 19.3-190 and 19.3-191 for CCTF and UPTF, respectively). The timing of the onset of downcomer boiling is ranged by varying the accumulator and pumped safety injection water temperatures, based on historical plant data.

# **3D Effects**

This refers to multidimensional flow that may occur in the downcomer and its impact on the transient. This is important for Large Break LOCA, where it was ranked high (H) for the refill phase. The FSLOCA methodology is based on relatively detailed modeling of the downcomer's 3D flow by including 3 circumferential nodes (channels) per cold leg. For a 3-loop plant this will result in a downcomer noding with 9 sectors in the circumferential direction. Code model uncertainties were assessed by comparisons with the UPTF ECC bypass test data (Test 6). Those assessments showed that there is a conservative bias, in that ECC bypass is overpredicted, which in turn extends the refill time period in a conservative direction (Section 19.3.5).

#### Mixture Level/Flashing/Void Fraction

For Small Break LOCA, Mixture Level was assigned a high (H) ranking for the final three phases of the transient since the downcomer level affects the level in the inner vessel. For Intermediate Break LOCA, the mixture level is assigned a high (H) ranking for the final two phases of the transient since the downcomer

level affects the level in the inner vessel. For Large Break LOCA, the downcomer level becomes the only driving force for the core inlet flow during reflood making the ranking high (H) for this phase.

The code's ability to predict the void distribution and mixture level for blowdown/flashing transients slower than a typical large break LOCA was assessed in the GE Vessel Blowdown Tests (Section 23.1.1). That facility contains no internal structures, and has hydraulic diameter similar to a PWR downcomer. It was confirmed that the code is able to adequately predict the void distribution [

]^{a,c}.

For large breaks, uncertainties in the flow regimes and void distributions affect the amount of ECC water bypassed at the end of blowdown and the beginning of refill. Code model uncertainties were assessed by comparisons with the UPTF ECC bypass test data (Test 6). Those assessments showed that there is a conservative bias, in that ECC bypass is overpredicted (Section 19.3.5).

#### **Entrainment/De-entrainment**

Uncertainties in entrainment/de-entrainment affect the amount of ECC water bypassed at the end of blowdown/beginning of refill and was ranked high (H) in both refill and reload phases of a large break LOCA. Code model uncertainties were assessed by comparisons with the UPTF ECC bypass test data (Test 6). Those assessments showed that there is a conservative bias, in that ECC bypass is overpredicted (Section 19.3.5). The amount of water entrained from the downcomer and out of the broken loop during reflood is also effectively ranged by varying the break type, flowrate, and broken loop nozzle resistance. Entrainment can also occur during reflood, due to the steam flow from the intact loops. Comparisons with CCTF Run 62 and UPTF Test 25 data indicated that entrainment during reflood is well predicted (Sections 19.6.5 and 19.3.11). Based on these assessments this uncertainty contributor is bounded in the analysis.

#### Liquid Level Oscillations

The liquid level in the downcomer during the reflood phase of a large break LOCA is affected by a number of parameters that are ranged, including accumulator and safety injection temperature, accumulator water volume, break type and flowrate, and broken cold-leg nozzle resistance. Manometric oscillations in the downcomer and core are evident during early reflood following a large break LOCA. Such is observed in integral effects tests (CCTF, see Section 19.6), where the oscillatory behavior is captured adequately. The oscillatory core injection on the reflood is expected to cause increased cooling (Section 23.2.2.6). The expected improvement in cooling is predicted to be much smaller by <u>WCOBRA/TRAC-TF2</u> judging from CCTF-62 (Section 19.6) and ACHILLES (Section 20.1) test comparisons.

#### 29.5.11 Lower Plenum

#### Hot-wall Effect (Void Generation or Boiling)

Heating of the water in the lower plenum during reflood eventually causes boiling, which results in level swell in the downcomer, spilling of water out of the broken loop, and a reduction in reflood rate. The timing of the onset of boiling in the lower plenum is ranged by varying the accumulator and pumped safety

injection water temperatures, based on historical plant data. See Reactor Pressure Vessel Internals/Vessel Wall Stored Energy discussion in Section 29.5.10.

#### 29.5.12 Break

# **Critical Flow**

The break flowrate is varied by [

]^{a,c} The development of the break flow multipliers is

described in Section 29.1.1.

#### **Containment Pressure**

A conservatively low containment pressure is used, which eliminates the need for a detailed uncertainty treatment.

#### **Upstream Flow Regime**

For small breaks, the upstream flow regime affects the inlet quality at the break depending on the assumed orientation of the break relative to the cold leg (top, side or bottom). Since the break flowrate largely determines the system inventory, a high (H) ranking is assigned to this process for all phases of the small break LOCA transient with exception of blowdown phase. As described in Section 29.2, [

]^{a,c}.

#### **Cold Leg Nozzle Flow Resistance**

The broken cold leg nozzle resistance influences the flow split between the vessel side flow path and the pump discharge side flow path, which then impacts the core flow during the blowdown for a large break LOCA. The flow split in the broken loop is ranged by varying the broken cold-leg nozzle resistance, among other parameters, by an amount that accounts for uncertainties in its value (Section 29.1.2). See also *Flow Reversal/Stagnation* discussion in Section 29.5.2.

# **29.6 EXPERIMENTAL UNCERTAINTIES (EMDAP STEP 9)**

As part of the evaluation model development, a large database of experiments was used to compare against code predictions. As stated in Regulatory Guide 1.203, Section 1.2.7:

"It is important to know the uncertainties in the database. These uncertainties arise from measurement errors, experimental distortions, and other aspects of experimentation. If the quantified experimental uncertainties are too large compared to the requirements for evaluation model assessment, the particular data set or correlation should be rejected."

Throughout this report (Volumes I and II in particular), when information regarding experimental uncertainty was available or could be derived from the data reports and references, it was presented in a way to reflect measurement uncertainties. In some cases, the experimental measurement uncertainty was

large and was therefore reflected and accounted for in the uncertainty analysis (see for example Section 17 regarding the safety injection condensation model). However, in some instances no uncertainty information could be found or could be inferred from the references. In those cases the measurement uncertainty is expected to be negligible when compared to the relatively large uncertainty and scatter in the data itself.

# **29.7 REFERENCES**

1. Akimoto, et al., 1984, J. Nucl. Sci. & Tech., 21[6], pp. 450-465, June 1984.

- Bajorek, S. M., et al., 1998, "Code Qualification Document for Best Estimate LOCA Analysis," WCAP-12945-P-A, Volume 1 Revision 2, and Volumes 2 through 5 Revision 1, and WCAP-14747.
- 3. Boyack, B., et al., "Quantifying Reactor Safety Margins," NUREG/CR-5249, (1989).
- 4. American Nuclear Society, 1979, "Decay Heat in Light Water Reactors," ANSI/ANS 5.1.
- Anklam, T. M., et al., 1982, "Experimental Investigations of Uncovered Bundle Heat Transfer and Two-Phase Mixture Level Swell Under High Pressure Low Heat Flux Conditions," NUREG/CR-2456.
- 6. Baum, A. J., 1977, "A Study of Transition and Film Boiling From Vertical Surfaces," Ph. D. Thesis, Carnegie-Mellon University.
- 7. Bordelon, F. M. and Murphy, E. T., 1974, "Containment Pressure Analysis Code (COCO)," WCAP-8327 (Proprietary), WCAP-8306 (Non-Proprietary).
- Broughton, J. M., 1981, "PBF LOCA Test Series, Test LOC-3 and LOC-5 Fuel Behavior Report," NUREG/CR-2073.
- Burman, D. L., 1980, "Comparison of Westinghouse LOCA Burst Tests Results with ORNL and Other Program Results," Specialist Meeting on Fuel Behavior Under Accident Conditions, September 1 – 4, Helsinki, Finland.
- 10. Cathcart, J. V., and Pawel, 1977, "Zirconium Metal-Water Oxidation Kinetics IV Reaction Rate Studies," ORNL/NUREG-17, Oak Ridge National Laboratory, Oak Ridge, TN.
- 11. Clifford, P. M., and Flanagan, M. E., 2009, "Proposed Modification of Cladding Embrittlement Criteria," Paper 2120, Proceedings of Top Fuel 2009, Paris, France.
- 12. Combustion Engineering, 1992, "Improvements to Fuel Evaluation Model," CEN-161(B)-P, Supplement 1-P-A.
- 13. Crane Co., 1988, "Flow of Fluids Through Valves, Fittings, and Pipes," Technical Paper No. 410.

- 14. Dhir, V. K., Duffey, R. B., and Catton, I., 1981, "Quenching Studies on a Zircaloy Rod Bundle," ASME J. Heat Transfer, Vol. 103, pp. 293-299.
- 15. Draper, N. and Smith, H., 1981, "Applied Regression Analysis, Second Edition," John Wiley and Sons.
- 16. Federal Register Notice, 2009, "Performance-Based Emergency Core Cooling System Acceptance Criteria," 74 FR 40765, August 13.
- 17. Foster, J.P., and Sidener, S., 1999, "Westinghouse Improved Performance Analysis and Design Model (PAD 4.0)," WCAP-15063-P, Rev. 1.
- 18. Frepoli, C., 2007, "Assessment of Rod-to-Rod Thermal Radiation Heat Transfer Contribution During Reflood in PWR Fuel Assemblies," ICAPP 2007, Nice, France, May 13-18, Paper 7323.
- 19. Ganic, E. and Rohsenow, W. M., 1977, "Dispersed Flow Heat Transfer," Int. J. Heat Mass Transfer, Vol. 20, pp. 855-866.
- 20. Henry, R. E., 1974, "A Correlation for the Minimum Film Boiling Temperature," AICHE Symposium Series, Vol. 138, pp. 81-90.
- 21. Holmes, B. J., 1991, "ISP 25 Comparison Report," AEA-TRS-1043.
- 22. Loftus, M. J., et al., 1980, "PWR FLECHT-SEASET Unblocked Bundle Forced and Gravity Reflood Task, Data Report," WCAP-9699.
- MPR, 1990, "Summary of Results From the UPTF Downcomer Separate Effects Tests, Comparison to Previous Scaled Tests, and Application to U.S. Pressurized Water Reactors," MPR Associates, MPR-1163.
- 24. Nissley, M. E., et al., 2005, "Realistic Large-Break LOCA Evaluation Methodology Using the Automated Statistical Treatment of Uncertainty Method (ASTRUM)," WCAP-16009-P-A and WCAP-16009-NP-A.
- Powers, D. A. and Meyer, R. O., 1980, "Cladding Swelling and Rupture Models for LOCA Analysis," NUREG/CR-0630.
- 26. Shumway, R., 1985, "Return to Nucleate Boiling," ANS Proceedings National Heat Transfer Conference, Denver, CO, pp. 372-388.
- 27. Spier, E. M., et al., 1988, "Evaluation of Nuclear Hot Channel Factor Uncertainty," WCAP-7308-L-P-A.
- 28. Tasaka, K., et al., 1988, "The Results of 5% Small Break LOCA Tests and Natural Recirculation Tests at the ROSA-IV LSTF," Nuclear Engineering and Design, 108.

- 29. Tregoning, Abramson, Scott, and Chokshi, "LOCA frequency evaluation using expert elicitation," Nuclear Engineering and Design 237 (2007) 1429-1436.
- 30. Vijaykumar, R. and Dhir, V. K., 1992, "An Experimental Study of Sub-cooled Film Boiling on a Vertical Surface Hydrodynamic Aspects," ASME J. Heat Transfer, Vol. 114, pp. 161-178.
- 31. Wong, S. and Hochreiter, L. E., 1981, "Analysis of the FLECHT-SEASET Unblocked Bundle Steam Cooling and Boiloff Tests," NRC/EPRI/Westinghouse-8.

32. Yoder, et al., 1982, "Dispersed Flow Film Boiling in Rod Bundle Geometry – Steady-State Heat Transfer Data and Correlation Comparisons," NUREG/CR-2435, ORNL-5822.

# **30 TECHNICAL BASIS OF STATISTICAL PROCEDURES APPLIED IN FULL SPECTRUM LOCA UNCERTANTY METHODOLOGY**

# 30.1 STATISTICAL METHODOLOGY ROADMAP

A realistic (best-estimate) safety analysis asks for the assessment of uncertainties associated with physical models, data uncertainties, and plant initial and boundary condition variability. The current safety regulations of the United States Nuclear Regulatory Commission (US NRC) are stipulated in 10 CFR Part 50, Section 50.46. Based on the 10 CFR 50.46 rule, an emergency core cooling system (ECCS) design is required to satisfy prescriptive criteria. The regulation identifies the following five criteria:

- 1. Peak cladding temperature (PCT) shall be less than 2200°F
- 2. Maximum local oxidation (MLO) shall be less than 17%
- 3. Core-wide oxidation (CWO) shall be less than 1% (to limit the maximum amount of hydrogen generated)
- 4. The core shall maintain a coolable geometry
- 5. Long term cooling shall be demonstrated

Code Scaling, Applicability, and Uncertainty (CSAU) Element 3, the sensitivity and uncertainty analysis element, aims to provide a simple Best-Estimate Plus Uncertainty (BEPU) statement (Boyack, et al. 1989) that satisfies the first three criteria above. To accomplish this objective, the effects of the important uncertainty contributors are determined. The uncertainty statement is based on the combined effect of the contributors.

The objective of a LOCA analysis is to address criteria (b)(1), (b)(2) and (b)(3) of 10 CFR 50.46, the determination of peak cladding temperature (PCT), maximum local oxidation (MLO) and core-wide oxidation (CWO). Typically the last two criteria (coolable geometry and long-term cooling), are satisfied outside the LOCA analysis once the LOCA calculation is demonstrated to be in compliance with the first three criteria. [

ahtforward approx

]^{a,c}

Regarding the treatment of uncertainties within the CSAU framework, the most straightforward approach is to combine the uncertainties with a direct Monte Carlo simulation. The procedure is designed to generate a sample of the short term LOCA 'population,' and then non-parametric statistical inference procedures are used to develop probabilistic statements that show compliance with the 10 CFR 50.46 criteria.

The code (WCOBRA/TRAC-TF2) is the 'black-box' which receives as input a set of random values, one for each uncertainty parameter, and outputs the three values that characterize a specific LOCA scenario (PCT, MLO and CWO). Several cases are executed until the sample size is large enough to represent the population and stabilize the estimates of the key parameters of interest. The issue is how results are interpreted to demonstrate compliance with the 10 CFR 50.46 requirements.

10 CFR 50.46 states that "[...] uncertainty must be accounted for, so that, when the calculated ECCS cooling performance is compared to the criteria set forth in paragraph (b) of this section, there is a high level of probability that the criteria would not be exceeded." Paragraph (b) of 10 CFR 50.46 contains the list of the acceptance criteria. 10 CFR 50.46 does not explicitly specify how this probability should be evaluated or what its value should be.

Additional clarification as to the US NRC expectations on the acceptable implementation of the "high probability" requirement is provided in Section 4 of Regulatory Guide 1.157 (Best-Estimate Calculations of Emergency Core Cooling System Performance) that states: "a 95% probability is considered acceptable to the NRC staff [...]." Further, Regulatory Guide 1.157 introduced the concept of confidence level as a possible refinement to the uncertainty treatment, but did not expand further on this concept.

As statistical methods are implemented to perform LOCA safety analyses, a statistical statement which estimates or bounds the 95th quantile of the population with a 95% confidence level has been suggested by the NRC as acceptable to demonstrate the required "high probability." In the previous approved methodology (ASTRUM, WCAP-16009-P-A) the 95th quantile of the joint-distribution of PCT, MLO and CWO is bounded with at least 95% confidence level. The Safety Evaluation Report (SER) of the Westinghouse Best-Estimate Large Break LOCA methodology (ASTRUM) states the following: "the staff determined that a 95th percentile probability level based on best approximations of the constituent parameter distributions and the statistical approach used in the methodology is appropriately high for this application."

Consistently with the previously approved methodology, the 95/95 criterion is also considered for the FULL SPECTRUM LOCA (FSLOCA) methodology.

One key difference between the previous LBLOCA methodology (ASTRUM, WCAP-16009-P-A) and FSLOCA is that the FSLOCA methodology extends the break area spectrum considered in the analysis to cover the full range from what is historically defined as Small Breaks (SB) to Large Breaks (LB) including break sizes typically not analyzed and classified as Intermediate Breaks (IB).

As discussed in Section 29.4, a simple extension of the ASTRUM approach to smaller break sizes was considered not appropriate because SBLOCA would not be properly considered in the sample by simply extending a uniform probability distribution of the split break sizes in the SB region. A more balanced approach has been developed and was discussed in Section 29.4.

]^{a,c}

ſ

# ]^{a,c}

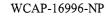
# **30.2 STATISTICAL SAMPLING APPROACH (MONTE CARLO)**

The run matrix is generated by using random numbers. The random numbers are obtained using a generator from Press, et al. This particular generator has a period of approximately  $2.3 \times 10^{18}$ , that is, the series of numbers generated would not be repeated before  $2.3 \times 10^{18}$  random numbers are used. For all practical purposes, this number is quite large and period exhaustion is considered impossible.

In addition, according to Press, et al., the output from this random number generator has passed standard statistical tests intended to detect lack of randomness (especially certain subtle serial correlations).

The random number generator returns a value, RND, between 0 and 1. To alter the range to [a,b] instead, a linear mapping is applied.:

$$VALUE = a + (b-a)*RND$$



The generation of normal (Gaussian) random variables is done by first generating RND and then using a rejection method that is efficient for distributions that have symmetric unimodal probability density functions (PDFs).

The random number generator depends on an initial seed to select the starting point in a random sequence. Having such algorithms allows for repeatability of results without compromising randomness. In the analysis, the initial seed is obtained randomly from the configuration control system. This system assigns a random identifier to each run, so that they can be uniquely identified. If the run matrix needs to be repeated or extended, repeatability is ensured by using the same seed.

# 30.3 NON-PARAMETRIC ORDER-STATISTICS TOLERANCE LIMITS FORMULATION

The consideration of nonparametric tolerance limits was originally presented by Wilks (Wilks, 1941). Wilks showed that for continuous populations, the distribution of P(i,j), the proportion of the population between the i-th and j-th order statistics, is independent of the population sampled.

The assumption of continuity is a rather mild one. In the present context, it means that the probability of getting two runs with precisely the same PCT or MLO is zero. Formally, we require that the cumulative distribution function (CDF) of the outcomes be continuous; the PDF, which is the derivative of the CDF, need not be continuous for the relevant results to hold.

Derivation of non-parametric tolerance limits is presented next. This derivation is based on the non-parametric multivariate tolerance limits formulation first proved by Wald (1943) and more recently adapted by Guba-Makai (Guba, et al., 2003) to the problem of making safety inferences based on the output of models of complex systems. The derivation provided here of the non-parametric tolerance limits follows the formulation by Guba-Makai.

For the sake of simplicity the case with a single output variable y with a probability density function g(y) is considered first. Assume that nothing is known about the probability density function g(y) except that it is continuous. If N runs are carried out with random input(s), then a sample  $\{y_1, y_2, ..., y_N\}$  of the random output y will be obtained.

Two functions  $L = L(y_1, y_2, ..., y_N)$  and  $U = U(y_1, y_2, ..., y_N)$  called tolerance limits can be defined such that:

$$P\left(\int_{L}^{U} g(y)dy > \gamma\right) = \beta$$
 (30-1)

where  $\beta$  represents the probability that a fraction  $\gamma$  of the random output variable y population falls within the tolerance limits U and L.



Now arrange the values  $y_1$ ,  $y_2$ , ...,  $y_N$  in increasing order (the probability of equal values of y occurring is neglected since g(y) has been assumed to be a continuous function), and denote by  $y_k$  the  $k^{th}$  of these ordered value.

Thus, in particular:

 $y(1) = \min y_k \quad \text{and} \quad y(N) = \max y_k \\ 1 \le k \le N \quad 1 \le k \le N$ (30-2)

and let by definition  $y(0) = -\infty$  and  $y(N+1) = +\infty'$ .

In this case, for some positive  $\gamma < 1$  and  $\beta < 1$ , it can be demonstrated that there can be constructed two functions  $L = L(y_1, y_2, ..., y_N)$  and  $U = U(y_1, y_2, ..., y_N)$ , such that the probability  $\beta$  that

$$\int_{L}^{0} g(y) dy > \gamma$$
 (30-3)

can be determined, as demonstrated in Guba, et al. (2003), as:

$$\beta = 1 - I(\gamma, s - r, N - s + r + 1) = \sum_{j=0}^{s-r-1} {N \choose j} \gamma^{j} (1 - \gamma)^{N-j}$$
(30-4)

where:

$$I(\gamma, j, k) = \int_{0}^{\gamma} \frac{u^{j-1}(1-u)^{k-1}}{B(j, k)} du$$
(30-5)

$$B(j,k) = \frac{(j-1)!(k-1)!}{(j+k-2)!}$$
(30-6)

$$0 \le r < s \le N$$
, and  $L = y(r), U = y(s)$ 

Equation 30-4 can be used to provide an answer to the question "for a given L = y(r) and U = y(s), what is the sampling size N of the output variable y that has to be collected so that there is a probability  $\beta$  that a fraction  $\gamma$  of the random output variable y population falls within the specified tolerance limits U and L?" It can be observed that Equation 30-4 does not depend on the probability density function g(y) or the number of input variables in the process.

In the particular case that the tolerance limits are selected such that r = 1 and s = N (i.e., the maximum and minimum value of the samples y(k) of the output variable y are used to define L and U), the two-sided tolerance level can be obtained as¹:

$$\beta = 1 - \gamma^{N} - N(1 - \gamma)\gamma^{N-1}$$
(30-7)

If interest is limited only to the upper tolerance limit (r = 0 and s = N),

$$\beta = 1 - \gamma^{N} \tag{30-8}$$

Guba, et al. (2003) also provides an extension of the single output variable formulation for the case of multiple variables. For this case, some additional definitions are required. Consider an output comprised of p variables,  $y_1, y_2, ..., y_p$ . Let g  $(y_1, ..., y_p)$  be the joint distribution of the output variables and let <u>Y</u> be defined as:

$$\underline{\mathbf{Y}} = \begin{pmatrix} y_{11} & y_{12} & \dots & y_{1N} \\ y_{21} & y_{22} & \dots & y_{2N} \\ \dots & \dots & \dots & \dots \\ y_{p1} & y_{p2} & \dots & y_{pN} \end{pmatrix}$$
(30-9)

Analogous to the single output case, the problem of setting tolerance limits for  $y_1, ..., y_p$  can be formulated as follows: for some given positive values  $\gamma < 1$  and  $\beta < 1$ , there can be constructed two random functions  $L_i = L_i (y_1, y_2, ..., y_N)$  and  $U_i = U_i (y_1, y_2, ..., y_N)$ , such that there is a probability  $\beta$  that:

$$\int_{L_{1}}^{U_{1}} \dots \int_{L_{p}}^{U_{p}} g(y_{1}, ..., y_{p}) dy_{1} \dots dy_{p} > \gamma$$
(30-10)

If  $g(y_1, ..., y_p)$  is continuous, it can be assumed that no two elements in  $\underline{Y}$  are equal. The sequence of rows in  $\underline{Y}$  is arbitrary, reflecting the fact that we number the output variables arbitrarily. Let us consider the first row of the sample matrix and arrange its elements in order of increasing magnitude  $y_1(1), y_1(2), ..., y_1(N)$ . Select now between these  $y_1(r_1)$  as  $L_1$  and  $y_1(s_1) > y_1(r_1)$  as  $U_1$ . Let  $i_1, i_2, ..., i_{s_1-r_1-1}$  stand for the original columns of the elements  $y_1(r_1 + 1), y_1(r_1 + 2), ..., y_1(s_1 - 1)$ . Next, the N observed values of the output variable  $y_2$  are considered, and the part  $y_{2,i_1}, y_{2,i_2}, ..., y_{2,i_{s_1-r_1-1}}$  of its elements are arranged in increasing order to obtain  $y_2(1), y_2(2), ..., y_2(s_1 - r_1 - 1)$ . Select now between these  $y_2(r_2)$  as  $L_2$  and  $y_2(s_2) > y_2(r_2)$  as  $U_2$ , where evidently  $r_2 \ge r_1$  and  $s_2 \le s_1$ - $r_1$ -1. If this process is applied to the end of the sample matrix, a p-dimensional space will be defined:

$$V_{p} = \{ [L_{1}, U_{1}]^{*} [L_{2}, U_{2}]^{*} \dots ^{*} [L_{p}, U_{p}] \}$$
(30-11)

^{1.} Note that Guba, et al. (2003) Equation 18 contains a typographical error in the definition of  $\beta$  for the two-sided case that is corrected in Equation 30-7.

where:

$$\begin{array}{lll} L_{j} & = & y_{j} \bigl( r_{j} \bigr) \\ U_{j} & = & y_{j} \bigl( s_{j} \bigr) \\ r_{j} \geq r_{j - 1} \geq ... \geq r_{1}, & \mbox{ for } j = 2, \, ..., \, p \\ r_{j} < s_{j} \leq s_{j - 1} - r_{j - 1} - 1, & \mbox{ for } j = 2, \, ..., \, p \end{array}$$

As demonstrated by Guba, et al. (2003), in the case of  $p \ge 2$  dependent output variables with continuous joint distribution function g (y₁, ..., y_p) it is then possible to construct p-pairs of random intervals [L_i, U_i], i = 1, ..., p such that the probability of the inequality:

$$\int_{L_{1}}^{U_{1}} \dots \int_{L_{p}}^{U_{p}} g(y_{1}, \dots, y_{p}) dy_{1} \dots dy_{p} > \gamma$$
(30-12)

is free of  $g(y_1, ..., y_p)$  and is given by

$$P\left(\int_{L_{1}}^{U_{1}} \dots \int_{L_{p}}^{U_{p}} g(y_{1}, \dots, y_{p}) dy_{1} \dots dy_{p} > \gamma\right) = 1 - I(\gamma, s_{p} - r_{p}, N - s_{p} + r_{p} + 1)$$
(30-13)

As demonstrated in Guba, et al. (2003), where I(..., ..., ...) is the incomplete beta function ratio defined in Equation 30-5 and

$$s_{p} \le s_{p-1} - r_{p-1} - 1 \le s_{1} - \sum_{j=1}^{p-1} (r_{j} + 1)$$
 (30-14)

$$\mathbf{r}_{\mathbf{p}} \ge \mathbf{r}_{\mathbf{p}-1} \ge \mathbf{r}_{\mathbf{l}} \tag{30-15}$$

In several practical applications,  $r_1 = r_2 = ... = r_p = 1$ , and  $s_p = N-2(p-1)$ , and the probability  $\beta$  from Equation 30-13 can be expressed as:

$$\beta = 1 - I(\gamma, N - 2p + 1, 2p) = \sum_{j=0}^{N-2p} {N \choose j} \gamma^{j} (1 - \gamma)^{N-j}$$
(30-16)

And for a one sided confidence level  $(r_1 = r_2 = ... = r_p = 0)$  and  $s_p = N-p+1$ , then²:

$$\beta = 1 - I(\gamma, N - p + 1, p) = \sum_{j=0}^{N-p} {N \choose j} \gamma^{j} (1 - \gamma)^{N-j}$$
(30-17)

2. Note that Guba, et al. (2003) Equation 25 contains a typographical error in the definition of  $\beta$  for the single-sided case that is corrected in Equation 30-17.

[

]^{a,c}

Table 30-1 [		] ^{a,c}				
· · · · · · · · · · · · · · · · · · ·						
				· · · · · · · · · · · · · · · · · · ·		
<u></u>						
<b></b>						
	· ·					
······································				·		
	······		· · · · · · · · · · · · · · · · · · ·			

However, there are important disadvantages of the distribution-free upper confidence bounds. First, the extreme order statistics generally tend to have high variance, so different sets of computer runs can give very high upper confidence bounds. The variance of the estimator can be reduced by extending the sample size. The effect of the sample size on the variance of the estimator is discussed next.

]^{a,c}

# **30.3.1 Tolerance Intervals and Sample Size**

The approach discussed in Section 30.3 is the so-called 'tolerance interval method.' The procedure is used to determine an upper bound estimate of a given quantile of the population, say the 95th quantile  $Q_{95}$ . The k-th estimator/rank (Table 30-1) bounds the proportion  $\gamma = 95\%$  of the population for the considered output variables [ ]^{a,c} with at least  $\beta = 95\%$  probability. Call this estimate  $Q_{95/95}$ . The procedure is known to be conservative (bounding) and the risk of excessively overestimating the fraction of the population of interest is very high, especially if the estimator is based on the extreme case, rank k=1.

]^{a,c}

ſ

Table 30-2         [			] ^{a,c}	
·····	-			
			· · ·	-
	· · · · · · · · · · · · · · · · · · ·			
			<u></u>	-
)				
,				
· · · ·			······································	
			· · · · · · · · · · · · · · · · · · ·	
				┨
			· · · · · · · · · · · · · · · · · · ·	-
				_
· .				-
	- - -			_
			·	
		·		

30.4 [

]^{a,c}

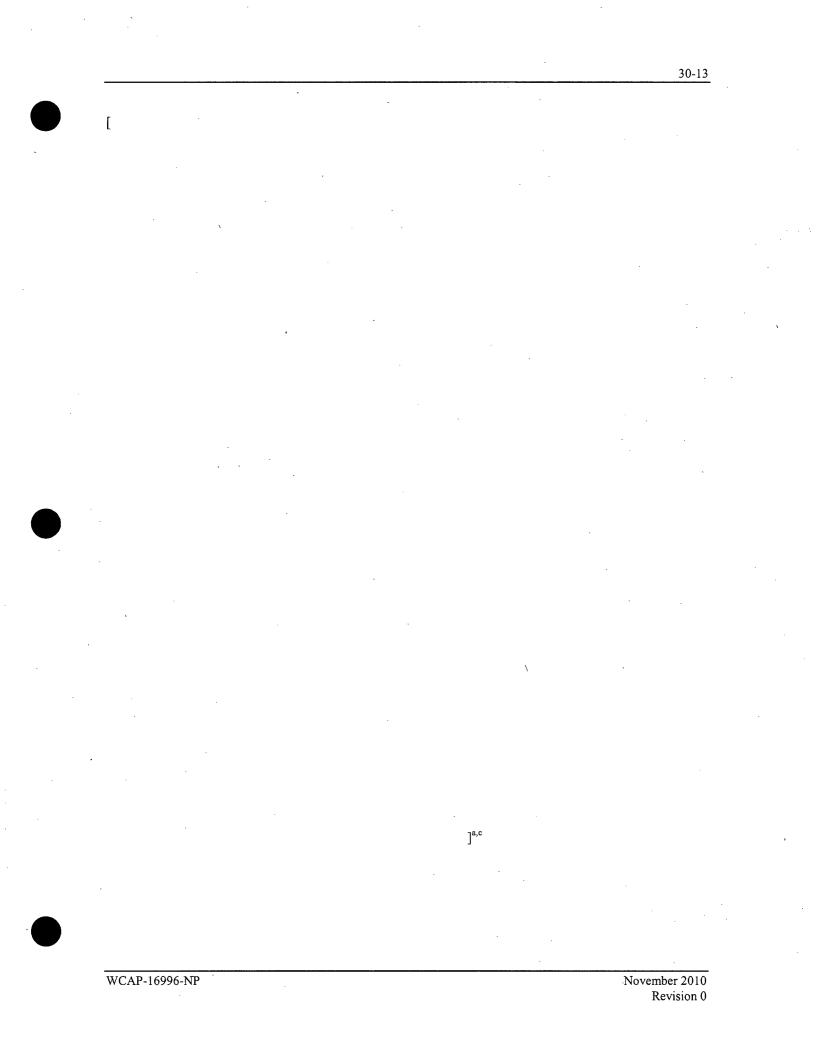
[

.

]^{a,c}

WCAP-16996-NP

November 2010 Revision 0



# 30.5 OVERVIEW OF FULL SPECTRUM LOCA STATISTICAL PROCEDURE (ASTRUM-FS)

Sections 30.3 and 30.4 provided the theoretical basis for the various statistical procedures needed to:

1. Generate a representative sample of the LOCA scenarios population;

2. Analyze the results and infer figures of merit that can satisfy compliance with the 10 CFR 50.46 design criteria.

[

]^{a,c}

]^{a,c}

[

# 30.6 CONCLUSIONS ON COMPLIANCE WITH 10 CFR 50.46 ACCEPTANCE CRITERIA

]^{a,c}

The previous Sections described the statistical theory used to determine the number of cases required to bound the 95th percentile of [  $]^{a,c}$ , with a joint probability of 95% confidence. This assures that there is a high probability that the first two acceptance criteria are met, consistent with the Code of Federal Regulations (CFR) 10 CFR 50.46 requirements and Regulatory Guide 1.157 guidance. Further insights on the full compliance with the 10 CFR 50.46 criteria are described below.

30.6.1 [

ſ

]^{a,c}

[...

]^{a,c}

WCAP-16996-NP

November 2010 Revision 0

]^{a,c}

#### **30.7 REFERENCES**

1. Boyack, B., et al., "Quantifying Reactor Safety Margins," NUREG/CR-5249, (1989).

2. [

[

- 3. Guba, A., et al., "Statistical Aspects of Best Estimate Method-I," Reliability Engineering and System Safety, 80, (2003), pp. 217-232.
- 4. Montgomery, D. C., "Design and Analysis of Experiments," 5th Edition, 2000.

- 5. Press, W. H., et al., "Numerical Recipes in FORTRAN: The Art of Scientific Computing," 2nd Edition, Cambridge University Press, 1992, Chapter 7.
- 6. Wald, A., "An Extension of Wilks' Method for Setting Tolerance Limits," Annals of Mathematical Statistics, Vol. 14 (1943), pp. 45-55.
- 7. Wilks, S. S., "Determination of Sample Sizes for Setting Tolerance Limits," The Annals of Mathematical Statistics, Vol. 12 (1941), pp. 91-96.

Table 30-3         Generic Rod Power Census Used for Core-Wide Oxidation Assessment						
		-		,		
· · · · · · · · · · · · · · · · · · ·				· · ·		
		· .				
				,		

# 31 FULL SPECTRUM LOCA DEMONSTRATION ANALYSIS

The nuclear power plant selected for the demonstration analysis of the FULL SPECTRUM LOCA (FSLOCA) methodology is V. C. Summer (CGE), a three-loop Westinghouse pressurized water reactor located approximately 20 miles northwest of Columbia, SC.

The development of the plant input model and input parameters was documented in Section 26. In Section 27, this plant model was exercised in the representative LOCA scenarios covering the full spectrum of break sizes to demonstrate that the dominant phenomena identified in the PIRT (Section 2) were properly captured.

To perform a realistic (best-estimate) safety analysis for an emergency core coolant system (ECCS), the associated uncertainties in the physical models, experimental data and plant initial and boundary conditions needed to first be identified and assessed as outlined in Section 29. With regard to the treatment of the identified uncertainties, Section 30 introduces the approach to combine the identified uncertainties along with the technical basis for doing so.

In this section, the demonstration plant model is exercised using the  $\underline{W}COBRA/TRAC-TF2$  code to demonstrate the FSLOCA methodology.

#### **31.1 DEVELOPMENT OF INITIAL RUN MATRIX**

As discussed in Section 30, a Monte Carlo simulation is to be carried out over the entire spectrum of LOCAs to combine the uncertainties and generate a representative sample of cases. The uncertainty attributes sampled include break size, plant initial and boundary conditions, global and local model uncertainty variables (Section 29), and the plant response to a LOCA event is computed with the <u>W</u>COBRA/TRAC-TF2 computer code.

Because the demonstration analysis was performed concurrently with the methodology development, three uncertainty parameters were treated differently than as described in Section 29. [

]^{a,c} The different distributions are not expected to qualitatively change the conclusions and observations drawn in this section regarding the influence of effective break area, and the overall results are expected to be comparable to those that would result from [

]^{a,c}. The downcomer condensation multiplier (XC) was [

]^{a,c} The minimum film

]^{a,c}. This does not affect the global response, but the PCT and MLO including local uncertainties are likely under-predicted in the demonstration analysis as a result.

The full sample of [  $]^{a,c}$  is generated according to Step 1 in Section 30.5, using the Monte Carlo sampling method described in Section 30.2. In this case, it was known that a maximum of [  $]^{a,c}$ 

WCAP-16996-NP

boiling temperature (TMIN) was [

Among all the uncertainty attributes, [

uncertainty values used in the CGE demonstration analysis are listed in Tables 31.1-2a and 31.1-2b.

]^{a,c}

#### **31.1.1 Break Area Ranges**

The break size is sampled [

During a small break LOCA, the system will initially drive to an equilibrium state between the primary and secondary side, which typically occurs at the lowest MSSV set pressure. To determine the minimum break area ( $A_{min}$ ), a simple TEE model, shown in Figure 31.1-2, is set up to check the critical break flow rate at the lowest MSSV set pressure.

First, the minimum safety injection flow at the lowest MSSV pressure of  $[ ]^{a,c}$  is determined. As described in Section 25.3,  $[ ]^{a,c}$ . The resulting high head safety injection (HHSI) flow is  $[ ]^{a,c}$ .

Next, the break flow from the RCS at the lowest MSSV pressure is determined using the WCT-TF2 model shown in Figure 31.1-2. The cold leg temperature is assumed to be [

Table 31.1-1 provides results for [

Based on the results in Table 31.1-1, for an equilibrium pressure of the lowest MSSV set pressure, the charging system can make up the mass loss out of the break for break sizes less than or equal to [

7^{a,c}

]^{a,c}

#### **31.1.2 Plant Operating Range**

In Section 29, the uncertainty contributors or parameters that are explicitly considered in the FSLOCA methodology are listed in Tables 29-1 through 29-5. As discussed there, the uncertainty contributors are grouped as:

]^{a,c}, break type (DEGCL vs. Split), Split break area (Table 29-1)

WCAP-16996-NP

ſ

ſ

1.

]^{a,c}.

]^{a,c}.

]^{a,c}. The plant-specific



- 2. Thermal-hydraulic (T/H) global models (Table 29-2)
- 3. Local models for the Hot Rod (Tables 29-3a and 29-3b)
- 4. Power related uncertainty parameters (Table 29-4)
- 5. Initial and boundary conditions (Table 29-5)

Table 31.1-2a and Table 31.1-2b summarize the plant operating range over which the uncertainty evaluation is to be performed for the demonstration plant. The PBOT, PMID data pairs in Table 31.1-2b define a closed shape in the PMID, PBOT plane (Figure 31.1-3) within which PBOT and PMID are sampled randomly.

Table 31.1-1         Calculation of Minimum Break Area					
Break Size (in)	Flow Area (ft ² )	Mass Flow (lbm/s)			

Parameter	Nominal	Range	Units
		х х	
	······································		

	Table 31.1-2b Une	certainty Range of P	lant Specific PBO	T, PMID Paramete	rs		
_	Parameter	Pair-1	Pair-2	Pair-3	Pair-4	Units	<u> </u>

WCAP-	16996-NP
-------	----------

November 2010 Revision 0 <u>a,c</u>

<u>a,c</u>

a,c



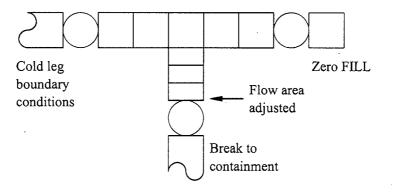


Figure 31.1-2 Noding Diagram for Minimum Break Area Determination



WCAP-16996-NP

31-6 . a,c

]^{a,c}

#### 31.2 [

Section 30.5 outlines the statistical procedures used to:

1. Generate a representative sample of the LOCA population;

2. Analyze the results and infer figures of merit that address compliance with the 10 CFR 50.46 design criteria.

The purpose of this section is to describe the generation of the LOCA database. The statistical analysis of the results and reporting relative to 10 CFR 50.46 acceptance criteria will be discussed in Section 31.5.

With Step 1 in Section 30.5, the process begins by [

]^{a,c}. For the demonstration

analysis, it was known that [

]^{a,c}. As described in Section 31.1, [

]^{a,c} are executed using the <u>WCOBRA/TRAC-TF2</u> code (Step 2).

1^{a,c}

31.2.1 [

ſ

[

 $]^{a,c}$  discussed in Section 30.4.

# 31.2.2 [

[

[

[

## 31.2.3 Conclusion

The analysis shows that [

]^{a,c} Details of the results are provided in Section 31.3.

]^{a,c} Details of the results are provided in Section 31.4.

]^{a,c}

]^{a,c}

Table 31.2-1a ]^{a,c} [ .

<u>a.c</u>

н Н

WCAP-16996-NP

Table 31.2-1b	[	] ^{a,c}
	•	
N		
		· .

<u>a,c</u>

Table 31.2-1c [					
	·				
·			· · · · ·		
	-				

Table 31.2-1	d (	] ^{a,c}
	ر	
-		

WCAP-16996-NP

_

a,c

a,c



Table 31.2-2a	[	] ^{a,c}

WCAP-16996-NP

Table 31.2-2b	[	] ^{a,c}
		· · · · ·
·		

WCAP-16996-NP

a,c

Table 31.2-2	d (	 	] ^{a,c}
		 · · · · · ·	
		 ÷.	
		τ.	

∖a,c

a,c

]^{a,c}

]^{a,c}

(31-1)

]^{a,c}.

### 31.3 ANALYSIS OF RESULTS [

The transients are inspected to ensure that transient termination was demonstrated for all cases. A transient is considered terminated if the following trends and conditions are met:

For example, Figure 31.3-1 to Figure 31.3-3 confirm that all of the transient termination criteria are met for  $[ ]^{a,c}$ . Inspection of similar figures for all the other transients in the database ensures the same.

]^{a,c}

The predicted PCTs for [

ſ

 $]^{a,c}$  are provided in Figure 31.3-4 as a function of [

Because the [

Figure 31.3-4 identifies the three cases that [

]^{a,c} Tables 31.3-1a and 31.3-1b provide the uncertainty attributes and the results for

the [

]^{a,c}.

Figure 31.3-5 shows PCT [

# Figure 31.3-6 shows the PCT sensitivity to [

In several of the cases, at the time of accumulator injection, [

]^{a,c}

Of the [

]^{a,c}

1 abit 31,3-14	Uncertainty Attributes [ ] ^{a,c}			
			•	
	· · · · · · · · · · · · · · · · · · ·			
	,			
	· · · · · · · · · · · · · · · · · · ·			
			· · · · · · · · · · · · · · · · · · ·	
	······			
				·
	,			
	·	· ·		
	······			
•				

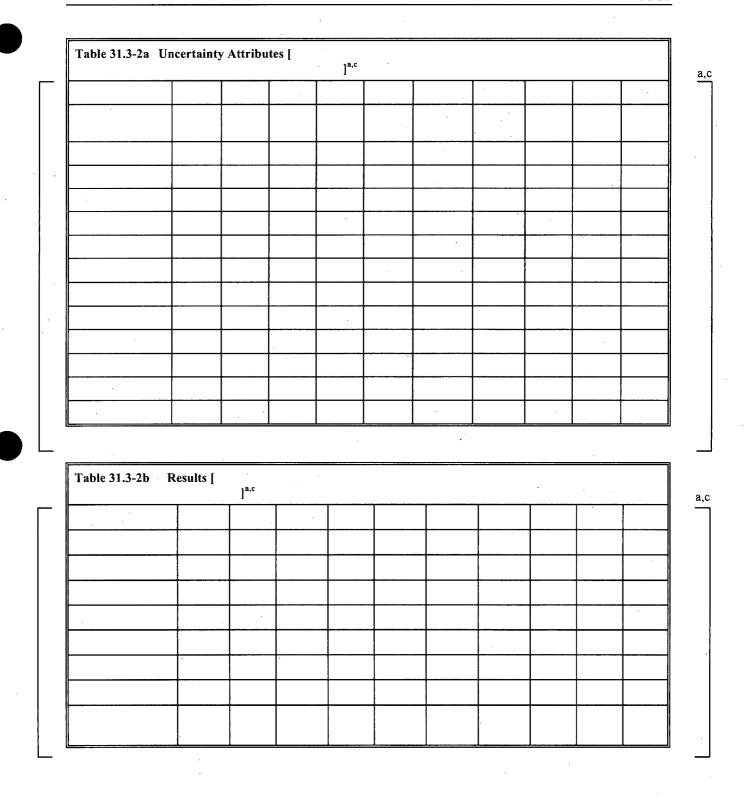
WCAP-16996-NP

able 31.3-1a Uncertainty Attributes [ ] ^{a,c}		
	· · · · ·	
· · · ·		
	 	<u> </u> [
<u>, ,,</u>		
	1	· · · · · · · · · · · · · · · · · · ·
		·

Table 31.3-1b   Results for [		] ^{a,c}
· ·		
	· · ·	
		·

		[		] ^{a,}							
						· · · · ·					
										· · ·	
							l				
						······			1		
	 				· · ·						
					•						
											i ·
<u> </u>	 					<u> </u>		· · ·			
			· · · · ·								
							c .				
								·····			

WCAP-16996-NP



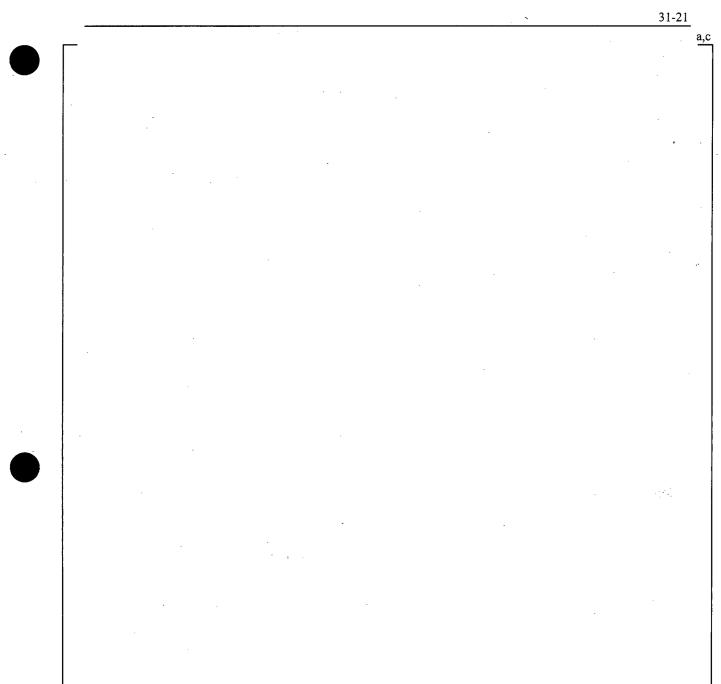


Figure 31.3-1 [

	· · · · · · · · · · · · · · · · · · ·						<u>-22</u> a,
		•				·	<u> </u>
					•		
	· · ·						
	·						
ļ	· · ·						
			· ·				
	·				· .		
	•			۰.			
L	Figure 31.3-2 [						<u></u>

WCAP-16996-NP

	 31-23
	•
- 1	
Χ.	

WCAP-16996-NP

November 2010 Revision 0

a,c

Figure 31.3-4 [

]^{a,c}

WCAP-16996-NP

a,c

]^{a,c}

Figure 31.3-5 [

WCAP-16996-NP

Γ				
	·			
· · · .				
2 2 2 3				· · ·
		· · · ·		,
н • •			:	

]^{a,c}

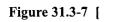
Figure 31.3-6 [

WCAP-16996-NP

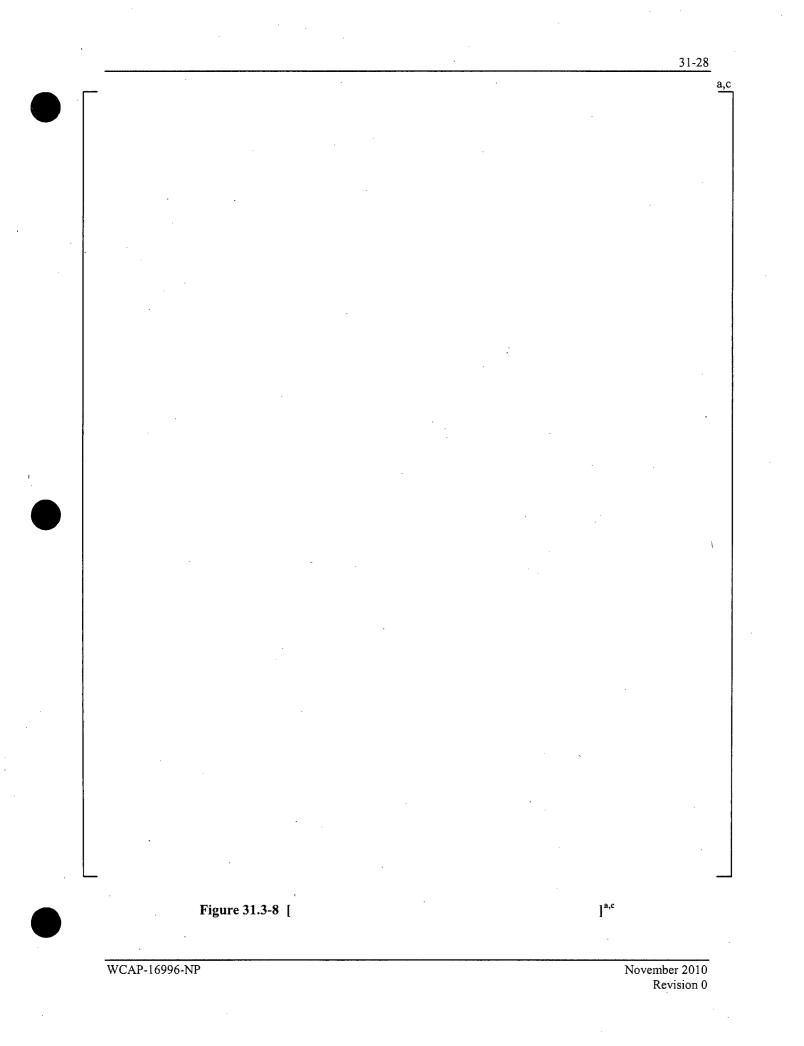
a,c



a,c



WCAP-16996-NP



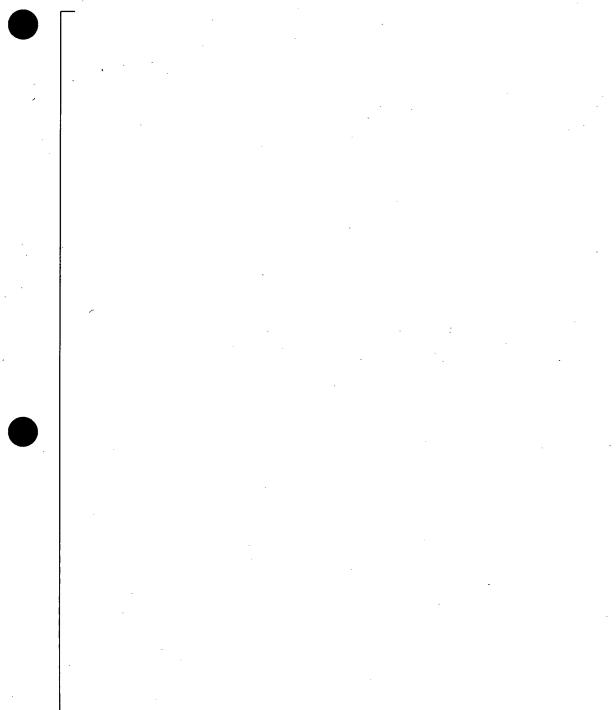


Figure 31.3-9 [

WCAP-16996-NP

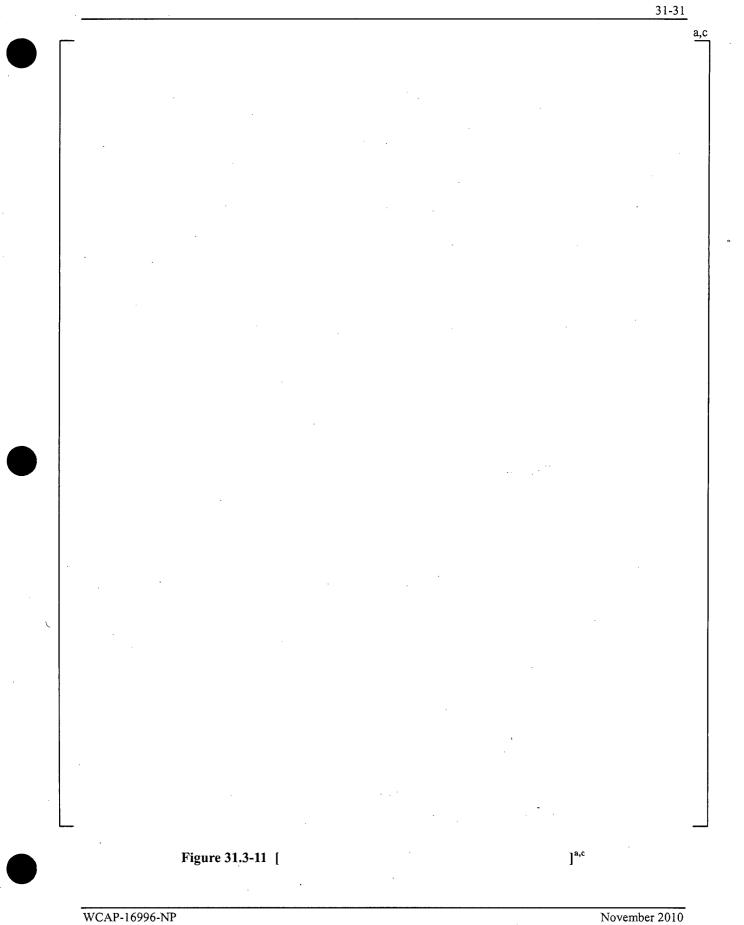
November 2010 Revision 0

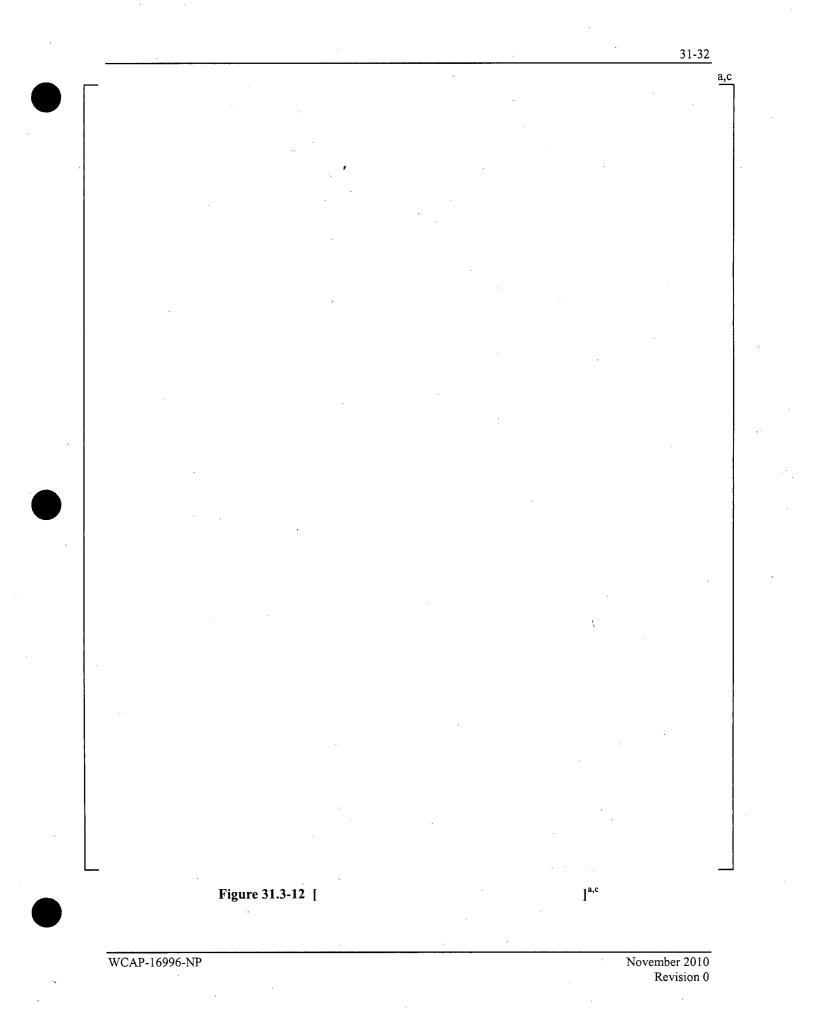
]^{a,c}

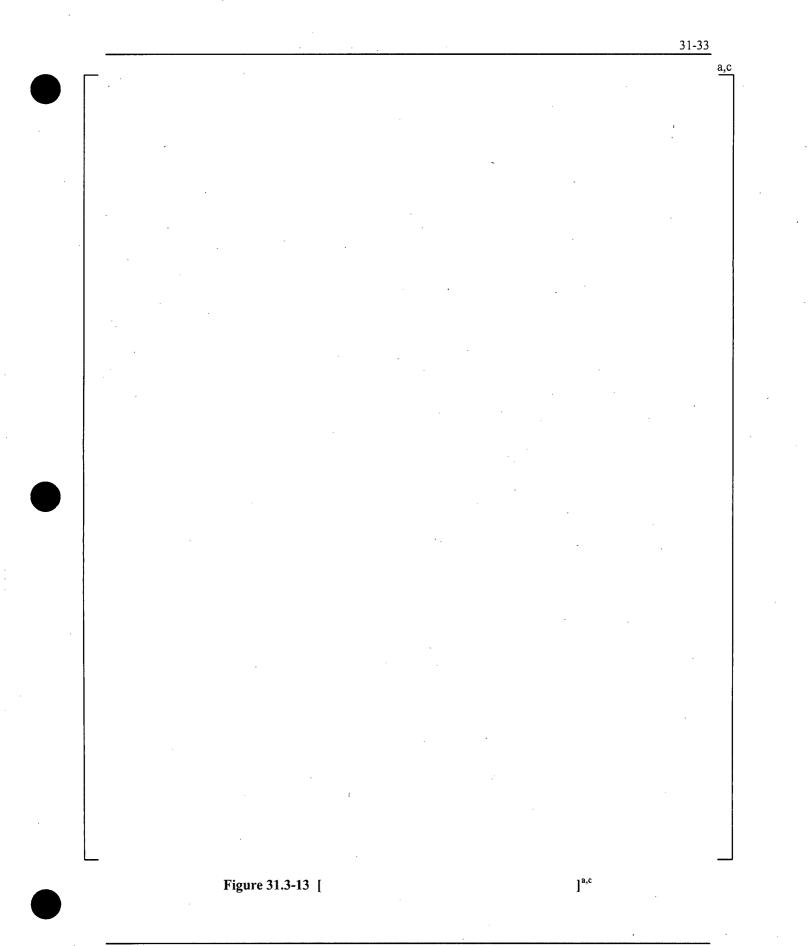
a,c

		 				<u>.</u>	31-30
							a
					, _		
			· .				
	•						
				·			
							-
	· .						
	_			•			_

WCAP-16996-NP







]^{a,c}

# 31.4 ANALYSIS OF RESULTS [

[

]^{a,c}

Table 31.4-1a provides the uncertainty attributes for the 10 most limiting runs [ ]^{a,c}, while Table 31.4-1b shows the PCT and MLO results. Figure 31.4-1 shows the influence of the effective break area [

]^{a,c} In the case of a DEG break, [

]^{a,c}

Figure 31.4-3 presents the PCT results as a function of [

]^{a,c} This effect, however, is expected to be limited as shown in Section 28.1.5.

]^{a,c}

ſ

]^{a,c} As reflood progresses and droplets become entrained to the upper elevations, the dispersed flow film boiling (DFFB) heat transfer regime becomes dominant. Figure 31.4-11 shows that [

Appreciable transient oxidation is expected to occur only above approximately [

]^{a,c}

Figure 31.4-14 shows the peak cladding temperatures [

ſ

]^{a,c} Each case

]^{a,c}

. ]^{a,c}.

indicates rod quench has occurred by [ ]^{a,c}. A comparison of the [ ]^{a,c} and the nominal DEG reference transient from Section 27.2.1 is provided in Figure 31.4-15, where the peak cladding temperature for the hot rod is shown [

Section 30.3.1 discusses the concept of tolerance intervals and sample size in the context of order statistics, while Section 30.5 describes [

]^{a,c} Figure 31.4-17 shows the upper bound predictor of the 95th quantile PCT with 95% confidence (95/95) [

]^{a,c}

WCAP-16996-NP

Table 31.4-1a	Uncertain	nty Attrib	outes [			] ^{a,c}			
				·		-			
n									
· · · · · · · · · · · · · · · · · · ·								 	1
······································									
		•.							
······································									
					-				
	-								
******	-						···· ·		
·								 · · ·	<u> </u>
	- i				×				

<b>Table 31.4-1a</b> ] ^{a,c}						
•						
					,	
				-		
· · ·						
					÷ ,	

ı

a,c

# Figure 31.4-1 [

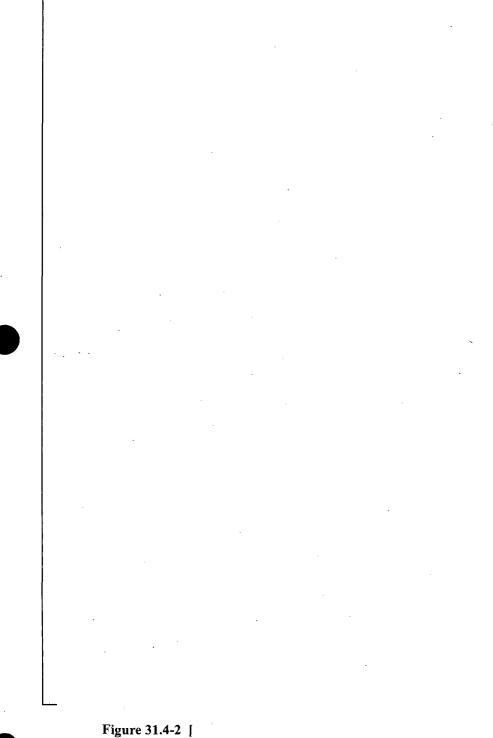
WCAP-16996-NP

November 2010 Revision 0

]^{a,c}

- 3	1	-39
~		

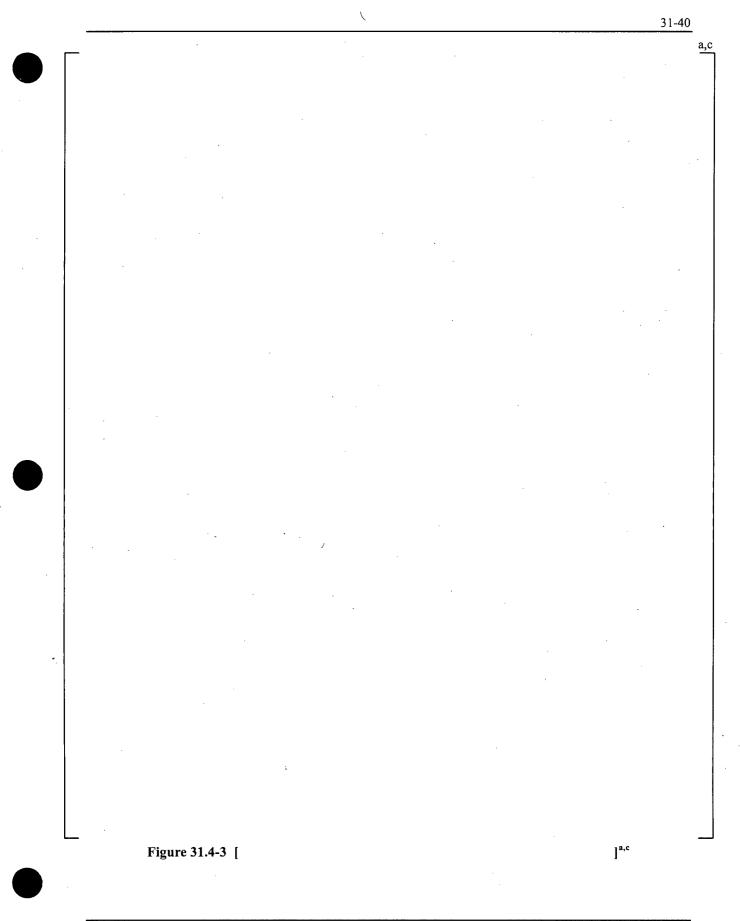
a,c



1

]^{a,c}

WCAP-16996-NP



a,c

Figure 31.4-4 [

]^{a,c}

WCAP-16996-NP

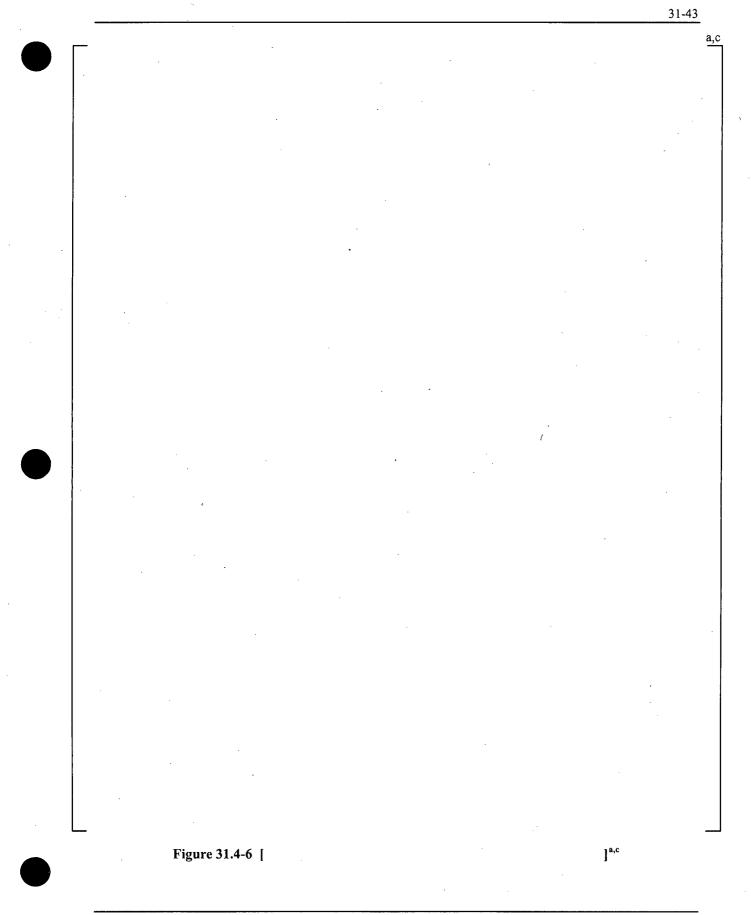
a,c

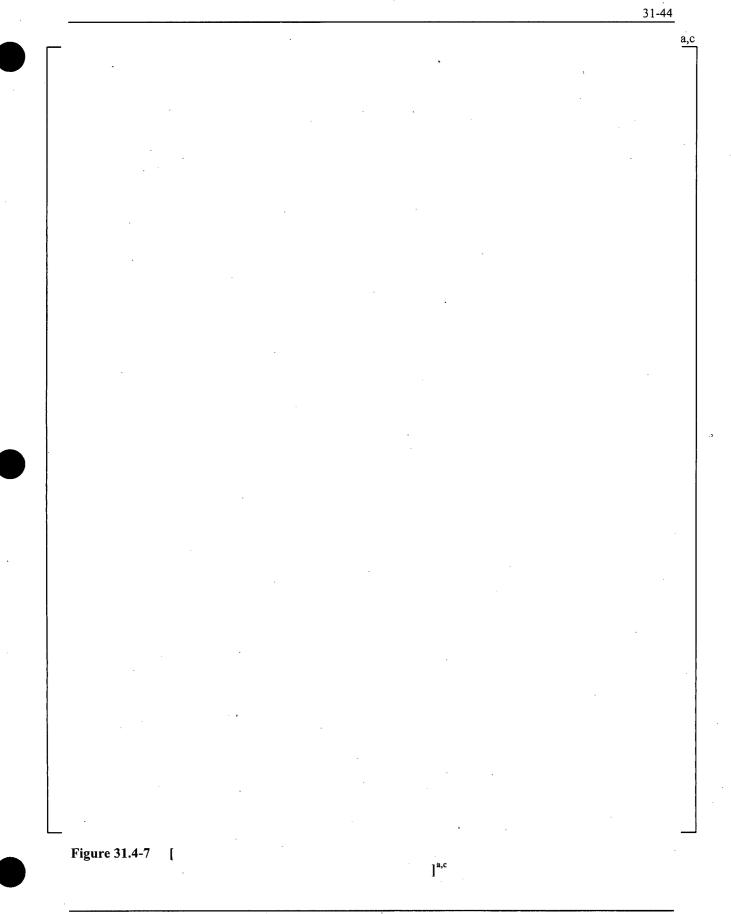
.

Figure 31.4-5 [

]^{a,c}

WCAP-16996-NP

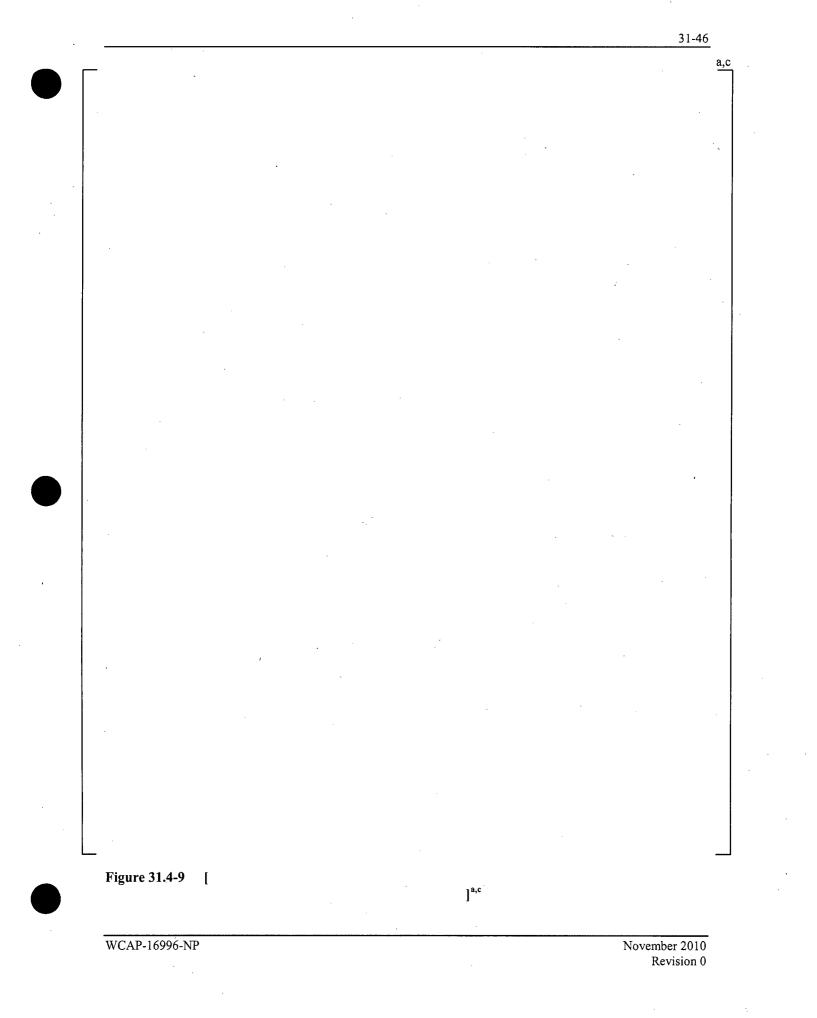




a,c

Figure 31.4-8 [

[^{a,c}



		51-47
, ,	· · ·	а
		-
<b>`</b>		
	ς	
	· · ·	
Ť		
· · ·		
	· · · · · · · · · · · · · · · · · · ·	
		,
		_
Figure 31.4-10 [		
-Bare over to I		] ^{a,c}

WCAP-16996-NP

		 	 		 31-48
					a,c
	· .				
		۰.			
			`		
Figure 31.4-11 [			∫] ^{a,}	c	

- 3	1	-49

a,c

•		·			
			<i>.</i>	•	
		·			
	·				
					•
,					

Figure 31.4-12 [

]^{a,c}

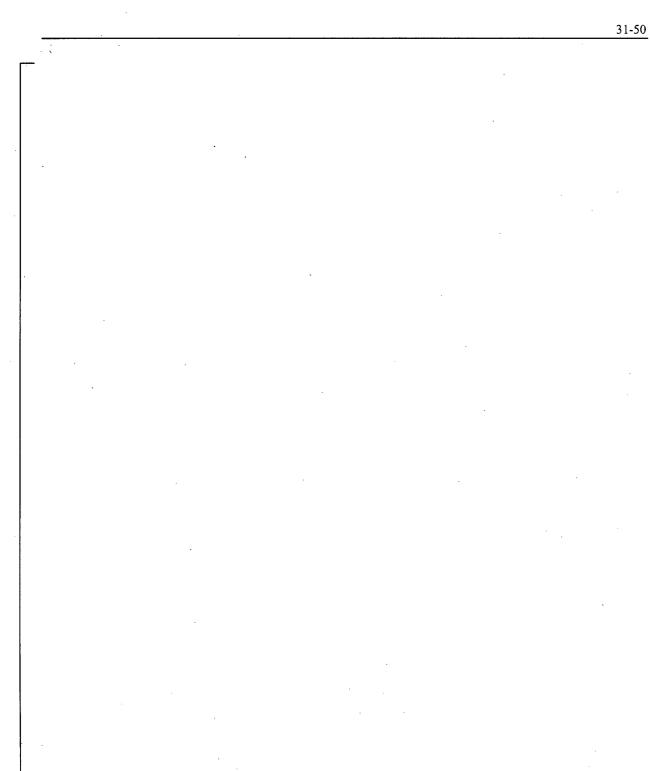


Figure 31.4-13 [

]^{a,c}

WCAP-16996-NP

November 2010 Revision 0 a,c

a,c

# Figure 31.4-14 [

]^{a,c}

WCAP-16996-NP

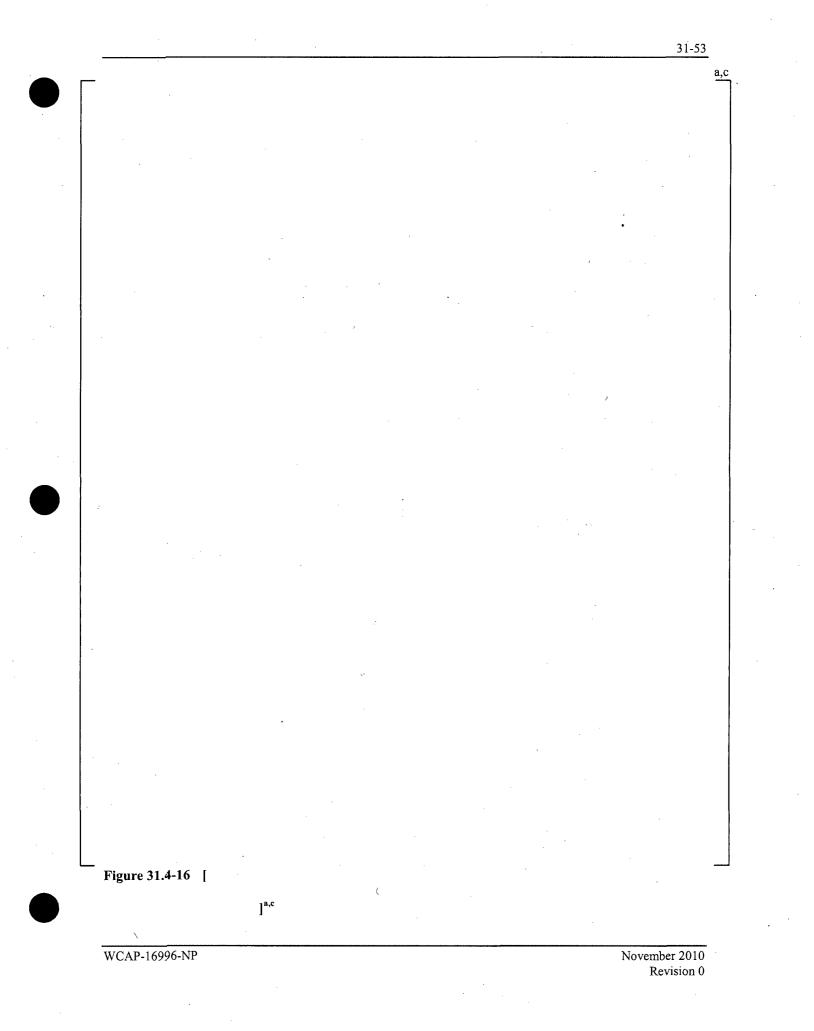
· · · · · ·

Figure 31.4-15 [

]^{a,c}

WCAP-16996-NP

November 2010 Revision 0 a,c



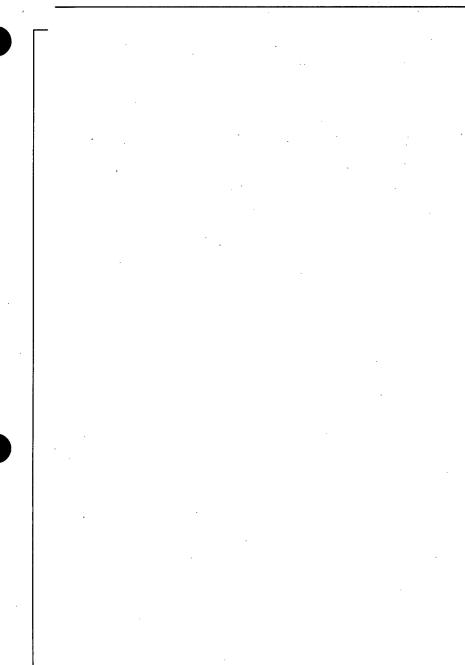


Figure 31.4-17 [

WCAP-16996-NP

November 2010 Revision 0

]^{a,c}

31-54

a,c

# 31.5 SUMMARY REPORT AND COMPLIANCE WITH 10 CFR 50.46 CRITERIA

The objective of the LOCA safety analysis is to provide upper bound values of PCT, MLO and CWO that can be directly compared against (b)(1), (b)(2) and (b)(3) of the 10 CFR 50.46 acceptance criteria. It is written that the "[...] uncertainty must be accounted for, so that, when the calculated ECCS cooling performance is compared to the criteria set forth in paragraph (b) of this section, there is a high level of probability that the criteria would not be exceeded."

]^{a,c}

The method chosen to accomplish such objectives was discussed in Section 30.6. [

WCAP-16996-NP

November 2010 Revision 0

]^{a,c}

[ ]^{a,c}

Table 31.5-1	l		] ^{a,c}	
· .				
	· .			
	.*		· ·	
		· .		
· ·	· · · ·			

`

WCAP-16996-NP

# **32 METHODOLOGY SUMMARY**

In this section, the FULL SPECTRUM LOCA (FSLOCA) evaluation model is assessed against applicable regulatory criteria and guidance.

# 32.1 COMPLIANCE WITH 10 CFR 50.46

- (i) This part briefly outlines the requirements for an acceptable evaluation model, and requires that demonstration be provided that the limits of the Code of Federal Regulations (CFR) 10CFR50.46 be met with a high degree of probability. Additional details concerning these requirements are spelled out in Regulatory Guides (RG) 1.157 (US Nuclear Regulatory Commission (NRC), 1989) and 1.203 (US Nuclear Regulatory Commission, 2005). Compliance of the best-estimate methodology with these requirements is addressed in detail in the next section.
- Peak Cladding Temperature The peak cladding temperature (PCT) is verified to remain below the limit of 2,200°F for loss-of-coolant accidents (LOCAs) of all break sizes, using the methods described in Section 30. A demonstrative application of the method is discussed in Section 31.
- 3. Maximum Cladding Oxidation The maximum cladding oxidation (MLO) is verified to remain below the regulatory limit of 17 percent of cladding thickness, using the procedure described in Section 30. A demonstrative application of the method is discussed in Section 31.
- 4. Maximum Hydrogen Generation The hydrogen generated in the core, as determined by estimating the total volume of cladding oxidized for the limiting conditions, is verified to be less than the regulatory limit of 0.01 times the maximum theoretical amount, using the procedure described in Section 30. A demonstrative application of the method is discussed in Section 31.
- 5. Coolable Geometry Westinghouse reload cores are analyzed using plant-specific or bounding seismic and LOCA loads to confirm that the core remains coolable during the LOCA. This acceptance criteria is met by compliance with acceptance criteria (b)(1), (b)(2), and (b)(3), and showing that grid crush due to combined seismic and LOCA loads does not extend to the in-board assemblies. Specific calculations are performed if grid crushing occurs in the in-board assemblies to assess the effects of the grid crush (Section 25.1).
- 6. Long-Term Cooling Long-term cooling is dependent on the demonstration of continued delivery of cooling water to the core. The actions, automatic or manual, that are currently in place at these plants to maintain long-term cooling remain unchanged.

The FULL SPECTRUM LOCA Evaluation Model (FSLOCA EM) has been developed consistently with Regulatory Guide (RG) 1.203 which represents an evolution and extension to the 1989 RG 1.157. RG 1.203 provides guidance on the Evaluation Model Development and Assessment Process (EMDAP). RG 1.203 extends on the regulatory positions of RG 1.157 which has been the basis of previously approved methodologies (2004 ASTRUM EM, WCAP-16009-P-A and 1996 CQD, WCAP-12945-P-A).

The EMDAP is the process utilized to define the function requirements of the EM and to guide through its assessment such that a decision on the EM adequacy for the purpose of LOCA safety analysis can be made. The EMDAP comprises 4 Elements and a total of 20 Steps which represent the Regulatory Position on the matter.

The mapping of the FSLOCA EM to the EMDAP was already provided in Section 1.2. The purpose of this section is to summarize main conclusions relative to compliance with regulatory guide RG 1.203 and aspect of RG 1.157 that are not already considered in RG 1.203.

# 32.2 COMPLIANCE WITH REGULATORY GUIDE 1.203

## 32.2.1 Regulatory Position 1, "Evaluation Model Development and Assessment Process"

The application envelope of Westinghouse FULL SPECTRUM LOCA (FSLOCA) Evaluation Model (EM) is defined in Sections 1 and 2. The scenario being addressed is a postulated loss of coolant accident that is initiated by an instantaneous rupture of a reactor coolant system (RCS) pipe in a Pressurized Water Reactor (PWR). The break type considered is either a double-ended guillotine, defined as a complete severance of the pipe resulting in unimpeded flow from either end, or a split break, defined as a partial tear. The break size considered for a split includes any break size such that break flow is beyond the capacity of the normal charging pumps up to and including the area of a double ended guillotine rupture with a break flow area two times the pipe area.

As far as the power plant class the PIRT developed in Section 2 is intended to be comprehensive and therefore to cover the same power plant class included in the previous methodology (ASTRUM) which include Westinghouse designed 3- and 4-loop plants with emergency core cooling system (ECCS) injection into the cold legs, Westinghouse designed 2-loop plants with upper plenum injection (UPI) and Combustion Engineering designs.

The FSLOCA EM development followed the EMDAP process of RG. 1.203 and the mapping of the development roadmap and documentation to the elements of the EMDAP was provided in Section 2. The focus here is in addressing the "EM Adequacy Decision" – Regulatory Position 1.5 of RG 1.203.

#### **Adequacy Decision**

The adequacy decision is based on the final assessment of the <u>WCOBRA/TRAC-TF2</u> performances. The standard suggested in the Regulatory Position 1.5 was followed here. The High-ranked PIRT phenomena are reviewed in the following Table. Some of processes have being combined to ease the analysis.

For each item, the EM capability is assessed following these standards

Excellent Agreement – Applies when the code exhibits no deficiencies in modeling a given behavior. Major and minor phenomena and trends are correctly predicted. The calculated results are judged to agree closely with data. Reasonable Agreement – Applies when the code exhibits minor deficiencies. Overall, the code provides an acceptable prediction. All major trends and phenomena are predicted correctly. Differences between calculated values and data are greater than are deemed necessary for excellent agreement.

Minimal Agreement – Applies when the code exhibits significant deficiencies. Overall, the code provides a prediction that is not acceptable. Some major trends or phenomena are not predicted correctly, and some calculated values lie considerably outside the specified or inferred uncertainty bands of the data.

Insufficient Agreement – Applies when the code exhibits major deficiencies. The code provides an unacceptable prediction of the test data because major trends are not predicted correctly. Most calculated values lie outside the specified or inferred uncertainty bands of the data.

For high-ranked phenomena in PIRT, the standard for acceptability with respect to fidelity is generally "<u>reasonable agreement</u>." For phenomena whose assessment are in Minimum agreement and insufficient agreement category would require conservative treatment in the EM. A conservative treatment for phenomena whose assessments are in Reasonable agreement is sometimes selected when the effort of developing an uncertainty range is not justified.

The assessment summary of high PIRT ranked phenomena and models is tabulated below in Table 32-1. The order of phenomena group in the table follows the PIRT given in Table 2-1. In addition to the adequacy rating, sections where assessments are described, and the main assessment findings, the uncertainty treatment for each phenomenon in the EM is shown.

Table 32-1	Summary of Assessment Results and Uncertainty Treatment for High PIRT Ranked Phenomena									
		~								
				· · · · · · · · · · · · · · · · · · ·						
				· · ·						
						· · ·				

November 2010 Revision 0



Table 32- (cont.)	1 Summary of A	ssessment Res	ults and Uncertainty	y Treatment for High PIRT Ranked Phenomena
-				

____



Summary of Assessment Results and Uncertainty Treatment for High PIRT Ranked Phenomena Table 32-1 (cont.) a,c





Table 32 (cont.)	2-1 Summary of As	ssessment Res	ults and Uncertainty	ty Treatment for High PIRT Ranked Phenomena
•				
	· .			

.~

November 2010 Revision 0

_	Table 32 (cont.)	2-1 Summary of A				
			· ·	- iet Alessee		
					· · · · · · · · · · · · · · · · · · ·	

.

Table 32-1       Summary of Assessment Results and Uncertainty Treatment for High PIRT Ranked Phenomena         (cont.)							
х.							
				· · · · · · · · · · · · · · · · · · ·			

WCAP-16996-NP

•

Image: A model

Table 32-1       Summary of Assessment Results and Uncertainty Treatment for High PIRT Ranked Phenomena         (cont.)							
					. •		· ·
							- - -
					· .		
						<u>, .i</u>	
					·		
			· · · ·				

Table 32-1 (cont.)	Summary of Assessment Results and Uncertainty Treatment for High PIRT Ranked Phenomena								
						-	•		
			- 					·	
		:							
								· ·	
								· · ·	
								:	
		· •							
								,	





Table 32-1 (cont.)		Summary of A	·			
			: :	<u>}.</u>		

----

November 2010 Revision 0

32-12

a,c

Table 32-1       Summary of Assessment Results and Uncertainty Treatment for High PIRT Ranked Phenomena (cont.)						
			-			
	· · ·					
	· · · · · ·					

November 2010 Revision 0

tu tu	

 Table 32-1       Summary of Assessment Results and Uncertainty Treatment for High PIRT Ranked Phenomena (cont.)							a,0	
-								
	~				· · · · · · · · · · · · · · · · · · ·	····	·	
							· · · · · · · · · · · · · · · · · · ·	

WCAP-16996-NP

# 32.2.2 Regulatory Position 2, "Quality Assurance"

Westinghouse QA procedures were followed for all aspects of methodology development related to documentation and review. User guidance was developed and cited in FSLOCA related calculation notes, independent verification of all FSLOCA related calculations notes was performed, and all records were archived in accordance with Westinghouse requirements. In addition, an independent and interdisciplinary design review team was convened five separate times over the course of the development of the FSLOCA-EM in order to review major components of the methodology and important decisions made during the methodology development.

## 32.2.3 Regulatory Position 3, "Documentation"

This document is intended to comply with the RG 1.203, Regulatory Position 3 which asks for "Proper documentation to allow appraisal of the EM application to the postulated scenario". The documentation material is organized in three volumes whose content is summarized in Section 1.3. In the following compliance with regulatory positions 3.1 through 3.7 is discussed.

#### Requirements

The FSLOCA EM functional requirements are presented in Volume I, Section 2 and are consistent with Element 1 of the EMDAP.

#### Methodology

The computer code  $\underline{W}COBRA/TRAC-TF2$  represents the engine of the FSLOCA EM and it is the only computational device. The uncertainty analysis methodology is [

]^{a,c}. Volume III documents the FSLOCA EM methodology. Section 25 is a compilation of the plant sources of uncertainty; Section 26 provides a detailed description of the <u>WCOBRA/TRAC-TF2</u> model for selected PWRs. Sections 27 and 28 describes the simulation of selected reference transients for the PWRs for the purpose of justifying specific methodology decisions. The uncertainty contributors are then summarized and discussed in Section 29 while Section 30 outlines the methodology used to combine those uncertainties.

#### **Computational Device Description Manuals**

The purpose of Volume I, particularly Section 3 through 11, is to describe the modeling theory and associated numerical scheme and solution models. Section 3 provides a "Top-Down" review of the computational device (WCOBRA/TRAC-TF2) that starts with the presentation of the governing equations, the discretization and linearization of those equations and the numerical algorithm used to solve the set of equations. The following Sections (from 4 to 11) provide a "Bottom-Up" review of the closure relations, their pedigree, applicability and scalability.

# User Manual and User Guidelines

<u>WCOBRA/TRAC-TF2</u> User's Manual is a separate document from this WCAP. Guidelines on noding and modeling strategy are discussed in Section 26 of this report (Volume III) for the purpose of ensuring consistency between the noding scheme used to model the PWRs and that used for the experiments which are used for validation of physical models in the code. Reinforcing noding consistency to the extent practical between the SETs, IETs and the PWR ensure that same conclusions with respect to biases and uncertainties derived from the code and model assessments are applicable to the PWR LOCA simulations for which the EM was designed. Exceptions to the general noding philosophy are discussed and justified on case by case basis throughout the report.

# **Scaling Reports**

Rather than providing a separate scaling report, scaling considerations are disseminated throughout this report. Scalability of model and correlations are discussed in Volume I as part of the "Bottom-Up" review as outlined here under the compliance to Regulatory Position 3.3. Scaling analyses used to support the viability of the experimental database are summarized within each section of Volume II (assessment report), for each test facility.

#### **Assessment Reports**

Volume II (Sections 12 through 24) can be seen as the "<u>W</u>COBRA/TRAC-TF2 assessment report". Volume II discussed the assessment of the code against Separate Effect Tests (SETs), Integral Effect Tests (IETs) and additional component assessments or thought problems. The content of Volume 2 is organized as discussed in Section 1.3. The intent of the assessment purposes (1)-(15) of Regulatory Position 3.6 has been followed. In particular Section 24 provides a compensating error analysis.

#### **Uncertainty Analysis Reports**

The FSLOCA EM uncertainty methodology is presented in Volume III which is organized as discussed before to comply with Regulatory Position 3.2

# 32.2.4 Regulatory Position 4, "General Purpose Computer Programs"

The <u>W</u>COBRA/TRAC-TF2 code used by Westinghouse for best-estimate LOCA analyses is an improved version of <u>W</u>COBRA/TRAC which is used in the Westinghouse's previously approved best-estimate large break loss-of-coolant accident (LBLOCA) methodology (or Evaluation Model (EM)) as described in WCAP-16009-P-A (Nissley et al., 2005). The 1D Module of the code was replaced with TRAC-PF1/MOD2 versions of the code which is the basis of the current NRC audit tool TRACE. The models in <u>W</u>COBRA/TRAC-TF2 are intended to provide realistic calculations of phenomena of importance to the behavior of a PWR during a LOCA transient. These models have been assessed using comparisons of code predictions several experiments conducted in a number of separate effects test facilities, and three integral test facilities (ROSA, LOFT and CCTF) and full-scale separate effects test (UPTF). The code validation matrix was selected to cover the range of conditions expected during a PWR LOCA transient, to the extent practical. Uncertainty in the experimental data was considered in the overall uncertainty assessment.

# 32.2.5 Regulatory Position 5, "Graded Approach to Applying the EMDAP Process"

FSLOCA EM is an evolution of the currently approved methodology (ASTRUM, WCAP-16009-P-A), however a graded approach to the EMDAP process was deemed not practical and justifiable in this case. The extent of the changes and the novelty of including Small Break LOCA scenarios required the application of the full EMDAP process.

# **32.3 COMPLIANCE WITH REGULATORY POSITION WITH RESPECT TO THE UNCERTAINTY METHODOLOGY**

Regulatory Guide 1.203 focuses primarily on the code development and assessment process (EMDAP). Appendix A.3 of RG 1.203 essentially points back to RG 1.157 and the CSAU as far as preferred method utilized to combine the uncertainties. It is noted that original CSAU suggested the use of response surfaces as a means of combining uncertainties. However, potential disadvantages are discussed. It is recognized that response surface techniques are limited because of "the dependency of the number of computer simulations on the number of phenomena or processes determined in the PIRT that may be needed to estimate the total uncertainty. That is, at least two "single parameter change" runs must be made for each required phenomenon or process. In addition, cross-product runs must be made when several of the phenomen or processes have significant covariance. The cross-product runs may involve change runs of two, three, or four parameters to adequately determine the effect of nonindependent phenomena or processes."

Such limitations were recognized during the development of the ASTRUM EM (WCAP-16009-P-A), and resolved by replacing the response surface step with a direct Monte Carlo sampling of the uncertainty combined with a non-parametric order statistics technique to obtained the 95/95 probability statement to show compliance with 10 CFR 50.46 acceptance criteria. [

]^{a,c}

In the following we will address specific regulatory positions of RG 1.157 specific to the uncertainty methodology.

# 32.3.1 Regulatory Position 4, "Estimation of Overall Calculational Uncertainty"

#### General

The Westinghouse approach to the overall calculational uncertainty has been to separate the uncertainty contributors into two general classifications; the code and models uncertainty contributors and the plant conditions uncertainty contributors. Each uncertainty contributor is varied simultaneously in the calculations performed for the uncertainty analysis.

The code and models uncertainty contributors account for the uncertainty in predicting the important thermal-hydraulic phenomena identified in the PIRT, and important modeling assumptions. Controlling parameters of the important phenomena are ranged via use of multipliers. Each multiplier is characterized by a Cumulative Distribution Function (CDF) which represents the bias and uncertainty for the corresponding model. Development of the CDFs is discussed in Section 29. The CDFs were developed by performing a systematic assessment of the uncertainty associated with the code prediction relative to the

data. [

]^{a,c}

The assessment of the thermal-hydraulic models in <u>W</u>COBRA/TRAC-TF2 used a large number of test comparisons to ensure that estimates of the model uncertainties were well-founded, and included potential scaling effects. Models were grouped in some cases as a package when it was considered more meaningful to validate a specific model package against experiments. For example, the <u>W</u>COBRA/TRAC-TF2 simulations of the FLECHT reflooding experiments in Sections 14 and 15 were used to validate many aspects of the heat transfer package, including specific heat transfer correlations, the prediction of the minimum film boiling temperature, the entrainment model, the heat flux split between evaporation and superheating, and calculated dispersed droplet flow behavior (drop sizes and velocities). The FLECHT and FLECHT-SEASET tests have sufficient independent sources of data that can be used to validate the computer code such that one is confident that the correct answer is being calculated for the correct reasons. A compensating error analysis is also provided in Section 24.

The plant conditions uncertainty contributors calculations account for the different possible operating conditions and accident initial conditions that the plant could experience. The plant specific sources of uncertainty are discussed in Section 25. Similarly to the code model uncertainty contributors, some are explicitly ranged in the uncertainty methodology, others are bounded to ease the analysis when it is not practical to treat these conditions in a statistical fashion.

10 CFR 50.46 states that "[...] uncertainty must be accounted for, so that, when the calculated ECCS cooling performance is compared to the criteria set forth in paragraph (b) of this section, there is a high level of probability that the criteria would not be exceeded." 10 CFR 50.46 does not explicitly specify how this probability should be evaluated or what its value should be. However additional clarification as to the US NRC expectations on the acceptable implementation of the "high probability" requirement is provided in this Regulatory Position 4.1 that states: "a 95% probability is considered acceptable by the NRC staff [...]". Further Regulatory Guide 1.157 introduced the concept of confidence level as a possible refinement to the uncertainty treatment, but did not expand further on this concept.

As statistical methods are implemented to perform LOCA safety analyses, a statistical statement which estimates or bounds the 95th quantile of the population with a 95% confidence level has been suggested by the NRC as acceptable to demonstrate the required "high probability." In the previous approved methodology (ASTRUM, WCAP-16009-P-A) the 95th quantile of the joint-distribution of PCT, MLO and CWO is bounded with at least 95% confidence level. [

]^{a,c}

#### **Code Uncertainty**

The best test of the overall accuracy of the computer code, and the accuracy of individual models, is to compare code predictions to data obtained from a wide range of experiments. Wherever possible, tests performed at full scale or large scale should be used, to eliminate or minimize uncertainties associated

with scalability. <u>WCOBRA/TRAC-TF2</u> was used to simulate several different experiments that capture the same phenomena at different scales. The <u>WCOBRA/TRAC-TF2</u> validation matrix includes tests with different bundle sizes, rod arrays, lengths, power shapes, and grid types, since the computer code will have to model these effects for different plant designs and conditions. Test rod bundles are prototypical of PWR fuel assemblies. Potential distortions induced by the apparatus and test geometry were addressed in the assessment. An assessment was made of the code's ability to predict PCT with varying power scales. For complex phenomena such as the ECC bypass the code was assessed against full scale data (UPTF test facility). In each case, the code predictions were shown to be conservative at full scale, or they reasonably predicted the phenomenon.

One measure of the accuracy of the code uses the comparisons of the predicted and measured PCTs. By selecting experiments with care and by comparing to data other than the measured cladding temperatures, it can be assured that the PCT is reasonably predicted for the correct reasons. The possibility of compensating errors being present was investigated. It was concluded that while compensating errors do exist, the net effect is a conservative prediction of a PWR LOCA transient.

While the available integral effects tests are useful for addressing the issues of scalability and compensating errors, there are insufficient data to address the potential for propagation of uncertainties as a LOCA transient progresses. A detailed study of uncertainty propagation requires that the effects be quantified using computer code calculations of a PWR LOCA transient. [

]^{a,c}

#### Other Sources of Uncertainty

#### Initial and Boundary Conditions and Equipment Availability

The treatment of important initial and boundary conditions, and assumptions of the availability of important equipment, are summarized below.

Initial Condition	Considered in Uncertainty Evaluation?
Core power level	Yes
Core power distribution	Yes
RCS fluid conditions	Yes
Accumulator conditions	Yes
Time in cycle	Yes
Hot assembly location	No (bounded)
Steam generator plugging	No (bounded)
Boundary Condition	
Break flow	Yes
SI temperature	Yes
SI flow and delay	No (bounded)
Containment pressure	No (bounded)
Containment pressure	No (bounded)

WCAP-16996-NP

Equipment Availability Offsite power Single failure Control rod insertion

No (bounded if statistically significant) No (bounded) No for Region II (bounded)

#### ]^{a,c}

#### Fuel Behavior

[

Uncertainties in the lead fuel rod initial conditions and its behavior during the LOCA transient are explicitly accounted for. These uncertainties include hot rod peaking, initial fuel temperature, cladding burst temperature, burst strain, fuel density after burst due to relocation, and metal-water reaction rates. The treatment of fuel behavior in the Westinghouse methodology is considered to be more complete than that used in the CSAU methodology, in that [

# ]^{a,c}.

#### Other Variables

Uncertainties in decay heat and break flowrate are included in the overall uncertainty assessment. The metal-water reaction rate uncertainty is also considered as one of the fuel rod uncertainty parameters, as noted in the Regulatory Position 4.3.2 Compliance Discussion.

#### **Statistical Treatment of Overall Calculational Uncertainty**

The overall calculational uncertainty statement is determined using a non-parametric statistical method. Uncertainties in [

7^{a,ç}

The FULL SPECTRUM LOCA methodology used by Westinghouse addresses the PCT, maximum cladding oxidation, maximum hydrogen generation, and coolable geometry criteria defined in 10 CFR 50.46(b)(1) through (b)(4).

Coolable geometry is demonstrated by ensuring that the [ ]^{a,c} criteria are satisfied, including any effects of combined LOCA and SSE loads on core geometry.

]^{a,c}

The Westinghouse methodology used to satisfy the long-term cooling criterion defined in 10 CFR 50.46(b)(5) is unaffected by the use of best-estimate techniques for the short-term transient calculation.

# **32.4 REFERENCES**

- 1. Bajorek, S. M., et al., 1998, "Code Qualification Document for Best Estimate LOCA Analysis," WCAP-12945-P-A, Appendix C (Proprietary).
- 2. Nissley, M. E., et al., 2005, "Realistic Large Break LOCA Evaluation Methodology Using Automated Statistical Treatment of Uncertainty Method (ASTRUM)," WCAP-16009-P-A, Revision 0, and WCAP-16009-NP-A, Revision 0 (Non-Proprietary).
- 3. NRC, 1989, "Best-Estimate Calculations of Emergency Core Cooling System Performance," Regulatory Guide 1.157.
- 4. NRC, 2005, "Transient and Accident Analysis Methods," Regulatory Guide 1.203.

WCAP-16996-NP